AD_____

Award Number: DAMD17-02-1-0461

TITLE: A High Resolution Clinical PET with Breast and Whole Body Transfigurations

PRINCIPAL INVESTIGATOR: Wai-Hoi Wong, Ph.D.

CONTRACTING ORGANIZATION: The University of Texas
M.D. Anderson Cancer Center
Houston, TX 77030

REPORT DATE: April 2005

TYPE OF REPORT: Annual

PREPARED FOR: U.S. Army Medical Research and Materiel Command
Fort Detrick, Maryland 21702-5012

DISTRIBUTION STATEMENT: Approved for Public Release;
Distribution Unlimited

REPORT DOCUMENTATION PAGE

Form Approved
OMB No. 074-0188

1. AGENCY USE ONLY	2. REPORT DATE	3. REPORT TYPE AND DATES COVERED
	April 2005	Annual(1 Apr 2004 - 31 Mar 2005)

4. TITLE AND SUBTITLE
A High Resolution Clinical PET with Breast and Whole Body Transfigurations

5. FUNDING NUMBERS
DAMD17-02-1-0461

6. AUTHOR(S)
Wai-Hoi Wong, Ph.D.

7. PERFORMING ORGANIZATION NAME(S) AND ADDRESS(ES)
The University of Texas
M.D. Anderson Cancer Center
Houston, TX 77030

E-Mail: gwong@di.mdacc.tmc.edu

8. PERFORMING ORGANIZATION REPORT NUMBER

9. SPONSORING / MONITORING AGENCY NAME(S) AND ADDRESS(ES)
U.S. Army Medical Research and Materiel Command
Fort Detrick, Maryland 21702-5012

10. SPONSORING / MONITORING AGENCY REPORT NUMBER

11. SUPPLEMENTARY NOTES
Original contains color plates: ALL DTIC reproductions will be in black and white

12a. DISTRIBUTION / AVAILABILITY STATEMENT
Approved for Public Release; Distribution Unlimited

12b. DISTRIBUTION CODE

13. ABSTRACT (Maximum 200 Words)

Despite advances in the last decade, the radiographic diagnosis of breast cancer remains uncertain. Of the annual 600,000 cases referred for biopsy by mammograms each year, 400,000 are unnecessary, costing $2 billion annually. The diagnosis of breast cancer in young women and women with silicone implants continues to be difficult. Accurate detection of small breast tumors (2-3 mm) is still to be achieved. Positron emission tomography(PET)has the potential to reduce this high healthcare cost, unnecessary painful anxiety, and to improve diagnosis and survivability for women of all ages. We have developed the detector and electronic technology for building an ultrahigh resolution PET camera. We propose to use such technology to construct an ultrahigh resolution PET that has a dedicated breast-diagnosis mode that has 13-26 times higher detection sensitivity than regular PET and an ultrahigh image resolution of 2.5mm compared to the 4.5-6 mm in today's PET cameras. We have already developed a scaled-down engineering prototype PET to confirm the feasibility that 2-3 mm tumor can be detected accurately. We propose to construct a scaled-up clinical version of the design so that it can be used for clinical human trials to confirm the clinical utility.

14. SUBJECT TERMS
Breast Cancer

15. NUMBER OF PAGES
166

16. PRICE CODE

17. SECURITY CLASSIFICATION OF REPORT	18. SECURITY CLASSIFICATION OF THIS PAGE	19. SECURITY CLASSIFICATION OF ABSTRACT	20. LIMITATION OF ABSTRACT
Unclassified	Unclassified	Unclassified	Unlimited

Table of Contents

INTRODUCTION

Despite advances in the last decade, the radiographic diagnosis of breast cancer remains uncertain. Also, the diagnosis of breast cancer in dense breasts continues to be difficult, whether the density is a result of fibrocystic diseases or young age. Accurate detection of very small breast tumors (2-3 mm) and small metastases, which is essential for survival and breast conservation, is still to be achieved. Positron emission tomography (PET) has the potential to improve in these areas as PET images physiologic differences between tumor and normal tissue, providing > 90% sensitivity and >95% specificity in many recent studies. It also eliminates imaging difficulties for women who have silicone implants and dense breasts, which have negligible effect in PET; hence, PET is useful for high-risk young women, and patients with implants, both from reconstructive surgery after mastectomy or cosmetic reasons.

However, for breast cancer diagnosis, there are technical limitations in current PET cameras that are designed for whole-body tumor staging instead of breast imaging. This goal of this project is to help the development of an ultrahigh resolution convertible-PET design that minimizes the limitations:
(1) A convertible gantry with a dedicated breast mode that has 10-15 times higher detection sensitivity for breast-tumor activities than a whole-body PET
(2) An intrinsic image resolution of 2.5-3.0 mm.

BODY

The statement of work or task planned for this period was as follows:

TASK 1. Developing a PET camera gantry that can be transformed between the whole-body mode and the breast mode (Months 1-30): Design and Construct the computer-controlled servo motor movement system for rotating the gantry with high precision (Month 24-30).

TASK 2. Developing the high-speed electronic system, 169 circuit boards (Month 1-30):
Design and build the digital multiplexer circuits, 12 boards (month 25-28)
Design and build and test the programmable coincidence-detection board (Month 20-30)
Design and build the data acquisition parallel-computer system.

TASK 3. Integrating all the subsystem to form the proposed PET and debug the whole system as an integral unit (Month 24-32).

TASK 4. Developing the software and image-process techniques (Month 1-30): Continuously developing the image reconstruction and image processing technique (Month 12-24).

TASK 5. Testing the imaging performance (Month 31-36)

For TASK 1-5, the accomplishments are as follows

About 2/3 of the task planned above has been accomplished. However, there has been a

significant modification in the mechanical design that we have developed in the last reporting period. During this reporting period, in a more detailed mechanical analysis, it became apparent that in the original mechanical design completed last year, the module-supporting structure (that facilitated the transformation) may sag excessively due to the weight of each detector module (25 Kg) and the long cantilever support design (fig.1). We reported the original design in the last reporting period (2). The sagging of the detector modules would increase the positioning error of the small 2.6mm detectors, thereby compromising the ultrahigh imaging resolution potentially allowed by the small crystals. In view of this design deficiency, we stopped the production of the gantry that was originally planned for this second period, and instead we used this period to redesign the gantry transformation structure. This redesign is near completion with the final design shown in fig.2. Thus the mechanical development has become the bottleneck of the whole project and has delayed the overall progress of the project by about 7-8 months.

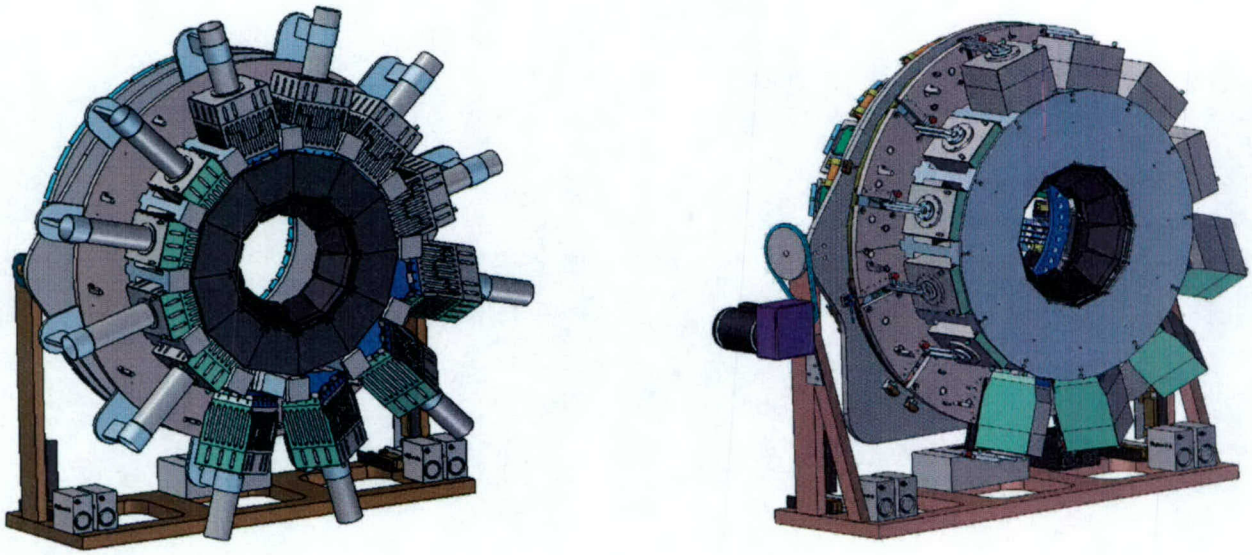

FIG. 1 *In the original design (left), the 12 detector heads or modules were supported by 12 long pipes, which would slide in-and-out to different patient openings rotating the detector modules. The pipe supporting structure (cantilever) would cause too much deflection from the heavy weight of the detector heads. In the redesign version (right), the cantilever pipes were replaced by a bearing structure that rides on tracks-and-rails, which eliminated the long cantilever thereby eliminating the mechanical deflections, which caused the mis-positioning of the 2-mm detectors inside the detector heads.*

Other than the detector module support rigidity, there is another user-friendly issue. In the original design, the simple pivoting trunnion for turning the whole PET horizontal is not friendly for the breast-imaging patients because the camera situates too high above ground, 1.57 meter or 5.2 ft, (fig.2) and a patient has to climb over a ladder or be hoisted to lie on top of the camera to be imaged. This was due to the large size of the camera and the typical pivoting trunnion design (2). Although the original design would do the job of turning the PET horizontal for breast imaging, we have not been happy with the design. We have been struggling with other design options trying to find a camera turning mechanism that would lower the camera as the camera is being turned, and also a mechanism that is simple to make and strong (and stable) enough to carry the 2 ton camera. After devising and studying many

design solutions, we have finally arrived at a mechanism satisfying all the above conditions (fig.3, right side). This new turning mechanism lowers the camera to 0.82 meter (2 ft 8 in) much less than the 5.2 ft in the original design. With a 2 ft 8 inch height, even a short woman can simply bend over to lie on top of the camera for breast imaging.

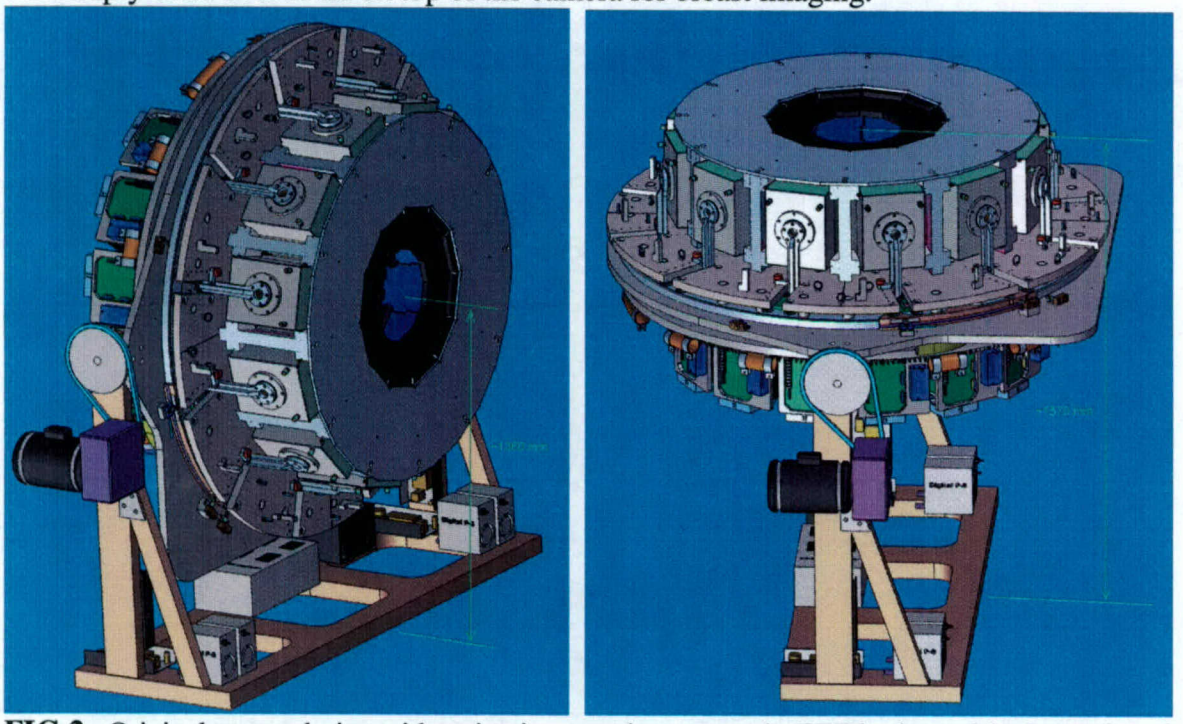

FIG.2 Original gantry design with a pivoting trunnion to turn the PET horizontal for breast imaging.

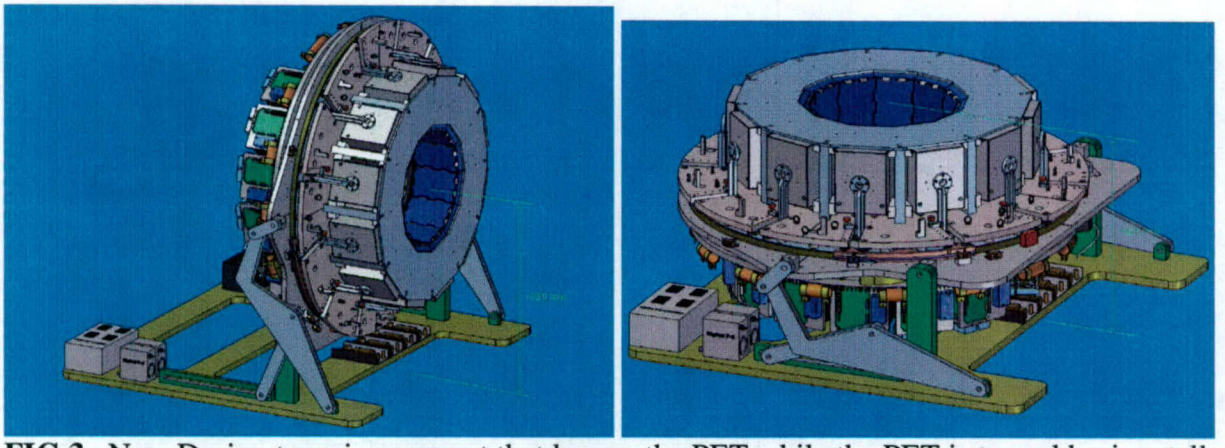

FIG.3 New Design trunnion support that lowers the PET while the PET is turned horizontally

These two mechanical redesigns have caused much delay and created manpower and resource problems for the project because other technical staffs (those involved in the development of detectors, electronics, firmware, software and the robotic motion-control system) would be idling because of their waiting on the sideline unable to install their subcomponents into the mechanical assembly for further testing and debugging. This idling and waiting would be wasteful in terms of grant funding and resource usage. We managed this problem by (a) redirecting most of the manpower into other ongoing research projects; (b) using the remaining manpower to construct a small table-top PET with a solid detector ring (fixed geometry) as a "test bench" to test and debug the complex electronic hardware and software

earmarked for the transformable PET rather than experiencing a total stop in work by the delay in the mechanical redesign development (fig.4). However, these steps to conserve funding and productivity to deal with the delay in mechanical development also led to budget carryover for this funding period. Hence, we have already requested and granted a 1-year no-cost extension for the project.

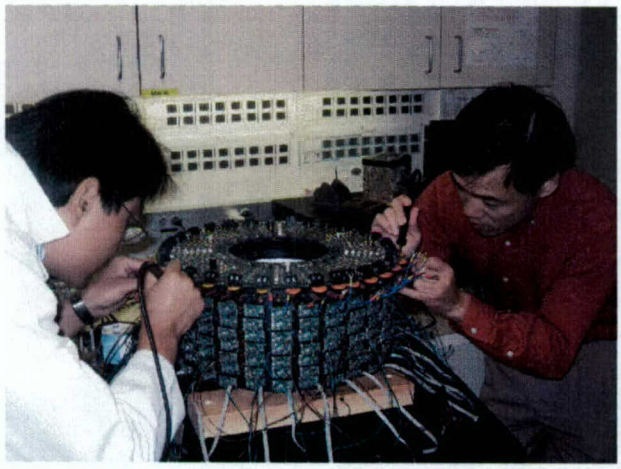

FIG. 4 *Small bench-top PET for testing electronics, Software and image processing technique*

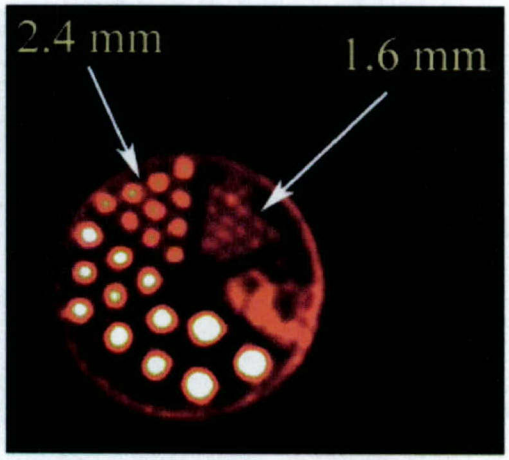

FIG. 5 *PET image of Micro-Delux Phantom*

With the small table-top PET detection ring as a substitute, we were able to integrate all the subcomponents of the PET cameras together for a total debugging of the front-end electronics (4, 8, 12), coincidence circuit (5), data-acquisition electronics and software (10), the communication interfaces between subsystems, system-tuning algorithm and control (15), and image processing algorithm and software (3, 6, 13, 14, 16) (TASK-2, TASK-3 and TASK-4). Hence, these other TASKS would not be delayed by the mechanical redesign. This small PET development has been a very useful exercise as it revealed some weaknesses and mismatches between components. Engineering changes have been made to hardware, software and optimization methodologies; these changes are being implemented to the electronics of the transformable PET.

The small test-bench PET camera has produced very high-resolution images, which means that all the complex PET electronics, software and image-process algorithm were functioning correctly and splendidly. We achieve 1.7-2.1 mm image resolution on this test-bench small PET, as demonstrated by the resolution phantom image (fig.5), testifying to the capability of the detector technology, the complex electronics and software developed.

To summarize the accomplishment of the project so far in the last three years:

The architecture of the system has been developed; unlike conventional PET with a fixed ring of detectors, this transformable PET divided into 12 **rectangular** detector modules. For wholebody imaging, a detector module is mated to the neighboring module on the shorter side of the rectangular module (fig.6, left side). For breast imaging, all the modules are rotated

along its axis so that the modules are mated together long the long side to shrink the detector ring diameter (fig.6, right side).

The detail design of the detector module is shown in fig.7. 12 such test-modules have been partially completed in the mechanical construction (fig.8, fig.9). We have also finished the construction of all 40,000 position-sensitive scintillation detectors (fig.10) (9, 11, 17).

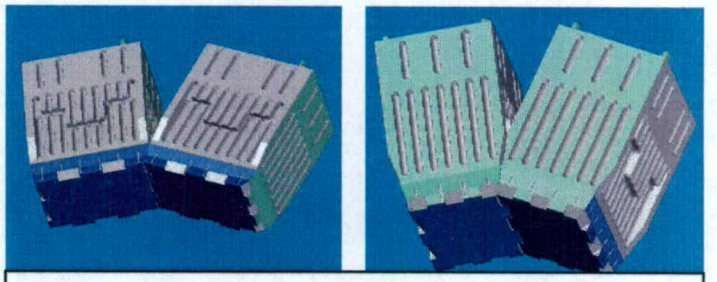

FIG. 6 Two of the 12 detector modules forming the detector ring: Left – large ring or wholebody imaging formation (83.5 cm diameter). Right – small ring or breast imaging formation (50 cm)

photomultipliers, front-end fast amplifier and control electonics incorporated (fig.6). The 2 test modules were mated together accurately mechanically with no gaps between the two detector modules to facilitate the body-breast conversion (fig.7).

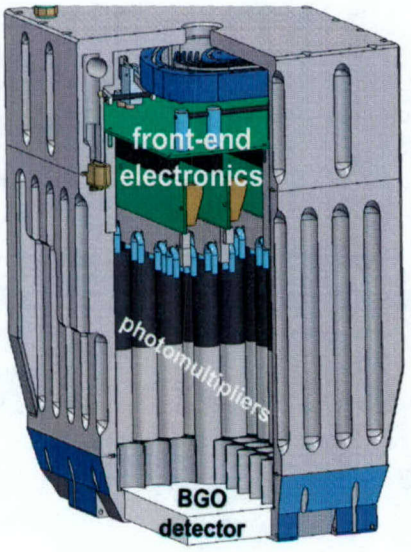

FIG. 7 Internal design of module

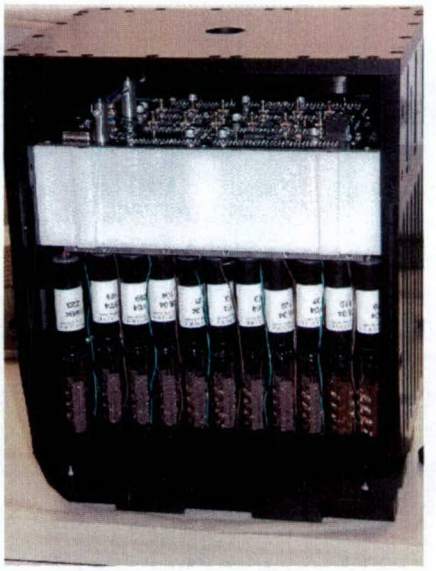

FIG. 8 Module construction

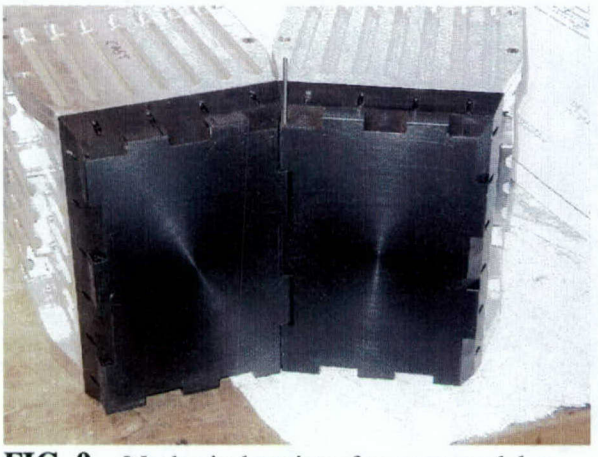

FIG. 9 Mechanical mating of two test-modules

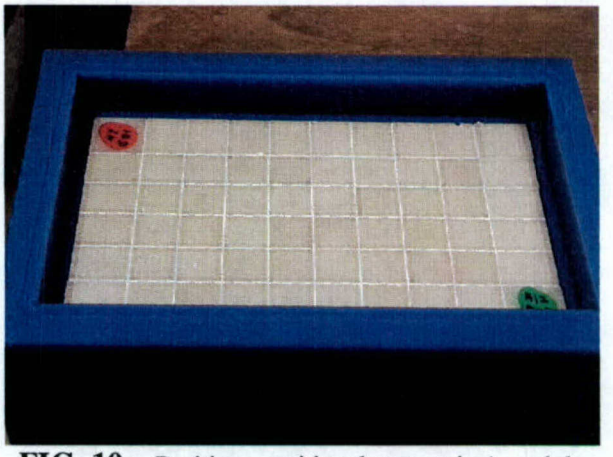

FIG. 10 Position-sensitive detectors in 1 module

The detector-position decoding of the constructed detectors were tested for all 40,000 position-sensitive crystals using the prototype electronics we designed and constructed for this PET camera. The crystal-position decoding test results have been excellent (fig.11).

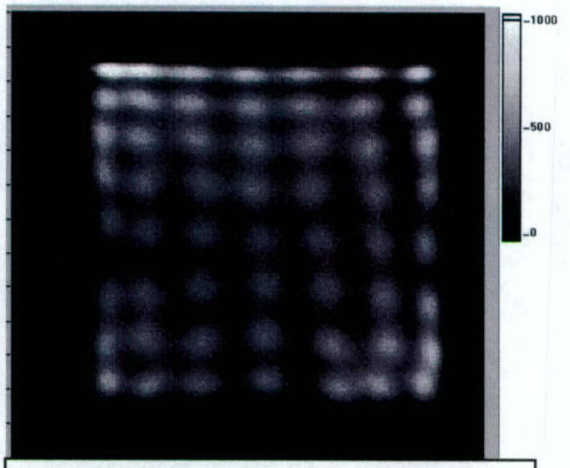

FIG. 11 detector-position decoding

Electronic Design and Construction

The patented high-speed pileup-recovery front-end electronics and decoding-electronics (HYPER) have been designed and all 12 sets of HYPER have been constructed (fig.12). This front-end electronics were tested and they performed well and were used to obtain the results shown in fig.5 and fig.11 (8, 12). The coincidence-timing and data sorting electronics has also been developed and built (5) for this transformable PET (fig.13). We have done partial testing on it.

We also developed a high-speed system-wide detector-tuning system for this PET camera and this BGO-detector-tuning system should take 1-2 minutes to retune all 40,000 detectors (15) instead of the 4-6 hours in current commercial systems, thereby allowing the whole PET to be re-calibrated for every patient to insure optimal imaging quality for every patient, instead of 1-3 months in current practice. This tuning system (using internal LED light) has been developed and tested and recently submitted for journal publication. Test results showed that all 40,000 detectors in the camera can be recalibrated in 1 minute. The detector-position-decoding test "before and after tuning" was excellent (fig. 14).

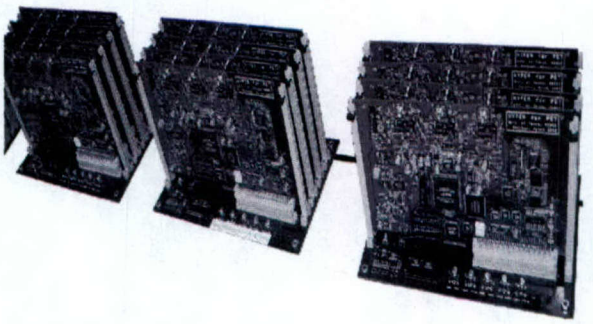

FIG. 12 3 of the 12 sets of HYPER electronics

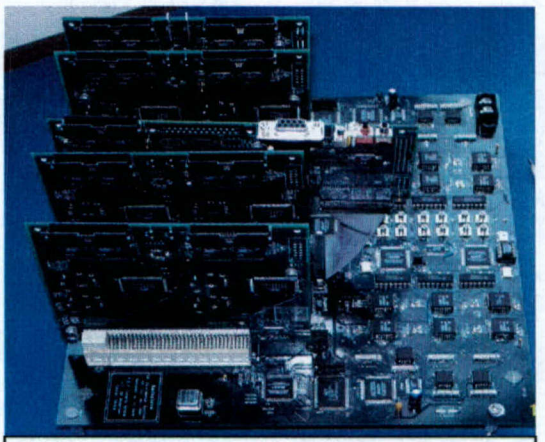

FIG. 13 Coincidence electronics

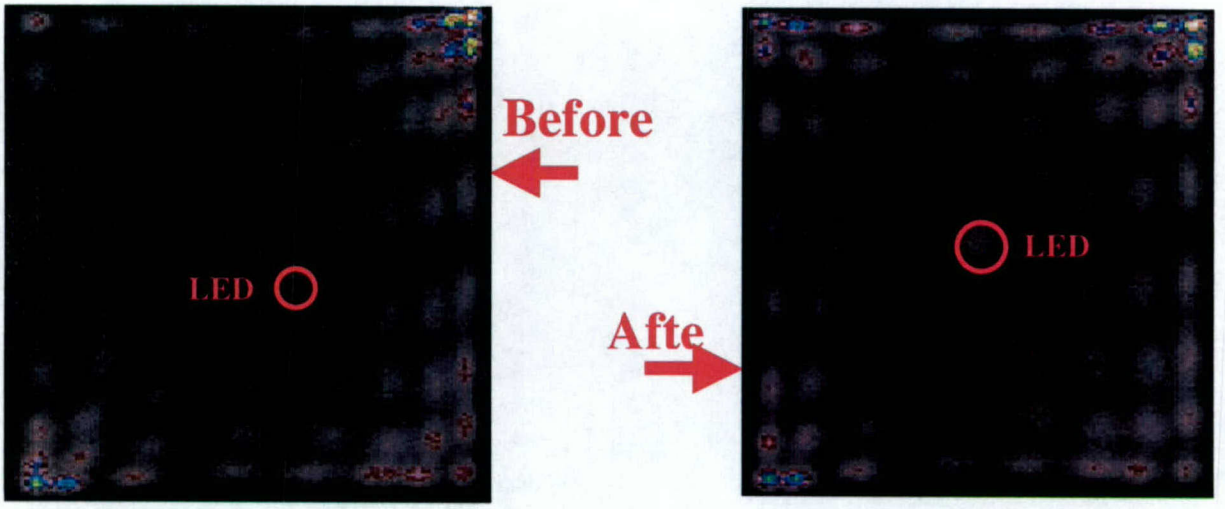

Before tuning

After tuning

FIG. 14 Before tuning, crystal positions were moved to the right and caused position-decoding errors. After tuning, the crystals positions were restored to the original positions

Because of the ultrahigh image resolution of the system, we are developing a breathing-cycle gating system to correct for the patient breathing moving. This system used a sensor in the patient's nostril air-flow and gating electronics to correct for the patient breathing movement (fig.15). A paper has been published (1). Test results of the system, using our existing prototype PET, showed that this gating-system increased lesion uptake in the image by an average of 2.2 time for 3-5 mm lesions.

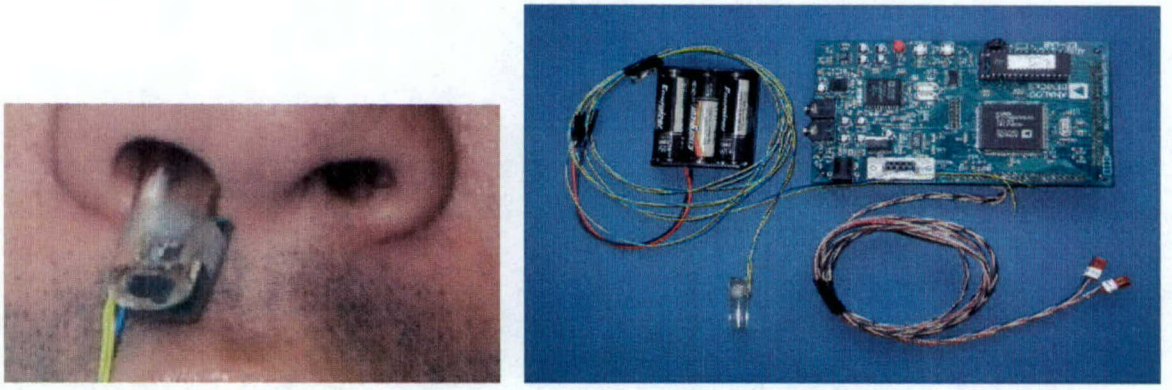

FIG. 15 LEFT---Nostril-air breathing cycle gating system improved lesion uptake in image

We have developed the image reconstruction and image processing software and methodology (3, 6, 13, 14) to study lesion detection in ultrahigh resolution PET cameras. We used this software to evaluate ways to achieve better lesion detection and published one peer-reviewed paper. Four different image-reconstruction software and different image processing filters were implemented, tested and compared.

KEY RESEARCH ACCOMPLISHMENTS

- The very complex transformable-PET mechanical design has been accomplished and all of the 12 detector heads (module) have been fabricated and are being put together.
- All the 40,000 position-sensitive detectors have been constructed and tested. The results have been good.
- The very complex front-end electronics (HYPER) has been developed and fabricated. The programmable coincidence-detection electronics has also been developed and fabricated. These electronics have been tested with the 2 prototype detector head and on the bench-top small PET.
- A new detector tuning system has been developed. This system can tune all the detectors in the system in less than 1 minute, which is significant improvement to existing commercial systems that take many hours to tune a PET with far fewer detectors. This system has also been tested on the small bench-top PET.
- A breathing-cycle movement-compensation method has also been developed to improve lesion detections in our system.
- All the basic data-acquisition software, image-reconstruction software and image-display software has been developed and tested on the bench-top PET
- The transformable mechanical gantry has been redesigned for better detector-positioning accuracy. The camera can now be lowered while being turned horizontally for breast imaging, so that patients do not have to climb onto the camera for breast imaging

---

REPORTABLE OUTCOMES

In this three years, our research effort have resulted in the publication of 11 peer-reviewed scientific papers, and 16 conference record papers:

A. Articles in Peer-Reviewed Journals

1. Wang, Y.; Baghaei, H.; Li, H.; Liu, Y.; Xing, T.; Uribe, J.; Ramirez, R.; Xie, S.; Kim, S.; Wong, W.-H. A Simple Respiration Gating Technique and Its Application in High-Resolution PET Camera. IEEE Transactions on Nuclear Science, Volume 52, Issue 1, Feb. 2005 Page(s):125-129.

2. Uribe, J.; Xie, S.; Li, H.; Baghaei, H.; Wang, Y.; Liu, Y.; Xing, T.; Ramirez, R.; Bushman, M.; Kim, S.; Wong, W.-H. Gantry Design With Accurate Crystal Positioning for a High-Resolution Transformable PET Camera. IEEE Transactions on Nuclear Science, Volume 52, Issue 1, Feb. 2005 Page(s):119-124.

3. Baghaei, H.; Wai-Hoi Wong; Uribe, J.; Hongdi Li; Yu Wang; Yaqiang Liu; Tao Xing; Ramirez, R.; Shuping Xie; Soonseok Kim.

A comparison of four-image reconstruction algorithms for 3-D PET imaging of MDAPET camera using phantom data. IEEE Transactions on Nuclear Science, Volume 51, Issue 5, Oct. 2004 Page(s):2563-2569.

4. Yaqiang Liu; Hongdi Li; Yu Wang; Tao Xing; Shuping Xie; Uribe, J.; Baghaei, H.; Ramirez, R.; Soonseok Kim; Wai-Hoi Wong.
A gain-programmable transit-time-stable and temperature-stable PMT Voltage divider. IEEE Transactions on Nuclear Science, Volume 51, Issue 5, Oct. 2004 Page(s):2558-2562.

5. Yu Wang; Hongdi Li; Yaqiang Liu; Tao Xing; Uribe, J.; Baghaei, H.; Farrell, R.; Wai-Hoi Wong. A modular low dead-time coincidence system for high-resolution PET cameras. IEEE Transactions on Nuclear Science, Volume 50, Issue 5, Oct. 2003 Page(s):1386-1391.

6. Baghaei, H.; Wai-Hoi Wong; Uribe, J.; Hongdi Li; Aykac, M.; Yu Wang; Yaqiang Liu; Tao Xing; Farrell, R. Brain lesion detectability studies with a high resolution PET operating in no-septa and partial-septa configurations. IEEE Transactions on Nuclear Science, Volume 50, Issue 5, Oct. 2003 Page(s):1364-1369.

7. Aykac, M.; Hongdi Li; Uribe, J.; Yu Wang; Baghaei, H.; Yaqiang Liu; Tao Xing; Wai-Hoi Wong. A study of coincidence line spread function (CLSF) estimation for small scintillators using quadrant sharing technique. IEEE Transactions on Nuclear Science, Volume 50, Issue 5, Oct. 2003 Page(s):1331-1338.

8. Yaqiang Liu; Hongdi Li; Yu Wang; Tao Xing; Baghaei, H.; Uribe, J.; Farrell, R.; Wai-Hoi Wong. A programmable high-resolution ultra-fast delay generator. IEEE Transactions on Nuclear Science, Volume 50, Issue 5, Oct. 2003 Page(s):1487-1490.

9. Uribe, J.; Wai-Hoi Wong; Baghaei, H.; Farrell, R.; Hongdi Li; Aykac, M.; Bilgen, D.; Yaqiang Liu; Yu Wang; Tao Xing. An efficient detector production method for position-sensitive scintillation detector arrays with 98% detector packing fraction
IEEE Transactions on Nuclear Science, Volume 50, Issue 5, Oct. 2003 Page(s):1469-1476.

10. Hongdi Li; Tao Xing; Yaqiang Liu; Yu Wang; Baghaei, H.; Uribe, J.; Ramirez, R.; Wai-Hoi Wong. A HOTLink/networked PC data acquisition and image reconstruction system for a high-resolution whole-body PET with respiratory or ECG-gated performance. IEEE Transactions on Nuclear Science, Volume 50, Issue 3, June 2003 Page(s):393-397.

11. Uribe, J.; Hongdi Li; Tao Xing; Yaqiang Liu; Baghaei, H.; Yu Wang; Aykac, M.; Ramirez, R.; Wai-Hoi Wong. Signal characteristics of individual crystals in high resolution BGO detector designs using PMT-quadrant sharing. IEEE Transactions on Nuclear Science, Volume 50, Issue 3, June 2003 Page(s):355-361.

B. Conference Record

1. Baghaei, H.; Wai-Hoi Wong; Uribe, J.; Hongdi Li; Aykac, M.; Yu Wang; Yaqiang Liu; Tao Xing; Farrell, R. Brain lesion detectability studies with a high resolution PET operating in no-septa and partial-septa configurations. Nuclear Science Symposium Conference Record, 2002 IEEE Volume 3, 10-16 Nov. 2002 Page(s):1736-1740 vol.3.

2. Hongdi Li; Wai-Hoi Wong; Yu Wang; Yaqiang Liu; Tao Xing; Uribe, J.; Baghaei, H.; Farrell, R. Front-end electronics based on high-yield-pileup-event-recovery method for a high resolution PET

camera with PMT-quadrant-sharing detector modules. Nuclear Science Symposium Conference Record, 2002 IEEE Volume 2, 10-16 Nov. 2002 Page(s):699-703 vol.2.

3. Yu Wang; Hongdi Li; Yaqiang Liu; Tao Xing; Uribe, J.; Baghaei, F.; Farrell, R.; Wai-Hoi Wong. A modular low dead-time coincidence system for high resolution PET cameras. Nuclear Science Symposium Conference Record, 2002 IEEE Volume 2, 10-16 Nov. 2002 Page(s):960-964 vol.2.

4. Uribe, J.; Hongdi Li; Yaqiang Liu; Tao Xing; Baghaei, H.; Yu Wang; Farrell, R.; Wai-Hoi Wong. Signal characteristics of individual crystals in a high resolution BGO detector design using PMT-quadrant sharing. Nuclear Science Symposium Conference Record, 2002 IEEE Volume 2, 10-16 Nov. 2002 Page(s):926-930 vol.2.

5. Yaqiang Liu; Hongdi Li; Yu Wang; Tao Xing; Baghaei, H.; Uribe, J.; Farrell, R.; Wai-Hoi Wong. A programmable high-resolution ultra fast delay generator. Nuclear Science Symposium Conference Record, 2002 IEEE Volume 2, 10-16 Nov. 2002 Page(s):1153-1157 vol.2.

6. Baghaei, H.; Uribe, J.; Hongdi Li; Yu Wang; Yaqiang Liu; Tao Xing; Farrell, R.; Wai-Hoi Wong. Effects of attenuation correction and 3D-reconstruction algorithms on brain lesions detectability. Nuclear Science Symposium Conference Record, 2002 IEEE Volume 3, 10-16 Nov. 2002 Page(s):1529-1533 vol.3.

7. Uribe, J.; Wai-Hoi Wong; Baghaei, H.; Farrel, R.; Li, H.; Liu, Y.; Wang, Y.; Xing, T. An efficient detector production method for position-sensitive scintillation detector arrays with 98% detector packing fraction. Nuclear Science Symposium Conference Record, 2002 IEEE Volume 2, 10-16 Nov. 2002 Page(s):1144 - 1148 vol.2.

8. Hongdi Li; Tao Xing; Yaqiang Liu; Yu Wang; Baghaei, F.; Uribe, J.; Farrell, R.; Wai-Hoi Wong. A HOTLink/networked PC data acquisition and image reconstruction system for a high resolution whole-body PET with respiratory or ECG-gated performance. Nuclear Science Symposium Conference Record, 2002 IEEE Volume 2, 10-16 Nov. 2002 Page(s):1135-1139 vol.2.

9. Baghaei, H.; Wong, W.-H.; Uribe, J.; Li, H.; Wang, Y.; Liu, Y.; Xing, T.; Ramirez, R.; Xie, S.; Kim, S. A comparison of four image reconstruction algorithms for detection of small lesions in brain phantom. Nuclear Science Symposium Conference Record, 2003 IEEE Volume 4, 19-25 Oct. 2003 Page(s):2584-2588 Vol.4.

10. Li, H.; Liu, Y.; Xing, T.; Wang, Y.; Uribe, J.; Baghaei, H.; Xie, S.; Kim, S.; Ramirez, R.; Wong, W.-H. An instantaneous photomultiplier gain calibration method for PET or gamma camera detectors using an LED network. Nuclear Science Symposium Conference Record, 2003 IEEE Volume 4, 19-25 Oct. 2003 Page(s):2447-2451 Vol.4.

11. Yaqiang Liu; Hongdi Li; Yu Wang; Tao Xing; Shuping Xie; Uribe, J.; Baghaei, H.; Ramirez, R.; Soonseok Kim; Wai-Hoi Wong. A gain-programmable transit-time-stable and temperature-stable PMT voltage divider. Nuclear Science Symposium Conference Record, 2003 IEEE Volume 5, 19-25 Oct. 2003 Page(s):3101-3104 Vol.5.

12. Uribe, J.; Xic, S.; Li, H.; Baghaei, H.; Wang, Y.; Liu, Y.; Xing, T.; Ramirez, R.; Bushman, M.; Kim, S.; Wong, W.-H. Gantry design with accurate crystal positioning for a high-resolution transformable PET camera. Nuclear Science Symposium Conference Record, 2003 IEEE Volume 3, 19-25 Oct. 2003 Page(s):2215-2219 Vol.3.

13. Yu Wang; H. Baghaei; Hongdi Li; Yaqiang Liu; Tao Xing; Uribe, J.; Ramirez, R.; Shuping Xie; Soonseok Kim; Wai-Hoi Wong. A simple respiration gating technique and its application in high-resolution PET camera. Nuclear Science Symposium Conference Record, 2003 IEEE Volume 3, 19-25 Oct. 2003 Page(s):2188-2191 Vol.3.

14. H. Baghaei; W.-H. Won; J. Uribe; H. Li; Y. Wang; T. Xing; R. Ramirez, S. Xie, S., S. Kim, and Y. Zhang. An Evaluation of the Effect of Partial-Septa on Detection of Small Lesions in Brain Phantom Study Using MDAPET Camera. IEEE Nuclear Science Symposium and Medical Imaging conference record, Rome, Italy, October 16-22, 2004.

15. R. Ramirez; W.H. Wong; J. Uribe; H. Li; T. Xing; Y. Wang; Y. Liu; H. Baghaei; S. Xie; S. Kim; and Y. Zhang; Characteristics of 40,000 Quadrant-Sharing BGO Detectors Made by the Slab-Sandwich-Slice Technique. IEEE Nuclear Science Symposium and Medical Imaging conference record, Rome, Italy, October 16-22, 2004.

16. H. Li, W.-H. Wong, S. Kim, R. Ramirez, S. Xie, Y. Wang, T. Xing, J. Uribe, H. Baghaei. A Simulation Study on Optically Decoding Reflecting Windows for PMT Quadrant Sharing Scintillation Detector Block. IEEE Nuclear Science Symposium and Medical Imaging conference record, Rome, Italy, October 16-22, 2004.

CONCLUSION

We have accomplished 85% of the tasks originally planned in these three years, including the 40,000 detectors fabrication, mechanical gantry design, all the electronics and software development. All the detectors, electronics and software have been fully debugged and tested on a small bench-top PET camera; these components are fully functional. Because of the mechanical gantry redesign, the gantry construction has been delayed. But the more accurate detector positioning mechanics and more breast-patient-friendly gantry turning system would significantly improve the usability of the PET camera. A one-year no-cost extension has been granted to finish the construction of this very complex PET camera.

REFERENCES

1. Wang, Y.; Baghaei, H.; Li, H.; Liu, Y.; Xing, T.; Uribe, J.; Ramirez, R.; Xie, S.; Kim, S.; Wong, W.-H. A Simple Respiration Gating Technique and Its Application in High-Resolution PET Camera. IEEE Transactions on Nuclear Science, Volume 52, Issue 1, Feb. 2005 Page(s):125-129.

2. Uribe, J.; Xie, S.; Li, H.; Baghaei, H.; Wang, Y.; Liu, Y.; Xing, T.; Ramirez, R.; Bushman, M.; Kim, S.; Wong, W.-H. Gantry Design With Accurate Crystal Positioning for a High-Resolution Transformable PET Camera. IEEE Transactions on Nuclear Science,
Volume 52, Issue 1, Feb. 2005 Page(s):119-124.

3. Baghaei, H.; Wai-Hoi Wong; Uribe, J.; Hongdi Li; Yu Wang; Yaqiang Liu; Tao Xing; Ramirez, R.; Shuping Xie; Soonseok Kim.
A comparison of four-image reconstruction algorithms for 3-D PET imaging of MDAPET camera using phantom data. IEEE Transactions on Nuclear Science, Volume 51, Issue 5, Oct. 2004 Page(s):2563-2569.

4. Yaqiang Liu; Hongdi Li; Yu Wang; Tao Xing; Shuping Xie; Uribe, J.; Baghaei, H.; Ramirez, R.; Soonseok Kim; Wai-Hoi Wong.
A gain-programmable transit-time-stable and temperature-stable PMT Voltage divider. IEEE Transactions on Nuclear Science, Volume 51, Issue 5, Oct. 2004 Page(s):2558-2562.

5. Yu Wang; Hongdi Li; Yaqiang Liu; Tao Xing; Uribe, J.; Baghaei, H.; Farrell, R.; Wai-Hoi Wong. A modular low dead-time coincidence system for high-resolution PET cameras. IEEE Transactions on Nuclear Science, Volume 50, Issue 5, Oct. 2003 Page(s):1386-1391.

6. Baghaei, H.; Wai-Hoi Wong; Uribe, J.; Hongdi Li; Aykac, M.; Yu Wang; Yaqiang Liu; Tao Xing; Farrell, R. Brain lesion detectability studies with a high resolution PET operating in no-septa and partial-septa configurations. IEEE Transactions on Nuclear Science, Volume 50, Issue 5, Oct. 2003 Page(s):1364-1369.

7. Aykac, M.; Hongdi Li; Uribe, J.; Yu Wang; Baghaei, H.; Yaqiang Liu; Tao Xing; Wai-Hoi Wong. A study of coincidence line spread function (CLSF) estimation for small scintillators using quadrant sharing technique. IEEE Transactions on Nuclear Science, Volume 50, Issue 5, Oct. 2003 Page(s):1331-1338.

8. Yaqiang Liu; Hongdi Li; Yu Wang; Tao Xing; Baghaei, H.; Uribe, J.; Farrell, R.; Wai-Hoi Wong. A programmable high-resolution ultra-fast delay generator. IEEE Transactions on Nuclear Science, Volume 50, Issue 5, Oct. 2003 Page(s):1487-1490.

9. Uribe, J.; Wai-Hoi Wong; Baghaei, H.; Farrell, R.; Hongdi Li; Aykac, M.; Bilgen, D.; Yaqiang Liu; Yu Wang; Tao Xing. An efficient detector production method for position-sensitive scintillation detector arrays with 98% detector packing fraction
IEEE Transactions on Nuclear Science, Volume 50, Issue 5, Oct. 2003 Page(s):1469-1476.

10. Hongdi Li; Tao Xing; Yaqiang Liu; Yu Wang; Baghaei, H.; Uribe, J.; Ramirez, R.; Wai-Hoi Wong. A HOTLink/networked PC data acquisition and image reconstruction system for a high-resolution whole-body PET with respiratory or ECG-gated performance. IEEE Transactions on Nuclear Science, Volume 50, Issue 3, June 2003 Page(s):393-397.

11. Uribe, J.; Hongdi Li; Tao Xing; Yaqiang Liu; Baghaei, H.; Yu Wang; Aykac, M.; Ramirez, R.; Wai-Hoi Wong. Signal characteristics of individual crystals in high resolution BGO detector designs using PMT-quadrant sharing. IEEE Transactions on Nuclear Science, Volume 50, Issue 3, June 2003 Page(s):355-361.

12. Hongdi Li; Wai-Hoi Wong; Yu Wang; Yaqiang Liu; Tao Xing; Uribe, J.; Baghaei, H.; Farrell, R. Front-end electronics based on high-yield-pileup-event-recovery method for a high resolution PET camera with PMT-quadrant-sharing detector modules. Nuclear Science Symposium Conference Record, 2002 IEEE Volume 2, 10-16 Nov. 2002 Page(s):699-703 vol.2.

13. Baghaei, H.; Uribe, J.; Hongdi Li; Yu Wang; Yaqiang Liu; Tao Xing; Farrell, R.; Wai-Hoi Wong. Effects of attenuation correction and 3D-reconstruction algorithms on brain lesions detectability. Nuclear Science Symposium Conference Record, 2002 IEEE Volume 3, 10-16 Nov. 2002 Page(s):1529-1533 vol.3.

14. Baghaei, H.; Wong, W.-H.; Uribe, J.; Li, H.; Wang, Y.; Liu, Y.; Xing, T.; Ramirez, R.; Xie, S.; Kim, S. A comparison of four image reconstruction algorithms for detection of small lesions in brain

phantom. Nuclear Science Symposium Conference Record, 2003 IEEE Volume 4, 19-25 Oct. 2003 Page(s):2584-2588 Vol.4.

15. Li, H.; Liu, Y.; Xing, T.; Wang, Y.; Uribe, J.; Baghaei, H.; Xie, S.; Kim, S.; Ramirez, R.; Wong, W.-H. An instantaneous photomultiplier gain calibration method for PET or gamma camera detectors using an LED network. Nuclear Science Symposium Conference Record, 2003 IEEE Volume 4, 19-25 Oct. 2003 Page(s):2447-2451 Vol.4.

16. H. Baghaei; W.-H. Wong; J. Uribe; H. Li; Y. Wang; T. Xing; R. Ramirez; S. Xie; S. Kim; and Y. Zhang. An Evaluation of the Effect of Partial-Septa on Detection of Small Lesions in Brain Phantom Study Using MDAPET Camera. IEEE Nuclear Science Symposium and Medical Imaging conference record, Rome, Italy, October 16-22, 2004.

17. R. Ramirez; W.H. Wong; J. Uribe; H. Li; T. Xing; Y. Wang; Y. Liu; H. Baghaei; S. Xie; S. Kim; and Y. Zhang; Characteristics of 40,000 Quadrant-Sharing BGO Detectors Made by the Slab-Sandwich-Slice Technique. IEEE Nuclear Science Symposium and Medical Imaging conference record, Rome, Italy, October 16-22, 2004.

18. H. Li; W.-H. Wong; S. Kim; R. Ramirez; S. Xie; Y. Wang; T. Xing; J. Uribe; and H. Baghaei. A Simulation Study on Optically Decoding Reflecting Windows for PMT Quadrant Sharing Scintillation Detector Block. IEEE Nuclear Science Symposium and Medical Imaging conference record, Rome, Italy, October 16-22, 2004.

IEEE TRANSACTIONS ON NUCLEAR SCIENCE, VOL. 52, NO. 1, FEBRUARY 2005

A Simple Respiration Gating Technique and Its Application in High-Resolution PET Camera

Yu Wang, *Member, IEEE*, Hossain Baghaei, *Member, IEEE*, Hongdi Li, *Member, IEEE*, Yaqiang Liu, Tao Xing, Jorge Uribe, *Member, IEEE*, Rocio Ramirez, Shuping Xie, Soonseok Kim, and Wai-Hoi Wong, *Member, IEEE*

***Abstract*—We have developed a simple technique to gate positron emission tomography (PET) imaging in synchronization with respiratory motion to reduce image blurring caused by breathing and to improve quantification of tracer uptake in lesions in the chest and abdomen, especially in very high-resolution PET systems. Taking advantage of the temperature differences in the air flow in a nostril due to inhalations and exhalations, a simple solid-state thermometer was used to construct a respiratory gating system to monitor the respiratory cycles. The gating system provided trigger signals indicating inspiration and expiration as well as periodic (about 40 Hz) timing-tick signals. These trigger and timing-tick signals were inserted into the data stream in real-time while the PET camera was taking data. The gating trigger signals represent particular phases of respiratory motion. This gating system was implemented and tested with our MDAPET, a very high-resolution (2.7-mm resolution) PET camera developed at The University of Texas M. D. Anderson Cancer Center. A volunteer with two spherical lesion phantoms (diameters 3 mm and 5 mm) placed on the abdomen close to the navel was scanned in the gated mode. The respiration-gated images of the lesion phantoms were compared and studied. The simple respiratory gating system worked well in terms of detecting the breathing cycle and providing gating trigger and timing-tick signals. Image blur and errors in the measurements of the lesions' volumes in the gated PET images were reduced, compared with those of the nongated PET images.**

I. Introduction

MOTION blurs images. The amplitude of respiratory motion can be as high as 20 mm, severely degrading the high-resolution performance of the modern medical imaging instruments if no anti-motion method is applied while scanning the chest and abdomen. In the cases of computed tomography (CT) or magnetic resonance imaging (MRI), because of their fast scanning speed, the respiratory motion can be eliminated by breath holding. However, for positron emission tomography (PET), due to its relatively slower scanning speed, it is not practical to apply breath holding to obtain motion-free images. Gating the respiration is a more practical approach to acquiring a more accurate and clearer image. Some recent studies have shown that respiratory-gated PET results in a reduction of the lesion volume measurement of up to 34%, and as much as a 159% change in SUV maximum value estimation [1]. Since PET (with 18F-fluorodeoxyglucose [18F-FDG] injection) has much better sensitivity (87%) and specificity (91%) than CT (68% and 61%, respectively) in lung cancer detection [2], it likely will be increasingly applied for lung cancer diagnosis. Consequently, easily available and usable respiration-gating techniques for PET imaging are in demand.

Many respiration-gating methods, such as video-camera-based motion detectors [1], pneumatic respiratory bellows [3], and air flow pressure sensors, have been developed over the past decades. Each of them works well but has some drawbacks such as patient discomfort, implementation complexity, or relatively high cost. In this paper, we propose and demonstrate a simple gating technique by sensing the temperature differences in the air flow in a nostril due to inhalations and exhalations. During expiration the air temperature in the nostril is expected to be higher than that during inspiration, since the exhaled air has been warmed by the lungs. An inexpensive solid-state thermometer can be used to construct circuitry to monitor the respiratory cycles.

Manuscript received November 12, 2003; revised October 4, 2004. This work was supported in part by the NIH-CA58980 PHS Grant, NIH-CA61880 PHS Grant, NIH-CA76246 PHS Grant, NIH-CA58980S PHS Grant, NIH-EB01481 PHS Grant, NIH-EB00217 PHS Grant, NIH-EB01038 PHS Grant, U.S. Army-Breast Cancer Research Grant, Texas ARP/ATP Grant 003657-0058-2001, and Analog Devices Incorporated University Program.

The authors are with University of Texas M. D. Anderson Cancer Center, Houston, TX 77030 USA (e-mail: wangy_km@yahoo.com; ywang@di.mdacc.tmc.edu).

Digital Object Identifier 10.1109/TNS.2004.843103

II. System Design

A. Design of the Nostril Sensor Piece

A solid-state temperature sensor (TMP04, Analog Devices Inc.) was used to measure the temperature of air flowing through a nostril. A plastic tube (Tycon R3603, Saint-Gobain Performance Plastics Corporation) about 3 cm long was used to construct the nostril piece to hold the temperature sensor and to conduct the air flow of respiration over the surface of the temperature sensor. A small window the size of the temperature sensor was cut on the side of the tube about 6 to 8 mm from one end. The sensor was wired and powered with 3 AA batteries, Fig. 1(a). The temperature signals from the sensor were fed into a digital signal processor (DSP) for further gating processing.

When a test or a gated scan was conducted, the sensor was placed at the end of the subject's nostril, as shown in Fig. 1(b). The air conducting tube should be inserted into the nostril 8 to 12 mm. None of the five volunteers who tested the sensor reported that the sensor interfered with their breathing.

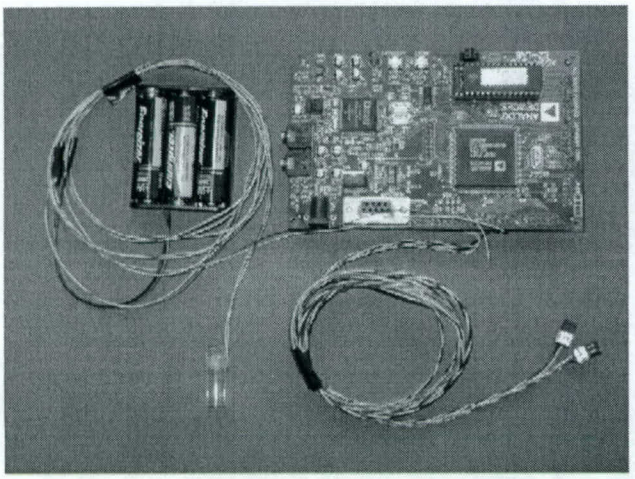

(a)

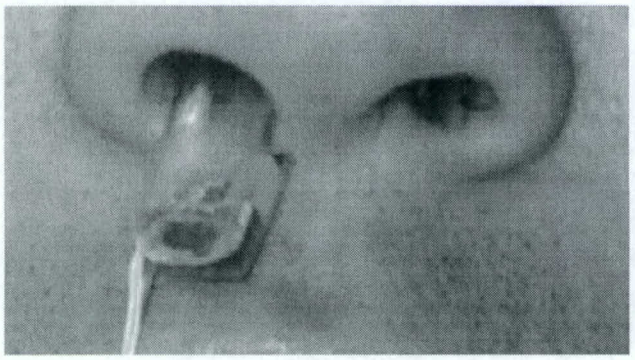

(b)

Fig. 1. (a) Proposed respiration gating system and (b) the nostril sensor piece was tested by a volunteer.

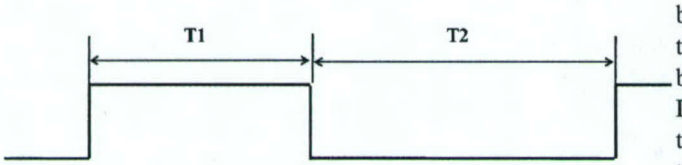

Fig. 2. TMP04 temperature sensor output waveform.

B. Signal Processing and Gate Generating

An inexpensive DSP development kit (ADSP2181 EZ-Kit, Analog Devices Inc.) was used to process the temperature information from the sensor, to trace the respiratory cycles, and to produce the respiration gating signals and the periodic timing-tick signals.

The TMP04 provides temperature information with a pulse-width-modulation (PWM) signal, as shown in Fig. 2. PWM signal facilitates the interface because the signal can be transferred with one single wire. Widths (T1, T2 in Fig. 2) of TTL (Transistor-Transistor-Logic) compatible high (logic 1) and low (logic 0) statuses, which represent the temperature information, can be measured easily by counting the duration of each status with digital devices including processors. Then, the temperature can be calculated by using widths of high and low statuses through (1) [4]. The DSP performs width measurement of the output signal from the TMP04 and the temperature calculation

$$\text{Temperature}(^{\circ}\text{C}) = 235 - \frac{400 \times T1}{T2}. \qquad (1)$$

The DSP generates the respiration gating signal from the current temperature through the following procedure: if the temperature is higher than a threshold value, then the gating signal is set to low (logic 0), denoting expiration; otherwise, the gating signal is set to high (logic 1), denoting inspiration.

Three major factors have an impact on the temperature measurement. First, the ambient environment affects the heat-transfer on the surface of the sensor and correspondingly changes the temperature measurement. Second, different people breathe in different ways, so that the temperatures measured by the sensor will be different. Third, the subject may change his breath pattern over the course of the acquisition. As a result, the DSP must track the variation in signal amplitude and adjust the threshold dynamically. Fig. 3 shows the relationships among the temperature sensor signal, gating threshold, and digital gating signal.

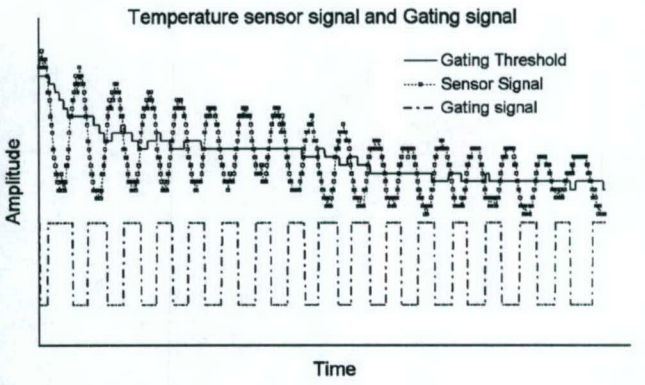

Fig. 3. Temperature-sensor signal and respiratory gating pulse. A DSP algorithm tracks the variation of the measured temperature (sensor signal) and adjusts the threshold automatically in order to generate the respiratory gating signal correctly. The y-scale of gating signal was adjusted so that all data fit into one graph.

C. Gated PET Data Acquisition and Processing

Although respiratory cycle-predicting algorithms, by which sinogram-mode data acquisition is possible, can be realized in DSP, we found that if a patient breathes freely without breath-guiding instruction, the cycles vary too quickly to be predicted correctly. Correspondingly, in this work, the data were taken in list mode rather than sinogram mode. In order to eliminate the influence of the respiratory cycle variation and register gating phases correctly, periodic (about 40 Hz) timing-tick signals were created by the DSP.

The gating signals and timing-tick signals were fed into the coincidence circuitry of the MDAPET [5]. Specific logic implemented in a complex programmable logic device (CPLD) generated unique codes corresponding to the gating signals of inhalation and expiration as well as the timing-tick signals and inserted these codes into the coincidence data stream from PET

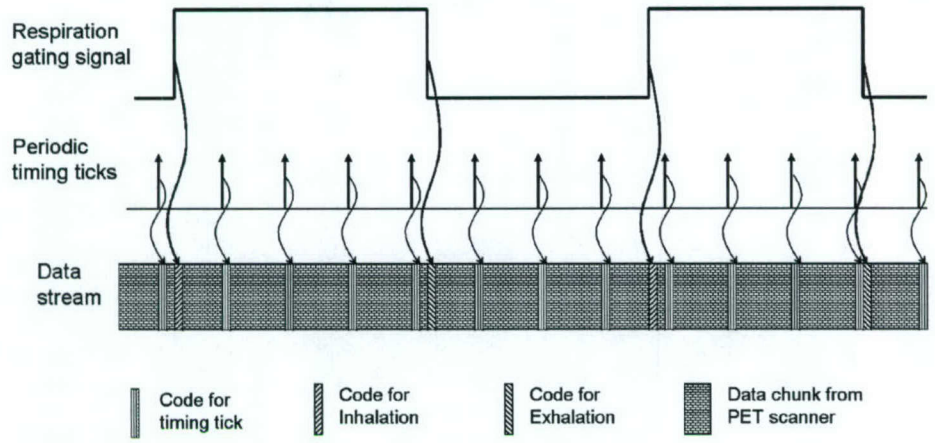

Fig. 4. Data acquisition scheme of the proposed respiration gating PET scan.

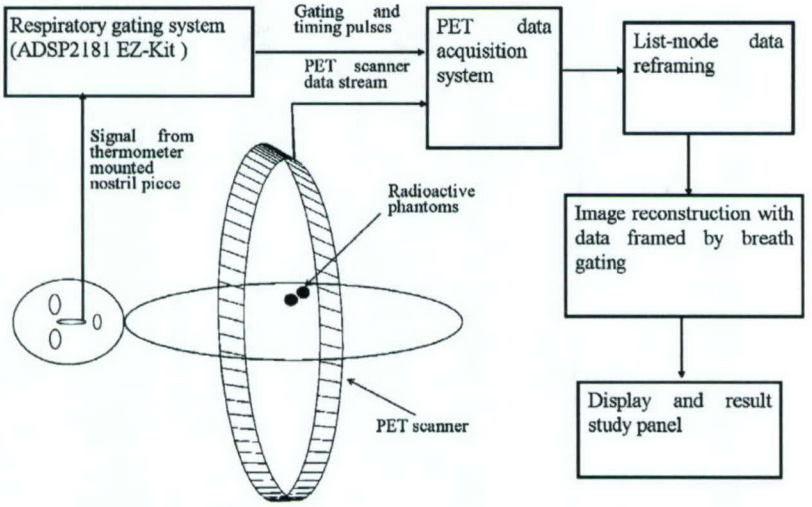

Fig. 5. Diagram of the respiration gating system experimental setup.

scanner in real time. The data acquisition scheme is shown in Fig. 4.

A program was written to process the list-mode data. The program extracted the codes of inhalation and expiration and the periodic timing-ticks from the data-stream and generated framed sinograms accordingly. By means of periodic timing-tick insertion and list-mode data acquisition, in which the frames don't have to be evenly distributed, not only can a patient breathe freely during a scan but also an investigator can adjust the frame pattern of the gated images to achieve the best observation. A Labview program for editing the frame patterns and displaying the gated images was created. The gated image frames can be displayed in both frame-selectable mode and sequential (movie) mode.

III. Test Method

The sensor was tested using an experimental setup shown in Fig. 5. Two lesion phantoms (diameters 3 and 5 mm) filled with 18F-FDG solution (SUV = 8) were attached to a volunteer's abdomen (near the navel). The volunteer was scanned with the gating device.

The 3-dimensional re-projection method (3DRP) [6] was used to reconstruct images. To minimize radiation exposure to the volunteer and to simplify the experiment, no transmission scan was performed, so the images were reconstructed without attenuation and scatter corrections.

IV. Results

Fig. 6 shows gated and nongated images of the two lesion phantoms. The gated images clearly show much better definition of lesions. The image artifacts in the X direction are attributable to the lack of an attenuation correction. Fig. 7 shows vertical profiles of 5 images with significant differences chosen from 8 frames shown in Fig. 6. For images of each phantom, the profiles were generated at the same X coordinate. Table I lists quantitative comparisons of gated and nongated images. The peak intensity values were increased about 137% for 5-mm phantom and 106% for 3-mm phantom

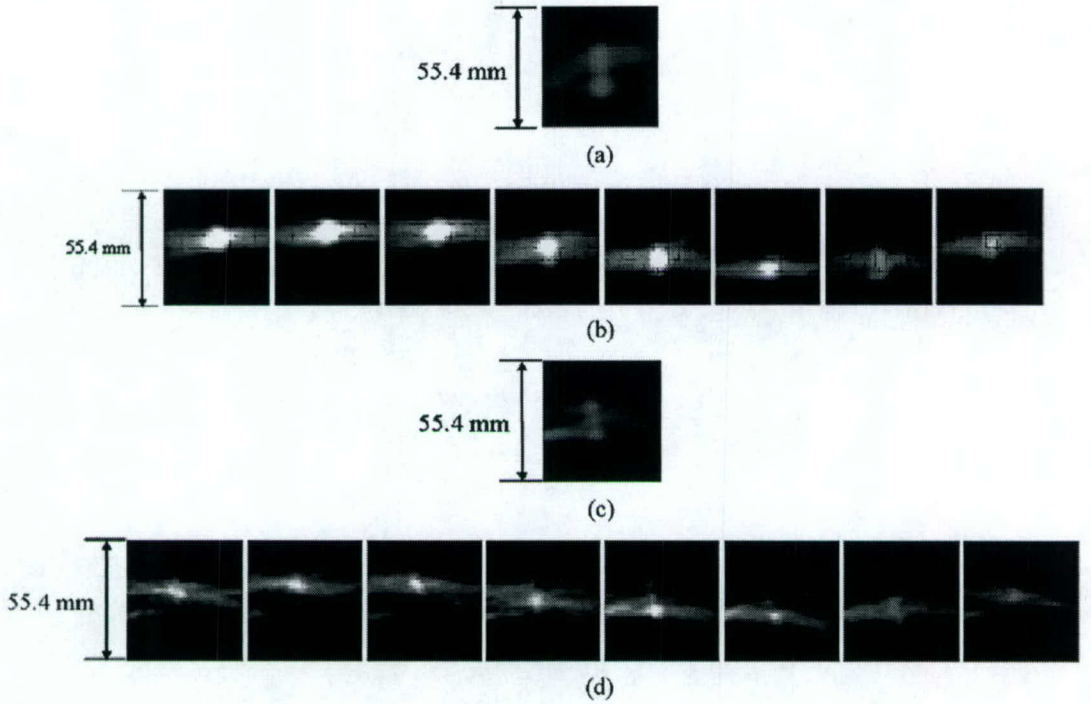

Fig. 6. Images of 5-mm and 3-mm lesion phantoms with and without respiration gating (same slice). (a) Nongated image of the 5-mm lesion phantom. (b) Respiration gated images of the 5-mm lesion phantom images. (c) Nongated image of the 3-mm lesion phantom. (d) Respiration gated images of the 3-mm lesion phantom images.

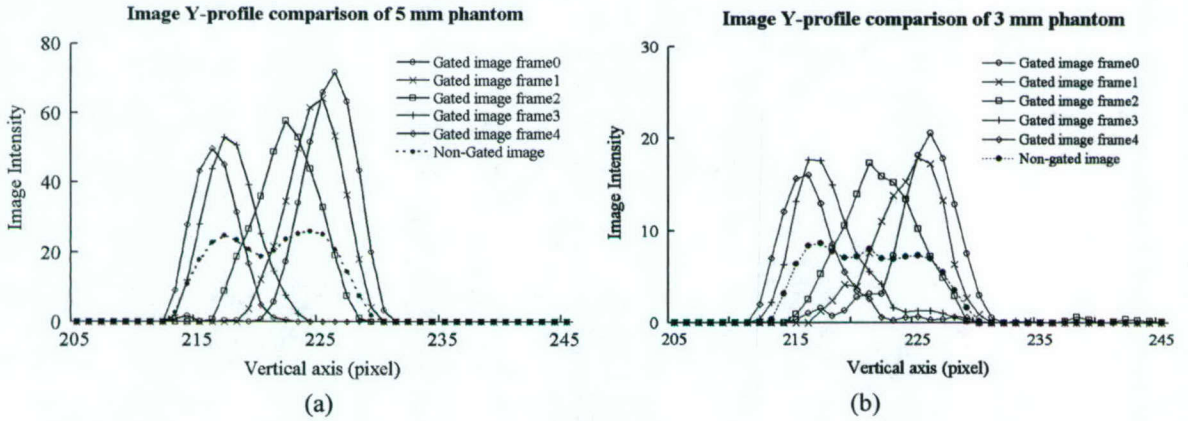

Fig. 7. Vertical profile comparisons of selected frames of gated images of lesion phantoms (diameters (a) 5 mm and (b) 3 mm).

on average. Meanwhile, the coarse measurements of lesion sizes (full width half measurement [FWHM] of profile) were reduced on average 59% and 57% for 5-mm and 3-mm phantoms, respectively. The respiration-gated data provide sharper images, improving the lesion definition over the nongated data.

V. Conclusions and Discussions

We have developed a simple respiration gating technique with a solid-state temperature sensor detecting the temperature difference of the air flow in the nostril due to inhalation and expiration. A gating apparatus based on this technique was designed using a low-cost DSP development kit. We have demonstrated the method with a simple experiment, in which a feature moving with a volunteer's respiratory motion was effectively deblurred. The respiration-gated data acquired with the proposed gating method provided much sharper and clearer images than the nongated data did. Thus, the gated images improved lesion definition.

Quantitative assessment of the accuracy of this method, whether in absolute terms or in comparison to other techniques, has not yet been undertaken. It is important to note that this apparatus generates trigger signals upon which time-based gating schemes are performed (in a manner like cardiac gating). Other transducers, such as a pneumatic respiratory bellows, may be

TABLE I
QUANTITATIVE COMPARISON OF IMAGE PROFILES

Phantom	Image frame No.	FWHM of profile (pixel)	SUV peak value (image intensity)
5mm diameter	0	5.3	71.7
	1	5.7	64.1
	2	6	57.7
	3	5	53
	4	4.7	49.7
	Average	5.3	59.2
	Non-gated	12.9	26
3mm diameter	0	5	20.6
	1	5.8	18
	2	7.5	17.4
	3	5.1	17.6
	4	5	16
	Average	5.7	17.9
	Non-gated	13.2	8.7

used to produce a direct position signal against which the PET data is binned. Such "signal level based" gating schemes may have inherently better performance than the time-based scheme which our apparatus employs. However, we are encouraged by our initial results, especially in light of the relative simplicity and low cost of our method.

REFERENCES

[1] S. A. Nehmeh, Y. E. Erdi, C. C. Ling, K. E. Rosenzweig, H. Schoder, S. M. Larson, H. A. Macapinlac, O. D. Squire, and J. L. Humm, "Effect of respiratory gating on quantifying PET images of lung cancer," *The J. Nucl. Med.*, vol. 43, no. 7, pp. 876–881, 2002.

[2] N. C. Gupta, W. C. Tamim, G. G. Graeber, H. A. Bishop, and G. R. Hobbs, "Mediastinal lymph node sampling following positron emission tomography with fluorodeoxyglucose imaging in lung cancer staging," *Chest*, vol. 120, no. 2, pp. 521–527, 2001.

[3] G. J. Klein, B. W. Reutter, M. H. Ho, J. H. Reed, and R. H. Huesman, "Real-time system for respiratory-cardiac gating in positron tomography," *IEEE Trans. Nucl. Sci.*, vol. 45, no. 4, pp. 2139–2143, 1998.

[4] Analog Devices Inc., "Serial Digital Output Thermometers (Temperature Sensor) Data Sheet," Rev. A, TMP03/TMP04, 2001.

[5] J. Uribe, H. Baghaei, H. Li, S. Yokoyama, N. Zhang, J. Wang, F. Dobbs, and W. Wong, "Basic imaging performance characteristics of a variable field of view camera using quadrant sharing detector design," *IEEE Trans. Nucl. Sci.*, vol. 46, pp. 491–497, 1999.

[6] P. E. Kinahan and J. G. Rogers, "Analytic 3D image reconstruction using all detected events," *IEEE Trans. Nucl. Sci.*, vol. 36, pp. 964–968, 1988.

IEEE TRANSACTIONS ON NUCLEAR SCIENCE, VOL. 52, NO. 1, FEBRUARY 2005

Gantry Design With Accurate Crystal Positioning for a High-Resolution Transformable PET Camera

Jorge Uribe, *Member, IEEE*, Shuping Xie, Hongdi Li, *Member, IEEE*, Hossain Baghaei, *Member, IEEE*, Yu Wang, Yaqiang Liu, Tao Xing, Rocio Ramirez, Mark Bushman, Soonseok Kim, and Wai-Hoi Wong, *Member, IEEE*

***Abstract*—A positron emission tomography (PET) camera capable of transforming its geometric configuration is being developed. This high-resolution oncologic transformable PET (HOTPET) can be modified from a large detector ring of 83 cm to a small diameter ring of 54 cm. The system consists of 12 rectangular detector modules arranged in a polygon. *The detector gap between modules remains constant in both configurations* because each module is rotated around its own axis and displaced radialy, bringing together adjacent modules. HOTPETs detectors are highly pixilated (crystal pitch 2.6 mm), requiring accurate placement of the modules relative to each other to ensure alignment of crystals within the same detector ring. We have designed a precise *detector bank holder* with keyways and complementary keys built onto its sides to allow interlocking with each other to form a polygon and maintain crystal coplanarity. Consequently, we were able to design the gantry supporting the modules using wider tolerances and so reduce its construction cost. The module provides support to 77 photomultiplier tubes (PMTs), the analog front-end electronics, and an automated PMT-gain control, all enclosed within a controlled environment. Potential development of light leaks was minimized with only two parting surfaces throughout the module's box, and tortuous-path air ducts inside the walls. Internal airflow allows temperature control. Simple removal of a back cover and a motherboard gives access to any part of the electronic components or a PMT with minimal disturbance to other components.**

I. Introduction

A HIGH-resolution positron emission tomography (PET) camera whose geometric configuration can be transformed is being developed [1]. This high-resolution oncologic transformable PET (HOTPET) camera can be modified from a large detector ring for whole-body scans (83-cm diameter), to a higher sensitivity, smaller port for brain/breast scans (54-cm diameter) [2]. The system was designed to allow both clinical and research applications with one camera, specially those requiring high sensitivity and resolution with geometric adjustment to a particular anatomy, e.g., dedicated breast or brain imaging [3]. At the same time it provides equivalent sensitivity and higher resolution [2.6-mm resolution expected at the center of the field of view (FOV) [2]] than a dedicated whole-body clinical scanner. The camera consists of 12 independent detector modules arranged in a regular 12-sided-polygon as shown in Fig. 1,

Manuscript received November 13, 2003; revised May 25, 2004. This work was supported in part by the NIH-CA58980 PHS Grant, NIH-CA61880 PHS Grant, NIH-CA76246 PHS Grant, NIH-CA58980S PHS Grant, NIH-EB01481 PHS Grant, NIH-EB00217 PHS Grant, NIH-EB01038 PHS Grant, U.S. Army-Breast Cancer Research Grant, and Texas ARP/ATP Grant 003657-0058-2001.

The authors are with the M. D. Anderson Cancer Center, the University of Texas, Houston, TX 77030 USA (e-mail: juribe@di.mdacc.tmc.edu; juribe@alumni.umass.edu).

Digital Object Identifier 10.1109/TNS.2004.843145

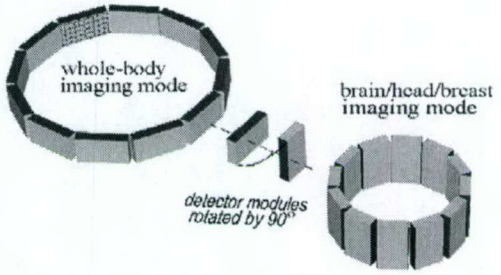

Fig. 1. HOTPET geometric transformation from large to small radius without changing the size of the gap between adjacent modules. Each block represents the scintillation detector bank inside a detector module.

with a 14.8-mm gap separation between detectors from adjacent modules. An important feature of this camera is that the *gap between modules remains constant in both configurations*. The versatile transformation between modes with no change in detector separation is possible by rotating the modules on their own axes and displacing them in the radial direction, bringing their rectangular faces side by side as depicted in Fig. 1.

II. Design

The mechanical design of this camera is challenging due to the convertible geometric configurations required and the small size of the detector crystals (2.68 mm × 2.68 mm). Complex mechanical assemblies could have large compound mechanical tolerances, which generate detector-positioning variations that create resolution degradation in the image. Therefore, mechanical tolerances of gantry components must be very small compared to the crystal detector size to minimize such degradation. In addition, this modular system must satisfy the following requirements and design considerations.

- Gantry must rotate 30° on main axis (patient's axial direction) with angular positioning accuracy of at least 1/5 the arch covered by one detector crystal (0.07°). This is needed for improving sampling and minimizes image artifacts caused by intermodule gaps [4].
- Gantry must turn 90° from the vertical whole-body mode to the horizontal/flat breast mode.
- Alignment of crystals belonging to the same detector ring must be assured within 1/10 crystal size (0.27 mm). This is needed to optimize axial resolution.
- Modules must be able to move independently or in tandem along the gantry's radial direction and rotate 90° on their axes to change scanning mode.

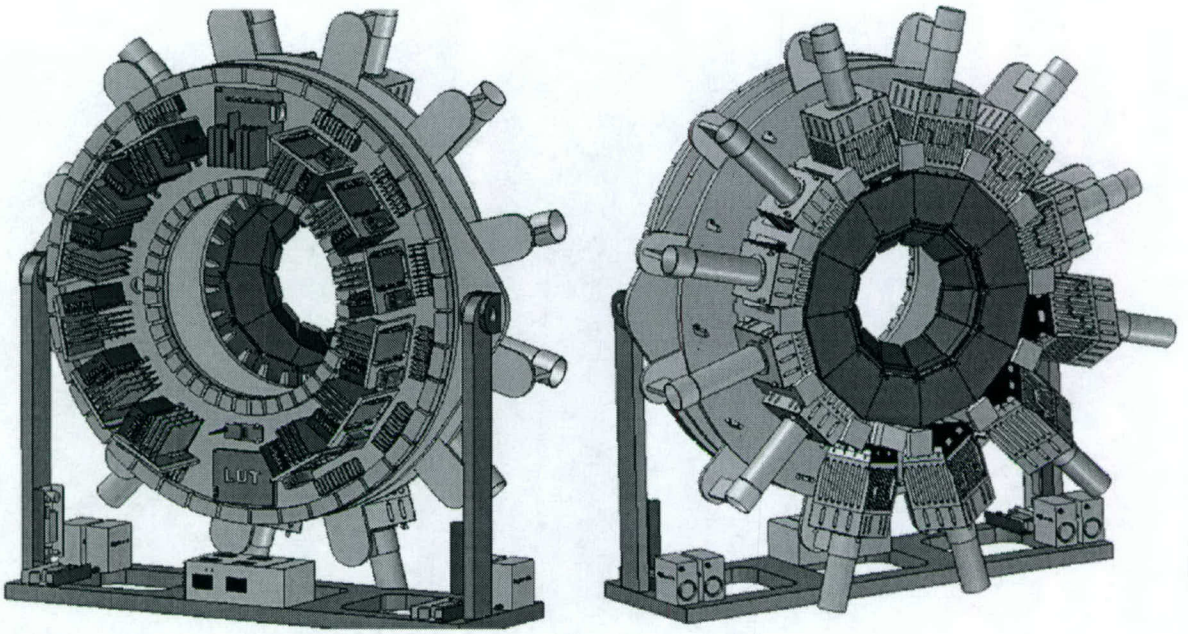

Fig. 2. Gantry design. Left: View of rear plate of the gantry supporting all the electronic components of the camera. Notice that both front and back lead shields are visible. Boxes on the floor are the power supplies. Right: Front view with 12 modules displayed in sets of four presenting the breast mode (left four modules), whole-body mode (top-right four modules) and transport mode (bottom-right four modules). Notice the movable lead shields partially open.

- Each module at the brain/breast and whole-body positions must be securely fixed with positive positioning stops for easy operation and repeatable configuration of the camera.
- Side shielding must be movable so that the patient opening can be changed from whole-body to brain/breast mode.
- Dead space between detector and patient chest wall must be minimized when configured in breast mode and the whole breast must be included in the FOV.
- The length of cables carrying fast/high-rate signals must be short to avoid signal degradation.
- Number of cables connecting rotating part of the gantry and fixed platform must be minimized (moving parts break easily).
- Front-end and processing electronics must be confined to the gantry. There should be no outside electronic racks except for computer performing image reconstruction and image display.
- Module design should allow easy maintenance with minimum disturbance to other components when serviced.
- Heat removal from the modules' inner volume must be provided. Temperature must be kept under 40°C.
- Number of parting surfaces in the module must be minimized to avoid the development of light leaks.

We have designed a gantry and detector module that satisfies the previous conditions. In addition, the design does not require extremely tight mechanical tolerances on the gantry parts because the factors that affect accuracy of the detector position have been confined to the front section of the module as explained below. The design process started with a module, which in turn determined the overall design of the gantry, but for clarity's sake we will describe the gantry design first.

A. Gantry Design

The gantry provides support for the twelve modules and all the electronics. Details on the electronic design can be found in [5]–[8]. To shorten the distance between a module and its electronics they have been placed on two large round plates as shown in Fig. 2, with each electronic set placed behind the corresponding module that it serves. The module support structure and the electronic support structure are bound together and rotate as one unit around the patient, riding on a large bearing system mounted on the third plate shown between the two plates mentioned before (Fig. 2). A "V" bearing system with a large "knife edge" ring and gear are used as riding/driving mechanism for rotating 30° around the patient. A stepper motor with a gear-head and a linear magnetic encoder form a closed system that can provide accurate rotation. A similar system was tested with our first PET prototype, MDAPET [9], and was accurate to 0.03°.

The middle plate can turn 90° on an axis horizontal and perpendicular to the patient axial direction; with it the entire gantry moves from the vertical orientation to the horizontal one. In the horizontal mode, a bed with an opening can be attached to the gantry and the breast of a person lying prone on the bed will suspend inside the FOV.

Each module is supported by a member attached to its backside that slides on a trunnion fixed to the gantry, as well as two Delrin guides, one on each side of the module (Fig. 2). Vertical tabs on the supporting round plate and the Delrin guides provide positive stops for module positioning in the breast/brain and whole-body modes. Calibration of the modules position is necessary only once; from then on, the tabs give a repeatable

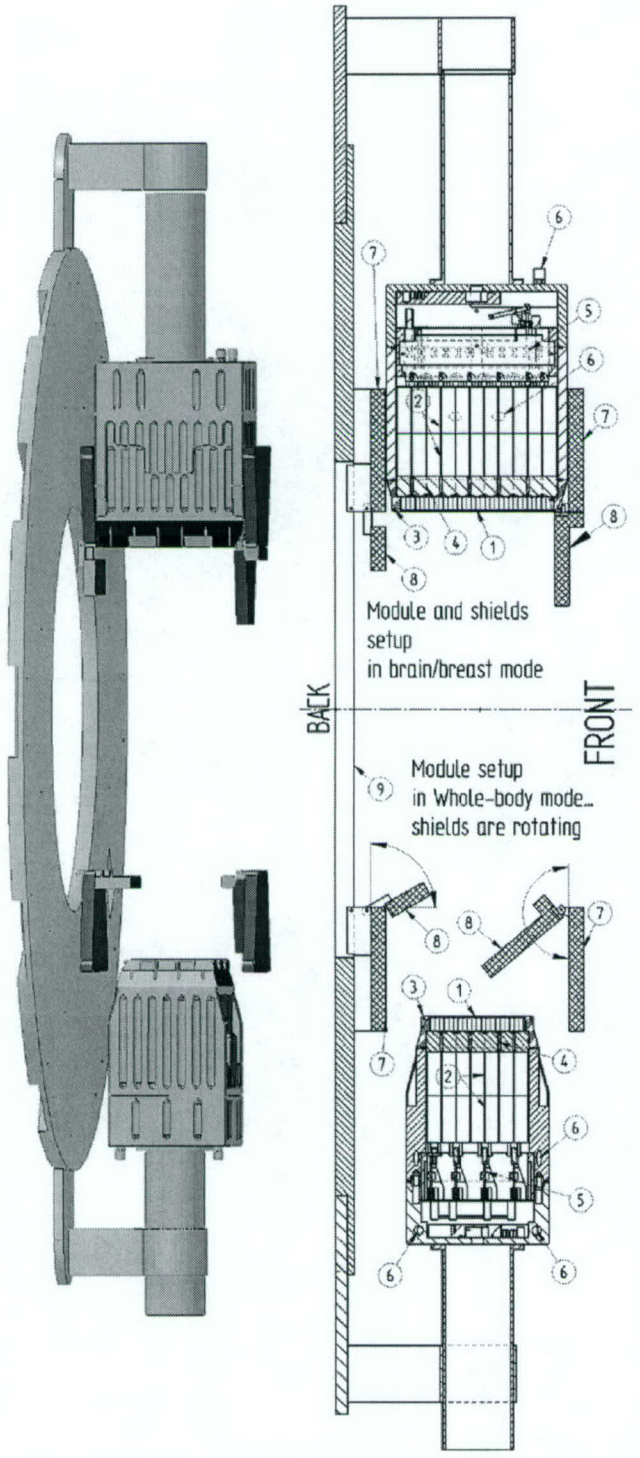

Fig. 3. Shielding configurations and cross sectional view. Left: Two of the 12 modules shown; bottom module configured in whole-body mode, top module configure in brain/breast mode. Corresponding shielding configurations are also shown (notice movable pieces). Right: Cross-sectional view showing modules' inner components. (1) BGO detector bank, (2) photomultipliers and voltage dividers, (3) *detector-bank holder*, (4) PMT holder, (5) front-end (analog and calibration) electronics, (6) air cooling ducts and air intake, (7) fix lead shields, (8) movable lead shields (left shield rotates 90°, right shield rotates 180°), and (9) large support plate with patient opening in the middle.

positioning pattern. These tabs allow only one direction of rotation for each module (Fig. 2).

TABLE I
HOPET MECHANICAL PARAMETERS

Mechanical parameters	Brain/breast mode	Whole-body mode
Number of detector modules	12	12
Detector bank axial dimension	207.9mm	129.3mm
Detector bank trans-axial dimension	129.3mm	207.9mm
Number of detector rings	72	44
Crystals per ring	528	864
Axial FOV	20.8 cm	12.9 cm
Diameter between facing detector banks	54 cm	83.3 cm
Shield-defined patient volume (trans-axial)	28 cm	53.6 cm
Shield-defined patient volume (axial)	22.9 cm	14.9 cm
Gap between adjacent detector banks	14.8 mm	14.8 mm
Detector gap angle span	3.06°	1.98°
Gantry rotation	30°	30°
Lead shield thickness	20 mm	40 mm (front only)

B. Shielding Design

Lead shielding is provided at the front and back of the patient opening, as shown in Fig. 3, for rejection of gamma rays generated outside the FOV. HOTPET will be a three-dimensional (3-D) acquisition PET camera with possibility for intermediate partial septa, manually placed, to reduce scattered and accidental coincidences [1], [10], [11]. Design consideration of the shielding called for a compromise between optimum placement of the shields for each configuration mode and the level of complexity of its supporting mechanism. A shield optimally placed will require both radial displacement as well as axial displacement on both sides of the modules as the modules move from breast/brain mode to whole-body mode. It would require a rather complicated mechanical support capable of holding the movable lead pieces (20-mm thick). Instead, we designed HOTPETs shielding using two sets of fixed lead pieces (one set on each side of the module) and separated enough to allow a module to slide in between shields while oriented in brain mode [Fig. 3 #(7)]; plus another two sets of movable flaps that can open and close like the petals of a flower [Fig. 3 #(8) and Fig. 2], also placed on two sides of the module. The movable shielding serves the dual purpose of narrowing the patient opening in the brain mode, as well as decreasing the exposed axial length of the patient to the detectors in whole-body mode (Fig. 3, left-bottom). In brain mode the movable shield extends away from the modules into the patient opening, whereas in the whole-body mode the pieces move closer to the modules and between the fixed pieces. As a result, however, the shielding in the whole-body mode does not block as many unwanted photons as it would if the shields were placed right next to the detector. From Table I one can realize that the axial length of the detector module in whole-body mode is 129.3 mm, whereas the axial length of the "shield-defined patient volume" is larger at 14.9 cm. Therefore, additional 2 cm of the patient's axial length will contribute with extra single-counts. In Table I, "shield-defined patient volume" refers to the section of the patient within the front and back lead shielding; the FOV is a part of the "shield-defined volume."

A steel plate supports the fixed lead pieces as well as the hinges of the movable pieces at the front of the scanner (plate

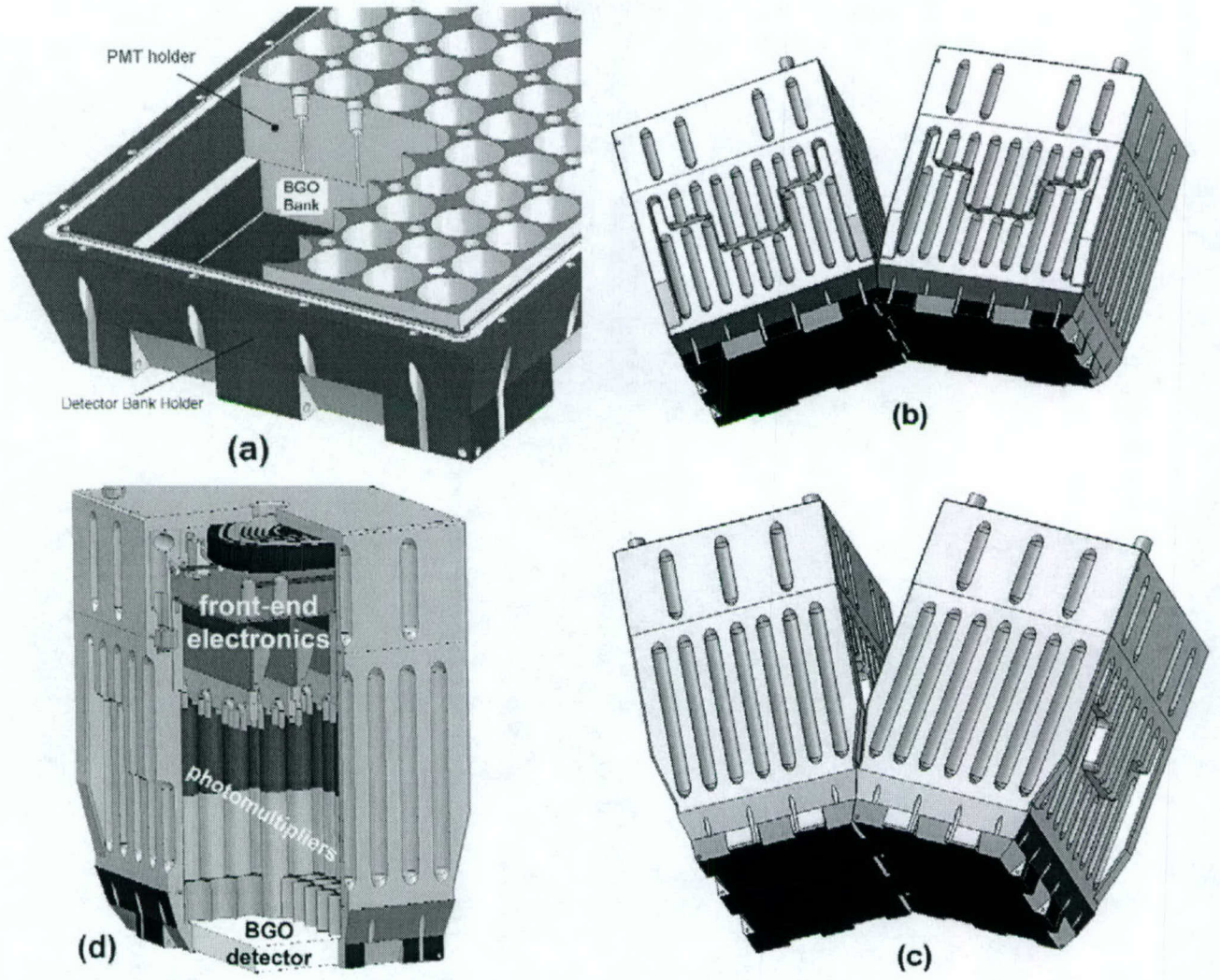

Fig. 4. HOTPETs detector module and its configurations. (a) *Detector-bank-holder*. (b) Short sides of the rectangular holder are mated together forming a 30° angle and a large-diameter polygon for whole-body imaging. (c) Long sides of the rectangular holder are mated together forming a 30° angle and a small-diameter polygon for brain/breast mode. (d) Detector module internal components.

not shown in Fig. 3). The large aluminum plate supporting the modules acts as support for the pieces on the back of the scanner. In addition, the steel and aluminum structures provide rigidity to prevent warping of the shields under their own weight.

C. Detector Module Mechanical Design

Each HOTPET detector module encases a highly pixilated *detector bank* of 60 blocks. The blocks are BGO crystal arrays with 7×7, 7×8 or 8×8 elements in them; combined, the detector bank has 3168 crystals with crystal-pitch ranging from 2.6 to 3.1 mm. The bank is 207.9 mm long by 129.3 mm wide (Table I). A detailed description of the detector bank design and the novel block production process can be found in [12].

Scintillation crystals are optically coupled to 19-mm round PMTs [Fig. 3 #(2)] using the photomultiplier quadrant sharing technique (PQS) developed in our group [12], [13]. The small size of the crystals requires that each module be accurately placed relative to each other to ensure alignment of crystals within the same detector ring. Misalignment of crystals will produce lower resolution and poor image quality. Thus, rather than placing the modules on a massive gantry to achieve the position accuracy of the modules and in turn of the detectors, we designed a precise *detector bank holder* as shown in Figs. 4(a) and 5. The bank holder has keyways and complementary keys built onto opposite sides of the holder to allow interlocking with each other to form a polygon and maintain detector rings coplanar (plane perpendicular to the patient's axial direction). Fig. 4(b) and (c) show two modules locked in the whole-body and brain/breast positions, respectively. By taking care of the tight mechanical tolerances and appropriate alignment of the detector elements with the polygon structure formed by the detector holders, the gantry design is greatly simplified, reducing its manufacturing cost.

The *detector-bank-holder* is a black Delrin cradle holding the BGO-bank and the PMT-holder mold as shown in Fig. 4(a) [see also #(3) and #(4) Fig. 3]. The bank holder was designed to keep equal separation (1.48 cm) between adjacent detector banks in the two camera modes. Consequently, the gaps in the sinograms are relatively small; slightly larger in the brain/breast mode due to the larger angle spanned by the fix module gap at the smaller radius of the brain/breast configuration (shown in Fig. 6).

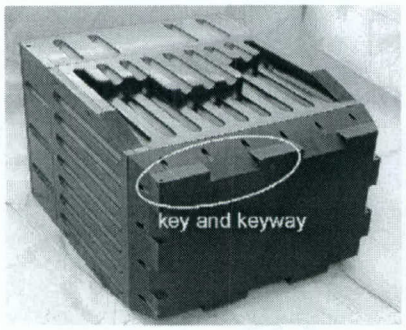

Fig. 5. Detector module. *Detector-bank-holder* with key and complementary keyway milled on its sides shown in the foreground. Back cover and sidewalls were black anodized to minimize light reflection inside the box and throughout the air-cooling ducts.

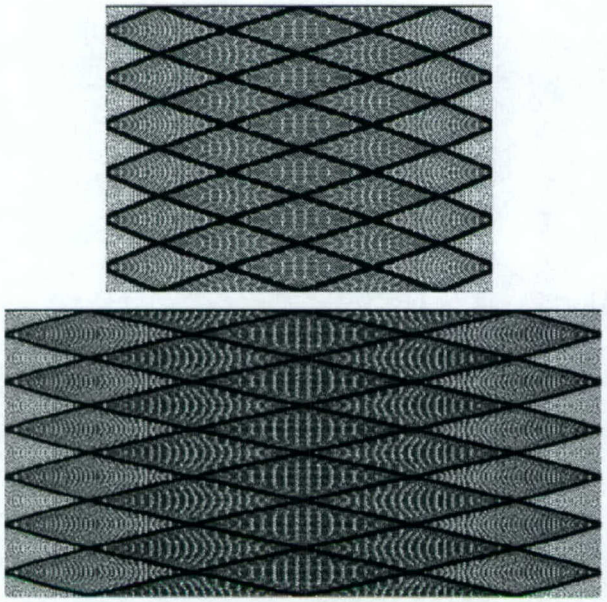

Fig. 6. Simulated sinograms showing all lines of response for the (top) brain/breast mode and the (bottom) whole-body mode. Both histograms were drawn on the same scale.

Accurate placement of the detector crystals within a ring is provided by the locking mechanism built in the front of each detector module. In turn, the module's support and the large-round plate provide placement to the detector modules in the laboratory reference and relative to the patient. Thus, it is expected to require accurate rotational positioning (0.03°), but there is no need for extremely accurate module support. The fact that the axis of rotation of a detector ring could precess around the patient axis due to variations from the module support should have little effect because the gantry has a total rotation of just 1/12 of a revolution.

The PMT-holder (Figs. 4(a)) and 7) aligns the photomultipliers over the BGO crystal arrays in PQS mode [13]. It also includes a network of light emitting diodes (LEDs) housed in small holes drilled between PMT holes. Light from the LEDs is collimated by 0.7-mm diameter holes onto the central crystal of the BGO blocks and used by the automated PMT gain-tuning technique featured in this camera [14].

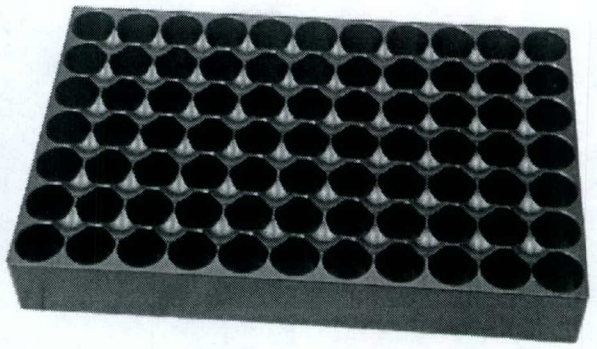

Fig. 7. Photomultiplier positioning holder. Accurately places PMT over the BGO bank of blocks using PQS technology. Holes of 0.7-mm diameter were drilled between four PMT holes to collimate light from LEDs embedded in the jig. These holes are not visible in the above picture due to their small size.

Photomultipliers inserted into the PMT-holder and their corresponding voltage dividers are shown in Fig. 4(d). Around the PMT and behind the outer walls of the module, there is a closed-loop sheet of mu-metal to minimize the presence of external magnetic fields in the PMT space [too thin to be observed in Fig. 4(d)]. Above the PMT-voltage dividers, there is a set of pressure-applying components (upside-down "U"s), exerting a light force on each PMT to preserve the optical coupling, which could deteriorate over time from mechanical vibration. Above the pressure bars, in the upper half of the module, there is a set of four printed circuit daughter-boards attached to a larger motherboard. Each module contains within: a) analog front-end electronics for signal amplification and discrimination, b) signal weighting circuit for Anger decoding of the location of gamma hits (first level decoding—prenormalized signals), c) distribution of high-voltage to PMTs, and d) the LED-PMT-gain tuning system [5], [14]. In order to service a module, e.g., to replace a voltage divider, it is necessary to remove the motherboard while keeping in place the daughter-boards. We have built a precision frame with pockets cut into its sides to hold the daughter-boards using a series of Delrin pieces wedged into these pockets. Fig. 4(d) shows two wedges next to the daughter boards; the mounting frame was cut out for clarity. The motherboard is removed using four levers operated in tandem and supported by the motherboard to impel itself up as the levers press against the edge of the daughter boards below [Fig. 3 #(5)].

A total of 12 RG-174 coaxial cables carry the information from each module. In addition, there is one high-voltage cable and one parallel-format cable for system control. These lines come out the back of the module. Before going through the back opening the cables are routed through a simple maze that block the light and makes the interior of the module light tight [round piece against the top cover in Fig. 4(d)]. Thus, there is no epoxy or gap-filling material to remove when servicing the interior of the module or replacing a cable.

Each module dissipates 45 W, which would increase the internal temperature if there were no cooling, thereby degrading the light output of the BGO scintillator. We built a simple network of air ducts inside the module walls with the intake and outlet couplings at the top of the box [Figs. 4(c) and 3 #(6)]. In addition, grooves were milled on the outside surface of the walls, increasing the total heat-radiating surface exposed to the outside air.

III. Conclusion

We have designed the detector modules and supporting gantry of a modular PET camera that can change geometric configurations from whole-body to brain mode without changing the separation between adjacent modules.

Sets of fixed and movable lead shields were designed to accommodate the changing geometry while maintaining adequate rejection of gammas rays from outside the FOV.

The gantry can rotate azimuthally 90° and turn the scanner into a dedicated high-sensitivity breast scanner.

Accurate positioning of detector crystals is essential in high-resolution PET systems. Such accuracy is provided in our design by a *detector bank holder* placed directly in the front section of the module where the detector crystals are located, rather than relying on accurate placement of the modules on the gantry. As a result, loose tolerances are permitted in the manufacturing of the gantry, producing a cost reduction.

Acknowledgment

The authors would like to thank the machinists at the Radiation Physics Machine Shop at the M. D. Anderson Cancer Center: P. Barnet, J. W. Griffin, C. D. Ziegler, and their supervisor L. K. Danniel for their support and careful manufacturing of the parts for this camera. They would also like to thank N. Goza for his support during the production phase of the modules and gantry components.

References

[1] W. H. Wong, J. Uribe, H. Li, H. Baghaei, Y. Wang, M. Aykac, Y. Liu, T. Xing, D. Bilgen, and R. Farrell, "The design of high-resolution transformable wholebody PET camera," *IEEE Trans. Nucl. Sci.*, vol. 49, no. 5, pp. 2079–2084, Oct. 2002.

[2] W. H. Wong, J. Uribe, H. Li, H. Baghaei, Y. Wang, M. Aykac, and Y. Liu, "Design of a wholebody high resolution PET with changeable transaxial and axial fields of view," in *Proc. SNM 48th Annu. Meet.*, Jun. 2001, pp. 98P–98P.

[3] M. Watanabe, K. Shimizu, T. Omura, M. Takahashi, T. Kosugi, E. Yoshikawa, N. Sato, H. Okada, and T. Yamashita, "A new high-resolution PET scanner dedicated to brain research," *IEEE Trans. Nucl. Sci.*, vol. 49, no. 3, pp. 634–639, Jun. 2002.

[4] H. Baghaei, H. Li, J. Uribe, Y. Wang, and W.-H. Wong, "Compensation of missing projection data for MDAPET camera," in *Proc. IEEE Nuclear Science Symp. Medical Imaging Conf. Record*, vol. 3, Lyon, France, Oct. 15–20, 2000, pp. 17/41–17/45.

[5] H. Li, W.-H. Wong, Y. Wang, Y. Liu, T. Xing, J. Uribe, and H. Baghaei, "Front-end electronic design based on high-yield-pileup-event-recovery method for a high-resolution PET camera with PMT-quadrant-sharing detector modules," presented at the IEEE Nuclear Science Symp. Medical Imaging Conference Record, Norfolk, VA, Nov. 10–16, 2002.

[6] Y. Liu, H. Li, Y. Wang, T. Xing, J. Uribe, H. Baghaei, and W.-H. Wong, "A programmable high-resolution ultra fast delay generator," *IEEE Trans. Nucl. Sci.*, vol. 50, no. 5, pp. 1487–1490, Oct. 2003.

[7] H. Li, T. Xing, Y. Liu, Y. Wang, H. Baghaei, J. Uribe, and W.-H. Wong, "A hotlink/network PC data acquisition and image reconstruction system for a high-resolution whole-body PET with respiratory and ECG-gated performance," *IEEE Trans. Nucl. Sci.*, vol. 50, no. 3, pp. 393–397, Jun. 2003.

[8] Y. Wang, H. Li, Y. Liu, T. Xing, J. Uribe, H. Baghaei, and W.-H. Wong, "A modular low dead-time coincidence system for high resolution PET cameras," *IEEE Trans. Nucl. Sci.*, vol. 50, no. 5, pp. 1386–1391, Oct. 2003.

[9] J. Uribe *et al.*, "Basic imaging performance characteristics of a variable field of view pet using quadrant sharing detectors," *IEEE Trans. Nucl. Sci.*, vol. 46, no. 3, pp. 491–497, Jun. 1999.

[10] M. Aykac, J. Uribe, H. Baghaei, H. Li, Y. Wang, Y. Liu, T. Xing, and W.-H. Wong, "Septa design study for volumetric imaging in positron emission tomography," *IEEE Trans. Nucl. Sci.*, vol. 49, no. 5, pp. 2097–2102, Oct. 2002.

[11] H. Baghaei, W.-H. Wong, M. Aykac, J. Uribe, H. Li, Y. Wang, Y. Liu, and T. Xing, "Brain lesions detectability studies with a high resolution PET operating in no-septa and partial-septa configurations," *IEEE Trans. Nucl. Sci.*, vol. 50, no. 5, pp. 1364–1369, Oct. 2003.

[12] J. Uribe, W.-H. Wong, H. Li, H. Baghaei, Y. Wang, Y. Liu, T. Xing, and R. Farrell, "An efficient detector production method for position-sensitive scintillation detector arrays with 98% detector packing fraction," *IEEE Trans. Nucl. Sci.*, vol. 50, no. 5, pp. 1469–1476, Oct. 2003.

[13] W.-H. Wong, "A positron camera detector design with cross coupled scintillators and quadrant sharing photomultipliers," *IEEE Trans. Nucl. Sci.*, vol. 40, no. 4, pp. 962–966, Aug. 1993.

[14] H. Li, Y. Liu, T. Xing, Y. Wang, J. Uribe, H. Baghaei, S. Xie, R. Ramirez, and W. H. Wong, "An instantaneous photomultiplier gain calibration method for PET or gamma camera detectors using LED network," presented at the IEEE Nuclear Science Symp. Medical Imaging Conf., Portland, OR, Oct. 2003.

IEEE TRANSACTIONS ON NUCLEAR SCIENCE, VOL. 51, NO. 5, OCTOBER 2004

A Comparison of Four-Image Reconstruction Algorithms for 3-D PET Imaging of MDAPET Camera Using Phantom Data

Hossain Baghaei, *Member, IEEE*, Wai-Hoi Wong, *Member, IEEE*, Jorge Uribe, *Member, IEEE*, Hongdi Li, *Member, IEEE*, Yu Wang, *Member, IEEE*, Yaqiang Liu, Tao Xing, Rocio Ramirez, Shuping Xie, and Soonseok Kim

***Abstract*—We compared two fully three-dimensional (3-D) image reconstruction algorithms and two 3-D rebinning algorithms followed by reconstruction with a two-dimensional (2-D) filtered-backprojection algorithm for 3-D positron emission tomography (PET) imaging. The two 3-D image reconstruction algorithms were ordered-subsets expectation-maximization (3D-OSEM) and 3-D reprojection (3DRP) algorithms. The two rebinning algorithms were Fourier rebinning (FORE) and single slice rebinning (SSRB). The 3-D projection data used for this work were acquired with a high-resolution PET scanner (MDAPET) with an intrinsic transaxial resolution of 2.8 mm. The scanner has 14 detector rings covering an axial field-of-view of 38.5 mm. We scanned three phantoms: 1) a uniform cylindrical phantom with inner diameter of 21.5 cm; 2) a uniform 11.5-cm cylindrical phantom with four embedded small hot lesions with diameters of 3, 4, 5, and 6 mm; and 3) the 3-D Hoffman brain phantom with three embedded small hot lesion phantoms with diameters of 3, 5, and 8.6 mm in a warm background. Lesions were placed at different radial and axial distances. We evaluated the different reconstruction methods for MDAPET camera by comparing the noise level of images, contrast recovery, and hot lesion detection, and visually compared images. We found that overall the 3D-OSEM algorithm, especially when images post filtered with the Metz filter, produced the best results in terms of contrast-noise tradeoff, and detection of hot spots, and reproduction of brain phantom structures. Even though the MDAPET camera has a relatively small maximum axial acceptance (± 5 deg), images produced with the 3DRP algorithm had slightly better contrast recovery and reproduced the structures of the brain phantom slightly better than the faster 2-D rebinning methods.**

***Index Terms*—Filtered backprojection, image reconstruction, ordered-subsets expectation-maximization, positron emission tomography (PET).**

I. Introduction

THREE dimensional (3-D) positron emission tomography (PET) data acquisition, which allows for the measurement of coincidences between all possible pairs of detectors, significantly improves scanner sensitivity over two-dimensional (2-D) acquisition. So, 3-D scanning can improve statistical accuracy in images for a given acquisition time. However, a fully utilization of the image-improving potential of the 3-D projection data may require using a fully 3-D reconstruction technique. A major problem is that fully 3-D image reconstruction is very time consuming and so not practical for routine clinical application. As a more practical approach, 3-D projection data can be rebinned into 2-D sinograms and then a 2-D image reconstruction method can be used to significantly reduce the computing time. However, due to the approximate nature of the rebinning methods, it could also degrade the image quality.

The relative performance of reconstruction methods can be strongly dependent on image analysis task. Kinahan and Karp compared 3-D reprojection (3DRP) [1] and single-slice rebinning (SSRB) [2] methods for two simulated scanners: one with standard axial acceptance (± 9 deg) and another one with large axial acceptance (± 27 deg) [3]. Simulations were for "perfect" data, that is, no scattered or random coincidences, no attenuation, and no detector resolution blurring. They found that for a standard camera for many studies the SSRB was essentially as accurate as the 3DRP method, except for a region at large radii near the axial center, but the large axial acceptance camera requires 3-D reconstruction. Matej *et al.*. evaluated performance of three fully 3-D PET reconstruction algorithms by comparing hot and cold spots detectability and structural accuracy [4]. They did not find a clear difference in the overall performance of a filtered-backprojection algorithm (3DRP), and two iterative methods: the expectation maximization maximum likelihood (EM-ML) [5] and the algebraic reconstruction technique (ART). Farquhar *et al.* compared the 3DRP, Fourier rebinning (FORE) [6], and SSRB for the high-resolution MicroPET [7]. They found that the 3DRP algorithm gives the best combination of resolution and noise performance. Reader *et al.* compared 3DRP, back-project then filter (BPF), FORE and ordered-subsets expectation-maximization (OSEM) [8] for a dual-headed camera with a very large field of view (FOV) [9]. They found that FORE +2D-FBP offered a better contrast-noise tradeoff than 3DRP and that 3D-OSEM gave the best contrast at the expense of greater image noise.

In this paper, we evaluated the relative performance of two fully 3-D image reconstruction algorithms and two 3-D rebinning algorithms for the prototype high resolution MDAPET camera. We compared a 3-D filtered-backprojection algorithm (3DRP), a 3-D iterative statistical method (3D-OSEM), and two rebinning methods, the SSRB and the FORE methods. The

Manuscript received November 9, 2003; revised April 27, 2004. This work was supported in part by the NIH-CA58980 PHS Grant, NIH-CA61880 PHS Grant, NIH-CA76246 PHS Grant, NIH-CA58980S PHS Grant, NIH-EB01481 PHS Grant, NIH-EB00217 PHS Grant, NIH-EB01038 PHS Grant, U.S. Army-Breast Cancer Research Grant, and the Texas ARP/ATP Grant 003657-0058-2001.

The authors are with the M. D. Anderson Cancer Center, University of Texas, Houston, TX 77030 USA (e-mail: hbaghaei @di.mdacc.tmc.edu).

Digital Object Identifier 10.1109/TNS.2004.834809

rebinned data were then reconstructed with the standard 2-D filtered-backprojection (2D-FBP) method.

II. Materials and Methods

A. Data Acquisition

The performance of the algorithms was evaluated by reconstructing three data sets acquired from the scan of three phantoms that were placed collinearly with the scanner axis: 1) a uniform cylindrical phantom with internal diameter of 21.5 cm; 2) a uniform 11.5-cm cylindrical phantom with four embedded small hot lesion phantoms having diameters of 3, 4, 5, and 6 mm placed at a radial distance of 2 cm near the center of the camera; and 3) the 3-D Hoffman brain phantom [10]. The brain phantom was scanned with and without embedded lesions. The three small hot lesion phantoms embedded in Hoffman brain phantom had diameters of 3, 5, and 8.6 mm. The 5-mm lesion was placed near the center of the brain phantom, and the other two lesions were placed near the periphery of the brain phantom. The 5- and 3-mm lesions were located at the central slices and the 8-mm lesion was placed in slices near the edge of the axial FOV. Since the noise and contrast performance will vary with both radial and axial position, the hot lesions were placed at different radial and axial distances and all data were acquired in 3-D.

We used the high-resolution MDAPET, a prototype 3D-PET camera, to scan the phantoms. This camera is a multiring scanner with an intrinsic transaxial resolution of 2.8 mm and a coincidence timing window of 20 ns. It has 14 detector rings covering an axial field-of-view of 3.85 cm. Each ring consists of 448 small bismuth germanate (BGO) crystals having an in-plane and axial crystal pitch of 2.66 and 2.80 mm, respectively. The camera's detection system is divided into eight independent and moveable modules. Each module can be translated radially to alter the size of the patient opening, optimizing the detection sensitivity for different body cross sections. In addition, the gantry can be tilted from vertical to horizontal positions. So, the camera has several modes of operations; we took the current data in the brain mode while gantry was in horizontal position. Fig. 1 shows the MDAPET camera in brain mode and vertical position, with the eight modules forming a closely packed octagon. In brain mode, the camera has a ring diameter of 44 cm and patient opening of 32 cm with a maximum axial acceptance angle of ± 5 deg. The detector module design, which is based on the quadrant-sharing technique, the electronics of the camera, and the imaging performance characteristics of the MDAPET camera have been previously described [11]–[17].

All data were acquired in 3-D mode with a maximum ring difference of 13 rings, which produced 196 sinograms. In the present study, each sinogram had 239 radial bins and 180 azimuthal views, and no axial or transaxial compression was performed on projection data. The radial sampling was 1.385 mm. The camera allows simultaneous imaging of 27 transaxial slices with 1.4 mm thickness. Data were acquired using ^{18}F-fluorodeoxyglucose (FDG) tracer.

To compensate for the lower sensitivity of the MDAPET camera, a result of its small axial FOV, phantoms were scanned for a longer period than is typical for a clinical size camera (13–15 cm axial FOV), and the measurements were started at a relatively higher activity (dead time maintained below 10%). For each scan we collected data comparable to what we expected for a 20-min scan with a clinical size camera. The activity concentration, at the beginning of scan, was about 1.2 μCi/ml for the noise variance study and 1.4 μCi/ml for the contrast recovery and brain phantom studies. Data acquisition time was about 1 h for each scan.

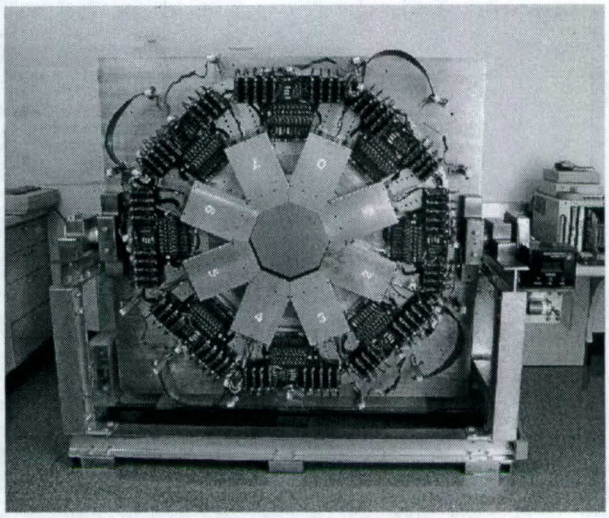

Fig. 1. The MDAPET camera in brain mode and vertical position.

Prior to 3-D image reconstruction and rebinning, several corrections were applied to the 3-D projection data. These corrections were for random coincidence, attenuation, geometric and detector pair efficiency [18]. The sinograms for random (accidental) coincidence events were measured using a second delayed coincidence window and then subtracted from the sinograms measured in the prompt window. Attenuation correction factors were calculated assuming a uniform attenuation with an attenuation coefficient equivalent to that of water. Geometric and detector pair efficiency (normalization) factors were extracted from a very high statistics data acquired with a uniform cylindrical phantom. The scatter contribution was not measured or estimated, and so no scatter correction was applied to data.

B. Reconstruction Algorithms

For the fully 3-D filtered backprojection reconstruction, we used an implementation of the 3DRP of Kinahan and Rogers [1]. The 3DRP algorithm incorporates a preliminary step in which projections that are partially measured in the 3-D data acquisition, because of the truncated cylindrical geometry of the scanner, are completed. This step is done by forward projection of an initial low statistics image obtained from the reconstruction of the sinograms with ring differences of 0 and ± 1. The calculated forward projected data are less noisy than their measured counterparts and show some loss in spatial resolution [19]. The 2-D filter was defined as the product of the 2-D filter derived by Colsher [20] and the Hamming low-pass apodization function [21]. The apodizing filter was assumed to be a radially symmetrical window [22]. The reconstruction

incorporated ring differences up to 13 and so could utilize all 196 sinograms.

For the fully 3-D iterative statistical method, we utilized an implementation of the ordered subsets expectation maximization (3D-OSEM) algorithm that was developed by the PARAPET project [23], [24]. The software was modified to include the sinogram parameters and specific geometry of the MDAPET camera. The OSEM algorithm expects Poisson distributed input data. Despite the fact that our projection data were corrected for attenuation and randoms, and were no longer Poisson distributed, we used them with OSEM method. The use of an appropriate statistical model that incorporates corrections during the reconstruction process has the potential to further improve the image quality [25], [26]. For the work presented here, we used nine subsets, so one full iteration corresponded to nine subiterations. We also studied the effect of postfiltering on the reconstructed images using a Metz filter with a full-width half-maximum of 4 mm and a power parameter of 1. For power of 0, the Metz filter is just a Gaussian filter and for higher power the midrange frequencies are more amplified than the Gaussian filter [27].

A simple way to rebin 3-D data into 2-D sinograms is the single-slice rebinning method [2]. In this method, the oblique lines of response are included in the sinogram midway between the two rings involved. Each transaxial plane is then reconstructed independently with a 2-D algorithm. This method is fast but also introduces distortions in the scanner's point-spread function. Axial blurring occurs for activity not located near the axial axis of the camera, which becomes more severe as the distance from the axis increases.

The FORE algorithm is based on an approximation of the exact Fourier rebinning formula, derived from the frequency-distance relation. The MDAPET implementation of the FORE algorithm is based on software developed by Defrise *et al.* [6], modified to include the sinogram parameters and specific geometry of the MDAPET camera.

For both rebinning methods, all 196 measured sinograms, corresponding to a maximum ring difference of 13, were rebinned into 27 planes and then reconstructed with a standard 2-D filtered-backprojection method. As we did in the case of 3DRP method, we used a Hamming apodizing window. The cutoff frequency was varied to control the contrast-to-noise tradeoff. The cutoff frequency for FBP images (3DRP and rebinning methods + FPB) and number of iterations for OSEM and parameters for postreconstruction smoothing filters were selected by making the image noise level among different techniques to be comparable. In all reconstructions, the full ring difference of 13 was used and the image pixel size was 1.385 mm by 1.385 mm. All the reconstruction algorithms were run on an Intel 2.8-GHz Pentium 4 personal computer. The typical reconstruction times for 3D-OSEM (for 5 full iterations), 3DRP, and 2D-FBP algorithms were about 32, 11, and 0.4 min, respectively.

III. Results

A. Noise Variance

For comparison of the noise level in the images reconstructed with different techniques, we calculated the coefficient of variation (CV) by using data acquired from the scan of a uniform cylindrical phantom. The phantom had an inner diameter of 21.5-cm and was filled up to height of 8 cm (about 2 cm above and 2 cm below the detector axial FOV). The total number of true + scatter counts collected was about 110 million. The CV was measured by computing σ/μ, in which σ and μ are the standard deviation and mean value over a region of interest (ROI), respectively. We used a circular ROI with a radius of 70 pixels (about 9.7 cm).

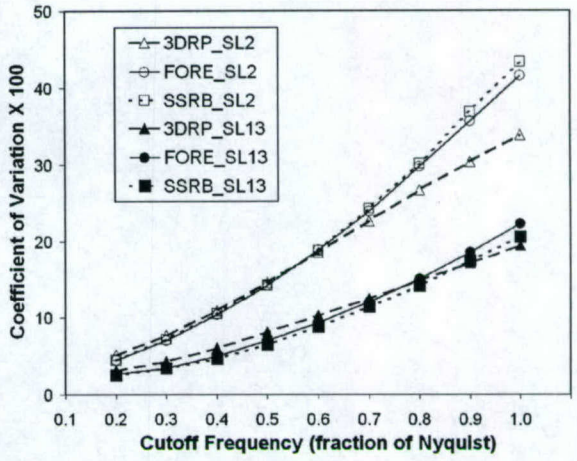

Fig. 2. CV for an edge slice (slice no. 2) and a central slice (slice no. 13) as a function of the cutoff frequency. The lines simply connect the points.

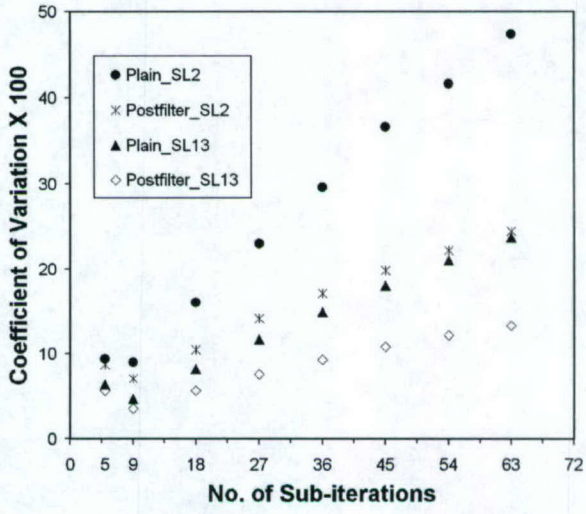

Fig. 3. Similar to Fig. 2, but for plain and postfiltered 3D-OSEM images.

The coefficient of variation for slice number 2 and number 13 versus the filter cutoff frequency is shown in Fig. 2 for FBP methods. For a cutoff frequency of 0.6–0.7 of Nyquist, all three methods had about the same CV. The CV for 3DRP algorithm showed slightly less sensitivity to change in cutoff frequency for both image planes.

In Fig. 3, the CV is plotted as a function of number of subiterations for plain 3D-OSEM (no postreconstruction smoothing) and for postfiltered images. For about 45–54 subiterations (5 to 6 full iterations), the postfiltered images showed noise variance comparable to FBP images for cutoff frequency of 0.6 to 0.7.

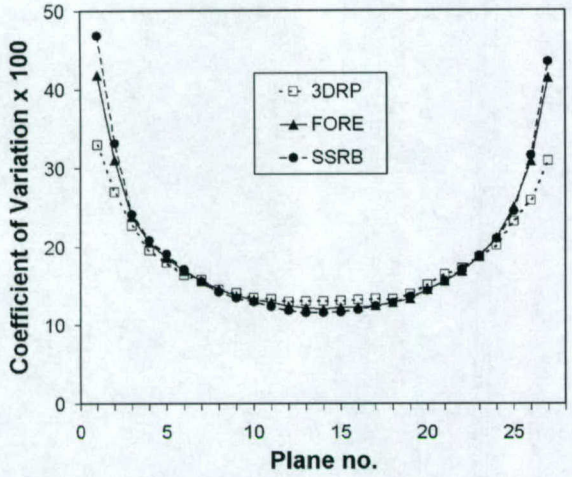

Fig. 4. Coefficient of variation plotted as a function of slice number for filtered backprojection methods. The lines simply connect the points.

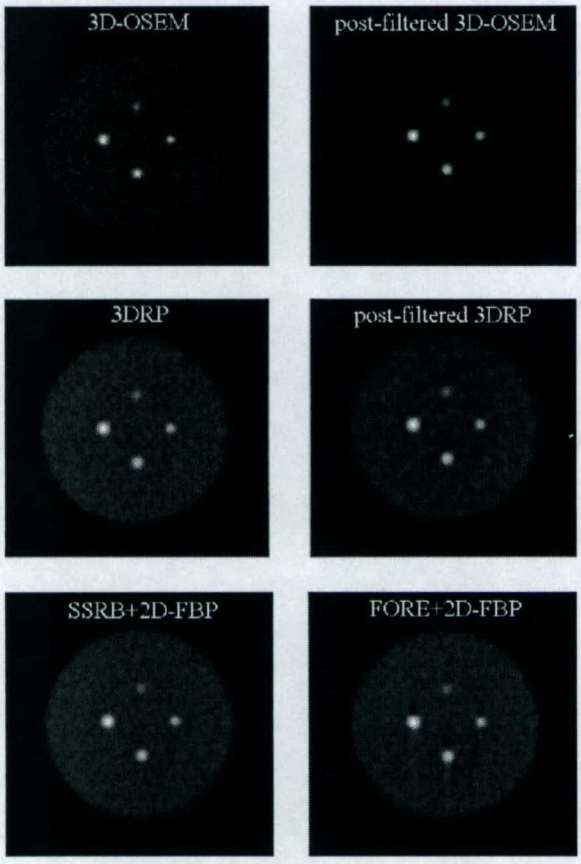

Fig. 5. Image of a central slice of the cylindrical phantom with four small lesions reconstructed with (top left) 3D-OSEM, (top right) postfiltered 3D-OSEM, (middle left) 3DRP, (middle right) postfiltered 3DRP, (bottom left) SSRB + 2D-FBP, and (bottom right) FORE + 2D-FBP. For FBP methods a hamming filter with cutoff frequency of 0.7 was used. For OSEM images five full iterations were used. The postfiltering was done with a Metz filter.

In Fig. 4, the coefficient of variation for each of the 27 image slices is shown for 3DRP and rebinning methods. We used a Hamming filter with a cutoff frequency of 0.7 of Nyquist. For all methods, the increase in noise variance seen in the edge planes, compared to the central planes, was expected because of the reduced sensitivity in planes at the edge of the axial field-of-view. For images obtained with rebinned sinograms and 2D-FBP reconstruction algorithm, compared to 3DRP images, the CV was higher for slices near the edge and slightly smaller for slices near the center. The CV for the FORE method, which was between the 3DRP and SSRB methods, was closer to the SSRB result.

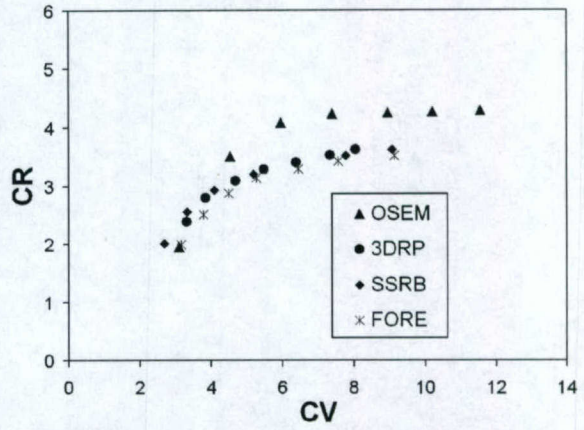

Fig. 6. The contrast-noise tradeoff for the 6 mm lesion using plain 3D-OSEM and FBP reconstruction methods (no postfiltering). A circular region of interest with a diameter of 4 pixels (about 5.5 mm) was used.

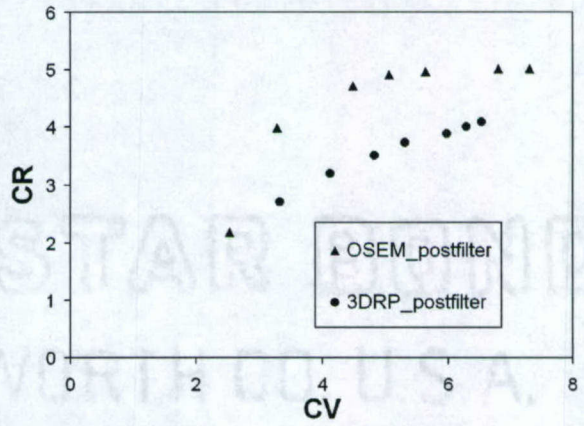

Fig. 7. The same as Fig. 6 for postfiltered images of 3D-OSEM and 3DRP algorithms with a Metz filter.

B. Contrast Recovery

For comparison of the contrast recovery (CR) we used data acquired from a scan of the 11.5-cm cylindrical phantom with four embedded small lesion phantoms. The sizes of the embedded lesion phantoms were 3, 4, 5, and 6 mm, and radioactivity concentration was the same for all lesions. The lesions were placed at the central slices (i.e., near the center of the camera axial-field-of-view) at a distance of 2 cm from the axial axis. The cylinder was uniformly filled with lower density activity up to height of 8 cm, forming a warm background. The total number of true + scatter counts collected was about 100 million.

A reconstructed image of a central slice of the warm cylinder with four hot lesions, for each of the four different methods, is shown in Fig. 5. The images of 3DRP and 3D-OSEM algorithms

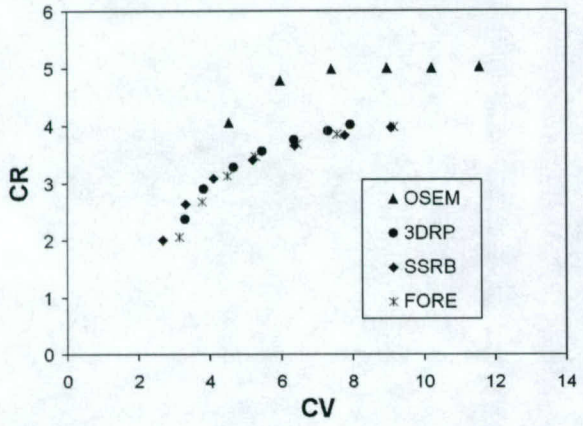

Fig. 8. The same as Fig. 6 for a ROI of one pixel (using maximum value).

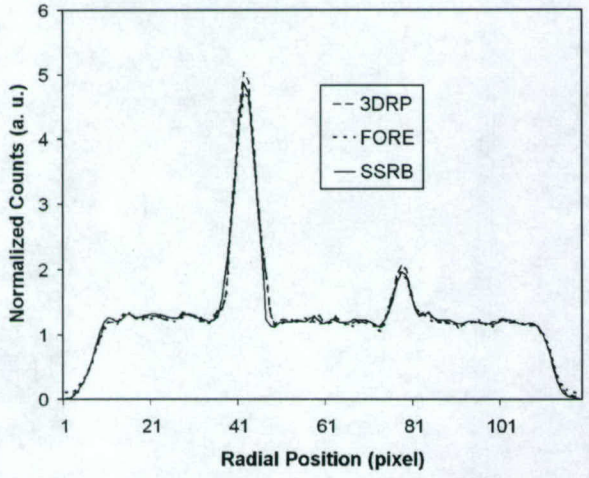

Fig. 9. A horizontal profile running along the middle of the image presented in Fig. 5 for lesions to background activity ratio of 6. The peak in the left (right) corresponds to the 6 mm (4 mm) lesion. The image was reconstructed with 3DRP, FORE + 2D-FBP, and SSRB + 2D-FBP methods (no postfiltering).

after postfiltering with a Metz filter are also shown. The Metz power was 1 and FWHM was 4 mm. The ratio of the activity concentration in the lesions to the background was 6:1. All four lesions were clearly observable for all methods.

The contrast recovery for the hot regions (small lesions) surrounded by a warm background was defined as (S-B)/B, where S and B are the average counts in a region of interest of the hot lesion and background, respectively.

Fig. 6 shows the contrast-noise tradeoff for a central slice for all methods. The CR values were extracted for the 6 mm lesion, and the CV values obtained from the warm background. In Fig. 7, results are shown for 3DRP and 3D-OSEM images after postfiltered with a Metz filter. To generate these figures, for filtered-backprojection methods the cutoff frequency was varied from 0.4 to 1 of Nyquist frequency and for the OSEM method the number of full iterations was varied from 1 to 7. We used a circular region of interest with a diameter of 4 pixels (about 5.5 mm) for hot spot. The CR was not extracted for the other lesions since their smaller sizes made defining the region of interest in a consistent way more difficult and we found the results to be less reliable. We did not observe any significant differences between

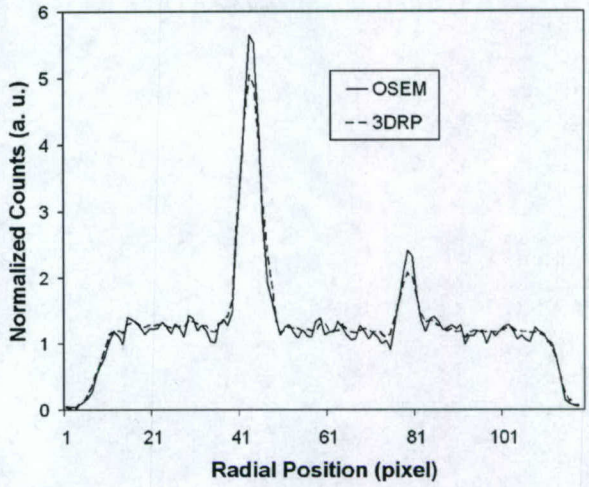

Fig. 10. Similar to Fig. 9, but for 3DRP and 3D-OSEM algorithms (no postfiltering).

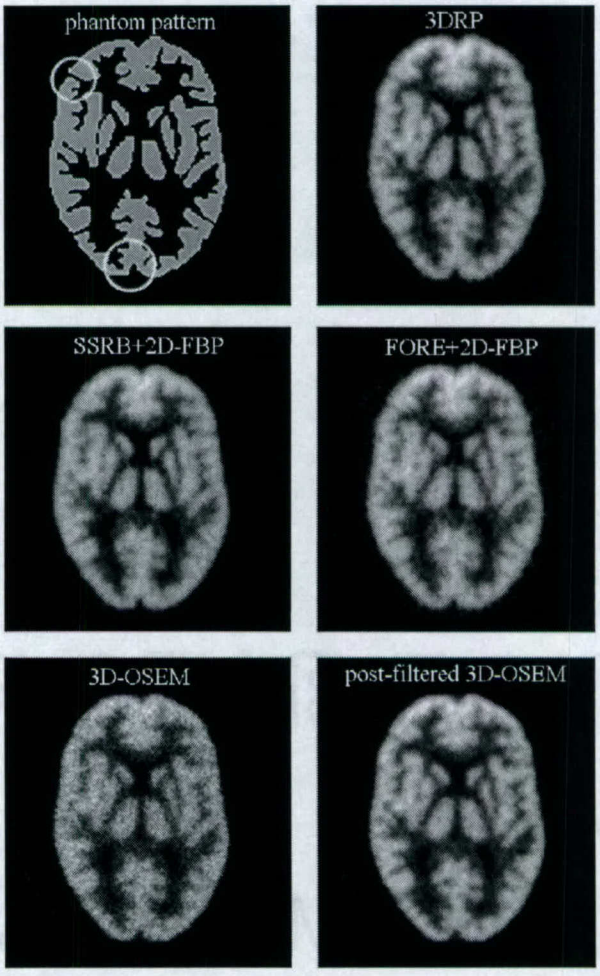

Fig. 11. A central image slice of the Hoffman brain phantom (no lesion) reconstructed with different methods compared to the phantom pattern: (top left) true phantom pattern, (top right) 3DRP, (middle left) SSRB + 2D-FBP, (middle right) FORE + 2D-FBP, (bottom left) plain OSEM, and (bottom right) 3D-OSEM + postfiltering. For better comparison two areas on the true phantom pattern are circled.

FBP methods; however, 3D-OSEM images showed higher contrast recovery for a given noise level which became more significant when followed with Metz postfiltering.

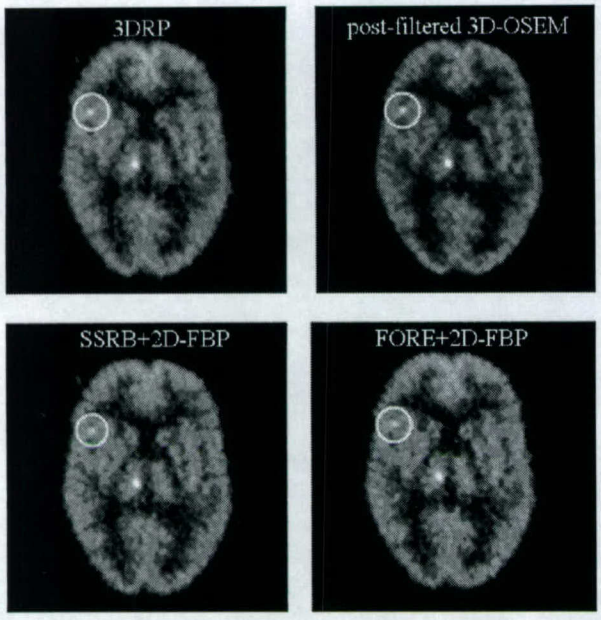

Fig. 12. An image slice (slice no. 15) of the Hoffman brain phantom with the 5-mm lesion (near center) and 3-mm lesion (circled) reconstructed with the (top left) 3DRP algorithm, (top right) 3D-OSEM + postfiltering, (bottom left) SSRB + 2D-FBP, and (bottom right) with FORE + 2D-FBP. The ratio of the activity concentration in the lesions to background was 4.3.

To study the effect of the number of samples (size of ROI) on the contrast-noise tradeoff, we repeated the calculation for the extreme case of using a ROI of only one pixel (using the maximum value) for the 6 mm lesion and results are shown in Fig. 8. Even though the results were different from those shown in Fig. 6, they showed similar behavior: no significant differences between FBP methods and 3D-OSEM images had higher contrast recovery for a given noise level.

A horizontal profile running through the middle of the 6 mm and 4 mm lesions for the image slice presented in Fig. 5 is plotted in Figs. 9 and 10. For filtered backprojection methods, the cutoff frequency was 0.7. For 3D-OSEM method, the image was obtained for five full iterations. The profile data for each image were normalized accordingly to the average counts in the background in each case. The peak to background ratio was slightly higher for the 3DRP than for rebinning methods, and the FWHM was slightly smaller for 3DRP. Images reconstructed with 3D-OSEM algorithm showed the highest contrast.

C. Brain Phantom Study

In Fig. 11, an image slice (slice no. 12) of the 3-D Hoffman brain phantom (no lesion) reconstructed with different methods are compared to the picture of the corresponding phantom's slice. The total number of true + scatter events collected was about 104 million. All methods reasonably reproduced the structures of the Hoffman brain phantom. However, the fully 3-D reconstruction methods slightly more accurately reproduced the structures of the phantom at the periphery (e.g., see the circled areas).

Fig. 12 shows a reconstructed image slice (slice no. 15) of the Hoffman brain phantom with the 5-mm and 3-mm embedded lesions when the ratio of the activity concentration in the lesion to background (gray matter) was 4.3. Fig. 13 shows a reconstructed image slice (slice no. 4) with 8.6-mm lesion when the ratio of the activity concentration in the lesions to the background was 1.46. To improve visualization of smaller lesions and also to study the effect of lesion positions, the 8.6 mm lesion phantom was placed such that it did not appear in the same slices as the smaller lesions.

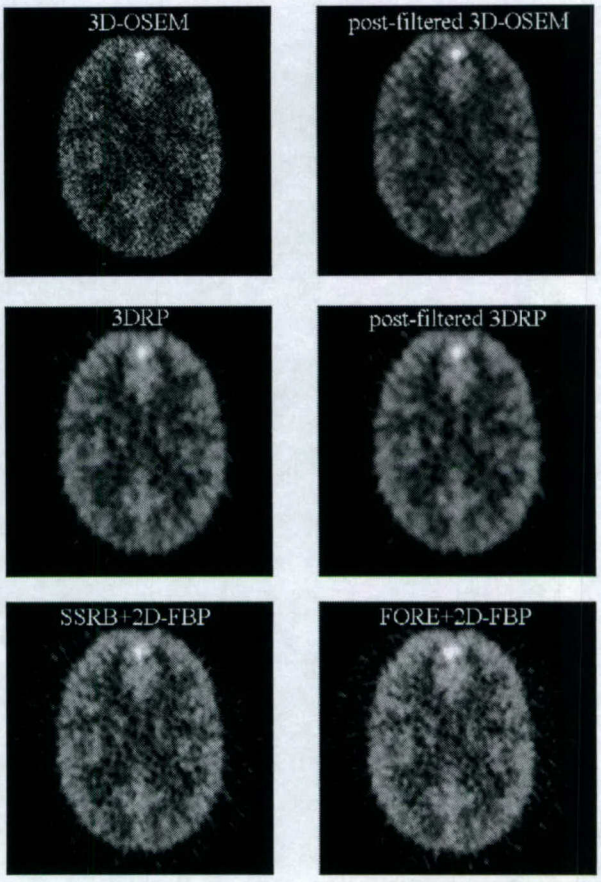

Fig. 13. An image slice (slice no. 4) of the Hoffman brain phantom with 8.6 mm lesion reconstructed with the (top left) 3D-OSEM, (top right) 3D OSEM + postfiltering, (middle left) 3DRP, (middle right) 3DRP + postfiltering, (bottom left) SSRB + 2D-FBP, and (bottom right) with FORE + 2D-FBP. The ratio of the activity concentration in the lesion to background was 1.46.

Visual comparison of the images did not show any significant differences between different reconstruction techniques in terms of detection of lesions. However, the images obtained with fully 3-D reconstruction algorithms, especially for the 3D-OSEM + postfilttered method, looked less noisy; this effect was clearer for the 8.6-mm lesion image (Fig. 13: plane no. 4). For a simple quantitative analysis we compared the profiles of the images. Fig. 14 shows the normalized horizontal profiles running through the middle of the images of the 5-mm lesion in warm background when the ratio of the activity in the hot lesion to the warm background was 5.4.

The profile figures showed that the ratio of the peak (lesion activity) to the background (gray matter) was slightly higher for the 3-D methods and highest for 3D-OSEM algorithm. The profile for the FORE + 2D-FBP, which was close to the profile for the SSRB + 2D-FBP, is not shown.

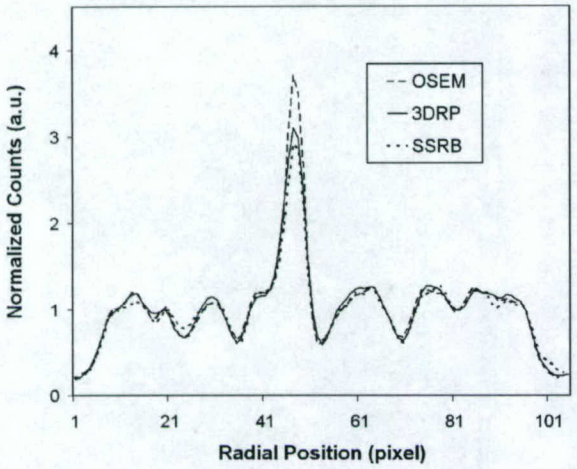

Fig. 14. A horizontal profile running along the middle of the slice presented in Fig. 12. The peak in the center corresponds to 5-mm lesion.

IV. Conclusion

We evaluated the performance of two fully 3-D reconstruction algorithms and two rebinning methods followed by 2-D image reconstruction for 3-D PET imaging of MDAPET camera. Reconstruction methods were evaluated by comparison of the noise level in images, contrast recovery of hot lesions, and by visual inspections of the reconstructed images. Small lesions were placed at different radial and axial positions in a uniform cylindrical phantom and the 3-D Hoffman brain phantom. We found that the 3D-OSEM algorithm, especially when followed by post filtering with a Metz filter, produced the best results in terms of contrast recovery, and images were less noisy, especially near the edge of the axial FOV. Both 3-D algorithms slightly better reproduced the structures of Hoffman brain phantom. The 3DRP algorithm produced images with slightly better contrast compared to the faster 3-D rebinning methods, especially at the larger radial distance. We did not observe any significant differences, in terms of contrast-noise tradeoff and visual comparison of images, between the results of SSRB and FORE algorithms perhaps because of the relatively small axial acceptance (± 5 deg) of the MDAPET camera.

Acknowledgment

The authors would like to thank the personnel of the clinical PET center of the University of Texas M. D. Anderson Cancer Center for their support in providing the FDG used for this paper.

References

[1] P. E. Kinahan and J. G. Rogers, "Analytic 3D image reconstruction using all detected events," *IEEE Trans. Nucl. Sci.*, vol. 36, pp. 964–968, Feb. 1989.

[2] M. E. Daube-Witherspoon and G. Muehllehner, "Treatment of axial data in three-dimensional PET," *J. Nucl. Med.*, vol. 28, pp. 1717–1724, 1987.

[3] P. E. Kinahan and J. S. Karp, "Figures of merit for comparing reconstruction algorithms with a volume-imaging PET scanner," *Phys. Med. Biol.*, vol. 39, pp. 631–642, 1994.

[4] S. Matej, G. T. Herman, T. K. Narayan, S. S. Furuie, R. M. Lewitt, and P. E. Kinahan, "Evaluation of task-oriented performance of several fully 3D PET reconstruction algorithms," *Phys. Med. Biol.*, vol. 39, pp. 355–367, 1994.

[5] L. A. Shepp and Y. Vardi, "Maximum likelihood reconstruction for emission tomography," *IEEE Trans. Med. Imag.*, vol. MI-1, pp. 113–122, Oct. 1982.

[6] M. Defrise, P. E. Kinahan, D. W. Townsend, C. Michel, M. Sibomana, and D. F. Newport, "Exact and approximation rebinning algorithms for 3-D PET data," *IEEE Trans. Nucl. Sci.*, vol. 16, pp. 145–158, 1997.

[7] T. H. Farquhar, A. Chatziioannou, and S. R. Cherry, "An evaluation of exact and approximate 3-D reconstruction algorithms for a high-resolution, small-animal PET scanner," *IEEE Trans. Med. Imag.*, vol. 17, pp. 1073–1080, Dec. 1998.

[8] H. M. Hudson and R. S. Larkin, "Accelerated image reconstruction using ordered subsets of projection data," *IEEE Trans. Nucl. Sci.*, vol. 13, pp. 601–609, Dec. 1994.

[9] A. J. Reader, D. Visvikis, K. Erlandsson, R. J. Ott, and M. A. Flower, "Intercomparison of four reconstruction techniques for positron volume imaging with rotating planar detectors," *Phys. Med. Biol.*, vol. 43, pp. 823–834, 1998.

[10] E. J. Hoffman, P. D. Cutler, W. M. Digby, and J. C. Mazziotta, "3-D phantom to simulate cerebral blood flow and metabolic images for PET," *IEEE Trans. Nucl. Sci.*, vol. 37, pp. 616–620, Apr. 1990.

[11] W.-H. Wong, "A positron camera detector design with cross-coupled scintillators and quadrant sharing photomultipliers," *IEEE Trans. Nucl. Sci.*, vol. 40, pp. 962–966, Aug. 1993.

[12] W.-H. Wong, J. Uribe, W. Lu, and K. Hicks, "Design of a variable field prototype PET camera," *IEEE Trans. Nucl. Sci.*, vol. 43, pp. 1915–1920, June 1996.

[13] W.-H. Wong, J. Uribe, K. Hicks, and M. Zambelli, "A 2-dimensional detector decoding study on BGO arrays with quadrant sharing photomultipliers," *IEEE Trans. Nucl. Sci.*, vol. 41, pp. 1453–1457, June 1994.

[14] W.-H. Wong, G. Hu, N. Zhang, J. Uribe, J. Wang, H. Li, H. Baghaei, and S. Yokoyama, "Front end electronics for a variable field PET camera using the PMT-quadrant-sharing detector array design," *IEEE Trans. Nucl. Sci.*, vol. 44, pp. 1266–1270, June 1997.

[15] H. Li, W.-H. Wong, N. Zhang, J. Wang, J. Uribe, H. Baghaei, and S. Yokoyama, "Prototype electronics for a variable field of view PET camera using the PMT-quadrant-sharing detector array," *IEEE Trans. Nucl. Sci.*, vol. 46, pp. 546–550, June 1999.

[16] J. Uribe, H. Baghaei, H. Li, S. Yokoyama, N. Zhang, J. Wang, F. Dobbs, and W.-H. Wong, "Basic imaging characteristics of a variable field of view PET camera using quadrant sharing detector design," *IEEE Trans. Nucl. Sci.*, vol. 46, pp. 491–497, June 1999.

[17] H. Baghaei, W.-H. Wong, J. Uribe, H. Li, N. Zhang, and Y. Wang, "Breast cancer studies with a variable field of view PET camera," *IEEE Trans. Nucl. Sci.*, vol. 47, pp. 1080–1084, June 2000.

[18] H. Baghaei, W.-H. Wong, J. Uribe, H. Li, N. Zhang, and J. Wang, "The correction factors for a high resolution variable field of view PET camera," *J. Nucl. Med.*, vol. 40, pp. 279P–279P, May 1999.

[19] S. R. Cherry, M. Dahlborn, and E. J. Hoffman, "Evaluation of a 3D reconstruction algorithm for multi-slice PET scanners," *Phys. Med. Biol.*, vol. 37, pp. 779–790, 1992.

[20] J. G. Colsher, "Fully three-dimensional positron emission tomography," *Phys. Med. Biol.*, vol. 25, pp. 103–115, 1980.

[21] H. Baghaei, W.-H. Wong, H. L. J. Uribe, Y. Wang, M. Aykac, Y. Liu, and T. Xing, "Evaluation of the effect of filtering apodization for volume PET imaging using the 3DRP algorithm," *IEEE Trans. Nucl. Sci.*, vol. 50, pp. 3–8, Feb. 2003.

[22] M. Defrise and P. E. Kinahan, "Data Acquisition and Image Reconstruction for 3D PET," in *The Theory and Practice of 3D PET*, B. Bendriem and D. W. Townsend, Eds. Dordrecht: Kluwer Academic, 1998, pp. 11–53.

[23] C. Labbe, K. Thielemans, H. Zaidi, and C. Morel, "An object-oriented library incorporating efficient projection/backprojection operators for volume reconstruction in 3D PET," in *Proc. 1999 Int. Meeting on Fully Three-Dimensional Image Reconstruction in Radiology and Nuclear Medicine*, 1999, pp. 137–140.

[24] M. Jacobson, R. Levkovitz, A. Ben-Tal, K. Thielemans, T. Spinks, D. Belluzzo, E. Pagani, V. Bettiardi, M. C. Gilardi, A. Zverovich, and G. Mitrai, "Enhanced 3D PET OSEM reconstruction using inter-update Metz filtering," *Phys. Med. Biol.*, vol. 45, pp. 2417–2439, 2000.

[25] E. U. Mumcuoglu, R. Leahy, and S. R. Cherry, "Bayesian reconstruction of PET images: Methodology and performance analysis," *Phys. Med. Biol.*, vol. 41, pp. 1777–1807, 1996.

[26] C. Comtat, P. E. Kinahan, M. Defrise, C. Michel, and D. W. Townsend, "Fast reconstruction of 3D PET data with accurate statistical modeling," *IEEE Trans. Nucl. Sci.*, vol. 45, pp. 1083–1089, June 1998.

[27] H. Baghaei, J. Uribe, H. Li, Y. Wang, M. Aykac, Y. Liu, T. Xing, and W.-H. Wong, "An evaluation of the effect of filtering in 3-D OSEM reconstruction by using data from a high-resolution PET scanner," *IEEE Trans. Nucl. Sci.*, vol. 49, pp. 2381–2386, Oct. 2002.

A Gain-Programmable Transit-Time-Stable and Temperature-Stable PMT Voltage Divider

Yaqiang Liu, Hongdi Li, *Member, IEEE*, Yu Wang, Tao Xing, Shuping Xie, Jorge Uribe, *Member, IEEE*, Hossain Baghaei, *Member, IEEE*, Rocio Ramirez, Soonseok Kim, and Wai-Hoi Wong, *Member, IEEE*

***Abstract*—A gain-programmable, transit-time-stable, temperature-stable photomultiplier (PMT) voltage divider design is described in this paper. The signal-to-noise ratio can be increased by changing a PMT gain directly instead of adjusting the gain of the preamplifier. PMT gain can be changed only by adjusting the voltages for the dynodes instead of changing the total high voltage between the anode and the photocathode, which can cause a significant signal transit-time variation that cannot be accepted by an application with a critical timing requirement, such as positron emission tomography (PET) or time-of-flight (TOF) detection/PET. The dynode voltage can be controlled by a digital analog converter isolated with a linear optocoupler. The optocoupler consists of an infrared light emission diode (LED) optically coupled with two phototransistors, and one is used in a servo feedback circuit to control the LED drive current for compensating temperature characteristics. The results showed that a six times gain range could be achieved; the gain drift was <0.5% over a 20 °C temperature range; 250 ps transit-time variation was measured over the entire gain range. A compact print circuit board (PCB) for the voltage divider integrated with a fixed-gain preamplifier has been designed and constructed. It can save about $30 per PMT channel compared with a commercial PMT voltage divider along with a variable gain amplifier. The preamplifier can be totally disabled, therefore in a system with a large amount of PMTs, only one channel can be enabled for calibrating the PMT gain. This new PMT voltage divider design is being applied to our animal PET camera and TOF/PET research.**

***Index Terms*—PET, PMT, voltage divider.**

I. Introduction

A HIGH resolution positron emission tomography (PET) detector usually has a large number of decodable crystals per photomultiplier (PMT), and the crystal decoding resolution is more dependent on a stable PMT gain; however, a PMT gain can change with many environmental factors, such as room temperature, operating time, radiation exposure, etc.; hence, a more frequent system-gain calibration is required. There are two ways to calibrate the PMT output: 1) using a variable-gain amplifier (VGA) to compensate the PMT gain and 2) adjusting the PMT gain directly. In our proposed whole-body PET camera [1], we used regular resistor voltage-dividers provided by the PMT manufacturer; hence, VGAs were used for gain calibration. However, a high-speed VGA usually has a large voltage output offset, which can vary randomly with its gain change. This requires a special baseline restoring circuit in data acquisition electronics, because all the signals are dc-coupled for high-count-rate application. In our low-cost animal PET camera [2], the detector is designed as showed in Fig. 1. An inexpensive PMT voltage divider has been designed for optimal PMT autogain calibration. The design goals for the voltage divider are low cost, compact size, a large programmable gain-range, a very small PMT signal transit-time variation, gain temperature stability, and simple control.

Manuscript received November 13, 2003; revised May 14, 2004. This work was supported in part by NIU under CA58980 PHS Grant, in part by the National Institutes of Health under PHS Grants CA61880, CA76246, CA58980S, EB01481, EB00217, and EB01038, in part by a grant from the U.S. Army-Breast Cancer Research, and in part by Texas ARP/ATP under Grant 003657-0058-2001.

The authors are with Anderson Cancer Center, The University of Texas, Houston, TX 70030 USA (e-mail: yaqiang_l@yahoo.com).

Digital Object Identifier 10.1109/TNS.2004.835776

II. Methods

For an N-stage PMT tube with a regular resistor voltage-divider, the PMT gain can be described as $G = \prod_{i=1}^{N} k_i V_i^{\alpha}$, where k_i is a proportionality constant, V_i is the interdynode voltage per stage, and the exponent α is usually between 0.6 and 0.8. Hence the PMT gain can be adjusted by changing the voltage. But by changing the high voltage, the total electron transit time inside the tube can also be changed which will require an additional lookup table to correct the time of flight for coincidence application. The transit time mean value, evaluated over a statistically large number of pulses, varies as $1/\sqrt{V}$ and is usually of the order of several tens of nanoseconds. If the PMT high voltage changes from 1150 to 1500 V, the transit time will decrease by 12%. This means that a difference of several nanoseconds in transit time should be corrected.

Fig. 2 shows our voltage divider design. A voltage between d_{N-3} and d_{N-2} should be decreased when some divider current flows in a phototransistor. This voltage drop is distributed to other dynode voltages, and then applied these voltages becomes higher slightly. This kind of varying of dynode d_{N-2} potential conduces the number of secondary electrons released from the dynode decreases and the whole PMT gain drops. However, the PMT total high voltage does not change, and transit time does not change so much. The low-voltage control electronics are isolated by an optocoupler that consists of an infrared light emission diode (LED) optically coupled with two phototransistors. For the last fourth resistor of the divider R_{N-2}, part of the current is drawn by the top phototransistor; the bottom phototransistor is used in a servo-feedback mechanism to control the LED drive current; which has the effect of compensating for the LED's nonlinear time and temperature characteristics. Changing the LED drive current will change the current of the

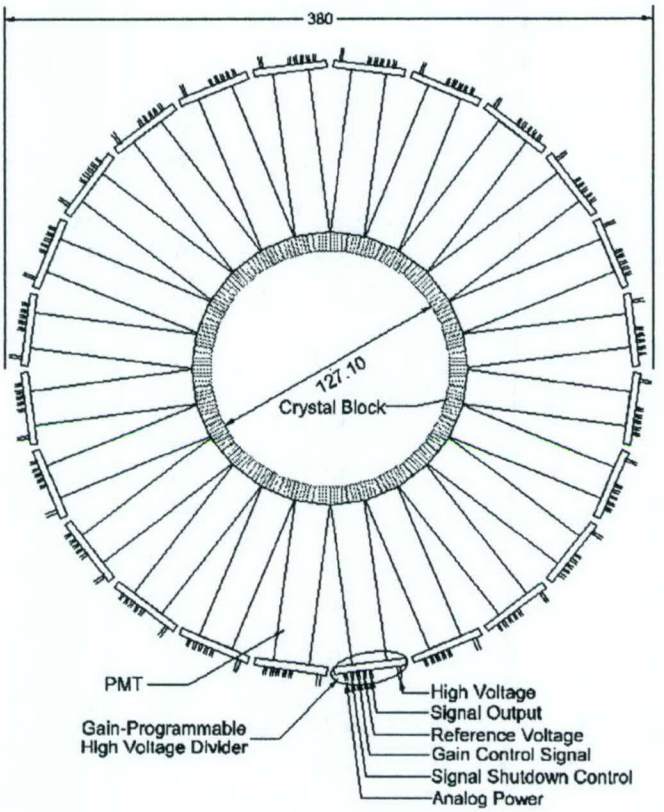

Fig. 1. The animal PET detection system where the PMT-quadrant-sharing (PQS) blocks are directly coupled to the PMT without light guides or optical fiber to maximize the light output. Each PMT mounts a gain-programmable high-voltage divider. The divider is very small to make the whole system compact.

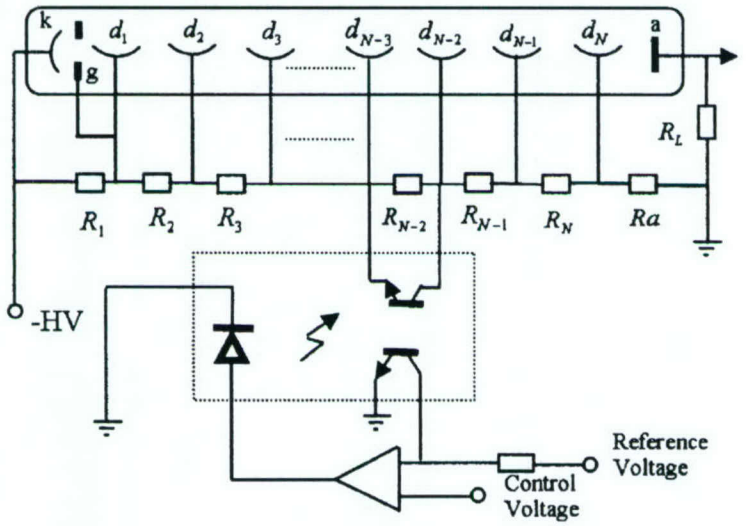

Fig. 2. A gain-programmable, transit-time-stable, and temperature-stable PMT divider design. The design maintains total high voltage, changing the distribution on the high voltage divider to adjust the PMTs gain.

top phototransistor. That will change the voltage on resistor R_{N-2}. The control voltage is driven by a digital analog converter. That makes the PMT gain programmable.

Because the cathode/first-dynode space is much larger than the space of neighboring dynodes, its contribution to transit time should be treated carefully. In our system, we used Philips XP1910 PMT, the electron path length L between the cathode and the first dynode is about three times as the length l between two neighboring dynodes. The emission photon wavelength of LSO is about 420 nm. As described in the Philips manual [3], the energy of photoelectron E_p is about 1.2 eV (written as eV_p), and the secondary-electron energy E_s is about 5 eV (written as eV_s). We have simulated the variation of PMT transit time. To make it easier, we consider the cathode, interdynodes and

TABLE I
A DIVIDER TYPE VOLTAGE RATIO. D_{10} DENOTES THE FINAL DYNODE OF THE PMT

A divider type voltage ratio (for maximum gain)							
K	D1	D2	D3	D4	...	D_{10}	A
2	1	1.5	1	1	1	1	

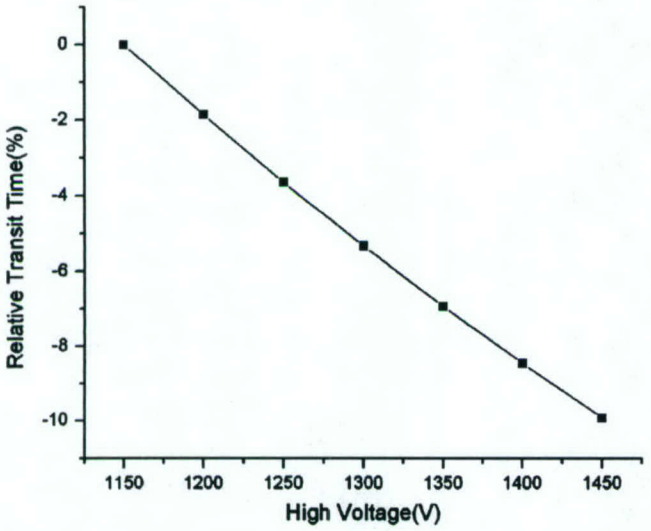

Fig. 3. Simulation result of the relative transit time as a function of the divider high voltage.

anode as parallel planes and ignore the distribution of illumination point at the cathode and the angle distribution of photoelectron and secondary emission electrons. The first time, we used the normal resistor divider, as the Photonis catalog suggests (see Table I). The transit time as a function of total high voltage can be described as shown in (1)

$$t_{\text{transit}} = \frac{l}{V}\sqrt{\frac{2m}{e}}[9(\sqrt{V+V_s}-\sqrt{V_s}) + (\sqrt{1.5V+V_s}-\sqrt{V_s})/1.5] + \frac{L}{2V}\sqrt{\frac{2m}{e}}(\sqrt{2V+V_p}-\sqrt{V_p}) \quad (1)$$

where m is the electron static mass, e is the electron charge, l represents the distance between two neighboring dynodes and the distance between the tenth dynode and the anode, L is the distance between the cathode and the first dynode, V is the voltage between the last two dynodes, $V_p = E_p/e \approx 1.2$ V, and $V_s = E_s/e \approx 5$ V. The simulation results are shown in Fig. 3.

Secondly, we adjusted the voltage V_{7_8} between the dynodes D_8 and D_7 and kept the total voltage value V_t. Transit time can be described as (2)

$$t_{\text{transit}} = \frac{l}{V}\sqrt{\frac{2m}{e}}[8(\sqrt{V+V_s}-\sqrt{V_s}) + (\sqrt{1.5V+V_s}-\sqrt{V_s})/1.5] + \frac{L}{V}\sqrt{\frac{2m}{e}}(\sqrt{2V+V_p}-\sqrt{V_p}) + \frac{l}{V_{7\_8}}\sqrt{\frac{2m}{e}}(\sqrt{V_{7\_8}+V_s}-\sqrt{V_s}) \quad (2)$$

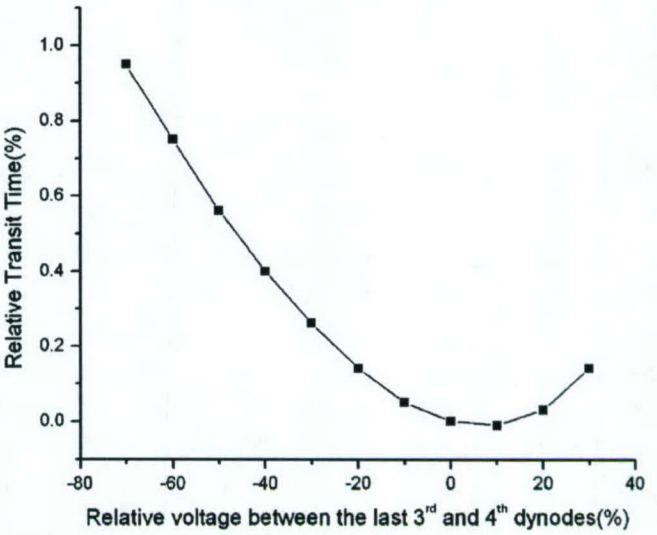

Fig. 4. Simulation of the relative transit time as a function of the relative voltage between the last third and fourth dynodes.

where m is the electron static mass, e is the electron charge, l represents the distance between two neighboring dynodes, and the distance between the tenth dynode and the anode, L is the distance between the cathode and the first dynode, V is the voltage between the last two dynodes and $V = (V_t - V_{7\_8})/10.5, V_p = E_p/e \approx 1.2$ V, and $V_s = E_s/e \approx 5$ V.

Fig. 4 shows the simulation result of the transit time as a function of the relative voltage between the two dynodes. The value changes are compared with the divider design as Table I. If you compare the two PMT gain adjustment methods, the transit time variation of the new divider is much smaller than the normal resistor divider.

III. PERFORMANCE

We have designed and implemented a gain-programmable, transit-time-stable, and temperature-stable PMT voltage divider. This divider will be used in our new animal PET system. All the performance tests have been done on an independent prototype circuit (see Fig. 5). A high-speed amplifier was built in the divider. The amplifier can be shut down totally by a control signal that makes instantaneous PMT gain calibration possible [4]. Except the high voltage supply wires, there is a flat cable that includes the gain control, reference voltage, shutdown control, output signal, and power supply.

A. Programmable Gain Range Measurement

We have implemented a new voltage divider for the Photonis XP1910 PMT and tested its range in gain variations. Fig. 6 shows that by adjusting the low control voltage from 0 V to 3.9 V, a total 6× PMT gain range can be achieved. For the same PMT and a regular resistor voltage divider, testing showed that high voltage changed from 1150 V to 1470 V, and there was 6× PMT gain change (see Fig. 7).

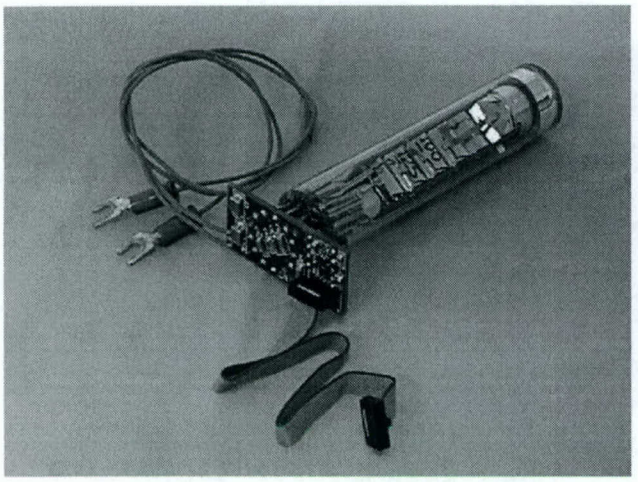

Fig. 5. A photograph of a prototype gain-programmable, transit-time-stable, and temperature-stable PMT voltage divider.

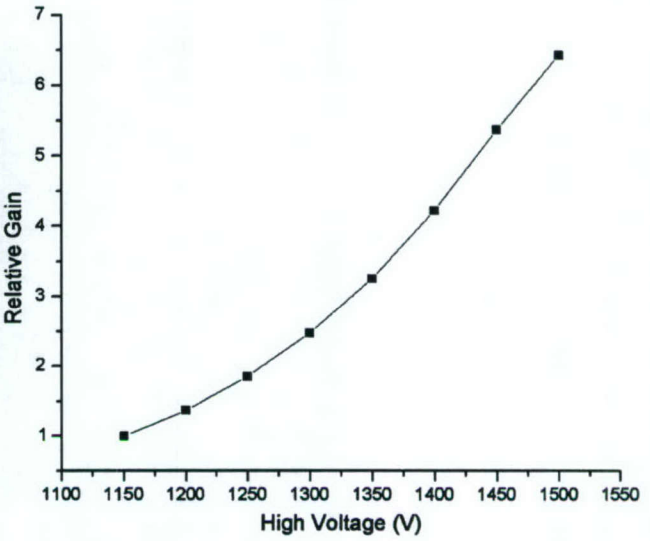

Fig. 7. The PMT gain changed about 6.4 times when the high voltage changed from 1150 V to 1500 V.

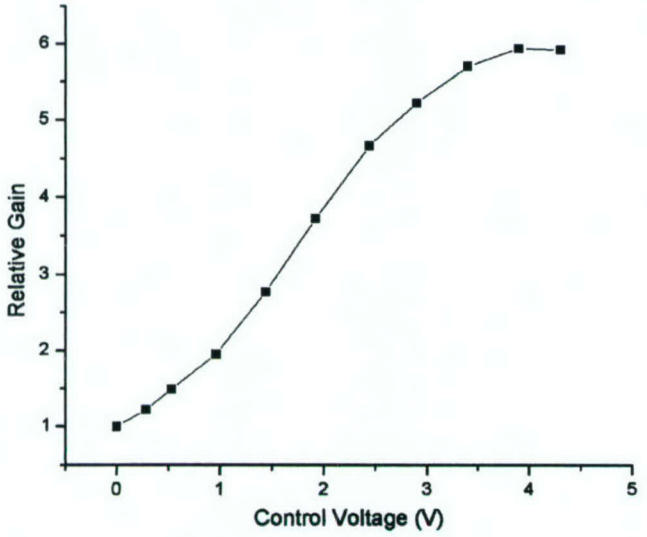

Fig. 6. The relative gain value was calculated as the gain compared with the control voltage was 0 V. It changed about six times at the whole control range. From 0 V to 3.9 V, the gain increased with the increasing control voltage.

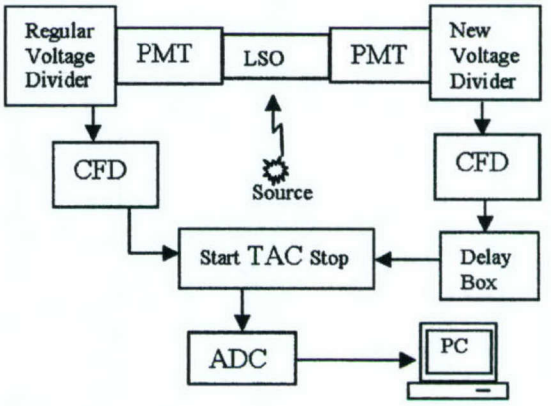

Fig. 8. PMT transit time measurement bench.

B. Transit-Time Variation Measurement

The gain-programmable voltage divider with a low transit-time variation is very important for coincidence application such as a PET, especially for time-of-flight (TOF)/PET. Our test bench was set up as shown in Fig. 8.

Two Photonis XP1912 PMTs coupled with a lutetium oxyorthosilicate (LSO) crystal were put into a black box. One PMT used a regular resistor voltage divider as the manufacture suggested; the other one used our newly proposed voltage divider. We setup a test bench with in a NIM bin: a CANBERRA time-to-amplitude (TAC) module (model 2145) was used to measure the variation of the PMT transit time. The signals from the two PMTs were triggered by two constant-fraction discrimination (CFD) modules; one CFD's output was used as the TAC's start signal, and the other one was delayed by a fixed-time and then used as stop signal. The TAC result was digitized by an analog-to-digital module (CANBERRA model 8075), and the spectrum was collected by a computer.

First, we measured the transit time for a regular resistor voltage divider. The new divider remained unchanged, but the voltage for the regular divider was changed from 1150 V to 1500 V continuously. TAC output change (transit-time change) was also measured as the PMT gain changed (Fig. 9). There was about a 2.8 ns transit-time variation.

Second, we measured transit time for our proposed gain-programmable voltage divider. The regular voltage divider remained unchanged, and the new divider's control voltage was changed from 0 V to 4.3 V. As shown in Fig. 9, there was only about 250 ps variation over the entire PMT gain range of six times.

C. Gain Temperature Drift Measurement

Using Cs-137, Photonis XP1912 PMT, and only changing the divider temperature, we also tested the new divider's gain-tem-

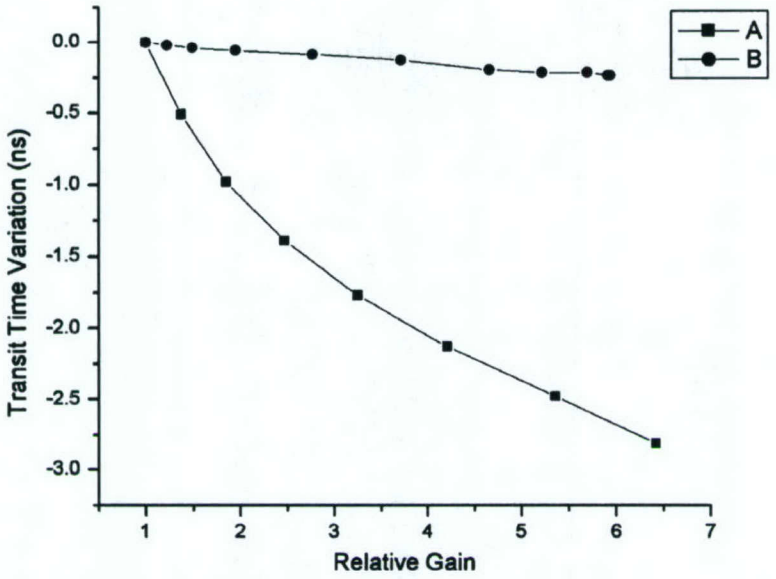

Fig. 9. Test results of transit-time variations as a function of the PMT relative gain. Curve A: regular divider. Curve B: new divider.

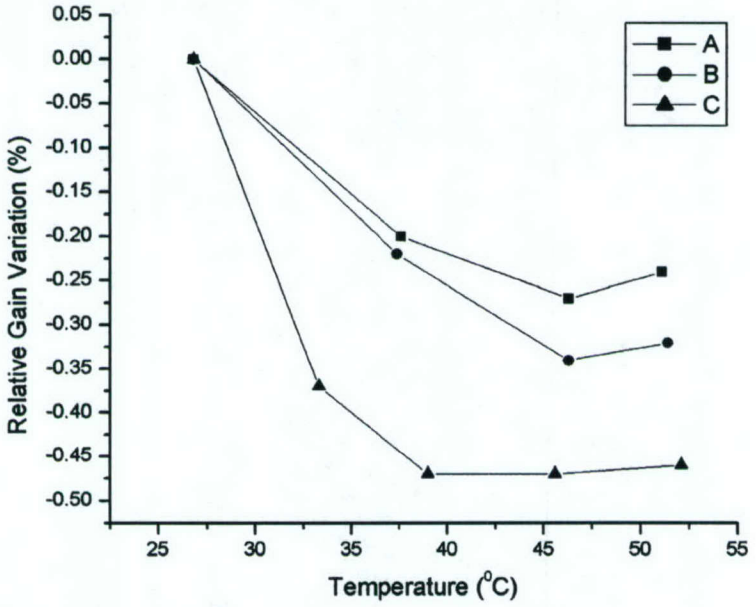

Fig. 10. Relative gain variation as a function of temperature. The new divider had good temperature stability when the divider's temperature changed from 26.8 °C to over 50 °C. Curve A: control voltage is 1.9 V; the PMT's gain change less than 0.3%. Curve B: control voltage is 2.9 V; the PMT's gain change less than 0.4%. Curve C: control voltage is 4.3 V; the PMT's gain change less than 0.5%.

perature stability at three different gain points. Fig. 10 shows that the temperature changed from 26.8 °C up to over 50 °C, and the gain change measured <0.5%.

IV. Conclusion

We have designed and constructed gain-programmable, transit-time-stable, and temperature-stable PMT voltage divider. Our test results showed that: 1) the PMT-gain had a 6× dynamic range; 2) the PMT transit-time varied less than 250 ps over the entire range; and 3) the PMT gain with the new divider design had good temperature stability. This new PMT voltage divider design is adopted for our proposed animal PET camera and can reduce camera size and production costs.

References

[1] H. Li, W. H. Wong, Y. Wang, Y. Liu, T. Xing, J. Uribe, H. Baghaei, and R. Ramirez, "Front-end electronics based on high-yield-pileup-event-recovery method for a high resolution PET camera with PMT-quadrant-sharing detector modules," in *Conf. Rec. 2002 IEEE MIC*.

[2] W. H. Wong, H. Li, S. Xie, R. Ramirez, J. Uribe, Y. Wang, Y. Liu, T. Ting, and H. Baghaei, "Design of an inexpensive high-sensitive small animal PET camera," in *Conf. Rec. 2003 IEEE MIC Conference*.

[3] Philips, "Photomultiplier tubes principles and applications,".

[4] H. Li, Y. Liu, T. Xing, Y. Wang, J. Uribe, H. Baghaei, S. Xie, R. Ramirez, and W. H. Wong, "An instantaneous photomultiplier gain calibration method for PET or gamma camera detector using a LED network," in *Conf. Rec. 2003 IEEE MIC*.

A Modular Low Dead-Time Coincidence System for High-Resolution PET Cameras

Yu Wang, Hongdi Li, *Member, IEEE*, Yaqiang Liu, Tao Xing, Jorge Uribe, *Member, IEEE*, Hossain Baghaei, *Member, IEEE*, Rocio Farrell, and Wai-Hoi Wong, *Member, IEEE*

***Abstract*—A high-resolution oncologic transformable positron emission tomography (HOTPET) is currently under development. The detector ring of the camera consists of 12 detector modules. Because the high-yield-pile-up-event-recovery (HYPER) front-end electronics are applied in this new-generation PET camera, a low-dead-time coincidence circuitry is needed to take advantage of the improved efficiency from this technology. The coincidence matching of events coming from different detector modules is performed by an AND-logic on the arriving edges of the module output timing pulses. A flexible modular architecture has been adopted to facilitate the use of the coincidence circuitry for different detector module configurations in addition to different electronic and mechanical implementations. The application of backplane/plug-in architecture and programmable devices (EPLD/FPGA) along with a digital signal processor (DSP) provide reprogrammable flexibility and expandability, allowing scans ranging from animal and breast PET to whole-body PET. There are 42 possible combinations of module pairs derived from the maximum 12 detector modules in coincidence with seven opposite modules. Both the accidental and total (true + accidental) coincidences are simultaneously collected in real time; the accidental timing shift is $\geq$200 ns relative to true events. The timing-gate window for the coincidence AND-logic can be dynamically, digitally adjusted during data acquisition between 6.5 and 16 ns to optimize the signal-to-noise ratio in the data. The prototype circuit showed that the timing accuracy is far better than 0.5 ns and the coincidence dead-time is less than 21 ns.**

***Index Terms*—Coincidence circuits, digital signal processor, positron emission tomography (PET), programmable logic array.**

I. Introduction

THE detection of coincident events is at the core of a positron emission tomography (PET) camera. In recent PET developments, the popular implementation of coincidence detection [1]–[3] is to use the digitized timing mark of the arrival of each gamma event. By comparing the timing-marks of the events from the pairs of the detector groups whose lines of response span the tomograph field-of-view, the coincidence can be picked up from the sea of the single events. This method has some advantages, such as reliability and less sensitivity to noise. On the other hand, it also has some drawbacks, such as relatively lower timing resolution, because the timing mark usually comes from a system main clock; and more bits of data to transfer requiring more complex front-end electronics and more connectors.

In our high-resolution oncologic transformable PET (HOTPET) [4], [5], we chose Pulse-AND logic as a coincidence-realization method because of its simplicity. By adopting a modular backplane/plug-in architecture and using modern programmable devices and a digital signal processor) (DSP), the coincidence circuitry is flexible and reprogrammable, so it can be used for different detector configurations to construct PET cameras for different purposes without redesigning the hardware.

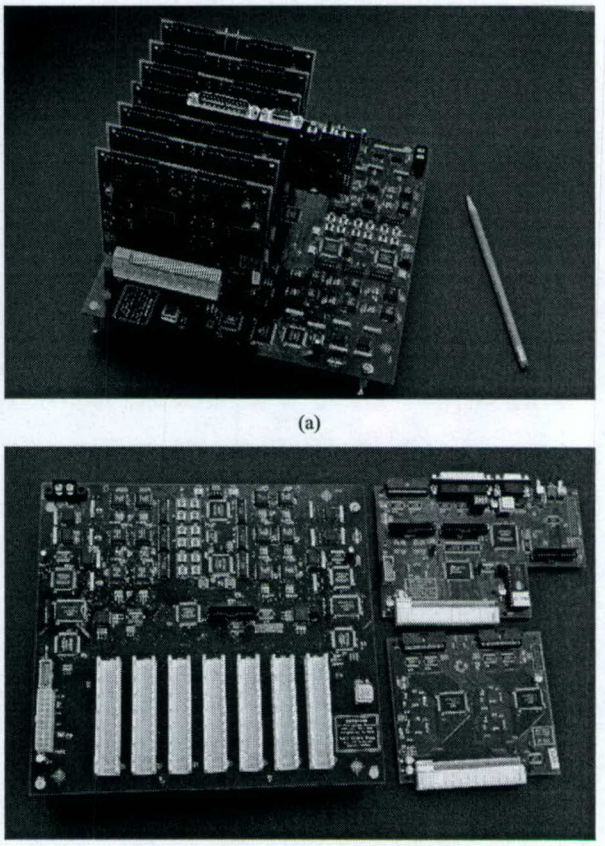

(a)

(b)

Fig. 1. Photos of (a) the whole coincidence system and (b) its comprising boards. The photo (b) shows the coincidence backplane (left), DSP controller (right top), and gamma-event FIFO buffer board (right bottom).

Manuscript received January 7, 2003; revised March 28, 2003. This work was supported in part by the NIH Grant ROI CA58980, NIH Grant ROI CA61880, NIH Grant ROI CA76246, NIH Grant ROI EB00217, NIH Grant ROI EB001038, the U.S. Army Breast Cancer Grant, the Texas Higher Education Advanced Technology Grant, the J.S. Dunn Research Foundation, and the Cobb Endowment for Cancer Research.

The authors are with University of Texas M. D. Anderson Cancer Center, Houston, TX 77030 USA (e-mail: wangy_km@yahoo.com).

Digital Object Identifier 10.1109/TNS.2003.817309

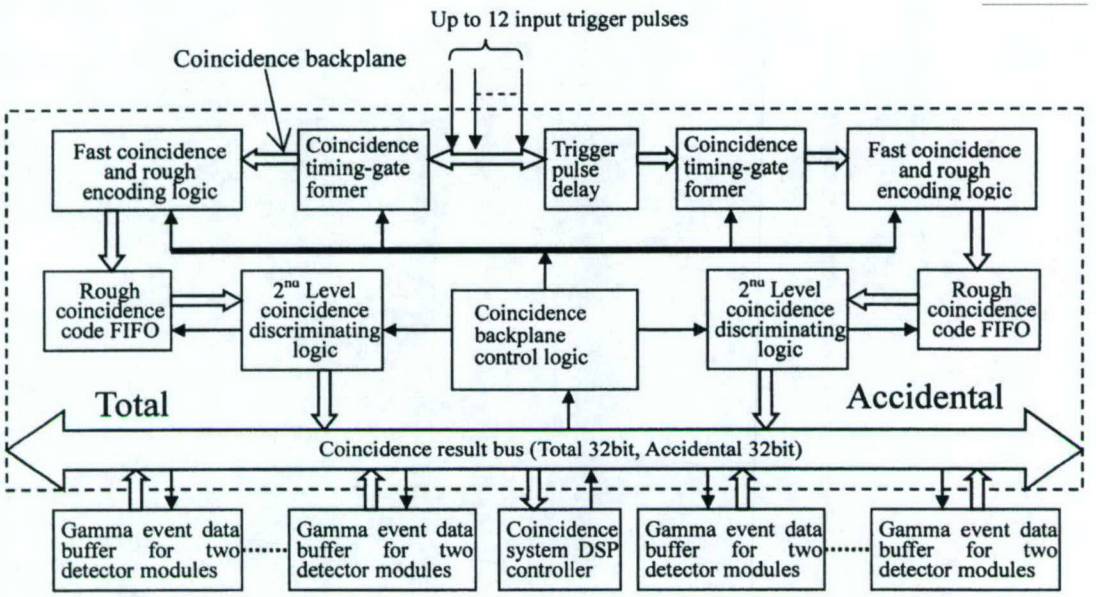

Fig. 2. Block diagram of the modular low dead-time coincidence system.

II. System Design

A. Overall Description

As shown in Figs. 1 and 2, the coincidence system is designed to be expandable/reprogrammable to cover from 2 to 12 detector modules. The backplane/plug-in architecture facilitates the tailoring of this system for different size cameras, ranging from animal and breast PET to whole-body PET. For handling up to 12 detectors, there are seven slots on the coincidence backplane to accommodate six data buffer plug-in modules and 1 DSP embedded controller. Each data buffer deals with data from two detector modules.

B. Coincidence-Logic Circuitry Backplane

The coincidence-logic circuitry is on the backplane board. Up to 12 trigger pulses from the front-end electronics [6] of the detector modules enter the backplane through coaxial cables. The rising edges of the trigger pulses represent the arrival of the gamma events. There are 42 module pair combinations derived from the 12 detector modules looking for coincidence with seven opposite modules. The events picked from the coincidence of the prompt trigger pulses are regarded as total (true + accidental) coincident events. Meanwhile, as shown in Fig. 3, each trigger pulse is delayed with a $\geq$200 ns timing shift to any of the other pulses. The events picked from coincidences of the delayed pulses are regarded as accidental coincident events. All of the delaying shifters are realized in two field-programmable gate array (FPGA) chips from Altera Inc. As a result, the logic circuits for both total and accidental coincidences are identical, simplifying the design and implementation. Moreover, performing the data delay and timing pulse delay within the coincidence system reduces the number of cables (both coaxial and flat ribbon cables) connecting the detector modules to the coincidence system and makes the design of the front-end electronics output simpler. The reduction in the number of cables has an appreciable advantage for simplifying the gantry assembly, especially for a rotating gantry.

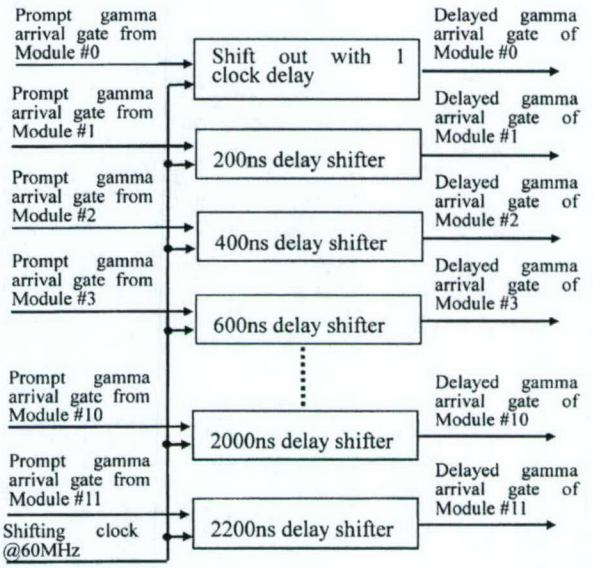

Fig. 3. Diagram of trigger shifting delay for accidental coincidences.

By using the digitally configurable delay lines, the coincidence windows can be easily changed on the fly to optimize for a better signal-to-noise ratio (SNR) in different countrate environments; for example, when scanning different parts of a body during a whole-body scan.

Because the high-yield pile up event recovery (HYPER) [5] front-end electronics are applied in this new PET camera, low dead-time is necessary for the coincidence circuitry to take advantage of its improved efficiency. To reduce the coincidence dead-time as much as possible, a two-level coincidence detection and selection logic structure has been

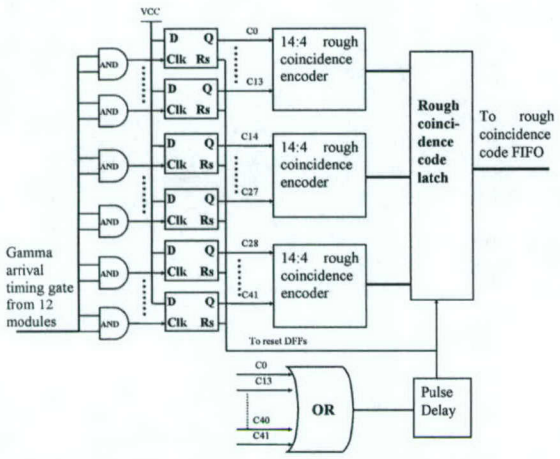

Fig. 4. The first-level rapid coincidence logic.

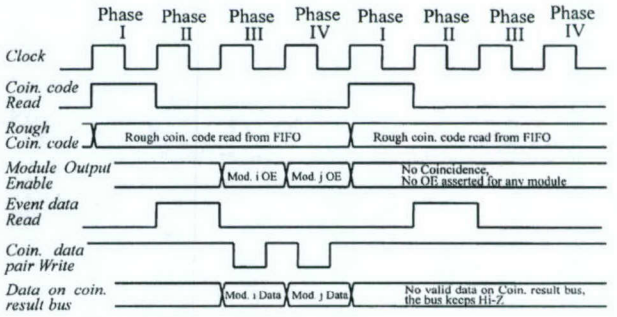

Fig. 5. Timing diagram of the second-level coincidence processing logic (module number $i < j$, $i, j \in 1, \ldots, 12$).

adopted. As Fig. 4 depicts, the first level is performed in a fast erasable programmable logic device (EPLD) for fast coincidence detection. This level basically is an AND-logic array that detects 42 probabilities of coincidences and encodes the detected coincidences roughly and rapidly, then writes the rough coincidence code into a first-in/first-out (FIFO) buffer for further selection and encoding. As long as the AND-logic detects a coincidence, it will generate a FIFO write signal to push the rough coincidence code and the data from all of the detector modules into the corresponding FIFOs at the same moment, regardless of whether some detector modules have invalid data output. The second-level discriminating logic then distinguishes and accepts the valid data while rejecting the invalid data.

Being driven by a 40-MHz clock, the second-level discriminating logic reads the rough coincidence code from the rough-coincidence-code FIFO, selects valid coincidences, then combines the data of two coincident gamma events into a 64-bit coincidence data unit. The logic monitors the almost-full and almost-empty flags of the rough-coincidence-code FIFO and performs selection operations when an almost-full flag is detected. Fig. 5 shows four phases needed for a second-level selection. In phase I, at the rising edge of the clock, a read pulse is sent to the rough-coincidence-code FIFO. A logic circuitry decodes the data fetched from the FIFO to check for a valid coincidence. If there is a valid coincidence, the logic will prepare the output-enable signals for the corresponding data-buffer FIFOs. If there is no valid coincidence, the output-enable signals will be kept invalid. In phase II, at the rising edge of the clock, a read pulse is sent to all data buffer FIFOs to pop out the data written by the write signal of the rough-coincidence-code FIFO; In phases III and IV, if a valid coincidence has been found in Phase I, the output-enable signals will allow the corresponding data FIFOs to place their data on the coincidence-result bus sequentially, and the write signal of coincidence-result FIFO will be generated once in each phase to store the 64-bit coincidence-result data. If no valid coincidence has been found in Phase I, neither the output-enable signals nor the coincidence result FIFO write signal will be asserted. The performance continues until an almost-empty flag is detected. Accordingly, the system can sustain a throughput of 10 million events per second.

Because many FIFOs are used to buffer the rough coincidence code and gamma-event data, a FIFO-output order mismatch will lead to unrecoverable coincidence misregistration. To avoid this kind of mishap, an order-checking mechanism is designed and implemented by pushing a toggling bit into all of the FIFOs. The toggling bit changes its status when there is a rough coincidence output from the first-level AND-logic. Dedicated logic circuitry on the DSP controller board monitors the output of the toggling bit from the gamma-event FIFOs and the rough-coincidence-code FIFO. If a status mismatch is detected, the monitoring logic will send an interrupt request to the DSP and then the DSP will reset and reinitialize the whole coincidence system to stop generating misregistration data.

The multiple coincident events are rejected from both the total and the accidental coincidences because the coincident events chosen from multiple coincidences will degrade the SNR rather than improve it, although the countrate may increase.

C. Gamma-Event Data FIFO Buffer

Because of the two-level coincidence-discrimination structure, fast coincidence data FIFO buffers are needed to match the speed of the low-dead-time first-level coincidence detection logic. The structure of the gamma-event data FIFO buffer is illustrated in Fig. 6. Data showing position and energy of a detected gamma-event are digitized and converted into a 32-bit data unit from the front-end electronics. The data from all detector modules are fed into the data buffer plug-in modules through flat ribbon cables. Each buffer module receives data from two detector modules. As mentioned above, once the first level coincidence circuit detects a rough coincidence, all prompt gamma-event data will be written into FIFOs synchronously. After the second-level coincidence-selection logic makes a final selection, the buffered data from the selected pair of detector modules will be sent to the coincidence-result bus on the backplane. Only FIFOs with valid coincidence data will have valid output-enable signals. Then, these data will be pushed into the coincidence-result FIFO buffer on the DSP controller board.

Since accidental coincidence detection is based on a digital timing-shift-delay method, the gamma-event data must be delayed to match their delayed trigger pulses. The data delay is

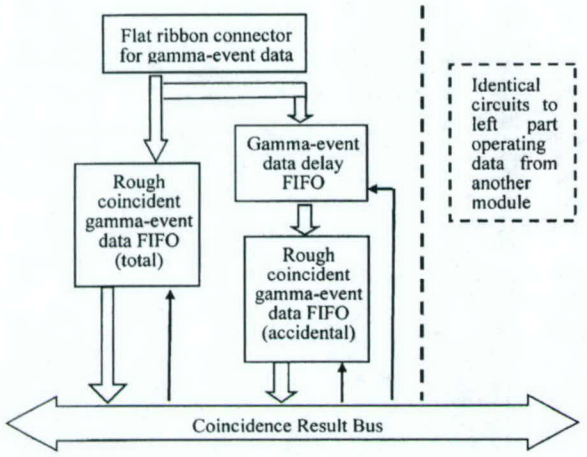

Fig. 6. Diagram of gamma-event data FIFO buffer.

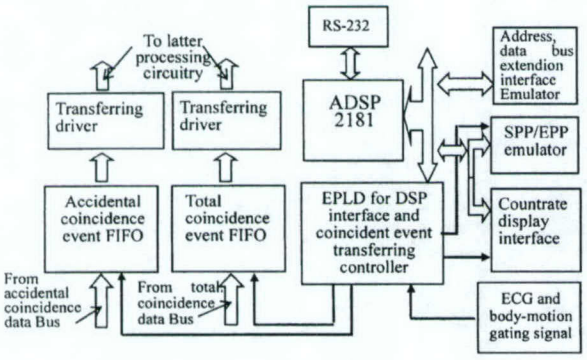

Fig. 7. Diagram of DSP-based coincidence system controller.

implemented by adding an extra FIFO before the rough-coincident-gamma-event-data FIFO, writing the data into the FIFO with a prompt trigger pulse and reading it out with a delayed trigger pulse. Then, the accidental data FIFOs perform operations similar to those of the total coincidence data FIFOs.

D. DSP-Based System Controller

The DSP controller resides in the middle slot of the seven-slot bus interface and has its own interface to the coincidence backplane to extend the control to the backplane. Fig. 7 shows the structure of the DSP-based system controller. The two major tasks of this controller are: 1) buffering the coincident result (as mentioned before) and interfacing to the latter processing circuitry, which could be a crystal look-up board or an interface to a data acquisition computer and 2) and controlling the coincidence system and potentially controlling the front-end electronics. It also has features such as: 1) communication with a host computer through an RS-232 port; 2) counting and displaying the coincidence countrate and the single countrate of each detector module in real time; and 3) monitoring and tracking electrocardiograph (ECG) signals or lung motion signals for cardiac and respiratory gating.

A custom made real-time monitor program running inside the ADSP2181 (40-Mhz clock DSP) carries out all the control tasks.

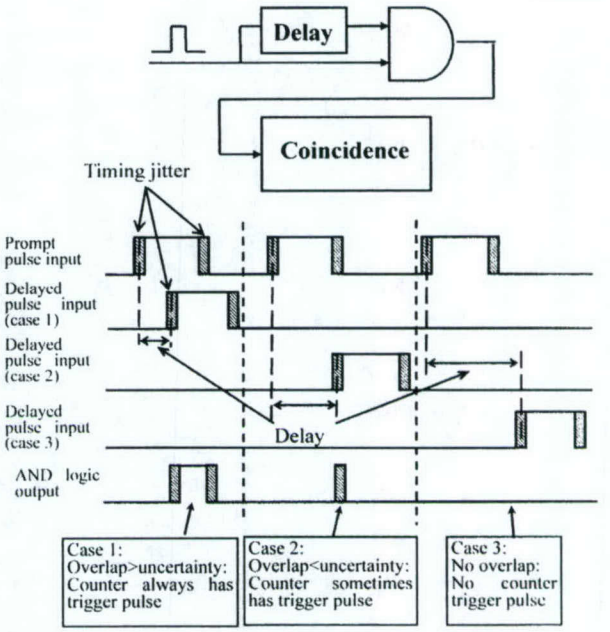

Fig. 8. Diagram of the coincidence timing uncertainty testing method.

Some basic operating-system-like functions are also available within the real-time monitor; such as loading a piece of program to the DSP, starting execution of a program, and loading the contents of a segment of memory from the DSP. These functions can facilitate some future functional development without the need to modify the monitor program and to burn it into an erasable programmable read only memory (EPROM) before finalization of the code.

A Labview based function library has also been developed to support the integration of the coincidence system with a host PC.

III. Results of Test

A. Coincidence Timing Uncertainty Test

The timing uncertainty is very important to a coincidence system. To test it, we used the method illustrated in Fig. 8. Three representative coincidence (timing overlap) cases were studied by using a variable delay to achieve the desirable timing overlap. In case 1, as illustrated in Fig. 8, the overlap between the pulse and its delayed counterpart was bigger than the timing uncertainty, so the AND-logic always enabled an output pulse. In case 2, the overlap between the pulse and its delayed counterpart was smaller than the timing uncertainty, so the AND-logic enabled an output pulse only when the timing jitter caused an overlap between the pulse and its delayed counterpart. In case 3, the overlap between the pulse and its delayed counterpart had no overlap anyway, so the AND-logic did not enable an output pulse. By counting the coincidences between a pulse and its delayed counterpart within a specific timing window, we can measure the coincidence countrate as a function of the delay. In the graph of coincidence countrate versus delay, (Fig. 9), 0.5-ns timing uncertainty is represented by the edge where the coincidence countrate drops from the maximum to zero. However, since the

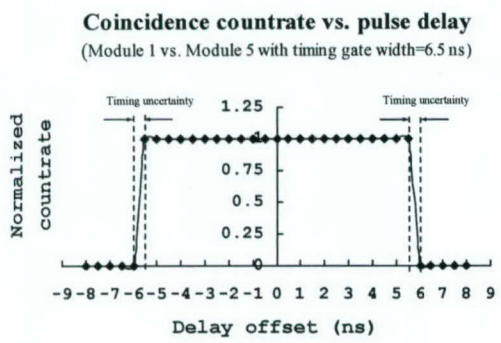

Fig. 9. Typical coincidence countrate and pulse delay relationship between two modules.

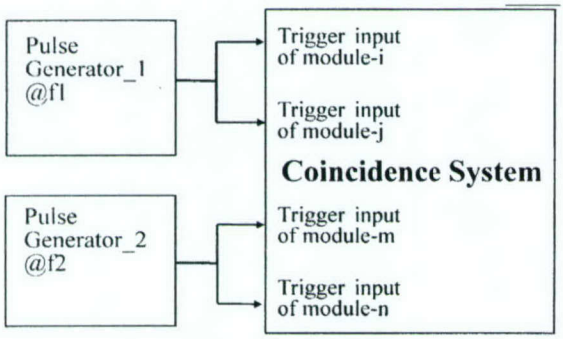

Fig. 10. Diagram of the coincidence dead-time testing method.

timing uncertainty measured in Fig. 9 was limited by the minimum delay step (0.5 ns) of our delay box (EGG DB463), we could not get a more accurate result. Therefore, the coincidence timing uncertainty induced by the coincidence system was expected to be far less than 0.5 ns.

B. Coincidence Circuitry Dead-Time Test

Encoding a coincident event takes some time. Before an encoding process is finished, the first-level coincidence detection and encoding logic must be paralyzed to guarantee that the correct module pair information is determined and recorded. The paralysis causes a short period of dead-time.

We tested the dead-time of the coincidence system and found that the dead-time was about 21 ns. The testing method is shown in Fig. 10. Two pulse generators fed pulses to the coincidence system, simulating trigger signals from front-end electronics. Each generator provided pulses to two module inputs, which were considered within the domain of coincidence combinations. Correspondingly, there were two coincidences occurring independently at the respective rates of the two generators. We can record the input pulse rate of each generator and the output rate of the coincidence logic on the system's countrate monitor. The dead-time of the circuit was calculated using (1) [7]. Table I shows the test result

$$\tau_{\text{dead}} = \frac{f_1 + f_2 - f_{\text{coin}}}{2 f_1 f_2} \tag{1}$$

TABLE I
COINCIDENCE DEAD-TIME TEST RESULT

Test-module combination	Generator_1 input rate (f_1) kHz	Generator_2 input rate (f_2) kHz	Coincidence output rate (f_{coin}) kHz	Dead-time (τ_{dead}) ns
Modules (1,4,7,10)	190.3	1303	1483	20.8
	4698	4658	8440	20.9
Modules (2,5,8,11)	721.7	788.8	1487	20.6
	4593	4442	8181	20.9
Modules (3,6,9,12)	1656	1310	2877	20.5
	4787	4066	8038	20.9
Average dead-time of all modules				20.8

where, τ_{dead} is the dead-time of the coincidence circuit, f_1 and f_2 are the input rates of the generators, and f_{coin} is the output rate of the coincidence system.

The dead-time measured with the above method is a feature of the coincidence electronics other than the dead-time of an entire system. Because of the arbitrary frequencies of two pulsers, the phase warble guaranteed the full coverage of all the timing relationships between two coincidences, although the dead-time was measured with periodic pulses, statistically it is completely equivalent to that being measured with random signal feeding.

IV. CONCLUSION AND DISCUSSION

In this paper, we present a modular, low-dead-time coincidence system for modular PET cameras. The system is based on a fast coincidence discrimination structure consisting of a first-level rapid AND-logic and a clock-driven second-level fine selection logic. A modular backplane/plug-in architecture that we have adopted supports different detector module configurations in addition to different electronic and mechanical implementations.

The coincidence system functionally works well for as many as 10 000 000 coincident events per second (with periodic testing pulses). The gate width for the AND-logic is on-line changeable from 6.5 to 16 ns and has better than 0.5 ns adjustment accuracy. The coincidence timing uncertainty is far less than 0.5 ns. The dead-time of coincidence logic is around 21 ns which is smaller than that found in normal designs.

The test results satisfy our design specifications. However, improvement will be pursued. The first improvement would be to reduce timing gate window from current 6.5 ns because a large timing gate limits the coincidence timing resolution. For a PET camera with bismuth germinate crystals (BGO), like our HOTPET, the relatively wide timing gate is good enough. However, for systems with faster scintillators, such as lutetium oxyorthosilicate (LSO) or gadolinium oxyorthosilicated (GSO), the 6.5 ns gate may not be suitable. Though the improvement might make the circuit a little more complex, we believe a narrower timing gate can be accomplished.

REFERENCES

[1] H. M. Dent *et al.*, "A real time digital coincidence processor for positron emission tomography," *IEEE Trans. Nucl. Sci.*, vol. NS-33, pp. 556–559, Feb. 1986.

[2] D. F. Newport *et al.*, "Coincidence detection and selection in positron emission tomography using VLSI," *IEEE Trans. Nucl. Sci.*, vol. 36, pp. 1052–1055, Feb. 1989.

[3] J. W. Young *et al.*, "Optimum bandwidth usage in digital coincidence detection for PET," in *Proc. Conf. Rec. 1993 IEEE MIC Conf.*, vol. 2, 1993, pp. 1205–1208.

[4] W. H. Wong *et al.*, "Feasibility of a high speed gamma camera using the high-yield-pile-up-event-recovery (HYPER) method," *J. Nucl. Med.*, vol. 42, no. 4, pp. 624–632, .

[5] W.-H. Wong *et al.*, "The design of a high-resolution transformable whole body PET camera," *IEEE Trans. Nucl. Sci.*, vol. 49, Oct. 2002. IEEE MIC Conf. Rec. 2001.

[6] H. Li *et al.*, "A new pileup-provention front-end electronic design for high resolution PET and Gamma Camera," in *Proc. IEEE Nuclear Science Symp. Conf. Rec.*, vol. 4, Nov. 2001, pp. 1969–1973.

[7] W. R. Leo, *Techniques for Nuclear and Particle Physics Experiment*. Berlin, Germany: Springer-Verlag, 1987, pp. 114–118.

Brain Lesion Detectability Studies With a High Resolution PET Operating in No-Septa and Partial-Septa Configurations

Hossain Baghaei, *Member, IEEE*, Wai-Hoi Wong, *Member, IEEE*, Jorge Uribe, *Member, IEEE*, Hongdi Li, *Member, IEEE*, Mehmet Aykac, Yu Wang, Yaqiang Liu, Tao Xing, and Rocio Farrell

Abstract—**Three-dimensional (3-D) positron emission tomography (PET) acquisition in comparison to two-dimensional (2-D) PET acquisition improves the sensitivity of the system at the cost of higher scatter and accidental coincidence contributions. A partial-septa system (i.e., some detector rings lack septa) allowing "partial" 3-D acquisition may provide a better alternative to the 2-D acquisition and full 3-D acquisition. We investigated the effect of partial-septa configuration on the noise equivalent sensitivity and lesion detectability for a high-resolution PET camera. We used the MDAPET camera to detect small lesions in brain images obtained from scan of the Hoffman brain phantom. For this work, three small lesion phantoms with diameters of 3, 5, and 8.6 mm were embedded into the 3-D Hoffman brain phantom. The activity concentration ratio of the lesions to the brain gray matter ranged from 1.5 to 10. Data for the hot lesion phantoms and the normal 3-D Hoffman brain phantom were taken separately. Then, the two sets of sinogram data were selectively combined to generate the sinogram data for the desired standard uptake values (SUVs). In the reconstructed images, we could clearly see the 8.6 mm lesion, with or without septa, at even the lowest activity ratio that we measured. The 5 mm and 3 mm lesions were observable at activity ratios of 2.2 and 5.4, respectively. We found that even though the use of septa increased the noise equivalent count rate and lowered the image noise, it did not necessarily improve lesion detectability. In partial-septa configurations, the white matter regions of the brain images had lower counts and the images visually looked better than no-septa images; however, images taken in the no-septa configuration had slightly higher contrast.**

Index Terms—**3-D PET data acquisition, lesion detectability, positron emission tomography (PET), septa.**

I. Introduction

THE three-dimensional (3-D) positron emission tomography (PET) acquisition has higher sensitivity than two-dimensional (2-D) PET acquisition, but at the cost of higher scatter and accidental coincidence. 3-D PET also has the potential to reduce data acquisition time compared to 2-D PET. Currently, commercial PET cameras operate in two extreme modes of no-septa (3-D acquisition mode) and all-septa (2-D acquisition mode) configurations. Several investigators have studied the effect of all-septa and no-septa configurations on lesion detectability and noise characteristics of images and have found that 3-D acquisition mode may have advantages in imaging brain, small patients, and animals, and especially at low activity levels they report that it can outperform 2-D mode acquisition [1]–[4]. Recently, a hybrid PET design was proposed to acquire projection data in both 2-D and 3-D modes simultaneously by using rotating partial-ring septa [5]. Several investigators also have studied optimal septa spacing in gamma cameras for PET imaging [6], [7].

A partial-septa system, in which full-ring septa are inserted between only some of the detector rings, may provide a better alternative than the 2-D acquisition and full (no-septa) 3-D acquisition. In this study, intermediate septa designs were used to reduce the scatter and accidental coincidence with an acceptable sensitivity loss by using a 3-D PET camera that could operate in no-septa mode or with a partial-septa system. In our previous work, a Monte Carlo simulation was performed to evaluate possible septa designs, and for several septa configurations the noise equivalent count (NEC) rate was measured and compared [8]. In this work, we studied the effect of using partial-septa on brain lesion detectability.

II. Materials and Methods

A. Scanner and Phantoms

For this study, three small lesion phantoms were embedded into the 3-D Hoffman brain phantom [9]. The inner diameters of the embedded lesion phantoms were 3, 5, and 8.6 mm, and all had the same standard uptake values (SUVs). The approximate ratio of the activity concentration in the lesions to the activity in the background (brain gray matter regions) ranged from 1.5 to 10. The lesions were placed into the brain phantom white matter regions. The 5 mm lesion was placed near the center of the brain phantom, and the other two lesions were placed near the periphery of the brain phantom.

To scan the phantoms, we used the high-resolution MDAPET, a prototype PET camera. This camera is a multiring scanner with an intrinsic transaxial resolution of 2.8 mm. Each ring contains 448 bismuth germanate (BGO) crystals having an in-plane and axial crystal pitch of 2.66 and 2.80 mm, respectively. The detectors are grouped into blocks of 7×7 crystals. The camera detection system is divided into eight independent, movable modules. Each module can be translated radially to alter the size of the patient opening, optimizing the detection sensitivity for different

Manuscript received December 3, 2002; revised June 28, 2003. This work was supported in part by the NIH Grant RO1 CA58980, NIH Grant RO1 CA61880, NIH Grant RO1 CA76246, NIH Grant RO1 EB00217, NIH Grant RO1 EB001038, U.S. Army Breast Cancer Grant, Texas Higher Education Grant, John S. Dunn Foundation Research Grant, and the Cobb Foundation for Cancer Research.

The authors are with the University of Texas M. D. Anderson Cancer Center, Houston, TX 77030 USA (e-mail: hbaghaei@di.mdacc.tmc.edu).

Digital Object Identifier 10.1109/TNS.2003.817967

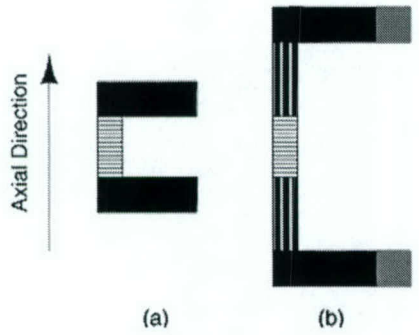

Fig. 1. (a) Original axial view of a detector module in MDAPET camera. (b) Axial view of a modified detector module.

body cross-sections. Also the gantry can be rotated during data acquisition in 0.10° steps up to 45°. For this study the gantry was rotated during the data acquisition in 1° steps to fill the gaps in the sinograms caused by the empty space between modules. The detector module design, which is based on a quadrant-sharing technique, and the electronics of the PET camera were described previously [10]–[14], [21]. The imaging performance characteristics of the camera were also discussed previously [15], [16].

MDAPET camera has 14 detector rings covering an axial field-of-view (FOV) of 38.5 mm, as shown in Fig. 1(a), which is much smaller than a clinical camera. In order to simulate more closely the performance of a clinical size camera, the detector modules were modified axially to extend from 38.5 mm to 131 mm by placing the side shields farther apart as shown in Fig. 1(b). Since there is no detector ring in the extended region, the maximum ring difference and corresponding axial acceptance angle of a clinical camera could be larger than those of the modified MDAPET camera. For this work we used a maximum ring difference of 13 for image reconstruction. Extensions added to each side of each detector module consisted of three layers of lead and aluminum as a BGO substitute to take into account for inter-crystal scattering. Each lead foil (3 mm thick) was sandwiched between two 1.5 mm thick aluminum foils. Each side shield was extended from 60 mm to 85 mm to reduce the radiation coming from outside the FOV.

Fig. 2 shows an axial view of the modified version of the MDAPET detector module for three septa configurations: (a) no-septa; (b) partial 5-septa with inter-gap separation between septa of 2.01 cm; and (c) partial 7-septa with inter-gap separation between septa of 1.46 cm. Septa consisted of 2 mm of lead in all designs.

B. Data Collection

To minimize the number of imaging sessions, we acquired two separate data sets. We first acquired data for the hot lesion phantoms and then acquired data for the warm (normal) Hoffman brain phantom. When the first data set (hot lesions data) were acquired, the hot lesions were placed inside the Hoffman brain phantom filled with nonradioactive water (cold background) to simulate the attenuation and scatter effects. For the second set of data, the lesion phantoms were removed and the Hoffman brain phantom was filled with FDG solution.

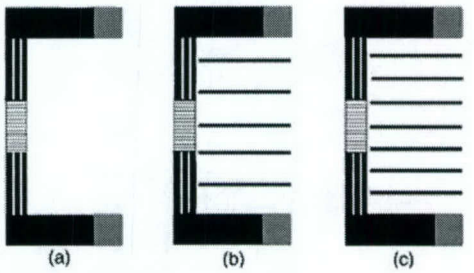

Fig. 2. Axial view of a modified MDAPET module with three different septa configurations: (a) no-septa; (b) partial 5-septa; and (c) partial 7-septa.

We took data in the brain mode, one of several modes of operation of the MDAPET camera. In this mode, the camera has a ring diameter (the distance between two facing detector modules) of 44 cm. To compensate for the lower sensitivity of the MDAPET camera, due to its small "real" axial field of view, the brain phantom was scanned for a longer period than is typical for a clinical study, and the measurements were started at a relatively higher activity and stopped at a lower activity than they would be in a clinical study. In addition, for the second set of data of measuring the warm background, scanning was repeated three times which required the phantom be positioned precisely. Then the data were summed to obtain a number of true events equivalent to that would be collected in a clinical study after a typical injected dose of 10 mCi ^{18}F-fluorodeoxyglucose (FDG) in a 20 minutes scan. This procedure could slightly blur the brain phantom structures but should not have any important effect on lesion detectability (the hot lesions data were all taken in one setup).

All data were acquired in 3-D mode with an axial acceptance of 13 rings, which produced 196 sinograms. In the present study, each sinogram had 239 radial bins and 180 azimuthal views, and no axial or transaxial compression was performed on projection data. The radial sampling was 1.385 mm.

C. Data Analysis

We selectively combined the two sets of sinogram data that were acquired separately to generate the sinogram data for the desired SUVs. This combination method greatly reduced the number of required measurements for different lesion uptake and also eliminated the effect of the 'cold' walls of the lesion phantoms that exists when hot lesions and the warm background are measured simultaneously [16], [17]. However, this technique requires the phantom be positioned precisely and the concentration ratio of the tissue and background and the accidental coincidence be known. Further, the effect of the dead time also becomes more important. This sinogram summing method allows all the different SUVs data for lesions to be taken in one experimental period by collecting the different SUVs data as the activity decays.

Prior to image reconstruction, the projection data were corrected. These corrections included random coincidence subtraction, attenuation correction, geometric, and detector-pair efficiency corrections [18]. The attenuation correction was obtained by calculating the attenuation length from the shape

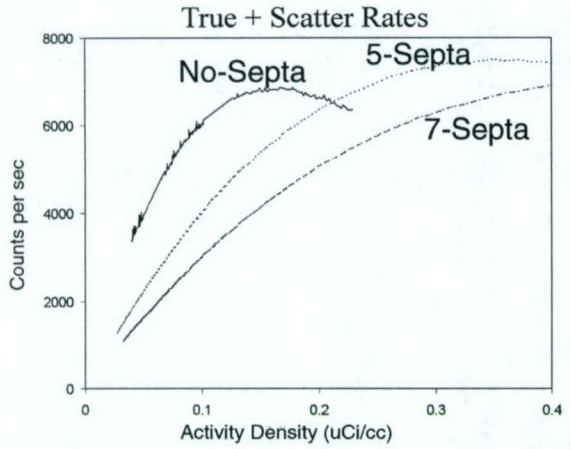

Fig. 3. Comparison of true+scatter count rates for three detector configurations: no-septa, 5-septa, and 7-septa.

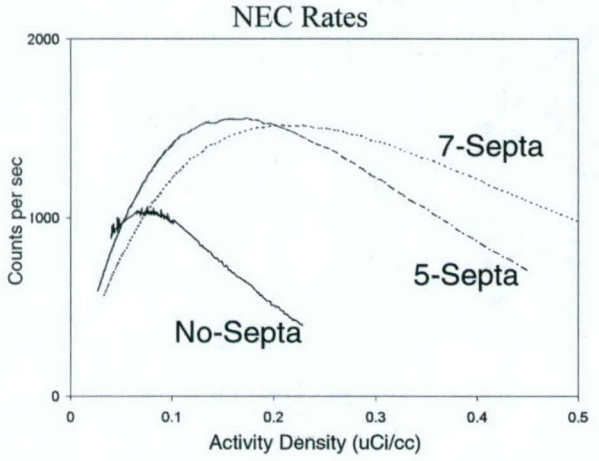

Fig. 4. Comparison of NEC rates for three detector configurations: no-septa, partial 5-septa, and 7-septa.

of the phantom (cylinder) and assuming uniform attenuation. All data were acquired with the FDG tracer.

For image reconstruction we used the 3-D-reprojection algorithm with a Butterworth filter [19], [20]. The camera allows simultaneous imaging of 27 transaxial image slices with 1.4-mm slice thickness. Each reconstructed image had 239 × 239 pixels.

III. Results

A. NEC Study

The NEC was measured for a standard uniform NEMA (National Electrical Manufacturers Association) phantom 21 cm in diameter and 18 cm high. For these measurements 1.5 mCi, 2.9 mCi and 3.5 mCi of FDG was added to the water phantom for no-septa, 5-septa, and 7-septa configurations, respectively. True (unscattered and scattered) and accidental coincidence count rates were measured in full 3-D acquisition mode as the activity decayed for each configuration. The true + scatter count rates for the three configurations are compared in Fig. 3. The scatter fraction values used for NEC calculation were 37.9% for no-septa, 27.0% for 5-septa and 24.5% for 7-septa configurations [8]. The NEC for the three configurations is shown in Fig. 4. It is clear that, in terms of NEC rate, for activity of 0.07 μCi/cc or higher the MDAPET scanner in brain mode performed much better for 5-septa, and 7-septa configurations than for the no-septa configuration.

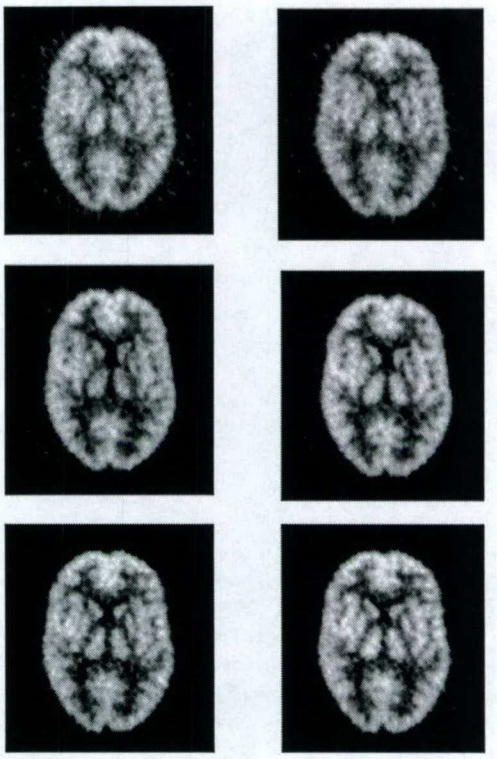

Fig. 5. Two image slices of the Hoffman brain phantom reconstructed with the 3-DRP algorithm for three different septa configurations: (top) no-septa, (middle) 5-septa, and (bottom) 7-septa.

The no-septa configuration reached its NEC peak rate around 0.07 μCi/cc. In the typical brain studies, activity concentration is much higher than 0.07 μCi/cc for a 10 mCi FDG injection. Therefore for the prototype MDAPET camera for a typical brain study such intermediate septa configurations as the partial 5-septa or 7-septa configurations may be more appropriate and for no-septa configuration a lower activity (e.g., 5 mCi) may be more appropriate.

B. Lesion Detectability Study

Fig. 5 shows two reconstructed image slices of the Hoffman brain phantom without embedded lesion phantoms for no-septa (top), 5-septa (middle), and 7-septa (bottom) configurations. The images show that, as the number of septa increased, the white matter (background) contribution became less observable, the gray matter contribution became more pronounced, and image quality visually improved. The total true coincidence events collected were 76 000 000, 57 000 000, and 33 000 000 for no-septa, 5-septa, and 7-septa configurations, respectively. The scatter fraction from Hoffman brain phantom studies was estimated to be 31.3%, 20.5% and 14% for the no-septa, 5-septa and 7-septa cases. The ratio of NEC for the 5-septa to no-septa case was calculated to be about 1.25.

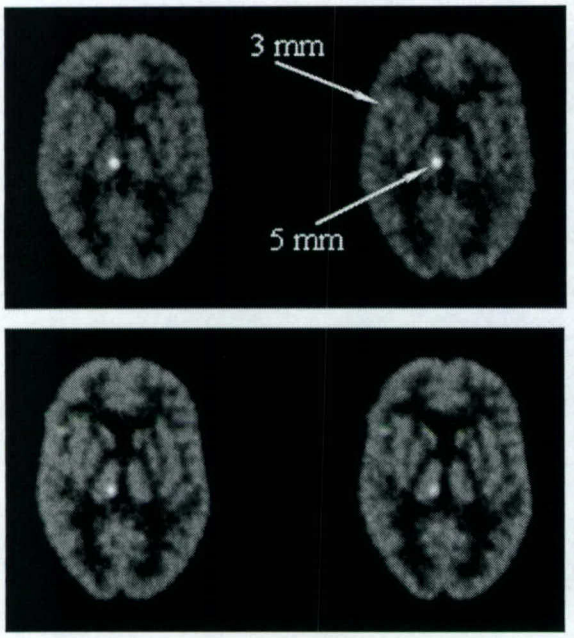

Fig. 6. Two image slices of the Hoffman brain phantom with 3 mm and 5 mm lesions for two different septa configurations: (top) no-septa and (bottom) 5-septa. The ratio of activity concentration of the lesions to gray matter was 5.4.

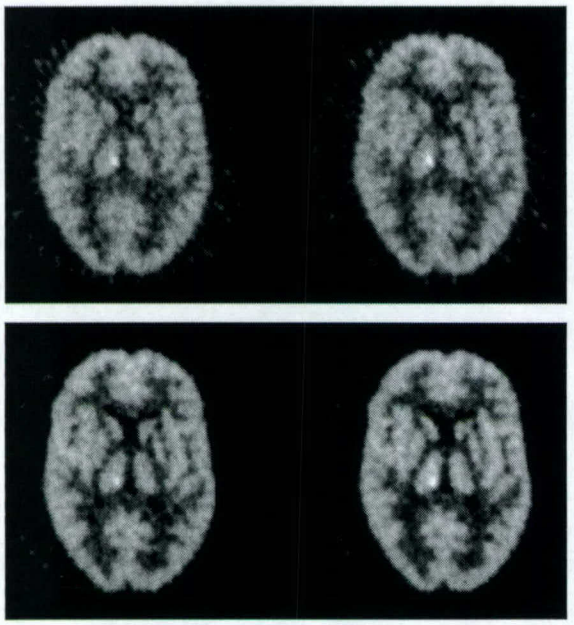

Fig. 7. Two image slices of the Hoffman brain phantom with 5 mm lesion for two different septa configurations: (top) no-septa and (bottom) 5-septa. The ratio of activity concentration of the lesions to gray matter was 2.2.

Fig. 6 shows two reconstructed image slices with 3 mm (left near edge) and 5 mm (near center) embedded lesion phantoms when the ratio of the activity concentration in the lesions to background (gray matter) was 5.4. In order to improve visualization of smaller lesions, the 8.6 mm lesion phantom was placed such that it did not appear in the same image slices as the others. The activity ratio of 5.4 was the lowest activity ratio at which the 3 mm lesion was observable.

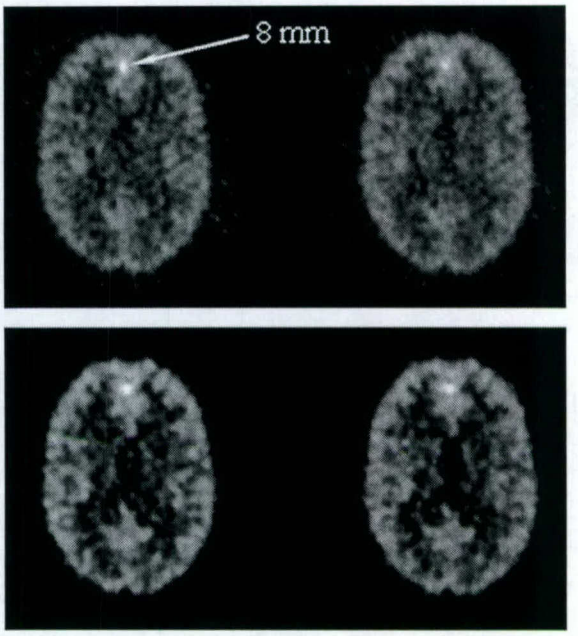

Fig. 8. Two image slices of the Hoffman brain phantom with 8 mm lesions for two different configurations: (top) no-septa and (bottom) 5-septa. The ratio of activity concentration of the lesions to gray matter was 1.5.

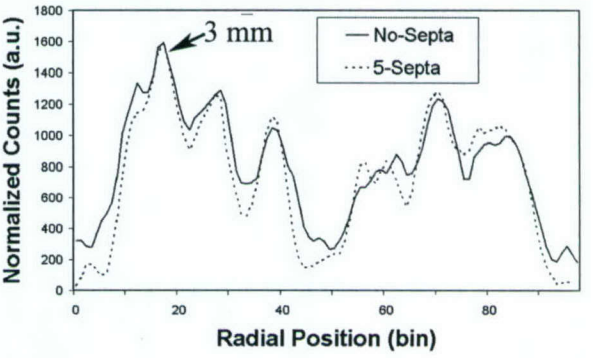

Fig. 9. Horizontal profiles through the middle of the images of 3 mm hot lesion in warm background shown in Fig. 6 for no-septa and partial 5-septa configurations. Ratio of activity concentration of the lesions to background (gray matter) was 5.4.

Fig. 7 shows two reconstructed image slices with 5 mm embedded lesion phantom when the ratio of the activity concentration in the lesions to background (gray matter) was 2.2. The activity ratio of 2.2 was the lowest activity at which this lesion was clearly observable.

Fig. 8 shows two reconstructed image slices with 8.6 mm lesion when the activity concentration in the lesions to the background was 1.5. This was the lowest activity ratio that we measured, and the 8.6 mm lesion was still clearly observable.

Visual comparison of the images did not show any significant differences between no-septa and the partial-septa configurations in terms of lesion detectability; however partial-septa images had less background noise compared to no-septa case. Fig. 9 shows the normalized horizontal profiles running through

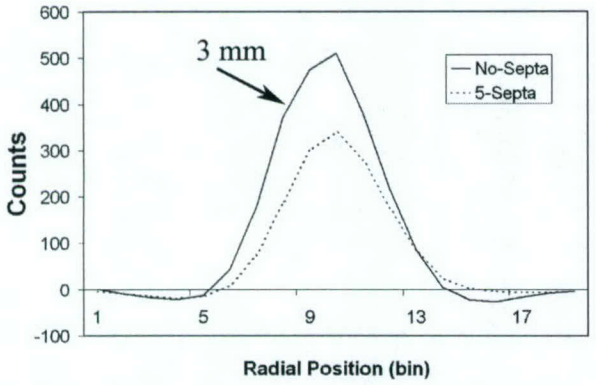

Fig. 10. Horizontal profiles through the middle of the images of the 3 mm hot lesion in cold background for no-septa and partial 5-septa configurations. Activity concentration of the 3 mm lesion was the same as data in Fig. 9.

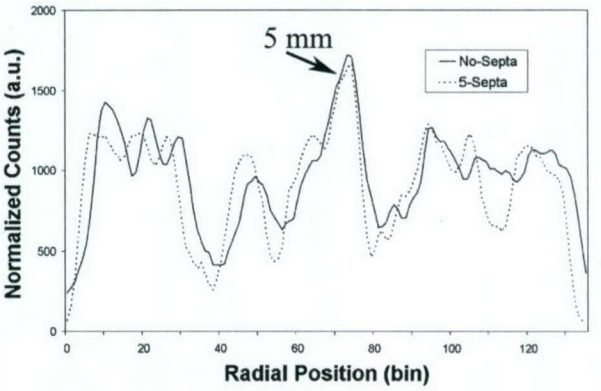

Fig. 12. Horizontal profiles through the middle of the 5 mm lesion image slices shown in Fig. 7 for no-septa and partial 5-septa configurations. Ratio of activity concentration of the lesions to gray matter was 2.2.

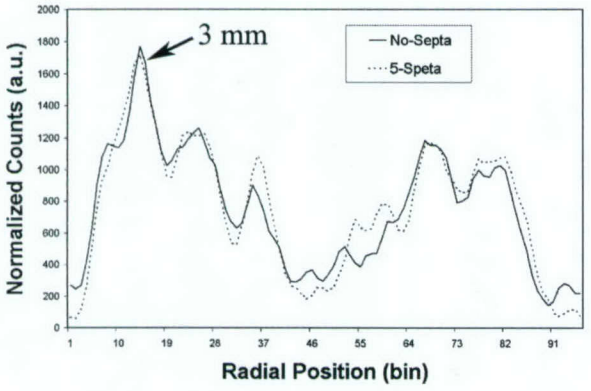

Fig. 11. Horizontal profiles through the middle of the 3 mm lesion images for no-septa and partial 5-septa configurations when ratio of activity concentration of the lesions to gray matter was 7.4.

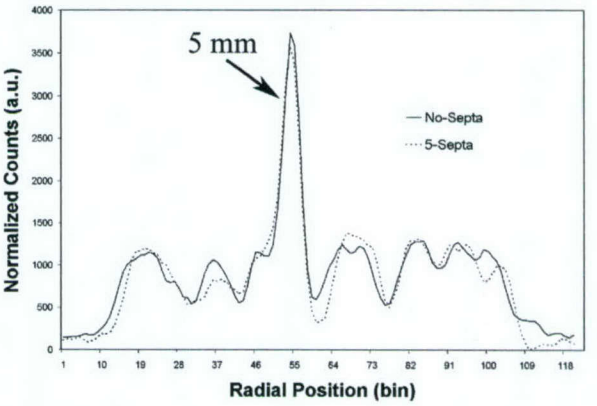

Fig. 13. Horizontal profiles through the middle of the 5 mm lesion images for no-septa and partial 5-septa configurations. Ratio of activity concentration of the lesions to gray matter was 7.4.

the middle of the images of 3 mm lesion in warm background for no-septa and 5-septa configurations (Fig. 6) when the ratio of the activity in the hot lesion to the warm background was 5.4. For comparison, in Fig. 10 the horizontal profile running along the middle of the hot 3 mm lesion in the cold background, when the hot lesion had the same activity as in Fig. 9, is shown. Fig. 11 shows the normalized horizontal profiles through the middle of the 3 mm lesion image at activity ratio of 7.4. Figs. 12 and 13 show the normalized horizontal profiles running along the middle of the 5 mm lesion image at activity ratios of 2.2 and 7.4, respectively. Figs. 14 and 15 show the normalized horizontal profiles through the middle of the 8.6 mm lesion image at activity ratios of 2.2 and 7.4, respectively. In profiles shown in Figs. 9–15 no averaging over rows or columns was done. The profile data for each image was normalized according to the average count in the background for each case.

The profile figures showed that the ratio of the peak (lesion activity) to the background (gray matter) was slightly higher for the no-septa configuration, especially for the largest lesion.

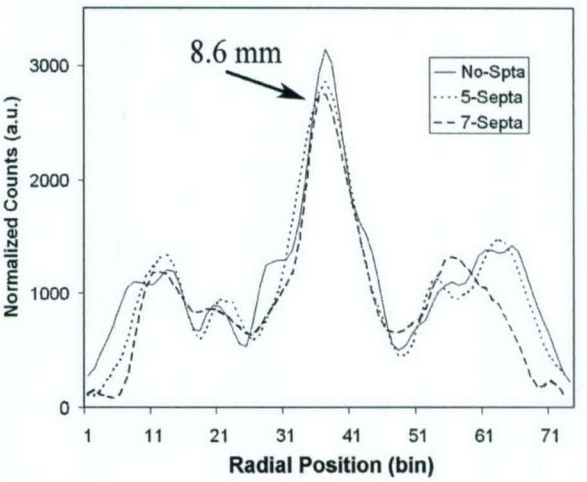

Fig. 14. Horizontal profiles through the middle of the 8.6 mm lesion images for no-septa, 5-septa and 7-septa configurations. Ratio of activity concentration of the lesions to gray matter was 2.2.

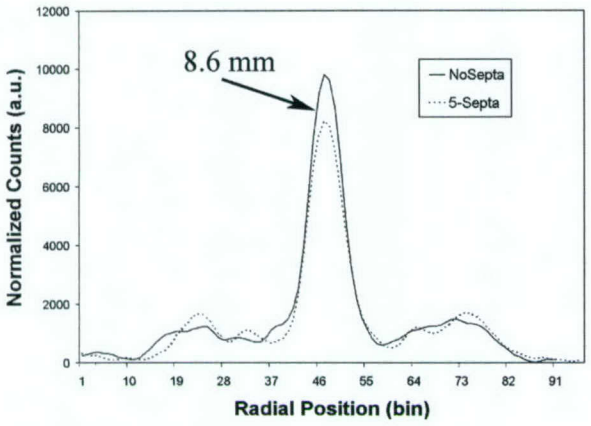

Fig. 15. Horizontal profiles through the middle of the 8.6 mm lesion images for no-septa and partial 5-septa configurations. Ratio of activity concentration of the lesions to gray matter was 7.4.

IV. Conclusion

The MDAPET camera operating in partial 5-speta and 7-septa configurations performed better than no-septa case in terms of peak NEC. For the 5-septa configuration the NEC peaked around 0.18 μCi/cc with $\sim$1.6 Kcps value, and the camera sensitivity was estimated to be 53% compared to the no-septa case. For 7-septa NEC peaked around 0.22 μCi/cc with $\sim$1.5 Kcps value and the camera sensitivity was estimated to be 35% compared to the no-septa case.

The visual inspection of the lesion images showed that the 3 mm lesion phantom embedded in the 3-D Hoffman brain phantom could be clearly observed, with or without partial septa, when the activity concentration ratio between the lesion and the background (gray matter) was greater than 5.4. The 5 mm lesion could be seen at an activity ratio greater than 2.2. The 8.6 mm lesion was observable even at the lowest activity ratio (1.5) we measured. We found that even though the use of partial septa increased the NEC rate, that increase did not translate into improved lesion detectability over no-septa case. We found that with septa the white matter regions of brain had lower counts and the brain images had less noise and images looked better compared to no-septa images; however, images without septa had slightly higher contrast.

The NEC measurement was done with a cylindrical phantom, which was larger than the Hoffman brain phantom. Since both scattered and accidental coincidence contributions are larger in NEMA phantom than in the brain phantom, partial septa would have a greater effect on NEC rate. In brain lesion measurements there was little contribution from activity outside the FOV of the camera. In more realistic conditions, when there are activities outside the FOV, the effect of partial-septa system could become more important.

Acknowledgment

The authors would like to thank the personnel of the clinical PET center of the University of Texas M. D. Anderson Cancer Center for their support in providing the FDG used for this work.

References

[1] D. J. Kadrmas, P. E. Christian, S. D. Wollenweber, S. G. Kohlmyer, and C. W. Stearns, "Comparative evaluation of 2-D and 3-D lesion detectability on a full-ring BGO PET scanner," *J. Nucl. Med.*, vol. 43, no. 5, p. 56P, May 2002.

[2] S. Pajevic, M. E. Dauve-Witherspoon, S. L. Bacharach, and R. E. Carson, "Noise characteristics of 3-D and 2-D PET images," *IEEE Trans. Med. Imaging*, vol. 17, pp. 9–23, Feb. 1998.

[3] D. L. Baily, T. Jones, T. J. Spinks, M. C. Gilardi, and D. W. Townsend, "Noise equivalent count measurements in a neuro-PET scanner with retractable septa," *IEEE Trans. Med. Imaging*, vol. 10, pp. 256–260, 1991.

[4] C. W. Stearns, S. R. Cherry, and C. J. Thompson, "NECR analysis of 3-D brain PET scanner designs," *IEEE Trans. Nucl. Sci.*, vol. 42, pp. 1075–1079, Aug. 1995.

[5] J. E. Tanaka, T. Hasegawa, T. Yamashita, H. Okada, and H. Murayama, "A 2-D/3-D hybrid PET scanner with rotating partial slice-septa and its quantitative procedures," *Phys. Med. Biol.*, vol. 45, pp. 2821–2841, 2000.

[6] T. G. Turkington and W. H. Sampson, "Optimizing septal spacing for gamma camera PET imaging," in *Proc. IEEE Medical Imaging Conf. Rec.*, vol. 3, 2000, p. 1767.

[7] S. J. Glick, C. J. Groiselle, J. A. Kolthammer, and R. Z. Stodilka, "Optimization of septal spacing in hybrid PET using estimation task performance," in *Proc. IEEE Medical Imaging Conf. Rec.*, San Diego, CA, 2001.

[8] M. Aykac, J. Uribe, H. Baghaei, H. Li, Y. Wang, Y. Liu, T. Xing, and W.-H. Wong, "Septa design study for volumetric imaging in positron emission tomography," *IEEE Trans. Nucl. Sci.*, vol. 49, pp. 2097–2102, Oct. 2002.

[9] E. J. Hoffman, P. D. Cutler, W. M. Digby, and J. C. Mazziotta, "3-D phantom to simulate cerebral blood flow and metabolic images for PET," *IEEE Trans. Nucl. Sci.*, vol. 37, pp. 616–620, Apr. 1990.

[10] W.-H. Wong, "A positron camera detector design with cross-coupled scintillators and quadrant sharing photomultipliers," *IEEE Trans. Nucl. Sci*, vol. 40, pp. 962–966, Aug. 1993.

[11] W.-H. Wong, J. Uribe, W. Lu, and K. Hicks, "Design of a variable field prototype PET camera," *IEEE Trans. Nucl. Sci.*, vol. 43, pp. 1915–1920, June 1996.

[12] W.-H. Wong, J. Uribe, K. Hicks, and M. Zambelli, "A 2-dimensional detector decoding study on BGO arrays with quadrant sharing photomultipliers," *IEEE Trans. Nucl. Sci.*, vol. 41, pp. 1453–1457, June 1994.

[13] W.-H. Wong, G. Hu, N. Zhang, J. Uribe, J. Wang, H. Li, H. Baghaei, and S. Yokoyama, "Front end electronics for a variable field PET camera using the PMT-quadrant-sharing detector array design," *IEEE Trans. Nucl. Sci.*, vol. 44, pp. 1266–1270, June 1997.

[14] R. H. Li, W.-H. Wong, N. Zhang, J. Wang, J. Uribe, H. Baghaei, and S. Yokoyama, "Prototype electronics for a variable field of view PET camera using the PMT-quadrant-sharing detector array," *IEEE Trans. Nucl. Sci.*, vol. 46, pp. 546–550, June 1999.

[15] J. Uribe, H. Baghaei, H. Li, S. Yokoyama, N. Zhang, J. Wang, F. Dobbs, and W.-H. Wong, "Basic imaging characteristics of a variable field of view PET camera using quadrant sharing detector design," *IEEE Trans. Nucl. Sci.*, vol. 46, pp. 491–497, June 1999.

[16] H. Baghaei, W.-H. Wong, J. Uribe, H. Li, N. Zhang, and Y. Wang, "Breast cancer studies with a variable field of view PET camera," *IEEE Trans. Nucl. Sci.*, vol. 47, pp. 1080–1084, June 2000.

[17] R. S. Miyaoka, S. G. Kohlmyer, and T. K. Lewellen, "Hot sphere detection limits for a dual head coincidence imaging system," *IEEE Trans. Nucl. Sci.*, vol. 46, pp. 2185–2191, Dec. 1999.

[18] H. Baghaei, W.-H. Wong, J. Uribe, H. Li, N. Zhang, and J. Wang, "The correction factors for a high resolution variable field of view PET camera," *J. Nucl. Med.*, vol. 40, p. 279P, May 1999.

[19] P. E. Kinahan and J. G. Rogers, "Analytic 3-D image reconstruction using all detected events," *IEEE Trans. Nucl. Sci.*, vol. 46, pp. 964–968, Feb. 1989.

[20] H. Baghaei, W.-H. Wong, H. Li, J. Uribe, Y. Wang, M. Aykac, Y. Liu, and T. Xing, "Evaluation of the effect of filtering apodization for volume PET imaging using the 3-DRP algorithm," *IEEE Trans. Nucl. Sci.*, vol. 50, pp. 3–8, Feb. 2003.

[21] W.-H. Wong, "A positron camera detector design with cross-coupled scintillators and quadrant sharing photomultipliers," in *Proc. Conf. Rec. 1992 IEEE Nuclear Science Symp./Medical Imaging Conf.*, Orlando, FL, 1992.

IEEE TRANSACTIONS ON NUCLEAR SCIENCE, VOL. 50, NO. 5, OCTOBER 2003

A Study of Coincidence Line Spread Function (CLSF) Estimation for Small Scintillators Using Quadrant Sharing Technique

Mehmet Aykac, *Member, IEEE*, Hongdi Li, *Member, IEEE*, Jorge Uribe, *Member, IEEE*, Yu Wang, Hossain Baghaei, *Member, IEEE*, Yaqiang Liu, Tao Xing, and Wai-Hoi Wong, *Member, IEEE*

Abstract—**Inter-crystal scatter and scintillation light spread are the primary factors for mispositioning of coincidence events in positron emission tomography (PET) for light sharing detectors. The probability of Compton scatter of a 511 keV photon within the crystal is more than 50% of the interactions. Inter-crystal scatter has been studied before and it was concluded that the coincidence line spread function (CLSF) was not significantly affected. Unlike one-to-one scintillator-photomultiplier tube (PMT) coupled (discrete) detectors, detector blocks utilizing the light sharing technique have additional degradation of their spatial resolution due to shared scintillation photons within the block. This study focuses on an estimation of CLSF for 7 × 7 BGO (bismuth germanate) detector blocks by comparing the simulation results for discrete and light shared detectors. The simulation model included inter-crystal scatter but the effect of scintillation light spread is the primary emphasis of our investigation. Based on experimental measurements, deterministic position profiles that calculate a spread (uncertainty) in positioning due to light sharing between neighboring crystals, were estimated from simple photoelectron statistics. The resultswere embedded in the Monte Carlo simulation to estimate the CLSF more accurately. Two 7 × 7 BGO detector blocks (2.68 mm × 2.68 mm × 18 mm) with different surface treatments coupled to 4 PMTs were used to estimate the positioning spread values. For discrete detectors, the FWHM values of CLSF for 7 × 7 BGO block with crystal dimensions of 2.68 mm × 2.68 mm × 18 mm were found to be approximately 1.47 mm for discrete detectors and 1.51 mm for light shared detectors. The intrinsic spatial resolutions of 7 × 7 light shared BGO block with crystal dimensions of 2.68 mm × 2.68 mm × 18 mm for 20 cm, 40 cm and 80 cm detector ring diameters were estimated as 1.57 mm, 1.75 mm and 2.30 mm, respectively.**

Index Terms—**Coincidence line, Monte Carlo methods, positron emission tomography.**

I. Introduction

POSITRON emission tomography (PET) detectors generally exhibit spatial resolution limits due to the choice of crystal length, crystal surface area, the gap between scintillators and the scatter between the crystals. Typically, 511 keV photons within the detector undergo Compton scatter (54%), Coherent scatter (6%) and photoelectric absorption (40%). Several investigators [1]–[4] discussed inter-crystal effects on spatial resolution for discrete detectors. Shao [1] concluded that the inter-crystal scatter has an insignificant effect on the FWHM of the CLSF. Murthy [2] reported experimental measurements of the coincidence response for the presence of neighboring crystals. Cho [3] also discussed the resolution limits of a PET system for narrow width crystal detector arrays. Comanor [4] investigated Compton scatter in PET detector modules.

The scope of this study is an examination of the effect on intrinsic detector resolution of the spread in the position profile due to light sharing between the neighbor crystals. The spread between neighboring crystals creates an uncertainty in positioning an event in the position profile as shown in Fig. 1. This uncertainty can be minimized significantly by using position-sensitive PMTs, however the cost of the detector increases dramatically. In the light sharing technique, crystal positioning in a block mainly depends on the total number of generated scintillation photons. Accuracy of controlling the light distribution is crucial to position the crystal elements in the block and will introduce degradation on the detector spatial resolution if not handled properly. Variation in the number of generated scintillation photons causes changes in the amount of spread in crystal position profile. An increase in the number of collected scintillation photons causes a decrease in the uncertainty regions between neighboring crystals, hence providing better position profiles.

II. Method

A. Basic Theory of Photoelectron Statistics

Components of a position profile, x and y shown in Fig. 2, can be computed by the following:

$$x = \frac{(E_A + E_C)}{(E_A + E_B + E_C + E_D)}$$
$$y = \frac{(E_A + E_B)}{(E_A + E_B + E_C + E_D).} \quad (1)$$

As suggested by Wong [5], each photoelectron exhibits a binomial distribution when detected by PMTs (A + C) with a probability (p) and PMTs (B + D) with a probability (1-p).

Manuscript received January 28, 2002; revised July 1, 2003. This work was supported by NIH Grants RO1 CA76246, RO1 CA61880, and RO1 CA58980, the J.S. Dunn Research Foundation, and the Cobb Endowment for Cancer Research.

M. Aykac was with the University of Texas, M.D. Anderson Cancer Center, Houston, TX 77030 USA. He is now with CPS Innovations, Rockford, TN 37853 USA (e-mail: aykac2000@yahoo.com).

H. Li, J. Uribe, Y. Wang, H. Baghaei, Y. Liu, T. Xing, and W.-H. Wong are with the University of Texas, M.D. Anderson Cancer Center, Houston, TX 77030 USA.

Digital Object Identifier 10.1109/TNS.2003.817965

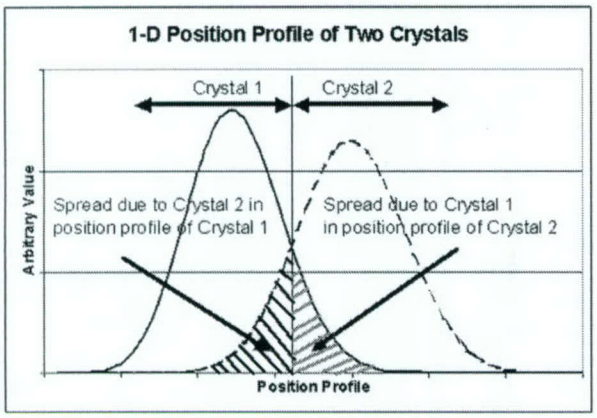

Fig. 1. Representative one-dimensional position profile for two neighbor crystals based on deterministic approach.

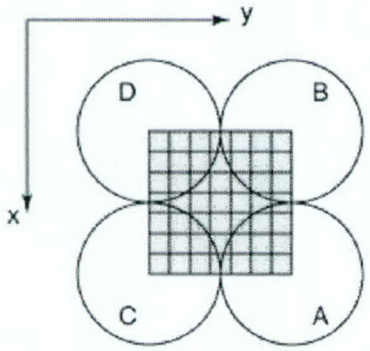

Fig. 2. 7 × 7 BGO block coupled to four PMTs A, B, C, D using quadrant sharing technique.

Therefore, the following deterministic equations can describe the photoelectron distribution in x and y dimensions:

$$Q(n) = \frac{N!}{(N-n)!n!}\left(\frac{E_{AC}}{N}\right)^{n}\left(1-\frac{E_{AC}}{N}\right)^{(N-n)} \quad (2)$$

$$Q(r) = \frac{N!}{(N-r)!r!}\left(\frac{E_{AB}}{N}\right)^{r}\left(1-\frac{E_{AB}}{N}\right)^{(N-r)} \quad (3)$$

$$\text{Single Crystal Position Profile} = Q(n)\,Q(r) \quad (4)$$

where $N = E_A + E_B + E_C + E_D$: total number of photoelectrons generated in each scintillation event; $E_{AC} = E_A + E_C$: average number of photoelectrons going to PMTs A and C; $E_{AB} = E_A + E_B$: average number of photoelectrons going to PMTs A and B; n, r ranges from 0 to E_{AC} and 0 to E_{AB}, respectively. Therefore, the position profile for a single crystal can be expressed by (4). Similarly, the entire position profile for a block can be calculated by summing all the probability functions defined in the form shown in (4) for all the crystals. Based on the deterministic approach explained above, spread values shown in Fig. 1 can be calculated for each crystal and therefore the spread from neighboring crystals can be estimated in percent. For example, a single crystal surrounded by 8 neighboring crystals, forming a 3 × 3 matrix will contain 1 true position (decoding certainty, $P_k(x_k, y_k)$) for the central crystal and eight spread

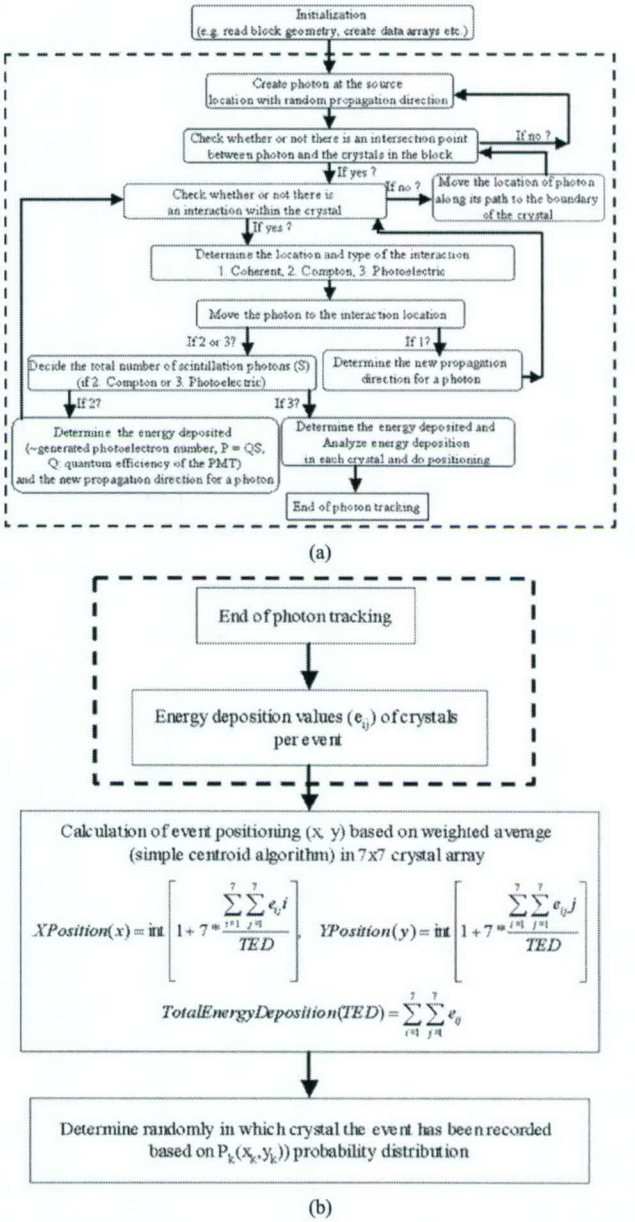

Fig. 3. (a) Algorithm of Monte Carlo code for single photon tracking. Steps in the box with dashed line were repeated for the second annihilation photon. (b) Algorithm to determine the event positioning using $P_k(x_k, y_k)$ probability distribution due to light spread.

values in percent due to eight surrounding crystals. This can be expressed as a probability distribution, $P_k(x, y)$, such that

$$\sum_{i=-1}^{1}\sum_{j=-1}^{1} P_k(x_k + i, y_k + j) = 1. \quad (5)$$

Crystals at four corners and four sides in the block have only three and five neighboring crystals, respectively.

It is worth saying that photoelectron statistics originate from the statistics of scintillation photons generated in the crystal. As mentioned above, the total number of photoelectrons generated in PMT A and C can be written as $E_{AC} = E_A + E_C = q_A n_A + q_C n_C$, where q_A, q_C are the quantum efficiency values

of the PMTs A and C, n_A, n_C are total number of scintillation photons collected by PMTs A and C. Assuming that the quantum efficiency values for the PMTs are very close to each other and equal to Q, E_{AC} is directly proportional to the number of scintillation photons collected by these PMTs and can be rewritten as $E_{AC} = Q(n_A + n_C)$. Therefore, instead of talking about the statistics of scintillation photons, it is fair to discuss simply photoelectron statistics for an event.

B. Monte Carlo Simulation

Our Monte Carlo simulation program models the photoelectric absorption, and Coherent and Compton scatter. The interaction probabilities were calculated based on the tabulated values of interaction cross sections for various scintillators such as BGO, LSO, NaI(Tl), and GSO. Klein–Nishina formulation was used to estimate the scattering angles for Compton interactions. Elastic scattering was modeled based on the Kaplan's [6] implementation. Coherent scatter angles were estimated based from the tabulated scatter amplitudes in the Evaluated Photon Data Library. Due to the difficulties of modeling the surface properties of the crystals, scintillation photons were not tracked individually in the scintillators. The photoelectron number generated by the scintillation photons at the photocathode of the PMT was assumed to be proportional to the total energy deposition in the crystal at every interaction. Positron motion and noncollinearity between annihilation photons were included by using a modified formula of Moses and Derenzo [7]. Equation (6), below, was used to estimate the intrinsic spatial resolution

$$\mathrm{FWHM}_{\mathrm{spa.res.}} = \left[\mathrm{FWHM}_{\mathrm{CLSF}}^2 + 0.0022^2 D^2 + s^2\right]^{\frac{1}{2}} \quad (6)$$

where D is detector ring diameter, $\mathrm{FWHM}_{\mathrm{CLSF}}$ is detector coincidence resolution coming out of the simulation, s (0.25 mm) is the ^{18}F positron range in tissue.

Our Monte Carlo program uses an input geometry file that contains information about the incident photon energy (in this case 511 keV was used), total number of annihilation photons generated, precalculated spread and decoding certainty values for all the crystals in a block using experimental and deterministic position profiles. Crystal boundaries were simply defined by rectangular planes. Fourdifferent types of crystals can be defined as media: BGO, LSO, NaI(Tl), and GSO. Since tracking of individual scintillation photons was not modeled, the energy deposition of an annihilation photon was stored for every crystal per event. At the end of photon tracking, simple weighted average was used to determine the positioning of an event. Fig. 3(a) shows the algorithm of the simulation program for the photon tracking section. Multiple scattering within the crystal and the block was modeled. The simulation program tracks the photon until the photon completely loses its energy through photoelectric and Compton interactions in the block or escapes.

C. Experimental Measurements of Position Profile and Estimation of Spread in the Position Profile

In the experimental measurements of this study, two 7 × 7 BGO blocks were used. A total of ninety-eight individual BGO crystals were cut with the size of 2.68 mm × 2.68 mm × 18 mm.

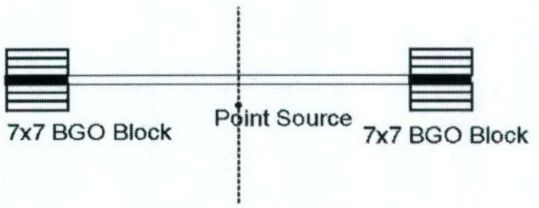

Fig. 4. Setup of 7 × 7 BGO blocks in coincidence for CLSF simulation for both light shared and discrete detectors. Point source was moved 0.2 mm along the dashed line. Total of 500 000 annihilation photons were simulated at each position. Coincident events were stored for only one line-of-response as shown.

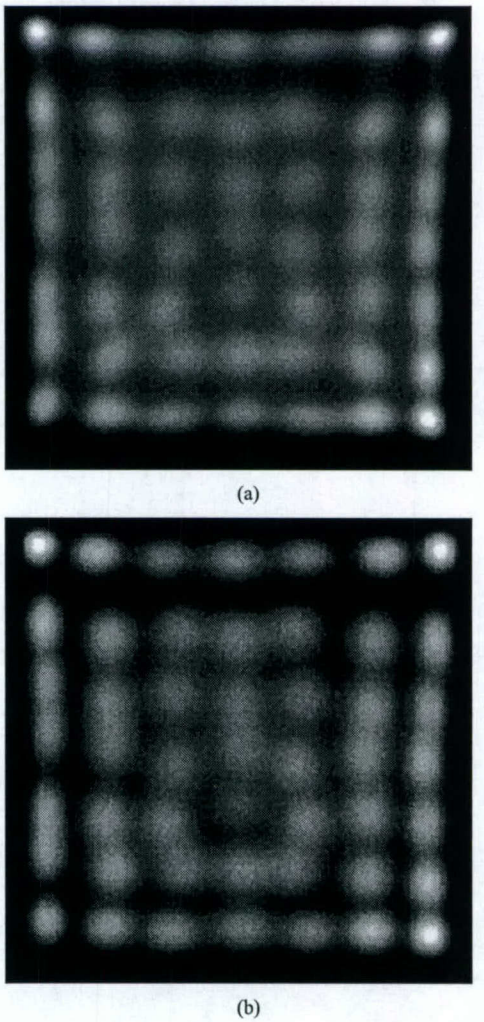

(a)

(b)

Fig. 5. Comparison of as Cut type 7 × 7 BGO block position profiles using ^{137}Cs source. (a) Experiment. (b) Deterministic method.

The crystals in one of the 7 × 7 blocks were left as cut and the crystals in the other block were finely roughened (lapped) to remove the blade marks and to produce relatively uniform surfaces. In both blocks, only one side of each crystal was polished and this side was used to couple to a 2 × 2 PMT array. To obtain a well-separated position profile, different paint levels were applied to the surfaces of each crystal by using reflector paint and crystals were glued by using optical cement. Thickness of

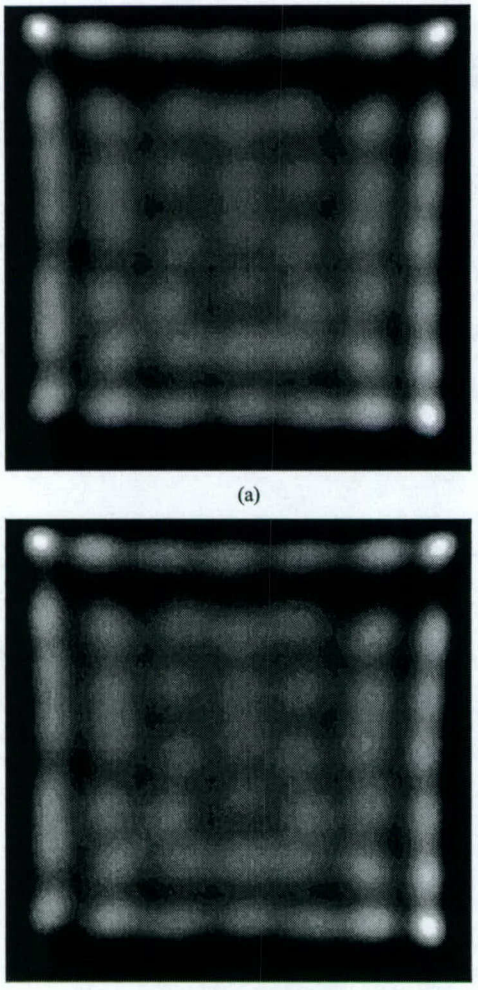

(a) (b)

Fig. 6. Comparison of as Cut type 7 × 7 BGO block position profiles using ^{68}Ga source. (a) Experiment. (b) Deterministic method.

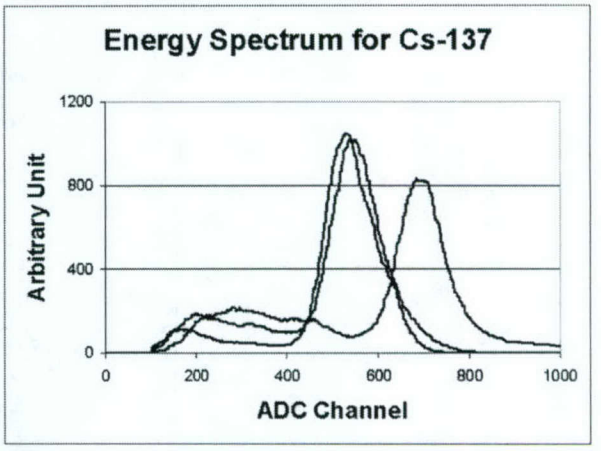

(a)

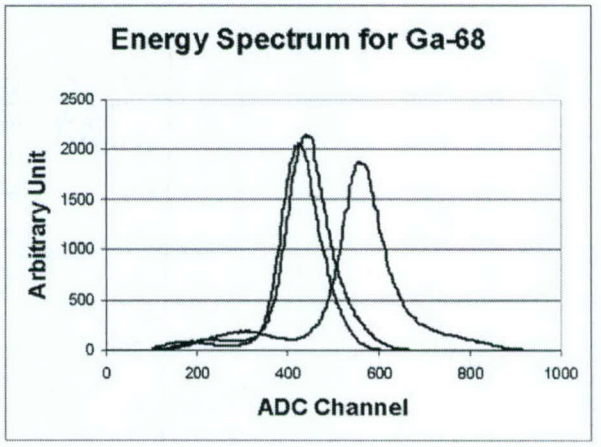

(b)

Fig. 7. Energy spectra of 3 individual crystals as Cut type 7 × 7 BGO block (center, bottom middle, bottom right corner see the detector block in Fig. 1). (a) ^{137}Cs source source 662 keV photopeak locations: center (532), bottom middle (550), bottom right corner (694). (b) ^{68}Ga source source 511 keV photopeak locations: center (428), bottom middle (443), bottom right corner (564).

the paint was roughly 0.1 mm resulting in a crystal pitch of 2.8 mm after the blocks were glued.

Position profile measurements of the blocks were performed by using ^{137}Cs and ^{68}Ga sources. Energy thresholds were set to 500 keV for ^{137}Cs and 380 keV for ^{68}Ga. Energy spectra were obtained for three individual crystals in each block using predefined rectangular regions in the position profiles. Using the flood source images, central points of each crystal were manually chosen. The ratios of central location (x_k, y_k) of each crystal to flood source image size (S) correspond to $E_{AC}/N(\sim x_k/S)$ and $E_{AB}/N(\sim y_k/S)$ ratios [recall (2) and (3)]. Therefore, the only unknowns in (2) and (3) are photoelectron (N) numbers for all the crystals.

The number of collected photoelectrons from each crystal was assumed proportional to the corresponding photopeak locations in their energy spectra. Based on this assumption, deterministic position profiles were calculated by using binomial probability equations given in (2)–(4). Total photoelectron numbers (N) for every crystal were changed iteratively while keeping the ratio of photopeak locations of the crystals fixed with respect to each other, until the deterministic position profile matched closely with the experimental flood source image.

TABLE I
ESTIMATED NUMBER OF PHOTOELECTRONS USING DETERMINISTIC METHOD FOR 7 × 7 BGO BLOCK AS *CUT* (^{137}CS)

176	164	146	150	162	169	178
162	156	143	152	157	157	163
159	152	132	148	152	156	165
154	152	143	138	153	145	164
153	150	143	144	150	146	164
157	147	145	152	157	170	177
158	154	150	143	159	171	181

TABLE II
ESTIMATED NUMBER OF PHOTOELECTRONS USING DETERMINISTIC METHOD FOR 7 × 7 BGO BLOCK AS *CUT* (^{68}GA)

142	132	120	120	130	134	144
131	124	115	122	126	126	131
128	123	106	120	122	122	133
122	122	113	110	123	122	132
124	123	126	116	120	120	132
126	122	126	122	126	137	143
127	124	121	115	128	138	145

TABLE III
ESTIMATED DECODING CERTAINTIES (%) FOR 7 × 7 BGO BLOCK AS *CUT* (^{137}CS)

99.2	97.0	94.3	93.4	95.7	98.3	99.1
94.4	91.3	84.1	79.7	88.1	93.8	96.0
85.2	77.5	78.3	68.5	81.5	80.5	87.4
87.5	79.4	77.4	67.6	72.9	78.4	85.7
84.1	82.0	74.4	74.9	74.3	83.9	90.3
85.0	83.3	78.3	76.6	77.1	89.6	92.9
98.0	92.9	91.0	89.8	91.3	93.3	96.5

TABLE IV
ESTIMATED DECODING CERTAINTIES (%) FOR 7 × 7 BGO BLOCK AS *CUT* (^{68}GA)

97.8	94.5	89.5	87.6	93.6	96.8	98.3
91.6	85.8	74.0	65.1	80.0	87.6	92.4
77.2	66.1	65.4	53.4	67.8	71.6	80.8
81.5	68.7	66.7	57.1	61.6	68.2	79.5
77.8	73.3	63.7	60.7	61.3	75.3	84.6
77.3	75.0	68.0	62.1	62.6	80.0	87.8
94.8	88.8	84.1	83.7	83.8	86.5	93.9

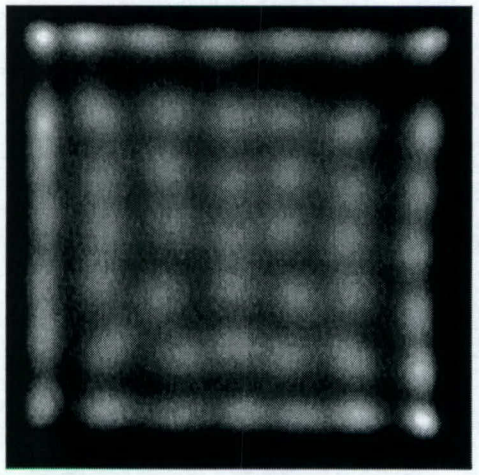

(a)

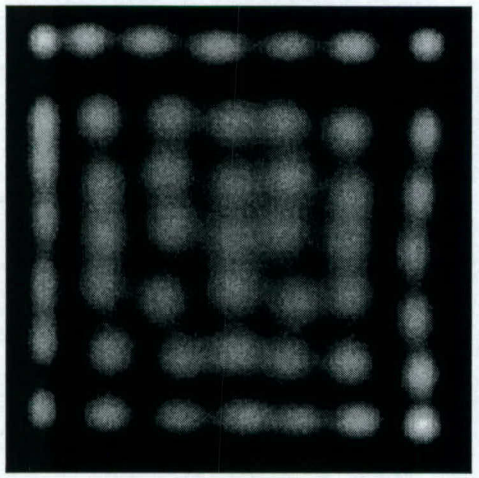

(b)

Fig. 8. Comparison of Lapped type 7 × 7 BGO block position profiles using ^{137}Cs source. (a) Experiment. (b) Deterministic method.

Once N values were determined, spreading and decoding certainty values were calculated using (4) for every crystal

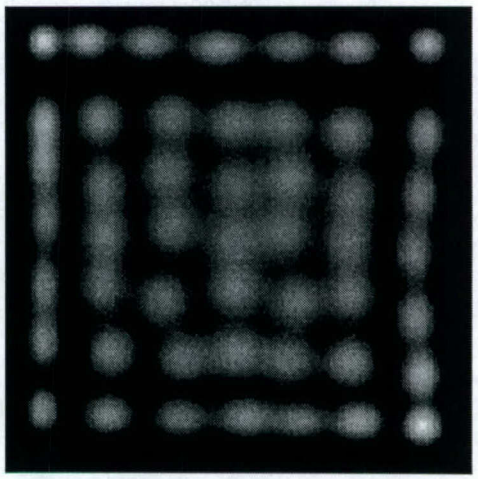

(a)

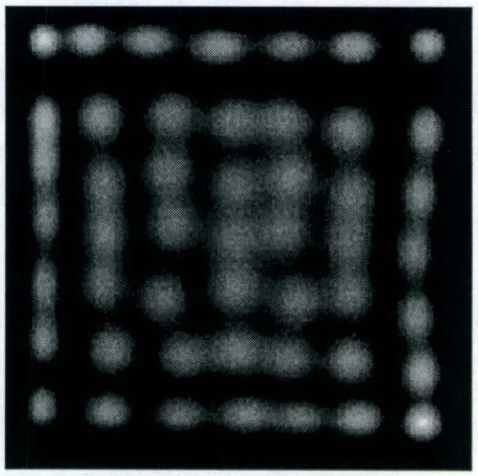

(b)

Fig. 9. Comparison of Lapped type 7 × 7 BGO block position profiles using ^{68}Ga source. (a) Experiment. (b) Deterministic method.

in the detector block. Average probability values to represent decoding certainties and spread values were estimated for 49 crystal elements in both as cut and lapped detector blocks. Because in the quadrant sharing technique, the crystals in the central region of the block are usually poorly decoded compared to the crystals at the edges, one would prefer to study and compare the CLSF in two regions. Probability values represented two regions for 7 × 7 BGO blocks: (a) "central" region (central 3 × 3 BGO array) and (b) "outer" region that surrounds the central region (40 crystals in total). Decoding certainties and spread values in percent were reported separately for two different regions and the entire block. At the end of each photon tracking, final positioning of the event was obtained by convolving the weighted positioning from the Monte Carlo code and the decoding certainties and spread values estimated from deterministic position profile.

D. Coincidence Line Spread Function Simulation

Having photon interactions modeled (recall Fig. 3) and decoding certainties calculated, two 7 × 7 BGO scintillator blocks (19.5 mm × 19.5 mm × 18 mmdimensions) were simulated in

coincidence at 20 cm, 40 cm and 80 cm apart (see Fig. 4). A point source in air at the center of two blocks was moved in 0.2 mm steps across the detectors and atotal of 500 000 annihilation photons were simulated at each position. Positioning of an event was achieved by using a weighted average result of energy deposition in the crystals. Decoding certainties and spread values were also taken into account for light shared detectors. In the discrete detector case, it was assumed that there was one-to-one crystal-PMT coupling. Therefore, no light spread was considered for the simulations of discrete detectors. Total numbers of coincident detected events were stored at each position and plotted to get CLSF for one line-of-response. FWHM values of CLSF were estimated by fitting a Gaussian function.

III. Results

Figs. 5 and 6 compare the results of experimental and deterministic position profiles for 7 × 7 BGO blocks in the "as Cut" case. The position profile obtained by using ^{137}Cs (662 keV) is slightly better than the one using ^{68}Ga (511 keV)(compare Fig. 5(a) to Fig. 6(a)) because more photoelectrons were collected for the case of ^{137}Cs source.

Fig. 7 compares the energy spectra for 3 individual crystals in the block. "Center" and "bottom middle" crystals lose more scintillation photons than the "bottom right corner" crystal because more light is spreading in those locations. Estimated photoelectron numbers are listed for individual crystals in Table I for ^{137}Cs and Table II for ^{68}Ga. The energy resolution values of selected crystals were calculated and found to be in the range of 22% to 32% in both as Cut and Lapped types for ^{68}Ga source.

Decoding certainties and spread values for as Cut type block, which were calculated from the results of deterministic method shown in Fig. 3 and Table I, are listed in Table III for 49 individual crystals for ^{137}Cs flood source. Similarestimations were performed for ^{68}Ga source using Fig. 4 and Table II. For this case, the decoding results are presented in Table IV. Same analyses were repeated for Lapped type BGO block and the results are shown in Figs. 8–10 and Tables V–VIII.

Decoding certainties and spread values in percent for as cut and lapped types of detector blocks were calculated. These values showed how much mispositioning occurred to neighboring scintillators on average. Results are listed in Tables IX and X. The center element of a 3 × 3 decoding probability matrix shows with what certainty the crystal was decoded. Other elements in the 3 × 3 matrix show the spreading probability to neighboring scintillators. CLSF simulation results were compared between light shared detectors and discrete detectors as shown in Figs. 11 and 12. Intrinsic spatial resolution values are listed in Table XI for as Cut, Lapped and discrete 7 × 7 BGO blocks.

Finally, Table XI compares the intrinsic spatial resolution (recall (6)) if we are to build a PET tomograph with ring diameters of 20 cm, 40 cm and 80 cm using three types of detectors mentioned above.

IV. Discussion and Conclusion

In this work, the effect of spread in the position profile on CLSF was studied for light shared detectors and compared to discrete detectors. It has been concluded that the CLSF was insensitive to this spread. Hence, intrinsic spatial resolutions for

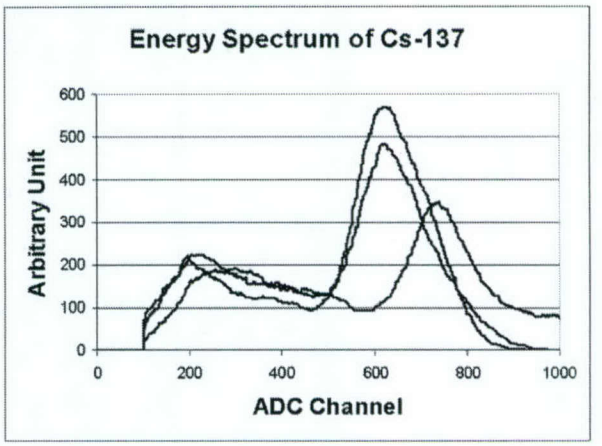

(a)

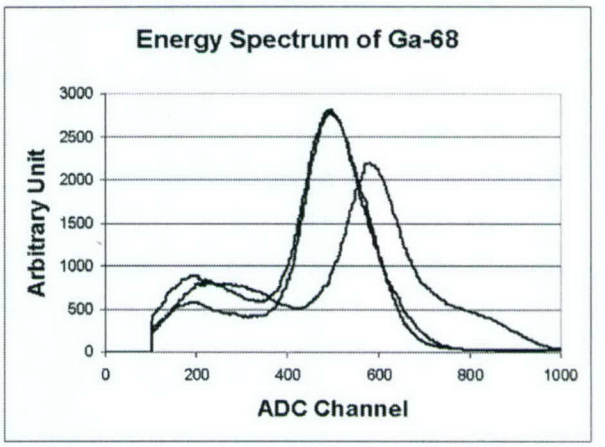

(b)

Fig. 10. Energy spectra of 3 individual crystals Lapped type 7 × 7 BGO block using (a) ^{137}Cs source 662 keV photopeak locations: center (633), bottom middle (634), bottom right corner (740). (b) ^{68}Ga source (511 keV photopeak locations: center (500), bottom middle (497), bottom right corner (586).

TABLE V
Estimated Number of Photoelectrons Using Deterministic Method for 7 × 7 BGO Block *Lapped* (^{137}CS)

184	169	161	159	174	177	184
172	162	159	161	171	163	168
163	159	158	167	162	161	171
159	158	162	157	157	161	169
153	158	157	159	156	157	169
159	156	157	163	166	177	183
164	163	157	158	175	179	184

TABLE VI
Estimated Number of Photoelectrons Using Deterministic Method for 7 × 7 BGO Block *Lapped* (^{68}GA)

150	138	130	130	142	144	150
140	132	130	131	139	133	137
133	130	129	136	132	131	139
130	129	129	128	128	131	138
124	129	126	130	127	128	138
129	127	128	133	135	144	149
133	133	128	129	143	146	150

TABLE VII
ESTIMATED DECODING CERTAINTIES (%) FOR 7 × 7 BGO BLOCK *LAPPED* (^{137}CS)

99.2	97.1	94.3	93.4	95.7	98.3	99.1
94.4	91.3	84.1	79.7	88.1	93.8	96.0
85.2	77.5	78.3	68.5	81.5	80.5	87.4
87.5	79.4	77.4	67.6	72.9	78.4	85.7
84.1	82.0	74.4	74.9	74.3	83.9	90.3
85.0	83.3	78.3	76.6	77.1	89.6	92.9
98.0	92.9	91.0	89.8	91.3	93.3	96.5

TABLE VIII
ESTIMATED DECODING CERTAINTIES (%) FOR 7 × 7 BGO BLOCK *LAPPED* (^{68}GA)

96.8	93.9	93.5	91.8	91.1	95.0	99.6
83.3	90.2	83.1	72.3	71.0	88.0	93.7
77.8	74.8	71,3	57.9	59.0	74.5	84.0
84.4	68.5	73.2	58.3	58.6	68.9	84.6
83.7	78.5	79.1	66.9	68.9	75.1	89.4
86.3	88.1	78.2	68.4	74.2	85.7	91.5
97.7	94.7	88.6	83.3	83.2	90.5	96.5

TABLE IX
AVERAGE DECODING CERTAINTIES AND SPREAD FOR AS *CUT* (^{68}GA). (i) INCLUDING ALL 49 CRYSTALS. (ii) OUTER REGION (40 CRYSTALS TOTAL). (iii) CENTRAL 3 × 3 BGO REGION (9 CRYSTALS) IN 7 × 7 BGO BLOCK

Block Region (i)			Block Region (ii)			Block Region (iii)		
0.79	5.28	1.04	1.16	6.74	1.44	2.03	7.96	2.18
3.92	78.07	3.73	1.17	89.45	4.81	6.44	61.96	5.88
1.10	5.32	0.75	1.61	6.91	1.14	2.79	8.66	2.10

TABLE X
AVERAGE DECODING CERTAINTIES AND SPREAD FOR *LAPPED* TYPE (^{68}GA). (i) INCLUDING ALL 49 CRYSTALS. (ii) OUTER REGION (40 CRYSTALS TOTAL). (iii) CENTRAL 3 × 3 BGO REGION (9 CRYSTALS) IN 7 × 7 BGO BLOCK

Block Region (i)			Block Region (ii)			Block Region (iii)		
0.61	4.45	0.71	0.30	3.79	0.42	1.98	7.38	2.01
3.56	81.37	3.49	3.10	84.85	2.79	5.61	65.90	6.61
0.74	4.47	0.60	0.50	3.94	0.31	1.79	6.82	1.90

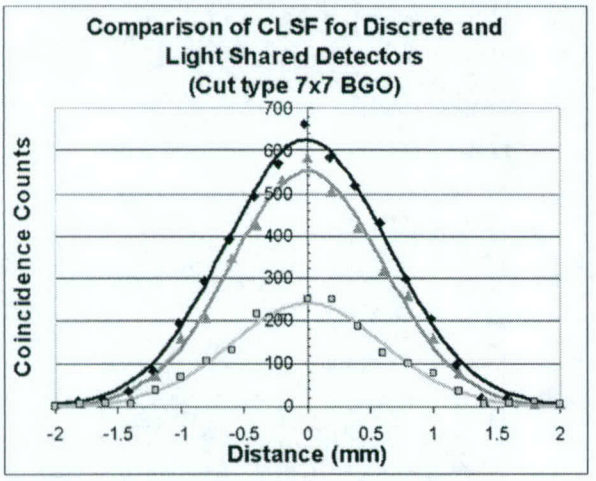

Fig. 11. Comparison of CLSF simulation results of 49 discrete detectors versus light shared detectors as *Cut Type* for "central" and "outer" regions. Simulation results are marked as ♦ (black) for discrete detectors, □ (light gray) *as Cut Type* (case (iii) in Table IX above) and ▲ (dark gray) *as Cut Type* (case (i) in Table IX above). The solid lines with the corresponding gray colors are Gaussian fits to simulation results.

different detector ring diameters were found to be very close

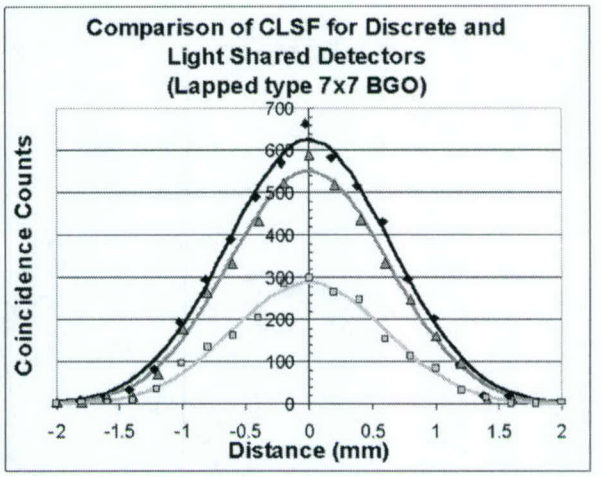

Fig. 12. Comparison of CLSF simulation results of 49 discrete detectors versus light shared detectors Lapped type for "central" and "outer" regions. Simulation results are marked as ♦ (black) for discrete detectors, □ (light gray) Lapped type (case (iii) in Table X above) and ▲ (dark gray) *Lapped Type* (case (i) in Table X above). The solid lines with the corresponding gray colors are Gaussian fits to simulation results.

TABLE XI
COMPARISON OF ESTIMATED INTRINSIC SPATIAL RESOLUTION (IN MILLIMETERS) FOR VARIOUS DETECTOR RING DIAMETERS BETWEEN DISCRETE AND LIGHT SHARED DETECTORS

Block Type	Ring Diameter (20cm)	Ring Diameter (40cm)	Ring Diameter (80cm)
As Cut	1.59	1.76	2.33
Lapped	1.57	1.75	2.32
Discrete	1.55	1.73	2.30

for discrete and light shared detectors. Even though the FWHM values of CLSFs were not changed significantly for different regions of the block, not surprisingly the coincidence sensitivity for the crystals in the central region decreased to 44% in lapped type and 37% in as cut type compared to discrete detectors (see Figs. 11 and 12) because of the misplaced coincidence events. It is worth saying that overall sensitivity of the blocks was remained unchanged, but the number of detected coincident events had been diminished because of mispositioning for a specific line-of-response. Average decoding certainty and spread values, shown in Tables IX and X, behaved similar to a simple low pass filter that degraded the CLSF. If the decoding certainty values were averaged for the entire 7 × 7 BGO block, the coincidence sensitivity values were calculated 86% in lapped type and 84% in as cut type compared to discrete detector block (recall Figs. 11 and 12). Estimation of total generated photoelectron numbers using deterministic approach was found to be consistent with the locations of the photopeaks in the energy spectra.

REFERENCES

[1] Y. Shao, S. R. Cherry, S. Siegel, and R. W. Silverman, "A study of inter-crystal scatter in small scintillator arrays designed for high resolution PET imaging," *IEEE Trans. Nucl. Sci.*, vol. 43, pp. 1938–1944, June 1996.

[2] K. Murthy, C. J. Thompson, I. N. Weinberg, and F. M. Mako, "Measurement of the coincidence response of very thin BGO crystals," *IEEE Trans. Nucl. Sci.*, vol. 41, pp. 1430–1435, Aug. 1994.

[3] Z. H. Cho, J. P. Jones, and M. Singh, *Foundations of Medical Imaging*. New York: Wiley, 1993, pp. 221–230.

[4] K. A. Comanor, P. R. G. Virador, and W. W. Moses, "Algorithms to identify detector Compton scatter in PET modules," *IEEE Trans. Nucl. Sci.*, vol. 43, pp. 2213–2218, Aug. 1996.

[5] W. H. Wong, J. Uribe, K. Hicks, and M. Zambelli, "A 2-dimensional detector decoding study on BGO arrays with quadrant sharing photomultipliers," *IEEE Trans. Nucl. Sci.*, vol. 41, pp. 1453–1457, Aug. 1994.

[6] M. S. Kaplan, R. L. Harrison, and S. D. Vannoy, "Coherent scatter implementation for SimSET," *IEEE Trans. Nucl. Sci.*, vol. 45, pp. 3064–3068, Dec. 1998.

[7] W. W. Moses and S. E. Derenzo, "Empirical observation of resolution degradation in positron emission tomographs utilizing block detectors," *J. Nucl. Medicine*, vol. 34, no. 5, p. 101P, 1993.

IEEE TRANSACTIONS ON NUCLEAR SCIENCE, VOL. 50, NO. 5, OCTOBER 2003

A Programmable High-Resolution Ultra-Fast Delay Generator

Yaqiang Liu, Hongdi Li, Yu Wang, Tao Xing, Hossain Baghaei, Jorge Uribe, Rocio Farrell, and Wai-Hoi Wong

Abstract—**This paper presents a high-resolution, low-dead-time digital delay method in which the performance is independent of the total delay time. We have implemented a low-dead-time (50 ns) and high-resolution (±0.9 ns) delay generator with delay times up to hundreds of milliseconds. We propose high-resolution whole-body positron emission tomograghy (PET) with a 12-module photomultiplier tube-quadrant- sharing (PQS) detector design. This high-resolution delay unit is an important part of the new PET electronics in which a high-yield pileup event recovery (HYPER) method is used. Using the HYPER method, the energy/position signals are generated or digitized upon the arrival of the next event (arriving at a random time after the present event). If the present event is piled up by the next event, the energy/position signals are no longer synchronized with the leading edge of the triggering signal. To detect a coincidence event by using the HYPER method, the original trigger signal must be delayed by a fixed time (1.5 μs for a PET using a bismuth germinate crystal) and a new synchronization process must also be set up between the delayed trigger and the energy/position signals before being passed to the coincidence detection electronics. Each HYPER processor requires one delay generator; there are 48 delay units inside the whole PET system. This high-resolution delay generator also can be used in other PET systems in which a delay is needed to synchronize the fast timing trigger to the slower integration or detection address outputs; this low timing jitter delay can also be applied to automatic test equipment and communications.**

Index Terms—**Delay generator, high-yield pileup event recovery (HYPER), positron emission tomograghy (PET), tube-quadrant-sharing (PQS).**

I. Introduction

WE PROPOSE a dynamic signal-integration approach called high-yield pileup event recovery (HYPER) [1] to prevent signal pileup for position emission tomography (PET) and gamma cameras. We have deployed the HYPER electronic processing in our modular high-resolution PET system that is under construction. This PET system has 12 detector modules. Each module has four HYPER-Anger-positioning zones generating 48 modular electronic channels [2], [3]. The HYPER method combined with multiple Anger-positioning zones can significantly increase the count-rate capability and dose efficiency of PET and gamma cameras. But for coincidence detection applications and other timing-detection applications, such as positron-coincidence imaging, an additional trigger-delay technique must be used. In traditional scintillation detector electronics, the signal integration time for each event is fixed. Hence, the end of the integration and the signal digitization time (for energy and position) are synchronized with the timing trigger signal but delayed by a fixed integration time. The trigger signal is generated at the leading edge of the timing trigger pulse or the arrival time of the event. Coincidence detection can be performed between the ends of the digitization signals or the trigger signals. However, since HYPER uses a dynamic integrating method in which the energy and position signals are digitized upon the arrival of the next event (arriving at a random time after present event), the measured energy and position signals are no longer synchronized with the leading edge of the present triggering signal. To detect a coincidence event using the HYPER method: (a) the original trigger signal must be delayed by a fixed time that is longer than the maximum possible integration and digitization time and (b) the current energy/position digitized signal must also be resynchronized to the delayed timing trigger. After the delay and resynchronization, all the signals relating to the current event can then be passed to the coincidence-checking processor. Except for the fixed delay time, both the timing trigger and the energy/position signals would maintain the fast timing integrity of the event if the delay circuit can maintain a negligible timing jitter. Hence, the coincidence timing resolution of the PET camera hinges on the timing resolution (fidelity) of this delay circuit. This type of accurate delay is not necessary in one conventional coincidence-processing method [4] that finds the coincidence event pairs by sorting (table lookup) the time marks generated by latching a master clock's time at the onset of an event. However, this type of "latching-sorting" design would be quite cumbersome for our system with 48 timing channels that will need 48 fast latches and ribbon cables with timing skews corrected. Hence, we developed this high-timing-fidelity delay circuit because of engineering requirements and practical necessity. This high-resolution delay circuit can also be used in other coincidence electronics designs that use the "timing-AND-logic" concept employed by some commercial PET systems, because such systems also require a long delay to synchronize the timing trigger and the energy/position signals.

Manuscript received December 6, 2002; revised April 1, 2003. This work was supported in part by NIH Grant RO1 CA58980, NIH Grant RO1 CA61880, NIH Grant RO1 CA76246, NIH Grant RO1 EB00217, NIH Grant RO1 EB001038, U.S. Army Breast Cancer Grant, Texas Higher Education Grant, John S. Dunn Foundation Research Grant, and Cobb Fund for Cancer Research.

The authors are with the University of Texas M. D. Anderson Cancer Center, Houston, TX 77030 USA (e-mail: yaqiang_l@yahoo.com).

Digital Object Identifier 10.1109/TNS.2003.817412

II. Methods

A. Pre-Coincidence Synchronization of Signals in the Dynamic Integrating Approach

As discussed earlier, the HYPER dynamic integration and correction method requires a timing delay and a resynchroniza-

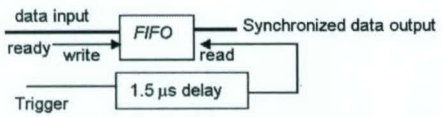

Fig. 1. Circuit to restore synchronization of HYPER signals before coincidence processing.

TABLE I
SYNCHRONIZATION RESTORING

TABLE 1					
Event number	1	2	3	4	5
Event arrival time (μs)	0	0.2	1.5	2.0	2.7
Event integration-sampling time = input time of event into FIFO (μs)	0.2	1.2	2.0	2.7	*
Event readout time from FIFO (μs)	1.5	1.7	3.0	3.5	4.2
Waiting (holding) time of event in FIFO (μs)	1.3	0.5	1.0	0.8	*

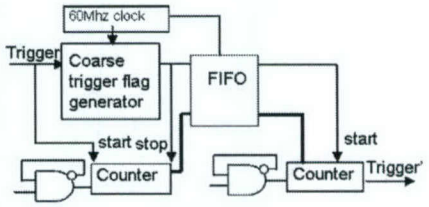

Fig. 2. Diagram of the digital delay unit.

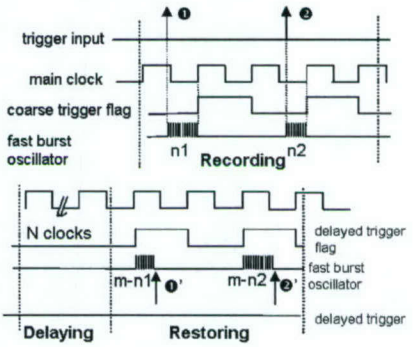

Fig. 3. Timing of the delay generator, which consists of three sections: time jitter recording, main time delaying, and fine-delay restoring.

tion between the timing trigger and the energy/position signal of the same events. In the synchronization process, the energy and position signals of all events are first pipeline buffered into a first-in/first-out (FIFO) temporary memory, then a delayed trigger signal is used to read them out individually so that the sequential order of events within the data stream can be maintained. Since the readout of the energy and position signals from the temporary holding FIFO memory is time-latched by the delayed trigger, and since the delayed trigger signal is synchronized with the trigger signal (except for the fixed delay-time shift), the energy and position signals are now synchronized to the trigger signal (Fig. 1).

The fixed delay time should be longer than the maximum integration time. The trigger delay circuit should have a good timing resolution and low dead time. Table I illustrates the processing of five continuous events using FIFO and delay technique to restore the synchronization between the event trigger signal and the data output signal (except for the fixed delay-time shift).

1) Event integration-sampling time equals next event's arrival time if the current event is piled up by the next event, if there is no pileup on the current event, it will be integrated for a fixed maximum period of 1 μs.
2) Waiting time is the time difference between the FIFO readout time and the event arrival time.
3) * *means that the value is dependent on the next event arrival time (not illustrated in Table I).*

Hence, the order of the data in a FIFO is the same as the order of events coming in. We are using the linear structure of a FIFO to line up all the events in the order in which they arrive. Then we apply a large fixed delay (larger than the longest integration time) for the event trigger, and use the delayed event trigger to "clock" the readout of events from the FIFO. Hence, each event in the FIFO is clocked out (read out) synchronously with the event triggering time (except for a fixed delay). It is the waiting (holding) time of an individual event in the FIFO (as controlled by the delayed trigger) that synchronizes the FIFO readout time to the original event-arrival time.

B. B Delay Method

Figs. 2 and 3 show the design and timing of the high-resolution pipeline delay unit. The design includes three sections: a high-resolution time recorder, a major/coarse time-delay, and a high-resolution trigger restoration. Each input trigger signal is recorded by a main clock (60 MHz) generating a clock-synchronized coarse trigger flag signal. Meanwhile an ultra-fast counter (see Fig. 2), driven by a 700-MHz burst oscillator, counts the time lapse between the original trigger and this coarse trigger flag. The arrival time of the trigger signal can be recorded very accurately by combining the coarse trigger flag and the fast counter. The burst oscillator only works for a very short time to reduce the system noise level and the power dissipation. The main time delay section consists of a synchronized FIFO memory. The coarse trigger flag and the recorded number from the fast counter will be put into the FIFO, which is driven by the same main clock to create the main time delay. The FIFO has a pipeline structure, and the length of the FIFO times the clock period determines the main time delay. To restore the delayed trigger accurately, the delayed number of the counter readout from the FIFO will be reloaded into another ultra-fast counter (see Fig. 2), and the delayed trigger flag output from the FIFO will start the second counter clocked by a second burst oscillator. The high-resolution delay trigger signal will be created when the second counter becomes full.

In Fig. 3, n1 is the time lapse between the event trigger input and the associated coarse trigger flag. This is the time jitter caused by the main clock. Here, we use a fast clock to record it. In the same figure, m is the full range or maximum count of the second fast counter, and $(m - n1)$ is the adjusted

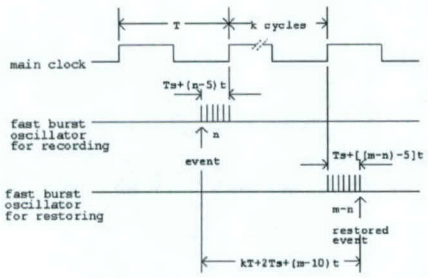

Fig. 4. The delay time is independent of the event arrival time by ensuring fast oscillators working more than five cycles in both recording and restoring signals. T is the main clock period; t is the period of burst oscillator; Ts is the time of the first five cycles of the burst oscillator.

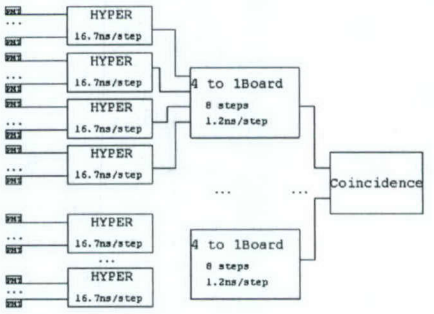

Fig. 5. Two programmable time alignment mechanism: coarse steps (16.7 ns/step) on the HYPER boards and fine steps (1.2 ns/step) on the 4-to-1 boards.

delay time needed to accurately restore the trigger signal from the delayed coarse trigger flag. To have the (m − n1) fine delay time in the second counter, it will be reset to n1 and then run until it reaches m when an accurate delay trigger is generated. Hence, the time difference between the recovered delay trigger and the original event trigger is equal to n1 + (main clock delay) + (m − n1) = (main clock delay) $+m$, therefore, it is a time constant, and the jitter n1 can be canceled. An additional fine delay time can be achieved by adding or subtracting a time offset to the preset time n1 for the second counter. Both the length of the FIFO and the time offset can be programmed using a field-programmable gate array. The programmable time-offset is useful if front-end electronic boards need a high-resolution time alignment for coincidence measurement. The counters and burst oscillators used for recording the time lapse and restoring the delay trigger are ultra-fast emitter-coupled logic (ECL) picoseconds devices. Since the jitter time n1 is measured by the first counter and the compensating delay time (m − n1) is clocked by the second counter, any difference between the two burst clock periods would cause an extra timing error. To reduce this timing error, we built the two burst oscillators in one ECL chip so that they could have the same frequency, unaffected by changes in the temperature and other environmental conditions such as the voltage of the power supply. To reduce system noise, the two burst oscillators work for only a very short time. This introduces a new technical problem, however, because the first several cycles after the oscillators start working are not very stable. Tests showed that the cycle time was not consistently stable until the fifth cycle. To solve this problem, a logic circuit is designed to have some selectable function: the trigger signal is caught by the main clock rising edge only when the count number n is greater than five; otherwise it will be caught by the next main clock rising edge. For the same reason, the counter's full number m is big enough to make the restoring number "m − n" greater than five. As shown in Fig. 4, if the two burst oscillators have the same characteristics, their first five cycles' total time is *Ts*, assuming the oscillators have stable cycles with time t after the first five cycles. If the number recorded by the first counter is n, the time lapse between the event trigger signal and the next main clock is $Ts + (n-5)t$. When restoring the signal, the time lapse between the main clock and the restoring signal is $Ts + [(m-n)-5]t$. If the main clock cycle time is T and there are k main clock cycles between the recording and restoring, the total delay time is $kT + 2Ts + (m-10)t$. The n is canceled, and we get a time constant. In designing the delay, temperature-effect monitoring is a very important to achieving the timing goal.

C. Time Alignment

In our design, each detector module is divided into four electronic zones; each zone has its own HYPER and trigger delay circuit. Before performing coincidence checking, there is a "4-to-1" board to combine the energy/position data and trigger signals of the four zones back into a single module. Thus, for the following circuits, all the signals would look like those from an integral module. All the modules' trigger signals will go to the coincidence board for time coincidence, as shown as Fig. 5.

Our PET system has 12 modules; and each module has four zones. Each zone has its own delay unit, but the delay times normally differ from each other. Hence, all the delayed signals should be aligned in time before time coincidence is performed. Each HYPER board has a software-controllable switch that can introduce a 16.7 ns delay. The 4-to-1 board has four simple delay units that could provide further delay times for each zone. This simple delay unit has eight steps, and each step has a 1.2 ns delay time. These two ways of adjusting time delay make it possible to align the time difference of the delayed signals among the different zones and modules. The delay time steps can be controlled by software through a parallel port, which makes time alignment easier than the traditional cable delay method.

III. Performance

We have designed and implemented a high-resolution delay generator with a very low dead time. This delay generator has also been integrated successfully into our HYPER circuit for the PET application. All the performance tests have been done on an independent prototype circuit (see Fig. 6).

Fig. 7 shows delayed pulse signals, produced by the delay generator, on a Tektronix digital oscilloscope (TDS3032) with an infinite display time. The oscilloscope was triggered by the rising edge of the same pulse input to the delay generator. Since the delay timing applied only to the rising edge and not to the falling edge, we found the delayed pulses had a larger jitter (16.7 ns) in the falling edge than in the rising edge. The rising edge time jitter (resolution) was less than ±0.9 ns. This delay

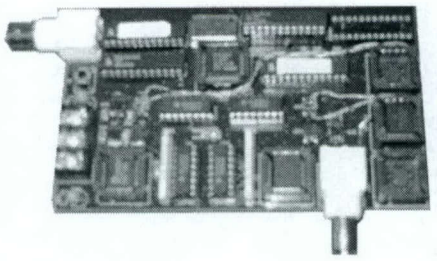

Fig. 6. A prototype delay generator.

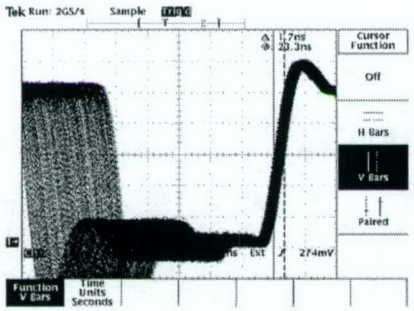

Fig. 7. The delay signal result observed from the oscilloscope.

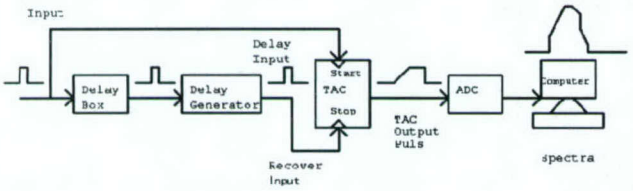

Fig. 8. The delay time distribution detection method.

timing resolution is good enough for the coincidence measurement of BGO PET detectors with a typical 12- to 20-ns coincidence-timing window. The circuit has a 50-ns dead time. Thus, if two pulses are too close together (less than the 50 ns dead time), they will not be delayed correctly. We also found the delay timing resolution and the dead-time performance were not degraded as the total delay time increased (by increasing the FIFO length for the main delay).

We also set up another test bench with nuclear instrumentation modules (see Fig. 8). A time-to-amplitude converter (TAC) module (model 2145) was used to measure the delay time. The TAC was started by the original pulse signal and stopped by its delayed pulse signal. The TAC result was digitized by an analog-to-digital converter (ADC) module (model 8075), and a spectrum was then created in a computer. To calibrate the time for an ADC channel, we added an extra 4.0-ns delay using an

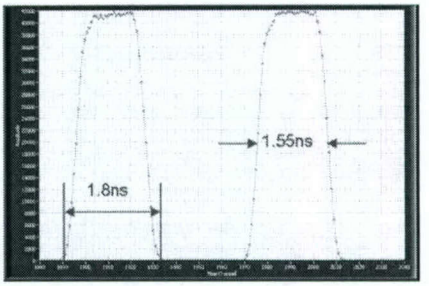

Fig. 9. The delay time distribution result.

analog delay box in the pulse delay channel. By adding this 4.0-ns delay, the spectrum was shifted to upper channels by an offset of 80 channels (see Fig. 9). Hence, each ADC channel indicated a 50-ps delay. The ideal spectrum of the delay time distribution is a rectangle. A full width at half maximum of 1.55 ns and a full width at tenth maximum of 1.80 ns for the spectrum were measured with this method.

IV. Conclusion and Discussion

A programmable, high-resolution, ultra-fast delay generator has been designed and constructed. Our test results showed: 1) the delay generator had a timing jitter of less than ± 0.9 ns, a figure small enough for timing and coincidence measurement; 2) the delay generator had a dead time of about 50 ns and could handle input pulse rates of up to 20 MHz; 3) the total delay range of the delay generator could be as long as hundreds of milliseconds with no performance degradation; and 4) the delay time can be programmed in coarse steps of 16.7 ns and in fine steps of 1.2 ns. This high-resolution delay generator is an important component when using dynamic scintillation integration such as the HYPER circuit we proposed for PET coincidence detection, and it has been successfully integrated into the HYPER electronics. This delay generator can also be used as a general device in other applications, such as automatic test equipment and communications.

References

[1] W. H. Wong, H. Li, J. Uribe, H. Baghaei, Y. Wang, and S. Yokoyams, "Feasibility study of a high speed gamma camera design using the high-yield-pileup-event-recovery (HYPER) method," *J. Nucl. Med.*, vol. 42, no. 4, Apr. 2001.

[2] W. H. Wong, "The design of a high resolution transformable whole body PET camera," *IEEE Trans. Nucl. Sci.*, vol. 49, Oct. 2002.

[3] H. Li *et al.*, "A new pileup-prevention front-end electronic design for high resolution PET and Gamma Camera," in *Proc. IEEE Nuclear Science Symp. Conf. Rec.*, vol. 4, Nov. 2001, pp. 1969–1973.

[4] J. P. Martin and K. Ragan, "A programmable nanosecond digital delay and trigger system," in *Proc. IEEE Nuclear Science Symp. Conf. Rec.*, vol. 2, Oct. 2000, pp. 141–144.

IEEE TRANSACTIONS ON NUCLEAR SCIENCE, VOL. 50, NO. 5, OCTOBER 2003

An Efficient Detector Production Method for Position-Sensitive Scintillation Detector Arrays With 98% Detector Packing Fraction

Jorge Uribe, *Member, IEEE*, Wai-Hoi Wong, *Member, IEEE*, Hossain Baghaei, *Member, IEEE*, Rocio Farrell, Hongdi Li, *Member, IEEE*, Mehmet Aykac, D. Bilgen, Yaqiang Liu, Yu Wang, and Tao Xing

***Abstract*—Position-sensitive scintillation-detector arrays (PSSDAs) are used in nuclear-imaging methods such as PET. The kind of technique selected in producing the PSSDA determines the imaging resolution, sensitivity, labor/part cost, and reliability of the system. Production of PSSDA is especially challenging and costly for ultra-high-resolution systems that have large numbers of very small crystal needles, so we developed a new slab-sandwich-slice (SSS) production method. Instead of using individual crystal needles, the construction started with crystal slabs that are 15-crystal-needles wide and 1-needle thick. White-paint was deposited onto slab surfaces to form shaped optical windows. The painted slabs were grouped into two crystal-sandwich types. Each sandwich type consisted of a stack of seven slabs painted with a distinctive set of optical windows, held together with optical glue. For a 40 000-crystal system, only 192 type A and 144 type B sandwiches are needed. Sandwiches were crosscut into another slab formation ("slices"). Each slice was again 1-needle thick; each slice was basically a stack of needles glued together, optically coupled by the glue and the painted windows. After a second set of white-paint optical-windows was applied on the slices' surface, three slices of type B were grouped between four slices of type A to form a 7 × 7 PSSDA. We used SSS production method to build 7 × 7, 7 × 8 and 8 × 8 crystal blocks needed for a high-resolution 12-module prototype PET camera. The method reduced the more than 400 000 precision painting and gluing steps into 55 500 steps for a 40 000-BGO-crystal system, thus lowering the labor cost. The detectors fabricated with the method were of high quality: 2.66 mm × 2.66 mm crystals were separated by only a 0.06-mm gap for a 98% linear detector packing fraction or 96% area packing fraction. Compared to 90% linear-packing (81% area) from conventional methods, the 20% increase in packing density translates into as much as a 1.2 to 1.4 coincidence sensitivity in PET. Crystal cost was halved, and production yield increased to 94%. It generated very small crystal-positioning errors ($\sigma = 0.09$ mm), required for ultrahigh resolution detectors.**

***Index Terms*—Photodetectors, position sensitive detectors, positron emission tomography (PET), quadrant sharing detectors, scintillation detectors.**

I. Introduction

POSITION-sensitive scintillation detector arrays (PSSDA) are commonly used in nuclear imaging, especially in PET cameras. Other than the design of the detector, the most important decision in building a PET is the detector production method, because it directly determines the ultimate imaging resolution, sensitivity, labor cost, and reliability. In position-sensitive scintillation array systems, each scintillation crystal distributes a unique amount of scintillation light to a number of photodetectors/photomultipliers (PMT). The PMT signals identify each firing crystal from each crystal's unique light-distribution pattern. Imaging resolution is determined by a) how finely the light distribution from each crystal can be controlled and b) the precision with which the light-distribution design is executed in a mass-production process.

We have developed a new production method for PSSDA that fulfills the following seven important conditions:

1) finely control the distribution of light from each crystal to achieve high imaging resolution;
2) efficiently distribute the scintillation light to photodetectors for maximum imaging resolution;
3) achieve a high crystal-packing density for maximum sensitivity;
4) precisely and reproducibly manufacture the light-distribution devices according to design specifications;
5) lower costs for both labor and raw material;
6) maintain long term reliability;
7) high yield detector production (less detector breakage or substandard detectors).

The process of producing a position-sensitive crystal array involves: a) cutting, lapping, etching, polishing, and cleaning each crystal, b) making the light-distributor for each crystal, c) optically mating each crystal to the light distributor, and d) assembling all the crystals and light distributor into an array. An ultra-high-resolution PET system may have more than 40 000 crystals (and light distributors), each as small as 2.66 mm × 2.66 mm as in our experimental high-resolution-oncologic-transformable-PET (HOTPET) [1]. The sheer number and small crystal size can make such a system unrealistic to produce both in terms of the raw material and the labor cost. Since the crystal pitch is very small in an ultrahigh resolution system, the traditional sawing technique (partial-depth sawing of a crystal block or a plastic light-guide) would significantly decrease the detection sensitivity. A diamond-blade's kerf of as little as 0.35 mm lowers the packing-area efficiency to $[2.66/(2.66 + 0.35)]^2 = 78\%$; translated into a coincidence efficiency of only 61% $(0.78)^2$. We remedied the sensitivity loss by first developing a partial-crystal-surface painting technique to control the light through the crystal surfaces; the shape of the mask depends on the location of the crystal in

Manuscript received December 3, 2002; revised July 20, 2003. This work was supported in part by the National Institutes of Health (NIH) under Grants RO1 CA58980, RO1 CA61880, RO1 CA76246, and RO1 CA58980S1, by the Texas Higher Education Advanced Technology Grant, by the John S. Dunn Foundation under a Research Grant, by The Mike Hogg Foundation, and by the Cobb Foundation for Cancer Research.

The authors are with the M.D. Anderson Cancer Center, University of Texas, Houston, TX 77030 USA (e-mail: juribe@mdanderson.org).

Digital Object Identifier 10.1109/TNS.2003.817959

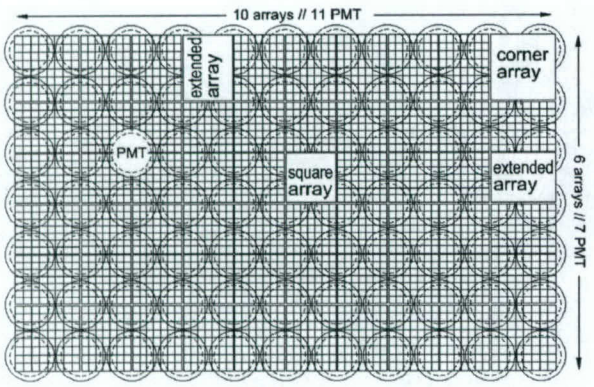

Fig. 1. HOTPET's detector module design requires three different types of PSSDA arranged in PQS mode for optimum use of the PMTs at the edge of the module. Edge blocks are knows as "extended" blocks.

the array and on the surface orientation. Second, by removing any gap between crystals except for the space occupied by the glue and paint layers (0.06 mm), which is less than one-fifth of the diamond-blade's kerf and increases the coincidence detection efficiency by 50% over the partial sawing technique. However, precise manufacturing, painting, and gluing of 40 000 tiny crystals would still require over 400 000 steps, which is extremely labor intensive and expensive.

A. Motivation

The PET instrumentation group at MD Anderson Cancer Center is involved in the design and development of a second generation, very-high resolution and versatile, PET camera for clinical and research applications. The camera can be transformed from an extra-large patient port for radiotherapy planning to a small-diameter high-sensitivity breast/animal system [1], [2]. It consists of 12 independent modules that move radially and turn around their own axis transforming the camera into the various configurations. The design of its highly pixilated detector modules is based on the photomultiplier quadrant sharing technology "PQS" [3], developed by the same group. PSSDAs arranged in PQS mode make optimum use of the PMT's photocathode (no gaps between arrays) except for the PMTs at the edge of the module, where just one half of the photocathode is utilized. We have developed asymmetrical crystal arrays [4], which extend the size of the detector module and include the unused part of the edge PMTs; double-extended crystal arrays for the module's four corners were also developed. Fig. 1 shows HOTPET's detector module design combining the three types of PSSDA, including 3168 crystal-needles (38 016 total system) coupled to 77 PMTs. This module design implements PQS's cost savings by using fewer PMTs, and improves sensitivity by minimizing the gaps between detector blocks, as compared to today's commercial PET cameras [1].

The first-generation PET camera developed by our group (MDAPET [5]) served as the testing ground for two PSSDA production techniques: "partial-depth sawing" and "paint and glue" masking [1]. Fig. 2 shows a BGO block from MDAPET build using these two techniques. The camera's axial resolution was the result of controlling the scintillation light throughout the block by "partial-depth sawing" light-barriers, whereas the

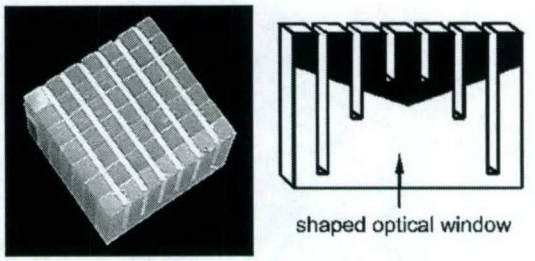

Fig. 2. (Left) MDAPET's 7 × 7-BGO-array combining the "partial-depth sawing" and the "paint and glue" mask techniques to control the scintillation light inside the block. (Right). Painted-mask used in the "paint and glue" direction for optimum gamma-hit crystal decoding.

trans-axial (in-plane) resolution was the result of the "paint and glue" light-blocking technique. The 2.8 mm transaxial resolution we achieved was superior to the 3.4 mm axial resolution of the "partial-depth sawing" proving the benefits of the "paint-and-glue" technique. Combined with better linear packing fraction, compared to the kerf left by the saw, the paint-and-glue technique was the obvious choice to design the detector of the second generation PET camera. The major drawback of this approach was that it turned each crystal into an individual element, rather than a section of a slab defined by the saw cuts (Fig. 2 right), which logically leads to the handling of nearly 40 000 separate pieces. An added complication came from the fact that the shape of the painted masks were more than simple bands across the crystal array. They had convoluted shapes optimized for better identification of gamma hits from different crystal needles within the block, as shown in Fig. 2 (right). Furthermore, the development of "extended" PSSDA for the edge and corners of HOTPET's modules was possible because asymmetrical masks of different shapes were applied along the extended direction.

The overall detector requirements, reproducibility, and the need for a low-cost production method to build HOTPET's detectors motivated us to develop the process described here. We have designed and implemented the "**slab-sandwich-slice**" (**SSS**) production technique necessary for efficiently producing large numbers of very small PSSDA with almost 100% packing fraction. Using it we can produce both symmetric and asymmetrical blocks and still allow use of fine-tuned convoluted light-barriers between needles. The SSS method lowered the production cost, increased yield, and increased detection efficiency.

II. The Slab-Sandwich-Slice Method

The SSS production algorithm topology is illustrated in Fig. 3. Instead of using individual crystal needles, we started the construction with BGO slabs that were 15 crystal-needles wide and 1 crystal-needle thick (2.66 mm × 50 mm, Fig. 4, top left). There was no actual constraint on the length of the slabs; they can be of arbitrary length. We chose the 15-needle length to accommodate the BGO supplier's tooling and production capabilities [6]; overall costs were reduced as a result. A stack of 7 slabs were painted with optical masks (window) and optically glued together [7] to form a crystal *sandwich* (top arrays Fig. 3, Fig. 4). The mask on each slab was a fixed height straight band of white paint [7] applied along the entire length of the slab

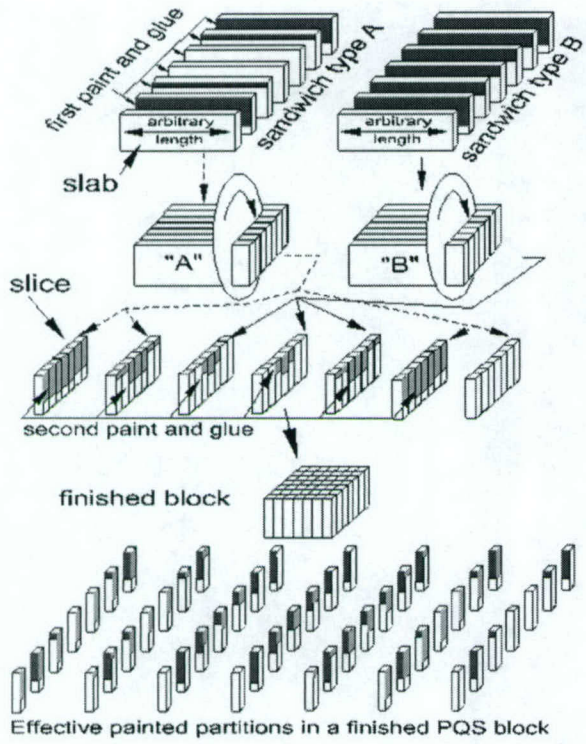

Fig. 3. The "slab-sandwich-slice" (SSS) production method for position-sensitive scintillator detector arrays (PSSDA).

[Fig. 3, Fig. 5(a)]. Then, the slabs were grouped into 2 different "sandwich types" (A and B in Fig. 3) following a specific order according to the size of their masks. For sandwich type A, only four of the seven slabs were painted with two different mask patterns (top-left—Fig. 3). For sandwich type B, six slabs were painted with a different set of masks (top right—Fig. 3).

All the sandwiches are crosscut into another slab formation, which we call "slices" (picture in Fig. 4). The thickness of each slice was again one crystal width (2.66 mm), and each slice was in essence a stack of individual crystal needles optically coupled together by the glue and paint masks between them. All the slices cut from a given sandwich had the same mask pattern between the crystal needles, defined by the parent sandwich. Three slices of type B were grouped between four slices of type A (follow the dash and solid arrows in Fig. 3) to form an array of slices. Before the seven slices of this new array were glued together to form the final PSSDA ("finished block" in the same figure), a new set of masks was painted (masks shown on the face of each slice).

Details of the 49 crystal needles that form the final PSSDA, with the correct masking, are shown in the block's exploded view at the bottom of Fig. 3. In this view, each crystal needle has a set of masks and windows that are relevant only to the specific crystal location and face orientation within the block. The PSSDA described in Fig. 3 is a square symmetric block, confirmed by observing that every set of masks facing a *column* of crystals also appears as a set of masks facing a *row* of crystals and they are repeated symmetrically from the center of the block (Fig. 3 bottom).

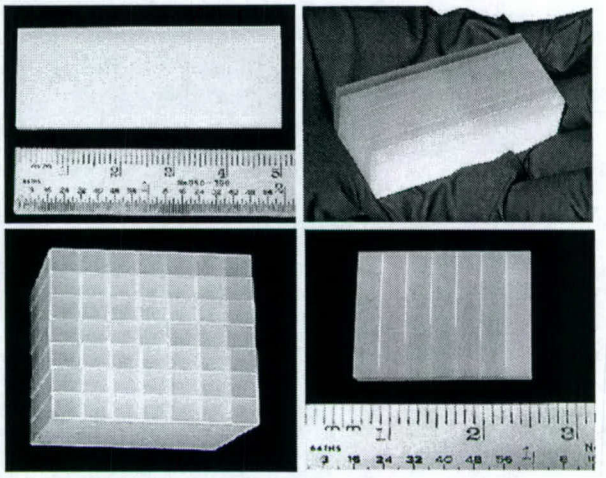

Fig. 4. Pictures showing the four stages of the SSS production process. Clockwise direction (from top left): slab, sandwich, slice, and 7 × 7 PSSDA.

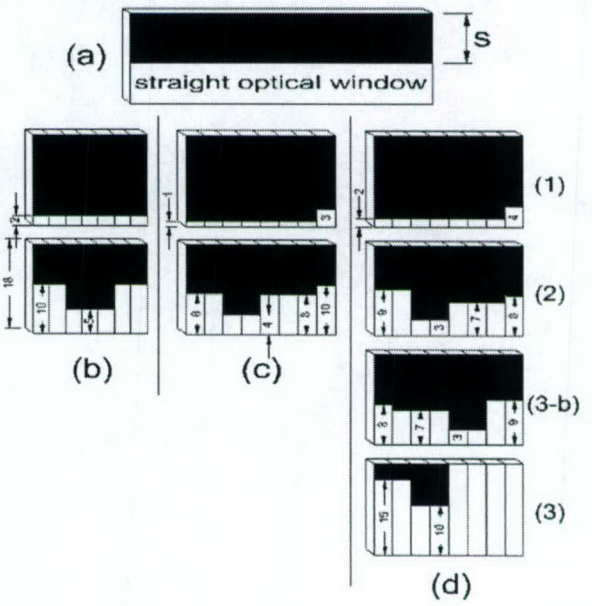

Fig. 5. Examples of slab and slice paint-masks used for HOTPET. (a) Masks for slabs that make up a sandwich; straight masks with constant height "s" covering the length of the slab. (b) Masks for slices of symmetric PSSDA (middle blocks Fig. 1). (c) Masks for slices of extended arrays placed at the edge of the detector module in Fig. 1. (d) Masks for the corner arrays of the same module.

Pictures of a slab, a sandwich, a slice, and the final 7 × 7 PSSDA are shown in Fig. 4. Comparison of this array with the one in Fig. 2 shows very small intercrystal separation, increasing packing fraction and detection sensitivity.

The SSS method is not limited to the production of symmetric or square detector arrays. In fact, it allows fine-tuning of the shaped optical windows between needles by introducing the "stepped" light barrier, which makes possible asymmetric light partitions. The paint-and-glue barrier used in the first-generation PET, shown in Fig. 2 (right), achieved nonuniform blocking of the light between this slice and an adjacent one. The crystals in the middle had a larger blocking mask than the end crystals,

TABLE I
SUMMARY OF HOTPET DETECTOR PRODUCTION (PARTS AND STEPS INVOLVED). 12 MODULE SYSTEM WITH 38 016 CRYSTALS

Block type	7x7 symmetric	7x8 extended	8x8 corner-extended	TOTAL CAMERA
Number of blocks	384	288	48	720
Types of Sandwich (Tot.Quantity)	2 (179)	4 (134)	4 (27)	10 (340)
Number of slabs	1253	1072	216	2541
Types of masks for slabs (painting steps)[1]	5 $\left(\frac{1077}{4}=270\right)$	11 $\left(\frac{828}{4}=207\right)$	11 $\left(\frac{258}{4}=64\right)$	27 $\left(\frac{2163}{4}=541\right)$
Number of slices (one cut/slice)	2688	2016	384	5088
Types of masks for slices (painting steps)[1]	3 $\left(\frac{2304}{4}=576\right)$	3 $\left(\frac{1728}{4}=432\right)$	10 $\left(\frac{480}{4}=120\right)$	16 $\left(\frac{4512}{4}=1128\right)$

[1]The ratios in parenthesis show the number of slabs or slices masked divided by four, because there were four pockets in each painting jig holder and all four are painted in one operation (see Tooling section).

but the shape of the mask was limited to two straight lines due to the masking process. In the second generation the stepped light-barrier has a straight horizontal boundary *at each* crystal and can be adjusted individually for every element, as shown in Fig. 5(b), (c), and (d). Fig. 5 shows the masks and values used in the production of the new detector for HOTPET. It shows symmetric patterns used for the symmetric 7 × 7 block [Fig. 5(b)], as well as nonsymmetric mask patterns used for the extended-rectangular 7 × 8 PSSDAs placed at the edges of the detector module [Fig. 5(c)] and masks for the larger square asymmetric 8 × 8 arrays for the module's corners [Fig. 5—column (d)].

The SSS method can use a larger number of sandwiches than the two shown in Fig. 3. More complicated crystal arrays, like the "extended" blocks for HOTPET (see Fig. 1 and Fig. 5), required four types of sandwiches due to asymmetry along the extended direction. For instance, the rectangular 7 × 8-crystal PSSDA was built by placing one slice from sandwich type A (not shown) between two slices from sandwich type B, these three slices were placed between two slices from type C, and slices from type D one on each end completed the block.

In some instances, light blocking provided by the white paint was not enough to decode the gamma hits from all needles in a PSSDA. We applied paint on facing surfaces of adjacent crystals, resulting in a double coat of paint for stronger light blocking. This technique is easily incorporated into the SSS production method by applying paint masks on both sides of the same slab or slice. For instance, three adjacent slices for HOTPET's corner block were painted using masks (d)(1), (d)(2), and (d)(3) from Fig. 5, but additional paint was needed between the last two slices. Thus, a fourth mask [Fig. 5(d)(3-b)], the mirror image of Fig. 5(d) (2), was applied on the backside of the third slice. A similar technique was used to mask the slabs of a sandwich, introducing double paint-coat along both axial and transaxial directions.

Table I summarizes the slab-sandwich-slice production process of the detector for HOTPET. A total of 720 PSSDAs of three different types were built starting with 2541 slabs. It is important to note that in spite of the variety of types and block-designs used for this detector, only two size slabs were purchased, i.e., 50 mm (15 needles long) by 2.68 mm thick and 50 mm long by 3.06 mm thick. Thus, the starting raw elements needed by the SSS method are simple large crystals (lower cost). The essence of the method rests in the *design of the painting masks and the layout of combinations of slices* from different sandwiches to form a PSSDA.

From Table I, the total number of steps (operations) needed to build the entire detector is as follows.

— Cut and lap of each element

(2541 slabs) × (3 cuts + 6 lap) = 22 869 operations
(5088 slices) × (1 cut + 2 lap) = 15 264 operations.

— Paint and glue

sandwich : 2705 mask & paint + 3941 clean & glue = 6646 operations
slices : 5640 mask & paint + 5040 clean & glue = 10 680 operations.

Thus, the total number of operations was 55 500, which is only one-eighth of the number of steps needed to build the same detector starting with individual needles (see Results section).

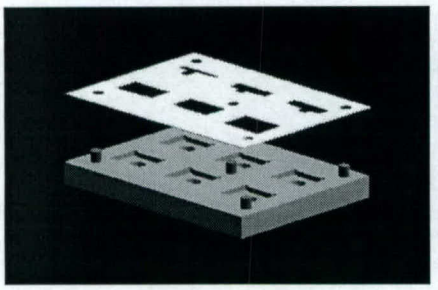

Fig. 6. Bottom: precision painting jig. Top: Laser-cut mask. The jig shown here was built for painting slices (six pockets). Jigs for painting slabs could hold only four slabs due to their larger size.

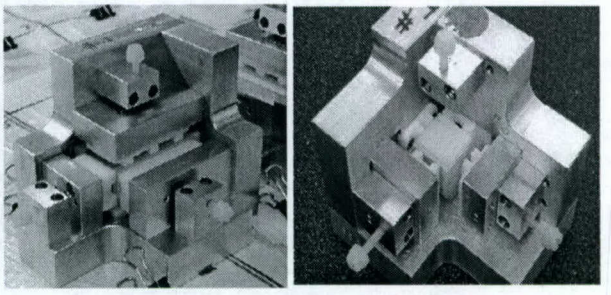

(a) (b)

Fig. 7. (a) Gluing jig with sandwich compressed in three dimensions. (b) Final PSSDA inside the jig with the top compression piece removed.

A. Tooling

A special set of tools was developed to assure the accuracy and reproducibility of crystal arrays built with the SSS technique.

To create the paint pattern, the slabs and slices need to be masked. Each slab/slice was mounted onto a painting jig and covered by a disposable painting mask. White paint was applied using an airbrush.

Developing a fast way to mask the crystals with high geometrical accuracy was essential. Masking and painting were performed on multiple slabs/slices simultaneously. Multiple slabs were placed in a precise masking painting jig. The jig has recesses that the slabs can slide into snugly, and the slab surfaces are flush with the jig surface (Fig. 6). The jig has five precisely placed steel studs for mask alignment. A paper mask with corresponding alignment holes to fit these studs was placed on the jig to cover both the jig and the slabs (Fig. 6). The masks were laser cut[1] from pressure sensitive stock [8]. Removable adhesive on one face of the mask kept it adhered to the jig and crystals while the paint was applied; yet it allowed easy removal of the paper mask leaving no residue on the BGO surface. A laser was used to precisely cut a stack of several sheets of paper at one time. Laser cut patterns are reproducible within 25-μm and accurate within 60-μm, and they cost only \$0.50 per sheet (including raw materials), which could be used to make up to six masks (Fig. 6). Ten jigs can be painted at one time.

The paint had to be applied evenly and with a precisely controlled thickness so that many layers of crystals (slabs) and paint could be stacked together with high precision. We used the airbrush technique driven by pressure-regulated N_2 gas from a gas cylinder. Pressure-regulated N_2 drove a constant rate of paint delivery to control the paint thickness. Each optical window required six coats, applied at 30-min intervals, with a final thickness of 45-μm.

A precise technique for gluing slabs and slices was needed. All the slabs and slices were glued together using optically transparent glue [7]. Because of high mechanical precision and optimum optical coupling requirements, the thickness of the glue layer and its application technique were carefully studied. We designed and built high-precision gluing jigs so that all three dimensions of a sandwich (made of slabs) or a PSSDA (made of slices) could be tightly compressed and dimensionally regulated (Fig. 7). From test run experiments we optimized precuring time of the glue to achieve ideal viscosity before application, as well as curing time while the glued array sits in the jig. Curing time needed to be long enough to harden and avoid compromising the mechanical tolerances at the time of disassembly, yet short enough to allow removal from the jig and easy cleaning of excess glue. From these studies we set up the following sequence for the gluing process: mix glue | precuring and air bubble removal (venting) | glue application and assembly of array into gluing jig | curing | disassembly and glue excess removal | remount into gluing jig | curing | disassembly and final cleaning.

[1]Lasercraft Inc., Santa Rosa, CA.

III. Results

The SSS method utilizes painted reflecting barriers on the crystal surfaces to precisely control the light distribution because *any shape can be painted*; this feature optimizes crystal decoding.

Throughout the entire process *no* single crystal needle is *handled individually,* making it a very efficient process.

Crystal needle separation is reduced to a few hundreds of a millimeter, improving detector sensitivity.

All these features of the SSS production method were evaluated with the construction of the detector for our high-resolution clinical-PET prototype HOTPET.

A. Cost and Production

Instead of working with each individual crystal needle, we bought slabs that have the same length as 15 needles stacked side by side. The price per BGO needle was \$4 (\$60 for 15), but the price for a BGO slab (15 wide) was \$31 (due to less processing). Hence, building the detectors from slabs instead of individual needles saved 50% in raw material costs.

The HOTPET detector has nearly 40 000 crystals in it (Table I). The number of steps (operations) involved in the construction of this detector starting with individual needles is shown below.

— Cut and lap each element

(38 016 needles) × (3 cuts + 6 lap) = 342 144 operations.

— Paint and glue:
  — Painting and masking 15 needles in one operation; from Table I

541 mask & paint + [541 sets × 4 (groups of 15) × 15 needles] clean = 33 001 operations.

— Gluing 7 (8) needles together into a slice and painting the slice

7×7 – crystal-block = 18 816 operations

7×8 and 8×8 blocks = 19 200 operations.

— Slice painting = 5640 operations.

— Final glue, put slices together into a PSSDA= 5040 operations.

Thus, the total number of operations would be 423 800, compared to 55 500 operations with the SSS production method. That is an 87% reduction in labor costs and lowers the probability of mistakes during assembly because fewer parts are handled. Notice the large disparity in the number of operations between the two methods, in spite of attempts to reduce the number of steps involving individual needles, e.g., 15 needles would be placed next to each other and painted together, as well as groups the size of a slice would be first glued and then painted together. If the process is not optimized, and every crystal is cut, lapped, painted, and glued *separately,* the production process for our new detector would require in excess of 0.5 million operations.

The SSS method has a high production yield because if a slice is broken during cutting, the broken slice can be replaced by the next cut from the same sandwich. Hence only 1/7 or 1/8 of the final block is wasted, whereas in the traditional partial-depth sawing method the whole block (49–64 crystals) would be wasted with one bad cut. Production of detector blocks for our first-generation camera MDAPET using the traditional partial-depth method had only a 70% production yield. In contrast, the SSS production method had a slice-cutting yield of 94%. The manufacturer of the BGO slabs [6] performed the slicing of the sandwiches once we have perfected the method.

The entire painting process including applications of masks on slabs and slices had a 98.9% yield.

B. Mechanical Tolerances

Nominally, we had set out to build three types of PSSDA with the following dimensions: 7×7-symmetric—19 mm × 19 mm × 18 mm, 7×8-nonsymmetric-extended—19 mm × 24.76 mm × 18 mm, 8×8-corner-nonsymmetric—24.76 mm × 24.76 mm × 18 mm. Most of the 720 blocks for HOTPET have been built and we studied their mechanical characteristics to evaluate the mechanical consistency of the SSS method.

The SSS method imposes no mechanical constraint on the length of the slabs that form a sandwich because they will be cut into slices. Thus, we purchased 50 mm long slabs with a wide tolerance of ±0.1 mm to lower material costs, but with tight enough tolerances to facilitate the assembly of the sandwich inside the painting and gluing jigs. The thickness of the slabs and slices, on the other hand, were crucial to the overall size of the finished PSSDA. We specified a tolerance of only (−)0.05 mm *below* the nominal thickness of 2.68 mm and 3.06 mm to the BGO manufacturer. These are the only two types of slabs purchased to produce all the detector arrays for HOTPET.

We evaluated size variations of nearly 200 slices and slabs and more than 120 assembled blocks, and have identified four factors that affect their dimensions. These variations are important because they directly affect the actual placement of a needle within the PSSDA. These factors are depicted in Fig. 8.

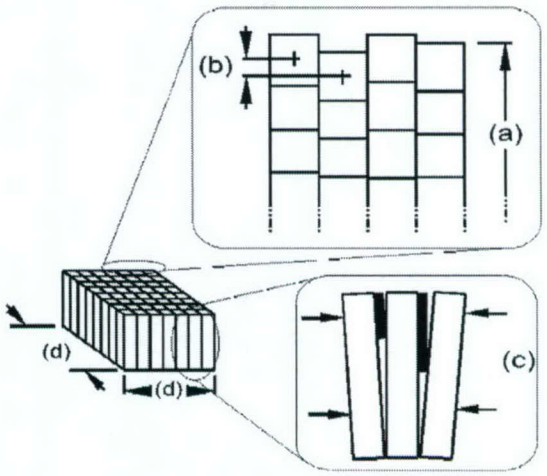

Fig. 8. Four sources of mechanical tolerances from the SSS manufacturing process: (a) glue, paint, and slab thickness (needle positioning error; measures repeatability); (b) systematic differences between sandwich types; (c) needle slant (paint placement, gluing jig limitations); (d) axial versus transaxial dimension differences (size of surface glued).

a) Length variations among slices from the *same* sandwich-type [nominal value 19 mm, and 24.76 mm; $\sigma = 0.04$ mm, Fig. 8(a)]. This variation, caused by differences in thickness of the slabs, paint layer, and/or glue layer, is a measure of the reproducibility of the SSS method.

b) Length differences in slices from *different* sandwich-types [average difference 0.1 mm, Fig. 8(b)]. These differences are due to the variation in number of masks painted in each sandwich type. Within the same PSSDA a slice cut from a parent sandwich with a fewer number of masks will be shorter than another slice cut from a sandwich with a greater number of masks. This is a source of systematic error in the SSS method.

c) Slices show vertical slant [average top–bottom difference 0.15 mm, Fig. 8(c)]. All masks are applied closer to the patient end of the PSSDA, with nothing on the PMT end to make up for this extra thickness. Therefore, slices can tilt. Inadequate sliding constraints of the compression pieces in the gluing jig allowed this displacement of the slices.

d) Axial and transaxial dimensions of square blocks are not equal [average difference 0.07 mm Fig. 8(d)]. This is due to the fact that equal force was applied by the compression pieces of the gluing jig to the side of a sandwich (50 mm × 18 mm surface—axial direction) and to the side of slice (19 mm × 18 mm surface—transaxial direction). Therefore, the pressure difference results in glue layers of different thickness.

The typical thickness of the paint plus glue layer between crystals was 0.06 mm.

Overall, the four factors described above combined with the intercrystal gap produced PSSDAs with the following dimensions: $7 \times 7 array$ – 18.97 mm × 19.12 mm × 18.1 mm; 7×8 – 19.13 mm × 24.85 mm × 18.1 mm; $8 \times 8 array$ – 25.48 mm × 25.39 mm × 18.1 mm. The variance of these dimensions were all

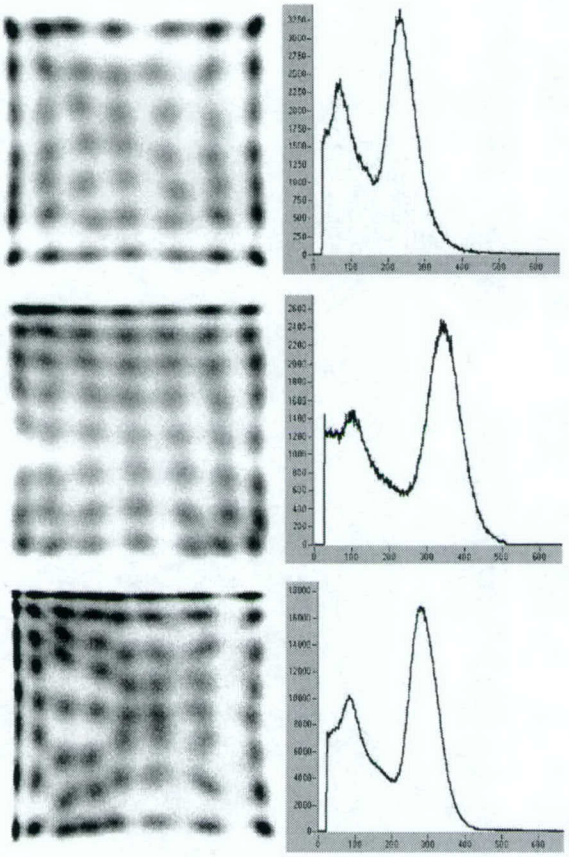

Fig. 9. Two-dimensional decoding map (left) and composite energy spectra (right) of all needles from the three types of PSSDA used in HOTPET (Fig. 1). (Top) 7 × 7 symmetrical array, (middle) 7 × 8 extended nonsymmetrical array, (bottom) 8 × 8 optically nonsymmetrical array used for the module's corners. (Electronic gain and PMT high-voltage settings not equal for all configurations).

under $\sigma^2 = (0.09\ \text{mm})^2$; and they were 98.5% to 99.8% within the target values. It is important to note that the variance and mechanical tolerances described above come from dimensions of complete slices and arrays; that is, they describe the positioning error of the last crystal in a stack of 7–8 needles. Thus, the *average* crystal-positioning error is smaller than the values shown above.

The very small gap between crystals results in a 98% linear detector packing fraction (96% in area). Compared with the typical 90% linear packing fraction (81% in area) in commercial systems [9], the 96/81 (1.2x) higher detector-packing density would result in a significantly higher coincidence detection sensitivity.

The solidly glued blocks are very robust mechanically. Note the superior mechanical tolerance of the block produced by the SSS production method in Fig. 4 bottom-left, compared to Fig. 2.

C. 2-D Map Decoding and Energy Spectra

We evaluated the crystal decoding capability of PSSDAs built with the SSS method. Fig. 9 presents the two-dimensional decoding map and the block's composite energy spectrum for the three types of arrays built for the prototype camera HOTPET. Energy resolution for these blocks is as follows: 7 × 7 − array = 25.6%; 7 × 8 − extended-array = 29%; and 8 × 8 − corner-array = 31%.

A detailed study of crystal signal characterization of the square-7 × 7 and extended-7 × 8 arrays can be found in [10].

IV. Conclusion

- The slab-sandwich-slice "SSS" production method for position sensitive scintillator detector arrays was developed and evaluated by building 720 PSSDA (40 000 crystals) for the high-resolution PET camera HOTPET.
- SSS utilizes painted reflecting barriers on the crystal surfaces to precisely control the scintillation-light distribution, allowing optical windows of *any shape*. Barriers were optimized for crystal identification of gamma hits on the PSSDA (Figs. 5 and 9), improving intrinsic detector resolution. Construction of asymmetric PSSDA was possible thanks to these versatile light barriers, minimizing the unused PMT potocathode area left by PMT-quadrant sharing detector technology.
- Instead of working with each individual crystal needle, the SSS method handles only arrays (sandwich, slices) of needles, making the production of PSSDAs eight times more efficient; and because the raw material is purchased in large slabs, many needles long, it cuts material cost by 50%.
- The average crystal-positioning error was very small ($\sigma <$ 0.09 mm), which is essential for an ultrahigh resolution detector. Sources of positioning error were linked to four mechanical variations in the PSSDA construction method.
- The gap between crystals was only 0.06 mm, producing PSSDAs with good linear packing fraction (98%, 96% area). A system built with such detectors would have improved sensitivity, which could range as much as 1.2 to 1.44 times, for the given resolution.
- The SSS method was flexible and easy to implement. It could be applied to detector arrays manufactured with other materials (LSO, GSO, etc.).
- Two *patents* titled "A Production Method for Making Position Sensitive Radiation Detector Arrays" and "Asymmetrically Placed Cross-coupled Scintillation Crystals" (U.S. Patents 60/353 136 and 60/353,135, filed February 2002) describe the SSS method.

Acknowledgment

The authors would like to thank the machinists at the Radiation Physics Shop at M.D. Anderson Cancer Center—M. Bushman, J. Bovin, P. Barnet, J. Griffin, K, Danniel, and T. Ziegler—for their support manufacturing the tools necessary for this project. They would also like to thank P. Mayes (Physical Plant Manager) for providing materials and making modifications to their laboratories to accommodate the detector construction.

References

[1] W.-H. Wong, J. Uribe, H. Baghaei, H. Li, Y. Wang, M. Aykac, and Y. Liu, "Design of a whole-body high resolution PET with changeable transaxial and axial fields of view," in *Proc. Soc. Nuclear Medicine 48th Annu. Meet.*, Toronto, ON, Canada, June 2001, p. 98P.

[2] W.-H. Wong, J. Uribe, H. Li, H. Baghaei, Y. Wang, M. Aykac, Y. Liu, T. Xing, D. Bilgen, and R. Farrell, "The design of a high resolution transformable wholebody PET camera," *IEEE Trans. Nucl. Sci.*, vol. 49, pp. 2079–2084, Oct. 2002.

[3] W.-H. Wong, "A positron camera detector design with cross coupled scintillators and quadrant sharing photomultipliers," *IEEE Trans. Nucl. Sci.*, vol. 40, pp. 962–966, Aug. 1993.

[4] W.-H. Wong, S. Yokoyama, and J. Uribe *et al.*, "An elongated position sensitive block detector design using the PMT quadrant sharing detector array," *IEEE Trans. Nucl. Sci.*, vol. 46, pp. 542–545, June 1999.

[5] J. Uribe, H. Baghaei, and H. Li *et al.*, "Basic imaging performance characteristics of a variable field of view PET using quadrant sharing detectors," *IEEE Trans. Nucl. Sci.*, vol. 46, pp. 491–497, Dec. 1999.

[6] Inst. Inorganic Chemistry, Siberian Branch, Russian Acad. Sci. 3, Acad. Lavrentyev Prospect, Novosibirsk, Russia.

[7] White Reflecting Paint BC-620 and Optical Cement BC-600, Saint-Gobain Crystals and Detectors, Newbury, OH.

[8] FASSON (r) Crack 'N peel Satin Litho, Pressure Sensitive Stock, Avery Dennison Corp., Pasadena, CA.

[9] S. R. Cherry, M. P. Tornai, C. S. Levin, S. Siegel, and E. J. Hoffman, "A comparison of PET detector modules employing rectangular and round photomultiplier tubes," *IEEE Trans. Nucl. Sci.*, vol. 42, pp. 1064–1068, Aug. 1995.

[10] J. Uribe, H. Li, T. Xing, Y. Liu, H. Baghaei, Y. Wang, M. Aykac, R. Farrell, and W.-H. Wong, "Signal characteristics of individual crystals in a high resolution BGO detector design using PMT-quadrant sharing," *IEEE Trans. Nucl. Sci.*, vol. 50, pp. 355–361, June 2003.

IEEE TRANSACTIONS ON NUCLEAR SCIENCE, VOL. 50, NO. 3, JUNE 2003

A HOTLink/Networked PC Data Acquisition and Image Reconstruction System for a High-Resolution Whole-Body PET With Respiratory or ECG-Gated Performance

Hongdi Li, *Member, IEEE*, Tao Xing, Yaqiang Liu, Yu Wang, Hossain Baghaei, *Member, IEEE*, Jorge Uribe, *Member, IEEE*, Rocio Ramirez, and Wai-Hoi Wong, *Member, IEEE*

Abstract—**An ultrahigh-resolution positron emission tomography (PET) camera in whole-body scanning or gated imaging study needs super computer-processing power for creating a huge sinogram as well as doing image reconstruction. A fast HOTLink serial bus attached to networked cluster personal computers (PC) has been developed for this special purpose. In general, the coincidence data from a PET camera is unidirectional; therefore, an additional daisy-chain bus using high-speed HOTLink (400 Mb/s, Cypress Semiconductor, inc.) transmitters and receivers is designed to carry the coincidence data to the entire networked (LAN) computers (PCs), the data from HOTLink are interfaced to a PC through a fast PCI I/O board (80 Mbyte/s). The overall architecture for the image acquisition and reconstruction computing system for a whole-body PET scanning is a pipeline design. One PC will acquire sinogram data for one bed position, and after completion of data acquisition that PC will begin to reconstruct the image. Meanwhile, another PC in the network will start data acquisition for the next bed position. The image results from the previous PC will be sent to a master computer for final tabulation and storage through the standard network, and then it will be free for processing a new bed position. In gated respiratory or gated ECG imaging study, each cycle is divided into many time segments and each PC will be reconfigured for processing one specified time-segment image. The authors are developing a high-resolution PET camera with 38,016 BGO crystal elements that requires 1 to 2 GB sinogram memory. This HOTLink/networked structure design also allows them to distribute the huge sinogram real-time binning into several PCs; the image reconstruction can be done in parallel.**

Index Terms—**Data acquisition, nuclear imaging, positron emission tomography (PET), serial bus.**

I. Introduction

WE HAVE proposed a high-resolution transformable whole body clinical positron emission tomography (PET) camera with 12 detector modules in a PMT-quadrant-sharing (PQS) design that decodes 38 016 BGO crystal elements [1]. This high-resolution PET camera doing a whole-body multiple bed position scanning will require a huge sinogram memory and a long-time for image reconstruction. Respiratory-gating or motion-tracking are also demanded in high-resolution PET study. The electrocardiogram-gated (ECG-gated) imaging method allows assessment of regional myocardial perfusion and evaluation of ventricular wall motion. Hence, to have a fast imaging performance, the computing power becomes more critical for a high-resolution clinical PET camera. The paper presents a method of implementing a fast but cheap data acquisition and image reconstruction computer system for a high-resolution PET camera. This method is also good for existing commercial PET cameras in order to achieve a higher patient throughput.

With the availability of inexpensive high-power PC-based computing, many of data acquisition and image reconstruction methods have been moving to a PC-based model. A data acquisition system with networked cluster PC structure will be widely accepted. We want to use the networked PC cluster design for both real-time data acquisition and image reconstruction in our PET camera. However, a standard PC networking has a problem in real-time broadcasting and the network protocol is not easy to be integrated into frond-end electronics without a special micro-processor involved. Since the coincidence data generated by a PET camera is unidirectional (from the camera to a data acquisition system), we can design another special fast bus attached to the standard networked computers for broadcasting the coincidence data to the entire networked PCs. This fast serial bus is daisy-chain linked with fiber optical or twisted-pair driving by 400 Mb/s HOTLink transmitter and receiver. Both the HOTLink transmitter and receiver are 32-pin chips and have a CMOS/TTL logic compatible interface, and further more, no special protocol is demanded for this additional bus. Hence, it is very easy to integrate the HOTLink components into front-end electronics. Each PC can real-time grab the data from the serial bus as demanded, and a master PC can order a slave PC to do a special task through the standard LAN. For example, to split a huge sinogram memory, the master PC would send a message to each slave PC through a TCP/IP specifying sub-sinograms to be processed.

Manuscript received December 2, 2002. This work was supported in part by the National Institute of Health under Grants RO1 CA58980, RO1 CA61880, RO1 CA76246, RO1 EB00217, RO1 EB001038, by the U.S. Army under a Breast Cancer Grant, by a Texas Higher Education Grant, by a J. S. Dunn Foundation Research Grant, and by the Cobb Fund for Cancer Research.

The authors are with the Department of Experimental Diagnostic Imaging, University of Texas M.D. Anderson Cancer Center, Houston, TX 77030 USA (e-mail: hli@di.mdacc.tmc.edu).

Digital Object Identifier 10.1109/TNS.2003.812441

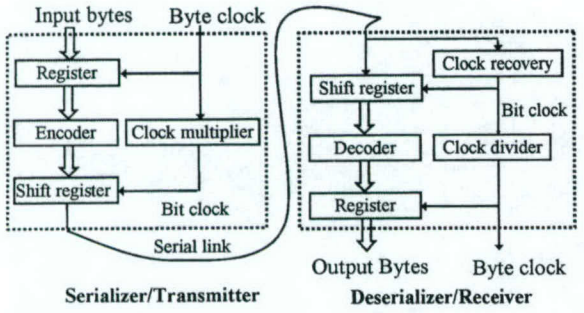

Fig. 1. HOTLink architecture.

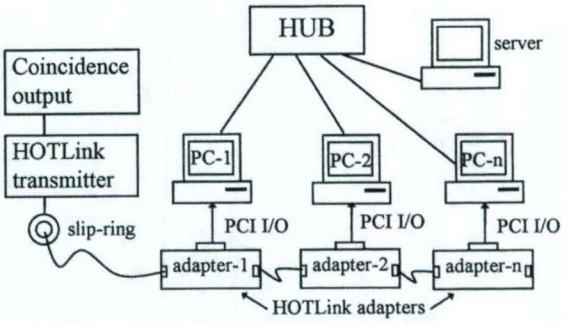

Fig. 2. Architecture of HOTLink/Networked computers.

II. Methods

A. Why HOTLink?

A high-resolution and high-sensitivity PET camera may generate 32-to-64 bits width parallel coincidence data with a rate up to 10 million coincidence events per second. Operating this high-speed parallel bus over significant distances can be problematic due to signal distortion, skew, and crosstalk. These effects can lead to loss of data and failure of the bus.

As system speeds increase, serial interfaces are often used to extend the high performance of a parallel interface well beyond the distances possible in parallel link. By only sending a single signal (though sending each bit much faster) both the signal-to-signal and signal-to-clock skew limits are removed. HOTLink (Cypress Semiconductor, Inc.) makes it easy and economical to move the same data over a high-speed serial connection using fiber-optic or twisted cables [2], [3].

Fig. 1 shows a serial link design using HOTLink (transmitter CY7B923 and receiver CY7B933, [4]) for moving streams of 8-bit parallel bytes from one location to another. HOTLink offers a built-in standard 8B/10B encoder/decoder and phase locked loop (PLL) based clock and data recovery circuits. These 8-bit data characters are encoded into 10-bit transmission characters and the 10-bit characters are sent serially across a link. At the receiving end of this link these serial bits are grouped together to 10 bits at a time (framed), and decoded back into their equivalent 8-bit data characters. Only 256 special 10-bit characters selected from the entire 1024 characters map to the 256 valid 8-bit input data characters. HOTLink also provides 12 valid special codes, selected from the 1024 characters, as different command codes. The communication synchronization character and violation symbol (RVS) are two of these special codes.

In summary, HOTLink is almost protocol-free for fast serial communication and has a COMS/TTL compatible interface, which can be easily integrated in an application system. And, it also reserves about ten special codes that you can use as commands in serial communications. In addition, serializing a parallel bus allows for operation of the bus over extended distance. The reduced bus width also makes it practical to pass the data through a simple slip-ring in a PET camera with CT function.

B. Whole-Body Scanning

A clinical PET camera usually needs to acquire five to eight bed positions in whole-body scanning. For our proposed high-resolution PET camera with 38 016 crystals and 5,184 sinograms, we estimated the reconstruction time with 15 minutes for two-dimensional (2-D) and 250 minutes for three-dimensional (3-D) filtered back-projection (FBP) for each bed position using a single 2.8 GHz Pentium-IV personal computer. Hence, about one to two reconstruction hours is demanded using 2-D FBP for whole-body scanning with five to eight bed positions, this is very time consuming. Definitely we need a super-power computing system for data acquisition and imaging reconstruction as well.

However, the coincidence data from a PET camera are always unidirectional; a fast serial bus is very suitable to carry the data to the acquisition computer. We have designed a data acquisition and image reconstruction system based on a fast HOTLink (400 Mb/s) daisy-chain bus combined with a standard local area network (LAN) that consists of six to eight personal computers (PCs); see Fig. 2. One PC will act as a master (server) computer, and the others will function as the slave (client) computers. The communication between the master and the other five to seven slave PCs is established through a standard LAN using TCP/IP. The server has a large hard disk that will be used to store the raw data as well as the reconstructed images. Each slave PC has 1–2 GB memory of its own for binning the sinogram data of one bed position in real time.

After the completion of the sinogram acquisition for one bed position, the sinogram for the just completed bed position will be used by the same slave PC in the network for image reconstruction. The image result from each slave PC will be sent to the master PC for final tabulation and storage. The overall architecture for the image acquisition and reconstruction computing system is a pipeline design. In this pipeline design, one PC will be used to reconstruct the image of one bed position. In scanning the first bed position, the first client PC (PC-1) will be instructed by the server to grab the data from the HOTLink daisy-chain bus. After scanning the first bed position, PC-1 will reconstruct the image of this bed position. In scanning the second bed position, PC-2 will grab the data from the HOTLink bus and after scanning the second bed position, PC-2 will reconstruct the image of this second bed position, while PC-1 may still be working on the reconstruction for the first bed position. If a whole-body scan takes eight bed positions, up to a maximum of eight reconstruction PCs will be needed. However, if the reconstruction time of each bed position is less than the scanning time of five bed positions (for example), then only five PCs will

be needed, because PC-1 will be free after scanning five bed positions and can be used for processing the bed position-6. For the same reason PC-2 can be used for position-7. We choose this multi-PC design instead of a typical SUN/HP workstation-based design using one to two high-power workstations or expensive VME system with multiple processors linked by RACEWAY crossbar, because this PC system is more flexible, cheaper, and easy to be maintained. Furthermore, performance of a PC-based system can be improved more frequently, cheaply, and compatibly.

C. Respiratory/ECG-Gated Imaging

In pulmonary nodules PET imaging, respiratory motion produces lesion blurring and an apparent increase in lesion size. This results in a decrease in the activity concentration per pixel within the lesion and an underestimation of SUV. Improved measurement of lesion volume and quantification of FDG uptake can be achieved with respiratory gated PET imaging [5]. In cardiac nuclear imaging, ECG-gating not only provides added information about global and regional left ventricular and right ventricular function, enhancing its prognostic value, but also helps to differentiate real defects from attenuation artifacts [6].

Recently, most of the gated high-resolution PET imaging is performed under list-mode only. Time-marks, generated by a respiratory or ECG sensor, are inserted into the coincidence data streams and recorded in list-mode. Each respiratory or ECG cycle is divided into many time-frames as demanded. And the time-frame sinogram-binning as well as image reconstruction will be performed after the data acquisition is finished.

The HOTLink/networked PC structure designed for whole-body scan discussed in Section II-B can also be used for real-time gated PET imaging. For example, each ECG period is divided into, say, six time-frames. The front-end electronics generates 25 ms free-running timing-ticks attached to the coincidence data streams broadcasting to the networked PCs through the HOTLink serial link. Each ECG cycle is divided into six time-frames according to those timing-ticks. Each slave computer is configured to process one specified time-framed sinogram binning and image reconstruction. Each slave PC has two memory buffers organized in ping–pong mode for recording the list-data from two most recent ECG cycles. The list-data will be sorted by frame-numbers; and only one specified frame will be processed by each PC, the data from rest frames will be discarded by this PC. If the total number of time-ticks in one ECG cycle is too long or too short that means an irregular ECG cycle has happened, and the entire list-data buffer for that ECG cycle will be discarded. This time-framed real-time data acquisition and image processing method can also be used for respiratory-gated imaging. However, since the respiratory cycle is more regular and slower than ECG cycle and patients can be further trained to have a regular cycle [5], we can predict the next respiratory period accurately by linear-fitting several measured previous periods. It is not necessary to attach the 25 ms timing-ticks into data streams for respiratory gating. With a predictable cycle time, the time-frame numbers can be generated ahead or real-time and we can attach frame-numbers to the coincidence data streams directly. Hence, a slave PC can process time-framed sinogram binning immediately without ping–pong buffering the list-data of the entire cycle as used in ECG-gating method mentioned above. If both the cardiac and respiratory gating is needed simultaneously, the maximum time-frame number for ECG and respiratory gating are limited to four. A maximum of 16 slave PCs are needed (since ECG and respiratory signals are not synchronized, there are 16 total combinations of the ECG and respiratory time-frames); however, if one slave PC can store two time-framed sinograms, then only eight slave computers are needed.

D. Network Parallel Subsinogram Reconstruction

It is very time consuming to reconstruct a high-resolution PET imaging. To speedup the processing, one solution is using multiple parallel processors to work on the huge sinogram data. However, accessing the same sinogram memory by the multiprocessors becomes a new bottleneck; the communication among the processors also needs some extra CPU time. Hence, the maximum processor number in this design is limited; the computing power is not increased linearly as the number of processors increased. Besides, the reconstruction algorithm has to be redesigned and optimized specially for this multi-CPU parallel processing system.

A new network parallel subsinogram reconstruction method has been designed that is benefited from the HOTLink/network PC structure. The huge sinograms (5184 sinograms for our proposed PET camera) are sorted into many groups. Each slave PC will do the sinogram rebinning of one group with its local memory. Only the coincidence data that belong to the group will be grabbed by the PC from the HOTLink serial bus. The reconstruction algorithm is simply modified so that each PC can start the reconstruction locally (with no necessary to access other sinogram groups) after the data acquisition is finished. This is a fully parallel processing design. In this design, there is no communication between PCs and no bottle-neck problem of accessing a common/shared memory. The reconstructed image results from each slave PC will be added together by a server.

III. Results and Discussion

A. Sending Coincidence Data Using HOTLink Transmitter

In the proposed high-resolution PET camera, the coincidence system will give two separate coincidence data outputs, one is for true coincidence and the other is for random coincidence [7]. The coincidence processing board passes through 64-bits prenormalized Anger-position and energy signals of the pair-events; another digital processing board will convert them into crystal and slice information by using lookup tables. Both the true and random coincidence data after the lookup-table-processing will become 32-bits (for gamma-1 position: 7-bits slice1, 6-bits crystal1; for gamma-2 position: 7-bits slice2, 6-bits crystal2; and 6-bits coincidence bank-pair number). The 32-bits true and random coincidence data are first shifted into a 2k $\times$ 8-bits first-in-first-out memory (FIFO) individually. Whenever the half-full flag of one FIFO is detected, that FIFO output will be switched to a HOTLink transmitter by a multiplexer; see Fig. 3. A selected HOTLink command identifying a true or random buffer will be sent first and then

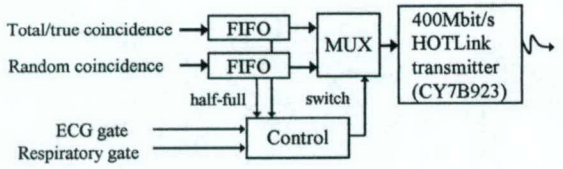

Fig. 3. Sending coincidence data with HOTLink transmitter.

immediately followed by the coincidence data with a half buffer size of that FIFO. In other words, the HOTLink command is a buffer-head indicating all the following data (with half of the FIFO length) will be either true or random events. In this way, the two coincidence outputs are simply merged and sent to a fast serial bus using a HOTLink (400 Mb/s, CY7B923) transmitter.

In the coincidence data format of our prototype MDAPET camera, one bit is used to identify true or random events and the data acquisition software needs to check that bit for every single event. In our new design, the software only needs to check the buffer-head once and then process the buffer continuously. Another big advantage is that the coincidence data are still limited within 32-bits width (33-bits were necessary if following the MDAPET data format) which simplified the PC I/O interface design.

The gate signals from ECG and respiratory sensors are also connected to the digital look-up-table processing board. The time-frame numbers or timing-ticks can be real-time inserted into the HOTLink data streams for further processing.

B. PC HOTLink Adapter

A custom-constructed PC HOTLink adapter has been developed to receive coincidence serial data from the front-end using a HOTLink receiver CY7B933, the received data are interfaced to a fast 32-bit PCI I/O board (National Instrument PCI-6534 [8]) inside each slave PC. Meanwhile, the same data from the receiver are feed back into another HOTLink transmitter on the adapter board passing the data to the next adapter board and slave PC as well. Hence, a fast daisy-chain serial bus is formed among these adapters for real-time broadcasting the coincidence data to the entire slave PC cluster at a rate up to 400 Mb/s. This serial bus can carry up to 10 million coincidence events per second, which is good enough for a high-efficient PET camera. Fig. 4 shows the design of HOTLink daisy-chain bus, data from the serial link are deserialized first and then will be interfaced to a PCI bus; meanwhile, the deserialied data will be serializered again and sent to next adapter through the onboard HOTLink transmitter. In fact, the deserializer and serializer act as an active serial bus driver, thus the entire link quality is not limited by the number of adapters inside the daisy-chain link. The twisted copper cable between two boards can be as long as 100 ft. By disabling/blocking the input deserialized data, a slave PC is able to send data from its memory to the serial link output so that data from one slave PC can be moved to next slave PC very fast.

Fig. 5 shows the HOTLink adapter-board design for PCI-6534 fast PCI I/O board. Fig. 6 is the photograph of the adapter board. The adapter-board can be initialized by the PCI-6534 through standard I/O and the data communication

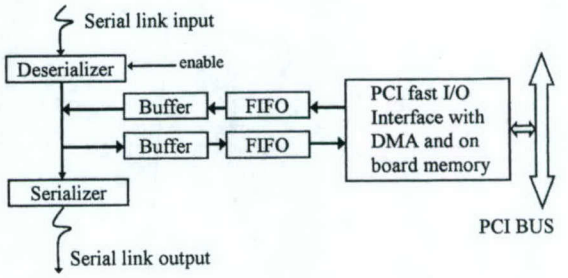

Fig. 4. PCI HOTLink daisy-chain serial bus.

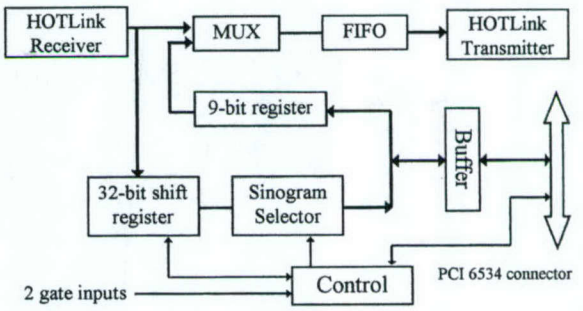

Fig. 5. PCI-6534 HOTLink adapter design.

between them is achieved by pattern I/O [8]. The PCI-6534 board has a 64 Mbyte onboard memory working as FIFO mode, data can be written into the memory as fast as 80 MB/s. The adapter-board can be initialized for different modes: HOTLink self-testing mode for checking the link quality, PC data acquisition mode, PC transferring mode for fast communication between PCs, and sinogram real-time selection mode for splitting a huge sinogram into several PCs. Two gate-signal inputs are reserved for some special purposes such as the position signals of a rotating rod for the data acquisition of transmission imaging. The entire logic was implemented by one Altera programmable logic device EPM7256SQC208.

The output of a HOTLink receiver is consisted of 8 bits data plus 1 bit data/command flag; however, the coincidence data in our PET system are 32-bits, therefore an 8-to-32-bits shifter register is demanded. Synchronization in data shift-processing should be carefully designed. Without the synchronization an error that happens in the shifter, such as one extra shift operation triggered by a noise, might kill the entire rest of the data. We use the HOTLink commands, such as the selected true/random buffer-head command or the ECG/respiratory start command, to reset/synchronize the 32-bits coincidence data so that one error may only kill a maximum of one buffer size (half length of the FIFO in the front-end processing board).

A normal HOTLink system rarely experiences one error per hour (a bit error rate of $1 \times 10^{-12} \approx 1$ error/h@ 266 Mbaud) [9]. When the receiver detects an error in the sequence of received transmission code (an error that corrupts a single bit), it asserts a RVS signal during the character-decoding-time following the error. Single-bit errors can cause changes in the data streams running disparity. In extreme cases, where the errors cause PLL cycle-slipping or loss of framing, the received streams will never

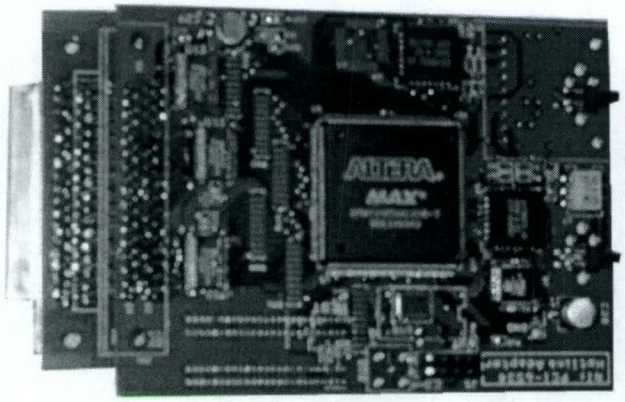

Fig. 6. Photograph of HOTLink adapter.

match. A special circuit has been developed by monitoring the status of RVS signal to automatically disconnect and reconnect the input signal continuously until the endless running errors disappeared. Our data showed that the system could be recovered less than 100 ms, if endless disparity errors were detected.

Another important application of the HOTLink adapter is to split a huge sinogram memory into the slave PC cluster; the image reconstruction algorithm can apply to those subsinograms individually. The reconstructed subimage results from the slave PCs are integrated together by a master computer for further processing. Hence, by using the HOTLink network design, we not only can handle the huge sinograms, but also can speed up the image reconstruction in a way of parallel processing.

The "sinogram selector" in Fig. 5 is designed specially for the purpose of real-time sinogram splitting mentioned above. The 5184 sinograms are sorted by the "slice-difference" of the two coincidence gamma events. Those sinograms will be grouped together if their "slice-differences" are within a specified range. Two registers in the "sinogram selector" can be initialized by a slave PC and define a range of a "slice-difference" window, so that if the difference of two slice numbers, identified by the coincidence-gamma events, belongs to that window, the coincidence event will be accepted by this slave PC. In order to reconstruct the image locally, the parallel reconstruction algorithm requires every slave PC to have directory sinograms (slice difference = 0). This can be achieved easily by the broadcasting capability of the HOTLink bus. The coincidence data belong to the direct sinograms or to the specified subsinograms defined by the "slice-difference" window can be real-time grabbed by a slave PC from the HOTLink daisy-chain bus. This parallel processing method has been proved by using two slave computers in our prototype MDAPET camera that we developed [10], [11].

IV. Conclusion

We have developed a high-speed HOTLink (400 Mb/s) serial bus that can broadcast 32-bits coincidence data of a PET camera to local networked computers. Using the HOTLink for serializing bus is very simple, no additional protocol is demanded and it can be easily integrated into a front-end electronics. The HOTLink/networked PC cluster design is very suitable for online pipeline data acquisition and image reconstruction for an ultrahigh-resolution PET camera doing whole-body multiple bed position scanning and respiratory/ECG gated imaging study. By using this design, a huge sinogram real-time binning can also be achieved by the slave PC cluster. The pipeline data acquisition and image reconstruction method will increase the throughput of patient scan.

This HOTLink/networked PC data acquisition system can be easily applied to an existing PET camera. It has been successfully used in our prototype MDAPET camera to replace the VME data acquisition system. Our VME data acquisition system is aged, unstable, and, furthermore, the IRONICS data interface board is no longer supported by the manufacturer.

The prototype HOTLink adapter combined with the National Instrument fast I/O board (PCI-6534) has strongly demonstrated the real-time processing power for PET study. A PCI HOTLink network board merging the functions of HOTLink and the fast PCI I/O will be designed in the future.

References

[1] W. H. Wong, "The design of a high resolution transformable whole body PET camera," *IEEE Trans. Nucl. Sci.*, vol. 49, Oct. 2002.

[2] "HOTLink design considerations," in *Application Notes in the HOTLink User's Guide*: Cypress Semiconductor Co..

[3] "Use HOTLink for 9- and 10-bit data," in *Application Notes for the HOTLink*: Cypress Semiconductor Co.

[4] *Datasheets for CY7B923, CY7B933*, Cypress Semiconductor Co.

[5] S. A. Nehmeh *et al.*, "Effect of respiratory gating on quantifying PET images of lung cancer," *J. Nucl. Medicine*, vol. 43, pp. 876–881, 2002.

[6] G. Germano *et al.*, "Automatic quantification of regional myocardial wall motion and thickening from gated technetium-99 m sestamibi myocardial perfusion single photon emission computed tomography," *J. Amer. Coll. Cardiol.*, vol. 30, pp. 1360–1367, 1997.

[7] Y. Wang *et al.*, "A modular low dead-time coincidence system for high resolution PET cameras," *Conf. Rec. 2002 IEEE MIC*.

[8] *User Guide for PCI-6534*, Nat. Instrument.

[9] "HOTLink built-in self-test (BIST)," in *Application Notes for the HOTLink*: Cypress Semiconductor Co.

[10] W. H. Wong, J. Uribe, W. Lu, and K. Hicks, "Design of a variable filed prototype PET camera," *IEEE Trans. Nucl. Sci.*, vol. 36, pp. 1915–1920, June 1996.

[11] J. Uribe, H. Baghaei, H. Li, S. Yokoyama, N. Zhang, J. Wang, F. Dobbs, and W. H. Wong, "Basic imaging characteristics of a variable field of view PET camera using quadrant sharing detector design," *IEEE Trans. Nucl. Sci.*, vol. 46, pp. 491–497, June 1999.

IEEE TRANSACTIONS ON NUCLEAR SCIENCE, VOL. 50, NO. 3, JUNE 2003

Signal Characteristics of Individual Crystals in High Resolution BGO Detector Designs Using PMT-Quadrant Sharing

Jorge Uribe, *Member, IEEE*, Hongdi Li, *Member, IEEE*, Tao Xing, Yaqiang Liu, Hossain Baghaei, *Member, IEEE*, Yu Wang, Mehmet Aykac, Rocio Ramirez, and Wai-Hoi Wong, *Member, IEEE*

***Abstract*—The PMT-quadrant sharing (PQS) detector design allows very high resolution detectors to be built with 70% fewer PMTs and lower cost. A common concern for the design is that there is a big gap (photo-insensitive area) between four circular PMTs and the photoelectron signal (pulse height) may be much lower for the central crystals. The concern increases with the use of smaller PMTs for high-resolution designs because small PMTs have relatively thicker walls and relatively larger tolerance spaces between them. The authors measured the pulse heights and energy resolution for each crystal in three different types of PQS blocks for 19 mm PMT. For a square 7 × 7 block detector (2.66 mm × 2.66 mm × 18 mm BGO needles), the maximum photopeak signals occurred at the corner crystal of the block. The signals for the worst central five crystals (sitting on space with no PMT connection) had pulse heights 0.87 as high as that of the corner crystals. The 12 crystals (outside the central five) with coupling only to the glass wall but not to the photocathode had a relative pulse height of 0.92. The eight crystals with partial exposure to photocathodes had a 0.94 relative pulse height. The energy resolution for individual crystals was 22%–30% with an average of 26%. Asymmetric photopeaks, especially for the corner crystals, were observed, and these were found to be the result of the depth-of-interaction effect. In the latest PQS design, extended blocks with asymmetric light distributions were used on the four edges and four corners of a large detector module so that the previously unused (wasted) half-row of peripheral PMT could be covered by crystals. An asymmetric block, single-extended (7 × 8 crystals) was also tested. The pulse-height ratio between the worst and best group of crystals in the single-extended block was 0.72 and that of the double-extended block was also 0.72. In a more demanding, higher spatial resolution 8 × 8 array (2.3 mm × 2.3 mm × 10 mm BGO) for mouse PET with shallower crystals, the pulse-height ratio was 0.73 with an average energy resolution of 20%. This study demonstrated that pulse height uniformity for the PQS design using circular PMT was excellent, better than the typical 3/1 pulse-height ratio in conventional block detectors.**

***Index Terms*—Photodetectors, position sensitive detectors, positron emission tomography (PET), quadrant sharing detectors, scintillation detectors.**

Manuscript received November 27, 2002. This work was supported in part by the National Institute of Health under Grants RO1 CA58980, RO1 CA61880, RO1 CA76246, RO1 EB00217, and RO1 EB001038, by the U.S. Army under a Breast Cancer Grant, by the Texas Higher Education Grant, by a John S. Dunn Foundation Research Grant, by a Mike Hogg Fund Research Grant, and by the Cobb Fund for Cancer Research.

The authors are with the University of Texas M.D. Anderson Cancer Center, Houston, TX 77030 USA (e-mail: juribe@di.mdacc.tmc.edu).

Digital Object Identifier 10.1109/TNS.2003.812478

I. Introduction

THE PMT-QUADRANT sharing (PQS) detector design [1]–[3] allows very high resolution detectors to be built with 70% fewer PMTs, fewer front-end electronic channels, and a lower cost. We used this design to build very high resolution positron emission tomography (PET) cameras [4], and it has been adopted by Siemens/CTI for its next generation LSO PET cameras [5]. A common concern for the design is that when four circular PMTs are used to further reduce the cost, the circular PMTs leave a big gap (photo-insensitive area) between the four PMTs. The dead-space issue is especially challenging with smaller diameter PMT ($D < 20$ mm), as the glass wall cannot be made proportionally thinner, which aggravates the dead-space problem. Furthermore, since the glass bottles of PMTs do not have high mechanical precision, a small amount of tolerance space between PMTs has to be built into the design (e.g., 0.5–1 mm), which further expands the dead-space. The dead space would imply that the photoelectron signal pulse heights may be much lower for the central crystals (of the crystal array) that sit on the dead space, thereby degrading imaging resolution and energy resolution. To determine whether these concerns are relevant, we evaluated the detail signal characteristics of PQS block detectors with respect to the large dead-space issues. The pulse heights and energy resolution for each crystal in three different types of PQS blocks based on 19 mm round PMT were measured and studied.

II. Methods

The experiments were performed with randomly chosen blocks among our stock of second-generation PQS BGO detector blocks. These blocks had painted interfaces between discrete crystals for distributing scintillation light, and the discrete crystals were optically glued together. The sizes and shapes of the painted areas were determined by the desired levels and directions of light distribution from each crystal. Three types of PQS block designs based on 19 mm round PMT were studied:

7 × 7 square block (each crystal was 2.66 mm × 2.66 mm × 18 mm);

8 × 8 square block (each crystal was 2.3 mm × 2.3 mm × 10 mm);

7 × 8 elongated asymmetric block (each crystal was 2.6 mm × 3.1 mm × 18 mm).

The in house developed front-end electronics of our prototype PET camera were used to acquire the data. The electronics employed the pileup-restoration technique recently developed by us [6], [7]. Four Photonis XP1911 PMT were used for the 19 mm circular PMT, with each PMT having one quadrant of its photocathode coupled to the BGO block by optical grease. The PMT high voltage was fixed at 1450 V, providing about 10^6 anode amplification gains. Cs-137 was used as the radiation source for all the studies. The gains of all four PMTs were equalized with their voltage-control variable-gain fast amplifiers by two different methods: 1) using just the crystal sitting at the center of each PMT and 2) using a region of 3×3 crystals corresponding to the relevant quadrant of the PMT. For the four PMTs used, both methods of equalization were within 5% of each other (data not shown), so the center-crystal equalization was used for all the studies. No particular criterion was followed while selecting the photomultipliers themselves from the pool of PMT used for the construction of our second-generation PET camera. PMTs for this camera were ordered from the manufacturer with relative gain values that differ by no more than 2.5 times.

The electronics were interfaced to a personal computer. We also developed the data-acquisition software, controlling the data-acquisition electronics, and the analysis software for this study for a PC platform. The hardware and software have been compared and validated against a commercial NIM multiparameter data-acquisition system (FAST from ComTec) by comparing both the pulse-height spectra and crystal-decoding map. Our system provides a higher data acquisition speed plus some custom-designed analysis capability such as recording the signal pulse-height spectrum for each pixel in the crystal-decoding map.

For each crystal block/array, the composite (total sum) pulse-height of all the crystals in the block was first measured with a distal point source. This composite pulse height measurement provided a first-pass energy-acceptance threshold for the whole array. The crystal position-decoding map as shown in Fig. 1 was acquired with this first-pass energy threshold. This first-pass crystal-decoding map was then used to draw a region-of-interest (ROI) map for each crystal in the array. The signal-pulse-height spectrum for each crystal region was analyzed and is presented in Section III.

From these results, the best energy-acceptance threshold for each crystal ROI was also determined; an energy-threshold lookup table for each crystal ROI in the crystal decoding map was created for each detector array tested. A second-pass data acquisition was then performed for each detector array to obtain a crystal-decoding map with individualized crystal-energy-thresholds. The results are presented in the next section.

III. Results

The second generation PQS BGO position-sensitive array has a much better production method [8] that mated all the crystals together with a minuscule gap of only 0.05–0.06 mm producing a very high packing fraction (Fig. 1). There was a white-paint window between crystals for controlling the distribution of light, and the crystal were optically glued together as a solid block. The painted windows allowed any shape and size to be painted thereby enabling optimal crystal decoding and the minimization of barrel or pincushion distortion in the decoding map. One such crystal block (7×7 array, 2.66 mm $\times$ 2.66 mm $\times$ 18 mm BGO) is shown in Fig. 1 with its raw position-decoding map.

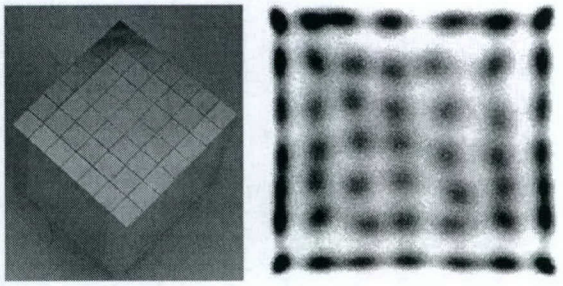

Fig. 1. Second-generation PQS position-sensitive BGO block and its raw crystal-decoding map without distortion correction and with only one energy acceptance threshold for the whole block.

A. 7 × 7 Array, 2.66 mm × 2.66 mm × 18 mm With 19 mm Round PMT

For this 7×7 block, the maximum photopeak signals occurred near the corner of the block as expected, while the signals for the worst central nine crystals (sitting on space with no photocathode coupling) were found to have the lowest pulse heights. The low pulse heights are due to the extra distance traveled by the scintillation light from the center crystals to the PMT windows through the block. This path for the light is possible thanks to finely tuned paint barriers placed between crystals. The ratio between the lowest pulse height to the highest was found to be

$$\frac{(\text{raw Min})}{(\text{raw Max})} = 0.78.$$

Hence, the worst crystal had 22% lower pulse height than the best crystal in the block. The raw pulse-height spectra of the worst (center crystal) and best crystal (near the corner) are shown in Fig. 2.

However, this raw ratio included the influence of all the regional nonuniformities of each PMT photocathode and the anisotropic orientation effect of each PMT [9]. To minimize such spatial PMT influences, we averaged values for crystals with the same rotational symmetry, i.e., the same up–down and left–right crystal-locations relative to the center of the block. After the symmetric averaging, the ratio between the lowest pulse height and the highest pulse height was found to be

$$\frac{(\text{symmetry-restored Min})}{(\text{symmetry-restored Max})} = 0.81.$$

This ratio may be a better measure of the geometrical optical efficiency difference between the worst crystal and the best crystal in a PQS block design, since the individual PMT variations and photocathode differences are thereby minimized. Hence, for the 7×7 BGO PQS array, the center crystal (the most disadvantageous, since it has no direct coupling to any PMT) had an optical efficiency 19% lower than that of a crystal that was directly coupled to the middle of a PMT, the most sensitive part of a PMT.

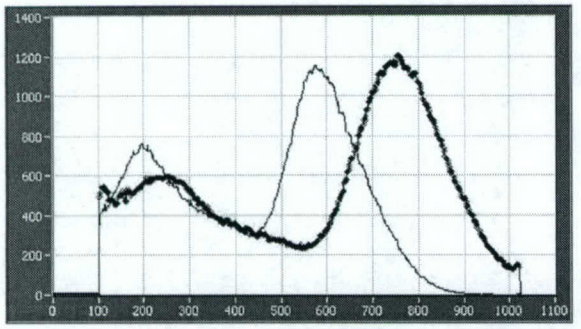

Fig. 2. Pulse-height spectra of the best and worst optical efficiency crystals.

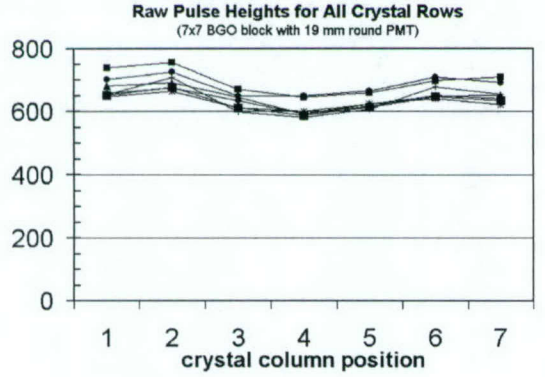

Fig. 3. Raw crystal pulse-heights for all seven rows of crystals.

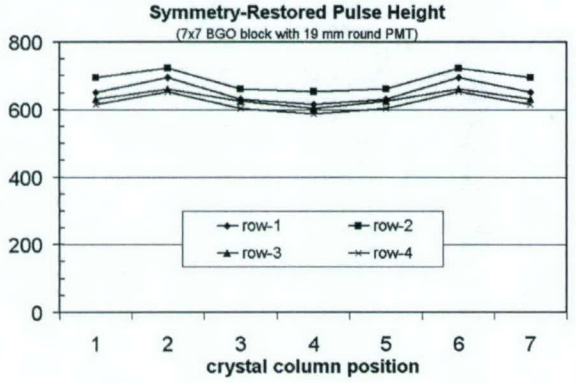

Fig. 4. Symmetry-restored pulse-heights for the first four crystal rows.

The pulse-height distribution of the upper four rows of crystals is shown in Fig. 3 for the raw signal and Fig. 4 after the above symmetry averaging.

The average pulse height was highest for the second row of crystals, although the first row of crystals was at the center of the PMT. This disparity was due to almost total (95%) optical isolation of the first and last row of crystals from the rest of the block; hence, all the scintillation light had to travel down the long and narrow crystal (2.66 mm × 2.66 mm × 18 mm) to be detected, during which some light was lost. This phenomenon was due to the very high spatial resolution of the block.

To categorize the crystal pulse height, the crystals were grouped into four types:

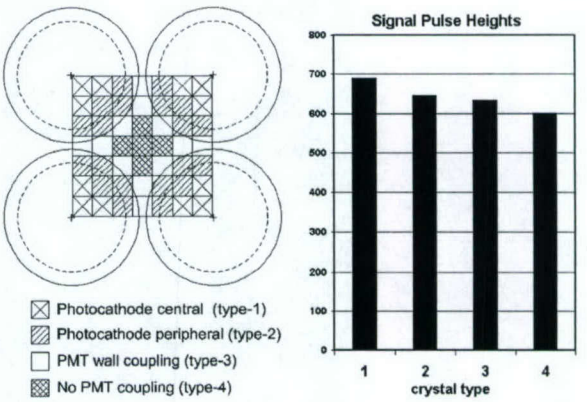

Fig. 5. Crystal-position types and their optical efficiencies.

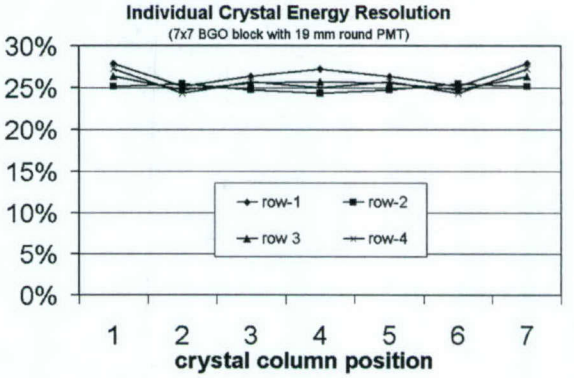

Fig. 6. Symmetry-restored energy resolution distribution.

Type-1: crystals on the photocathode central region;
Type-2: crystals on the photocathode edge and sidewall;
Type-3: crystals only coupled to the glass side wall;
Type-4: crystals with no PMT connection (five crystals).

The types and their optical efficiencies are shown in Fig. 5.

The optical efficiency ratio between the least efficient type and best type was found to be

$$\frac{(\text{Type-4 pulse height})}{(\text{Type-1 pulse height})} = 0.87.$$

Hence, as a group the central five crystals, which were just hanging in space without any optical coupling to a PMT, lost only 13% of the light compared to the ideal crystal group (type-1).

The measured energy-resolution distribution, after the symmetry restoration discussed earlier, is shown in Fig. 6.

The average energy resolution including all the crystal was found to be 25.6%.

The average energy resolution was also measured in a different way. The photopeaks of all the crystals were normalized to the same standard pulse height and then normalized by the counts in the ROI of each crystal. The normalized pulse-height spectra for all the crystals were summed, and the energy resolution for the normalized-sum spectrum was calculated. This "normalized-sum" energy resolution was found to agree with that of the first method.

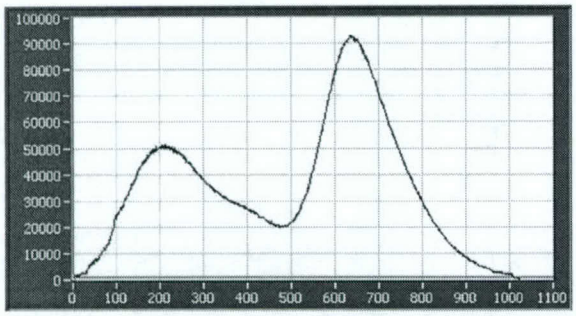

Fig. 7. Normalized-array-average spectrum for the 49 BGO in array.

In the normalized-sum spectrum for the whole array (Fig. 7), an asymmetry in the photopeak can be observed. We determined that it was due to the variation of light output with the depth of interaction. By collimating the beam toward the first one-third and the last one-third of the crystal depth on the last row of crystals in the array, two different photopeak pulse heights appeared. Because of the high stopping power of BGO, most of the interaction occurred at the front-end of the crystal (farther away from the PMT); this gave rise to the lower overall pulse-height. But some interactions occurred near the back-end (the PMT end), thereby yielding a higher pulse height than the average peak energy.

The normalized-sum spectrum of the whole array (Fig. 7) was also used to calculate the average photo-fraction of the small BGO crystals (2.66 mm × 2.66 mm × 18 mm) in the array

$$\text{Average detection photofraction} = 70\%.$$

B. 8 × 8 Array, 2.3 mm × 2.3 mm × 10 mm With 19 mm Round PMT

This BGO crystal-block geometry can be used for building a less expensive mouse-PET system, since its crystal dimension is close to that of the MicroPET (2.4 mm × 2.4 mm pitch and 10 mm deep) and it uses the large low-cost 19 mm PMT and BGO instead of the more expensive design of the MicroPET that uses LSO crystals with position-sensitive PMT together with an optical fiber bundle. For this 8 × 8 block, the ratio of the lowest pulse height to the highest was found to be

$$\frac{(\text{raw Min})}{(\text{raw Max})} = 0.67.$$

Hence, the worst crystal had 33% lower pulse height than the best crystal in the block. As discussed earlier, to minimize the PMT regional gain variation and anisotropy, crystals with the same rotational, up–down and left–right symmetries (relative to the center of the block) were averaged, and the symmetry-restored ratio min / max was

$$\frac{(\text{symmetry-restored Min})}{(\text{symmetry-restored Max})} = 0.72.$$

Hence, for the 8 × 8 BGO PQS array, the central crystal (worst case with no connection to PMT) had an optical efficiency 28% lower than that of a crystal that is directly coupled to the middle of a PMT.

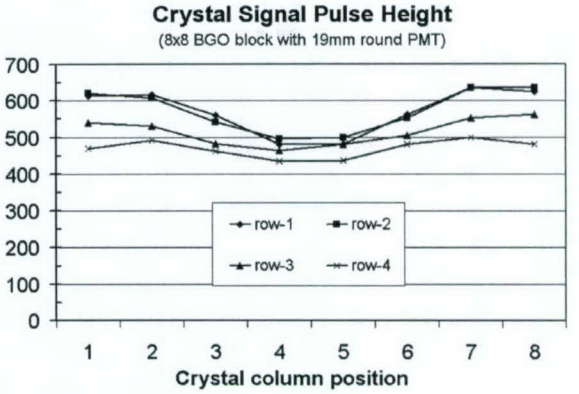

Fig. 8. Raw pulse-height distribution for 8 × 8 array with 19 mm PMT.

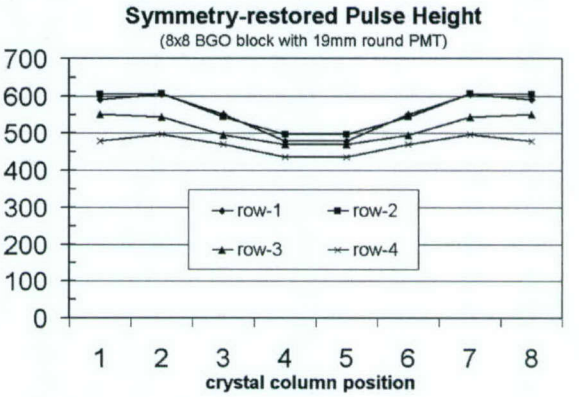

Fig. 9. Symmetry-restored pulse height distribution.

The pulse-height distribution of the upper four rows of crystals is shown in Fig. 8 for the raw signal and Fig. 9 after the above symmetry averaging.

As discussed earlier, the crystals were grouped into four types:

Type-1: crystals on the photocathode central region;
Type-2: crystals on the photocathode edge and sidewall;
Type-3: crystals only coupled to the glass side wall;
Type-4: crystals with no PMT connection (four crystals).

The types and their optical efficiencies are shown in Fig. 10.

The optical efficiency ratio between the least efficient type and best type was found to be

$$\frac{(\text{Type-4 pulse height})}{(\text{Type-1 pulse height})} = 0.73.$$

Hence, as a group the central four crystals that were just hanging in space without any optical coupling to a PMT lost 27% of the light compared to the ideal group (type-1). This is not as good as the 13% difference in the 7 × 7 array with the same PMT. It is, however, significantly better than the traditional block detectors used in current commercial PET cameras, where the most optically efficient crystal has three times higher pulse height than the least efficient crystal [10]. Similar to the 7 × 7 case, there was some asymmetric photopeak shape. But because of the shorter

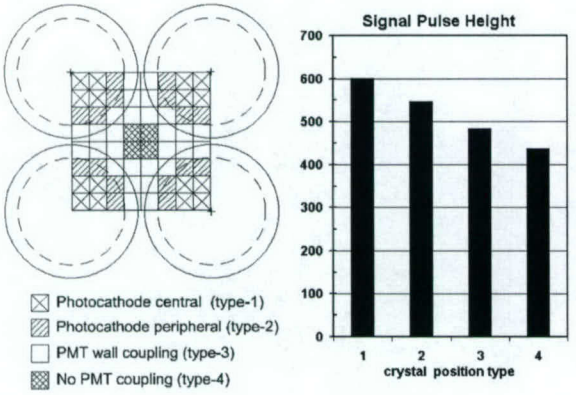

Fig. 10. Crystal-position types and their optical efficiencies.

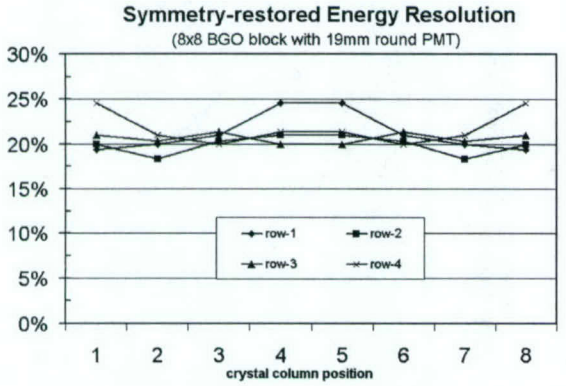

Fig. 11. Symmetry-restored energy resolution distribution.

crystals used in this array (10 mm), the asymmetry in the photopeak was smaller. The shorter array decreased the light-output variation as a function of the depth of interaction, even though the crystals here were also narrower (2.3 mm × 2.3 mm).

The measured energy-resolution distribution (symmetry restored) is shown in Fig. 11. The four abnormally large energy resolutions in Fig. 11 had asymmetric photopeaks. Overall, asymmetry of the energy spectrum due to depth of interaction in taller crystals, as discussed earlier, did not occur with shorter crystals (presented later in this section). However, in shorter crystals larger number of gamma interactions might take place deep inside the crystal and just outside the PMTs sensitive area in places with impaired light distribution; for instance, on the edge-crystals of the block between the glass bottles. The four crystals with large energy resolution in Fig. 11 are this type of crystal.

The normalized or equalized pulse-height spectra for all the crystals were summed, and the energy resolution for the normalized-sum spectrum was calculated. The normalized-sum spectrum of the whole array is shown in Fig. 12. The average energy resolution including all the crystal was found to be

$$\text{Average energy resolution} = 20.9\%.$$

If only the regularly shaped photopeaks were used, the "screened" averaged energy resolution was 20.4%. This energy

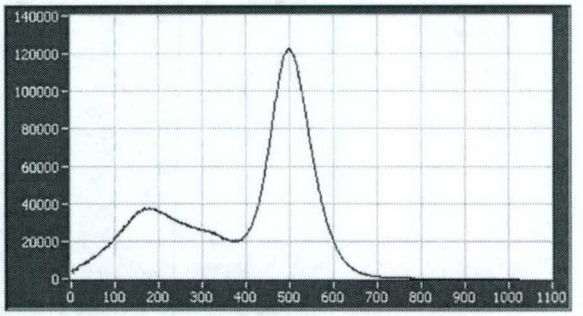

Fig. 12. Array-average spectrum for the 2.3 mm × 2.3 mm × 10 mm BGO.

resolution for this shallower block (10 mm) was better than the 25.6% for the deep crystals (18 mm) used in the 7 × 7 array, a difference that may be due to higher light-output efficiency of the shallower block. This 20.4% average energy resolution is comparable to the 19% average energy resolution measured for the LSO detectors (2.2 mm × 2.2 mm × 10 mm) in the MicroPET that uses LSO's much higher light output (5 times) and position-sensitive PMT (PSPMT) for position decoding [11].

Because the light output of an event is less dependent on the depth of interaction in shorter crystals, the photopeak in the normalized-sum spectrum for all 64 crystals (Fig. 12) was found to be symmetrical for this 10 mm deep array, compared to the asymmetrical photopeak observed in Fig. 7 for the 18-mm-deep array.

The normalized-sum spectrum of the whole array (Fig. 12) was also used to calculate the average photo-fraction of the small BGO crystals (2.3 mm × 2.3 mm × 10 mm) in the array

$$\text{Average detection photofraction} = 62.3\%.$$

Because the crystals in this array were smaller, this photofraction was smaller than the 70% of the 2.66 mm × 2.66 mm × 18 mm BGO reported above.

C. 7 × 8 Elongated Array, 2.66 mm × 3.1 mm × 18 mm With 19 mm Round PMT

This BGO elongated block was designed for use at the edge of a panel-detector module for extending the useful field of view to the edge of the last row of PMT [3]. Without the extended block design, half of the edge row of PMT in a panel detector module would be wasted, thereby reducing the advantage of the quadrant-sharing design. The pulse-height distribution (symmetry averaged) is shown in Fig. 13.

For this 7 × 8 block, the raw ratio between the lowest pulse height to the highest was found to be

$$\frac{(\text{raw Min})}{(\text{raw Max})} = 0.71.$$

Hence, the worst crystal had 29% lower pulse height than the best crystal in the block. The symmetry-restored ratio min/max was

$$\frac{(\text{symmetry-restored Min})}{(\text{symmetry-restored Max})} = 0.72.$$

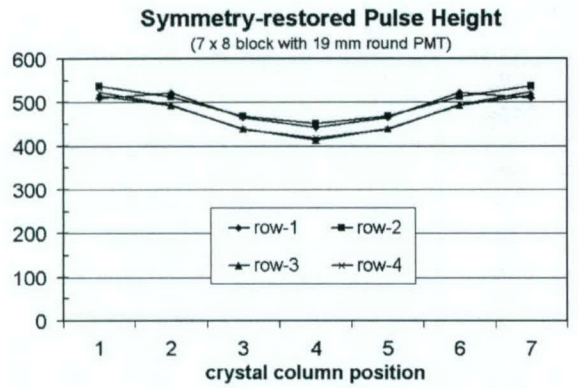

Fig. 13. Pulse-height distribution for the 7 × 8 array with 19 mm PMT.

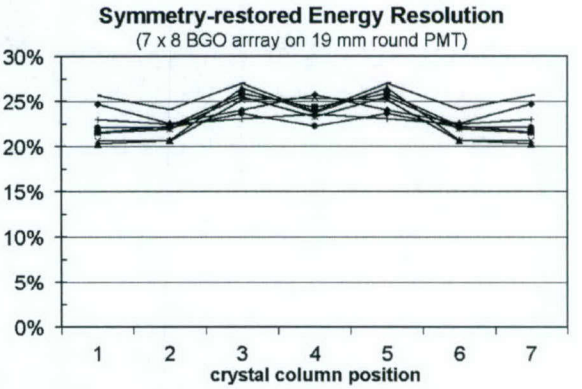

Fig. 15. Symmetry-restored energy resolution distribution for 7 × 8 array.

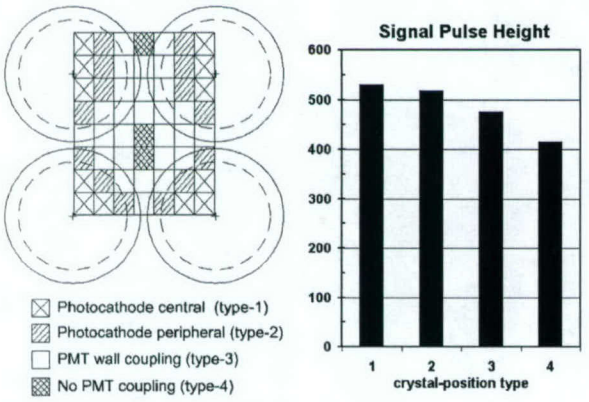

Fig. 14. The crystal-position types and their optical efficiencies.

As earlier, the crystals were grouped into four types. Each geometrical coupling types and their optical efficiencies are shown in Fig. 14.

For this 7 × 8 block, the ratio of the pulse heights of the type-4 (worst) to type-1 (best) crystals was found to be

$$\frac{(\text{Type-4 pulse height})}{(\text{Type-1 pulse height})} = 0.79.$$

Hence, the worst crystal group had a 21% lower pulse height than the crystals with the best geometry in the block.

The measured energy-resolution distribution (symmetry restored) is shown in Fig. 15. The average energy resolution for this 7 × 8 block was 23%, which is better than the 25% in the 7 × 7 array because of more favorable optical geometry.

IV. Conclusion and Discussion

Detailed signal characteristics for a very high resolution BGO detector design using the low cost quadrant-sharing (PQS) block decoding scheme with less expensive 19 mm round PMT were analyzed. There are some disadvantages in this type and size of PMT: 1) the relatively large gap (photo-insensitive area) between four round PMTs; 2) the dead-space of the 1-mm glass wall; and 3) the 0.8–1.0 mm mechanical tolerance space between PMTs due to the lack of mechanical precision in glass bottles. These disadvantages compounded the dead photo-detection area in the detector. The dead space would imply that the photoelectron-signal pulse heights may be much lower for the crystals sitting on the dead space, thereby degrading imaging resolution and energy resolution.

This study showed that for the very high resolution BGO detectors using the second-generation PQS block design and production, the worst crystal positions had signal pulse heights that were only 13%–27% lower than that of the best crystal group sitting on the middle of a PMT. The 7 × 7 block showed the most uniform light output (13%), while the 8 × 8 block was the worst (27%).

These individual crystal pulse-height measurements compare favorably to typical 3:1 difference in pulse heights in the conventional PET block-detector designs [10], [12]. Another similar pulse-height measurement for the Siemens HR-plus PET detectors using the same 19 mm circular PMT showed a 3:1 difference in pulse-height between the best and worst crystals [12]. Hence, the crystal optical-efficiency uniformity of the PQS block-detector design is better than the conventional PET block-detector design.

The high optical uniformity of the design is advantageous in that it simplifies the fast front-end electronics by using only one energy-discrimination level (one analog discriminator) for the entire detector module and still producing good crystal decoding (Fig. 1). In fact, energy discrimination is a two step process as we have implemented it in both generations of PET cameras built by our group using the PQS decoding technology. The first level rejection is based on one module-wide discrimination value significantly reducing the number of hits that need processing by the front-end analog electronics, whereas the second crystal-by-crystal cutoff is performed to fine tune rejection of scattered events. Quality of the two-dimensional decoding map alone is not enough test for the quality of the final image. Therefore, both levels of discrimination are needed for the whole system.

The 8 × 8 BGO array results also demonstrated that 64 crystals with a detector pitch of 2.3 mm × 2.3 mm can be decoded with 23% energy resolution (normalized from our test source Cs-137 to Ga-68) using low-cost BGO and effectively one $140 circular PMT. These results approach those of the MicroPET that also decoded 64 crystals (2.4 mm × 2.4 mm pitch) with 19%

energy resolution. It should be remembered, however, that the MicroPET detectors use more expensive LSO crystals (which generate five times more light), an optical fiber bundle, and a $4500 position-sensitive-photomultipliers (PSPMT) for every 64 crystals to achieve the decoding [11]. This study showed that a very low-cost mouse PET camera may be developed with the PMT quadrant-sharing technology.

REFERENCES

[1] W.-H. Wong, "A positron camera detector design with cross-coupled scintillators and quadrant-sharing photomultipliers," *IEEE Trans. Nucl. Sci*, vol. 40, Aug. 1993.

[2] W.-H. Wong, J. Uribe, K. Hicks, M. Zambelli, and G. Hu, "A 2-dimensional detector decoding study on BGO array with quadrant-sharing photomultipliers," *IEEE Trans. Nucl. Sci.*, vol. 41, pp. 1453–1457, Aug. 1994.

[3] W.-H. Wong, S. Yokoyama, J. Uribe, H. Baghaei, H. Li, J. Wang, and N. Zhang, "An elongated position sensitive block detector design using the PMT quadrant sharing detector array," *IEEE Trans. Nucl. Sci.*, vol. 46, pp. 542–545, June 1999.

[4] J. Uribe, H. Baghaei, H. Li, S. Yokoyama, N. Zhang, J. Wang, F. Dobbs, and W.-H. Wong, "Basic imaging performance characteristics of a variable field of view PET camera using quadrant sharing detector design," *IEEE Trans. Nucl. Sci.*, vol. 46, pp. 491–497, June 1999.

[5] C. Nahmias, R. Nutt, R. Hichwa, J. Czernin, C. Melcher, M. Schmand, L. Andreaco, L. Eriksson, C. Moyers, C. Michel, M. Bruckbaur, M. Conti, B. Bendriem, and J. Hamill, "PET tomography designed for five minute routine whole body studies," *J. Nucl. Medicine*, vol. 43, no. 5, p. 11, May 2002.

[6] W.-H. Wong and H. Li, "A scintillation detector signal processing technique with active pileup prevention for extending scintillation count rates," *IEEE Trans. Nucl. Sci.*, vol. 45, pp. 838–842, June 1998.

[7] H. Li, W.-H. Wong, J. Uribe, H. Baghaei, Y. Liu, Y. Wang, T. Xing, and M. Aykac, "A new pileup prevention front-end electronic design for high resolution PET and gamma cameras," *IEEE Trans. Nucl. Sci.*, vol. 49, pp. 2051–2056, Oct. 2002.

[8] J. Uribe, W.-H. Wong, H. Baghaei, R. Farrell, H. Li, M. Aykac, D. Bilgen, Y. Liu, Y. Wang, and T. Xing, "An efficient detector production method for position-sensitive scintillation detector arrays with 98% detector packing fraction," *Proc. IEEE, Nuclear Science and Medical Imaging Conf.*, Nov. 2002.

[9] J. Uribe, W.-H. Wong, G. Hu, K. Hicks, J. Wang, H. Baghaei, N. Zhang, H. Li, and S. Yokoyama, "Effect of the rotational orientation of circular photomultipliers in a PET camera block detector design," *IEEE Tran. Nucl. Sci.*, vol. 44, pp. 1266–1270, June 1997.

[10] M. Tornai, M. Germano, and E. J. Hoffman, "Position and energy response of PET block detectors with different light sharing schemes," *IEEE Trans. Nucl. Sci.*, vol. 41, pp. 1458–1463, Aug. 1994.

[11] S. R. Cherry, Y. Shao, R. W. Silverman, K. Meadors, S. Siegel, A. Chatzioannou, J. W. Young, W. Jones, J. C. Moyers, D. Newport, A. Boutefnouchet, T. H. Farquhar, M. Andreaco, M. J. Paulus, D. M. Binkley, R. Nutt, and M. E. Phelps, "MicroPET: A high resolution PET scanner for imaging small animals," *IEEE Trans. Nucl. Sci*, vol. 44, pp. 1161–1166, June 1997.

[12] S. R. Cherry, M. P. Tornai, C. S. Levin, S. Siegel, and E. J. Hoffman, "A comparison of PET detector modules employing rectangular and round photomultiplier tubes," *IEEE Trans. Nucl. Sci.*, vol. 42, pp. 1064–1068, Aug. 1995.

Brain Lesion Detectability Studies with a High Resolution PET Operating in No-Septa and Partial-Septa Configurations

Hossain Baghaei, Wai-Hoi Wong, Jorge Uribe, Hongdi Li, Mehmet Aykac, Yu Wang, Yaqiang Liu, Tao Xing, and Rocio Farrell

Abstract--**We investigated the effect of partial-septa on the noise equivalent sensitivity and lesion detectability for a high resolution PET camera. For this purpose we used the MDAPET camera to detect small lesions in brain images obtained from the scan of the Hoffman brain phantom. The three-dimensional (3-D) positron emission tomography (PET) acquisition in comparison to two-dimensional (2-D) PET acquisition improves the sensitivity of the system at the cost of higher scatter and accidental coincidence contributions. A partial-septa allowing 3D-acquisition may provide a better alternative. For this work, three small lesion phantoms with diameters of 3, 5 and 8.6 mm were embedded into the Hoffman brain phantom. The activity concentration ratio of the lesions to the surrounding brain gray matter was ranging from 1.5 to 10. For this study, the eight detectors modules of the prototype MDAPET scanner were modified axially to extend from 38.5 mm to 131 mm in order to simulate more closely the performance of a clinical size camera. Data for the hot lesion phantoms and the normal Hoffman brain phantom were taken separately. Then, the two sets of the sinograms data were selectively combined to generate the sinograms data for the desired SUVs. Visual inspection of the lesion images show that we could clearly see the 8.6 mm lesion, with or without septa, at even the lowest activity ratio that we measured. The 5 mm and 3 mm lesions were observable at activity ratio of 2.2 and 5.4, respectively. We found that even though the use of septa could increase the noise equivalent count rate and lower the image noise, it does not necessary translate into improvement of the lesion detectability. For partial-septa configurations the white matter regions of brain have less count and the brain images visually looked better; however, images from no-septa data had slightly higher contrast.**

I. INTRODUCTION

THE three dimensional (3-D) positron emission tomography (PET) acquisition in comparison to two-dimensional (2-D) PET acquisition improves the sensitivity of the system at the cost of higher scatter and accidental coincidence contributions. 3-D has the potential to reduce data acquisition time compared to the 2-D. Currently, commercial PET cameras operate in two extreme modes of no-septa (3-D acquisition) mode and all-septa-in (2-D acquisition) mode. Several investigators have studied the effect of all-septa and no-septa cases on the lesion detectability and noise characteristics of the images and have found that 3-D acquisition mode may have advantage in imaging brain, small patient and animal and especially at low activity levels it could outperform 2-D mode acquisition [1]-[4]. Recently, a hybrid PET design was proposed to acquire projection data in both 2-D and 3-D modes simultaneously by using rotating partial septa [5]. Several investigators have studied optimal septa spacing in gamma cameras for PET imaging [6], [7].

A partial-septa system, allowing 3-D acquisition, may provide a better alternative. In this study, intermediate septa designs have been used to reduce the scatter and accidental coincidence with an acceptable sensitivity loss by using a 3-D PET camera that could operate in no-septa mode or with a partial-septa system. In our previous work, a Monte Carlo simulation was performed to evaluate possible septa designs and for several septa configurations the noise equivalent count rate (NEC) was measured and compared [8]. In this work, we studied the effect of partial-septa on lesion detectability for brain cancer imaging.

II. METHODS

We used the high-resolution MDAPET, a prototype PET camera, to scan the phantoms. This camera is a multi-ring scanner with an intrinsic transaxial resolution of 2.8 mm. Each ring contains 448 bismuth germanate (BGO) crystals having an in-plane and axial crystal pitch of 2.66 and 2.80 mm, respectively. The detectors are grouped into blocks of 7X7 crystals. The camera detection system is divided into eight independent, movable modules. Each module can be translated radially to alter the size of the patient opening, optimizing the detection sensitivity for different body cross-sections. Also the gantry can be rotated during data acquisition in 0.10° steps up to 45°. For this study the gantry was rotated during the data

This work was supported in part by the NIH Grant ROI CA58980, NIH Grant ROI CA61880, NIH Grant ROI CA76246, NIH Grant ROI CA58980S1, Texas Higher Education Advanced Technology Grant, John S. Dunn Foundation Research Grant, and by the Cobb Foundation for Cancer Research.

The authors are with the University of Texas M. D. Anderson Cancer Center, Houston, TX 77030 USA (H. Baghaei's telephone: 713-794-5270, e-mail: hbaghaei @di.mdacc.tmc.edu).

0-7803-7636-6/03/$17.00 ©2003 IEEE.

acquisition in 1° steps to fill the gaps in the sinograms caused by the empty space between modules. The detector module design, which is based on quadrant sharing technique, and electronics of the PET camera were described previously [9]-[13]. The imaging performance characteristics of the camera were discussed in [14], [15].

MDAPET camera has 14 detector rings covering an axial field-of-view of 38.5 mm, as shown in Fig 1a, which is much smaller than a clinical size camera. In order to simulate more closely the performance of a clinical size camera, the detectors modules were modified axially to extend from 38.5 mm to 131 mm by placing the side shields farther apart as shown in Fig. 1b. Extended parts on both sides of the modules were replaced with three layers of lead (3 mm thick) + aluminum (1.5 mm thick) sandwiches as BGO substitute to take into account for inter-crystal scattering. Each shield was extended from 60 mm to 85 mm to reduce the radiation coming from out-of-FOV.

Fig. 2 shows axial view of the modified version of MDAPET detector module for three septa configurations: (a) no-septa, (b) partial 5-setpa with inter-gap between septa of 1.46 cm, and (c) partial 7-septa with inter-gap separation between septa of 2.01 cm. Septa thickness was chosen to be 2 mm lead in both.cases.

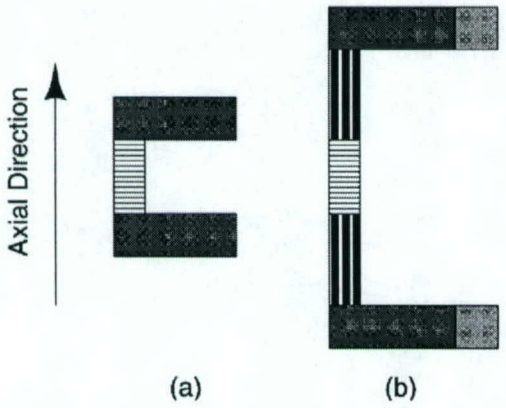

Fig. 1. (a) Original axial view of a detector module in MDAPET camera, (b) axial view of a modified detector module.

The MDAPET camera has several modes of operations and we took data in the brain mode. In this mode, the camera has a ring diameter (the distance between two facing detector modules) of 44 cm and patient opening of 32 cm. To compensate for the lower sensitivity of the MDAPET camera, due to the small "real" axial field of view, the brain phantom was scanned longer at relatively higher activity and repeated several times so that the data can be summed to obtain an equivalent number of true events as that a clinical version of the camera would collect in a typical injected dose of 10 mCi ^{18}F -fluorodeoxyglucose (FDG) in a 20 minutes scan.

For lesion detectability study three small lesion phantoms were embedded into the Hoffman brain phantom. The diameters of the embedded lesion phantoms were 3, 5 and 8.6 mm and all have the same standard uptake values (SUVs). The approximate activity concentration ratio of the lesions to the brain gray matter regions was ranging from 1.5 to 10.

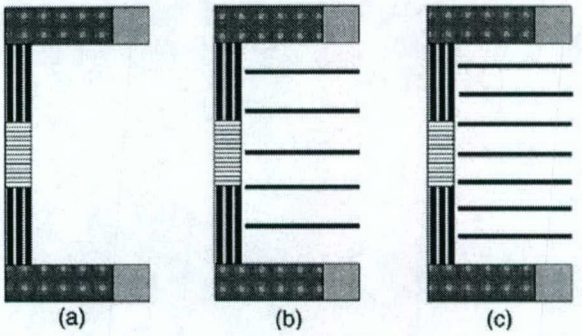

Fig. 2. Axial view of a modified MDAPET module with three different septa configurations: (a) no-septa, (b) partial 5-septa, and (c) partial 7-septa.

For practicality, to minimize the number of data taking imaging sessions, data for the hot lesion phantoms embedded in the Hoffman brain phantom filled with water and the warm (normal) Hoffman brain phantom without lesions were taken separately. Then, before applying any corrections, the two sets of the sinograms data were selectively combined to generate the sinograms data for the desired SUVs. This combination method greatly reduces the number of required measurements for different lesion uptake and also eliminates the effect of the 'cold' walls of the tissue phantoms that exits when hot lesions and the warm background are measured simultaneously. However, this technique requires the phantom be positioned precisely, the concentration ratio of the tissue and background be known, the accidental coincidence be known and also the effect of the dead time becomes more important [16]. When the lesions data were taken, the lesions were placed inside the Hoffman brain phantom filled only with water to provide the attenuation and scatter effects. This sinogram summing method allows all the different SUVs data for lesions to be taken in one experimental period by collecting the different SUVs data as the activity decays.

Prior to image reconstruction, the projection data were corrected. These corrections included random coincidence subtraction, attenuation correction, geometric and detector-pair efficiency corrections [17]. The attenuation correction was performed by calculating the attenuation length from the shape of the phantom (cylinder) and assuming a uniform attenuation coefficient. All data were acquired with the FDG tracer. For image reconstruction we used the 3-D reprojection algorithm with a Butterworth filter [18].

All data were acquired in 3-D mode with an axial acceptance of 13 rings which produced 196 sinograms and no averaging was performed. In the present study, each sinogram had 239 radial bins and 180 azimuthal views. The radial sampling was 1.385 mm. The camera allows simultaneous imaging of 27 transaxial slices with 1.4 mm thickness.

III. RESULTS

The NEC was measured for a standard uniform NEMA phantom with 21 cm diameter and 18 cm height. For these measurements 1.5 mCi, 2.9 mCi and 3.5 mCi of FDG was added to the water phantom for no-septa, 5-septa and 7-septa configurations, respectively. True (un-scattered and scattered) and accidental coincidence count rates were measured in full 3-D acquisition mode as the activity decayed for each configuration. The true count rates for three configurations are compared in Fig. 3. The scatter fraction values used for NEC calculation were 37.9% for no-septa, 27% for -5-septa and 24.5% for 7-septa configurations. The NEC for three configurations is shown in Fig. 4. It is clear that, in terms of NEC, for activity of 0.07 μCi/cc or higher the MDAPET scanner in brain mode performs much better for, 5-septa and 7-septa configurations than no-septa configuration.

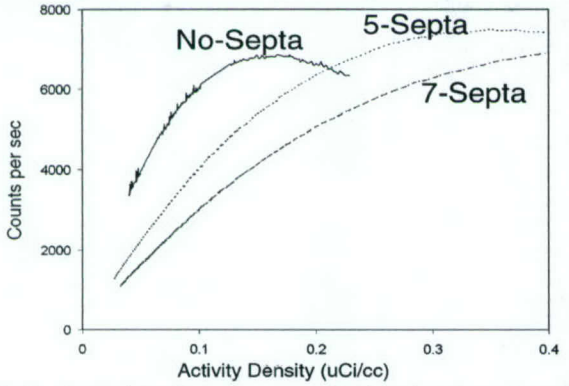

Fig. 3. Comparison of true count rates for three detector configurations: no-septa, 5-septa and 7-septa.

In the brain studies, typical activity concentration value ranges between 0.15 μCi/cc and 0.30 μCi/cc for 10 μCi FDG injection. In this range, intermediate septa configurations such partial 5-septa or 7-septa may be more appropriate. No-septa configuration reaches its NEC peak rate around 0.07 μCi/cc. As a result, in no-septa configuration less amount of activity (e.g. 5 mCi) could be more appropriate for MDAPET.

Figure 5 shows two reconstructed image slices of the Hoffman brain phantom without embedded lesion phantoms for no-septa (top row), 5-septa (middle row), and 7-septa (bottom row) configurations. The images show that for septa configurations the white matter (background) contribution become less observable and gray matter contribution become clearer and image quality visually improve. The total true coincidence events collected were 76 million, 57 million, and 33 million for no-septa, 5-septa and 7-septa configurations, respectively. The scatter fraction from Hoffman brain phantom studies estimated to be 31.3%, 20.5% and 14% for no-septa, 5-septa and 7-septa cases. The ratio of NEC for 5-septa to no-septa case was calculated to be about 1.25.

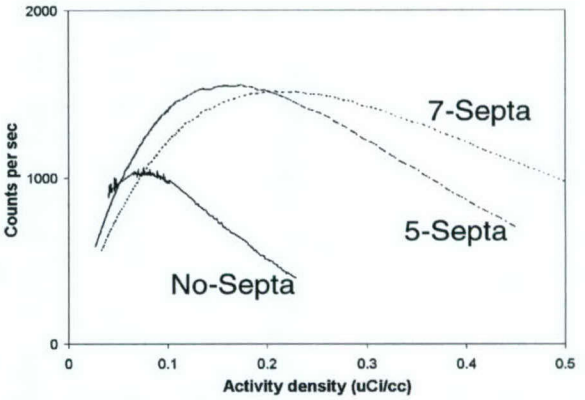

Fig. 4. Comparison of NEC rates for three detector configurations: no-septa, partial 5-septa and 7-septa.

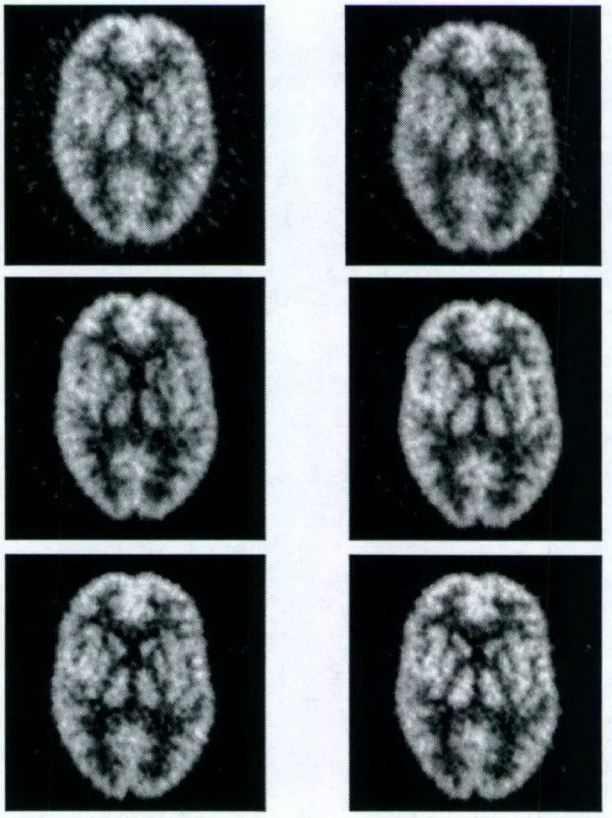

Fig. 5. Two image slices of the Hoffman brain phantom reconstructed with the 3DRP algorithm for three different configurations: (top) no-septa, (middle) 5-septa and (bottom) 7-septa.

Fig. 6 shows two reconstructed image slices with 3 mm and 5 mm embedded lesion phantoms when the ratio of the activity concentration in the lesions to surrounding tissue (brain gray matter) was 5.4. In order to better observe the lesion images, the 8.6 mm lesion phantom was placed such that does not appear at the same slices with the others. Top images are for no-septa and bottom images for 5-septa cases. The activity

ratio of 5.4 was the lowest activity ratio that the 3 mm lesion was observable.

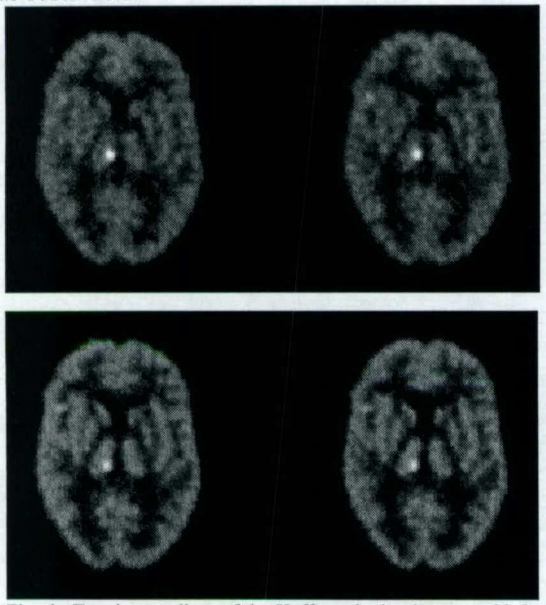

Fig. 6. Two image slices of the Hoffman brain phantom with 3 mm and 5 mm lesions for two different configurations: (top) no-septa and (bottom) 5-septa. Ratio of activity concentration of the lesions to gray matter was 5.4.

Fig. 7 shows two reconstructed image slices with 5 mm embedded lesion phantom when the ratio of the activity concentration in the lesions to the surrounding tisuue was 2.2. The activity ratio of 2.2 was the lowest activity that this lesion was clearly observable. Top images are for no-septa and bottom images for 5-septa cases.

Fig. 8 shows two reconstructed image slices with 8.6 mm lesion when the activity concentration in the lesions to the background was 1.5. This was the lowest activity ratio that we measured and the 8.6 mm lesion was clearly observable.

Figs. 9, 10 and 11 show a horizontal profiles running along the middle of the 3 mm lesion, 5mm lesion and 8.6 mm lesion, respectively. The ratio of the activity density of the lesions to the surrounding tissue was 7.4. The profile data for each image was normalized according to the average counts in the background for each case. Figs. 9-11 show that the ratio of the peak (lesion activity) to the background (gray matter) is higher for no-septa configuration especially for the largest lesion.

IV. CONCLUSION

The MDAPET camera operating in Partial 5-speta and 7-septa configurations performed better than no-septa case in terms of NEC. For 5-septa configuration the NEC peaked around 0.18 mCi/cc with ~1.6 Kcps value and the camera sensitivity was estimated 53% compared to no-septa case. For 7-setpa NEC peaked around 0.22 mCi/cc with ~1.5 Kcps value and the camera sensitivity was estimated 35% compared to no-septa case.

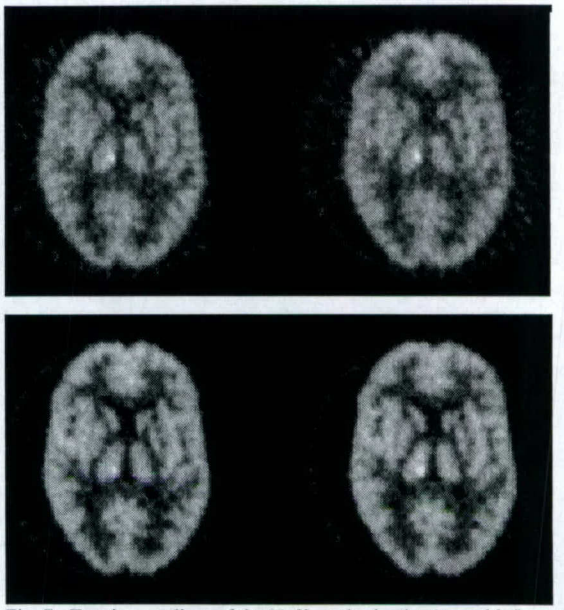

Fig. 7. Two image slices of the Hoffman brain phantom with 5 mm lesions for two different configurations: (top) no-septa and (bottom) 5-septa. Ratio of activity concentration of the lesions to gray matter was 2.2.

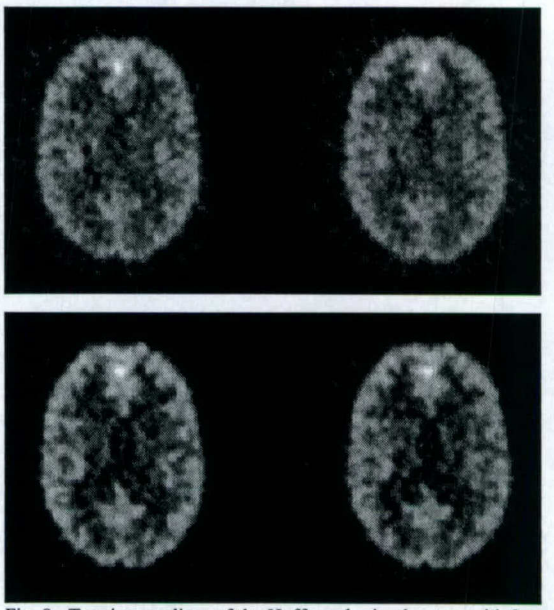

Fig. 8. Two image slices of the Hoffman brain phantom with 8 mm lesions for two different configurations: (top) no-septa and (bottom) 5-septa. Ratio of activity concentration of the lesions to gray matter was 1.5.

The Visual inspection of the lesion images show that we could clearly see the 3 mm lesion phantom embedded in the Hoffman brain phantom, with or without partial 5-septa, when the activity concentration ratio between the lesion and the surrounding tissue (gray matter) was greater than 5.4. The 5 mm lesion could be seen at the activity ratio greater than 2.2. The 8.6 mm was observable even at the lowest activity ratio (1.5) that we measured.

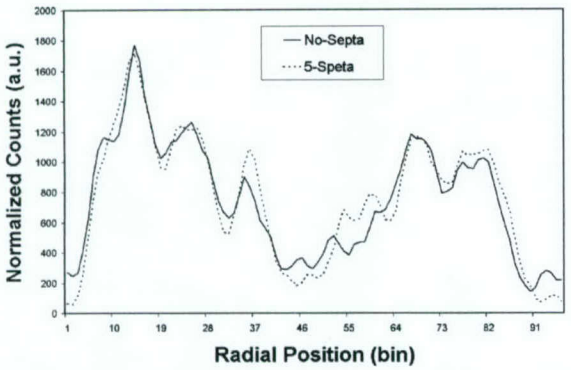

Fig. 9. A horizontal profile running through the middle of the 3 mm lesion images for no-septa and partial 5-septa configurations.

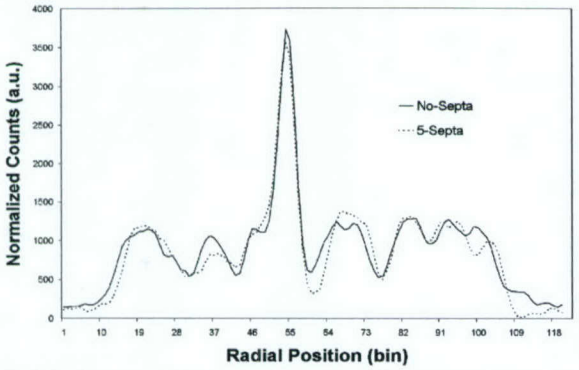

Fig. 10. A horizontal profile running through the middle of the 5 mm lesion images for no-septa and partial 5-septa configurations.

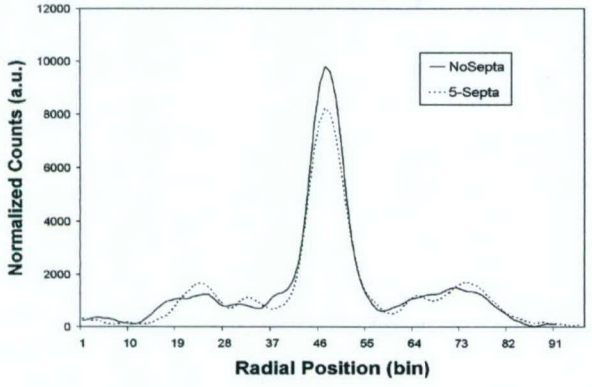

Fig. 11. A horizontal profile running through the middle of the 8.6 mm lesion images for no-septa and partial 5-septa configurations.

We found that even though the use of septa could increase the NEC rate, it does not necessary translate into improvement of the lesion detectability. With partial septa the white matter regions of brain have less count and the brain images have less noise; however, images without septa have slightly higher contrast especially for 8.6 mm lesion We are currently extending these measurements to lower activities and also planning to complete our measurement with 7-septa configuration for lesion imaging.

The NEC measurement was done with a cylindrical phantom which is larger than the Hoffman brain phantom. Since both scattered and accidental coincidence contributions are larger in NEMA phantom than the brain phantom, partial septa would have greater effect on NEC.

V. References

[1] D. J. Kadrmas, P. E. Christian, S. D. Wollenweber, S. G. Kohlmyer, C. W. Stearns, "Comparative evaluation of 2D and 3D lesion detectability on a full-ring BGO PET scanner," *J. Nucl. Med.*, vol. 43, no. 5, p. 56P, May 2002.

[2] S. Pajevic, M.E. Dauve-Witherspoon, S. L. Bacharach, and R. E. Carson, "Noise characteristics of 3-D and 2-D PET images," *IEEE Trans. Med. Imag.*, vol. 17, pp. 9-23, February 1998.

[3] D. L. Baily, T. Jones, T. J. Spinks, M. C. Gilardi, and D. W. Townsend, "Noise equivalent count measurements in a neuro-PET scanner with retractable septa," *IEEE Trans. Med. Imag.*, vol. 10, pp. 256-260, 1991.

[4] C. W. Stearns, S. R. Cherry, C. J. Thompson, "NECR analysis of 3D brain PET scanner designs," *IEEE Trans. Nucl. Sci.*, vol. 42, no. 4, pp. 1075-1079, xxx.1995.

[5] J. E.Tanaka, T.Hasegawa, T.Yamashita, H.Okada and H.Murayama "A 2D/3D hybrid PET scanner with rotating partial slice-septa and its quantitative procedures", *Phys. Med. and Biol.*, 45 pp. 2821-2841, 2000.

[6] Turkington,T.G., Sampson, W.H., "Optimizing septal spacing for gamma camera PET imaging", *IEEE Medical Imaging Conference Record*, vol. 3 pp. 1767, 2000.

[7] S.J.Glick, C.J.Groiselle, J.A.Kolthammer, R.Z.Stodilka, "Optimization of septal spacing in hybrid PET using estimation task performance", *IEEE Medical Imaging Conference Record*, 2001.

[8] M. Aykac, J. Uribe, H. Baghaei, H. Li, Y. Wang, Y. Liu, T. Xing and W-H. Wong, "Septa Design Study for Volumetric Imaging in Positron Emission Tomography," *IEEE Trans. Nucl. Sci.*, vol. 49, no. 5, October 2002.

[9] W.-H. Wong, "A positron camera detector design with cross-coupled scintillators and quadrant sharing photomultipliers," *IEEE Trans. Nucl. Sci*, vol. 40, pp.962-966, August 1993.

[10] W-H. Wong, J. Uribe, W. Lu, and K. Hicks, "Design of a variable field prototype PET Camera," *IEEE Trans. Nucl. Sci.*, vol. 43, pp. 1915-1920, June 1996.

[11] W-H. Wong, J. Uribe, K. Hicks, and M. Zambelli, "A 2-dimensional detector decoding study on BGO arrays with quadrant sharing photomultipliers," *IEEE Trans. Nucl. Sci.*, vol. 41, pp. 1453-1457, June 1994.

[12] W-H. Wong, G. Hu, N. Zhang, J. Uribe, J. Wang, H. Li, H. Baghaei, and S. Yokoyama, "Front end electronics for a variable field PET camera using the PMT-quadrant-sharing detector array design," *IEEE Trans. Nucl. Sci.*, vol. 44, pp. 1266-1270, June 1997.

[13] R. H. Li, W-H Wong, N. Zhang, J. Wang, J. Uribe, H. Baghaei, and S. Yokoyama, "Prototype electronics for a variable field of view PET camera using the PMT-quadrant-sharing detector array," *IEEE Trans. Nucl. Sci.*, vol. 46, pp. 546-550, June 1999.

[14] J. Uribe, H. Baghaei, H. Li, S. Yokoyama, N. Zhang, J. Wang, F. Dobbs, and W-H. Wong, "Basic imaging characteristics of a variable field of view PET camera using quadrant sharing detector design," *IEEE Trans. Nucl. Sci.*, vol. 46, pp. 491-497, June 1999.

[15] H. Baghaei, W-H. Wong, J. Uribe, H. Li, N. Zhang, and Y. Wang, "Breast cancer studies with a variable field of view PET camera," *IEEE Trans. Nucl. Sci.*, vol. 47, pp. 1080-1084, June 2000.

[16] R.S. Miyaoka, S.G. Kohlmyer, T.K. Lewellen, "Hot Sphere Detection Limits for a Dual Head Coincidence Imaging System," *IEEE Transaction on Nuclear Science*, vol. 46, pp.2185-2191, December 1999.

[17] H. Baghaei, W-H. Wong, J. Uribe, H. Li, N. Zhang, and J. Wang, "The correction factors for a high resolution variable field of view PET camera," *J. Nucl. Med.*, vol. 40, p.279P, May 1999.

[18] P. E Kinahan, J. G. Rogers, "Analytic 3D Image Reconstruction Using all Detected Events," *IEEE Transaction on Nuclear Science*, vol. 46 pp.964-968, 1989.

Front-end Electronics Based on High-yield-pileup-event-recovery Method for a High Resolution PET Camera with PMT-quadrant-sharing Detector Modules

Hongdi Li, Wai-Hoi Wong, Yu Wang, Yaqiang Liu, Tao Xing,
Jorge Uribe, Hossain Baghaei, Rocio Farrell

Abstract-- **Front-end electronics based on a high-yield-pileup-event-recovery (HYPER) method has been developed for a high resolution PET camera with 12 PMT-quadrant-sharing (PQS) detector modules that decoding 38,016 BGO crystal elements. Each module has 60 BGO blocks coupled to 77 PMTs that are organized as four Anger cameras in electronics. Each Anger camera is served by one HYPER decoding board to solve the pileup problem in order to have better count-rate and dead-time performance. There are 48 HYPER boards and only 144 A/D converters are used in the entire PET scanner. EPLD/FPGA based real time pileup remnant-correction algorithm and high-resolution digital trigger delay unit are developed for HYPER in PET coincidence application. Random coincidence events can also be acquired with the same digital delay method. A fast automatic PMT gain equalization method has been proposed to equalize the gains of 924 PMTs within two minutes. This instantaneous LED tuning can be performed between patient scans, hence it gives a better PET quality control. A standard daisy parallel port is used to control all the parameters such as gains of preamplifiers, trigger thresholds, signal DC offset control, trigger delay alignment, and as well as the coincidence time windows. A fast HOTLink (400Mbit/s, Cypress Semiconductor inc.) serial bus is used to transfer the coincidence data to networked data acquisition and image processing computers, and the sinogram binning and image reconstruction can be processed in parallel. This camera also has an ECG/respiratory gated imaging capability.**

I. INTRODUCTION

WE have introduced a high resolution transformable whole-body clinical PET camera with 12 PQS modular detector design where 924 PMTs decode 38,016 BGO crystal elements [1]. This camera has 6 times more decoded crystal elements than our prototype MDAPET camera [2, 3] that will require more complicated electronics and much higher count-rate performance. This is paper presents a new flexible modular electronic architecture and design for this particular PET camera. The modular electronics can be easily integrated for different PET configurations such as four module animal or mammography PET camera.

The PQS design increases the number of decoded crystal elements per PMT, therefore increased the resolution. In the proposed PET camera, each PMT can decode about 41 crystal elements in average. However, the increased number of crystals to be served by each PMT will inevitably increased the chance of signal pileup in the detection system. Pileups degrade image quality and creased image distortions. Due to the significant increase in the number of small detector elements the system requires the properties of a high resolution decoding, low imaging artifacts and as well as a better quality control. Hence, to fully realize the benefits of the PQS detector design, we apply the HYPER processing electronics [4] developed by us to process the pileup events in high count-rate situation in order to lower the image artifacts. To further increase the count-rate capability and have a better dead-time performance, we divide each detector module into 4 "Anger-gamma-camera" zones by Anger-weighting the PMT signals electronically according to their physical locations. Each Anger-camera has one HYPER electronic board to do real-time pileup signal processing. Hence, there are 48 high speed Anger-HYPER cameras inside each PET scanner. Figure 1 shows one detector module design, in this design 60 BGO blocks (32 standard blocks with 7x7 elements, 24 extended blocks with 8x7 elements and 4 extended blocks with 8x8 elements) are coupled to 77 PMTs.

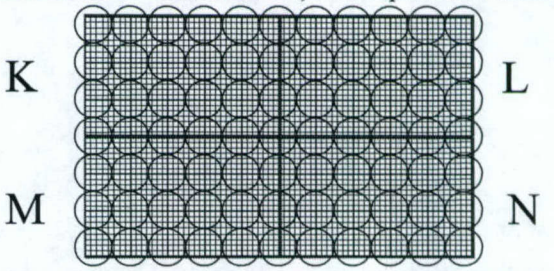

Fig.1 Large-field-of-view PQS detector module with 10x6 BGO blocks (3168 crystal elements) coupled to 77 PMTs (18.7mm diameter) is divided into four HYPER zones (K, L, M and N).

This work was supported in part by NIH under Grant RO1 CA76246, RO1 CA61880, RO1 CA58980 and RO1 EB001038, by Texas Higher Education Advanced Technology Grant No. 003657-0058-2001, the J.S. Dunn Research Foundation, the Cobb Endowment for Cancer Research.

Hongdi Li, Wai-Hoi Wong, Yu Wang, Yaqiang Liu, Tao Xing, Jorge Uribe, Hossain Baghaei and Rocio Farrell are with the University of Texas M.D. Anderson Cancer Center, Houston, TX 77030 USA (H. Li's telephone: 713-745-3732, e-mail: hli@di.mdacc.tmc.edu).

0-7803-7636-6/03/$17.00 ©2003 IEEE.

II. METHODS

A. Overall architecture

The electronics has been developed for the proposed whole-body clinical PET camera with 12 BGO detector modules in PQS design. Each module has one set of electronics including 'pre-amplifier', 'Anger positioning', 'HYPER' and 'digital multiplexer'. Inside each module, the 77 PMT signals are amplified and Anger-weighted as four Anger-cameras by a position matrix board generating four set of pre-normalized position and energy signal outputs. Each Anger-camera is served by one individual real-time pileup prevention HYPER circuit. A digital multiplexer, also working as a motherboard for the HYPER circuits, merges the four HYPER outputs for further coincidence processing. The coincidence board is also based on a modular architecture with daughter-boards sitting on a mother-board. It can be reprogrammed for a new PET configuration with different number of modules. In the 12-module camera, each module will have both the true and random coincidence with other 7 opposing modules. All the electronics are mounted on the gantry and can be rotated with the gantry. The gains of pre-amplifiers, analog trigger thresholds, digital energy thresholds, the width of coincidence timing window, the front-end LEDs for PMT' auto-tuning, and as well as the PMT high voltage can be controlled through a computer parallel port.

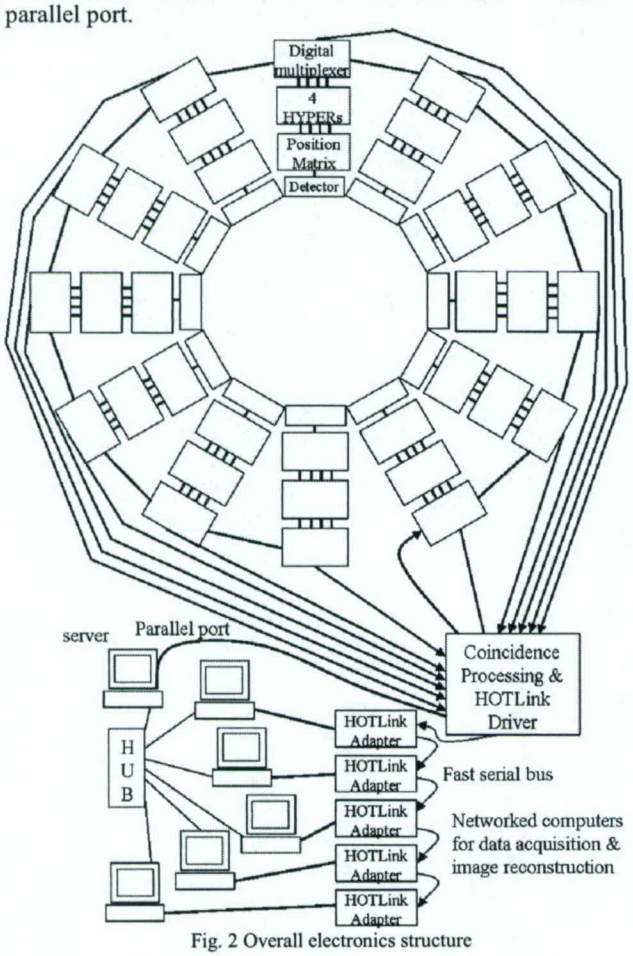

Fig. 2 Overall electronics structure

This is an inexpensive, flexible and easy to be maintained electronics design comparing to the traditional PET electronics. By using Anger-HYPER design, we do not need one HYPER circuit for each PMT; otherwise 924 HYPER channels would be used (costly). Only 144 ADCs are used in the whole camera with 924 PMTs, and still can work in high count-rate situation that benefited from the pileup prevention techniques. An important advantage of the HYPER design is that HYPER electronics works on both the total-energy signal (E) and the total-position signals (X', Y') in the same way. Hence, only 3 HYPER channels (X', Y', E) are used for each Anger-camera zone. Furthermore, dividing a detector module into 4 zones in electronics, each of which is served by 3 HYPER channels (X', Y', E), that increases the count rate by a total of 30X over the conventional processing method [4].

Another important improvement that reduces the components and simplifies the electronic design is that we assigned the functions of position normalization, the crystal identification lookup table and the fine crystal energy-threshold lookup table after the coincidence board. Generally the decoding electronics needs one real-time processing board doing these functions mentioned above, hence the entire camera needs 48 processing boards; and by applying these functions after coincidence, the 48 processing boards can be reduced to one board, because the event-rate after the coincidence board is much lower and further more the real-time performance is not necessary after coincidence. Hence, the lookup processing board is easier to be implemented, and on the same board we use HOTLink to serialize the processed coincidence data into 1 bit output. There are two reasons that can allow those processing functions to be done after coincidence: (1) the coincidence circuit only uses the time information of events, and the energies and positions of the events are simply passed through. Hence, the above functions can be done either before or after coincidence. (2) A major concern is that many scatter-events may be sent to the coincidence board if there is no fine crystal energy cut-off in the front-end, which will increase the dead-time of the coincidence processing. However, an advantage of the PQS design is that the difference of the photo-peak signal amplitude for all crystals is less than 30% [5], and one universal energy low threshold can reject most of the scatter-events for all crystals. Therefore, we don't need to perform the above functions until the coincidence finished. This PQS advantage allows us to greatly simplify the front-end electronics.

B. HYPER method for PET

We have suggested a HYPER method to solve the pileup problem and recover the events at very high count-rate [4]. The main idea is: **a.** estimating a weighted value to indicate the total energy inside the detector; **b.** the energy of this event can be derived by subtracting a residual signal from the previous weighted value; **c.** this method is also correct for Anger-energy and pre-normalized position signals.

energy of this pulse = weighted value of a pulse - (weighted value of the preceding pulse) x $e^{-(\text{time difference between this and the preceding event})}$

In HYPER method the event processing time is not fixed. If there is no pileup on the event, the signal will be integrated

for a maximum time of 1μs, however, if the circuit detects a pileup, the integrating stops immediately and A/D converter samples the weight-sum signal. Because of this dynamic processing time in HYPER method, the ready signal given by A/D converter is not synchronized with the trigger. It is all right for gamma camera; as for coincidence application, an additional high-resolution delay component has to be implemented in the HYPER circuit to restore the synchronization between data and the trigger. Other special techniques associated with HYPER and PQS detector design will be addressed in the following section.

III. Results and Discussion

A. An improved HYPER method

We have addressed different improved HYPER methods in a recent publication [6]. An improved HYPER method of applying multi-sampling on the weight-sum signal was adopted by this PET electronics. The weighted-sum signal of the integrated signal and the instantaneous signal amplified by τ is a constant in time, and is always a measure of the total radiation energy before the next event is detected, regardless of when the sum-signal is sampled. Since the instantaneous signal is noisier than the integrated signal, a low-pass smoothing circuit is applied to the weighted-sum signal in order to reduce the noise. The advantages of using a weight-sum signal/multi-sampling to estimate the total energy in implementation are: (a) it can produce the total energy directly; no further calculation will be involved; (b) since the sampling time for the time-constant sum signal is not critical, instead of using the expensive flash ADC, a very cheap pipe-line sampling ADC with a fixed sampling period can be used to digitize the sum signal. Sampling ADCs are widely used in telecommunications, digital cameras and high definition TV; the price of an ADC with 80MSPS sample-rate with 10 bit resolution is only about US $10.

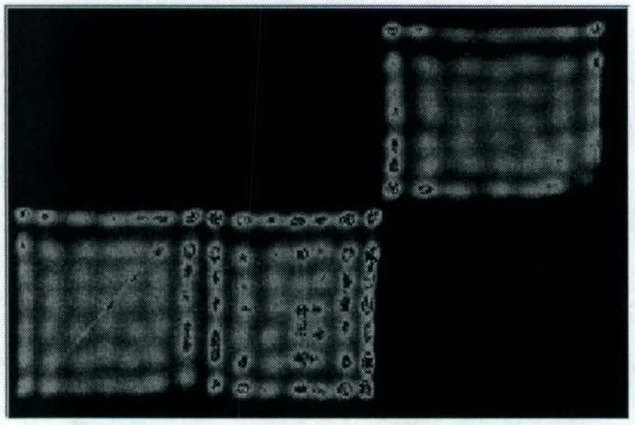

Figure 3: Crystal decoding map acquired by Anger-Hyper unit

We have tested the electronics of one Anger-camera zone with three BGO detector blocks, each block has 7x7 elements with a size of 2.7x2.7x1.8mm, coupled to Photonis 19mm PMTs (XP1911) in PQS design setup in a dark box. Figure 3 showed all the crystals are well decoded by this Anger-HYPER design. The entire system has 48 Anger-HYPER cameras (with multiple zones design); our target single rate is about 30 Mcps.

Following listed some additional techniques developed for the HYPER in PET application.

(1) *Trigger synchronization recovering*

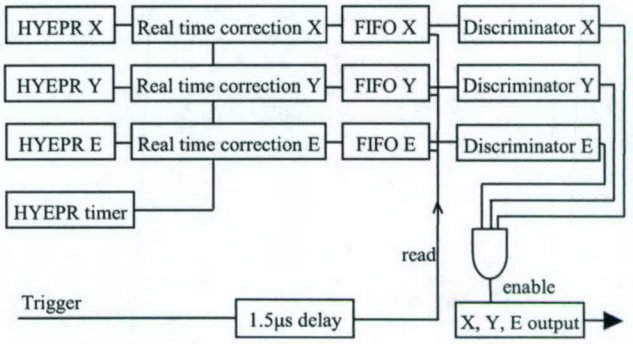

Figure 4: The HYPER design for PET application.

In the HYPER method, a random next-event can terminates the integrating of the current-event; hence the data-ready signal of the A/D converter is not synchronized with the event-trigger anymore. Figure 4 shows the concept of recovering the synchronization. The data from the A/D converter are stored into a FIFO (first in first out memory) and then will be read out by a delayed trigger signal. The trigger delay time should be longer than the maximum event processing time, for example here it is 1.5 μs and the maximum event processing time is 1.0 μs. We have developed a very high resolution (±0.9ns) and small dead-time (50ns) delay unit for this special purpose. The data readout from the FIFO is synchronized to the delayed trigger and the original trigger as well (only a fixed 1.5 μs time offset). The coincidence processing will apply on the delayed trigger signals.

(2) *Signal baseline restoring*

The dynamic integrating time in HYPER method needs a DC couple signal input that requires a big challenge to eliminate the signal's DC offset which can be caused by the pre-amplifier's input bias current or output voltage offset. The DC offset may also drift as the system temperature changes. A longer integrating time will create a larger error than a short integrating time due to the DC offset. Since this error is sensitive to the integrating time, we can not easily correct it after digitization. In the traditional method with a fixed integrating time, this error is fixed and can be derived after energy calibration.

We have developed a new method to measure the signal DC offset and then generate a compensative DC signal to cancel it directly. This method can work with or without radioactivity. To measure the DC offset, the circuit continuously generates automatic self-triggers at 750Kcps rate (dash arrows in Fig. 5); each self-trigger starts integrating the input signal for a fixed period of 1μs and then digitizes the integrator output. However, if a real gamma-event trigger

is detected within a self-trigger integration period, this self-trigger will be rejected, and meanwhile the circuit for generating self-triggers will be reset. A new self-trigger signal will start in about 1.5μs waiting time, see Fig. 5. The 1.5μs waiting time is to guarantee that no signal from the real event could contribute to the next self-trigger integration. Hence, the "baseline spectrum" is separated from the gamma spectrum; and according to the "baseline-peak" location, a DAC is initialized (according to a DC offset lookup table) and its output is feed-back to the pre-amplifier to cancel the DC offset therefore to restore the baseline back to the ground level. Since the "baseline spectrum" is always sharp and narrow, a few thousand events are enough to locate the "baseline-peak" accurately. Hence, it only takes a few milliseconds to restore the baseline. The baseline restoring can be done before every patient scan or even within a scan in the period of camera rotating or bed positioning.

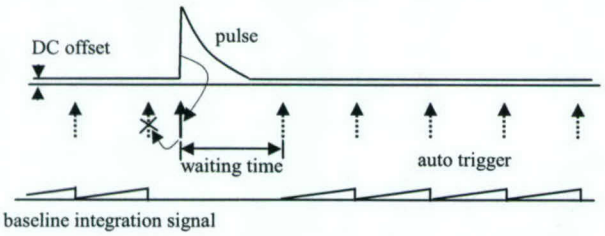

Figure 5: A method of DC offset measurement

(3) *Multiple HYPER zones design*

To further increase the count-rate capbility, a large detector is divided into several local Anger-camera zones by weight positioning PMTs in electronics. Figure 1 shows the detector module is divided into four zones (zone K, L, M and N). Since every two neighbor zones share one row or one column PMTs, one gamma hit may trigger two zones simulatanously if its energy is collected by the shared PMTs. A new simple method has been invented to identify a zone that is hit by a real gamma and to reject the false hit in other zones. To find out the zone that has a real hit, a threshold is set for the pre-normalized position signals of each zone (discriminator-X, -Y in figure 3). To demonstrate the idea, fig. 6 shows a simple example of two zones design, each zone has one independent block detector coupled to 4 PMTs in PQS. The pre-normalized position of zone-1is X1=A+D, and pre-normalized position of zone-2 is X2=C+F. If a gamma hits zone-2, there is no contribution of light to X1. However, if a gamma hits zone-1 (even in the corner crystal located in the center of PMT-B or PMT-E), it still has more than 3-5% of total light/energy going to PMT-A and PMT-D benefited from the PQS block design. That means the pre-normalized position signal (A+D) will have more than 3-5% of total energy of a real hit. Therefore, in data acquisition, a real hit in a zone should pass both the energy-acceptance threshold and pre-normalized position-acceptance threshold which are about 3-5% of E0 (the zone-l energy-acceptance threshold); however, a false hit in zone-1 caused by its neighbor's zone may be accepted by the energy threshold but it will not be accepted by the pre-normalized position threshold that is set to 3-5% of E0. The simulataneous acceptance of the energy threshold and the pre-normalized position threshold is a simple way to reject the false trigger (event) within a zone. This is a very robust discrimination because it is immune to differences in electronic-gain balance between different zones. This design also reduces electronic complexity and cost.

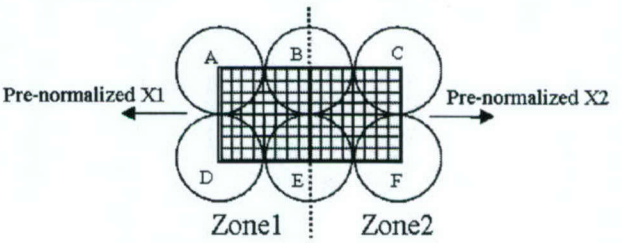

Figure 6: A simple example for zone identifying

B. Digital multiplexer--HYPER motherboard

Digital signal outputs from the four HYPER zones are merged into one output by a real-time digital multiplexer for further coincidence processing. The multiplexer board is also a mother-board, all the four HYPER boards are sitting on it (see Fig. 7); it reads the energy and pre-normalized position results from the four HYPER boards and meanwhile it distributes the parallel port control signals as well as the DC power supplies to all the four HYPER boards. The 12 modular electronics are controlled by a computer parallel port linked in daisy-chain. The parallel port cable is driven by a HYPER motherboard and goes to the next motherboard.

The digital multiplexer board has a dead time about 30ns, and the dead time for each HYPER board is about 50ns. If two HYPER outputs are detected within the 30ns dead time, the multiplexer-board will pickup the one with a large energy; and if more than two HYPER outputs are found within the dead time, it will pickup one in random or by a token ring.

There are four individual programmable delay units on each multiplexer board with about 1.2ns resolution to align the timing of the four HYPER boards. The HYPER board also has a limited delay adjustment capability in about 0.8ns resolution. Since the multiplexer outputs will directly go to the coincidence processing, those timing adjustments are necessary to balance the time delay difference caused by digital multiplexer, components, cables and connectors.

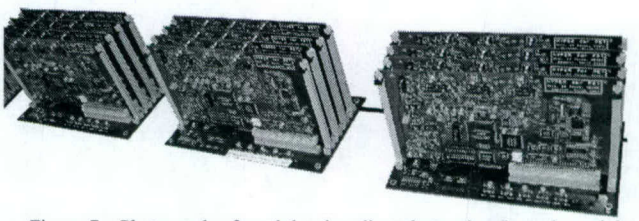

Figure 7: Photograph of modular decoding electronics. In each module there are four HYPER boards sitting on one multiplexer mother-board.

C. Coincidence electronics

A coincidence electronic system with backplane/plug-in architecture has been developed specially for the PET camera with modular detector design [7]. Benefited from the DSP and programmable EPLD/FPGA technology, the coincidence hardware can be reprogrammed for different PET configuration that is consisted of from 2 modules up to 12

modules. For 12 detector modules, see Fig. 8, each module will have the coincidence with other 7 opposite modules. Each event will generate a gate signal with a specify time width, and a traditional AND logic is used to detect the true coincidence events among those single gate signals. Simultaneously, pipeline delayed gate signals are generated (a varied delay time for each module, from 200ns to 2200ns), and another AND logic is used to detect the random coincidence events among those delayed gate signals. Our test result shows the system has 21ns dead-time and is able to operate up to 10million events per second, and the gate width can be on-line programmed from 6.5ns to 16ns at 0.5ns resolution.

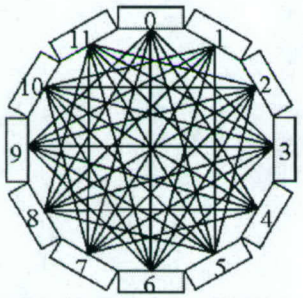

Figure 8: Coincidence design for 12 detector modules

D. *Instantaneous PMT auto-tuning*

The high decoding power of the PQS technique has more stringent requirement that the amplification of PMT needs to be more accurately equalized. Since all PMT-gain drifts with time, temperature and extended radiation exposure [8, 9], we have developed an ultra fast LED auto-tuning method to equalize the PMT gains for a better quality control. With this new method the gains of 924 PMT can be tuned within 2 minutes. Hence, the camera tuning can be done between patient scans.

One true blue LED is placed in the center of the empty space of every 4-PMT group in a detector module (fig. 9). The light of LED is directly injected into the center of a crystal array from the coupling side and distributed by the array back into the four decoding PMT. Each PMT has a variable-gain-amplifier (VGA) connected to the output and the VGA can be turned on/off individually. The four PMT gains are balanced by changing the four VGA gains to have a same amount of light output. The light outputs of every two neighboring LEDs can be aligned by adjusting the LED pulse width to have a same light output on a common PMT that is shared by the two LEDs. The LED tuning control logic is implemented in the front-end Anger-positioning matrix board inside the detector module.

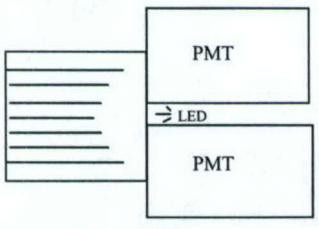

Figure 9: LED is used for PMT gain equalization in PQS detector

E. *HOTLink/networked computer system*

We have developed a HOTLink/networked computer system for the high resolution PET camera in whole-body scanning or gated imaging study [10]. A 400Mbit/s daisy-chain HOTLink is used to serialize the coincidence output and broadcast the data to networked PC cluster. The data will be interfaced to PC through a fast PCI I/O board. The overall architecture is good for pipeline processing. In a whole-body scanning, each PC will acquire sinogram data for one bed position, and after completion of data acquisition the PC begins to reconstruct the image meanwhile another PC will start data acquiring for the next bed position. And after sending its result to a server for final tabulation and storage through a standard TCP/IP network, this PC will be free for processing a new bed position. In gated respiratory or gated ECG imaging study, each PC will be reconfigured for processing a specified time-frame image of a respiratory or ECG cycle. The HOTLink/networked structure design also allows us to split the huge sinogram into several PCs in real-time and the image reconstruction can be done in parallel.

IV. Conclusions

A very low cost and high performance with large-field-of-view PET camera can be achieved by combining both PMT-quadrant-sharing and HYPER state-of-the-art designs. This paper presented an inexpensive, flexible (programmable) front-end modular electronics for PQS detector based on an Anger-HYPER method. The designs of coincidence, LED auto-tuning method as well as HOTLink/networked computer system are also addressed in this paper. All the electronics have been designed and implemented. More performance tests will be done in the near future.

V. References

[1] W.H. Wong, "The design of a high resolution transformable whole body PET camera," *IEEE Trans. Nucl. Sci.*, vol. 49(5), October, 2002.

[2] W.H. Wong, J. Uribe, W. Liu, K. Hicks, "Design of a variable field prototype PET camera," *IEEE Trans. Nucl. Sci.*, vol. 43 pp, 1915-1920, June 1996.

[3] H. Li, W.H. Wong, N. Zhang, J. Wang, J. Uribe, H. Baghaei, S. Yokoyama, "Prototype electronics for a variable field of view PET camera using the PMT-Quadrant-Sharing detector array," *IEEE Trans. Nucl. Sci.*, vol. 46, pp. 546-550, June 1999.

[4] W.H. Wong, H. Li, J. Uribe, H. Baghaei, Y. Wang, S. Yokoyams, "Feasibility study of a high speed gamma camera design using the high-yield-pileup-event-recovery (HYPER) method," *The Journal of Nuclear Medicine,* vol.42, no. 4, April 2001.

[5] J.Uribe, W.H. Wong, et al, "Signal characteristics of individual crystals in a high resolution BGO detector design using PMT-Quadrant-Sharing", *Conference record of the 2002 IEEE MIC Conference.*

[6] H. Li, W.H. Wong, et al, "A new pileup-prevention front-end electronics design for high resolution PET and gamma cameras," *IEEE Trans. Nucl. Sci.*, vol. 49(5), October 2002.

[7] Y. Wang, et al, "A modular low dead-time coincidence system for high resolution PET cameras," *Conference record of the 2002 IEEE MIC Conference.*

[8] Matheoud R, Zito F, Canz C, Voltini F, Gerundini P. "Changes in the energy response of a dedicated gamma camera after exposure to a high-flux irradiation," *Phys. Med. Biol., 44, N129-N135*, 1999.

[9] J. Uribe, et al, "Effect of photomultiplier gain-drift and radiation exposure on 2D-map decoding of detector arrays used in positron emission tomography," *Conference record of the 2001 IEEE MIC Conference.*

[10] H. Li, T. Xing, et al, "A HOTLink/networked PC data acquisition and image reconstruction system for a high resolution whole-body PET with respiratory or ECG gated performance," *Conference record of the 2002 IEEE MIC Conference.*

A Modular Low Dead-time Coincidence System For High Resolution PET Cameras

Yu Wang, Hongdi Li, *Member, IEEE*, , *IEEE*, Yaqiang Liu, Tao Xing, Jorge Uribe, *Member, IEEE*, Hossain Baghaei, *Member, IEEE*, Rocio Farrell, Wai-Hoi Wong, *Member, IEEE*

Abstract-- **A high-resolution-oncologic-transformable PET (HOTPET) is currently under development. The detector ring of the camera consists of 12 detector modules. Because the High-Yield-Pile-Up-Event-Recovery (HYPER) front-end electronics is applied in this new generation PET camera, a low dead-time coincidence circuitry is needed to take advantage of the efficiency improvement from this new technology. The coincidence matching of events coming from different detector modules is performed by an AND-logic on the arriving edges of the module output timing-pulses. A flexible modular architecture has been adopted to facilitate the use of the coincidence circuitry for different detector module configurations as well as different electronic and mechanical implementation. The application of backplane/plug-in architecture and programmable devices (EPLD/FPGA) and DSP (Digital Signal Processor) provide enough reprogrammable flexibility and expandability, ranging from animal and breast PET to whole-body PET. There are 42 possible pair combinations of modules derived from maximum 12 detector modules in coincidence with 7 opposite modules. Both the total (true + accidental) and accidental coincidences are simultaneously collected in real time; the accidental timing shift is ≥200ns relative to true events. The timing-gate window for the coincidence AND-logic can be dynamically digitally adjusted during data acquisition between 6.5-16ns to optimize signal/noise in the data. The prototype circuit showed that the timing accuracy is far better than 0.5 ns and the coincidence dead-time is less than 21ns.**

I. Introduction

The detection of coincident events is the core of a PET camera. In recent PET development, the popular implementation of coincidence detection [1, 2, 3] is to use the digitized timing-mark (or timing-code) of the arrival of each gamma event. By comparing the timing-marks of the events from the pairs of the detector groups whose lines-of-response (LOR) span the tomograph field-of-view (FOV), the coincidence can be picked up from the sea of the single events. This kind of method has some advantages such as (1) good reliability, (2) less sensitive to noises. On the other hand, it also has some drawbacks such as (1) relatively lower timing resolution because the timing-mark usually comes from a system main clock, (2) more bits of data needed to transfer so that more complex front-end electronics and more connectors are required.

In our HOTPET [4, 5], we chose Pulse-AND logic as coincidence-realizing method because of its simplicity. By adopting a modular backplane/plug-in architecture and using modern programmable EPLD/FPGA devices and DSP (Digital Signal Processor), the coincidence circuitry is flexible and reprogrammable so it can be used for different detector configurations to construct PET cameras for different purposes without redesigning the hardware.

II. System Design

A. Overall Description

As shown in Fig.1, 2, the coincidence system is designed to be expandable/reprogrammable to cover from 2 to 12 detector modules. The backplane/plug-in architecture facilitates the tailoring of this system for different size cameras ranging from animal and breast PET to whole-body PET. For handling up to 12 detectors, there are 7 slots on the coincidence backplane to accommodate 6 data buffer plug-in modules and 1 DSP embedded controller. Each data buffer handles data from two detector modules.

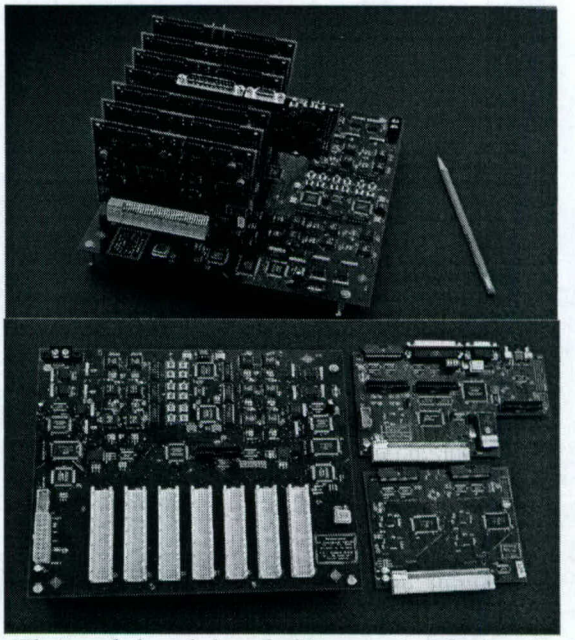

Fig.1Photos of the whole coincidence system (top) and its comprising boards (bottom). In bottom photo, coincidence backplane (left), DSP controller (right top), gamma-event FIFO buffer board (right bottom).

Manuscript received November , 2002. This work was supported in part by the NIH ROI CA58980, NIH Grant ROI CA61880, NIH Grant ROI CA76246, NIH Grant ROI CA58980S1, Texas Higher Education Advanced Technology Grant, the J.S. Dunn Research Foundation, and by the Cobb Endowment for Cancer Research.

Yu Wang, Hongdi Li, Yaqiang Liu, and Tao Xing, Jorge Uribe, Hossain Baghaei, Rocio Farrell, Wai-Hoi Wong are with University of Texas, M.D. Anderson Cancer Center, Houston, TX 77030 USA (Y. Wang's telephone:713-745-1671, e-mail:wangy_km@yahoo.com)

0-7803-7636-6/03/$17.00 ©2003 IEEE.

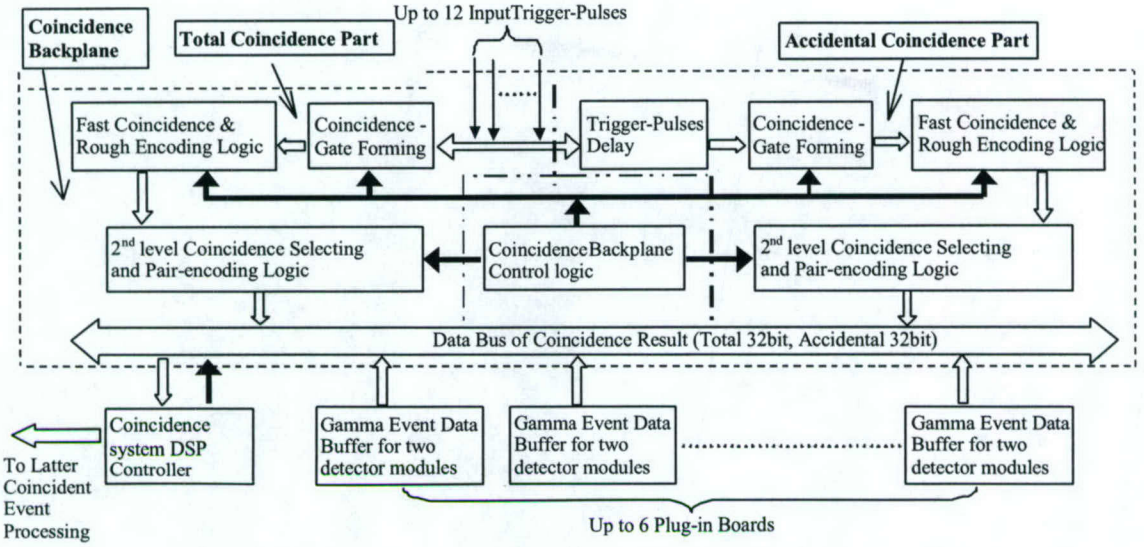

Fig.2 Block diagram of the Modular Low Dead-time Coincidence System

B. Coincidence Logic Circuitry Backplane

The coincidence-logic circuitry is on the backplane board. Up to 12 trigger pulses from the front-end electronics [6] of the detector modules enter the backplane through co-axial cables. The rising edges of the trigger pulses represent the arrival of the gamma events. There are 42 module-pair combinations derived from each of the 12 detector modules looking for coincidence with 7 opposite modules. The events picked from the coincidence of the prompt trigger pulses are regarded as total (true + accidental) coincident events. Meanwhile, as shown in Fig.3 each trigger pulse is delayed with a ≥200ns timing shift to any of the other pulses. The events picked from the delayed pulses are regarded as accidental coincident events. All of the delaying shifters are realized in 2 FPGA chips from Altera Inc. As a result, the logic circuits for both total and accidental coincidences are identical that simplifies the design and the implementation. Moreover, performing the data delay and timing pulse delay within the coincidence system reduces the number of cables (both coaxial and flat ribbon cables) connecting the detector modules to the coincidence system and makes the design of the front-end electronics output simpler. The reduction in the number of cables has an appreciable advantage for simplifying the gantry assembly, especially for rotating gantry.

By using the digitally configurable delay-lines, the coincidence windows can be easily changed on-the-fly to optimize for better signal/noise ratio in different countrate environment, for example, when scanning different parts of a body during a whole-body scan.

Because the High-Yield-Pile-Up-Event-Recovery (HYPER) [5] front-end electronics is applied in this new PET camera, low dead-time is a necessary feature of the coincidence circuitry to take advantage of the efficiency improvement. To reduce the coincidence dead-time as much as possible, 2-level coincidence detecting and selecting logic structure has been adopted. As Fig.4 depicts, the first level is performed in a fast EPLD for the fast coincidence detection. This level basically is an AND-logic array which detects 42 probabilities of coincidences and encodes the detected coincidences roughly and rapidly, then writes the rough coincidence code into a FIFO for further selecting and encoding. As long as the AND-logic detects a coincidence, it will generate a FIFO write signal to push the rough coincidence code and the data from all of the detector modules into the respectively corresponding FIFOs at the same moment no matter that some detector modules may not have valid data outputs. The second level discriminating logic then distinguishes and accepts the valid data while rejecting the invalid data.

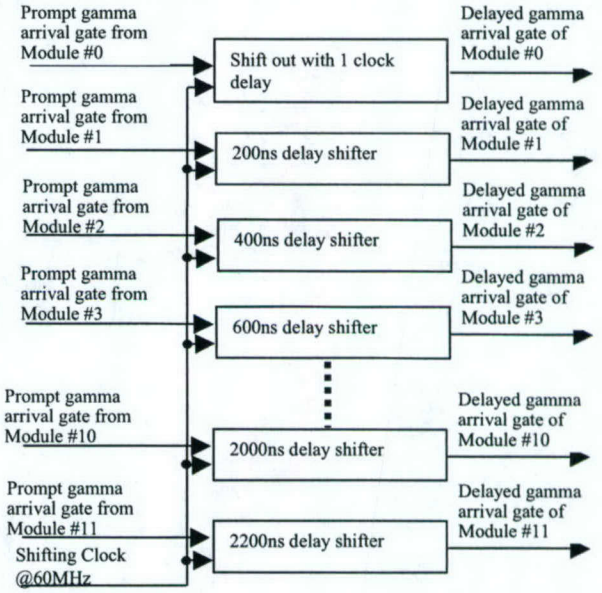

Fig.3 Diagram of trigger shifting delay for accidental coincidences

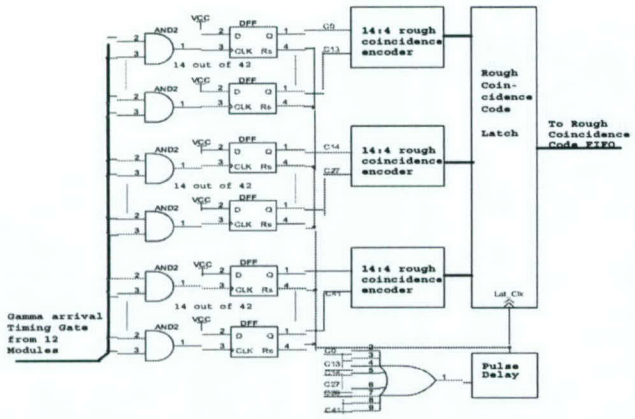

Fig.4 Diagram of the first level rapid coincidence logic

Being driven by a 40MHz clock, the second level discriminating logic reads the rough coincidence code from the rough-coincidence-code FIFO and selects valid coincidences and then combines the data of 2 coincident gamma events into a 64bit coincidence data. The logic monitors the Almost-Full and Almost-Empty flags of the rough-coincidence-code FIFO and performs selecting operations after an Almost-Full flag is detected. There are 4 phases to accomplish a selection, Fig.5. In phase I, at the rising edge of the clock, a read pulse is sent to the rough-coincidence-code FIFO. A logic decodes the data fetched from the FIFO to check if there is a valid coincidence. If there is a valid coincidence, the logic will prepare the output-enable signals for the corresponding data-buffer FIFOs. If there is no valid coincidence, the output-enable signals will be kept invalid. Phase II, at the rising edge of the clock, a read pulse is sent to all data buffer FIFOs to pop out the data written by the write signal of the rough-coincidence-code FIFO; Phase III and IV, if a valid coincidence has been found in Phase I, the output enable signals will allow the corresponding data FIFOs to place their data on the coincidence-result bus sequentially and the write signal of coincidence-result FIFO will be generated once in each phase to store the 64bit coincidence-result data. If no valid coincidence has been found in Phase I, neither output enable signals nor the coincidence result FIFO write signal will be asserted. The performance continues until an Almost-Empty flag is detected. Accordingly, the system can sustain 10M events per second throughput.

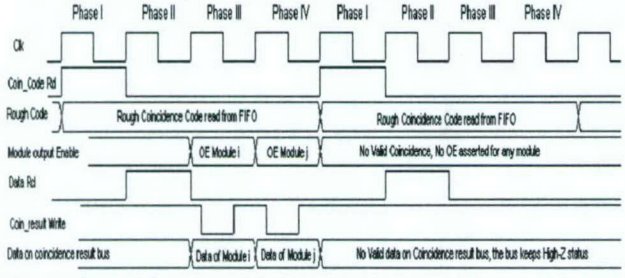

Fig. 5 Timing diagram of the second level coincidence processing logic (module number $i<j$, $i, j \in 1,\ldots,12$)

Because many FIFOs are used to buffer the rough coincidence code and gamma-event data, a FIFO-output order mismatch will lead to unrecoverable coincidence mis-registration. To avoid the occurrence of this kind of detrimental mishap, an order-checking mechanism is designed and implemented by pushing a toggling bit into all of the FIFOs. The toggling bit changes its status when there is a rough coincidence output from the first level AND-logic. There is a dedicated logic circuitry locating on the DSP controller board monitoring the output of the toggling bit from the gamma-event FIFOs and the rough-coincidence-code FIFO. If a status mismatch is detected, the monitoring logic will assert an interrupt request to the DSP then the DSP will reset and reinitialize the whole coincidence system to stop generating mis-registration data.

The multiple coincident events are rejected from both the total and the accidental coincidences because the coincident events chosen from multiple coincidences will degrade the signal-noise ratio rather than improve it although the countrate may increase.

C. Gamma-event data FIFO buffer

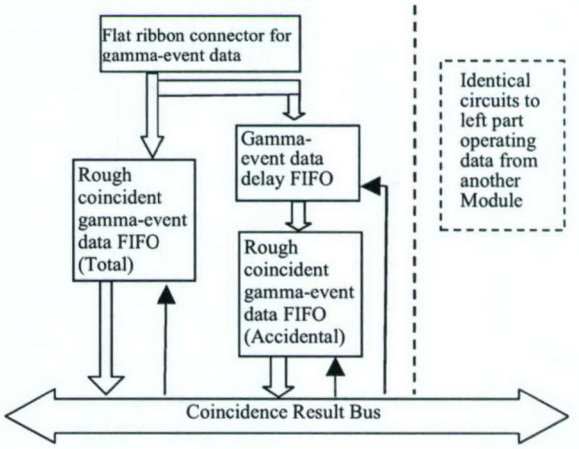

Fig. 6 Diagram of Gamma-event data FIFO buffer

Due to the 2-level coincidence-discriminating structure, the fast coincidence data FIFO buffers are needed to match the speed of the low dead-time first level coincidence detection logic. The position and energy information of a detected gamma-event are digitized and converted into a 32bit data from the front-end electronics. The data from all detector modules are fed into the data buffer plug-in modules through flat ribbon cables. Each buffer module receives the data from 2 detector modules. As mentioned above, once the first level coincidence circuit detects a rough coincidence, all prompt gamma-event data will be written into FIFOs synchronously. After the second level coincidence-selecting logic makes a final selection, the buffered data from the selected pair of detector modules will be sent to the coincidence-result bus on the backplane by means of only asserting the output-enable signals to the FIFOs which have the data of a valid coincidence. Then, these data will be pushed into the coincidence-result FIFO buffer on the DSP controller board.

Since the accidental coincidence detection is based on digital timing-shift-delay method, the gamma-event data must be delayed to match their delayed trigger pulses. The data delay is implemented by adding an extra FIFO before the rough-coincident-gamma-event-data FIFO, writing the data into the FIFO with prompt trigger pulse and reading it

out with delayed trigger pulse. Then, the accidental data FIFOs perform similar operation as the total coincidence data FIFOs.

D. DSP based System Controller

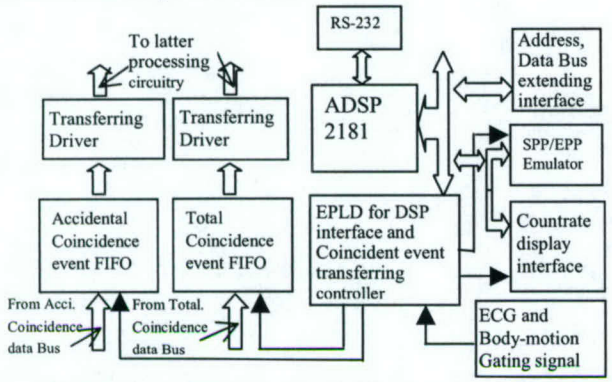

Fig.7 Diagram of DSP based coincidence system controller

The DSP controller resides in the middle slot of the 7-slot interface and has its own interface to the coincidence backplane to extend the control to the backplane. The 2 major tasks of this controller are (1) buffering the coincident result (as mentioned before) and interfacing to the latter processing circuitry which could be a crystal look-up board or an interface to a data acquisition computer, (2) controlling the coincidence system and potentially controlling the front-end electronics. It also has features such as: (1) communication with a host computer via RS-232, (2) counting and displaying the coincidence countrate and the single countrate of each detector module in real-time, and (3) monitoring and tracking electrocardiograph (ECG) signal or lung motion signal for cardiac and respiratory gating.

A custom made real-time monitor program running inside the ADSP2181 (40Mhz clock DSP) carries out all the control tasks. Some basic OS alike functions are also available within the real-time monitor such as loading a piece of program to the DSP, starting an execution of a program, loading the contents of a segment of memory from the DSP. These functions can facilitate some future functional development without the need to modify monitor and to burn it into an EPROM before finalization of the code.

A Labview based function library has also been developed to support the integration of the coincidence system to a host PC.

III. Results of Test

A. Coincidence timing-uncertainty test

The timing-uncertainty is very important to a coincidence system. To test it, we used the method illustrated in Fig.8. Three representative coincidence (timing overlap) cases were studied by using a variable delay to achieve the desirable timing overlap. Case 1, as illustrated in Fig.8, the overlap between the pulse and its delayed counterpart was bigger than the timing-uncertainty, the AND-logic always gave out an output pulse. Case 2, the overlap between the pulse and its delayed counterpart was smaller than the timing uncertainty, the AND-logic gave out an output pulse only when the time-jitter made an overlap between the pulse and its delayed counterpart. Case 3, the overlap between the pulse and its delayed counterpart had no overlap anyway, the AND-logic gave out no output pulse. By counting the coincidences between a pulse and its delayed counterpart within a specific timing window, we can measure coincidence countrate as a function of delay. Within the coincidence countrate vs delay graph, Fig. 9, 0.5ns timing-uncertainty is represented by the edge where the coincidence countrate drops from maximum to zero. However, since the timing-uncertainty measured in Fig.9 was limited by the minimum delay step (0.5ns) of our delay box (EGG DB463), we could not approach more accurate result. Therefore, the coincidence timing-uncertainty induced by the coincidence system was expected to be far less than 0.5ns.

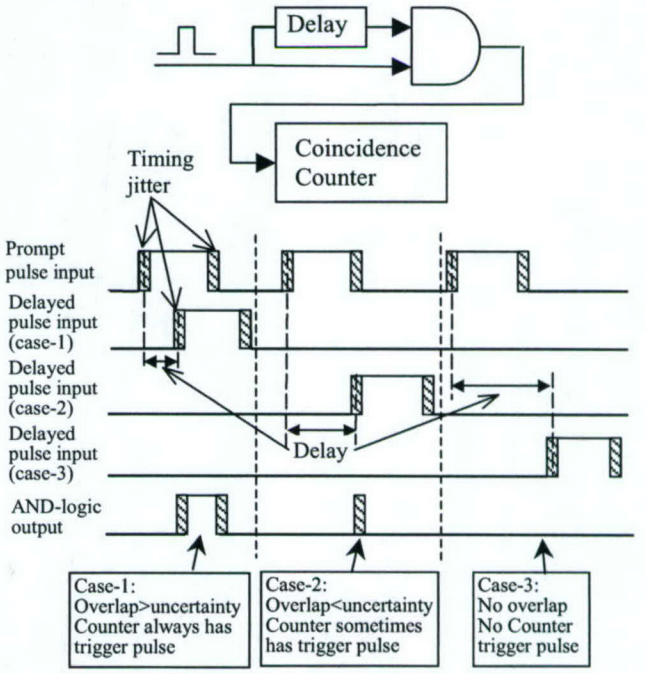

Fig.8 Diagram of the coincidence timing-uncertainty testing method

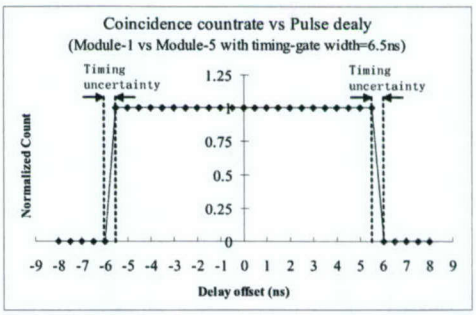

Fig.9 Typical coincidence countrate and pulse delay relationship between two modules

B. Coincidence circuitry dead-time test

Encoding a coincident event takes some time. Before an encoding process is finished, the first level coincidence detecting and encoding logic must be paralyzed to guarantee that the correct module-pair information is determined and recorded. The paralyzation causes a short period of dead-time.

We tested the dead-time of the coincidence system and found that the dead-time was about 21ns. The testing method is shown in Fig.10. Two pulse generators fed pulses to the coincidence system simulating trigger signals from front-end electronics. Each generator provided pulses to 2 module inputs which were considered within the domain of coincidence combinations. Correspondingly, there were 2 coincidences occurring independently at the respective rates of the 2 generators. We can record the input pulse rate of each generator and the output rate of the coincidence logic on the countrate monitor of the system. The dead-time of circuit was calculated using equation (1) [7]. Table 1 shows the test result.

$$\tau_{dead} = \frac{f_1 + f_2 - f_{coin}}{2 f_1 f_2} \quad (1)$$

where, τ_{dead} is the dead-time of coincidence circuit, f_1 and f_2 are the input rates of the generators, f_{coin} is the output rate of the coincidence system.

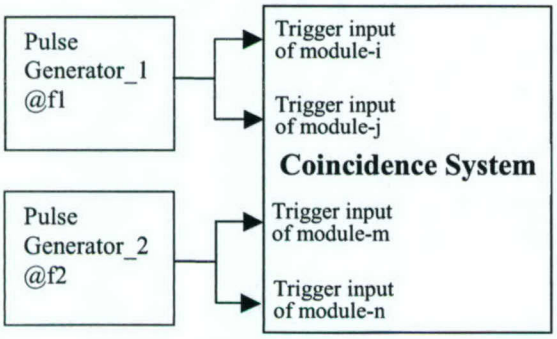

Fig. 10 Diagram of the coincidence dead-time testing method

IV. Conclusion and Discussion

In this paper, we present a modular, low dead-time coincidence system for modular PET cameras. The system is based on a fast coincidence discriminating structure consisting of a first level rapid AND-logic and a clock driving second level fine-selection logic. A modular backplane/plug-in architecture which we've adopted supports different detector module configurations as well as different electronic and mechanical implementation.

The coincidence system functionally works well up to 10 million coincident events per second (with periodic testing pulses). The gate width for AND-logic is on-line changeable from 6.5ns to 16ns and has better than 0.5ns adjusting accuracy. The coincidence timing-uncertainty is far less than 0.5ns. The dead-time of coincidence logic is around 21ns that is significantly smaller than conventional designs.

Table 1 Coincidence Dead-time test result

Test-module combination	Generator_1 input rate (f_1) kHz	Generator_2 input rate (f_2) kHz	Coincidence output rate (f_{coin}) kHz	Dead-time (τ_{dead}) ns
Modules (1.4.7.10)	190.3	1303	1483	20.8
	4698	4658	8440	20.9
Modules (2.5.8.11)	721.7	788.8	1487	20.6
	4593	4442	8181	20.9
Modules (3.6.9.12)	1656	1310	2877	20.5
	4787	4066	8038	20.9
Average Dead-time of all modules				20.8

The test results satisfy our design specification. However, improvement will be pursued. The first improvement would be to minimize timing gate window from current 6.5ns because a large timing gate limits the coincidence timing resolution. For a PET camera with BGO, like our HOTPET, the relatively wide timing gate is good enough. However, for the systems with faster scintillator, such as LSO or GSO, the 6.5ns gate may not be suitable. Though the improvement might make the circuit a little more complex, we believe a narrower timing gate can be accomplished.

V. References

[1] H.M. Dent, et al, " A Real Time Digital Coincidence Processor for Positron Emission Tomography", *IEEE Transaction on Nuclear Science, vol. 33, pp 556-559, February 1986.*

[2] D.F. Newport, et al, "Coincidence Detection and Selection in Positron Emission Tomography Using VLSI", *IEEE Transaction on Nuclear Science, vol. 36, pp.1052-1055, February 1989.*

[3] J.W. Young, et al, "Optimum Bandwidth Usage in Digital Coincidence Detection for PET", *Conference Record of the 1993 IEEE MIC Conference, Vol. 2, pp 1205-1208.*

[4] W.H. Wong, et al, "Feasibility of a High Speed Gamma Camera Using the High-Yield-Pile-Up-Event-Recovery (HYPER) Method", *J. Nucl. Med., 42(4), pp 624-632.*

[5] W-H. Wong, et al., "The Design of a High Resolution Transformable Whole body PET camera". *IEEE Transactions on Nuclear Science, 49(5): October, 2002 and. IEEE MIC Conference Record 2001.*

[6] H. Li, et al, "Front-end electronics Based on High-yield-pileup-event-recovery Method for a High Resolution PET Camera with PMT-quadrant-sharing Detector Modules", *IEEE MIC Conference Record 2001.*

[7] Glenn F. Knoll, Radiation Detection and Measurement (the third edition), John Wiley and Sons, 2000.

Signal Characteristics of Individual Crystals in a High Resolution BGO Detector Design Using PMT-Quadrant Sharing

Jorge Uribe, *Member, IEEE* ., Hongdi Li, *Member, IEEE.*, Yaqiang Liu, Tao Xing, Hossain Baghaei, *Member, IEEE.*, Yu Wang, *Member, IEEE.*, Rossio Farrell, Wai-Hoi Wong, *Member, IEEE.*

Department of Nuclear Medicine, University of Texas M.D. Anderson Cancer Center, Houston, Texas 77030

Abstract—**The PMT-quadrant sharing (PQS) detector design allows very high resolution detectors to be achieved with 70% fewer PMT and cost. A common concern for the design is that there is a big gap (photo-insensitive area) between 4 circular PMT, and the photoelectron signal (pulse height) may be much lower for the central crystals. The pulse heights and energy resolution for each crystal in 3 different types of PQS blocks for 19 mm PMT have been measured. For a regular square 7 x 7 block (2.66 x 2.66 x 18 mm BGO): the maximum photopeak signals occurred at the corner crystal of the block. The signals for the worst central-5 crystals (sitting on space with no PMT connection) was found to have pulse heights of 0.87 that of the corner crystals. The 12 crystals (outside the central-5) coupling only to the glass wall but not photocathode had a relative pulse height of 0.92. The 8 crystals with partial exposure to photocathodes had 0.94. The energy resolution for individual crystal was found to be 22-30% with an average of 26%. Asymmetric photopeaks, especially for the corner crystals, were observed, which was found to be from the depth-of-interaction effect. In the latest PQS design, extended blocks with asymmetric light distributions were used on the 4 edges and 4 corners of a large detector module so that the previously unused (wasted) half-row of peripheral PMT are now covered by crystals. An asymmetric blocks, single-extended (7 x 8 blocks) was also tested. The pulse-height ratio between the worst and best group of crystals in the single-extended block was found to be 0.72 and that of the double extended block was also found to be 0.72. In a more demanding, higher spatial resolution 8 x 8 array (2.3 x 2.3 x 10 mm BGO) for mouse PET with shallower crystals, the pulse-height ratio was 0.73 with an average energy resolution of 20%. This study demonstrated that pulse height uniformity for the PQS design using circular PMT was excellent, which is better than the typical 4/1 pulse-height ratio in conventional block detectors.**

Manuscript received Nov 5, 2001. This work was supported in part by NIH Grant RO1 CA58980, NIH Grant RO1 CA61880, NIH Grant RO1 CA76246, NIH Grant RO1 CA58980S1, US Army Breast Cancer Grant, Texas Higher Education Grant, John S. Dunn Foundation Research Grant, Cobb Foundation for Cancer Research

Jorge Uribe, Wai-Hoi Wong, Hongdi Li, Hossain Baghaei, Yu Wang, Yaqiang Liu, Tao Xing and Rossio Farrell are with the University of Texas M.D. Anderson Cancer Center, Box 217, 1100 Holcombe Blvd., Houston, Texas 77030, USA.

(Contact person: Jorge Uribe (e-mail: juribe@di.mdacc.tmc.edu)

I. Introduction

The PMT-quadrant sharing (PQS) detector design [1-2] allows very high resolution detectors to be achieved with 70% fewer PMT, front-end electronic channels and cost. This design has been used by us to build very high resolution PET cameras and adopted by Siemens/CTI for its next generation LSO PET cameras. A common concern for the design is when 4 circular PMTs are used to further reduce cost. The circular PMTs leave a big gap (photo-insensitive area) between 4 PMTs. The dead-space issue is especially challenging with smaller diameter PMT (D < 20 mm) as the glass wall cannot be made proportionally thinner, which aggravates the dead-space problem. Furthermore, since the glass bottles of PMTs do not have high mechanical precision, a small amount of tolerance space between PMTs has to be built into the design (e.g. 0.5-1 mm), which further expands the dead-space. The dead space would imply that the photoelectron signal pulse heights may be much lower for the central crystals (of the crystal array) that sit on the dead space, thereby degrading imaging resolution and energy resolution. This study evaluated the detail signal characteristics of PQS block detectors with respect to the large dead-space issues. The pulse heights and energy resolution for each of the 169 crystals in 3 different types of PQS blocks based on 19 mm round PMT were measured and studied.

II. Methods

The experiments were performed with randomly chosen blocks among our stock of second generation PQS BGO detector blocks. These blocks had painted interfaces between discrete crystals for distributing scintillation light, and the discrete crystals were optically glued together. The sizes and shapes of the painted areas were determined by the desired levels and directions of light distribution from each crystal. Three types of PQS block designs based on 19 mm round PMT were studied:

7 x 7 square block (each crystal is 2.66 x 2.66 x 18 mm)
8 x 8 square block (each crystal is 2.3 x 2.3 x 10 mm)
7 x 8 elongated asymmetric block (2.6 x 3.1 x 18 mm)

0-7803-7636-6/03/$17.00 ©2003 IEEE.

The in-house developed front-end electronics of our prototype PET camera were used to acquire the data. This in-house electronics employed the pileup-restoration technique developed by us recently [3]. Four Photonis XP1911 PMT were used for the 19 mm circular PMT. The PMT high voltage was fixed at 1450 V providing about 10^6 anode amplification gains. The gains of all four PMT were equalized with their respective voltage-control variable-gain fast amplifiers by two different methods: (a) using just the crystal sitting at the center each PMT and (b) using a region of 3x3 crystals corresponding to the relevant quadrant of the PMT. For the four PMT used, both methods of equalization were within 5% of each other. Hence, the center-crystal equalization method was used for all the studies.

The in-house developed electronics [3] were interfaced to a PC computer. The data-acquisition software controlling the data acquisition electronics and analysis software for this study were also developed in-house for the PC computer platform. The in-house hardware and software have been compared and validated against a commercial NIM multi-parameter data-acquisition system (FAST from Com Tec) by comparing both the pulse-height spectra and crystal decoding map. The in-house system provides a higher data acquisition speed and some custom-designed analysis capability such as keeping the signal pulse-height spectrum for each pixel in the crystal decoding map.

For each crystal block/array, the composite (total sum) pulse-height of all the crystals in the block was first measured with a distal point source. This composite pulse height measurement provided a first-pass energy-acceptance threshold for the whole array. The crystal position-decoding map as shown in fig.1 was acquired with this first-pass energy threshold. This first-pass crystal-decoding map was then used to draw a region-of-interest map for each crystal in the array. The signal-pulse-height spectrum for each crystal region was analyzed and presented in the next Result section.
From these results, the best energy-acceptance threshold for each crystal region-of-interest (ROI) was also determined; an energy–threshold lookup table for each crystal ROI in the crystal decoding map was created for each detector array tested. A second-pass data acquisition was then performed for each detector array to obtain a crystal decoding map with individualized crystal-energy-thresholds. The results are presented in the next section.

III. Results

The second generation PQS BGO position-sensitive array has a much better production method that mated all the crystals together with a minuscule gap of only 0.05-0.06mm providing very high packing fraction, fig.1. There was a white-paint window between crystals for controlling the distribution of light and the crystal were optically glued together as a solid block. The painted windows allowed any shape and size to be painted thereby enabling optimal crystal decoding and the minimization of barrel or pincushion distortion in the decoding map. One such crystal block (7 x 7 array, 2.66 x 2.66 x 18 mm BGO coupled to 19 mm round PMT) is shown in fig.1 with its raw position-decoding map.

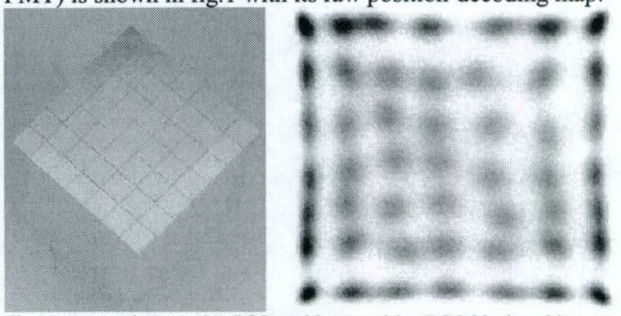

Fig.1. A second-generation PQS position-sensitive BGO block and its raw crystal-decoding map without distortion correction and with only one energy acceptance threshold for the whole block.

IIIa 7x7 array, 2.66 x 2.66 x 18 mm with 19mm round PMT

For this 7 x 7 block, the maximum photopeak signals occurred near the corner of the block as expected, while the signals for the worst central-9 crystals (sitting on space with no photocathode coupling) were found to have the lowest pulse heights. The ratio between the lowest pulse height to the highest was found to be,

(raw Min) / (raw Max) = 0.78

Hence, the most worst crystal has 22% lower pulse height than the best crystal in the block. The raw pulse-height spectra of the worst (center crystal) and best crystal (near the corner) are shown in fig.2.

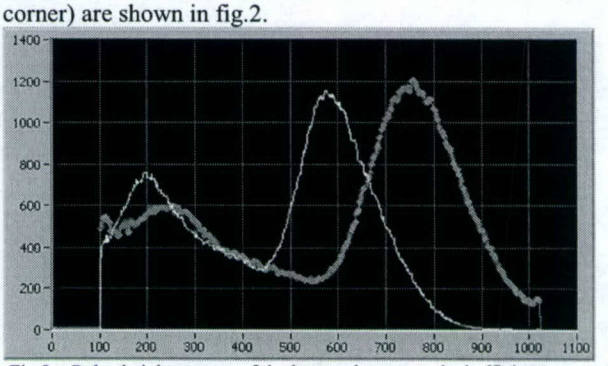

Fig.2. Pulse-height spectra of the best and worst optical efficiency crystals

However, this raw ratio included the influence of all the regional non-uniformity of each PMT photocathode and the anisotropic orientation effect of each PMT. To minimize such spatial PMT influences, crystals with the same rotational symmetry, the same up-down and left-right symmetries (relative to the center of the block) were averaged. After the symmetric averaging, the ratio between the lowest pulse height and the highest pulse height was found to be,

(symmetry-restored Min) / (symmetry-restored Max) = 0.81

This ratio may be a better measure of the geometrical optical efficiency difference between the worst crystal and the best crystal in a PQS block design as the individual PMT variations and photocathode differences have been

minimized. Hence, for the 7x7 BGO PQS array, the center crystal (most disadvantageous with no direct coupling to any PMT) had an optical efficiency 19% lower than that of a crystal that is advantageously directly coupled to the middle of a PMT, the most sensitive part of a PMT.

The pulse-height distribution of the upper 4-rows of crystals is shown in fig.3 for the raw signal and fig. 4 after the above symmetry averaging.

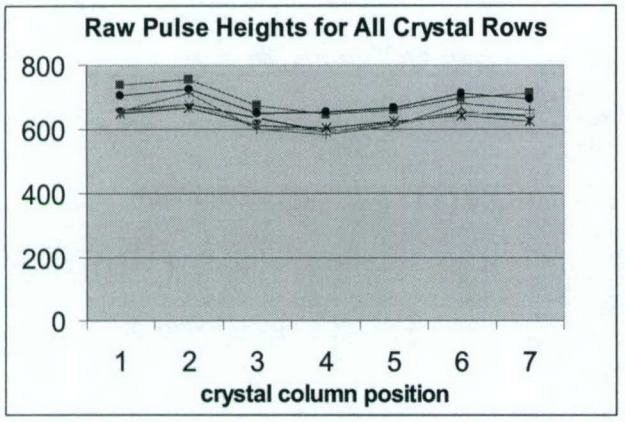

Fig.3. The raw crystal pulse-heights for all 7 rows of crystals

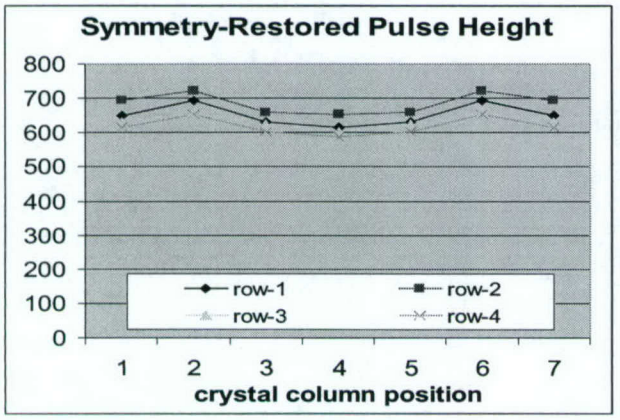

Fig.4. The symmetry-restored pulse-heights for the first 4 crystal rows

The average pulse height was highest for the second row of crystal although the first row of crystals was at the center of the PMT. This is due to the fact that the first and last row of crystals are almost totally (95%) optically isolated from the rest of the block; hence all the scintillation light had to travel down the long and narrow crystal 2.66 x 18 mm to be detected, thereby losing some light. This phenomenon was due to the very high spatial resolution of the block.

To categorize the crystal pulse height, the crystals are grouped into four types:

Type-1: the crystals on the photocathode central region
Type-2: the crystals on the photocathode edge and sidewall
Type-3: the crystals only coupled to the glass side wall
Type-4: the crystals with no PMT connection (5 crystals)

The types and their optical efficiencies are shown in fig.5.

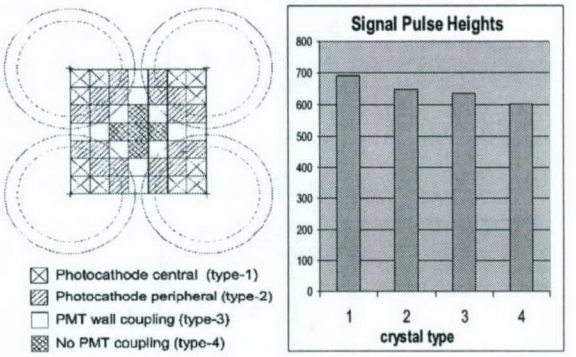

Fig.5. The crystal-position types and their optical efficiencies

The optical efficiency ratio between the least efficient type and best type is 0.87. Hence, as a group the central 5 crystals that were just hanging in space without any optical coupling to a PMT was found to lose only 13% of the light compared to the ideal group (type-1).

The measured energy-resolution distribution is shown in fig.6, after the symmetry restoration discussed earlier.

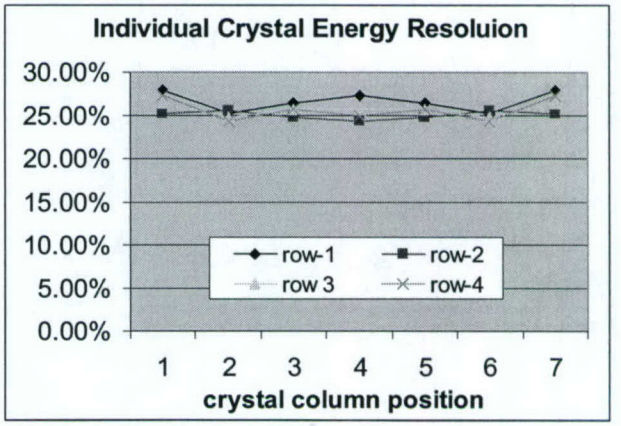

Fig. 6. The symmetry-restored energy resolution distribution

The average energy resolution including all the crystal was found to be 25.6 %.

The average energy resolution was also measured in a different way. The photopeaks of all the crystals were normalized to the same standard pulse height, with the normalization weighted by the counting sensitivity (counts in its ROI) of that crystal. The normalized or equalized pulse-height spectra for all the crystals were summed and the energy resolution for the normalized-sum spectrum was calculated. This "normalized-sum" energy resolution was found to agree with that of the first method.

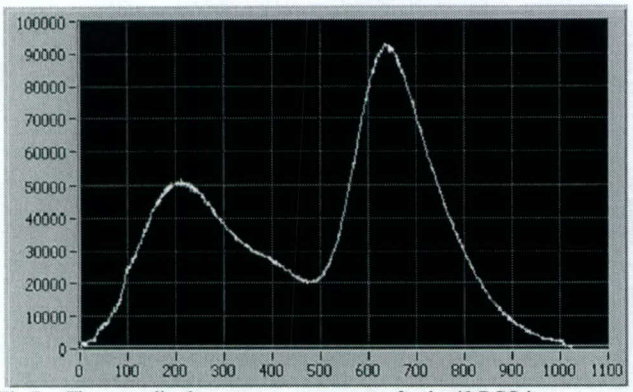

Fig.7. The normalized-array-average spectrum for the 49 BGO in array

In the normalized-sum spectrum for the whole array (fig.7), an asymmetry in the photopeak can be observed. We determined that it was due to the variation of light output with the depth of interaction. By collimating the beam toward the first 1/3 and the last 1/3 of the crystal depth on the last row of crystals in the array, 2 different photopeak pulse heights were observed. Because of the high stopping power of BGO, most of the interaction occurred at the front-end of the crystal (farther away from the PMT); this gave rise to the lower overall pulse-height. But some interactions occurred near the back-end (the PMT end) thereby yielding a higher pulse height than the average peak energy.

The normalized-sum spectrum of the whole array (fig. 7) was also used to calculate the average photo-fraction of the small BGO crystals (2.66 x 2.66 x 18 mm) in the array:

Average detection photofraction = 70%

IIIb 8x8 array, 2.3 x 2.3 x 10 mm with 19mm round PMT

This crystal and block geometry can be used for building less expensive mouse-PET system since its crystal dimension is quite close to that of the MicroPET (2.2 x 2.2 mm pitch and 10 mm deep) and it uses the large low-cost 19 mm PMT instead of the more expensive position-sensitive PMT. For this 8 x 8 block, the ratio between the lowest pulse height to the highest was found to be,

(raw Min) / (raw Max) = 0.67

Hence, the worst crystal has 33% lower pulse height than the best crystal in the block. As discussed earlier, to minimize the PMT regional gain variation and anisotropy, crystals with the same rotational, up-down and left-right symmetries (relative to the center of the block) were averaged, and the symmetry-restored min/max was:

(symmetry-restored Min) / (symmetry-restored Max) = 0.72

Hence, for the 8x8 BGO PQS array, the central crystal (most disadvantageous with no direct coupling to any PMT) had an optical efficiency 28% lower than that of a crystal that is advantageously directly coupled to the middle of a PMT. This is not as good as the 19% measured for the 7x7 array.

The pulse-height distribution of the upper 4-rows of crystals is shown in fig.8 for the raw signal and fig.9 after the above symmetry averaging.

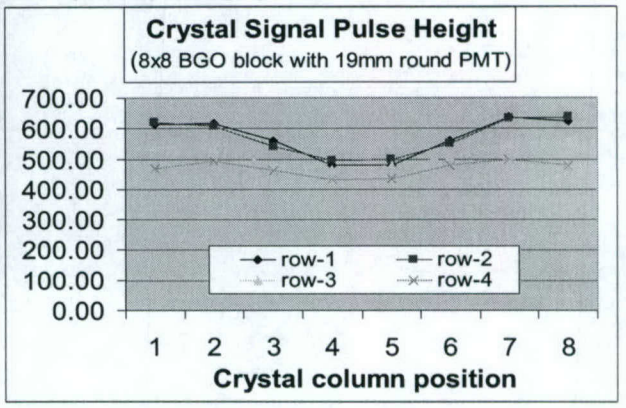

Fig. 8. Raw pulse-height distribution for 8x8 array with 19mm PMT

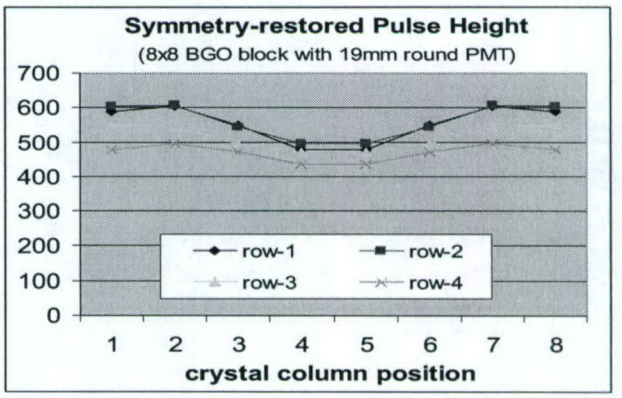

Fig. 9. Symmetry-restored pulse height distribution

As discussed earlier, the crystals are grouped into four types:

Type-1: the crystals on the photocathode central region
Type-2: the crystals on the photocathode edge and sidewall
Type-3: the crystals only coupled to the glass side wall
Type-4: the crystals with no PMT connection (5 crystals)

The types and their optical efficiencies are shown in fig.10.

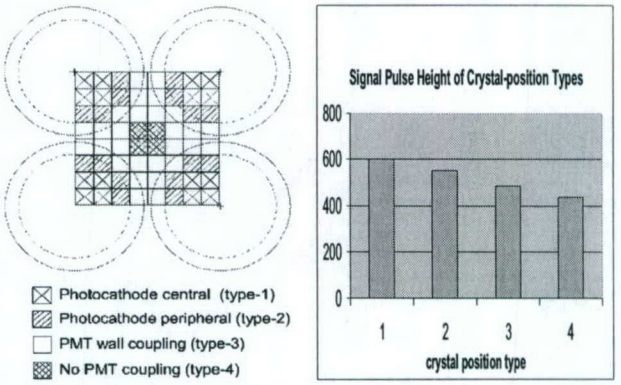

Fig.10. The crystal-position types and their optical efficiencies

The optical efficiency ratio between the least efficient type and best type is 0.73. Hence, as a group the central 4 crystals

that were just hanging in space without any optical coupling to a PMT was found to lose 27% of the light compared to the ideal group (type-1). This is worse than the 13% in the 7x7 array with the same PMT. It is, however, significantly better than the traditional block detectors used in current commercial PET cameras where the most optically efficient crystal has 4 times higher pulse height than the least efficient crystal [4]. Similar to the 7x7 case, there was some asymmetric photopeak shape. But because of the shorter crystals used in this array (10 mm), the asymmetry in the photopeak was smaller. The shorter array decreased the light-output variation as a function of the depth of interaction, even though the crystals here were also narrower (2.3 x 2.3 mm).

The measured energy-resolution distribution (symmetry restored) is shown in fig.11. The 4 abnormally large energy resolution in fig.11 had the asymmetric photopeaks due to the depth-of-interaction effect discussed earlier.

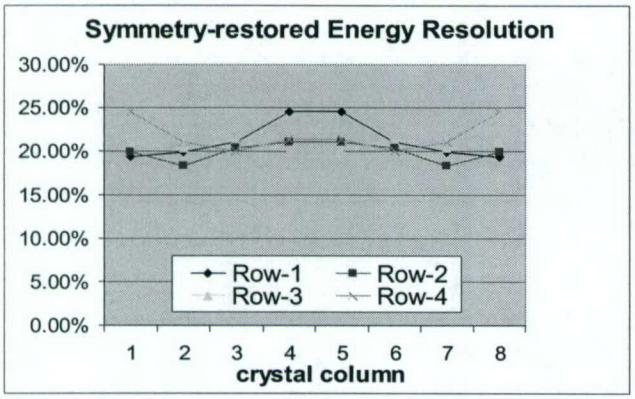

Fig. 11. Symmetry-restored energy resolution distribution

The average energy resolution including all the crystal was found to be 20.9 %. If only the regularly shaped photopeaks were used, the "screened" averaged energy resolution was found to be 20.4%. This energy resolution for this shallower block (10 mm) is better than the 25.6% for the deep crystals (18 mm) used in the 7x7 array, which may be due to higher light-output efficiency of the shallower block.

IIIc 7x8 elongated array, 2.66 x 3.1 x 18mm BGO

This is an elongated block to be used at the edge of a panel-detector module for extending the useful field of view to the edge of the last row of PMT. For this 7 x 8 block, the ratio of the pulse heights of the type-4 (worst) to type-1 (best) crystals was found to be,

(Type-4 pulse height) / (Type-1 pulse height) = 0.79

Hence, the worst crystal group has 21% lower pulse height than the crystals with the best geometry in the block. The symmetry-restored pulse-height distribution of its crystals is shown in fig.12.

The average energy resolution was for this 7x8 block was found to be 29%.

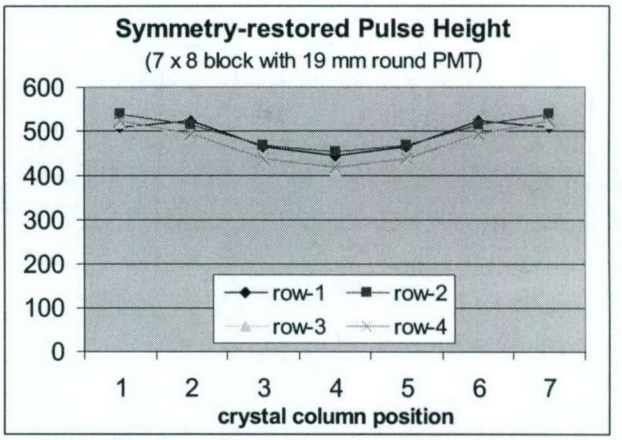

Fig. 12. Pulse-height distribution for the 7x8 array with198mm PMT

IV. Conclusion and Discussions

Detail signal characteristics for a very high resolution BGO detector design using the low cost quadrant-sharing (PQS) block decoding scheme with less expensive 19 mm round PMT has been studied. There are some disadvantages in this type and size of PMT: (a) the relatively large gap (photo-insensitive area) between 4 round PMTs, (b) the dead-space of the 1-mm glass wall, and (c) the 0.8-1.0 mm mechanical tolerance space between PMTs due to the lack of mechanical precision in glass bottles. These disadvantages compounded the dead photo-detection area in the detector. The dead space would imply that the photoelectron-signal pulse heights may be much lower for the crystals sitting on the dead space, thereby degrading imaging resolution and energy resolution. This study showed that, for the very high resolution BGO detectors using the second-generation PQS block design and production, the worst crystal positions had signal pulse heights that were only 13-27% lower than that of the best crystal group sitting on the middle of a PMT. The 7x7 block showed the most uniform light output (13%), while the 8x8 block was the worst (27%). These pulse-height uniformity results are better than the typical 4:1 difference in pulse heights in the conventional PET block-detector designs. The high optical uniformity of the design is advantageous in simplifying the fast front-end electronics since only one reasonable good energy discrimination level (one analog discriminator) would be needed for the entire detector module to get a good crystal decoding (fig.1).

V. References

[1] Wong W-H, Uribe J, Hicks K, Zambelli M, Hu G. A 2-dimensional detector decoding study on BGO array with quadrant-sharing photomultipliers. IEEE Transactions on Nuclear Science, 41(4), pp. 1453-1457, August 1994.

[2] W-H. Wong, S. Yokoyama, J. Uribe, et al, "An elongated position sensitive block detector design using the PMT quadrant sharing detector array," *IEEE Trans. Nucl. Sci.*, vol 46(3), pp. 542-545, 1999

[3] H. Li, W-H Wong, J. Uribe, et al, "A new pileup prevention front-end electronic design for high resolution PET and gamma cameras," *IEEE MIC Conference Record 2001.*

[4] M. P. Tornai, G. Germano, E. J. Hoffman, "Position and energy response of PET block detectors with different light sharing schemes," *IEEE Trans. Nucl. Sci.*, vol 41 (4), pp. 1458-1463, 1994

A Programmable High-resolution Ultra Fast Delay Generator

Yaqiang Liu, Hongdi Li, Yu Wang, Tao Xing, Hossain Baghaei, Jorge Uribe, Rocio Farrell, Wai-Hoi Wong

Abstract-- **This paper presents a high-resolution, small dead-time digital delay method where the performance is independent of the total delay time. We have implemented a small dead-time (50ns) and high-resolution (±0.9ns) delay generator with delay time up to hundreds of milliseconds. We have proposed a high-resolution whole-body PET with 12 module PMT-quadrant-sharing (PQS) detector design. This high-resolution delay unit is an important part in the new PET electronics where a high-yield-pileup-event-recovery (HYPER) method is used. Using HYPER method, the energy/position signals are generated or digitized at the arrival of the next event(arriving at a random time from present event) if the the present event was piled-up by the next event, so the energy/position signals are no longer synchronized with the leading edge of the trigggering signal. To detect a coincidence event by using the HYPER method, the original trigger signal has to be delayed by a fixed time (1.5μs for BGO) and a new synchronization process has to be setup between the delayed trigger and the energy/position signals before they can go to the coincidence detection electronics. Each HYPER processor needs one delay generator; there are 48 delay units inside the whole PET system. This high resolution delay generator also can be used in other PET systems where a delay is needed to synchronize the fast timing trigger to the slower integration or detector address outputs; this low timing-jitter delay can also be applied to automatic test equipment and communications.**

I. INTRODUCTION

WE have proposed a dynamic signal-integration approach called HYPER [1] to prevent signal pileup for the PET and gamma cameras. We have deployed the HYPER electronic processing to our modular high resolution PET system that is under construction. This PET system has 12 detector modules. Each module has 4 HYPER-Anger-positioning zones generating 48 modular electronic channels [2-3]. The HYPER method combined with multiple Anger-positioning zones can significantly increase the count-rate capability and dose efficiency of PET and gamma cameras. But for coincidence detection applications and other timing-detection applications such as positron-coincidence imaging, an additional trigger-delay technique has to be used. In traditional scintillation detector electronics, the signal integration time for each event is fixed. Hence, the end of integration and signal digitization time (for energy and position) are synchronized with the timing-trigger signal (except delayed by the fixed integration time). The trigger signal is generated at the leading edge of timing trigger pulse or the arrival time of the event. Coincidence detection can be performed between the end of digitization signals or the trigger signals. However, since HYPER uses a dynamic integrating method where the energy and position signals are digitized at the arrival of the next event (arriving at a random time from present event), the measured energy and position signals are no longer synchronized with the leading edge of the present triggering signal. To detect a coincidence event using the HYPER method, (a) the original trigger signal has to be delayed by a fixed time that is longer than the maximal possible integration and digitization time, and (b) the current energy/position digitized signal has to be re-synchronized to the delayed timing trigger with a new re-synchronization. After the delay and resynchronization, all the signals relating to the current event can then be passed to the coincidence-checking processor. Except for the fixed delay time, both the timing trigger and the energy/position signals would maintain the fast timing integrity of the event, if the delay circuit can maintain a negligible timing jitter. Hence, the coincidence timing resolution of the PET camera is hinged on the timing resolution (fidelity) of this delay circuit. This type of accurate delay is not necessary in one conventional coincidence-processing method[4] that finds the coincidence event-pairs by sorting (table lookup) the time-marks generated by latching a master-clock's time at the onset of an event. However, this type of "latching-sorting" design would be quite cumbersome for our system with 48 timing channels that will need 48 fast latches and ribbon cables with timing-skews corrected. Hence, we developed this high timing-fidelity delay circuit because of engineering requirement and practical necessity. This high resolution delay circuit can also be used in other coincidence electronics designs that use the "timing-AND-logic" concept employed by some commercial PET systems because such systems also require a long delay to synchronize the timing trigger and the energy/position signals.

This work was supported in part by NIH under Grant RO1 CA76246, RO1 CA61880 and RO1 CA58980, by Texas Higher Education Advanced Technology (ARP/ATP) Grant No. 003657-0058-2001, the J.S. Dunn Research Foundation, the Cobb Endowment for Cancer Research.

Yaqiang Liu, Hongdi Li, Yu Wang, Tao Xing, Hossain Baghaei, Jorge Uribe, Rocio Farrell and Wai-Hoi Wong are with the University of Texas M.D. Anderson Cancer Center, Houston, TX 77030 USA (Yaqiang Liu's telephone: 713-745-1671, e-mail: yaqiang_l@yahoo.com).

0-7803-7636-6/03/$17.00 ©2003 IEEE.

II. METHODS

A. Pre-coincidence synchronization of signals in the dynamic integrating approach.

As discussed earlier, the HYPER dynamic integration and correction method requires a timing delay and a re-synchronization between the timing trigger and the energy/position signal of the same events. The synchronization process works as follows. The energy and position signals of all events are first pipeline buffered into a FIFO (first-in-first-out) temporary memory, then a delayed trigger signal is used to read them out individually so that the sequential order of an event within the data stream can be maintained. Since the readout of the energy and position signals from the temporary-holding FIFO memory is time-latched by the delayed trigger and since the delayed trigger signal is synchronized with the trigger signal (except for the fixed delay-time shift), the energy and position signals are now synchronized to the trigger signal (figure 1).

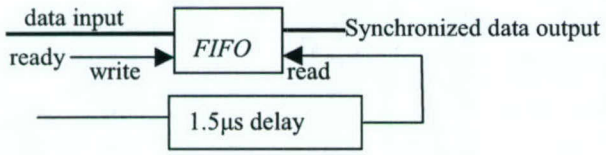

Figure 1: Circuit to restoring synchronization of HYPER signals before coincidence processing.

The fixed delay time should be longer than the maximum integration time. The trigger-delay circuit should have a good timing resolution and small dead time. Table-1 illustrates the processing of five continuous events by using FIFO and delay technique to restore the synchronization between the event-trigger signal and the data output signal (except for the fixed delay-time shift).

TABLE 1

Event number	1	2	3	4	5
Event arrived Time (us)	0	0.2	1.5	2.0	2.7
Event integration Sampling time = input time of event into FIFO (us)	0.2	1.2	2.0	2.7	*
Event readout time From FIFO (us)	1.5	1.7	3.0	3.5	4.2
Waiting (holding) Time of event in FIFO (us)	1.3	0.5	1.0	0.8	*

- Event integration-sampling time = next event's arrived time, if the current event is piled-up by the next event. If there is no pileup on the current event, it will be integrated for a fixed maximum time period of 1 microsecond.
- Waiting time is the time difference between the FIFO readout time and the event arrived time.
- * Means that the value is dependent on the next event arrived time (not illustrated in Table-1).

Hence, the order of the data in a FIFO is the same as the order of events coming in. We are using the linear structure of a FIFO to line up all the events in the order that they come in. Then we apply a large fixed delay (larger than the longest integration time) for the event-trigger, and use the delayed event trigger to "clock" the readout of events from the FIFO. Hence, each event in the FIFO is clocked out (readout) synchronously with the event triggering time (except for a fixed delay). It is the waiting (holding) time of an individual event in the FIFO (as controlled by the delayed trigger) that synchronizes the FIFO readout time to the original event-arriving time.

B. Delay Method

Figure 2 and 3 show the design and timing of the high-resolution pipeline delay unit. The design included three sections: a high-resolution time recorder, a major/coarse time-delay and a high-resolution trigger restoration.

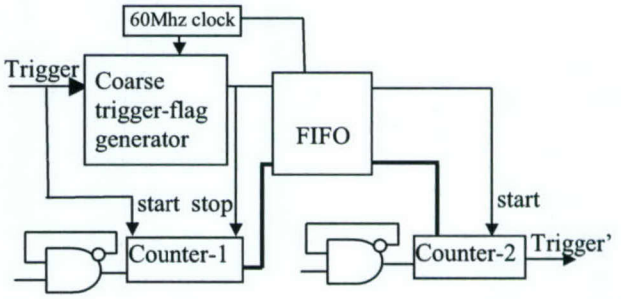

Figure 2: Diagram of the digital delay unit

Each input trigger signal is recorded by a main clock (60 MHz) generating a clock synchronized coarse trigger-flag signal. Meanwhile an ultra fast counter-1 (see figure 2), driven by a 700MHz burst oscillator-1, counts the time lapse between the original trigger and this coarse trigger-flag. The arrival-time of the trigger signal can be recorded very accurately by combining both coarse trigger-flag and the fast counter-1. Burst oscillator only works for a very short time in order to reduce the system noise level as well as the power dissipation. The main time-delay section is consisted of a synchronized FIFO memory. The coarse trigger-flag as well as the recorded number from the fast counter-1 will be put into the FIFO, which is driven by the same main clock to create the main time-delay. The FIFO has a pipeline structure and the length of the FIFO times the clock period determines the main time-delay. To restore the delayed trigger accurately, the delayed number of counter-1 readout from the FIFO will be reloaded into another ultra fast counter-2 (see figure 2) and the delayed trigger-flag output from the FIFO will start the

counter-2 clocked by burst oscillator-2. The high-resolution delay trigger signal will be created when the counter-2 becomes full.

In figure 3, n1 is the time lapse between the event trigger input and the associated coarse trigger-flag, it is the time jitter caused by the main clock. Here we use a fast clock to record it. m is the full range or maximum count of the fast counter-2, and (m-n1) is the adjusted delay time needed for accurately restoring the trigger signal from the delayed coarse trigger-flag. To have a (m-n1) fine delay time in counter-2, the counter-2 will be reset to n1 and then start running until it reaches full when an accurate delayed trigger is generated. Hence, the time difference between the recovered delayed trigger and the original event trigger is equal to n1+ (main clock delay) + (m-n1) = (main clock delay) + m, therefore it is a time constant and the jitter n1 can be cancelled. An additional fine delay time can be achieved by adding or subtracting a time-offset to the preset time n1 for counter-2. Both the length of the FIFO and the time-offset can be programmed using a FPGA. The programmable time-offset is useful if front-end electronic boards need a high-resolution time alignment for coincidence measurement. The counters and burst oscillators used for recording the time lapse and restoring the delay trigger are ultra fast ECL picoseconds devices.

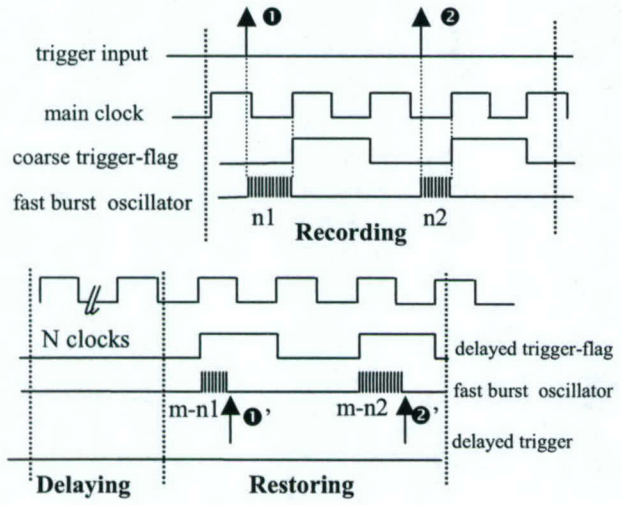

Figure 3: Timing of the delay generator, which is consisted of three sections: time jitter recording, main time delaying and fine-delay restoring.

Since the jitter time n1 is measured by counter-1 and the compensate delay time (m-n1) is clocked by counter-2, therefore any difference of the two burst clock periods would cause an extra timing error. In order to lower this timing error, we built the two burst oscillators in one ECL chip so that they could have a same frequency that is not affected by the temperature and other environment condition changes such as the voltage of power supply.

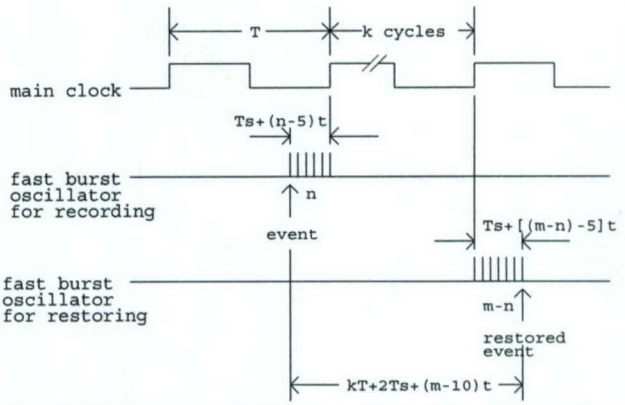

Figure 4: The delay time is independent of the event arrival time by ensuring fast oscillators working more than 5 cycles in both recording and restoring signals. T is the main clock period; t is the period of burst oscillator; Ts is the time of the first 5 cycles of the burst oscillator.

To reduce the system noise, the two burst oscillators only work for a very short time. There is a new technical problem, however, because the oscillators' first several cycles are not very stable when they are start working. Tests showed that the cycle time would not be stable until the 5th cycle. To solve this problem, a logic circuit is designed to have some selectable function: the trigger signal is caught by the main clock only when the count number n is bigger than 5, otherwise it will be caught by the next main clock. For the same reason, the counter's full number m is big enough to make the restoring number "m-n" bigger than 5. As shown as Figure 4, if the two burst oscillators have the same characteristic, and their first 5 cycle's total time is Ts, assuming the oscillators have stable cycles with time t after the first 5 cycles. If the counter-1 recorded number is n, the time lapse between the event trigger signal and the next main clock is $Ts + (n-5)t$. When restoring the signal, the time lapse between the main clock and the restoring signal is $Ts + [(m-n)-5]t$. If the main clock cycle time is T and there are k main clock cycles between the recording and restoring, the total delay time is $kT + 2Ts + (m-10)t$. n is cancelled, and we get a time constant. In designing the delay, temperature effect monitoring is a very important to archive the timing goal.

C. *Time alignment*

In our design, each detector module is divided into 4 electronic zones; each zone has its own HYPER and triggers delay circuit. Before performing coincidence checking, there is a "4-to-1" board to combine the energy/position data and trigger signals of the 4 zones back into a single module. So for the following circuits, all the signals would look like those from an integral module. All the module's trigger signals will go to coincidence board to do time coincidence. As shown as Fig. 5.

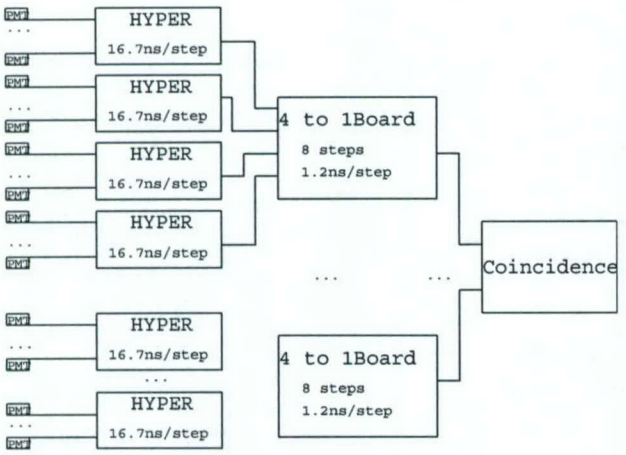

Figure 5: Two programmable time alignment mechanism: coarse steps (16.7ns/step) on the HYPER boards and fine steps (1.2ns/step) on the 4-to-1 boards.

In our PET system, there are 12 modules and each module has 4 zones, each zone has its own delay unit, the delay times normally have some difference each other. Hence all the delayed signals should be aligned in time before performing time coincidence. Each HYPER board has a software controllable switch that can optionally assert a 16.7ns delay. On the 4-to-1 board, there are four simple delay units that could provide another delay times for each zone. This simple delay unit has 8 steps, and each step has 1.2ns delay time. These two ways of adjusting time delay make it possible to alignment the time difference of the delayed signals among the different zones and different modules. The delay time steps can be controlled by software through a parallel port, which makes time alignment easier than the traditional cable delay method.

III. PERFORMANCE

We have designed and implemented a high resolution and very small dead-time programmable delay generator. This delay generator has also been integrated successfully into our HYPER circuit for the PET application. All the performance tests have been done on an independent prototype circuit see figure 6.

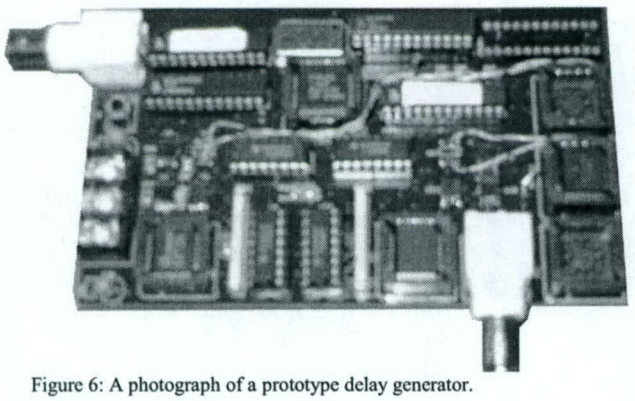

Figure 6: A photograph of a prototype delay generator.

Figure 7 shows delayed pulse signals, produced by the delay generator, on a Tektronix digital oscilloscope TDS3032 with an infinite display time. The oscilloscope was triggered by the rising-edge of the same pulse input to the delay generator. Since the delay timing only applied to the rising-edge not to the falling-edge, we found the delayed pulses had a larger jitter (16.7ns) in the falling-edge than that in the rising-edge. A less than ±0.9ns time jitter (resolution) of the rising-edge was measured. This delay timing resolution is good enough for the coincidence measurement of BGO PET detectors with a typical 12-20 ns coincidence-timing window. The circuit has a 50ns dead time; if two pulses are too close in time (less than the 50ns dead-time), they could not be delayed correctly. We also found the delay timing resolution as well as the dead-time performance was not degraded as the total delay time increased (by increasing the FIFO length for the main delay).

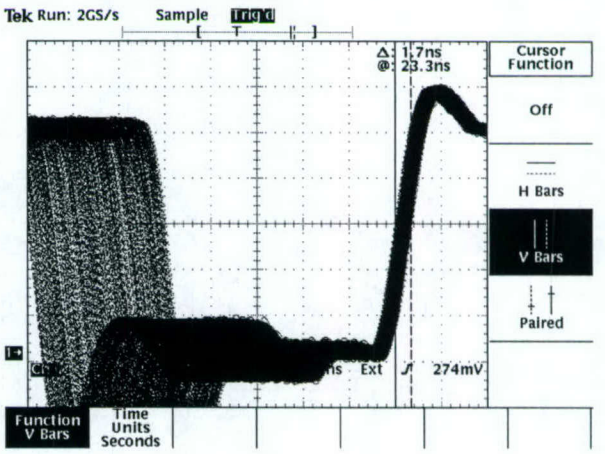

Figure 7: The delay signal result observed from scope.

We also setup another test bench with NIM, see figure 8. A CANBERRA time-to-amplitude (TAC) module (model 2145) was used to measure the delay time. The TAC was started by the original pulse signal and stopped by its delayed pulse signal, the TAC result was digitized by an analog-to-digital (ADC) module (CANBERRA model 8075) and after then a spectrum was created in a computer.

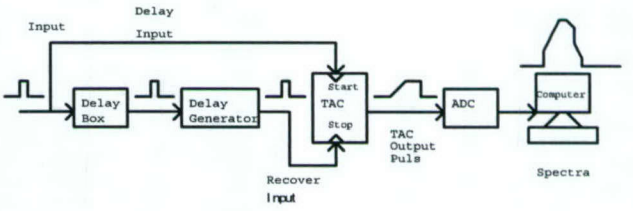

Figure 8: The delay time distribution detection method.

In order to calibrate the time for one ADC channel, we added a 4.0ns extra delay time using an analog delay box in the pulse delay channel. By adding this 4.0ns delay time, the spectrum was shifted to upper channels by an offset of 80 channels, see figure 9. Hence, each ADC channel indicated a 50ps delay time. The ideal spectrum of the delay time

distribution should be a rectangle. A FWHM of 1.55ns and a FWTM of 1.80ns for the spectrum were measured with this method.

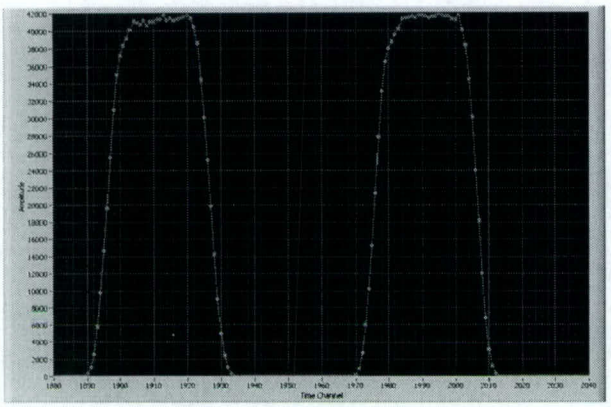

Figure 9: the delay time distribution result.

IV. CONCLUSIONS AND DISCUSSION

A programmable high-resolution ultra fast delay generator has been designed and constructed. Our test results showed: (1) the delay generator had a less than ±0.9ns timing jitter that was essential for timing and coincidence measurement; (2) the delay generator had a small dead-time of about 50ns that could handle a fast input pulse rates of up to 20 MHz; (3) the total delay range of the delay generator could be as long as hundreds milliseconds with no performance degraded; (4) the delay time can be programmed at a coarse step of 16.7ns and a fine step of 1.2ns. This high-resolution delay generator is an important component when using dynamic scintillation integration such as the HYPER circuit we proposed for PET coincidence detection and it has been successfully integrated in the HYPER electronics. This delay generator can also be used as a general device in other applications such as automatic test equipments and communications.

V. REFERENCES

[1] W.H. Wong, H. Li, J. Uribe, H. Baghaei, Y. Wang, S. Yokoyams, "Feasibility study of a high speed gamma camera design using the high-yield-pileup-event-recovery (HYPER) method," The Journal of Nuclear Medicine, vol.42, no. 4, April 2001.

[2] W.H. Wong, "The design of a high resolution transformable whole body PET camera," IEEE Trans. Nucl. Sci., vol. 49(5), October, 2002.

[3] H. Li, et al, "Front-end electronics based on high-yield-pileup-event-recovery method for a high resolution PET camera with PMT-quadrant-sharing detector modules," Conference record of the 2002 IEEE MIC Conference.

[4] J.P. Martin and K. Ragan, "A programmable nanosecond digital delay and trigger system," Conference record of the 2000 IEEE MIC Conference.

Effects of Attenuation Correction and 3D-Reconstruction Algorithms on Brain Lesions Detectability

Hossain Baghaei, Jorge Uribe, Hongdi Li, Yu Wang, Yaqiang Liu, Tao Xing, Rocio Farrell, and Wai-Hoi Wong

Abstract—**We compared lesion detectability in the brain images reconstructed with the three-dimensional (3-D) reprojection algorithm, with and without attenuation correction, and with the 3-D ordered subsets expectation maximization (OSEM) algorithm with and without post-filtering. For this purpose, three small lesion phantoms with diameters of 3, 5 and 8.6 mm were embedded into the Hoffman brain phantom. The approximate ratio of the activity concentration in the lesions to the surrounding brain gray matter was ranging from 1.5 to 10. We used the high-resolution MDAPET, a prototype 3D-PET camera, to scan the phantoms. This camera is a multi-ring scanner with an intrinsic transaxial resolution of 2.8 mm. For practicality, to minimize the number of imaging sessions to be taken, data for the hot lesion phantoms and the normal warm Hoffman brain phantom were taken separately. Then, before performing image reconstruction, the two sets of the sinograms data were selectively combined to generate the sinograms data for the desired SUVs. When the lesions data were taken, the lesions were placed inside the Hoffman brain phantom filled only with water to provide the attenuation and scatter effects. We observed a slight improvement in lesion detectability for the 5 mm lesion located near the center of image for attenuation corrected over non-attenuation corrected sinograms when images were reconstructed with the 3D-reprojection algorithm and also images visually looked better. Images reconstructed with 3-D OSEM followed by post-filtering show slight improvement in lesion detection over 3DRP.**

I. Introduction

MANY researchers have investigated different techniques for improving the quality of the reconstructed images in PET study. Some of these investigators have studied the effects of attenuation correction on the quality of images [1]-[3]. Some have used iterative methods as an alternative to filtered back projection for reconstruction of PET images [4]-[6]. In this work, we studied the effects of attenuation correction and two different 3D-reconstruction algorithms on lesions detectability in images obtained from the scan of three small lesion phantoms embedded into the Hoffman brain phantom [7]. The diameters of the lesions were 3 mm, 5 mm and 8.6 mm. The approximate ratio of the activity concentration in the lesions to the surrounding brain gray matter was ranging from 1.5 to 10. For image reconstruction we used the three-dimensional (3-D) reprojection [8] and 3-D ordered subsets expectation maximization (OSEM) algorithms [6].

This work was supported in part by the NIH Grant ROI CA58980, NIH Grant ROI CA61880, NIH Grant ROI CA76246, NIH Grant ROI CA58980S1, Texas Higher Education Advanced Technology Grant, John S. Dunn Foundation Research Grant, and by the Cobb Foundation for Cancer Research.

Hossain Baghaei, Jorge Uribe, Hongdi Li, Yu Wang, Mehmet Aykac, Yaqiang Liu, Tao Xing and Wai-Hoi Wong are with the University of Texas M. D. Anderson Cancer Center, Houston, TX 77030 USA (H. Baghaei's telephone: 713-794-5270, e-mail: hbaghaei @di.mdacc.tmc.edu).

II. Methods and Results

A. Methods

We used the high-resolution MDAPET, a prototype PET camera, to scan the phantoms. This camera is a multi-ring scanner with an intrinsic transaxial resolution of 2.8 mm. Each ring contains 448 bismuth germanate (BGO) crystals having an in-plane and axial crystal pitch of 2.66 and 2.80 mm, respectively. The detectors are grouped into blocks of 7X7 crystals. The camera detection system is divided into eight independent, movable modules. Each module can be translated radially to alter the size of the patient opening, optimizing the detection sensitivity for different body cross-sections. Also the gantry can be rotated during data acquisition in 0.10° steps up to 45°. The gantry rotation is necessary to fill the gaps in the sinograms caused by the empty space between modules. The standard procedure for this camera is to acquire data in 1° steps. The detector module design, which is based on the quadrant sharing technique, and electronics of the MDAPET camera were described previously [9]-[13]. The imaging performance characteristics of the camera were discussed previously [14], [15].

The MDAPET camera has several modes of operations and we took data in the brain mode. In this mode, the camera has a ring diameter (the distance between two facing detector modules) of 44 cm and patient opening of 32 cm. Camera has 14 detector rings covering an axial field-of-view (FOV) of 3.85 cm. To compensate for the lower sensitivity of the MDAPET camera, due to its small axial FOV, the Hoffman brain phantom was scanned longer at relatively higher activity and repeated several times so that the data can be summed to obtain an equivalent number of true coincidence events as that a clinical version of the camera would collect in a typical

0-7803-7636-6/03/$17.00 ©2003 IEEE.

injected dose of 10 mCi ^{18}F -fluorodeoxyglucose (FDG) in a 20 minutes scan. All measurements were done in 3-D mode.

For this work three small lesion phantoms were embedded into the Hoffman brain phantom. The diameters of the embedded lesion phantoms were 3, 5 and 8.6 mm and all have the same standard uptake values (SUVs). The approximate ratio of the activity concentration in the lesions to the background brain gray matter regions was ranging from 1.5 to 10.

For practicality, to minimize the number of imaging sessions to be taken, data for the hot lesion phantoms and data for the warm (normal) Hoffman brain phantom were taken separately. Then, before applying different corrections, the two sets of the sinograms data were selectively combined to generate the sinograms data for the desired SUVs. This combination method greatly reduces the number of required measurements for different lesion uptake and also eliminates the effect of the 'cold' walls of the tissue phantoms that exits when hot lesions and the warm background are measure simultaneously [15],[16]. However, this technique requires that phantom to be positioned precisely, the concentration ratio of the tissue and background be known, the accidental coincidence be known and also the effect of the dead time becomes more important. When the lesions data were taken, the lesions were placed inside the Hoffman brain phantom filled only with water to provide the attenuation and scatter effects. This sinogram summing method allows all the different SUVs data for lesions to be taken in one experimental period by collecting the different SUVs data as the activity decays.

Prior to image reconstruction, the projection data were corrected. These corrections included random coincidence subtraction, attenuation correction, geometric and detector-pair efficiency corrections [17]. The attenuation correction was performed by calculating the attenuation length from the shape of the phantom (cylinder) and assuming a uniform attenuation coefficient.

All data were acquired in 3-D mode with an axial acceptance of 13 rings which produced 196 sinograms and no averaging was performed. The camera allows simultaneous imaging of 27 transaxial slices with 1.4 mm thickness. In the present study, each sinogram had 239 radial bins and 180 azimuthal views. The radial sampling was 1.385 mm.

B. Results

Figure 1 shows two reconstructed slice images of the normal (without lesions) Hoffman brain phantom as they are compared to the phantom's pattern which indicates how well the phantom structures are reproduced. These results which are for a high statistics acquisition (200 million true coincidence events in all sinograms) were reconstructed with the 3D-reprojection algorithm.

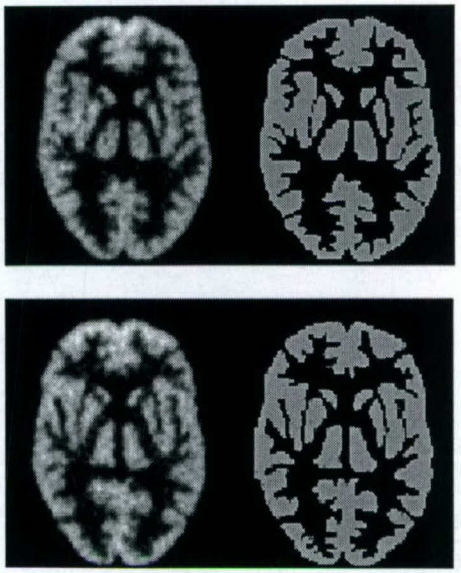

Fig. 1. Two image slices of the Hoffman brain phantom (without any lesions) reconstructed with the 3DRP algorithm compared to the true phantom's pattern on the right side.

Figure 2 shows two transaxial slices of the Hoffman brain phantom with three embedded lesion phantoms when the ratio of the activity concentration in the lesions to the surrounding background tissue (gray matter) was about 5. Top row images were reconstructed from attenuation corrected sinograms and bottom row images were obtained from the non-attenuation corrected sinograms.

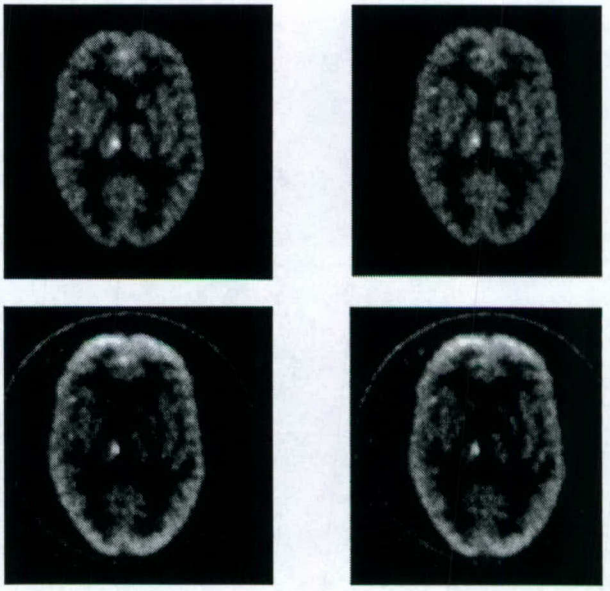

Fig. 2. Two image slices of the Hoffman brain phantom with three embedded lesions reconstructed with 3DRP algorithm: (top row) sinogram data were attenuation corrected; (bottom row) data were not attenuation corrected. Ratio of the activity density of lesions to the surrounding tissue (gray matter) was 5.

Figure 3 show the two image slices when lesion-to-surrounding tissue density ratio was 2.2. In both Figs. 2 and 3, the 5 mm lesion can clearly be seen near the center of the images. The 8.6 mm lesion is located near the top of the image and 3 mm lesion located on the left side of the image. The 3 mm and 8.6 mm lesion can only be seen in Fig. 2. In order to better observe the lesion images, the 8.6 mm lesion phantom was placed such that does not peak at the same slices with the other two that is why the 8.6 mm lesion is not as observable as the 5 mm lesion. By visually inspecting the images we observed that 5 mm lesion can be seen better in attenuation corrected data.

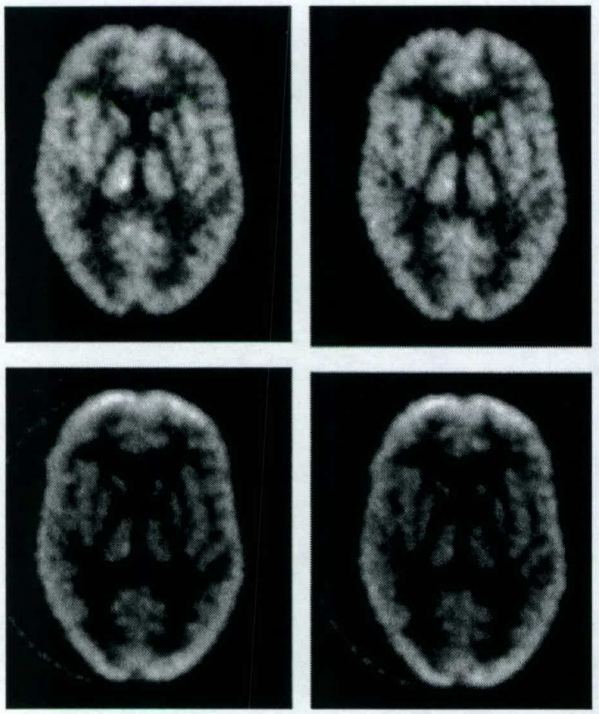

Fig. 3. Two image slices of the Hoffman brain phantom with three embedded lesions reconstructed with 3DRP algorithm: (top row) sinogram data were attenuation corrected; (bottom row) data were not attenuation corrected. Ratio of the activity density of the lesions to surrounding tissue was 2.2.

Fig. 4 shows two reconstructed image slices with the 5 mm lesion near the center of the images when the ratio of the activity concentration in the lesions to the background is about 2.2. Top row images were reconstructed with the 3D-reprojection algorithm, the middle row images were reconstructed with 3-D OSEM and the ones in the bottom row by 3D-OSEM followed by post-filtering with a Metz filter after the 40th sub-iteration. Fig. 5 shows two image slices with the 3mm and 5 mm lesions reconstructed with 3DRP algorithm and OSEM algorithm followed by post-filtering when lesion-to-surrounding tissue activity density ratio was 5.8. Data used for comparison of the 3DRP and 3D-OSEM algorithms were corrected for attenuation.

Figure 6 shows a horizontal profile running through the middle of the 5 mm lesion image at the activity ratio of 5.8. The 3D-OSEM results were post-filtered with a Metz filter after the 40th iteration. Figure 7 shows a horizontal profile running through the middle of the 5 mm lesion image at the activity ratio of 2.2. The 3D-OSEM results were post-filtered with a Metz filter after the 40th iteration. Figs. 6 and 7 show that the OSEM algorithm has a slight advantage over the 3DRP algorithm.

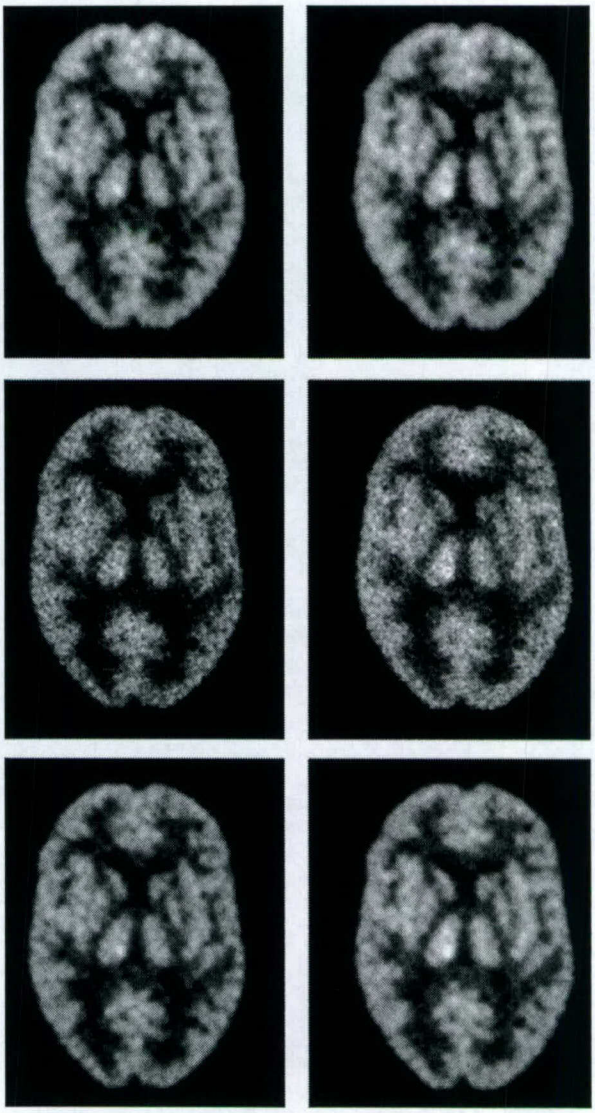

Fig. 4. Two images slices of the Hoffman brain phantom with 3 lesion phantoms: (top) reconstructed with the 3DRP algorithm, (middle) reconstructed with the 3D OSEM algorithm, and (bottom) reconstructed with 3D-OSEM followed by post-filtering using a Metz filter. Ratio of the activity density of the lesions to surrounding tissue was 2.2.

III. Conclusions

Images reconstructed, with the 3DRP algorithm, from the attenuation corrected data visually "looked" better than the

images reconstructed from the non-attenuation corrected data and structures of the Hoffman brain phantom are better observable. In terms of lesion detectability, for the 3 mm and 8.6 mm lesions which were located near the peripheral of the images, by visually inspecting images, we did not observe any significant differences between the attenuation corrected and non-corrected methods. For the 5 mm lesion placed near the center of the images, attenuation correction has a slight advantage over non-corrected.

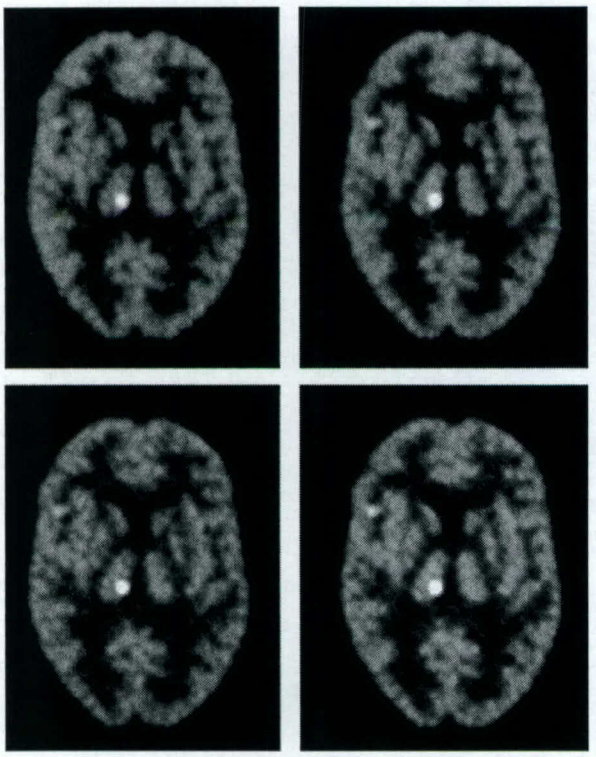

Fig 5. Two images slices of the Hoffman brain phantom with 3 lesion phantoms: (top) reconstructed with the 3DRP algorithm, (bottom) reconstructed with 3D-OSEM followed by post-filtering. Ratio of the activity density of the lesions to surrounding tissue was 5.8.

Both the 3DRP and 3D-OSEM algorithms were able to reasonably reproduce the detailed structures of the Hoffman brain phantom. The images reconstructed by the OSEM algorithm visually "looked" better if they were followed by post-filtering. In terms of lesion detectability, by visually inspecting the images constructed by two different methods, we did not observe any significant differences between them. However, by studying the horizontal profiles running along the middle of lesions, the OSEM algorithm, followed by post-filtering, showed a slight advantage over the 3DRP algorithm which may become important when the lesion detection is marginal.

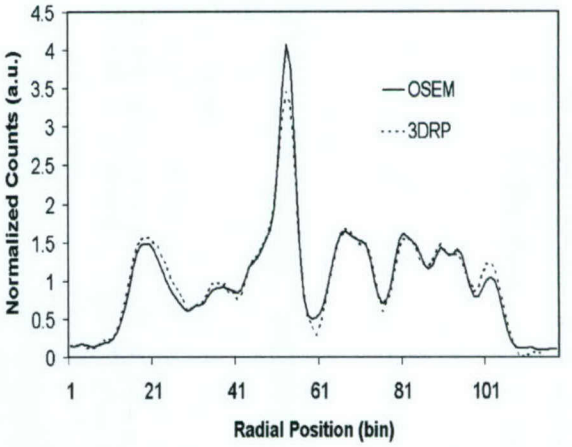

Fig. 6. A horizontal profile running through the middle of the 5 mm lesion images shown in Fig. 5 for the 3D-reprojection method and the 3D-OSEM algorithm followed by post-filtering. Ratio of the activity density of the lesions to surrounding tissue was 5.8.

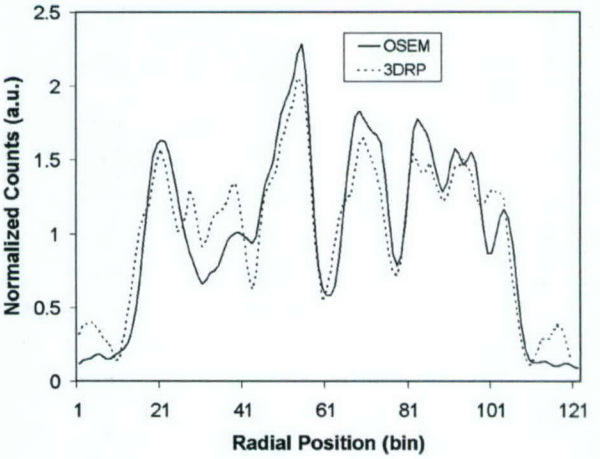

Fig. 7. A horizontal profile running through the middle of the 5 mm lesion images shown in Fig. 4 for the 3D-reprojection method and the 3D-OSEM algorithm with post-filtering. Lesion to surrounding tissue activity density ratio was 2.2.

IV. Acknowledgment

The authors would like to thanks the personnel of the clinical PET center of the University of Texas M. D. Anderson Cancer Center for their support in providing the FDG used for this work.

V. References

[1] C. Bleckmann, J. Dose, K. H. Bohuslavizki, R. Buchert, S. Klutmann, J. Msester, F. Janicke, and M. Clausen, "Effect of attenuation correction on lesion detectability in FDG PET of breast cancer," *J. Nucl. Med.*, vol. 40, no. 12, pp. 2021-2024, December 1999.

[2] R. L. Wahl, "To AC or not to AC: That is the question," *J. Nucl. Med.*, vol. 40, no. 12, pp. 2025-2028, December 1999.

[3] F. M. Bengel, S. I. Zeiegler, N. Avril, W. Weber, C. Laubenbacher, and M. Schwaiger, "Whole-body positron emission tomography inclinical

oncology: comparison between attenuation –corrected and uncorrected images," *Eur. J. Nucl. Med.*, vol. 24, pp. 1091-1098, 1997.

[4] H. M. Hudson, and R. S. Larkin, "Accelerated image reconstruction using ordered subsets of projection data," *IEEE Trans. Nucl. Sci.*, vol. 13, no. 4, pp. 601-609, Dec. 1994.

[5] A. J. Reader, D. Visvikis, K. Erlandsson, R. J Ott, and M. A. Flower, "Intercomparison of four reconstruction techniques for positron volume imaging with rotating planar detectors, " *Phys. Med. Biol.*, vol. 43, pp. 823-834, 1998.

[6] M. Jacobson, R. Levkovitz, A. Ben-Tal, K. Thielemans, T. Spinks, D. Belluzzo, E. Pagani, V. Bettiardi, M. C. Gilardi, A. Zverovich, and G. Mitrai, "Enhanced 3D PET OSEM reconstruction using inter-update Metz filtering," *Phys. Med. Biol.*, vol. 45, pp. 2417-2439, 2000.

[7] E. J. Hoffman, P. D. Cutler. W. M. Digby, and J. C. Mazziotta, "3-D phantom to simulate cerebral blood flow and metabolic images for PET," *IEEE Trans. Nucl. Sci.*, vol. 37, no. 2, pp. 616-620, April 1990.

[8] P. E Kinahan, J. G. Rogers, "Analytic 3D Image Reconstruction Using all Detected Events," *IEEE Transaction on Nuclear Science*, vol. 46 pp.964-968, 1989.

[9] W.-H. Wong, "A positron camera detector design with cross-coupled scintillators and quadrant sharing photomultipliers," *IEEE Trans. Nucl. Sci*, vol. 40, pp.962-966, August 1993; and *Conference Record of the 1992 IEEE Nuclear Science Symposium and Medical Imaging Conference (Orlando, FL)*, 1992.

[10] W-H. Wong, J. Uribe, W. Lu, and K. Hicks, "Design of a variable field prototype PET Camera," *IEEE Trans. Nucl. Sci.*, vol. 43, pp. 1915-1920, June 1996.

[11] W-H. Wong, J. Uribe, K. Hicks, and M. Zambelli, "A 2-dimensional detector decoding study on BGO arrays with quadrant sharing photomultipliers," *IEEE Trans. Nucl. Sci.*, vol. 41, pp. 1453-1457, June 1994.

[12] W-H. Wong, G. Hu, N. Zhang, J. Uribe, J. Wang, H. Li, H. Baghaei, and S. Yokoyama, "Front end electronics for a variable field PET camera using the PMT-quadrant-sharing detector array design," *IEEE Trans. Nucl. Sci.*, vol. 44, pp. 1266-1270, June 1997.

[13] R. H. Li, W-H Wong, N. Zhang, J. Wang, J. Uribe, H. Baghaei, and S. Yokoyama, "Prototype electronics for a variable field of view PET camera using the PMT-quadrant-sharing detector array," *IEEE Trans. Nucl. Sci.*, vol. 46, pp. 546-550, June 1999.

[14] J. Uribe, H. Baghaei, H. Li, S. Yokoyama, N. Zhang, J. Wang, F. Dobbs, and W-H. Wong, "Basic imaging characteristics of a variable field of view PET camera using quadrant sharing detector design," *IEEE Trans. Nucl. Sci.*, vol. 46, pp. 491-497, June 1999.

[15] H. Baghaei, W-H. Wong, J. Uribe, H. Li, N. Zhang, and Y. Wang, "Breast cancer studies with a variable field of view PET camera," *IEEE Trans. Nucl. Sci.*, vol. 47, pp. 1080-1084, June 2000.

[16] R.S. Miyaoka, S.G. Kohlmyer, T.K. Lewellen, "Hot Sphere Detection Limits for a Dual Head Coincidence Imaging System," *IEEE Transaction on Nuclear Science*, vol. 46, pp.2185-2191, December 1999.

[17] H. Baghaei, W-H. Wong, J. Uribe, H. Li, N. Zhang, and J. Wang, "The correction factors for a high resolution variable field of view PET camera," *J. Nucl. Med.*, vol. 40, p.279P, May 1999.

An Efficient Detector Production Method for Position-Sensitive Scintillation Detector Arrays with 98% Detector Packing Fraction

J. Uribe, *Member, IEEE,* Wai-Hoi Wong, *Member, IEEE,* H. Baghaei, *Member, IEEE,* R. Farrel, H. Li, *Member, IEEE,* Y. Liu, Y. Wang, , and T. Xing

Abstract—**Position-sensitive scintillation-detector arrays (PSSDA) are used in nuclear imaging such as PET. The PSSDA-production method determines the imaging resolution, sensitivity, labor/part cost, and reliability of the system. It is especially challenging and costly for ultrahigh-resolution systems that have large numbers of very small crystal-needles. A new slab-sandwich-slice (SSS) production method was developed. Instead of using individual crystal needles, the construction started with crystal slabs that are 15-crystal-needles wide and 1-needle thick. White-paint was deposited onto slab surfaces to form shaped optical windows. The painted slabs were grouped into two crystal-sandwich types. Each sandwich-type was a stack of 7 slabs painted with a distinctive set of optical windows, held together with optical glue. For a 40,000-crystal system, only 192 type-A and 144 type-B sandwiches are needed. Sandwiches were crosscut into another slab formation ("slices"). Each slice was again 1-needle thick; each slice is basically a stack of needles glued together, optically coupled by the glue and the painted windows. After a second set of white-paint optical-windows was applied on the slices' surface, 3 slices of type-B are grouped between 4 slices of type-A forming a 7x7 PSSDA. The SSS production method was applied in the construction of high-resolution 12-module prototype PET camera (HOTPET). The method reduces the more than 400,000 precision painting and gluing steps into 55,000 steps for a 40,000-BGO-crystal system, leading to lower labor cost. Detectors were fabricated with the method with good results. 2.66x2.66 mm^2 crystals are separated only by a 0.06-mm gap; this is a 98% linear detector packing fraction or 96% area packing fraction. Compared to 90% linear-packing (81% area) from conventional methods, the 20% higher crystal-packing density would translate into a 1.2-1.44 times higher coincidence-detection sensitivity in PET. The SSS method cut the crystal cost by half, and improved production yield by 94%. Crystal-positioning error was σ=0.09mm.**

Manuscript received November 16, 2002. This work was supported in part by the NIH Grant RO1 CA58980, NIH Grant RO1 CA61880, NIH Grant RO1 CA76246, NIH Grant RO1 CA58980S1, Texas Higher Education Advanced Technology Grant, John S. Dunn Foundation Research Grant, The Mike Hogg Foundation, and by the Cobb Foundation for Cancer Research.

Jorge Uribe, Hongdi Li, Hossain Baghaei, Yu Wang, ,Yaqiang Liu, Tao Xing, Rocio Farrel and Wai-Hoi Wong are with the University of Texas, M.D. Anderson Cancer Center, Houston, TX 77030 USA (J. Uribe's telephone: 713-745-1179, e-mail: juribe@mdanderson.org).

I. Introduction

Position-sensitive scintillation detector arrays (**PSSDA**) are commonly used in nuclear imaging, especially in PET cameras. Other than detector designs, the most important execution in building a PET is the detector production method, because it directly determines the ultimate imaging resolution, sensitivity, the labor cost, and the reliability of a PET system. In position-sensitive scintillation array systems, each scintillation crystal distributes a unique amount of scintillation light to a number of photomultipliers (PMT). The PMT signals identify each firing crystal from each crystal's unique light-distribution pattern. Imaging resolution is determined by (a) how finely the light distribution from each crystal can be controlled, and (b) the precision of executing the light-distribution design in a mass-production process. We have developed a production method that fulfills the following 7 important conditions:

(1) Finely control the distribution of light from each crystal to achieve high imaging resolution,
(2) Efficiently distribute the scintillation light to PMTs for maximum imaging resolution,
(3) The crystal array and light-distribution system achieve a high crystal-packing density for maximum sensitivity,
(4) Precisely and reproducibly produce the light-distribution devices according to design specifications,
(5) Lower costs for both labor and raw material,
(6) Be mechanically robust for maintaining long term reliability, and
(7) Have a high detector yield (less detector breakage or substandard detectors).

The production process of a position-sensitive crystal array involves (a) cutting, lapping, etching, polishing, and cleaning each crystal, (b) making the light-distributor for each crystal, (c) optically mating each crystal to the light-distributor, and (d) assembling all the crystals and light distributor into an array. An ultrahigh resolution PET system may have more than 40,000 crystals (and light distributors), each as small as 2.66x2.66mm^2 as in our experimental **High-resolution-Oncologic-Transformable-**PET **HOTPET** [1], [2]. The sheer large number and the small crystal size can make such a system unrealistic in both raw material and labor cost. Since the crystal pitch is very small in ultrahigh resolution system,

0-7803-7636-6/03/$17.00 ©2003 IEEE.

the traditional sawing technique (**partial-depth sawing** of a crystal block or a plastic light-guide) would significantly decrease the detection sensitivity. A diamond-blade's kerf of as little as 0.35 mm lowers the packing-area efficiency to $[2.66/(2.66+0.35)]^2$ = 78%; translated into a coincidence efficiency of only 61% $(0.78)^2$ (Fig. 1).

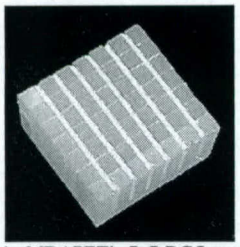

Fig. 1. MDAPET's 7x7-BGO-array combining the "partial-depth sawing" and the "paint and glue mask" techniques to control the scintillation

The first generation PET camera (MDAPET [3],[5]) developed by our group, served as the testing ground for two PSSDA production techniques "partial-depth sawing" and "**paint and glue masking**" [1]. The second method remedied the sensitivity loss by first using a partial-crystal-surface painting technique to distribute the light through the crystal surfaces. Second, by removing any gap between crystals except for the space occupied by the glue and paint layers (0.06mm). However, precise manufacturing, painting and gluing of 40,000 tiny crystals would require over 400,000 steps, which is extremely labor intensive and expensive. An additional complication came from HOTPET's detector design. Figure 2 shows this modular design combining symmetric and non-symmetric [4] PSSDA. It includes 3168 crystal-needles (38,016 total system) coupled to 77 PMTs.

Results of the "paint-and-glue" method, the overall detector requirements, reproducibility, and the need for a low cost production method, to build thousands of detectors for HOTPET, motivated us into the development of the process described here.

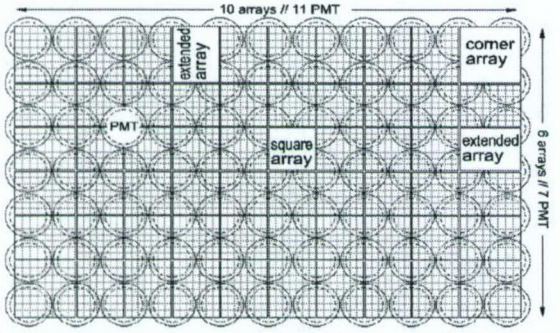

Fig. 2. HOTPET's detector module design requires three different types of PSSDAs arranged in PQS [3] mode for optimum use of the photocathode surfaces of PMTs at the edge of the module. Edge blocks are knows as "extended" blocks.

II. The Slab-Sandwich-Slice Method

The SSS production algorithm topology is illustrated in Fig.3. Instead of using individual crystal-needles, we start the construction with BGO **slabs** that are 15 crystal-needles wide and 1 crystal thick (2.66 mm). There is no actual constrain on the length of the slabs and can be of arbitrary length. We have chosen slabs 15 needles in length to accommodate the BGO supplier's tooling and production capabilities [6]; it reflected in overall cost reduction. A stack of 7 slabs painted with

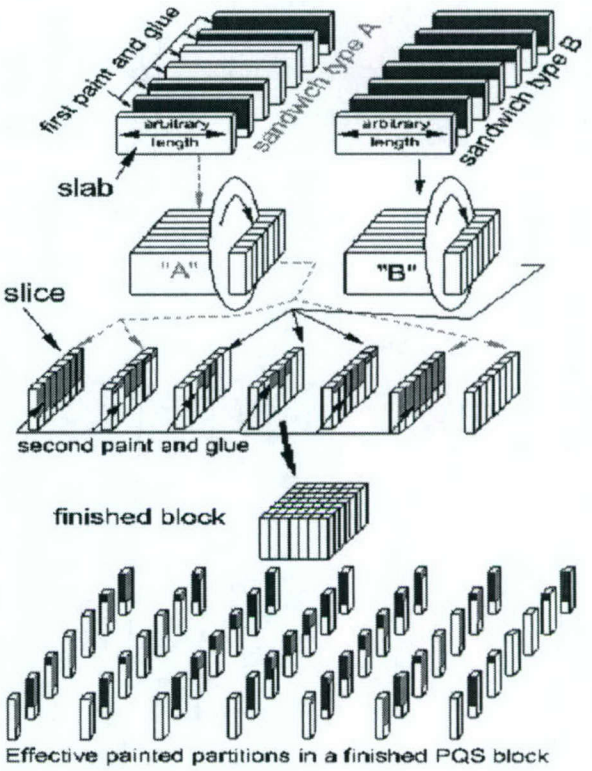

Fig. 3. The "slab-sandwich-slice" (SSS) production method for position-sensitive scintillator detector arrays (PSSDA).

optical masks (window) and optically glued together form a crystal **sandwich** (top arrays Fig. 3). The mask on each slab is a fix-height straight band of white paint applied along the entire length of the slab (Fig. 3,Fig. 5(a)). Then, the slabs are grouped into 2 different "sandwich types" (A and B in Fig.3) according to a specific order and size of their masks. For sandwich type-A only four of the seven slabs are painted with two different mask patterns (top-left -- Fig.3). For sandwich type-B, six slabs are painted with a different set of masks (top right – Fig. 3). All the sandwiches are crosscut into another slab formation, which we call "**slices**." The thickness of each slice is again one crystal width (2.66 mm), and each slice is in essence a stack of individual crystal needles optically coupled together by the glue and paint-masks between them. Three slices of type B are grouped between 4 slices of type A (follow the dash and solid arrows in fig.3) to form an "array of slices." Before the 7 slices of this new array are glued together, to form the final PSSDA ("finished block" in the same figure), a new set of masks are painted on their surface (masks shown on the face of each slice).

Details of the 49 crystal needles that form the final PSSAD, with the correct masking, are shown in the block's exploded view at the bottom of Fig.3. In this view, each crystal needle shows a set of masks and windows that are relevant only to the specific crystal location and face orientation within the block.

Pictures of a slab, a sandwich, a slice and the final 7x7 PSSDA are shown in Fig. 4. Comparison of this array with the one in Fig. 1 shows considerable decrease of inter-crystal

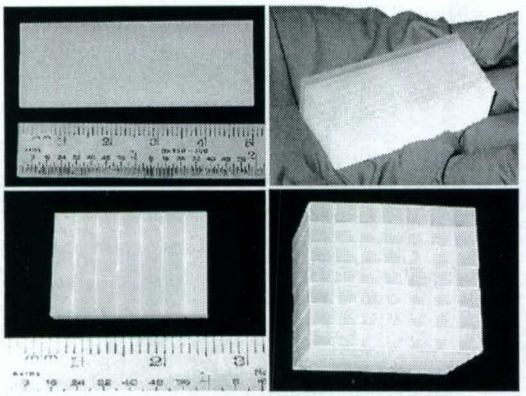

Fig. 4. Four stages of the SSS production process (clockwise direction) Pictures of a slab, sandwich, slice and 7x7- PSSDA

separation, increasing packing fraction and detection sensitivity.

The SSS method is not limited to the production of symmetric or square detector arrays. Figure 5 shows the mask types used in the production of the new detector for HOTPET. It shows symmetric patterns used for the symmetric 7x7 block (Fig. 5(b)); non-symmetric mask patterns used for the extended-rectangular 7x8 PSSDAs placed at the edges of the detector module (Fig. 5(c)); and masks for the larger-square non-symmetric 8x8 arrays for the module's corners (Fig. 5 -- column (d)).

In some instances, light blocking provided by the white paint is not enough to decode the gamma hits from all needles in a PSSDA. We have applied paint on facing surfaces of adjacent crystals; resulting in a double coat of paint for stronger light blocking. An example is shown in Fig 5(d), where a set of 3 adjacent slices for HOTPET's corner block were painted using masks (d)(1), (d)(2), and (d)(3), but additional paint was needed between the last two slices. Thus, a fourth mask (Fig. 5(d)(3-b)), mirror image of Fig. 5(d)(2), was applied on the backside of the third slice. The construction of HOTPET's detector required a total of 720 PSSDAs built from 2,541 slabs. It is important noticing that in spite of the variety on types and block-designs used by this detector, only two size slabs were purchased (50mm long by 2.68mm or 3.06mm thick).

The total number of steps/operations needed to build the entire detector is as follows:

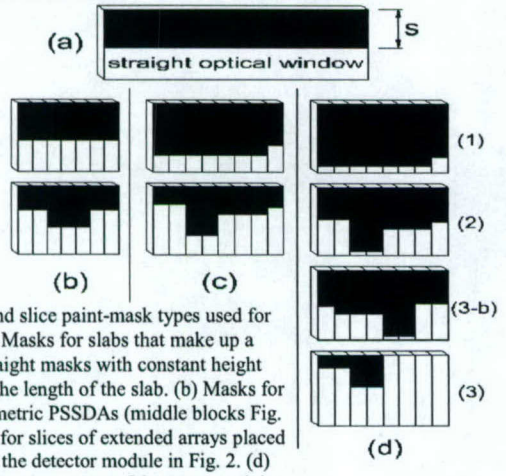

Fig. 5. Slab and slice paint-mask types used for HOTPET. (a) Masks for slabs that make up a sandwich; straight masks with constant height "s" covering the length of the slab. (b) Masks for slices of symmetric PSSDAs (middle blocks Fig. 2). (c) Masks for slices of extended arrays placed at the edge of the detector module in Fig. 2. (d) Masks for the corner arrays of the same module

- Cut and lap of each element:
  (2541 slabs) x (3 cuts + 6 lap) = 22,869 operations.
  (5088 slices) x (1 cut + 2 lap) = 15,264 operations.
-Paint & glue:
  sandwich: 2705 mask & paint + 3941 clean & glue = 6646 operations.
  slices: 5640 mask & paint + 5040 clean & glue = 10680 operations.

Thus, the total number of operations was 55,500, which is only one eighth of the number of steps needed to build the same detector starting with individual needles (see Results section).

A. Tooling

A special set of tools was developed to guarantee the accuracy and reproducibility of crystal arrays built with the SSS technique.

To create the painted pattern, the slabs and slices need to be masked. Each slab/slice was mounted onto a painting jig and covered by a disposable painting mask; the masks block the paint to form a shaped optical window.

Developing a fast way of masking the crystals with high geometrical accuracy is essential. To expedite the masking and painting processes, these processes were performed on multiple slabs/slices simultaneously. Multiple slabs were placed in a precise masking painting jig. The jig has recesses that the slabs can slide in snugly, and the slab surfaces are flush with the jig surface (Fig. 6). The jig has 5 precisely placed steel studs for mask alignment. A paper mask with removable adhesive on it and corresponding alignment holes to fit these studs was placed on the jig to cover both the jig and the slabs (Fig. 6). The masks were laser cut [7] from pressure sensitive stock [8]. Laser cutting provides very good accuracy (60μm), reproducibility (25μm) and very low cost ($0.50 per sheet-mask).

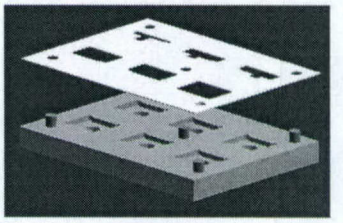

Fig. 6. Bottom: precision painting jig. Top. Laser-cut mask.

White paint [9] was applied with the airbrush technique driven by pressure-regulated N_2 gas from a gas cylinder.

A precision-gluing technique for the Slabs and Slices is needed. All the slabs and slices have to be glued together using optically transparent glue. Because of high mechanical precision and optimum optical coupling requirements, the thickness of the glue layer and its application technique were carefully studied. From test run experiments we optimized pre-curing time of the glue to achieve ideal viscosity before

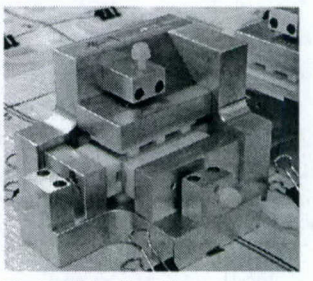

Fig. 7. Gluing jig with sandwich compressed in 3 dimensions.

application. We designed and built high-precision gluing jigs so that all three dimensions of a sandwich or PSSDA can be tightly compressed and dimensionally regulated (Fig. 7). The setting time of the glue while the array sits in the jig was also studied. It needed to be long enough to harden and avoid compromising the mechanical tolerances at the time of disassembly; yet fresh enough to allow removal from the jig and easy cleaning of excess glue.

III. Results

The SSS method utilizes painted reflecting barriers on the crystal surfaces to precisely control the light distribution because any shape can be painted; this feature optimizes crystal decoding.

Throughout the entire process no single crystal needle is handled individually, making it a very efficient process.

Crystal needle separation is reduced to a few hundreds of a millimeter, improving detector sensitivity.

All these features of the SSS production method were evaluated with the construction of the detector for our high-resolution clinical-PET prototype HOTPET.

A. Cost and Production

Instead of working with each individual crystal needle, we bought a slab that has the same length as 15 needles stacked together side by side. The price per BGO needle is $4 ($60 for 15), but the price for a BGO slab (15 wide) is $31 (due to less processing). Hence, building the detectors from slabs instead of individual needles saved 50% in raw material costs.

HOTPET's detector has near 40,000 crystals in it. The number of steps/operations involved in the construction of this detector starting with individual needles is shown below.

- Cut and lap of each element:
  (38,016 needles) x (3 cuts + 6 lap) = 342,144 operations.
- Paint & glue:
  - 541 mask, paint & clean = 33001 operations.
  - Gluing: 7x7-block + 8x8-block = 38,016 operations.
  - Slice painting + Final glue = 10,680 operations.

Thus, total number of operations would be 423,800, compared to 55,500 operations with the SSS production method. That is an 87% reduction in labor costs and lowers the probability of making mistakes during assembly because fewer parts are handled.

The SSS method has a very high production yield because if a slice is broken during cutting, the broken slice can be replaced by the next cut from the same sandwich. Hence only 1/7 or 1/8 of the final block is wasted, whereas in the traditional partial-depth sawing method the whole block (49-64 crystals) would be wasted with one bad cut. Detector production yield using the traditional method (partial-depth cut) was only 70%. In contrast, the SSS production method had a slice-cutting yield of 94%.

B. Mechanical Tolerances

Nominally, we set out to build three types of PSSDA for HOTPET with the following dimensions: 7x7-symmetric -- 19x19x 18mm^3, 7x8-non-symmetric-extended – 19x24.76x18mm^3, 8x8-corner-non-symmetryc – 24.76x24.76x18mm^3.

The SSS method imposes no mechanical constrain on the length of the slabs that form a sandwich because they will be cut into slices. Thus, we purchased 50mm long slabs with a wide tolerance of □0.1mm to lower material costs, but tight enough to facilitates the assembly of the sandwich inside the painting and gluing jigs. On the other hand, we requested the BGO manufacturer to allow only 0.05mm below the nominal thickness of 2.68mm and 3.06mm.

From evaluation of 200 slices and slabs and more than 120 assembled blocks, the following factors were identified to affect the block dimensions (depicted in Fig. 8).

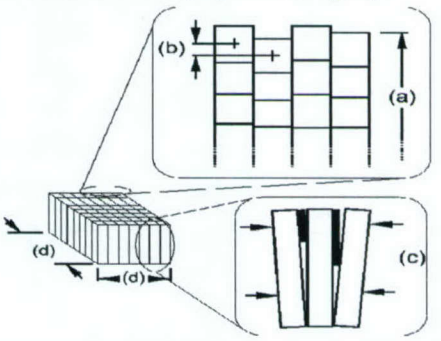

Fig. 8. Fours sources of mechanical tolerances from the SSS manufacturing process: (a) glue, paint and slab thickness (needle positioning error; measures repeatability.); (b) systematic differences between sandwich types; (c) needle slant (gluing jig limitations, paint placement); (d) axial vs. trans-axial dimension differences (size of surface glued).

(a) Variations in length of slices from the same sandwich type (nominal value 19mm, and 24.76mm; σ=0.04mm, Fig. 8(a)). This is due to variation in thickness of the slabs, paint layer, and/or glue layer. It is a measure of the reproducibility of the SSS method.

(b) Length differences in slices from different sandwich types (average difference 0.1mm, Fig. 8(b)). This is due to the number of masks painted in each sandwich type. Not all needles have masks painted on them; consequently the parent sandwich of such needle will yield shorter slices compared to another sandwich type providing the adjacent slice for the same PSSDA. This is a source of systematic error of the SSS method.

(c) Slices show vertical slant (average top-bottom difference 0.15mm, Fig. 8(c)). All masks are painted closer to the patient end of the PSSDA; with nothing on the PMT end to make up for this extra thickness; slices can tilt. Inadequate sliding constrains of the compression pieces in the gluing jig allowed this displacement of the slices.

(d) Axial and trans-axial dimensions of square blocks are not equal (average difference 0.07mm Fig. 8(d)). This is due to the fact that equal force was applied by the compression pieces of the gluing jig to the side of a sandwich (50x18mm^2 surface – axial direction), and to the side of slice (19x18mm^2 surface – trans-axial direction). Therefore, the pressure difference results in glue layers of different thickness.

The typical thickness measured of the paint plus glue layer between crystals was 0.06 mm.

Overall, the four factors described above combined with the inter-crystal gap produced PSSDAs with the following dimensions: 7x7 array – 18.97x19.12x18.1mm^3; 7x8array – 19.13x24.85x18.1mm^3; 8x8array – 25.48x25.39x18.1mm^3. The variance of these dimensions are all under $\sigma^2=(0.09mm)^2$; and they are all within 98.5% to 99.8% of the intended target values.

The very small gap between crystals results in a 98% linear detector packing fraction (96% in area). Compared with the typical 90% linear packing fraction (81% in area) in commercial systems [10], the 96/81 (1.2x) higher detector-packing density would provide a 1.2-1.44 times higher coincidence detection sensitivity in PET.

The solidly glued blocks are very robust. Note the excellent mechanical tolerance of the block produced by this slab-based production method (Fig. 4 bottom-right).

C. 2D map decoding and energy spectra

Ultimately, we must evaluate the crystal decoding capability of PSSDAs built with the SSS method. Figure 9 presents two-dimensional decoding map and block's composite energy spectrum for the three types of arrays built for the prototype camera HOTPET. Energy resolution for these blocks is: 7x7-array = 25.6%; 7x8-extended-array = 29%; and for the 8x8-corner-array = 31%.

A detailed study of crystal signal characterization of the square-7x7 and extended-7x8 arrays can be found in ref [11].

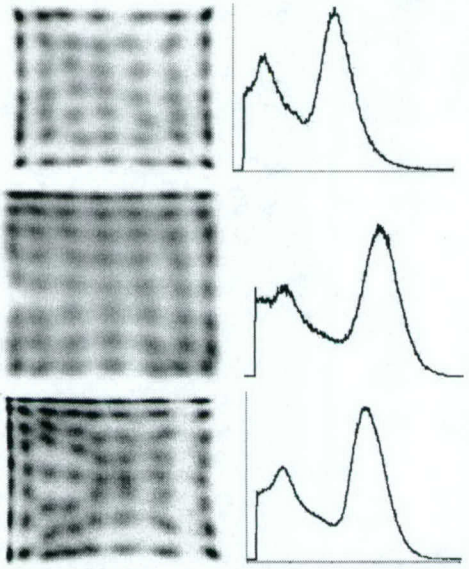

Fig. 9. Two-dimensional decoding map and composite energy spectra of all needles from the three types of PSSDA used in HOTPET (Fig. 2). (top) 7x7 symmetric array, (middle) 7x8 extended non-symmetric array, (bottom) 8x8 optically-non-symmetric array used for the module's corners.

IV. CONCLUSIONS

- The Slab-Sandwich-Slice "SSS" production method for position sensitive scintillator detector arrays (PSSDA) has been developed and evaluated by building 720 PSSDA (40,000 crystals) for a high-resolution PET camera HOTPET
- SSS utilizes painted reflecting barriers on the crystal surfaces to precisely control the scintillation-light distribution allowing shaped-optical-windows of any shape. It optimized crystal identification of gammas hitting the PSSDA; improving intrinsic detector resolution. Construction of non-symmetric PSSDA was possible thanks to these versatile light barriers; minimizing the unused PMT potocathode area left by PMT-quadrant sharing detector technology.
- Instead of working with each individual crystal needle, the SSS method handles only arrays (sandwich, slices) of needles, making the production of PSSDAs 8 times more efficient; and because the raw material is purchased in large slabs, many needles long, it cuts material cost by 50%.
- The average crystal-positioning error was very small ($\sigma <$ 0.09mm), which is essential for ultrahigh resolution detector. Sources of positioning error were tied to four mechanical variations in the PSSDA construction method.
- The gap between crystals was only 0.06mm, giving these PSSDAs extremely good linear packing fraction (98%, 96% area) and the coincidence efficiency (92%) is 1.4 times higher than commercial cameras.
- The SSS method was found easy to implement, flexible, and can be applied to detector arrays of any material.
- Two patents titled "A Production Method for Making Position Sensitive Radiation Detector Arrays" and "Asymmetrically Placed Cross-coupled Scintillation crystals" (U.S. patent office, Feb/2002), describe the SSS method.

V. REFERENCES

[1] W-H. Wong, J. Uribe, H. Baghaei, H. Li, Y. Wang, M. Aykac, Y. Liu, "Design of a Whole-body High Resolution PET with Changeable Transaxial and Axial Fields of View". Society of Nuclear Medicine 48th Annual Meeting, Toronto, Canada, June 23-27, 2001.

[2] W-H. Wong, J. Uribe, H. Li, H. Baghaei, Y. Wang, M. Aykac, Y. Liu, T. Xing, "The Design of a High Resolution Transformable Wholebody PET Camera". Accepted for publication IEEE Trans. Nucl. Sci. October, 2002.

[3] W-H. Wong,, "A positron camera detector design with cross coupled scintillators and quadrant sharing photomultipliers," *IEEE Trans. Nucl. Sci.*, vol 40, pp. 962-966, 1993.

[4] W-H. Wong, S. Yokoyama, J. Uribe, et al, "An elongated position sensitive block detector design using the PMT quadrant sharing detector array," *IEEE Trans. Nucl. Sci.*, vol 46(3), pp. 542-545, 1999.

[5] J Uribe, H. Baghaei, H. Li, et al, "Basic imaging performance characteristics of a variable field of view PET using quadrant sharing detectors," *IEEE Trans. Nucl. Sci.*, vol 46, no.6, pp. 491-497, 1999.

[6] Institute of Inorganic Chemistry, Siberian Branch, Russian Academy of Science 3, Acad.Lavrentyev Prospect, 630090 Novosibirsk, Russia.

[7] Lasercraft Inc. 3300 Coffey Ln. Santa Rosa, CA 95403-1917.

[8] FASSON ® Crack 'N peel Satin Litho, #316, pressure sensitive stock. Avery Dennison Corp. 150 North Orange Grove Blvd. Pasadena, CA 91103-3596.

[9] BC-620 reflector paint. SaintGobain, Newbury, OH 44065.

[10] S.R. Cherry, H.P. Tornai, C.S. Levin, S. Siegel, E.J. Hoffman, "A comparison of PET detector modules employing rectangular and round photomultiplier tubes," *IEEE Trans. Nucl. Sci.*, Vol. 42, no 4 pp. 1064 –1068, Aug. 1995.

[11] J. Uribe, H. Li, Y. Liu, T. Xing, H. Baghaei, Y. Wang, Rocio Farrell, W-H. Wong,"Signal Characteristics of Individual Crystals in a High Resolution BGO Detector Design Using PMT-Quadrant Sharing", conference proceedings IEEE, Nuclear Science and Medical Imaging conference, Norfolk, VA, November, 2002.

A HOTLink/Networked PC Data Acquisition and Image Reconstruction System for a High Resolution Whole-Body PET with Respiratory or ECG-Gated Performance

Hongdi Li, Tao Xing, Yaqiang Liu, Yu Wang, Hossain Baghaei, Jorge Uribe, Rocio Farrell, Wai-Hoi Wong

Abstract--**An ultra high resolution PET camera in whole-body scanning or gated imaging study needs super computer-processing power for creating a huge sinogram as well as doing image reconstruction. A real-time HOTLink attached to networked cluster personal computers (PC) has been developed for this special purpose. In general, the coincidence data from a PET camera is unidirectional; therefore an additional daisy-chain bus using high speed HOTLink (400Mbit/s, Cypress Semiconductor, inc.) transmitters and receivers is designed to carry the coincidence data to networked (LAN) computers (PCs). In whole-body scanning, each PC will acquire sinogram data for one bed position, the data from HOTLink is interfaced to a PC through a fast PCI I/O board (80Mbyte/s); and after completion of data acquisition the PC begins to reconstruct the image meanwhile another PC will start data acquisition for the next bed position. The overall architecture for the image acquisition and reconstruction computing system is a pipeline design. The image result from one PC will be sent to a master computer for final tabulation and storage through the standard network, and this PC will be free for processing a new bed position. In gated respiratory or gated ECG imaging study, each PC will be reconfigured for processing a specified time-section image of a respiratory or ECG cycle. We are developing a high resolution PET camera with 38,016 BGO crystal elements which needs 1 to 2 gigabytes sinogram memory; the HOTLink/networked structure design allows us to split the huge sinogram into several PCs in real-time and the image reconstruction can be done in parallel.**

I. INTRODUCTION

WE have introduced a high resolution clinical PET camera with the PMT-Quadrant-Sharing modular detector design [1]. The high resolution PET camera doing a whole-body multiple bed position scanning will generate a huge sinogram data and need a long time for image reconstruction. Respiratory-gating or motion-tracking are also demanded in high resolution PET study. The electrocardiogram-gated (ECG-gated) imaging method allows assessment of regional myocardial perfusion and evaluation of ventricular wall motion. The paper presents a method of implementation a fast data acquisition and image reconstruction computer system for a high resolution PET camera.

With the availability of inexpensive high power PC-based computing, many of data acquisition and image reconstruction have been moving to PC based model. A data acquisition system with networked cluster PC structure will be widely accepted. We want to use the networked PC cluster design for both real-time PET data acquisition and image reconstruction purpose. The standard PC networking has a problem with real-time broadcasting and it is not easy to be integrated into the frond-end electronics without a special micro-processor involved. Since the coincidence data generated by a PET camera is unidirectional (from camera to computing system), we implemented another special fast bus attached to the standard networked computers for broadcasting the coincidence data to the entire networked PCs. This daisy-chain fast fiber optical or twisted pair serial bus is based on 400Mbit/s HOTLink transmitter and receiver (Cypress Semiconductor Inc.). Both the HOTLink transmitter and receiver are 32 pins and have a CMOS/TTL logic compatible interface, and further more no special protocol is demanded for this additional bus. Hence, it is very easy to integrate the HOTLink components to front-end electronics. Each PC can real time grab the data from the serial bus as demanded. A master PC can order a slave PC to do a special task through the standard LAN. For example, to split a huge sinogram memory, the master PC will send a message to each slave PC through the TCP/IP to specify a sub-sinogram that each slave PC should deal with.

II. METHODS

A. Why HOTLink?

A high sensitivity and high resolution PET camera may generate 32-to-64-bit width parallel coincidence data with a

This work was supported in part by NIH under Grant RO1 CA76246, RO1 CA61880, RO1 CA58980 and RO1 EB001038, by Texas Higher Education Advanced Technology (ARP/ATP) Grant No. 003657-0058-2001, the J.S. Dunn Research Foundation, the Cobb Endowment for Cancer Research.

Hongdi Li, Tao Xing, Yaqiang Liu, Yu Wang, Hossain Baghaei, Jorge Uribe, Rocio Farrell and Wai-Hoi Wong are with the University of Texas M.D. Anderson Cancer Center, Houston, TX 77030 USA (H. Li's telephone: 713-745-3732, e-mail: hli@di.mdacc.tmc.edu).

0-7803-7636-6/03/$17.00 ©2003 IEEE.

rate up to 10 million coincidence events per second. Operation this high speed parallel bus over significant distances can be problematic due to signal distortion, skew, and crosstalk. These effects can lead to loss of data and failure of the bus.

As system speeds increase, serial interfaces are often used to extend the high performance of a parallel interface well beyond the distances possible in parallel link. By only sending a single signal (though sending each bit much faster) both the signal-to-signal and signal-to-clock skew limits are removed. HOTLink (Cypress Semiconductor inc.) makes it easy and economical to move the same data over a high-speed serial connection using fiber-optic or twisted cables [2, 3].

Figure 1 shows a serial link design using HOTLink (transmitter CY7B923 and receiver CY7B933, [4]) for moving streams of 8-bit parallel bytes from one location to another. HOTLink offers a built-in standard 8B/10B encoder/decoder and PLL (Phase Locked Loop) based clock and data recovery circuits. These 8-bit data characters are encoded into 10-bit transmission characters and the 10-bit characters are sent serially across a link. At the receiving end of this link these serial bits are grouped together to 10 bits at a time (framed), and decoded back into their equivalent 8-bit data characters. 256 special 10-bit characters selected from the entire 1024 characters map to the 256 valid 8-bit input data characters. HOTLink also provides 12 valid special codes as different command codes. The synchronize character and violation symbol (RVS) are two of these special codes.

In a sum, HOTLink is almost protocol-free for fast serial communication and has a COMS/TTL compatible interface, which can be easily integrated in an application system. And it also reserves about 10 special codes that you can use as commands in serial communications. In addition, serializing a parallel bus allows for operation of the bus over extended distance. The reduced bus width also makes it practical to pass the data through a simple slip-ring in a PET camera with CT function.

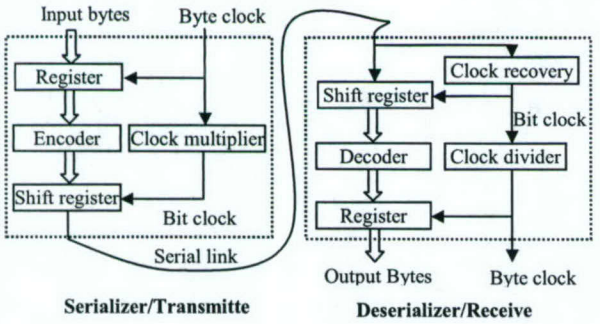

Figure 1: HOTLink architecture

B. *Whole-body scanning*

A clinical PET camera usually needs to scan 5-to-8 bed positions in a whole-body mode. For our high resolution PET camera with 38016 crystals and 5184 sinograms, we estimated the reconstruction time of 15 minutes for 2D and 250 minutes for 3D filtered back-projection (FBP) for each bed position using a single 2.8 GHz personal computer. It is very time consuming, about one to two reconstruction hours is required even for 2D FBP for 5-8 bed positions in whole-body scanning.

Since the coincidence data from a PET camera is always unidirectional, a fast serial bus is very suitable to carry the data to the acquisition computer. We have designed a data acquisition and image reconstruction system based on a fast HOTLink (400 Mbit/s) daisy-chain bus combined with a standard local area network (LAN) consists of 6-8 personal computers (PCs), see figure 2. One PC will function as the master (server) computer, and the others will be functioning as the slave (client) computers. The communication between the master and the other 5-7 slave PCs is established through standard LAN using TCP/IP. The server has a large hard disk that will be used to store the raw data as well as the reconstructed images. Each slave PC has 1-2 gigabytes memory of its own for binning the sinogram data of one bed position in real time.

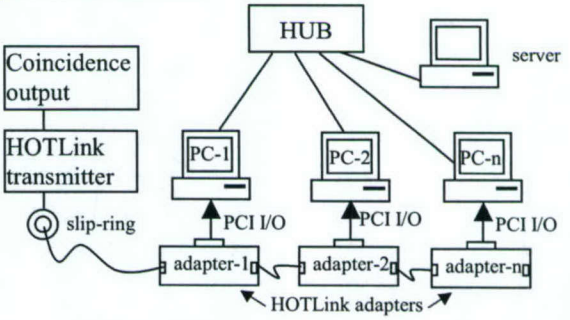

Figure 2: Architecture of HOTLink/Networked computers

After the completion of the sinogram acquisition for one bed position, the sinogram for the just completed bed position will be used by the same slave PC in the network for image reconstruction. The image result from each slave PC will be sent to the master PC for final tabulation and storage. The overall architecture for the image acquisition and reconstruction computing system is a pipeline design. In this pipeline design, one PC will be used to reconstruct the image of one bed position. In scanning the first bed position, the first client PC (PC-1) will be instructed by the server to grab the data from the HOTLink daisy-chain bus. After scanning the first bed position, PC-1 will reconstruct the image of this bed position. In scanning the second bed position, PC-2 will grab the data from the HOTLink bus and after scanning the second bed position, PC-2 will reconstruct the image of this second bed position while PC-1 may be still working on the first bed position. If a whole-body scan takes 8 bed positions, up to a maximum of 8 reconstruction PCs will be needed. However, if the reconstruction time of each bed position is equal to the scanning time of 5 bed positions, then only 5 PC will be needed, because PC-1 can be used for processing bed position-1 and bed position-6. We choose this multi-PC design instead of a typical SUN/HP workstation-based design using 1-2 high power workstations because the PC system is more flexible and cheaper. Furthermore, performance of a PC-based system can be improved more frequently, cheaply, and compatibly.

C. *Respiratory/ECG-gated imaging*

In pulmonary nodules PET imaging, respiratory motion produces lesion blurring and an apparent increase in lesion size. This results in a decrease in the activity concentration per pixel within the lesion and an underestimation of SUV. Improved measurement of lesion volume and quantification of FDG uptake can be achieved with respiratory gated PET imaging [5]. In cardiac nuclear imaging, ECG-gating not only provides added information about global and regional left ventricular and right ventricular function, enhancing its prognostic value, but also helps to differentiate real defects from attenuation artifacts [6].

Recently most of the gated high resolution PET imaging is performed under list-mode only. Time-marks, generated by a respiratory or ECG sensor, are inserted into the coincidence data stream and recorded in list-mode. Each respiratory or ECG cycle is divided into many time-fames as demanded. And time-framed sinogram-binning as well as image reconstruction will be performed after the data acquisition is finished.

The HOTLink/networked PC structure designed for whole-body scan discussed earlier can also be used for real-time gated PET imaging. For example, each ECG period is divided into, say, 6 time-frames; and each slave computer is configured to process one specified time-framed sinogram binning and the image reconstruction as well. The front-end electronics generates 25 milliseconds free-running timing-ticks attached to the coincidence data stream and broadcasting to the networked PCs through the HOTLink serial link. Each slave PC has two memory buffers organized in ping-pong mode for recording the list-data from two most recent ECG cycles. The list-data will be sorted by time-frames; and only a specified frame will be processed in one PC, the data from rest frames will be discarded by this PC. If the total number of time-ticks in one ECG cycle is too long or too short that means an irregular ECG cycle has happened, and the entire list-data buffer for that ECG cycle will be removed. The time-frames real time data acquisition and image processing method can also be used for respiratory-gated imaging. However, since the respiratory cycle is more regular and slower than ECG cycle and patients can be further trained to have a regular cycle [7], therefore we can predict the next respiratory period accurately by linear-fitting several measured previous cycles. With a predicable cycle time, the time-frame number can be generated ahead/real-time. The respiratory-frame numbers are also attached to the coincidence data stream. And a slave PC can process time-framed sinogram binning immediately without ping-pong buffering the list-data of the entire cycle as used in ECG-gating method mentioned above. If both the cardiac and respiratory gating is needed simultaneously, the maximum time-frame number for ECG and respiratory gating are limited to four. A maximum of 16 client PCs are needed (since ECG and respiratory signals are not synchronized, there are total 16 combinations of the ECG and respiratory time-frames); however, if one slave PC can store 2 time-framed sinograms, then only 8 slave computers are needed.

III. Results and Discussion

A. *Sending coincidence data using HOTLink transmitter*

There are two independent coincidence outputs in our coincidence system for the clinical high resolution PET camera, one is for true coincidence and the other is for random coincidence [8]. The coincidence board passes through 64bits signals of the pre-normalized Anger-position and energy of the pair-events; and another processing board will convert them into crystal and slice information by using lookup tables. Both the total/true and random coincidence data after the lookup-table-processing will become 32-bits (gamma-1 position: 7bits slice1, 6bits crystal1; gamma-2 position: 7bits slice2, 6bits crystal2; and 6bits coincidence bank-pair number). The 32bits true and random coincidence data are first shifted into a 2k x 8-bits FIFO (first-in-first-out memory) individually. If a half-full flag of one FIFO is detected, that FIFO output will be switched to a HOTLink transmitter through a multiplexer, see figure 3. A selected HOTLink command identifying a total/true or random buffer will be sent first and then immediately followed by the coincidence data with a half buffer size of that FIFO. In other words, the HOTLink command is a buffer-head indicating all the following data with half of FIFO length will be either true or random events. Hence, the two coincidence outputs are simply merged and sent to a fast serial bus using a HOTLink (400Mbits/s, CY7B923) transmitter.

In the coincidence data format of our prototype MDAPET camera, one bit is used to identify true or random event, and the data acquisition software has to check that bit for every event. In this design, the software only needs to check the buffer-head once and then processes the buffer continuously. Another big advantage is that the coincidence data are still limited within 32bits (33bits were necessary if followed the MDAPET data format) which simplified the interface design for 32bit PC data I/O.

The gate signals from ECG and respiratory sensors are also connected to the processing board. The time-frame numbers or timing-ticks can be real-time inserted into the HOTLink data stream for further processing.

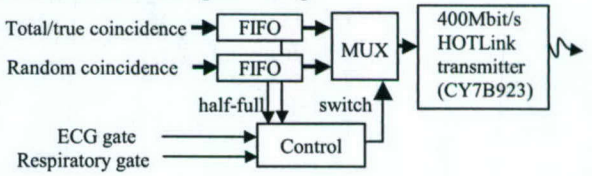

Figure 3: Sending coincidence data with HOTLink transmitter

B. *PC HOTLink adapter*

A custom-constructed PC HOTLink adapter has been developed to receive coincidence HOTLink serial data from the front-end using a HOTLink receiver CY7B933 and the received data are interfaced to a fast 32-bit PCI I/O board (National Instrument PCI-6534 [9]) inside each slave PC. Meanwhile the same fast serial data is feed back into another HOTLink transmitter on the adapter board passing the data to the next adapter board as well as the next slave PC. Thus, a fast daisy-chain serial bus is formed among these adapters for

real-time broadcasting the coincidence data to the entire slave PC cluster at a rate 400Mbit/sec. This serial bus can carry up to 10 million coincidence events per second, which is good enough for a high efficient PET camera. Figure 4 shows the design of HOTLink daisy-chain bus, data from the serial link are deserialized first and then will be interfaced to a PCI bus, meanwhile the deserialied data will be serializered again and sent to next adapter through the onboard HOTLink transmitter. In fact, the deserializer and serializer act as an active serial bus driver, thus the entire link quality is not limited by the number of adapters inside the daisy-chain. The twisted copper cable between two boards can be as long as 100 feet. By disabling/blocking the input deserialized data, a slave PC is able to send data from its memory to the serial link output, so that data from one slave PC can be moved to next slave PC very fast.

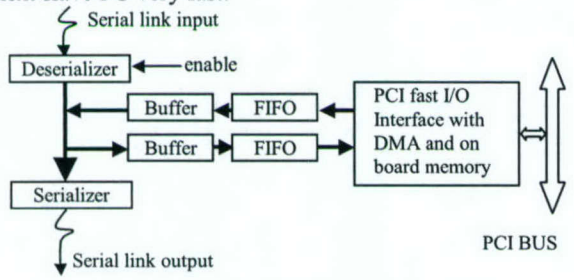

Figure 4: PCI HOTLink daisy-chain serial bus

Figure 5 and 6 shows HOTLink adapter-board design for the PCI-6534 (National Instrument) fast PCI I/O board. The adapter-board can be initialized by the PCI-6534 through standard I/O and the data communication between them is achieved by pattern I/O [9]. The PCI-6534 board has a 64Mbyte onboard memory working as first-in-first-out mode, data can be written into the memory as fast as 80Mbytes/sec. The adapter-board can be initialized for different modes: HOTLink self-testing mode for checking the link quality, PC data receiving mode for data acquisition, PC transferring mode for fast communication between PCs, and sinogram real-time selection mode for splitting a huge sinogram into several PCs. Two gate-signal inputs are reserved for some special purposes such as the position signals of a rotating rod for the acquisition of transmission imaging. The entire logic is implemented by one Altera programmable logic device EPM7256SQC208.

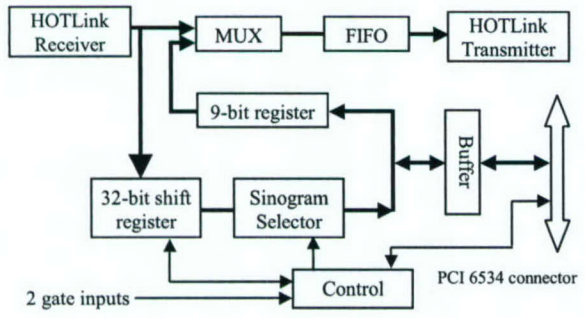

Figure 5: PCI-6534 HOTLink adapter design

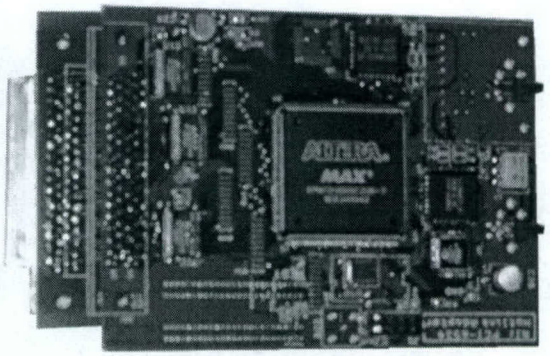

Figure 6: Photograph of HOTLink adapter

Since the output of the HOTLink receiver is an 8-bit data plus 1 bit data/command flag, however the coincidence data in our PET system are 32bits, therefore an 8-to-32bit shifter register is needed. Synchronization for data shift-processing should be carefully designed. Without the synchronization an error happened in the shifter, such as an extra shift operation triggered by a noise, might kill the entire rest of the data. We use the HOTLink commands, such as the selected true/random buffer-head command or the ECG/respiratory start command, to alignment/synchronize the 32bit coincidence data so that one error may only kill a maximum of one buffer size (half length of the FIFO in the front-end processing board).

A normally HOTLink system rarely experiences one error per hour (a bit error rate of $1x10^{-12} \approx$ 1error/hour @ 266 Mbaud) [10]. When the receiver detects an error in the sequence of received transmission code (an error that corrupts a single bit), it asserts a RVS signal during the character-decoding-time following the error. Single-bit errors can cause changes in the data stream running disparity. In extreme cases, where the errors cause PLL cycle-slipping or loss of framing, the received stream will never match. A special circuit has been developed to automatically disconnect and reconnect the input signal continuously until the endless running error stops by checking the status of the RVS signal. Our data showed the system could be recovered no more than 100ms.

Another important application of the HOTLink adapter is for splitting a huge sinogram into several slave PC clusters; and the image reconstruction algorithm can apply to those sub-sinograms individually. The reconstructed sub-image results from the slave PCs are integrated together in a master computer for further processing. Thus by using the HOTLink network design, we not only can handle the huge sinogram, but also can speed up the image reconstruction in a way of parallel processing.

The sinogram selector in figure 5 is designed for this special purpose mentioned above. Two registers which can be initialized by a slave PC define a range for a "slice-difference" window, so that if the difference of two slice numbers identified by the coincidence-gamma events is belonged to that window, the coincidence event will be accepted by this slave PC. In other words, the "slice-difference" window specifies the sub-sinograms that should assigned to this slave PC. The reconstruction algorithm

requires every slave PC to keep the directory sinograms (slice difference = 0) used for parallel processing. Since the HOTLink is broadcasting the coincidence data, every slave PC can real-time pickup those events that belong to the direct sinograms or to the specified sub-sinograms defined by the "slice-difference" window. This parallel processing method has been proved by using two slave computers in our prototype MDAPET camera we have developed [11, 12].

IV. CONCLUSIONS

We have developed a high speed HOTLink (400Mbit/s) serial bus that can broadcast the 32bit coincidence data of a PET camera to local networked computers. Using HOTLink for serializing bus is very simple, no additional protocol is demanded and it can be easily integrated into the front-end electronics. The HOTLink/networked PC cluster design is very suitable for online pipeline data acquisition and image reconstruction for an ultra-high resolution PET camera doing whole-body multiple bed position scanning and respiratory/ECG gating study. By using this design, a huge sinogram real-time binning can also be achieved by the slave PC cluster. The pipeline data acquisition and image reconstruction performance will increase the throughput of patient scan.

The HOTLink/networked PC data acquisition has been successfully used in our prototype MDAPET camera to replace the VME data acquisition system. Our VME data acquisition system is aged, slow and further more it is no longer supported by the manufacturer.

The prototype HOTLink adapter combined with the National Instrument fast I/O board (PCI-6534) has strongly demonstrated the real-time processing power for PET study. A PCI HOTLink network board merging the functions of HOTLink and the fast PCI I/O will be designed in future.

V. REFERENCES

[1] W.H. Wong, "The design of a high resolution transformable whole body PET camera," *IEEE Trans. Nucl. Sci.,* vol. 49(5), October, 2002.

[2] "HOTLink Design Considerations", application notes in the HOTLink User's Guide, Cypress Semiconductor Co.

[3] "Use HOTLink for 9- and 10-Bit Data", application notes for the HOTLink, Cypress Semiconductor Co.

[4] Datasheets for CY7B923, CY7B933, Cypress Semiconductor Co.

[5] Nehmeh SA, et al. "Effect of respiratory gating on quantifying PET images of lung cancer". J Nucl Med 2002; 43: 876-881

[6] Germano G, Erel J, Lewin H, et al. "Automatic quantification of regional myocardial wall motion and thickening from gated technetium-99m sestamibi myocardial perfusion single photon emission computed tomography," J Am Coll Cardiol 30: 1360-1367, 1997

[7] Sadek Nehmeh, Yusuf Eridi, Clifton Ling, et al. "Effect of respiratory gating on quantifying PET images of lung cancer", *The Journal of Nuclear Medicine*, vol. 43, No.7, pp. 876-881, July 2002.

[8] Y. Wang, et al, "A modular low dead-time coincidence system for high resolution PET cameras," *Conference record of the 2002 IEEE MIC Conference.*

[9] User guide for PCI-6534, National Instrument

[10] "HOTLink built-in self-test (BIST)", application notes for the HOTLink, Cypress Semiconductor Co.

[11] W.H. Wong, J. Uribe, W. Lu, K. Hicks, "Design of a variable filed prototype PET camera," *IEEE Trans. Nucl. Sci.,* vol. 36, pp. 1915-1920, June 1996.

[12] J. Uribe, H. Baghaei, H. Li, S. Yokoyama, N. Zhang, J. Wang, F. Dobbs, W.H. Wong, "Basic imaging characteristics of a variable field of view PET camera using quadrant sharing detector design," *IEEE Trans. Nucl. Sci.,* vol. 46, pp. 491-497, June 1999.

A Comparison of Four Image Reconstruction Algorithms for Detection of Small Lesions in Brain Phantom

H. Baghaei, *Member, IEEE,* W.-H. Wong, *Member, IEEE,* J. Uribe, *Member, IEEE,* H. Li, *Member, IEEE,* Y. Wang, *Member, IEEE,* Y. Liu, T. Xing, R. Ramirez, S. Xie, and S. Kim

***Abstract*--We compared two fully three-dimensional (3-D) image reconstruction algorithms and two 3-D rebinning algorithms followed by reconstruction with a two-dimensional (2-D) filtered backprojection algorithm. The two 3-D image reconstruction algorithms were ordered subsets expectation maximization (3D-OSEM) and 3-D reprojection (3DRP). The two rebinning algorithms were Fourier rebinning (FORE) and single slice rebinning (SSRB). The 3-D projection data used for this work were acquired with a high-resolution PET scanner (MDAPET) with an intrinsic transaxial resolution of 2.8 mm. The scanner has 14 detector rings covering an axial field-of-view of 38.5 mm. We scanned three phantoms: (1) a uniform cylindrical phantom with inner diameter of 20.5 cm, (2) a 11.5-cm cylindrical phantom with four embedded small lesions with diameters of 3, 4, 5, and 6 mm, and (3) the 3-D Hoffman brain phantom with three embedded small lesion phantoms with diameters of 3, 5, and 8.6 mm. We evaluated the different reconstruction methods by comparing the noise variance of images, contrast recovery and contrast-noise trade-off, lesion detectability, and by visually inspecting images. We found that overall the 3D-OSEM algorithm followed by post filtering produced the best results. Even though the MDAPET camera has a relatively small maximum axial acceptance (±5 deg), the 3DRP algorithm produced slightly better images compared to the faster 2-D rebinning methods.**

I. Introduction

THERE dimensional (3-D) positron emission tomography (PET) data acquisition, which allows for the measurement of coincidences between all possible pair of detectors, leads to a significant improvement in scanner sensitivity that can improve statistical accuracy in images for a given acquisition time. To fully utilize the image-improving potential of the 3-D projection data, it is necessary to use a fully 3-D reconstruction technique. A major problem is that fully 3-D image reconstruction is very time consuming and so not practical for routine clinical application. As a more practical approach, the 3-D projection data can be rebinned into 2-D sinograms and then a 2-D image reconstruction method can be used to significantly reduce the computing time. However, due to the approximate nature of the rebinning methods, it could also degrade the image quality. In this work, we evaluated the relative performance of a 3-D filtered back-projection algorithm [1], a 3-D iterative method, ordered subsets expectation maximization (3D- OSEM) [2,3], and two rebinning methods, the single slice rebinning (SSRB) [4] and Fourier rebinning (FORE) [5]. The rebinned data were then reconstructed with the standard 2-D filtered backprojection (2D-FBP) method.

This work was supported in part by the NIH-CA58980 PHS Grant, NIH-CA61880 PHS Grant, NIH-CA76246 PHS Grant, NIH-CA58980S PHS Grant, NIH-EB01481 PHS Grant, NIH-EB00217 PHS Grant, NIH-EB01038 PHS Grant, U.S. Army-Breast Cancer Research Grant, Texas ARP/ATP Grant 003657-0058-2001.

H. Baghaei, W.-H. Wong , J. Uribe, H. Li, Y. Wang, Y. Liu, T. Xing, R. Ramirez, S. Xie, and S. Kim, are with the University of Texas M. D. Anderson Cancer Center, Houston, TX 77030 USA (H. Baghaei's telephone: 713-794-5270, e-mail: hbaghaei @di.mdacc.tmc.edu).

II. Materials and Methods

A. Data Acquisition

The performance of the algorithms was evaluated by reconstructing three data sets acquired from the scan of three phantoms: (1) a uniform cylindrical phantom with internal diameter of 20.5 cm, (2) a 11.5-cm cylindrical phantom with four embedded small lesion phantoms having diameters of 3, 4, 5, and 6 mm, and (3) the 3-D Hoffman brain phantom [6] with three embedded small lesion phantoms with diameter of 3, 5 and 8.6 mm. All phantoms were placed collinearly with the scanner axis.

We used the high-resolution MDAPET, a prototype 3D-PET camera, to scan the phantoms. This camera is a multi-ring scanner with an intrinsic transaxial resolution of 2.8 mm. It has 14 detector rings covering an axial field-of-view of 3.85 cm. Each ring consists of 448 small bismuth germanate (BGO) crystals having an in-plane and axial crystal pitch of 2.66 and 2.80 mm, respectively. This prototype PET camera has several modes of operations; we took the current data in the brain mode. In brain mode, the camera has a ring diameter of 44 cm and patient opening of 32 cm with a maximum axial acceptance angle of ±5 deg. The detector module design, which is based on the quadrant-sharing technique, the electronics of the camera, and the imaging performance characteristics of the camera have been previously described [7-13].

All data were acquired in 3-D mode with the axial acceptance of 13 rings, which produced 196 sinograms. In the present study, each sinogram had 239 radial bins and 180 azimuthal views, and no axial or transaxial compression was

0-7803-8257-9/04/$20.00 © 2004 IEEE.

performed on projection data. The radial sampling was 1.385 mm. The camera allows simultaneous imaging of 27 transaxial slices with 1.4 mm thickness.

Prior to 3-D image reconstruction and rebinning, projection data were corrected. These corrections were for random coincidence, attenuation, geometric and detector pair efficiency [14]. The sinograms for random (accidental) coincidence events were measured using a second delayed coincidence window and then subtracted from the sinograms measured in the prompt window. Attenuation correction was calculated assuming a uniform attenuation coefficient. No scatter correction was applied.

B. *Reconstruction Algorithms*

For the fully 3-D filtered backprojection reconstruction, we used an implementation of the 3D-reprojection (3DRP) method of Kinahan and Rogers [1]. The 3DRP algorithm incorporates a preliminary step in which projections that are partially measured in the 3-D data acquisition, because of the truncated cylindrical geometry of the scanner, are completed. This step is done by forward projection of an initial low statistics image obtained from the reconstruction of the sinograms with ring differences of 0 or ±1. The calculated forward projected data are less noisy than their measured counterparts and show some loss in spatial resolution [15]. The two-dimensional filter was defined as the product of the 2-D filter derived by Colsher [16] and the Hamming low-pass apodization function [17]. The reconstruction incorporates ring differences up to 13 and so utilizes all 196 sinograms.

For the fully 3-D iterative method, we utilized an implementation of the ordered subsets expectation maximization (3D-OSEM) algorithm that was developed by the PARPET project [18, 19]. The software was modified to include the sinogram parameters and specific geometry of the MDAPET camera. We also post-filtered the reconstructed images using a Gaussian or a Metz filter with a full-width half maximum of 4 mm.

A simple way to rebin 3-D data into 2-D sinograms is the single-slice rebinning method [4]. In this method the oblique lines of response are included in the sinogram midway between the two rings involved. Each transaxial plane is then reconstructed independently with a 2-D algorithm. This method is fast but also introduces distortions in the scanner's point-spread function. Axial blurring occurs for activity not located near the axial axis of the camera which becomes more severe as the distance from the axis increases.

The FORE algorithm is based on an approximation of the exact Fourier rebinning formula, derived from the frequency-distance relation. The MDAPET implementation of the FORE algorithm is based on software developed by Defrise *et al.* [5], modified to include the sinogram parameters and specific geometry of the MDAPET camera.

For both rebinning methods, all 196 measured sinograms, corresponding to maximum ring difference of 13, were rebinned into 27 planes and then reconstructed with a standard 2-D filtered backprojection method.

III. Results

A. *Noise Variance*

For comparison of the noise level in the images reconstructed with different techniques, we calculated the coefficient of variation (CV) by using data acquired from the scan of the 20.5-cm uniform cylindrical phantom. The total number of true+scatter counts collected was about 110 million. CV was measured by computing σ/μ, in which σ and μ are the standard deviation and mean value over a region of interest, respectively. We used a circular region of interest with a radius of 70 pixels (about 9.7 cm).

The coefficient of variation for slice number 2 and number 13 versus the filter cutoff frequency is shown in Fig. 1 for 3DRP and rebinning methods. For a cutoff frequency around 0.7 of Nyquist, all three methods had about the same CV. The CV for 3DRP algorithm showed relatively less sensitivity to change in cutoff frequency for both image planes. In Fig. 2 the CV is plotted as a function of number of sub-iterations for plain 3D-OSEM and for post-filtered images. One full iteration was nine sub-iterations.

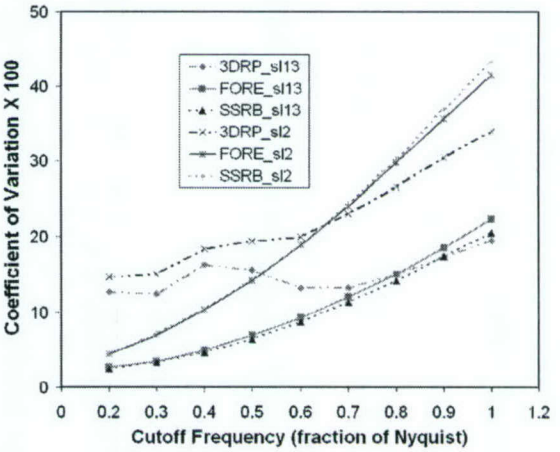

Fig. 1. CV for an edge slice (slice no. 2) and a central slice (slice no. 13) as a function of the cutoff frequency. The lines simply connect the points.

In Fig. 3 the coefficient of variation for each of the 27 image slices is shown for 3DRP and rebinning methods. We used a Hamming filter with a cutoff frequency of 0.7 of Nyquist. For all methods, the increase in noise variance seen in the edge planes, compared to the central planes, was expected because of the reduced sensitivity in planes at the edge of the axial field-of-view. For images obtained with rebinning techniques and 2D-FBP reconstruction, compared to 3DRP images, the CV was higher for slices near the edge and slightly smaller for slices near the center. The CV for FORE method, which was between the 3DRP and SSRB methods, was closer to the SSRB result.

B. *Contrast Recovery*

For comparison of the contrast recovery (CR) we used data acquired from a scan of the 11.5-cm cylindrical phantom with

four embedded small lesion phantoms. The sizes of the embedded lesion phantoms were 3, 4, 5, and 6 mm, and all of them had the same standard uptake value (SUV). The lesions were placed at the central slices (i.e., near the center of the camera axial-field-of-view) at a distance of 2 cm from the axial axis. The cylinder was uniformly filled with lower density activity, forming a warm background.

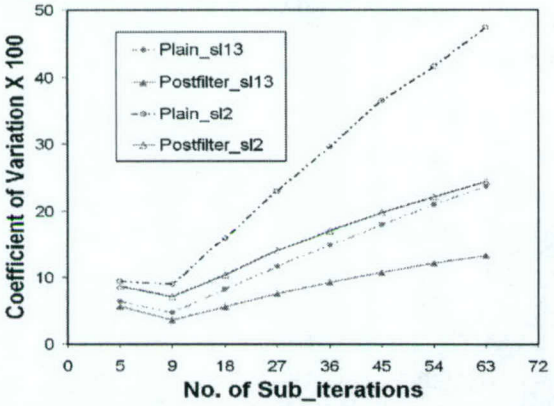

Fig. 2. Similar to Fig. 1, but for plain 3D-OSEM and post-filtered images. The lines simply connect the points.

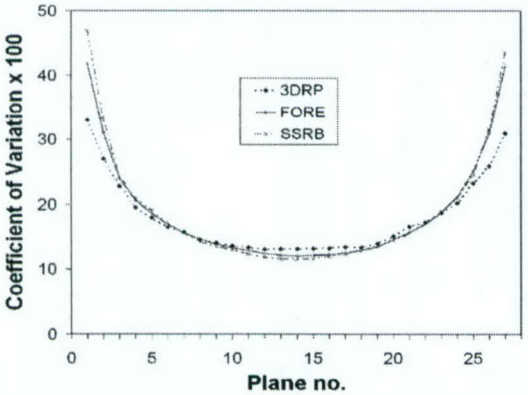

Fig. 3. Coefficient of variation plotted as a function of slice number for filtered backprojection methods. The lines simply connect the points.

A reconstructed image of central slice of the warm cylinder with four hot lesions, for each of the four different methods, is shown in Fig. 4. The activity ratio was chosen such that the smallest 3-mm lesion was barely observable for fully 3-D reconstruction. The 3D-OSEM image was post-filtered with a Metz filter with power of 1 after four full iterations [21].

The contrast recovery for the hot regions (small lesions) surrounded by a warm background was defined as (S-B)/B, where S and B are the average counts in a region of interest of the hot lesion and background, respectively. For the 6 mm lesion, the extracted contrast as a function of the cutoff frequency is shown in Fig. 5 for filtered backprojection methods. The images obtained with 3DRP algorithm had higher contrast recovery. The CR was not extracted for the other lesions since their smaller sizes made defining the region of interest in a consistent way more difficult and we found the results to be less reliable.

Fig. 6 shows the contrast-noise trade-off for a central slice. The CR values were extracted for the 6 mm lesion, and the CV values obtained from the warm background. A horizontal profile running through the middle of the 6 mm and 4 mm lesions, for the image slice presented in Fig. 4, is plotted in Figs. 7 and 8. For filtered backprojection methods, the cutoff frequency was 0.7. For 3D-OSEM method, the image was obtained for four full iterations and was post-filtered with a Metz filter. The profile data for each image was normalized accordingly to the average counts in the background in each case. The peak to background ratio was higher for the 3DRP than for rebinning methods and the FWHM was smaller for 3DRP. Images reconstructed with 3D-OSEM algorithm showed the highest contrast.

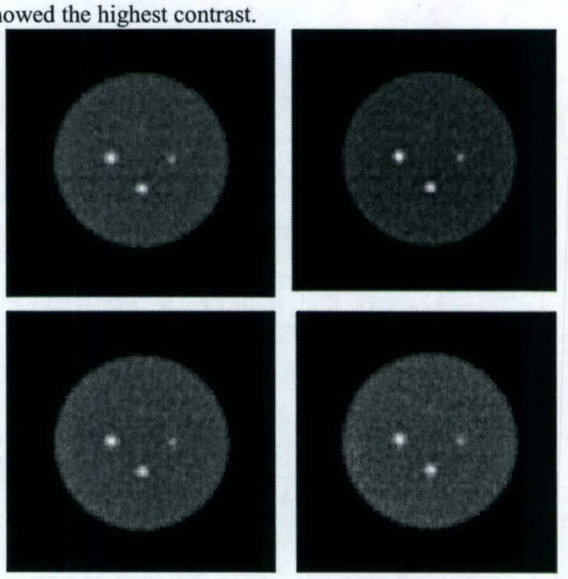

Fig. 4. Image of a central slice of the cylindrical phantom with four small lesions reconstructed with (top left) 3DRP, (top right) 3D-OSEM, (bottom left) SSRB+2D-FBP, and (bottom right) FORE+2D-FBP. For FBP methods a Hamming filter with cutoff frequency of 0.7 was used. The OSEM image was post-filtered with a Metz filter after four full iterations.

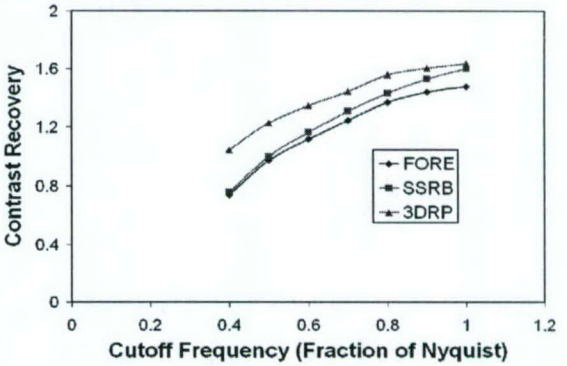

Fig. 5. Contrast recovery for the 6 mm lesion using the Hamming apodization function as a function of the cutoff frequency. The lines simply connect the points.

C. *Brain Lesion Detectability*

Fig. 9 shows for four reconstruction methods a reconstructed image slice (slice no. 14) of the Hoffman brain phantom with the 5 mm embedded lesion when the ratio of

activity concentration in the lesion to background (gray matter) was 5.4. Fig. 10 shows a reconstructed image slice (slice no. 4) with 8.6 mm lesion when the activity concentration in the lesions to the background was 1.46. In order to improve visualization of smaller lesions, the 8.6 mm lesion phantom was placed such that it did not appear in the same slices as the others.

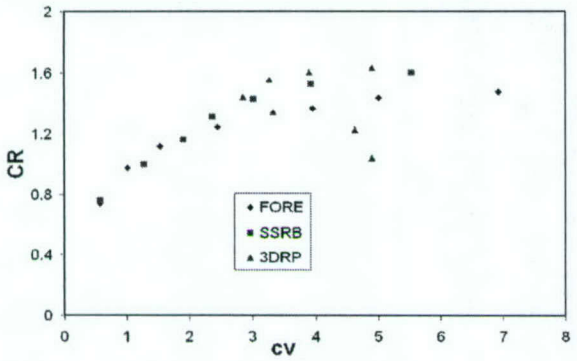

Fig. 6. The contrast-noise trade-off for the 6 mm lesion.

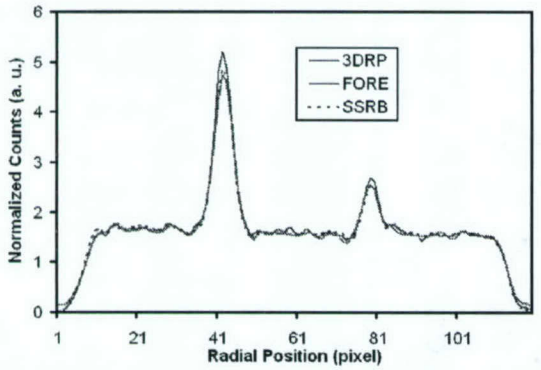

Fig. 7. A horizontal profile running along the middle of the image presented in Fig. 4 for activity ratio of 6. The peak in the left (right) corresponds to the 6 mm (4 mm) lesion. The image was reconstructed with 3DRP, FORE+2D-FBP, and SSRB+2D FBP methods.

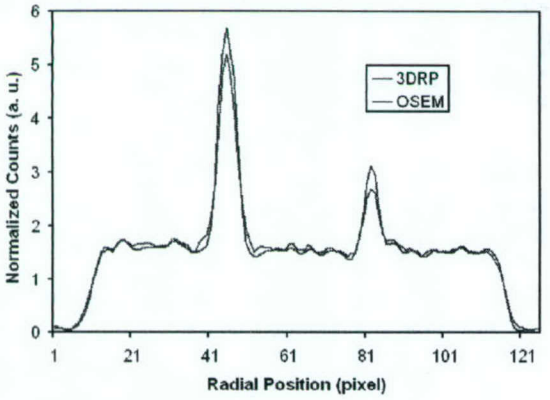

Fig. 8. Similar to Fig. 7, but for 3DRP and 3D- OSEM algorithms.

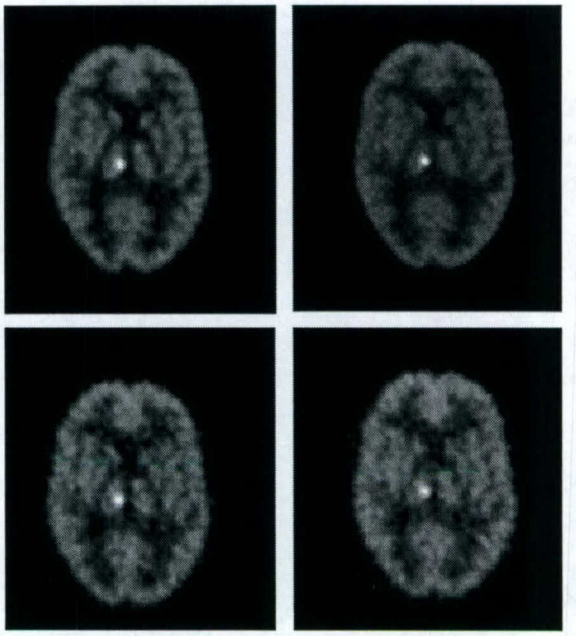

Fig. 9. An image slice (slice no. 14) of the Hoffman brain phantom with 5 mm lesion reconstructed with the (top left) 3DRP algorithm, (top right) 3D-OSEM + post filtering, (bottom left) SSRB + 2D-FBP, and (bottom right) with FORE + 2D-FBP. The ratio of the activity concentration in the lesion to background was 5.4.

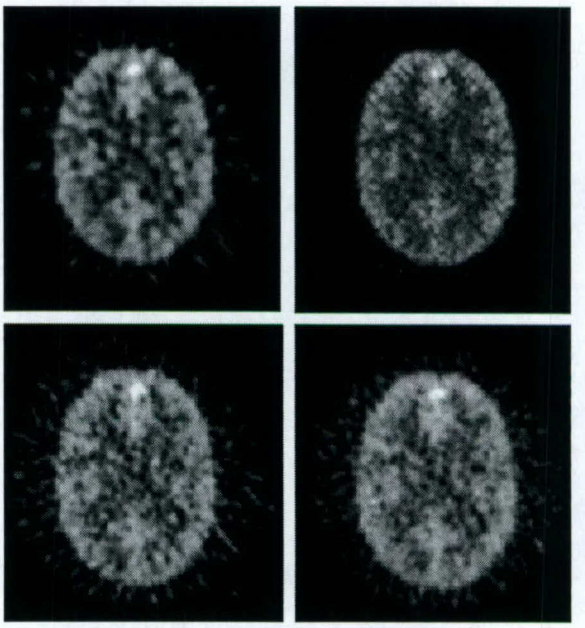

Fig. 10. An image slice (slice no. 4) of the Hoffman brain phantom with 8.6 mm lesion reconstructed with the (top left) 3DRP algorithm, (top right) 3D OSEM + post filtering, (bottom left) SSRB + 2D-FBP, and (bottom right) with FORE + 2D-FBP. The ratio of the activity concentration in the lesion to background was 1.46.

Visual comparison of the images did not show any significant differences between different reconstruction techniques in terms of lesion detectability. However, the images obtained with fully 3-D reconstruction algorithms,

especially for the 3D-OSEM+post-filttered method, looked less noisy; this effect was clearer for the 8.6 mm lesion image (plane no. 4). For further evaluation we compared the profiles of the images. Fig. 11 shows the normalized horizontal profiles running through the middle of the images of the 5-mm lesion in warm background when the ratio of the activity in the hot lesion to the warm background was 5.4.

The profile figures showed that the ratio of the peak (lesion activity) to the background (gray matter) was slightly higher for the 3-D methods and highest for 3D-OSEM. The profile for the FORE+2D-FBP, which was close to the profile for the SSRB+2D-FBP, is not shown.

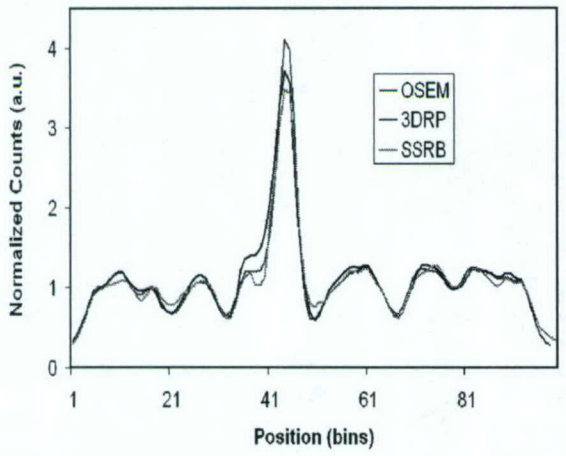

Fig. 11. A horizontal profile running along the middle of the slice presented in Fig. 8. The peak in the center corresponds to 5 mm lesion.

IV. Conclusions

We evaluated the performance of two fully 3-D reconstruction algorithms and two rebinning methods followed by 2-D image reconstruction. Methods were evaluated by comparison of the noise level in images, contrast recovery and lesion detectability and also by visual inspection of the reconstructed images. We found that the 3D-OSEM algorithm, when followed by post filtering, produced the best results. The 3DRP algorithm produced better images compared to the faster 3-D rebinning methods. We did not observe any significant differences, in lesion detectability, between the results of SSRB and FORE algorithms which were perhaps due to the relatively small axial acceptance (±5 deg) of the MDAPET camera.

V. Acknowledgment

The authors would like to thank the personnel of the clinical PET center of the University of Texas M. D. Anderson Cancer Center for their support in providing the FDG used for this work.

VI. References

[1] P. E Kinahan, J. G. Rogers, "Analytic 3D Image Reconstruction Using all Detected Events," *IEEE Trans. Nucl. Sci.*, vol. 46 pp.964-968, 1989.

[2] L. A. Shepp, and Y. Vardi, "Maximum likelihood reconstruction for emission tomography," *IEEE Trans. Med. Imag.*, vol. MI-1, pp. 113-122, October 1982.

[3] H. M. Hudson, and R. S. Larkin, "Accelerated image reconstruction using ordered subsets of projection data," *IEEE Trans. Nucl. Sci.*, vol. 13, no. 4, pp. 601-609, Dec. 1994.

[4] M. E. Daube-Witherspoon and G. Muehllehner, "Treatment of Axial Data in Three-Dimensional PET," *J. Nucl. Med.*, vol. 28, pp. 1717-1724, 1987.

[5] M. Defrise, P. E Kinahan, D.W. Townsend, C. Michel, M. Sibomana, and D.F. Newport, "Exact and Approximation Rebinning Algorithms for 3-D PET Data," *IEEE Trans. on Nucl. Sci.*, vol. 16, pp. 145-158. 1997.

[6] E. J. Hoffman, P. D. Cutler. W. M. Digby, and J. C. Mazziotta, "3-D phantom to simulate cerebral blood flow and metabolic images for PET," *IEEE Trans. Nucl. Sci.*, vol. 37, no. 2, pp. 616-620, April 1990.

[7] W.-H. Wong, "A positron camera detector design with cross-coupled scintillators and quadrant sharing photomultipliers," *IEEE Trans. Nucl. Sci*, vol. 40, pp.962-966, August 1993.

[8] W-H. Wong, J. Uribe, W. Lu, and K. Hicks, "Design of a variable field prototype PET Camera," *IEEE Trans. Nucl. Sci.*, vol. 43, pp. 1915-1920, June 1996.

[9] W-H. Wong, J. Uribe, K. Hicks, and M. Zambelli, "A 2-dimensional detector decoding study on BGO arrays with quadrant sharing photomultipliers," *IEEE Trans. Nucl. Sci.*, vol. 41, pp. 1453-1457, June 1994.

[10] W-H. Wong, G. Hu, N. Zhang, J. Uribe, J. Wang, H. Li, H. Baghaei, and S. Yokoyama, "Front end electronics for a variable field PET camera using the PMT-quadrant-sharing detector array design," *IEEE Trans. Nucl. Sci.*, vol. 44, pp. 1266-1270, June 1997.

[11] H. Li, W-H Wong, N. Zhang, J. Wang, J. Uribe, H. Baghaei, and S. Yokoyama, "Prototype electronics for a variable field of view PET camera using the PMT-quadrant-sharing detector array," *IEEE Trans. Nucl. Sci.*, vol. 46, pp. 546-550, June 1999.

[12] J. Uribe, H. Baghaei, H. Li, S. Yokoyama, N. Zhang, J. Wang, F. Dobbs, and W-H. Wong, "Basic imaging characteristics of a variable field of view PET camera using quadrant sharing detector design," *IEEE Trans. Nucl. Sci.*, vol. 46, pp. 491-497, June 1999.

[13] H. Baghaei, W-H. Wong, J. Uribe, H. Li, N. Zhang, and Y. Wang, "Breast cancer studies with a variable field of view PET camera," *IEEE Trans. Nucl. Sci.*, vol. 47, pp. 1080-1084, June 2000.

[14] H. Baghaei, W-H. Wong, J. Uribe, H. Li, N. Zhang, and J. Wang, "The correction factors for a high resolution variable field of view PET camera," *J. Nucl. Med.*, vol. 40, p.279P, May 1999.

[15] S. R. Cherry, M. Dahlborn, and E. J. Hoffman, "Evaluation of a 3D reconstruction algorithm for multi-slice PET scanners," *Phys. Med. Biol.*, vol. 37, pp. 779-790, 1992.

[16] J.G. Colsher, "Fully three-dimensional positron emission tomography," *Phys. Med. Biol.*, vol. 25, pp. 103-115, 1980.

[17] H. Baghaei, W-H. Wong, H. Li, J. Uribe, Y. Wang, M. Aykac, Y. Liu, T. Xing, and, "Evaluation of the effect of filtering apodization for volume PET imaging using the 3DRP algorithm," *IEEE Trans. Nucl. Sci.*, vol. 50, pp. 3-8, February 2003.

[18] M. Jacobson, R. Levkovitz, A. Ben-Tal, K. Thielemans, T. Spinks, D. Belluzzo, E. Pagani, V. Bettiardi, M. C. Gilardi, A. Zverovich, and G. Mitrai, "Enhanced 3D PET OSEM reconstruction using inter-update Metz filtering," *Phys. Med. Biol.*, vol. 45, pp. 2417-2439, 2000.

[19] C. Labbe, K. Thielemans, H. Zaidi, and C. Morel, "An object-oriented library incorporating efficient projection/backprojection operators for volume reconstruction in 3D PET," Proc. 1999 Int. meeting on fully three-dimensional image reconstruction in radiology and nuclear medicine, pp. 137-140, 1999.

[20] H. Baghaei, W-H. Wong, H. Li, J. Uribe, Y. Wang, M. Aykac, Y. Liu, T. Xing, and, "Evaluation of the effect of filtering apodization for volume PET imaging using the 3DRP algorithm," *IEEE Trans. Nucl. Sci.*, vol. 49, pp.2381-2386, October 2002.

An Instantaneous Photomultiplier Gain Calibration Method for PET or Gamma Camera Detectors Using an LED Network

Hongdi Li, *Member, IEEE*, Yaqiang Liu, Tao Xing, Yu Wang, *Member, IEEE,* Jorge Uribe, *Member, IEEE,* Hossain Baghaei, *Member, IEEE*, Shuping Xie, Soonseok Kim, Rocio Ramirez, Wai-Hoi Wong, *Member, IEEE*

Abstract—**In current clinical positron emission tomography (PET) cameras, there are about 1000 photomultiplier tubes (PMTs) in the detector system. Even a less-complicated gamma camera has many dozens of PMTs. Image quality and resolution of a camera is dependent on the proper equalization of all the PMT gains. However, a PMT gain can change with many environmental factors, such as room temperature, patient load, short-term or long-term radiation exposure, and time. Hence, an instantaneous automated PMT gain calibration method is especially important for an ultrahigh-resolution PET camera. We have developed a new PMT gain auto-tuning method using a blue light-emitting diode (LED) network. Each LED shines directly into the center of a scintillation crystal block from the PMT side, and the light is collected by the surrounding PMTs. The effects of crystal optical transferring efficiency and PMT optical coupling efficiency have been considered. The calibration is done by changing the gains of these surrounding PMTs or their following amplifiers to have the same signal output. An LED has well known problems of large light-yield varieties and is very sensitive to temperature. To overcome these problems, the light outputs of two neighboring LEDs are aligned first by a shared PMT. Each LED flashes individually and is driven by a 250 KHz pulse generator. At such a high pulse rate, the data acquisition for the gain calibration can be finished within a very short time so the LED temperature effect can be ignored. The amount of LED light output is set as close as possible to the amount of scintillation light by programming the width or height of the pulses; therefore, the same system electronics can be used for both purposes. Our proposed high-resolution whole-body PET camera with 924 PMTs in a PMT-quadrant-sharing (PQS) design can be calibrated in 1 minutes or less.**

I. INTRODUCTION

PET scans are very expensive; currently, some patient scans may cost $4,000. It is important to provide the highest quality image for such an expensive study and to provide the best patient care. A higher-resolution PET camera usually has a larger number of decodable crystals per photomultiplier tube (PMT), requiring each PMT gain to be more stable. Long-term PMT stability and decoding-resolution studies have been conducted, and it was found that there was a long-term ambient PMT-gain variation (5-10% in 100 days) that could be recovered by a system-wide tuning every few weeks or months in current commercial PET or gamma cameras. It typically takes many hours (a long down time for a clinical camera) to re-tune the whole system. The studies also found a short-term PMT gain variation due to changes in temperature and the level of radiation exposure in the last few hours that was as large as or even larger than the long-term variations in 100 days [1], [2]. This short-term variation cannot be overcome by retuning every few weeks or months. On our prototype MDAPET camera, which has 216 PMTs [3], the gain calibration takes many hours using conventional photo-peak pulse-height tuning. For our proposed clinical PET with 924 PMTs [4], that method is very tedious and time-consuming.

We developed a new instantaneous LED auto-tuning method that allows 1000 PMTs to be calibrated in 1 minute or less meaning that a PET camera can always be in the best condition for each patient scan. This ultra-fast PMT calibration method can also improve the quality of a mobile PET. As the location or orientation of a mobile PET changes, PMT gains affected by the Earth's magnetic field cannot be ignored, and a system-wide retuning is necessary. This new method can immediately realign the PMT gains for a mobile PET at a new location.

Using LEDs to calibrate PMT gains is not a new idea. However, all LEDs have 2 problems that prevent them from being used directly for PMT calibration/tuning for PET cameras: (1) the light output can vary by more than 2 times between different LEDs, even though the driving signals are identical, so it is not possible to directly generate an equal light level from each LED inside the detector head for calibration purposes, and (2) LED light output is very sensitive to the environment's temperature, and different LEDs respond differently to temperature. These two problems limit its applications. We used an LED network to solve these problems: light outputs from two neighboring LEDs can be aligned by one common PMT; and an LED light is shared by a cluster of PMTs, and the light is used only as a reference level for aligning the PMT gains. Once the critical light-output variation problem is solved, the LED can be used for very fast PMT tuning because it can easily be force-trigged 10 times faster than in a traditional gamma-ray detection method.

This work is support in part by the NIH-CA58980 PHS Grant, NIH-CA61880 PHS Grant, NIH-CA76246 PHS Grant, NIH-CA58980S PHS Grant, NIH-EB01481 PHS Grant, NIH-EB00217 PHS Grant, NIH-EB01038 PHS Grant, U.S. Army-Breast Cancer Research Grant, Texas ARP/ATP Grant 003657-0058-2001.

H. Li, Y. Liu, T. Xing, Y. Wang, J. Uribe, H. Baghaei, S. Xie, S. Kim, R. Ramirez and W.-H. Wong are with the Department of Experimental Diagnostic Imaging, University of Texas M.D. Anderson Cancer Center, Houston, TX 77030 USA (H. Li's telephone: 713-745-3732, e-mail: hli@di.mdacc.tmc.edu).

0-7803-8257-9/04/$20.00 © 2004 IEEE.

II. METHODS

A. Detector calibration method using LED

Fig. 1 shows a new detector configuration that could eliminate the LED weakness. In this basic unit, one LED is physically placed in an empty space at the center of a PMT cluster. The LED light shines directly into the central crystal from the PMT side (with no light leaking to the PMT's sidewall), reflecting inside the crystal block, and is collected by the surrounding PMTs. For most scintillation detectors, only a true-blue LED (or whatever true-color LED is close to the color of the scintillation light) will be used for matching the photo-characteristics of the PMT and scintillation crystals. LED light simulates the scintillation events hitting the central crystal. Physically, the LED light spot always marks the central crystal, and by decoding the LED signals with the surrounding PMTs, we can get the location of the central crystal. Since the LED light shines directly into the crystal and goes through the same path as the scintillation light, the LED signal output from a PMT already includes the effects of the crystal optical transferring efficiency and the PMT optical coupling efficiency. (An optical grease/glue is used to optically couple the crystals to the PMT, so there may be air bubbles in the coupling that reduce optical efficiency.) Therefore, by aligning the PMT outputs to the same value, we not only tune the PMT gains but also balance these optical effects.

Fig. 1: An LED at the center of a cluster of PMTs is used to tune a scintillation detector regardless of the temperature sensitivity of its light output.

As long as all the surrounding PMTs generate the same amount of light (photo-peak) from the LED, by adjusting either the gains of the PMTs directly or the gains of their following amplifiers, this detector unit is well balanced, and the location of the LED light spot (identifying the central crystal) is put at the center of the decoding map.

Since the LED light is shared by its surrounding PMTs, if the LED light output increases, all the PMT outputs will increase. In other words, the LED light is only used as a reference for aligning the PMT outputs, regardless of the amount of light yielded by the LED, which could be affected by temperature. Suppose the total gain for a signal channel is G; and G_{PMT} and G_{VGA} are the gains of the PMT and VGA, respectively; and G_{OPT} is the optical coupling efficiency. Then we have

$$G = G_{PMT} \times G_{VGA} \times G_{OPT} \qquad (1).$$

And if L is the light output from an LED (number of photoelectrons collected by the PMT) and V is the LED signal amplitude after VGA. The light output (L) is very sensitive to temperature for each LED, but if 2 PMT channels share the same LED light, the ratio of the two L signals (the number of photons going to PMT 1 divided by the number of photons going to PMT 2) will be independent of temperature and time. In equation (2), the optical coupling efficiency (G_{OPT}) is also a time constant; hence, the PMT gains can be equalized by changing only the gain of the VGA (G_{VGA}) to get the same photo-peak for the LED signal.

$$\frac{V_1}{V_2} = \frac{G_{PMT\,1}}{G_{PMT\,2}} \times \frac{G_{VGA\,1}}{G_{VGA\,2}} \times \frac{G_{OPT\,1}}{G_{OPT\,2}} \times \frac{L_1}{L_2} \qquad (2)$$

This PMT tuning mechanism can be extended to a larger detector system. In Fig. 2, detector 2 extends from the side of detector 1, sharing PMTs B and E, while detector 3 extends diagonally and shares only PMT F with detector 1. Suppose detector 1 has already been tuned by its LED using the above method. To tune detector 2, first change its LED pulse width or pulse height to yield the same light output (a reference) in the shared PMT B as given by detector 1, and then align the outputs of PMTs A and D to the reference value by adjusting the PMT or amplifier gains. In fact, PMT B is a cross reference for detector 1 and 2 in aligning the LED light outputs and PMT gains. In Fig. 2, PMT F also is a cross reference for aligning detector 3 with detector 1.

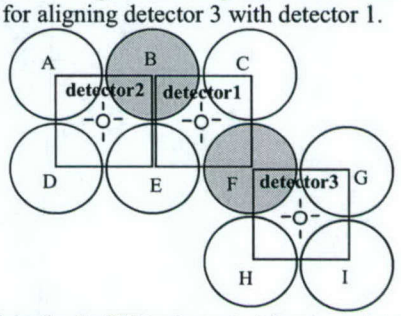

Fig. 2: Extending the LED tuning method for a larger detector design.

Fig. 3 shows our proposed PQS detector module integrated with the LED network for automatic detector calibration. Each LED can be powered ON individually, and the LED driving pulse width can be programmed to adjust its light output. In this design, it is not necessary to have one LED in every scintillation block, but every PMT is able to be tuned by at least one LED, and at least one shared PMT can be found to collect and align the amount of light emitted from two neighboring LEDs.

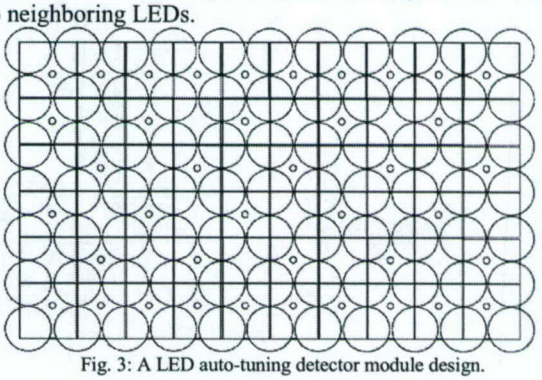

Fig. 3: A LED auto-tuning detector module design.

B. LED Configuration

To better simulate the scintillation light, the LED wavelength should be as close as possible to that of the scintillation light; for example, the wavelength of BGO scintillation light is about 480 nm, so we can choose a true-green or true-blue LED for calibration purposes.

Normally, an LED will yield many more photons than the scintillation light, which means an LED gives a much higher PMT output than a gamma event. To avoid overloading the electronics, the traditional method requires a special circuit to process the LED signal, increasing the cost and size of the electronics. Our design does not require any additional data acquisition electronics for the LED signal. Instead, we limit the number of LED photons injected into the crystal block and match the number of photons as closely as possible to those produced by the scintillation light. Two methods are used to reduce the number of photons shooting into the crystals. The first involves driving the LED by electrical pulses with very small pulse widths. To emit the light, different LEDs may require different minimum pulse widths. To further limit the light output, each LED is forced to work in the non linear range; the driving pulse changes from high (on) to low (off) before the LED reaches its stable maximum light output range. In our system, the pulse width can be computer programmed from 100 ns to 800 ns with a resolution of < 1 ns. With this adjustable pulse width range, the electrical pulses can drive the LEDs with as much as a 5X difference in light output efficiency. The second method involves using a small-hole light collimator to reject most of the photons and to focus the light onto the center part of the scintillation block. (See the structure in Fig. 4.) The LED housing and light collimator are located inside the PMT holder made of black delrin. Alternative design is leaving the LED outside and using an optical fiber to carry the light to the central part of the scintillation block. By limiting the LED light output, we can still use the same data acquisition electronics (preamplifier, integrator, A/D converter, etc.) in detector calibration.

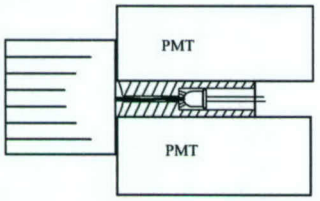

Fig. 4: A true-blue LED is placed inside the PMT holder, and the light is collimated for detector calibration.

Unlike the real scintillation signal generated in the scintillation crystals by gamma rays, the LED light has a much slower rise edge. Hence, the fast triggering circuit for the gamma signal cannot be used to trigger or detect the LED signal correctly. Fortunately, since the LED light is driven by an on-board pulsing circuit, we can use the same pulser to directly trigger the signal integration and digitization (processing) of the LED signal synchronously, bypassing the original fast triggering and gating circuit for gamma events.

Since the LED signal is processed by the same original gamma-ray decoding electronics, turning on multiple LEDs synchronously will result in pile-up in the decoding circuit. Hence, in a detector with a front-end analog Anger-weighted electronics design, only one LED at a time is allowed to be turned on, and all the LEDs can share one pulse-generating circuit (see Fig. 5) to simply the design and minimize the cost. The electronic components for the automatic LED calibration in our proposed PET detector model (Fig. 3) cost less than US $100. Each LED requires a different pulse width, and even for a given LED the pulse width may vary as the temperature changes; therefore, the pulse width will be calibrated online before a gain calibration starts.

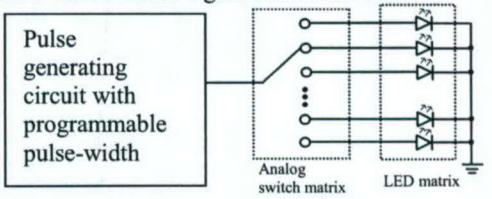

Fig. 5: Only one computer-programmable pulse generator is needed to drive the LED network.

III. Results

A. 2D crystal decoding map tuned with an LED

Fig.7 compares the crystal decoding maps before and after tuning by an LED. The LED was turned on for a short period after the crystal decoding map had been acquired with a gamma source; the LED map and crystal map were overlapped. The LED map was well centered in the tuned decoding map.

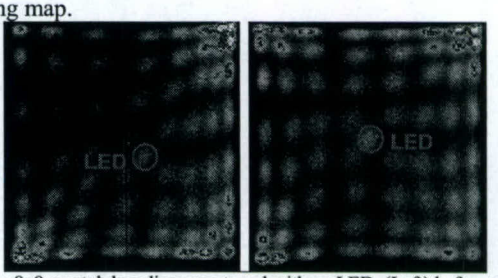

Fig. 6: An 8x8 crystal decoding map tuned with an LED. (Left) before tuning the LED map was not centered; (right) the LED map was centered after tuned.

B. Fast LED tuning

The LED network detector design can overcome typical LED difficulties, and once the critical light-output variation problem is solved, aligning the PMT gains can be very fast because of two important attributes: higher pulse rates and a Gaussian light output distribution. Fig. 7 shows a measured pulse-height distribution spectrum (PHS) of gamma and LED energy.

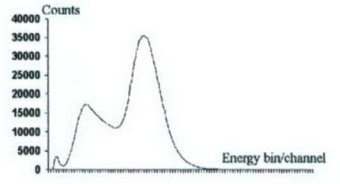

Fig. 7a: Gamma pulse-height distribution spectrum (PHS).

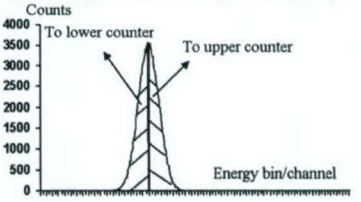

Fig. 7b: LED pulse-height distribution spectrum (PHS).

The PHS of an LED is a narrow symmetrical Gaussian distribution about the mean energy, without the low-energy scatter events of a gamma-counting PHS; this Gaussian distribution is caused statistical variations in the LED light output. To find the LED photo-peak (mean value of PHS), all the LED pulses are counted; however, in the gamma-ray PHS, the scatter events are useless for finding its photo-peak. Furthermore, since the LED pulses fall into fewer bins than the gamma-events, fewer total counts are required to find the LED photo-peak. Thus, it will be at least 10 times faster to locate an LED photo-peak than to locate a gamma-ray photo-peak.

An LED can be pulsed at a much higher repletion rate than the detection rate of the traditional gamma-ray detection-tuning method. In our study, the LED was pulsed at a rate of 250 KHz. In some advanced commercial detector-tuning methods, many PMTs can be calibrated at the same time with a uniform flood gamma source, but the LED pulsing rate still can be at least 2times faster than the total gamma-event rate.

C. *Parallel tuning method*

Aided by the Gaussian symmetric energy distribution of the LED, we have developed a new method with only a few electronic components for tuning the LED peak to a target location. The energy of each LED pulse is compared with a target LED peak value, and the low-energy events are counted into a lower counter and the high-energy events are counted into an upper-counter (Fig. 6b). Since all the events are summed into as few as 2 bins (2 counters), it gives better statistics and requires less time to get a VGA gain adjustment direction (high or low) than the peak-location method using the maximum number of counts. As long as one counter is full, the number of the other counter will be compared with a threshold (reference count), and if the number is over the threshold, meaning the numbers in the 2 counters are close enough, the tuning is done. Otherwise, if the lower counter is bellow the threshold (the 2 counters are not balanced), the gain is too high and the VGA gain needs to be decreased. On the other hand, if the upper counter is bellow the threshold, the VGA gain needs be higher. After setting a new VGA gain, the above 2 counters will be cleared, and the 2-counting measurement will be restarted. Hence, this simple continuous comparison of the two counters will guide the gain auto-adjustment of the VGA until both counters have a balanced number of events.

The upper counter, lower counter and digital comparators can be easily built into existing front-end electronics such as a FPGA or EPLD in every detector module, and only 2 bit output signals are required to identify all the four states: wait for the first full flag, VGA needs a lower gain, VGA needs a higher gain, and the tuning is satisfied. Since the 2 bit status signal changes only after one counter is full, the status changing rate is very slow (few hundred Hertz). Therefore, the status can be read out through a computer parallel port, which already has been used to initialize the PET camera.

To use the computer parallel port for tuning, bypassing all the coincidence procedures is very important for online detector calibration. The data acquisition computer cannot get the single LED energy information after the digital coincidence circuit (there is no coincidence between modules for LEDs at all) unless they are reconfigured for this special tuning purpose. With this technique, a module-based PET camera can be tuned in parallel. After initializing the LED and VGA in the sequence of modules, all the 2-counter peak-detection circuits start working individually, and the status of the 2-counter for every module is read out one by one through the parallel port. Since most of the tuning time is to collect the LED pulses by the 2 counters, paralleling this procedure will dramatically cut the total calibration time. Our study shows that tuning a 12 module camera with this parallel tuning method takes about the same time as tuning one module detector.

To further increase its flexibility, we have developed an interface board using a wireless microprocessor (CC1010 from Chipcon, Inc.) to drive the parallel port. This board will be mounted on the gantry and rotated with the camera; it will also reduce the number of wires going through a sleeping ring in a CT-PET camera.

However, in the conventional nuclear-counting method, the tuning electronics are much more complicated. In an asymmetric gamma-ray PHS, a full energy spectrum with more than 100 bins (in random-access memory) is needed, and a micro-processor is also involved to build a histogram of the events and to search for the photo-peak.

Therefore, in summary, with performance 10 times faster in LED photo-peak locating, 2times faster in the pulsing rate, and 12 times faster in parallel tuning, our LED automatic tuning method is a total of 240 times faster than the traditional gamma-ray detection tuning method. A system tuning for a 1000 PMT PET camera takes less than 1 minute. Repeating the calibration procedure many times, we found that the tuning was very stable and repeatable and the equalization could be achieved with errors of $< 1\%$.

IV. Discussion

There is a hidden hurdle in this PMT equalization method that needs to be overcome. Generally, because of geometric asymmetries, the sensitivity response of a PMT is not uniform across the entrance optical window (photocathode); the sensitivity difference can be as large as 20% [5]. In a PQS detector, only one quarter of a PMT is used for block decoding, and each of the 4 quadrants of the entrance window will have a different sensitivity or gain. This variability should be considered in designing the real-time LED light-output alignment method. A lower-sensitivity quarter will tune the VGA gain higher, while a higher-sensitivity quarter will set the VGA gain lower, even though the two adjacent LEDs have the same light output. To measure the regional sensitivity variations in each PMT, all the PMTs in the whole detector module or system should be equalized the first time (and only once) by the traditional nuclear photo-peak pulse-height matching technique. The nuclear counting equalization or an iterative energy-centroid method [6] is performed using the VGA connected to the output of each PMT. Each VGA can be addressed and its gain controlled by the data acquisition computer until the preset equalization conditions are met. After the PMTs are balanced by the traditional nuclear-counting or energy-centroid method, a few crystals situated inside each quarter of the shared PMT are selected,

0-7803-8257-9/04/$20.00 © 2004 IEEE.

and the average photo-peak pulse-height of those crystals indicates the sensitivity of the quarter. With these data, a lookup-table is created in the data acquisition computer to store the measured sensitivity of each quadrant of the PMTs. This lookup table is temperature independent, because the regional sensitivity is defined mainly by the mechanical architecture and is not affected by the temperature. The quadrant-sensitivity lookup table will be used to generate a correction factor to the real-time LED light-output alignment control for all subsequent LED tuning. The above initialization tuning (to set up the permanent PMT quadrant lookup table) would take a few hours, much like the current PMT tuning methods in commercial PET, but subsequent tunings with the LED method would take only 1 minute.

In the proposed module design, all the edge blocks are elongated. More than a quarter of the edge PMTs are involved in the elongated block decoding, which means the edge PMTs will collect more LED light than the inner PMTs. Therefore, the gain balance for the edge PMTs also needs to compensate for this overestimated LED peak. The effect of the elongated block is a similar to that of the PMT non-uniformity regional sensitivities in PMT gain tuning and can be recorded in a lookup table. Hence, only one lookup table for a detector module will be generated after the detector is assembled, and it will include the effects of both the asymmetric position of the edge PMTs and the PMTs' non-uniformity sensitivities.

What we have discussed is a method of adjusting the gain of each PMT channel (a PMT and its following amplifier) so that all PMT channels will provide the same output amplitude. However, there is another equalization issue: what should be the output amplitude for all the PMTs? There should be an optimal range or value for all the PMT channels. In the traditional equalization process using a radioisotope, the known gamma-ray energy of the reference radioisotope is used as the reference, and all the PMT channels are equalized to produce the same signal amplitude for the characteristic/reference gamma ray used.

In our LED tuning method, we only need one energy reference to calibrate the output amplitude of one PMT in each detector module, and the calibration of the rest of the PMTs is still performed by the LED automatic tuning method. Hence, only 12 PMTs (one for each module) need to be calibrated by the traditional nuclear-counting or energy-centroid method in the entire camera, and this can be done very quickly. We can use a standard radioisotope or even the gamma-ray reference source obtained from a patient who has been injected with a radiotracer before imaging (during the patient positioning period). Another simple method is to select a PMT with the most stable gain from the previous equalization record/log file. This PMT could be used as a reference to keep the same VGA gain as in the previous tuning. All the other PMT channels are then equalized to this reference channel by using the LED tuning technique. After all the PMTs are calibrated, a follow-up gain-change statistical analysis will be performed automatically. If it turns out that most of the PMT channels required the same percentage change on average (i.e., a 10% lower gain than the last value), this systematic change is a good indication that the reference PMT has in fact changed by that percentage (i.e., the reference PMT gain has decreased by 10%) instead of being stable. Hence, all the other PMT channels were "misled" by following the leader (the reference PMT). In this case, all the PMT channels in the detector module will be increased by the same percentage (10%) to get back to the true target value. The reference may not need to be perfectly accurate or perfectly reproducible every time, because what is more important in crystal decoding is the precision of uniformly setting the outputs of all the PMT channels.

V. Conclusions

An instantaneous PMT automatic calibration method using an LED network has been developed. This ultra-fast PMT gain calibration method is adopted by our proposed high-resolution PET camera with 12 PQS modules. Each module has independent tuning electronics, and the calibrations of the 12 modules can be operated in parallel mode through a regular computer parallel port. Our study shows a PET camera with 1000 PMTs can be tuned in about 1 minute without human involvement so that, before each patient scan, the entire detector system can be completely tuned. This ensures optimal image quality for each patient and provides a warning for any sudden mishap in the detector system before scanning each patient. This new method can immediately realign the PMT gains for a mobile PET at a new location to provide better quality control. This LED auto-tuning method can also be used in a traditional gamma camera.

VI. References

[1] J. Uribe, H. Li, H. Baghaei, M. Aykac, Y. Wang, Y. Liu, T. Xing, W.-H. Wong: "Effect of photomultiplier gain-drift and radiation exposure on 2D-Map decoding of detector array used in positron emission tomography," 2001 *IEEE Nuclear Science Symposium and Medical Imaging Conference Record,* San Diego, CA., November 6-10, 2001.

[2] R. Matheoud, F. Zito, C. Canz, F. Voltini, P. Gerundini. "Changes in the energy response of a dedicated gamma camera after exposure to a high-flux irradiation," *Phys. Med. Biol.* 44, N129-N135, 1999.

[3] W.-H. Wong, J. Uribe, K. Hicks, G. Hu, W. Lu: "Design of a variable field prototype PET camera," *IEEE Trans. Nucl. Sci.*, 43:1915-1920, June 1996.

[4] W.-H. Wong, J. Uribe, H. Li, H. Baghaei, Y. Wang, M. Aykac, Y. Liu, T. Xing, D. Bilgen, R. Ramirez: "The design of a high resolution transformable whole-body PET camera," *IEEE Trans. Nucl. Sci.*, 49(5), 2079-2084, October 2002.

[5] J. Uribe, W-H. Wong, G. Hu, K. Hicks, J. Wang, H. Baghaei, N. Zhang, H. Li, S. Yokoyama. "Effect of the rotational orientation of circular photomultipliers in a PET camera block detector design," *IEEE Trans. Nucl. Sci.*, 44(3): 1266-1270, June 1997.

[6] Y. Wang, W.-H. Wong., M. Aykac, J. Uribe, H. Li, H. Baghaei, Y. Liu, T. Xing. "An iIterative energy-centroid method for recalibration of PMT gain in PET or gamma camera," *IEEE Trans. Nucl. Sci.*, 49(5), 2047-2050, October 2002.

Electronics Design for a Low-Cost High-Sensitivity Rodent-Research PET (RRPET)

Hongdi Li, *Member, IEEE*, Yaqiang Liu, Tao Xing, Yu Wang, Shuping Xie, Jorge Uribe, *Member, IEEE*, Hossain Baghaei, *Member, IEEE*, Rocio Ramirez, Soonseok Kim, Wai-Hoi Wong, *Member, IEEE*

Abstract—**We designed and implemented electronics for a low-cost high-sensitivity positron emission tomography camera for research involving rodents. To reduce cost and increase sensitivity, we used continuous full-ring photomultiplier tube (PMT) with quadrant sharing (PQS) detector design. In this prototype camera, 168 PMTs decode 144 scintillation detector blocks consisting of 9216 crystal elements. An Anger position matrix board weight sums the 144 detector blocks as eight individual gamma camera zones. The full-ring detector decoding is performed by eight fixed local zones. However, in the PMT-quadrant-sharing design, every two adjacent zones share seven axial PMTs. A boundary processing technique has been developed for the PMT-quadrant-sharing detector blocks so that the decoding of the full-ring detector can be performed by individual zones. A high-yield-pileup-event-recovery decoding board, a module-based coincidence processing system and a data acquisition computer, which were originally developed for a whole-body PET, can still be used by this rodent PET camera. The camera needs only eight decoding boards, and each board decodes 18 detector blocks of one detector zone. The entire decoding electronics need only 24 ADCs and can handle about six million events/second of single-rate. A motherboard decodes the control commands from the data acquisition computer, performs the real-time boundary processing and distributes DC power signals to all the eight decoding boards. To further reduce the cost and size of the camera, we have developed a new compact PMT voltage divider with adjustable PMT gain that can be controlled by programming the dynode high voltages directly. The very front-end preamplifier is also integrated into this divider board to increase the signal-to-noise ratio. A new instantaneous light-emitting diode automatic PMT gain calibration method is also used in this camera for better quality control; the gains of 168 PMTs can be equalized within 1 minute.**

I. INTRODUCTION

TO significantly reduce the cost and improve the sensitivity of a positron-emission tomography (PET) camera for rodent research, we have developed a full-ring BGO detector in a PMT-quadrant-sharing (PQS) design [1]. The detector has no gap, and the camera does not rotate. In this camera, seven rings of PMTs decode six rings of PQS blocks. Each ring has 24 PMTs and 24 PQS scintillation blocks (Fig. 1). A pentagonal PQS BGO block has been successfully developed for this ring detector [2]. The same electronics architecture that we previously proposed for a whole-body 12-module PET camera [3] was adopted for this animal PET camera. We divide the entire camera into many high-speed gamma camera zones by Anger weighting the PMT signals in analog. Each Anger camera zone has its own energy and pre-normalized position signal outputs. We use high-speed high-yield-pileup-event-recovery (HYPER) decoding electronics [4] to deal with the pileup events at high count rate situations. Finally, we use a module-based coincidence processing system [5] to detect true and random coincidence events. The HYPER electronics and the coincidence processing system are exactly the same as those used in the whole-body PET camera; hence, we dramatically cut the electronics developing time and cost. Also there are fewer types of electronics boards to be maintained for both the whole-body PET camera and rodent PET camera in our laboratory.

The main difference between the decoding method of a ring detector and the decoding method of a modular detector with a PQS design is the boundary processing. A modular detector does not have decoding difficulty because the boundary is physically isolated; however, in the ring detector, because the boundary of two adjacent zones shares some PMTs, the lights of boundary events detected by one zone can be carried to the neighboring zone by the shared PMTs and affect its decoding. Hence, a special boundary processing technique is necessary for the ring decoding.

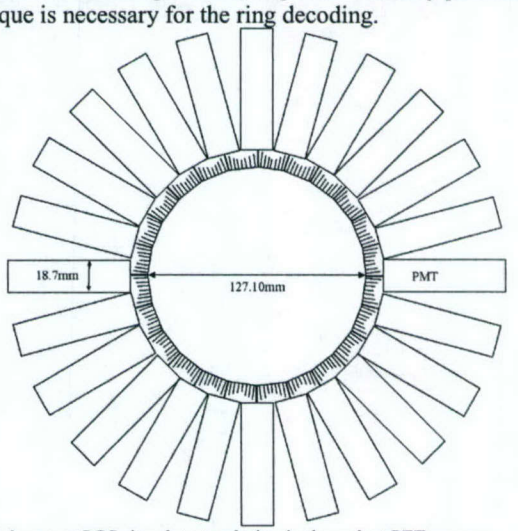

Fig.1: A low-cost PQS ring detector design in the rodent PET camera.

This work is support in part by the NIH-CA58980 PHS Grant, NIH-CA61880 PHS Grant, NIH-CA76246 PHS Grant, NIH-CA58980S PHS Grant, NIH-EB01481 PHS Grant, NIH-EB00217 PHS Grant, NIH-EB01038 PHS Grant, U.S. Army-Breast Cancer Research Grant, Texas ARP/ATP Grant 003657-0058-2001.

H. Li, Y. Liu, T. Xing, Y. Wang, S. Xie, J. Uribe, H. Baghaei, R. Ramirez Soonseok Kim, and W.-H. Wong are with the Department of Experimental Diagnostic Imaging, University of Texas M.D. Anderson Cancer Center, Houston, TX 77030 USA (H. Li's telephone: 713-745-3732, e-mail: hli@di.mdacc.tmc.edu).

0-7803-8257-9/04/$20.00 © 2004 IEEE.

II. METHODS

A. Overall architecture

Instead of implementing a dynamic zone locating technique for crystal decoding used by the Penn-PET head scanner [6], [7] or our prototype MDAPET scanner [8], we use a fixed zone decoding method for the continuous full-ring block detector system. The fixed zone decoding method simplifies the event triggering circuit and modularizes the crystal decoding processing circuit. Hence, the system is very flexible, and the electronics can be easily reconfigured and transplanted to a different PET camera.

In our proposed full-ring rodent research PET camera (RRPET), 144 scintillation detector blocks consisting of 9216 crystal elements are divided into eight individual decoding zones by electronics. Each zone has 18 detector blocks with 3 blocks in the transaxial direction by 6 blocks in the axial direction. To decode 3 x 6 blocks of one zone 4 x 7 PMTs with a PQS design are needed (Fig. 2). The 28 PMT signals in each zone are weight summed by fast amplifiers according to their physical locations as a regular Anger camera and generate analog energy and pre-normalized position signal outputs. Each zone shares seven axial PMTs with each neighbor (one PMT signal is shared by two zones). To reduce the output number of coaxial cables for the shared PMTs, we used printed-circuit-board wires instead, and all eight Anger positioning circuits were put on one positioning matrix board, which is mounted inside the camera (on top of detectors parallel to PMTs) with the center of the board open for animal loading.

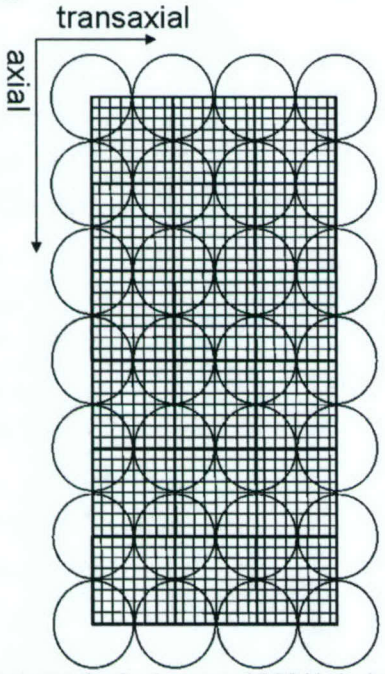

Fig. 2: One detector zone has 3 x 6 pentagonal BGO blocks decoded by 4 x 7 PMTs in a PQS design; every two adjacent zones share 7 boundary PMTs in the axial direction.

The energy output in one decoding zone is the sum of all the 4 x 7 PMT signals. Hence, if a neighboring-zone detects a gamma hit and most of its scintillation lights are collected by these shared PMTs, this event from the neighboring-zone still contributes greatly to the energy signal of the current zone and, therefore, triggers the decoding circuit. In other words, the decoding electronics of one zone handles a much higher event rate than what can be obtained by the 3 x 6 detector blocks originally assigned to the zone. Our simulation study showed that the zone had to handle a total rate of about 24 detector blocks (33% more than the rate of an independent zone).

Although the count rate for a single block may be low for a rodent PET camera because the total rate for one zone is about 24 times higher than a single block rate, the summed energy and position signals may have a pileup problem in particular applications. To perform the pileup event decoding, each Anger camera zone is served by one individual pileup prevention HYPER circuit that can handle a single event rate up to one million events per second.

Eight HYPER decoding boards sit on a custom-designed motherboard. The functions of the motherboard are to identify the actual location of a gamma event hitting the boundary of every two neighboring zones, to encode all the commands from a master computer for the HYPER boards and the front-end analog board, to find the light-emitting diode (LED) photo peak location for automatic PMT calibration, and to distribute the DC powers to the eight HYPER boards. Each zone has one ribbon cable on the motherboard that directly passes the digitized energy and position signals for every energy qualified event to the coincidence processing system for further coincidence events selection. Fig. 3 shows the electronics architecture designed for the RRPET camera.

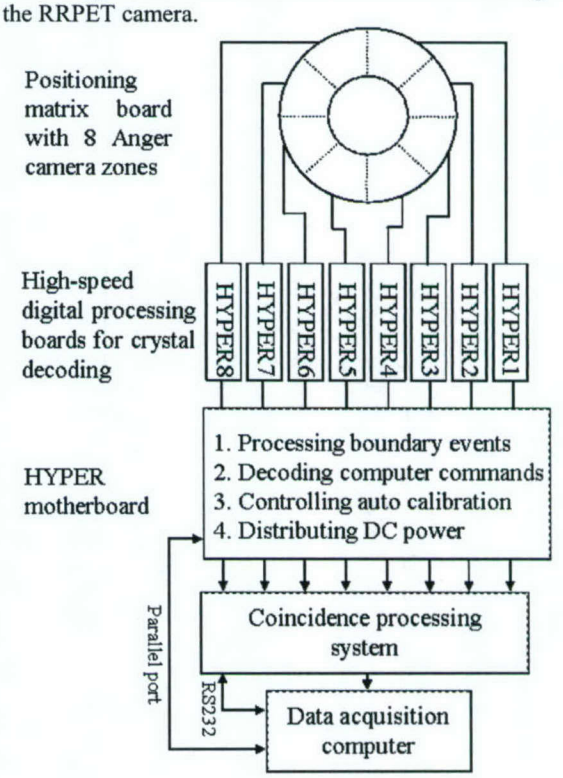

Fig. 3: Electronics architecture for the rodent PET camera.

The coincidence system, the eight HYPER boards, and their motherboard are outside the camera, while the programmable custom-made PMT voltage dividers and the Anger weighting matrix board are mounted inside the camera.

We have developed a coincidence processing system based on back-plane or plug-in architecture for PET cameras with a modular electronics structure [5]. Using digital signal processor (DSP) and field programmable gate array (FPGA) technology and without redesigning the printed-circuit-board layout, we can reprogram the coincidence hardware for a different PET configuration with a varying number of modules. The coincidence system can support up to 12 modules. For the RRPET with eight electronic zones (modules), each zone will have coincidence with five opposing zones. Hence, the ring detector has 20 coincidence bank pairs. Each bank pair has two individual output channels for true and random coincidence detection. The coincidence time window can be programmed through an RS232 serial port.

Real-time electronics for a traditional PET camera usually include position normalization, a look-up table for crystal identification, and a look-up table of the digital energy threshold of each crystal [8], [9]. In the RRPET electronics design, all the above procedures are performed by software, which reduces the number of electronics components and the production cost. The coincidence system produces the raw pre-normalized position and energy signals for the pair events that are selected by the coincidence time window. Only one raw digital energy threshold on the HYPER decoding board is used to reject most of the low energy scatter events. We realized that in a well-calibrated PQS detector block, the difference among the photo peak positions for all the crystals in the entire block is less than 22%; corner crystals have the highest photo peaks, and center crystals have the lowest photo peaks [10]. Hence, one universal energy threshold can reject most of the low energy scatter events for every crystal, and it does not allow too many scatter coincidence events. (Scatter events increase the dead time in coincidence processing.) Because scatter coincidence events will blur the image, all the coincidence events must be checked by a fine digital energy threshold look-up table using software to reject these scatter events. Each crystal has an individual energy cut off. We will do a simulation study to find out the maximum event processing rate with different computer CPU speeds. A real-time processing hardware is still an option; in fact, we already have built a processing board for a human PET camera that can also be used by the rodent PET camera.

The coincidence outputs are buffered and clocked to a fast PCI data I/O board in a personal computer. The data transfer rate is about 2.5 million events per second, which is fast enough for rodent PET applications.

To further reduce the RRPET production cost, we designed a compact, low-power, inexpensive PMT voltage divider [11]. A fly lead PMT can be directly soldered to this voltage divider board without using an expensive PMT socket. High voltages for PMT dynodes can be programmed by a data acquisition computer through this voltage divider. The programmable gain range is about 5 times. This voltage divider can save US$30 per channel in production cost; furthermore, it has more features than does a commercial PMT voltage divider using a standard socket. An ultra fast preamplifier (MAX4223) is on board to improve the signal-to-noise ratio. This amplifier also has a shut-down feature that can be used in automatic gain calibration. In the calibration mode, only one PMT channel is on, the rest of the channels are off.

The RRPET uses a new instantaneous LED automatic PMT gain calibration method for better quality control; the gains of all 168 PMTs can be equalized within 1 minute [12]. The tuning is managed through a computer parallel port that includes the controls of each PMT gain, amplifier gains for weighted sum signals, analog trigger thresholds, and digital energy thresholds, as well as the front-end PMT gain calibration LEDs. A RF wireless interface board (an optional part) has also been developed to simulate the parallel control signals using the RF microprocessor CC1010 (Chipcon, Inc.), which supports wireless communication with a master computer.

B. Detector boundary decoding method

Because every two adjacent detector zones share seven axial PMTs one gamma ray hitting a boundary block of the two zones may trigger both decoding electronics at the same time if these shared PMTs collect enough lights from that event. A crystal that is closer to the boundary has a greater chance of creating these "twin" triggers. Unfortunately, a simple energy threshold can do nothing to distinguish the real gamma hit from the "twin" triggers, because both events, of which one is true and one is false, create a lot of energy that is collected by the shared PMTs and qualified by the energy threshold.

However, in the PQS block design, the scintillation lights from each crystal are shared by four PMTs, and the percentage of the light sharing for each PMT can vary according to the crystal's location. For a corner crystal, most of the lights go directly to the nearest PMT, but about 3% of the total lights can be collected by the other three PMTs. To explain the concept of the boundary decoding method, a simple two-zone model with

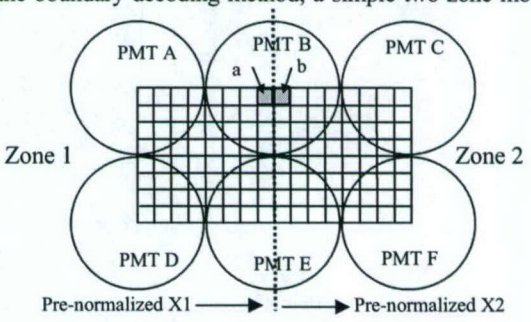

Fig. 4: A simple detector with two neighboring zones sharing two PMTs. "a" and "b" indicate two boundary crystals.

only one block is used in each zone (Fig. 4), and the two blocks share PMT B and PMT E. Hence, both blocks are the boundary blocks. According to Anger logic in the ring camera, the position signals for zone 1 is described by equation (1) and zone 2 is decribed by equation (2).

$$X1 = (A+D) \times 0 + (B+E) \times 1 = B+E \qquad (1)$$

$$X2 = (B+E) \times 0 + (C+F) \times 1 = C+F \qquad (2)$$

In additional to the traditional energy threshold needed for rejecting scatter events, the boundary decoding method uses another pre-normalized position threshold to identify a real gamma event hit on the boundary crystals. In Fig. 4, the lights contributed to position X1 (X1=B+E) in zone 1 from both crystal "a" and "b" would be almost the same because most of their lights would go to PMT B, even though crystal b is located in a different zone (zone 2). As for position X2 (X2=C+F) in zone 2, because the weight factor for PMT B is 0 and the lights from crystal a could not go to PMT C or PMT F (all the detector blocks are light isolated), no signal would be contributed to position X2 from crystal a. However, a percentage of lights from crystal b could be collected by PMT C and PMT F; hence, a simple threshold for position X2 in zone 2 could be used to identify the events from the two crystals. If the position X2 signal were above the threshold, b would be accepted and a would be rejected. On the other hand, if X2 were below the threshold, b would be rejected and a would be accepted. Although in both cases position X1 is above the position threshold, X1 would not be used in this boundary event identification.

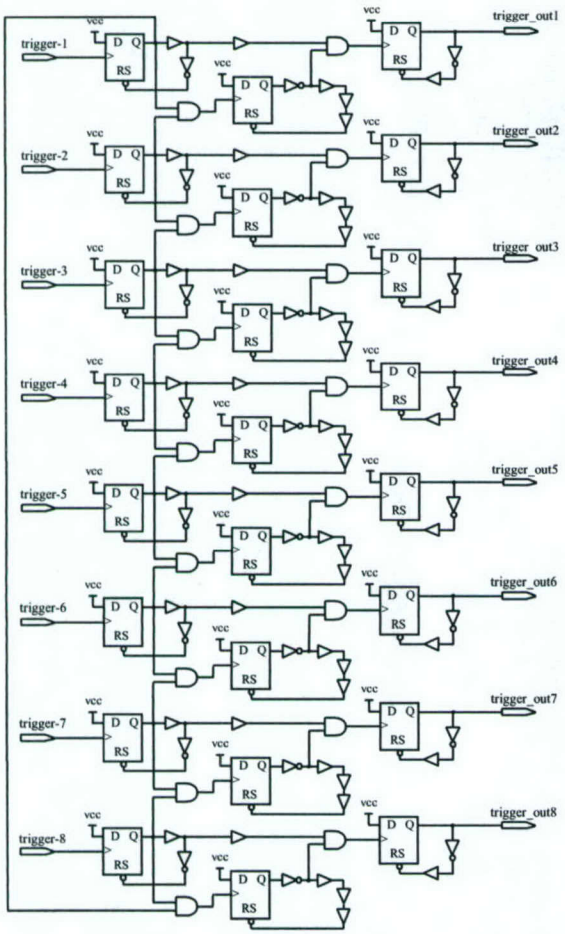

Fig. 5: Trigger selection circuit with boundary identification logic for eight full-ring detector zones.

Fig. 5 shows the trigger selection circuit for eight boundary identifications in the full-ring rodent PET camera. Each individual input trigger signal has already been qualified by both the energy threshold and the pre-normalized position threshold in its own decoding HYPER board. Therefore, for the boundary identification between two adjacent zones i-th and zone (i+1)-th, a false trigger (one of that twin triggers) in zone (i+1)-th has already been rejected by its decoding board. If both trigger-i and trigger-(i+1) were to have signals, then only trigger-(i+1) would be selected, and trigger-i would be rejected automatically.

III. Results

The BGO scintillation blocks for the proposed rodent PET camera are under development. Our prototype electronics were used as a standard tool to test the decoding quality of the scintillation blocks. The optimization of the decoding mask for the scintillation block has been finished. Fig. 6 shows a decoding image of four blocks (each block has 8 x 8 crystals) built with four different decoding masks. To test the electronics four detector blocks were assembled as one Anger camera and the two dimensional crystal decoding map was acquired by one HYPER decoding circuit. The result shows that all four blocks are clearly decoded and the third block from the left has the best mask.

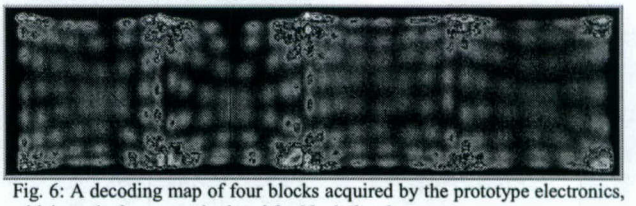

Fig. 6: A decoding map of four blocks acquired by the prototype electronics, which worked as a standard tool for block development.

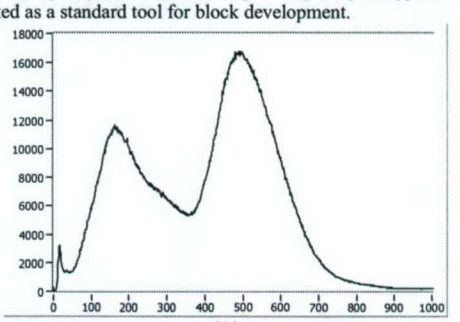

(A)

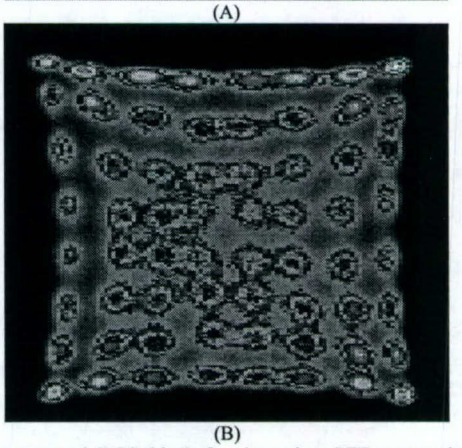

(B)

Fig. 7: A pentagonal BGO block for the rodent PET camera has been developed and tested. (A) Energy spectrum of the block. (B) Two-dimensional crystal decoding map.

The decoding map for two boundary blocks (one block in each zone) was taken with and without the boundary decoding technique discussed above. Without the boundary decoding technique the edge column crystals (circled by a white curve in Fig.8 (A)) got about four times more counts than the normal crystals. This was caused by false triggers from adjacent blocks. Ideally the image of these false events should be one straight line sitting right at the edge of the block map that can be rejected or cut off by a look-up table. However, because of the electronics noise from the Anger weighting amplifiers and ADCs, the image of the false events can spread and mix into the edge column crystals' real image and cannot be rejected by a look-up table. Fig. 8 (B) was acquired using the boundary decoding technique. The result shows all of the boundary crystals are clearly identified.

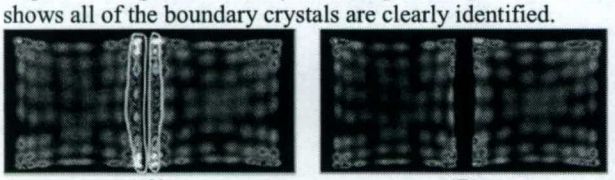

Fig. 8: The effect of a two-dimensional crystal decoding map without (A) and with (B) the boundary decoding technique involved.

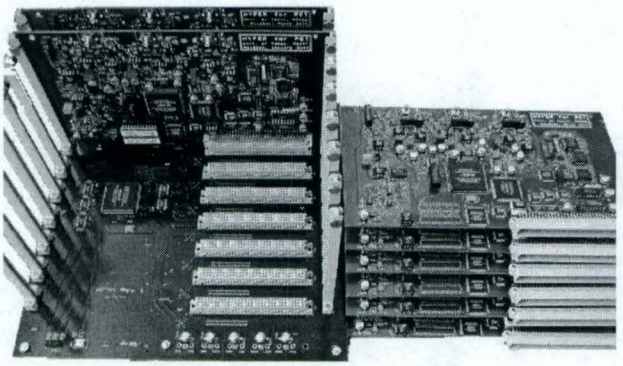

Fig. 9: A photo of the decoding electronics for the rodent PET camera.

IV. Conclusions

We have designed and implemented a special electronics for a low-cost high-sensitivity rodent PET camera. This camera uses a full-ring PMT-quadrant-sharing detector design and the production cost is less than US$100,000. The full-ring PQS scintillation detector with 144 scintillation blocks was divided into eight fixed local decoding zones. Each zone is served by one HYPER decoding board that has been designed for a module-based whole-body PET camera. The entire decoding system only needs 24 ADCs and still can handle about six million events per second of single event rate. A new boundary decoding method has been implemented. A compact PMT voltage divider and a new fast light-emitting diode PMT gain calibration method are used for better quality control. Because in this electronic architecture, we can use the HYPER decoding boards and coincidence system that we designed for a human PET camera, the developing time and cost are greatly reduced.

V. References

[1] W.-H. Wong, H. Li, S. Xie, R. Ramirez, J. Uribe, Y. Wang, Y. Liu, T. Xing, H. Baghaei "Design of an inexpensive high-sensitivity rodent-research PET (RRPET)," 2003 *IEEE Nuclear Science Symposium and Medical Imaging Conference Record, M6-20,* Portland, OR, October 19-25, 2003.

[2] S. Xie, R. Ramirez, Y. Liu, J. Uribe, H. Li, Y. Wang, T. Xing, H. Baghaei, W.-H. Wong "A pentagon photomultiplier-quadrant-sharing BGO detector design for small animal PET," 2003 *IEEE Nuclear Science Symposium and Medical Imaging Conference Record, M3-25,* Portland, OR, October 19-25, 2003.

[3] H. Li, W.-H. Wong, Y. Wang, Y. Liu, T. Xing, J. Uribe, H. Baghaei, R. Ramirez, "Front-end electronics based on high-yield-pileup-event-recovery method for a high resolution PET camera with PMT-quadrant-sharing detector modules," *IEEE Nuclear Science Symposium and Medical Imaging Conference Record, M3-51,* October 2002.

[4] W.-H. Wong, H. Li, J. Uribe, H. Baghaei, Y. Wang, S. Yokoyama, "Feasibility of a high speed gamma camera design using the high-yield-Pileup-evevnt-recovery (HYPER) method," *J. Nucl. Med.* vol. 42, pp. 624-632, 2001.

[5] Y. Wang, H. Li, T. Xing, J. Uribe, H. Baghaei, W.H. Wong, " A modular low dead-time coincidence system for high resolution PET cameras" *IEEE Trans. Nucl. Sci.*, vol. 50, pp. 1386-1391, October 2003.

[6] J. S. Karp, G. Muehllehner, D. Beerbolm, and D. Mankoff, "Event localization on a continuous scintillation detector using digital processing," *IEEE Trans. Nucl. Sci.*, vol. 33, pp. 550-555, February 1986.

[7] D. A. Mankoff, G. Muehllehner, and G. E. Miles, "A local coincidence triggering system for PET tomographs composed of large-area position-sensitive detectors," *IEEE Trans. Nucl. Sci.,* vol 37, pp. 730-736, April 1990.

[8] H. Li, W.-H. Wong, N. Zhang, J. Wang, J. Uribe, H. Baghaei, S. Yokoyama, "Electronics for a prototype variable field of view PET camera using the PMT-quadrant-sharing detector array," *IEEE Trans. Nucl. Sci.,* vol. 46, pp. 546-550, June 1999.

[9] J. W. Young, J. C. Moyers, and M. Lenox, "FPGA based front-end electronics for a high resolution PET scanner," *IEEE Trans. Nucl. Sci.,* vol 47, pp. 1672-1680, August 2000.

[10] J. Uribe, H. Li, T. Xing, Y. Liu, H. Baghaei, Y. Wang, M. Aykac, R. Ramirez, W.H. Wong, "Characteristics of individual crystals in a high resolution BGO detector design using PMT-quadrant-sharing," *IEEE Trans. Nucl. Sci.,* vol 50, pp. 355-361, June 2003.

[11] Y. Liu, H. Li el at. "A gain-programmable transit-time-stable and temperature-stable PMT voltage divider," 2003 *IEEE Nuclear Science Symposium and Medical Imaging Conference Record, M14-231,* Portland, OR, October 19-25, 2003.

[12] H. Li, Y. Liu, T. Xing, Y. Wang, J. Uribe, H. Baghaei, S. Xie, R. Ramirez, "An instantaneous photomultiplier gain calibration method for PET or gamma camera detectors using a LED network," 2003 *IEEE Nuclear Science Symposium and Medical Imaging Conference Record, M7-150,* Portland, OR, October 19-25, 2003.

A Gain-Programmable Transit-Time-Stable and Temperature-Stable PMT Voltage Divider

Yaqiang Liu, Hongdi Li, *Member,IEEE*, Yu Wang, Tao Xing, Shuping Xie, Jorge Uribe, *Member, IEEE,* Hossain Baghaei, *Member, IEEE,* Rocio Ramirez, Soonseok Kim, and Wai-Hoi Wong, *Member, IEEE*

Abstract--**A gain-programmable, transit-time-stable, temperature-stable photomultiplier (PMT) voltage divider design is described in this paper. The signal-to-noise ratio can be increased by changing a PMT gain directly instead of adjusting the gain of the pre-amplifier. PMT gain can be changed only by adjusting the voltages for the dynodes instead of changing the total high voltage between the anode and the photo-cathode, which can cause a significant signal transit-time variation that cannot be accepted by an application with a critical timing requirement, such as positron emission tomography (PET) or time-of-flight (TOF) detection/PET. The dynode voltage can be controlled by a digital analog converter (DAC) isolated with a linear optocoupler. The optocoupler consists of an infra-red light emission diode (LED) optically coupled with two phototransistors, and one is used in a servo feedback circuit to control the LED drive current for compensating temperature characteristics. The results showed that a 6 times gain range could be achieved; the gain drift was < 0.5% over a 20$^{\circ}C$ temperature range; 250ps transit-time variation was measured over the entire gain range. A compact print circuit board (PCB) for the voltage divider integrated with a fixed-gain pre-amplifier has been designed and constructed. It can save about $30 per PMT channel compared with a commercial PMT voltage divider along with a variable gain amplifier. The pre-amplifier can be totally disabled, therefore in a system with large amount of PMTs, only one channel can be enabled for calibrating the PMT gain. This new PMT voltage divider design is being applied to our animal PET camera and time-of-flight/PET research.**

I. Introduction

A high resolution positron emission tomography (PET) detector usually has a large number of decodable crystals per photomultiplier (PMT), and the crystal decoding resolution is more dependent on a stable PMT gain; however, a PMT gain can change with many environmental factors, such as room temperature, time and radiation exposure, etc.; hence, a more frequent system-gain calibration is required. There are two ways to calibrate the PMT output: (1) using a variable-gain amplifier (VGA) to compensate the PMT gain and (2) adjusting the PMT gain directly. In our proposed whole-body PET camera [1], we used regular resistor voltage-dividers provided by the PMT manufacturer; hence, VGAs were used for gain calibration. However, a high-speed VGA usually has a large voltage output offset, which can vary randomly with its gain change. This requires a special baseline restoring circuit in data acquisition electronics, because all the signals are DC-coupled for high-count-rate application. In our low-cost animal PET camera [2], the detector is designed as showed in Figure 1. An inexpensive PMT voltage divider has been designed for optimal PMT auto-gain calibration. The design goals for the voltage divider are low-cost, compact size, a large programmable gain-range, a very small PMT signal transit-time variation, gain-temperature-stability, and simple control.

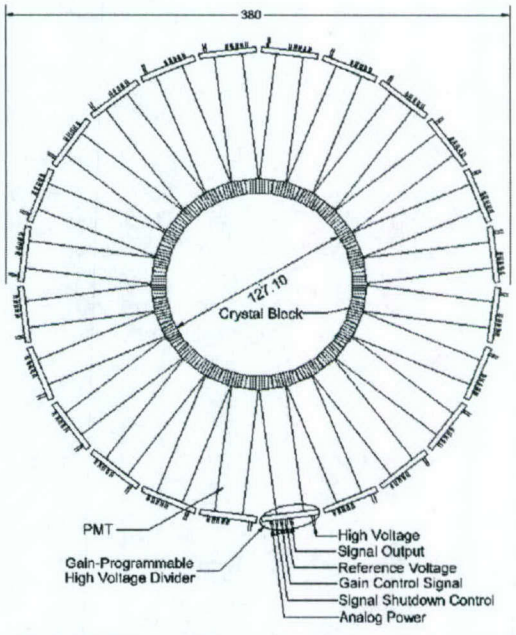

Fig. 1 The animal PET detection system where the PQS blocks are directly coupled to the PMT without light guides or optical fiber to maximize the light output. Each PMT mounts a gain-programmable high-voltage divider. The divider is very small to make whole system compact.

This work is support in part by the NIU-CA58980 PHS Grant, NIH-CA61880 PHS Grant, NIH-CA76246 PHS Grant, NIH-CA58980S PHS Grant, NIH-EB01481 PHS Grant, NIH-EB00217 PHS Grant, NIH-EB01038 PHS Grant, U.S. Army-Breast Cancer Research Grant, Texas ARP/ATP Grant 003657-0058-2001.

Yaqiang Liu, Hongdi Li, Yu Wang, Tao Xing, Shuping Xie, Hossain Baghaei, Jorge Uribe, Rocio Ramirez, soonseok kim, and Wai-Hoi Wong are with The University of Texas M. D. Anderson Cancer Center, Houston, TX 70030 USA (Yaqiang Liu's telephone: 713-745-1671; e-mail: yaqiang_l@yahoo.com).

0-7803-8257-9/04/$20.00 © 2004 IEEE.

II. METHODS

For an N-stage PMT tube with a regular resistor voltage-divider, the PMT gain can be described as $G = \prod_{i=1}^{N} k_i V_i^{\alpha}$, where k_i is a proportionality constant, V_i is the interdynode voltage per stage, and the exponent α is usually between 0.6 and 0.8. Hence the PMT gain can be adjusted by changing the voltage. But by changing the high voltage, the total electron transit time inside the tube can also be changed which will require an additional look-up table to correct the time of flight for coincidence application. The transit time mean value, evaluated over a statistically large number of pulses, varies as $1/\sqrt{V}$ and is usually of the order of several tens of nanoseconds. If the PMT high voltage changes from 1150v to 1500v, the transit time will decrease by 12.4%. This means that a difference of several nanoseconds in transit time should be correct.

Figure 2 shows a modified voltage divider design. In this design we only control the voltage between the last 3rd and 4th dynodes; the total high voltage remains the same so that by increasing the stage voltage, the rest stage voltages will drop a little; therefore the total transit time does not change that much. The low-voltage control electronics are isolated by an optocoupler that consists of an infra-red light emission diode (LED) optically coupled with two phototransistors. For the last 4th resistor of the divider R_{N-2}, part of current is drawn by the top phototransistor; the bottom phototransistor is used in a servo-feedback mechanism to control the LED drive current; which has the effect of compensating for LED's nonlinear time and temperature characteristics. Changing the LED drive current will change the current of the top phototransistor. That will change the voltage on resistor R_{N-2}. The control voltage is driven by a digital analog converter (DAC). That makes the PMT gain programmable.

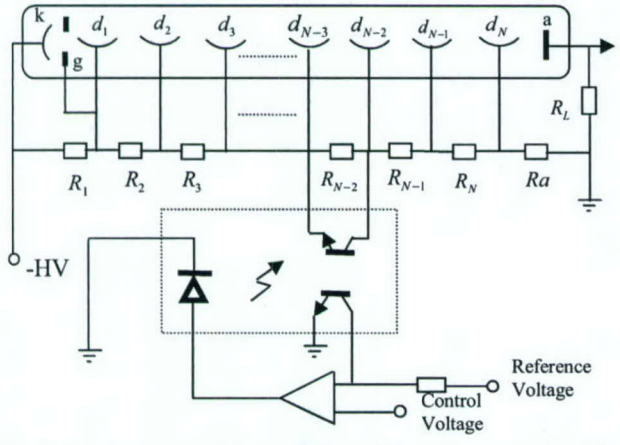

Fig. 2 A gain-programmable, transit-time-stable, and temperature-stable PMT divider design. The design maintains total high voltage, changing the distribution on the high voltage divider to adjust the PMT's gain.

Because the cathode/first-dynode space is much larger than the space of neighboring dynodes, its contribution to transit time should be treated carefully. In our system, we used Philips XP1910 PMT, the electron path length L between the cathode and the first dynode is about 3 times as the length l between two neighboring dynodes. The emission photon wavelength of LSO is about 420 nanometers. As described in the Philips manual [3], the energy of photoelectron E_p is about 1.2 eV (written as eV_p), and the secondary-electron energy E_s is about 5 eV (written as eV_s). We have simulated the variation of PMT transit time. To make it easier, we consider the cathode to first-dynode and other inter-dynodes as parallel planes and ignore the distribution of illumination point at the cathode and the angle distribution of photoelectron and secondary emission electrons. The first time, we used the normal resistor divider, as the Philips catalog suggests (see Table I). The transit time as a function of total high voltage can be described as shown in equation (1),

$$t_{transit} = \frac{l}{V}\sqrt{\frac{2m}{e}}\left[+8\left(\sqrt{V+V_s}-\sqrt{V_s}\right)+\left(\sqrt{1.5V+V_s}-\sqrt{V_s}\right)/1.5\right] + \frac{L}{2V}\sqrt{\frac{2m}{e}}\left(\sqrt{2V+V_p}-\sqrt{V_p}\right) \quad (1)$$

where m is the electron static mass, e is the electron charge, l is the distance between two neighboring dynodes, L is the distance between the cathode and the first-dynode, V is the voltage between the last two dynodes, $V_p = E_p / e \approx 1.2volt$, and $V_s = E_s / e \approx 5volt$. The simulation results are shown in Figure 3.

TABLE I A DIVIDER TYPE VOLTAGE RATIO. D_{10} DENOTES THE FINAL DYNODE OF THE PMT.

A divider type voltage ratio (for maximum gain)							
K	D1	D2	D3	D4	…	D_{10}	A
2	1	1.5	1	1	1	1	

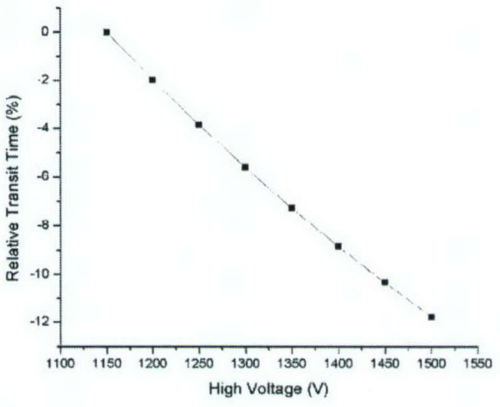

Fig. 3 Simulation result of the relative transit time as a function of the divider high voltage.

Secondly, We adjusted the voltage V_{7_8} between the dynodes D_8 and D_7 and kept the total voltage value V_t. Transit time can be described as equation (2),

$$t_{transit} = \frac{l}{V}\sqrt{\frac{2m}{e}}\left[7\left(\sqrt{V+V_s}-\sqrt{V_s}\right)+\left(\sqrt{1.5V+V_s}-\sqrt{V_s}\right)/1.5\right] + \frac{L}{V}\sqrt{\frac{2m}{e}}\left(\sqrt{2V+V_p}-\sqrt{V_p}\right)+\frac{l}{V_{7\_8}}\sqrt{\frac{2m}{e}}\left(\sqrt{V_{7\_8}+V_s}-\sqrt{V_s}\right) \quad (2)$$

where m is the electron static mass, e is the electron charge, l is the distance between two neighboring dynodes, L is the distance between the cathode and the first-dynode, V is the voltage between the last two dynodes and $V = (V_t - V_{7\_8})/10.5$, $V_p = E_p / e \approx 1.2volt$, and $V_s = E_s / e \approx 5volt$.

Figure 4 shows the simulation result of the transit time as a function of the relative voltage between the two dynodes. If you compare the two PMT gain adjustment methods, the transit time variation of the new divider is much small than the normal resistor divider.

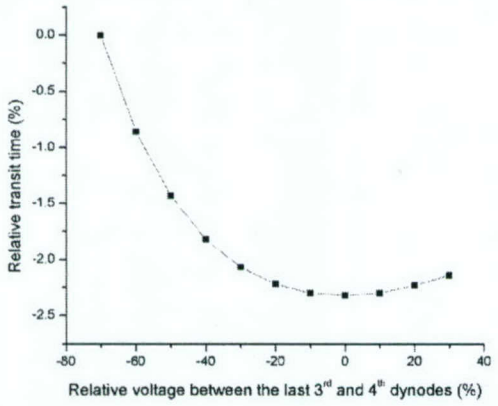

Fig. 4 Simulation of the relative transit time as a function of the relative voltage between the last 3rd and 4th dynodes.

III. Performance

We have designed and implemented a gain-programmable, transit-time-stable, and temperature-stable PMT voltage divider. This divider will be used in our new animal PET system. All the performance tests have been done on an independent prototype circuit (see Figure 5). A high-speed amplifier was build in the divider, the amplifier can be shutdown totally by a control signal that makes instantaneous PMT gain calibration possible [4]. Except the high voltage supply wires, there is a flat cable that includes the gain control, reference voltage, shutdown control, output signal, and power supply.

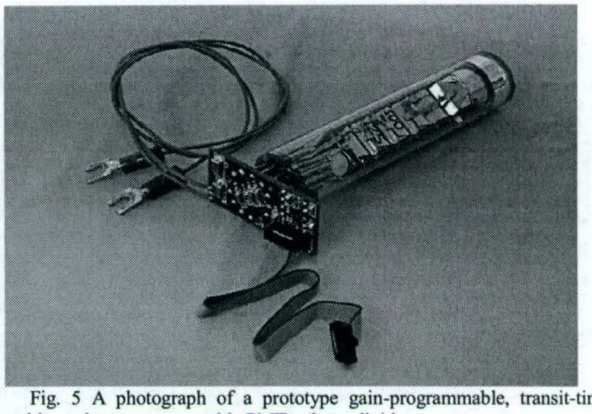

Fig. 5 A photograph of a prototype gain-programmable, transit-time-stable, and temperature-stable PMT voltage divider.

A. *Programmable gain range measurement*

We have implemented a new voltage divider for the Philips 1910 PMT and tested its range in gain variations. Figure 6 shows that by adjusting the low control voltage from 0V to 3.9V, a total 6x PMT gain range can be achieved. For the same PMT and a regular resistor voltage divider, testing showed that high voltage changed from 1150V to 1470V, there was 6x PMT gain change (see Figure 7).

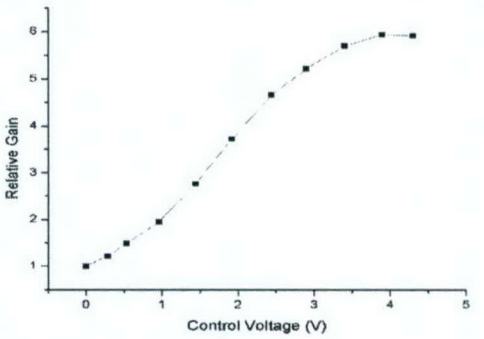

Fig. 6 The relative gain value was calculated as the gain compared with the control voltage was 0V. It changed about 6 times at the whole control range. From 0V to 3.9V, the gain increased with the increasing control voltage.

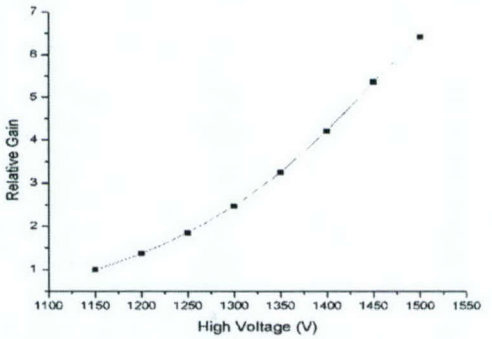

Fig. 7: The PMT gain changed about 6.4 times when the high voltage changed from 1150V to 1500V.

B. *Transit-time variation measurement*

The gain-programmable voltage divider with a low transit-time variation is very important for coincidence application such as a PET, especially for time-of –flight (TOF)/ PET. Our test bench was set up as shown in Figure 8.

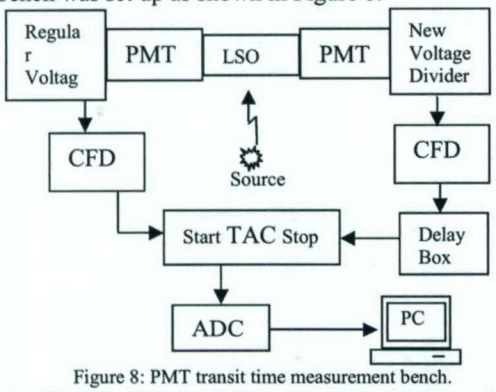

Figure 8: PMT transit time measurement bench.

Two Philips 1912 PMTs coupled with a lutetium oxyorthosilicate (LSO) crystal were put into a black box. One PMT used a regular resistor voltage divider as the manufacture suggested; the other one used our newly proposed voltage divider. We setup a test bench with in a NIM bin: a CANBERRA time-to-amplitude (TAC) module (model 2145) was used to measure the variation of the PMT transit time. The signals from the two PMTs were triggered by two constant-fraction discrimination (CFD) modules; one CFD's output was used as the TAC's start signal, and the other one was delayed by a fixed-time and then used as stop signal. The TAC result was digitized by an analog-to-digital (ADC) module (CANBERRA model 8075), and the spectrum was collected by a computer.

First, we measured the transit time for a regular resistor voltage divider. The new divider remained unchanged, but the voltage for the regular divider was changed from 1150V to 1500V continuously. TAC output change (transit-time change) was also measured as the PMT gain changed, (Figure 9). There was about a 2.8ns transit-time variation.

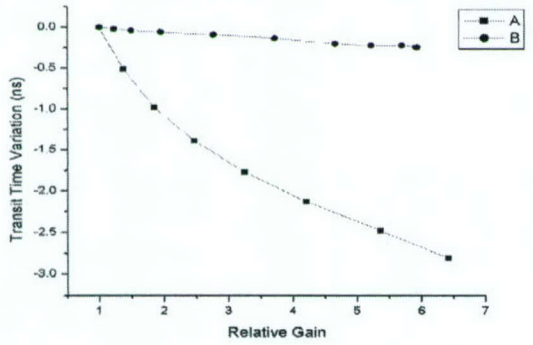

Fig. 9 Test results of transit-time variations as a function of the PMT relative gain

Curve A: Regular divider.

Curve B: New divider.

Second, we measured transit time for our proposed gain-programmable voltage divider. The regular voltage divider remained unchanged, and the new divider's control voltage was changed from 0V to 4.3V. As shown in Figure 9, there was only about 250ps variation over the entire PMT gain range of 6 times.

C. *Gain temperature drift measurement*

We also tested the new divider's gain-temperature stability at three different gain points. Figure 10 shows that the temperature changed from $26.8\,^{o}C$ up to over $50\,^{o}C$, and the gain change measured < 0.5%.

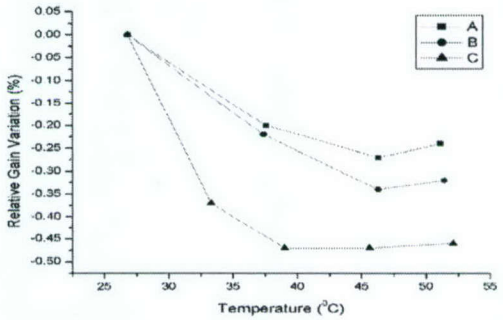

Fig. 10 Relative gain variation as a function of temperature. The new divider had good temperature stability when the divider's temperature changed from $26.8\,^{o}C$ to over $50\,^{o}C$.

Curve A: control voltage is 1.9V; The PMT's gain change less than 0.3%.

Curve B: control voltage is 2.9V; The PMT's gain change less than 0.4%.

Curve C: control voltage is 4.3V; The PMT's gain change less than 0.5%.

IV. Conclusions

We have designed and constructed gain-programmable, transit-time-stable, and temperature-stable PMT voltage divider. Our test results showed that: (1) the PMT-gain had a 6x dynamic range; (2) the PMT transit-time varied less than 250ps over the entire range; and (3) the PMT gain with the new divider design had good temperature stability. This new PMT voltage divider design is adopted for our proposed animal PET camera and can reduce camera size and production costs.

V. References

[1] H. Li, W.H. Wong, Y. Wang, Y. Liu, T. Xing, J. Uribe, H. Baghaei, and R. Ramirez, "Front-end electronics based on high-yield-pileup-event-recovery method for a high resolution PET camera with PMT-quadrant-sharing detector modules," Conference record of the 2002 IEEE MIC Conference.

[2] W.H. Wong, H. Li, S. Xie, R.Ramirez, J. Uribe, Y. Wang, Y. Liu, T. Ting, and H. Baghaei "Design of an inexpensive high-sensitive small animal PET camera," Conference record of the 2003 IEEE MIC Conference.

[3] PHILIPS "Photomultiplier Tubes Principles & Applications" pgs1.33-36.

[4] H. Li, Y. Liu, T. Xing, Y. Wang, J. Uribe, H. Baghaei, S. Xie, R. Ramirez, and W.H. Wong "An instantaneous photomultiplier gain calibration method for PET or gamma camera detector using a LED network," Conference record of the 2003 IEEE MIC Conference.

Gantry Design with Accurate Crystal Positioning for a High-Resolution Transformable PET Camera

J. Uribe, *Member, IEEE,* , S. Xie, H. Li, *Member, IEEE,* H. Baghaei, *Member, IEEE,* Y. Wang, Y. Liu, T. Xing, R. Ramirez, M. Bushman, S Kim, W-H. Wong, *Member, IEEE*

University of Texas M.D. Anderson Cancer Center, Houston, Texas 77030

Abstract— **A PET camera capable of transforming its geometric configuration is being developed. This high-resolution oncologic transformable PET (HOTPET) can be modified from a large detector ring of 83 cm to a small diameter ring of 54 cm. The system consists of 12 rectangular detector modules arranged in a polygon. The detector gap between modules remains constant in both configurations because each module is rotated around its own axis and displaced radialy, bringing together adjacent modules. HOTPET's detectors are highly pixilated (crystal pitch 2.6 mm), requiring accurate placement of the modules relative to each other to ensure alignment of crystals within the same detector ring. We have designed a precise *detector bank holder* with keyways and complementary keys built onto its sides to allow interlocking with each other to form a polygon and maintain crystal co-planarity. Consequently we were able to design the gantry supporting the modules using wider tolerances and so reduce its construction cost. The module provides support for 77 PMT, the analog front-end electronics, and an automated PMT-gain control, all enclosed within a controlled environment. By having only 2 departing surfaces throughout the module's box we minimize light leaks, and with air ducts inside the walls, its temperature can be controlled. Removal of just a back cover and a motherboard gives access to any part of the electronic components or a PMT with minimal disturbance to other components.**

I. Introduction

A high resolution positron emission tomography (PET) camera whose geometric configuration can be transformed is being developed [1]. This high-resolution oncologic transformable PET (HOTPET) camera can be modified from a large detector ring for whole-body scans (83 cm diameter), to a higher sensitivity, smaller port for brain/breast scans (54 cm diameter) [2]. The system was designed to allow both clinical and research applications with one camera, specially those requiring high sensitivity and resolution with geometric adjustment to a particular anatomy, e.g., dedicated breast or brain imaging. At the same time it provides equivalent sensitivity and higher resolution (2.6 mm resolution expected at the center of the FOV) [2] than a dedicated whole-body clinical scanner. The camera consists of 12 independent detector modules arranged in a regular 12-sided-polygon as shown in Fig. 1, with only 14.8 mm gap between detectors of adjacent modules. An important feature of this camera is that the gap between modules remains constant in both configurations. The versatile transformation between modes with no change in detector separation is possible by rotating each module on its own axis and displacing them in the radial direction, bringing their rectangular faces side by side as depicted in Fig. 1.

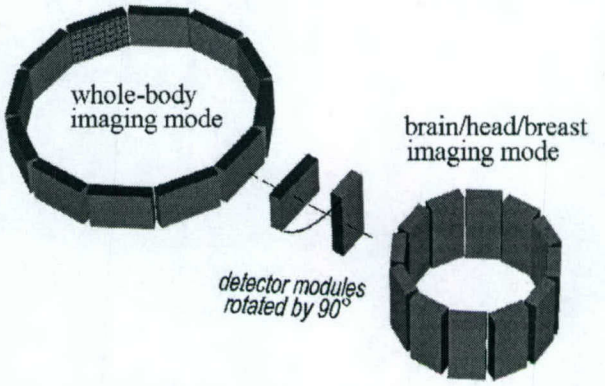

Fig. 1. HOTPET geometric transformation from large to small radius without changing the size of the gap between adjacent modules. Each block represents the scintillation detector bank inside a detector module

II. The Design

The mechanical design of this camera is challenging due to the convertible geometric configurations required and the small size of the detector crystals (2.68 mm x 2.68 mm). Complex mechanical assemblies could have large compound mechanical tolerances, which generate detector-positioning variations that create resolution degradation in the image. Therefore, mechanical tolerances of gantry components must be very small compared to the crystal detector size to minimize such degradation. In addition this modular system must satisfy the following requirements:

Manuscript received October 22, 2003. This work is support in part by the NIH-CA58980 PHS Grant, NIH-CA61880 PHS Grant, NIH-CA76246 PHS Grant, NIH-CA58980S PHS Grant, NIH-EB01481 PHS Grant, NIH-EB00217 PHS Grant, NIH-EB01038 PHS Grant, U.S. Army-Breast Cancer Research Grant, Texas ARP/ATP Grant 003657-0058-2001.

The authors are with the University of Texas, M.D. Anderson Cancer Center, Houston, TX 77030, USA (J. Uribe's telephone: 713-745-1179, e-mail: juribe@di.mdacc.tmc.edu).

0-7803-8257-9/04/$20.00 © 2004 IEEE.

- Gantry must rotate 30° on main axis (patient's axial direction) with 0.18° (11') or better angular positioning accuracy (this is 1/20th of the arch covered by one crystal detector). This is needed to improve sampling and minimize image artifacts caused by inter-module gaps.
- Gantry must turn 90° from the vertical whole-body mode, to the horizontal/flat breast mode.
- Alignment of crystals belonging to the same detector ring must be assured within 1/10th crystal size (0.27 mm). This is needed to optimize axial resolution.
- Modules must be able to move independently or in tandem along the gantry's radial direction and rotate 90° on their axes so as to allow change of scanning mode.
- Each module at the brain/breast and whole-body positions must be securely fixed with positive positioning stops for easy operation and repeatable configuration of the camera.
- Side shielding must be movable so that the patient opening can be changed from whole-body to brain/breast mode.
- Dead space between detector and patient chest wall must be minimized when configured in breast mode and the whole breast must be included in the FOV.
- The length of cables carrying fast/high-rate signals must be short to avoid signal degradation.
- Number of cables connecting rotating part of the gantry and fix platform must be minimized (moving parts break easily).
- Front end and processing electronics must be confined to the gantry. There should be no outside electronic racks except for computer performing image reconstruction and image display.
- Module design should allow easy maintenance with minimum disturbance to other components when serviced.
- Heat removal from each module's inner volume must be provided.
- Number of departing surfaces in the module must be minimized to avoid developing light leaks.

We have designed a gantry and detector module that satisfies the above conditions. In addition, the design does not require extremely tight mechanical tolerances on the gantry parts because the factors that affect accuracy of the detector position have been confined to the front section of the module as explained below. Thus, the design process started with a module, which in turn determined the overall design of the gantry, but for clarity's sake we will describe the gantry design first.

A. Gantry Design

The gantry provides support for the twelve modules and all the electronics. Details on the electronic design can be found in [3]-[6]. To shorten the distance between a module and its electronics they have been placed on two large round plates as shown in Fig. 2., with each electronic set placed behind the corresponding module that it serves. The module support structure and the electronic support structure are bound together and rotate as one unit around the patient, riding on a large bearing system mounted on the third plate shown between the two plates mentioned above (Fig. 2). A "V" bearing system with a large "knife edge" ring and gear will be used as riding/driving mechanism for rotating 30° around the patient. A stepper motor with a gear-head and an optical rotational encoder form a closed system that can provide accurate rotation, as it was tested in our first PET prototype, MDAPET [7]. It was accurate to 0.03°.

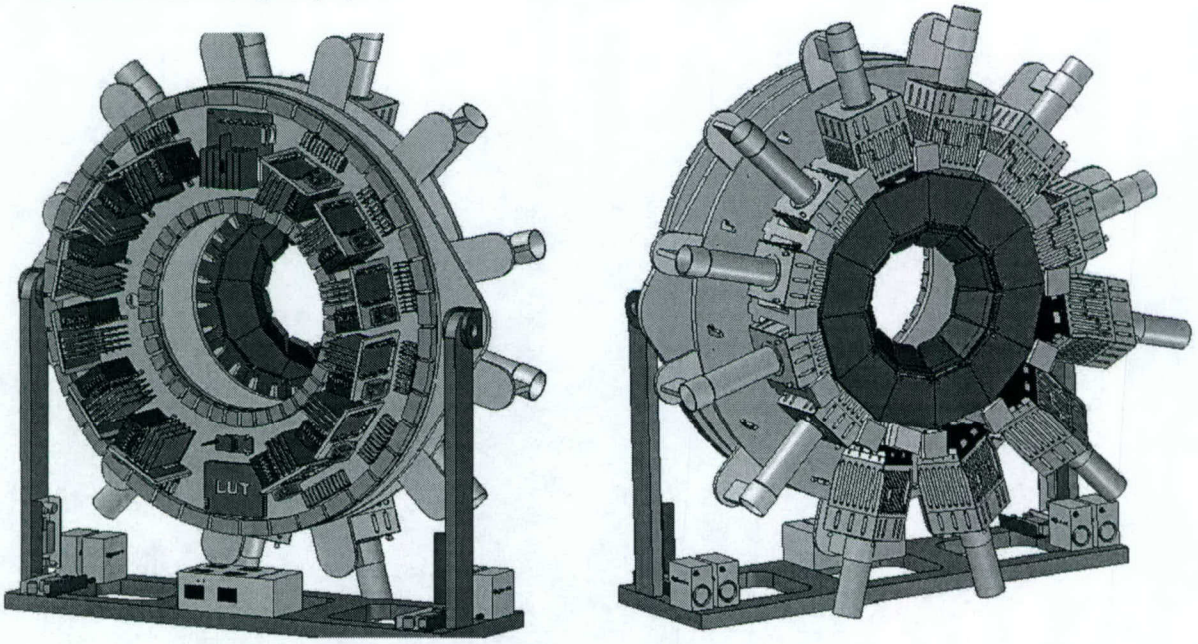

Fig. 2. Gantry design. **Right**: front view with 12 modules displayed in sets of four presenting the breast mode (left four modules), whole-body mode (top-right four modules) and transport mode (bottom-right four modules). Notice the movable lead shields partially open. **Left**: rear view of the gantry supporting all the electronic components of the camera. Notice that both front and back lead shields are visible. Boxes on the floor are the power supplies.

The middle plate can turn 90° on an axis horizontal and perpendicular to the patient axial direction; with it the entire gantry moves from the vertical orientation to the horizontal one. In the horizontal mode a bed with an opening can be attached to the gantry and the breast of a person lying prone on the bed will fall inside the FOV.

Each module is supported by a telescopic member attached to its backside, which slides on a trunnion fixed to the gantry, as well as two Delrin guides, one on each side of the module (Fig. 2). Vertical tabs on the supporting round plate and the Delrin guides provide positive stops for module positioning in the breast/brain and whole-body modes. Calibration of the modules position is necessary only once; from then on the tabs give a repeatable positioning pattern. These tabs allow only one direction of rotation for each module (Fig. 2).

Side lead shielding is provided for rejection of gamma rays generated outside the field of view (FOV). HOTPET will be a 3D acquisition PET camera with possibility for intermediate partial septa, manually placed, for rejection of scattered and accidental coincidences [1], [8], [9]. The shielding design required a compromise between optimum placement of the shields for each configuration mode and the level of complexity of its supporting mechanism. A shield optimally placed next to the modules will require both radial displacement as well as axial displacement on both sides of the modules as the modules move from breast/brain mode to whole-body mode, making very complicated the mechanical support of the heavy lead pieces (20 mm thick). We designed HOTPET's shielding using fixed sets of lead pieces placed on two sides of the detector modules (front and back of patient opening) configured in the brain mode, along with a set of movable pieces that can open and close like the petals of a flower. The movable shielding serves the dual purpose of narrowing the patient opening in the brain mode as well as decreasing the axial length of the FOV when the shields are flipped under the fixed pieces in the whole-body configuration (Fig. 2.). As a result, however, the shielding in the whole-body mode does not block as many photons generated in the FOV as it would if the shields were placed right next to the detector. From Table I one can realize that the axial extent of the detector module in whole-body mode is 129.3 mm, whereas the "shield-defined patient opening (axial)" is larger at 20.8 cm. In Table I "shield-defined opening" refers to the volume defined by the front and back lead shielding; the FOV is only part of the "shield-defined patient opening".

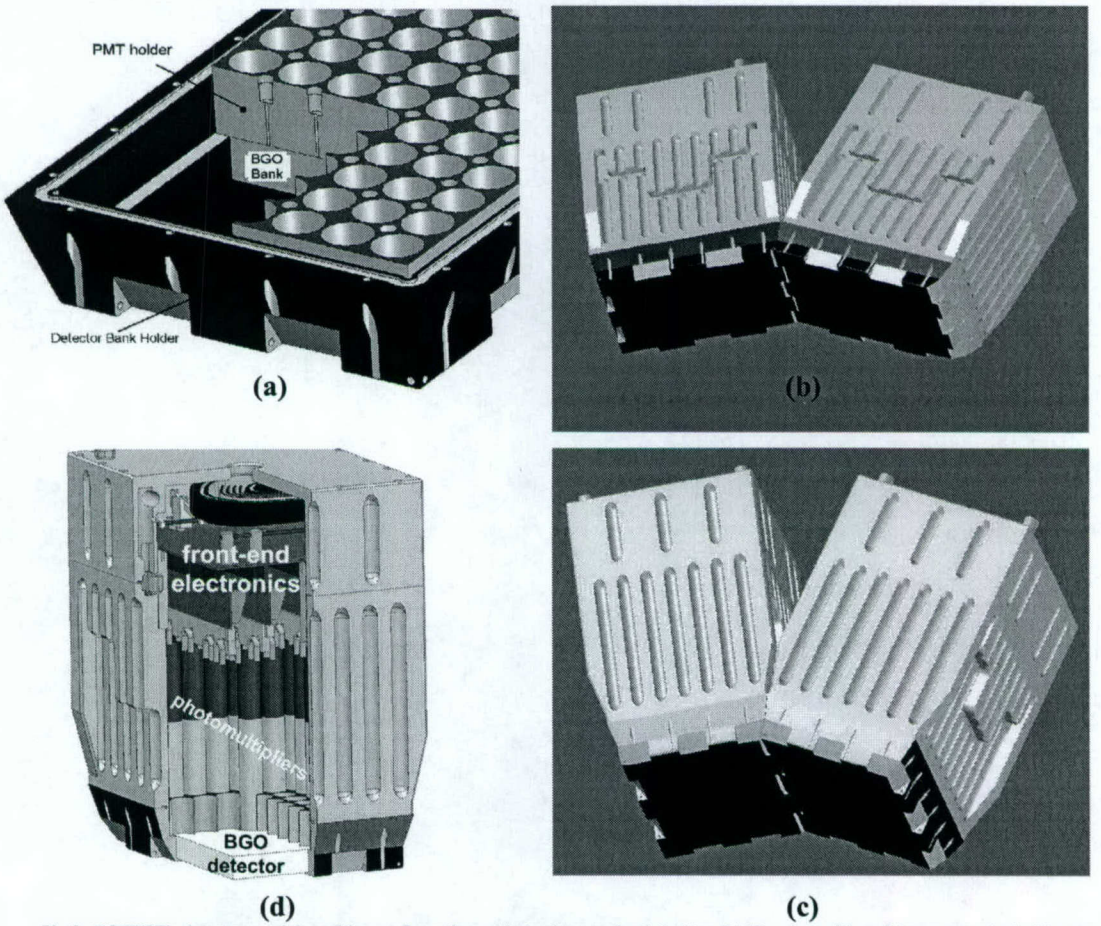

Fig.3. HOTPET's detector module and its configurations. (a) the detector-bank-holder. (b) The short sides of the rectangular holder are mated together forming a 30° angle and a large-diameter polygon for whole-body imaging. (c) The long sides of the rectangular holder are mated together forming a 30° angle and a small-diameter polygon for brain/breast mode. (d) Detector module internal components.

TABLE I

HOTPET MECHANICAL PARAMETERS

Mechanical parameters	Brain/breast mode	Whole-body mode
Number of detector modules	12	12
Detector bank axial dimension	207.9mm	129.3mm
Detector bank trans-axial dimension	129.3mm	207.9mm
Number of detector rings	72	44
Crystals per ring	528	864
Axial FOV	20.8 cm	12.9 cm
Distance between facing detector banks	54 cm	83.3 cm
Shield-defined patient opening (trans-axial)	28 cm	53.6 cm
Shield-defined patient opening (axial)	22.9 cm	20.8 cm
Gap between detector banks	14.8 mm	14.8 mm
Detector gap angle span	3.06°	1.98°
Gantry rotation	30°	30°
Lead shield thickness	20 mm	40 mm (front only)

B. Detector Module Mechanical Design

Each HOTPET detector module encases a highly pixilated *detector bank* of 60 blocks. The blocks are BGO crystal arrays with 7x7, 7x8 or 8x8 elements in them; combined, the detector bank has 3168 crystals with crystal pitch ranging from 2.6 mm to 3.1 mm. The bank is 207.9 mm long by 129.3 mm wide (Table I). A detailed description of the detector bank design and the novel block production process can be found in [10].

Scintillation crystals are optically coupled to 19 mm round photomultiplier tubes (PMT) using the photomultiplier quadrant sharing technique (PQS) developed in our group [10], [11]. The small size of the crystals requires that each module be accurately placed relative to each other to ensure alignment of crystals within the same detector ring.

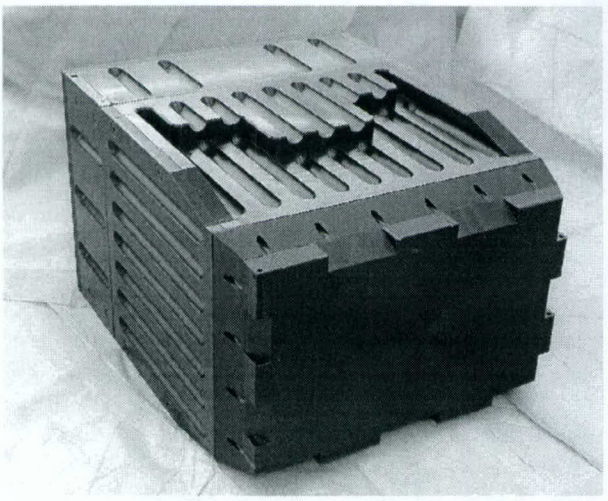

Fig. 4. Detector module. *Detector Bank Holder* shown in the foreground. Black anodized applied to minimize light reflection inside the box and throughout the air-cooling ducts.

Misalignment of crystals will produce lower resolution and poor image quality. Thus, rather than placing the modules on a massive gantry to achieve the position accuracy of the modules and in turn of the detectors, we designed a precise **detector bank holder** as shown in Fig. 3(a) and Fig. 4. The bank holder has keyways and complementary keys built onto opposite sides of the holder to allow interlocking with each other to form a polygon and maintain detector rings co-planar (plane perpendicular to the axial direction). Figures 3(b) and 3(c) show two modules locked in the whole-body and brain/breast positions respectively. By taking care of the tight mechanical tolerances and appropriate alignment of the detector elements with the polygon structure formed by the detector holders, the gantry design is greatly simplified, reducing its manufacturing cost.

The *bank holder* is a black Delrin cradle holding the BGO-bank and the PMT-holder mold as shown in Fig.3(a). The bank holder was designed to keep equal separation (1.48 mm) between adjacent detector banks in the two camera modes. Consequently the gaps in the corresponding sinograms are small and slightly larger in the brain/breast mode due to the larger angle spanned by the same distance at a smaller radius, as shown in Fig. 5.

The PMT mold aligns the photomultipliers over the BGO

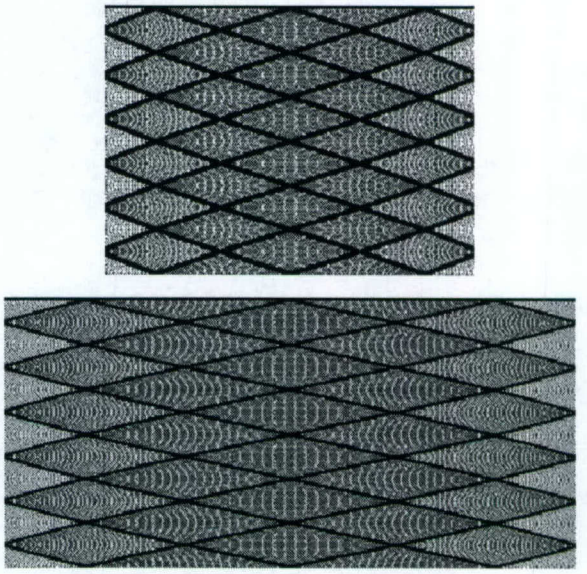

FIG. 5. Simulated sinograms showing all lines of response for the brain/breast mode (top), and the whole-body mode (bottom). Both histograms were drawn on the same scale

crystal arrays in PQS mode [11]. It also includes a network of light emitting diodes (LED) housed in small holes drilled between PMT holes (Fig. 6). Light from the LEDs is collimated by 0.7 mm diameter holes onto the central crystal of the BGO blocks and used by the automated PMT gain-tuning technique featured in this camera [12].

Figure 3(d) shows the PMTs and their corresponding voltage dividers. Around the PMT and behind the outer walls of the module, there is a closed-loop sheet of mu-metal to minimize the presence of external magnetic fields in the PMT space (too thin to be observed in Fig.3(d)). Above the PMT-voltage dividers there is a set of pressure-applying

components (upside-down "U"s), exerting a light force on each PMT to help preserve the optical coupling, which could deteriorate over time from mechanical vibration. Above the pressure bars, in the upper half of the module, there is a set of

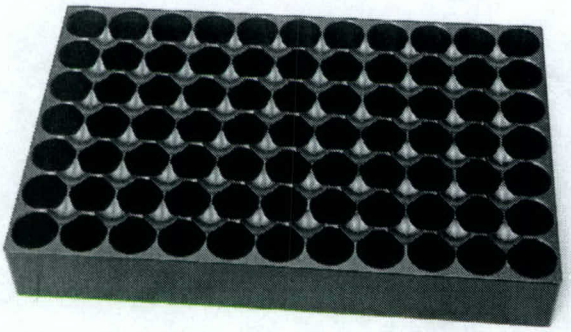

Fig. 6. Photomultiplier positioning grid. Accurately places PMT over the BGO bank of blocks using PQS technology.

four printed circuit daughter-boards attached to a larger motherboard. Each module contains within (a) analog front-end electronics for signal amplification and discrimination, (b) signal weighting circuit for Anger decoding of the location of gamma hits (first level decoding – prenormalized signals), (c) distribution of high-voltage for PMTs, and (d) the LED-PMT-gain tuning system [3]. In order to service a module, e.g. to replace a voltage divider, it is necessary to remove the motherboard while keeping in place the daughter-boards. We have built a precision frame with pockets cut into its sides to hold the daughter-boards using a series of brass pieces wedged into these pockets. Fig.3(d) shows two wedges next to the daughter boards; the mounting frame was cut out for clarity. The motherboard is removed using four levers operated in tandem and supported by the motherboard to impel itself up as the levers press against the edge of the daughter boards below.

A total of 12 RG-174 coaxial cables carry the information from each module. In addition, there is one high-voltage cable and one parallel cable for system control. These lines come out the top of the module. Before going through the opening the cables are routed through a simple maze partly filled with dark epoxy to make the interior of the module light tight (round piece against the top cover in Fig 3-d).

Each module dissipates 45 W, which would increase the internal temperature if there were no cooling, thereby degrading the light output of the BGO scintillator. We built a simple network of air ducts inside the module walls with the intake and outlet couplings at the top of the box (Fig 3-b and 3-c). In addition, grooves were milled on the outside surface of the walls, increasing the total heat-radiating surface exposed to the outside air.

III. Conclusions

We have designed the detector modules and supporting gantry of a modular PET camera that can change geometric configurations from whole-body to brain mode without changing the separation between adjacent modules.

A set of fixed and movable lead shields was also designed to accommodate the changing geometry while maintaining adequate rejection of gammas rays from outside the FOV.

The gantry can rotate azimuthally 90° and turn the scanner into a dedicated high-sensitivity breast scanner.

Accurate positioning of detector crystals is essential in high-resolution PET systems. Such accuracy is provided in our design by a **detector bank holder** placed directly in the front section of the module where the detector crystals are located, rather than relying on accurate placement of the modules on the gantry. As a result loose tolerances are permitted in the manufacturing of the gantry, producing a cost reduction.

IV. References

[1] W.H. Wong, J. Uribe, H. Li, H. Baghaei, Y. Wang, M. Aykac, Y. Liu, T. Xing, D. Bilgen, R. Farrell. The Design of High-Resolution Transformable Wholebody PET Camera. *IEEE Trans. Nucl. Sci.*, vol 49, pp.2079-2084, October 2002.

[2] W.H. Wong, J. Uribe, H. Li, H. Baghaei, Y. Wang, M. Aykac, Y. Liu. Design of a Wholebody High Resolution PET with Changeable Transaxial and Axial Fields of View. Proceedings of the SNM 48th Annual Meeting, p98P. June 2001.

[3] H. Li, W-H. Wong, Y. Wang, Y. Liu, T. Xing, J. Uribe, H. Baghaei. Front-End Electronic Design Based on High-Yield-Pileup-Event-Recovery Method for a High-Resolution PET Camera with PMT-Quadrant-Sharing Detector Modules. IEEE Nuclear Science Symposium and Medical Imaging conference record, Norfolk, VA, November 10-16, 2002.

[4] Y. Liu, H. Li, Y. Wang, T. Xing, J. Uribe, H. Baghaei, W-H. Wong. A Programmable High-Resolution Ultra Fast Delay Generator. IEEE Transactions on Nuclear Science, *50(5)*, 1487-1490, October, 2003.

[5] H. Li, T. Xing, Y. Liu, Y. Wang, H. Baghaei, J. Uribe, W-H. Wong. A Hotlink/Network PC Data Acquisition and Image Reconstruction System for a High Resolution Whole-Body PET with Respiratory and ECG-Gated Performance. IEEE Transactions on Nuclear Science, *50(3)*, 393-397, June, 2003.

[6] Y. Wang, H. Li, Y. Liu, T. Xing, J. Uribe, H. Baghaei, W-H. Wong, A Modular Low Dead-Time Coincidence System for High Resolution PET Cameras. IEEE Transactions on Nuclear Science, *50(5)*, 1386-1391, October, 2003.

[7] J. Uribe, H. Baghaei, H. Li, et al, "Basic imaging performance characteristics of a variable field of view PET using quadrant sharing detectors," *IEEE Trans. Nucl. Sci.*, vol 46, no.6, pp. 491-497, 1999.

[8] M. Aykac, J. Uribe, H. Baghaei, H. Li, Y. Wang, Y. Liu, T. Xing, W-H. Wong. Septa Design Study for Volumetric Imaging in Positron Emission Tomography. IEEE Transactions on Nuclear Science, *49(5)*, 2097-2102, October, 2002.

[9] H. Baghaei, W-H. Wong, M. Aykac, J. Uribe, H. Li, Y. Wang, Y. Liu, T. Xing. Brain Lesions Detectability Studies with a High Resolution PET Operating in No-Septa and Partial-Septa Configurations. IEEE Transactions on Nuclear Science, *50(5)*, 1364-1369, October, 2003.

[10] J. Uribe, W-H. Wong, H. Li, H. Baghaei, Y. Wang, Y. Liu, T. Xing, R. Farrell. An Efficient Detector Production Method For Position-Sensitive Scintillation Detector Arrays with 98% Detector Packing Fraction. IEEE Transactions on Nuclear Science, *50(5)*, 1469-1476, October, 2003.

[11] W-H. Wong, "A positron camera detector design with cross coupled scintillators and quadrant sharing photomultipliers," *IEEE Trans. Nucl. Sci.*, vol 40, pp. 962-966, 1993.

[12] H. Li, Y. Liu, T. Xing, Y. Wang, J. Uribe, H. Baghaei, S. Xie, R. Ramirez, W.H. Wong. An Instantaneous Photomultiplier Gain Calibration Method for PET or Gamma Camera Detectors Using LED Network. IEEE Nuclear Science Symposium and Medical Imaging Conference Record, Portland, Oregon, October 2003.

0-7803-8257-9/04/$20.00 © 2004 IEEE.

A Simple Respiration Gating Technique and its Application in High-Resolution PET Camera

Yu Wang, *Member, IEEE*, Hossain Baghaei, *Member, IEEE,* Hongdi Li, *Member, IEEE,* Yaqiang Liu, Tao Xing, Jorge Uribe, *Member, IEEE,* Rocio Ramirez, Shuping Xie, Soonseok Kim, and Wai-Hoi Wong, *Member, IEEE*

Abstract—**We have developed a simple technique to gate positron emission tomography (PET) imaging in synchronization with respiratory motion to reduce image blurring caused by breathing and improve quantification of tracer uptake in lesions in the chest and abdomen, especially in very high-resolution PET systems. Taking advantage of the temperature differences in the air flow in a nostril due to inhalations and exhalations, a simple solid thermometer was used to construct a respiratory gating system to monitor the respiratory cycles. The gating system provided trigger signals synchronous with respiration and 40Hz timing marks. These trigger signals and timing marks were inserted into the data stream in real-time while the PET camera was taking data. The gating trigger signals represent a particular phase of respiratory motion, and the evenly cycled timing marks were designed for motion-image frame registration. This gating system was implemented and tested with our MDAPET, a very high-resolution (2.7-mm resolution) PET camera developed at The University of Texas M. D. Anderson Cancer Center. A volunteer with 2 spherical lesion phantoms (diameters 3mm and 5mm) placed on the abdomen close to the navel was scanned in the gated mode. The respiration-gated images of the lesion phantoms were compared and studied. The simple respiratory gating system worked well in terms of detecting the breathing cycle and providing gating trigger signals and timing marks. Image blur and errors in the measurements of the lesions' volumes in the gated PET images were reduced, compared with those of the non-gated PET images.**

I. Introduction

Motion blurs images. The amplitude of respiratory motion can be as high 20 mm, severely degrading the high-resolution performance of the modern medical imaging instruments if no anti-motion method is applied while scanning the chest and abdomen. In the cases of computed tomography (CT) or magnetic resonance imaging (MRI), because of their fast scanning speed, the respiratory motion can be eliminated by breath holding. However, for positron emission tomography (PET), due to its relatively slower scanning speed, it is not practical to apply breath holding to obtain motion-free images. Gating the respiration is a more practical approach to acquiring a more accurate and clearer image. Some recent studies have shown that respiration gated PET images resulted in a 34% [1] or 28% [2] reduction of the error in lesions' measured volumes and as much as 159% [1] or 56.5% [2] in the maximum standardized uptake value (SUV). Meanwhile, PET (with 18F-fluorodeoxyglucose [18F-FDG] injection) has much better sensitivity (87%) and specificity (91%) than CT (68% and 61%, respectively) in lung cancer detection [3].

Many respiration-gating methods, such as pneumatic respiratory bellows, air flow pressure sensors and video-camera-based motion detectors, have been developed over the past decades. Each of them works well but has some drawbacks such as patient discomfort, implementation complexity, or relatively high cost. We proposed and designed a simple gating technique by sensing the temperature differences in the air flow in a nostril due to inhalations and exhalations. A cheap solid-state thermometer can be used to construct a circuitry to monitor the respiratory cycles. With only a small solid-state thermometer mounted nostril piece, patients can breathe more freely and comfortably during a scan.

II. System Design

A. Design of the nostril sensor piece

A solid-state temperature sensor (TMP04, Analog Devices Inc.) was used to measure the temperatures of air flowing through a nostril. A plastic tube (Tycon R3603, Saint-Gobain Performance Plastics Corporation) about 3 cm long was used to construct the nostril piece to hold the temperature sensor and to conduct the air flow of respiration over the surface of the temperature sensor. A small window the size of the temperature sensor was cut on the side of the tube about 6 to 8 mm from one end. The sensor was wired and powered with 3 AA batteries, Fig. 1a. The temperature signals from the sensor were fed into a digital signal processor (DSP) for further gating processing.

This work is supported in part by the NIH-CA58980 PHS Grant, NIH-CA61880 PHS Grant, NIH-CA76246 PHS Grant, NIH-CA58980S PHS Grant, NIH-EB01481 PHS Grant, NIH-EB00217 PHS Grant, NIH-EB01038 PHS Grant, U.S. Army-Breast Cancer Research Grant, Texas ARP/ATP Grant 003657-0058-2001 and Analog Devices Inc. university program.

Yu Wang, Hossain Baghaei , Hongdi Li, Yaqiang Liu, Tao Xing, Jorge Uribe, Rocio Ramirez, Soonseok Kim, Wai-Hoi Wong are with The University of Texas M. D. Anderson Cancer Center, Houston, TX 77030, USA (Yu Wang's telephone:713-745-1671, e-mail: wangy_km@yahoo.com).

0-7803-8257-9/04/$20.00 © 2004 IEEE.

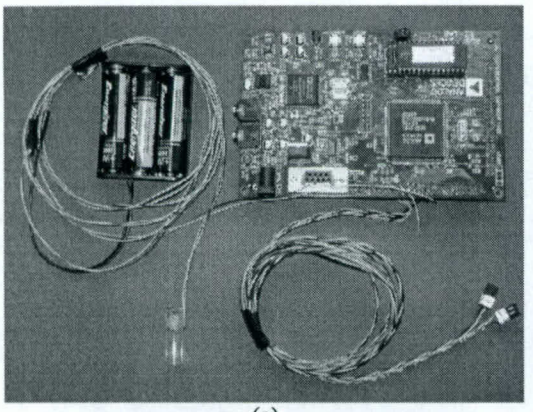

(a)

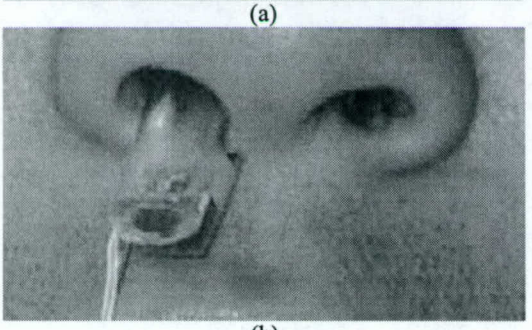

(b)

Fig. 1 (a) the proposed respiration gating system; (b) the nostril sensor piece was tested by a volunteer.

B. *Signal processing and gate generating*

An inexpensive DSP development kit (ADSP2181 EZ-Kit, Analog Devices Inc.) was used to process the temperature information from the sensor, to trace the respiratory cycles, and to produce the respiration gating signals and the evenly cycled timing marks.

The TMP04 provides temperature information with a pulse width modulation (PWM) signal. PWM signal facilitates the interface because the signal can be transferred with one single wire. Widths of high and low statuses representing the temperature information can be measured easily by counting the duration of each status. Then, the temperature can be calculated using widths of high and low statuses. The DSP performs width measurement of the PWM signal from the TMP04 and the temperature calculation. Due to the respiratory strength variation, the temperature on the thermometer varies too much to discriminate respiratory cycles with a fixed threshold. As a result, the DSP must track the variation and adjust the threshold dynamically. In addition, due to the respiratory cycle variation, periodic timing marks are needed to register gating phases correctly. The DSP creates evenly cycled (about 40-Hz) timing marks along with a digital respiration gating signal obtained through the above processing. Fig. 2 shows the relationships among the temperature sensor signal, gating threshold, and digital gating signal.

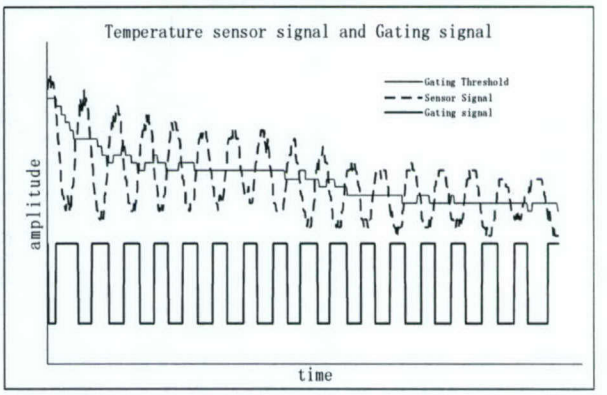

Fig. 2 Temperature sensor signal and respiratory gating signal; the gating threshold tracks the variation of the sensor signal automatically with a DSP tracking algorithm.

C. *Gated PET data acquisition and processing*

The gating signals and timing marks were fed into the coincidence circuitry of the MDAPET [4]. Thus, a specific logic implemented in a complex programmable logic device (CPLD) generated unique codes corresponding to the gating signals of inhalation and expiration along with the timing marks and inserted these codes into the coincidence data stream in real time.

Although respiratory cycle-predicting algorithms, by which sonogram-mode data acquisition is possible, can be realized in DSP, we found that if a patient breathes freely without breath-guiding instruction, the cycles vary too quickly to be predicted correctly. Correspondingly, in this work, the data were taken in list mode rather than sonogram mode.

A program was written to process the list-mode data. The program extracted the codes of inhalation and expiration and the evenly cycled timing marks and generated framed sinograms according to the gating and timing codes. By means of evenly cycled timing mark insertion and list-mode data acquisition, not only can a patient breathe freely during a scan but also an investigator can adjust the frame pattern of the gated images to achieve the best observation. A Labview program for editing the frame patterns and displaying the gated images was created. The gated image frames can be displayed in both frame-selectable mode and sequential (movie) mode.

III. Test Method

As shown in Fig. 3, 2 lesion phantoms (diameters 3 mm and 5 mm) filled with 18F-FDG solution (SUV=8) were attached to a volunteer's abdomen (near the navel). The volunteer was scanned with the gating device.

The 3-dimensional re-projection method (3DRP) [5] was used to reconstruct images. To simplify the experiment, the images were reconstructed without attenuation and scattering corrections. However, a better result could be expected if those corrections were applied.

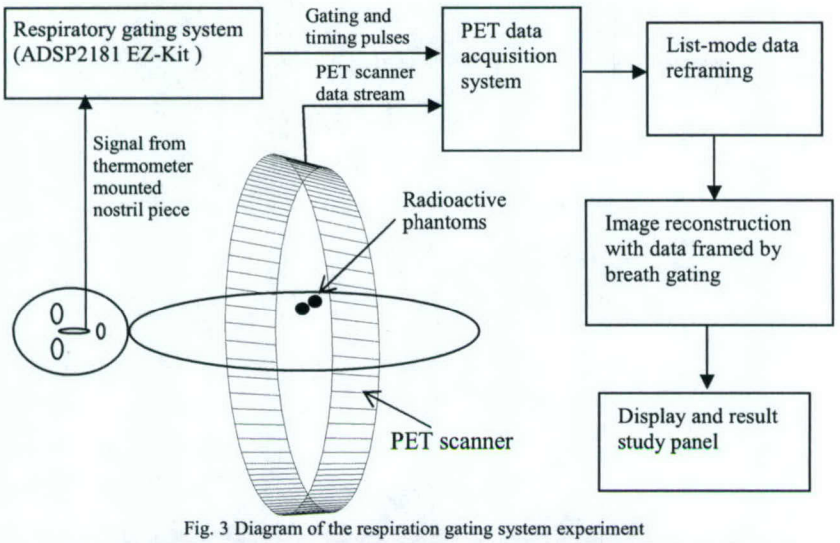

Fig. 3 Diagram of the respiration gating system experiment

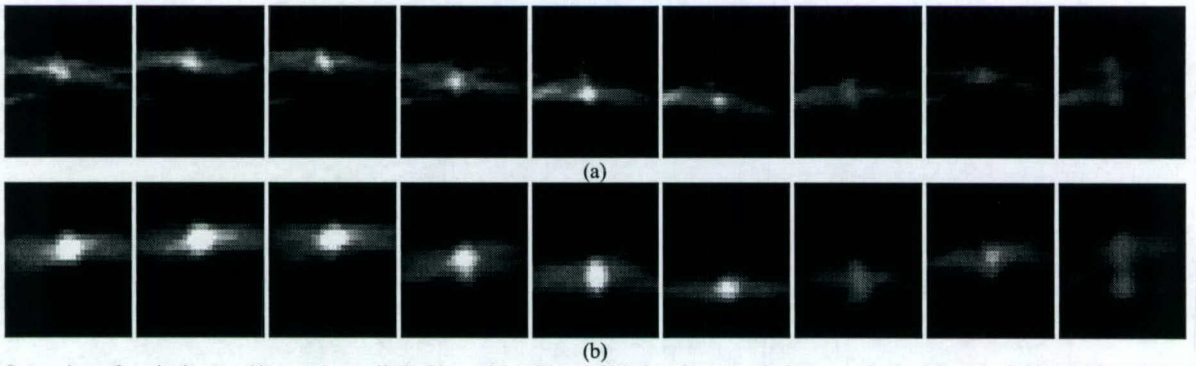

Fig. 4 Comparison of respiration gated images (same slice) of 3-mm (a) and 5-mm (b) lesion phantoms, the images at the far right in both (a) and (b) are the images without respiration gating.

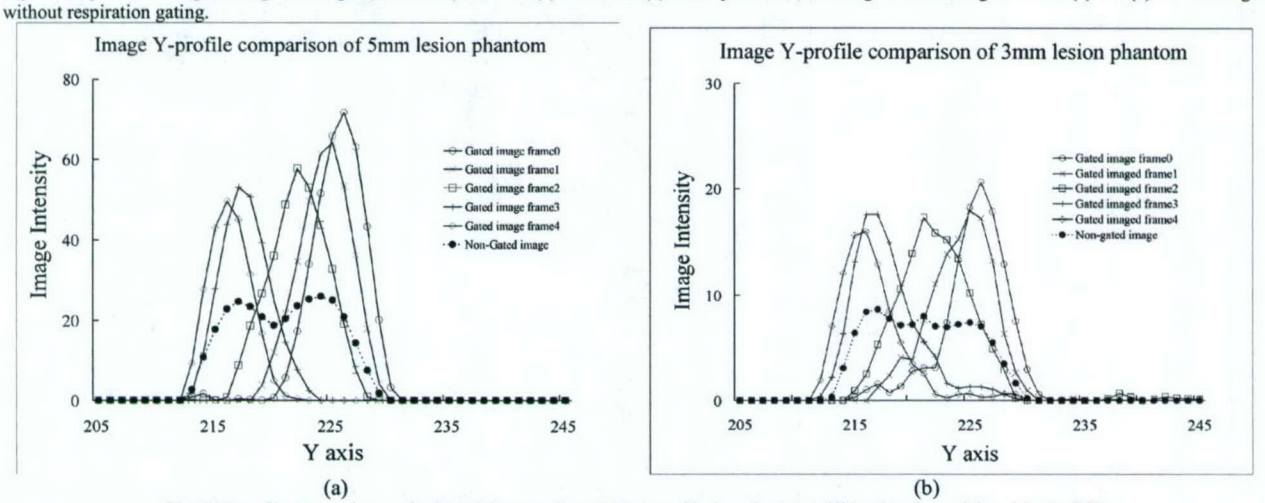

Fig. 5 Y-profile comparisons of selected frames of gated images of lesion phantoms (diameters 5 mm [a] and 3 mm [b]).

IV. Results

Fig. 4 visually shows much better lesion detection among respiration-gated images. Fig. 5 gives the profiles of the images shown in Fig. 3. For images of each phantom, the profiles were generated at the same X coordinate. Table 1 lists quantitative comparisons of gated and non-gated images. In terms of SUV contrast detection, respiration-gated images improved SUV peak value about 137% for 5-mm phantom and 106% for 3-mm phantom on average. Meanwhile, the lesion size (full width half measurement [FWHM] of profile) measurement was reduced on average 59% and 57% for 5-mm and 3-mm phantoms, respectively. Obviously, the respiration-gated data provide much sharper images,

improving the lesion detection significantly over the non-gated data. The reconstructed images of the 3-mm phantom are slightly worse than those of the 5-mm phantom, probably because of statistical error resulting from fewer counts.

V. Conclusions and Discussions

Table 1 Quantitative comparison of image profiles

Phantom	Image frame No.	FWHM of profile	SUV peak value
5mm diameter	0	5.3	71.7
	1	5.7	64.1
	2	6	57.7
	3	5	53
	4	4.7	49.7
	Average	5.3	59.2
	Non-gated	12.9	26
3mm diameter	0	5	20.6
	1	5.8	18
	2	7.5	17.4
	3	5.1	17.6
	4	5	16
	Average	5.7	17.9
	Non-gated	13.2	8.7

We developed a simple respiration gating technique with a solid-state temperature sensor detecting the temperature difference of the air flow in the nostril due to inhalation and expiration. A gating apparatus based on this technique was designed using a low-cost DSP development kit. Also an experiment was done to evaluate the proposed gating method. The respiration-gated data acquired with the proposed gating method provided much sharper and clearer images than the non-gated data did. Furthermore, the gated images improved lesion detection tremendously.

References

[1] S. A. Nehmeh, "Effect of respiratory gating on quantifying PET images of lung cancer," *The Journal of Nuclear Medicine*, 2002, pp. 876–881.

[2] S.A. Nehmeh, "Effect of respiratory gating on reducing lung motion artifacts in PET imaging of lung cancer", *Medical Physics*, 2002, pp. 366–371.

[3] N.C. Gupta, "Mediastinal lymph node sampling following positron emission tomography with fluorodeoxyglucose imaging in lung cancer staging", *Chest*, 2001 pp. 521-527.

[4] J. Uribe, "Basic imaging performance characteristics of a variable field of view camera using quadrant sharing detector design", *IEEE Transaction on Nuclear Science*, 1999, vol. 46, pp.491-497.

[5] P.E. Kinahan, "Analytic 3D image reconstruction using all detected events", *IEEE Transaction on Nuclear Science*, 1988, vol. 36, pp. 964-968.

0-7803-8257-9/04/$20.00 © 2004 IEEE.

An Evaluation of the Effect of Partial-Septa on Detection of Small Lesions in Brain Phantom Study Using MDAPET Camera

Hossain Baghaei, *Member, IEEE* , Wai-Hoi Wong, *Member, IEEE* , Jorge Uribe, *Member, IEEE,* Hongdi Li, *Member, IEEE,* Yu Wang, Tao Xing, Rocio Ramirez, Shuping Xie, Soonseok Kim, and Yuxuan Zhang

***Abstract*--We investigated the effect of partial-septa on detection of small lesions embedded into the Hoffman brain phantom using a high resolution PET camera. Three-dimensional (3-D) positron emission tomography (PET) acquisition in comparison to two-dimensional (2-D) PET acquisition improves the sensitivity of the system at the cost of higher random and scatter coincidence contributions. A partial-septa system, in which full ring septa are inserted between only some of the detector rings, allowing "partial" 3-D acquisition may provide a better alternative than the 2-D acquisition and full 3-D acquisition for reducing the scatter and random coincidence with less sensitivity loss. We used the MDAPET camera to detect small lesions in brain images obtained from the scan of the 3-D Hoffman brain phantom with three embedded small lesion phantoms with diameters of 3, 5, and 8.6 mm. To include the effect of background from activity outside the FOV, a large cylindrical uniform phantom with diameter of 21.5 cm filled with lower activity was placed near the Hoffman brain phantom. Data were acquired in three separate scans for 3 phantoms: (1) The large uniform cylindrical phantom; (2) the Hoffman brain phantom; (3) the 3 small lesions embedded in brain phantom. For scan of each phantom, the other phantoms were filled only with water. For lesions, data were collected for several SUVs as activity decayed. The three sets of data were selectively combined to generate the sinograms for the desired standard uptake values (SUVs). In partial-septa configurations, the white matter regions of the brain images had lower counts and the images visually looked better than no-septa images. Images taken in the partial-septa configuration had slightly higher contrast.**

I. Introduction

THE three-dimensional (3-D) positron emission tomography (PET) acquisition has higher sensitivity than two-dimensional (2-D) PET acquisition, but at the cost of higher random and scatter coincidence. Currently, commercial PET cameras operate in two extreme modes of full-septa (2-D mode) and no-septa (3-D mode) configurations. 3-D PET has the potential to reduce data acquisition time compared to 2-D PET. Several investigators have studied the effect of full-septa and no-septa configurations on lesion detectability and noise characteristics of images and have found that 3-D acquisition mode may have advantages in imaging brain, small patients, and animals, and especially at low activity levels they report that it can outperform 2-D mode acquisition [1]-[4]. Recently, a hybrid PET design was proposed to acquire projection data in both 2-D and 3-D modes simultaneously by using rotating partial-ring septa [5]. Several investigators also have studied optimal septa spacing in gamma cameras for PET imaging [6], [7].

A partial-septa system, in which full-ring septa are inserted between only some of the detector rings, may provide a better alternative than the 2-D acquisition and no-septa 3-D acquisition. In this study, intermediate septa designs were used to reduce the scatter and accidental coincidence with less sensitivity loss by using a 3-D PET camera that could operate in no-septa mode or with a partial-septa system. In our two previous works, we measured the noise equivalent count (NEC) rate for several partial-septa configurations [8] and we studied the effect of partial-septa on brain lesion detection without activity outside the field-of-field (FOV) [9]. In this work, we placed a large uniform cylindrical phantom with lower activity (SUV=1) outside FOV and further studied the effect of using partial-septa on detection of brain lesion.

II. Materials and Methods

A. Scanner and Phantoms

We used the MDAPET, a high-resolution PET camera, to scan the phantoms. This camera is a 14-ring scanner with an intrinsic transaxial resolution of 2.8 mm. Each ring contains 448 bismuth germanate (BGO) crystals having an in-plane and axial crystal pitch of 2.66 and 2.80 mm, respectively. The detectors are grouped into blocks of 7X7 crystals. The camera detection system is divided into eight independent, movable modules. Each module can be translated radially to alter the

This work was supported in part by the NIH Grant RO1 CA58980, NIH Grant RO1 CA61880, NIH Grant RO1 CA76246, NIH Grant RO1 EB00217, NIH Grant RO1 EB001038, US Army Breast Cancer Grant, Texas Higher Education Grant, John S. Dunn Foundation Research Grant, and by the Cobb Foundation for Cancer Research.

The authors are with the University of Texas M. D. Anderson Cancer Center, Houston, TX 77030 USA (H. Baghaei's telephone: 713-794-5270, e-mail: hbaghaei @di.mdacc.tmc.edu).

size of the patient opening, optimizing the detection sensitivity for different body cross-sections. The detector module design, which is based on a quadrant-sharing technique, its electronics, and the imaging performance characteristics of the camera are reported previously [10-16].

MDAPET camera has an axial field-of-view (FOV) of 38.5 mm which is much smaller than a typical clinical camera. In order to simulate more closely the performance of a clinical size camera, the detector modules were modified axially to extend from 38.5 mm to 131 mm by placing the side shields farther apart as shown in Fig. 1a [8]. Since there is no detector ring in the extended region, the maximum ring difference and corresponding axial acceptance angle of a clinical camera could be larger than those of the modified MDAPET camera. For this work we used a maximum ring difference of 13 for image reconstruction. Extensions added to each side of each detector module consisted of three layers of lead and aluminum as a BGO substitute to take into account for inter-crystal scattering. Each lead foil (3 mm thick) was sandwiched between two 1.5 mm thick aluminum foils. Each side shield was extended from 60 mm to 85 mm to reduce the radiation coming from outside the FOV.

Fig. 1 shows an axial view of the modified version of the MDAPET detector module for three septa configurations: (a) no-septa, (b) partial 5-septa with inter-gap separation between septa of 2.01 cm, and (c) partial 7-septa with inter-gap separation between septa of 1.46 cm. Septa consisted of 2 mm of lead in all designs.

The phantom system consisted of three phantoms: a uniform phantom with diameter of 21.5 cm, a 3-D Hoffman brain phantom, and three small lesion phantoms with inner diameters of 3 mm, 5 mm, and 8.6 mm embedded into the Hoffman brain phantom. All lesions had the same standard uptake values (SUVs). The approximate ratio of the activity concentration in the lesions to the activity in the background (brain gray matter regions) ranged from 2 to 10. The lesions were placed into the brain phantom white matter regions. The 5 mm lesion was placed near the center of the brain phantom, and the other two lesions were placed near the periphery of the brain phantom. Fig. 2 shows a schematic axial view of the phantoms setup.

B. *Data Collection*

To minimize the number of imaging sessions, we acquired three separate data sets for: (1) the hot lesion phantoms, (2) the warm Hoffman brain phantom without lesions, and (3) the uniform phantom outside the FOV. When the first data set (hot lesions data) were acquired, the hot lesions were placed inside the Hoffman brain phantom filled with non-radioactive water (cold background) to simulate the attenuation and scatter effects. For the second set of data, the lesion phantoms were removed and the Hoffman brain phantom was filled with FDG solution. For the third set of the data, the uniform phantom was filled with FDG solution and the Hoffman brain phantom was filled with water and no lesions.

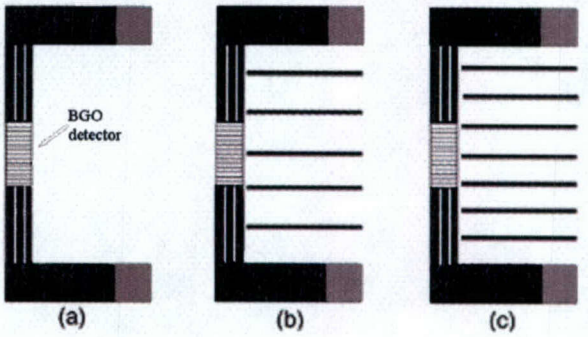

Fig. 1 Axial view of a modified MDAPET module with three different septa configurations: (a) no-septa, (b) partial 5-septa, and (c) partial 7-septa.

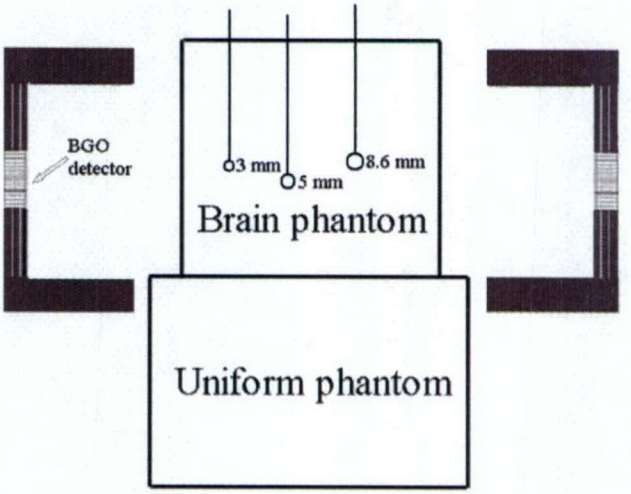

Fig. 2. A schematic axial view of the modified MDAPET modules and the phantoms set up.

All data were acquired in 3-D mode with an axial acceptance of 13 rings, which produced 196 sinograms. In the present study, each sinogram had 239 radial bins and 180 azimuthal views, and no axial or transaxial compression was performed on projection data. The radial sampling was 1.385 mm.

C. *Data Analysis*

We selectively combined the three sets of sinogram data that were acquired separately to generate the sinogram data for the desired SUVs for the uniform phantom, brain and lesions. This combination method greatly reduced the number of required measurements for different lesion uptake and also eliminated the effect of the 'cold' walls of the lesion phantoms that exists when hot lesions and the warm background are measured simultaneously [16-17]. This sinogram summing method allows all the different SUVs data for lesions to be taken in one experimental period by collecting the different SUVs data as the activity decays.

Prior to image reconstruction, the projection data were corrected. These corrections included random coincidence subtraction, attenuation correction, geometric, and detector-pair efficiency corrections [18]. The attenuation correction was estimated by calculating the attenuation length from the shape of the phantom (cylinder) and assuming uniform attenuation. All data were acquired with the ^{18}F-fluorodeoxyglucose (FDG) tracer. For all data presented in this work, the uniform phantom had SUV of 1 and the Hoffman brain phantom had SUV of 6 (only SUVs of lesions were varied).

For image reconstruction we used the 3D-reprojection algorithm (3DRP) with a Butterworth filter [19-20]. The camera allows simultaneous imaging of 27 transaxial image slices with 1.4-mm slice thickness. Each reconstructed image had 239 X 239 pixels.

III. RESULTS

Figure 3 shows two reconstructed image slices of the Hoffman brain phantom without embedded lesion for no-septa (top), 5-septa (middle), and 7-septa (bottom) configurations. The contribution from activity outside the FOV (from uniform phantom) was included in the data. The images show that, as the number of septa increased, the white matter (background) contribution became less observable, the gray matter contribution became more pronounced, and image quality visually improved.

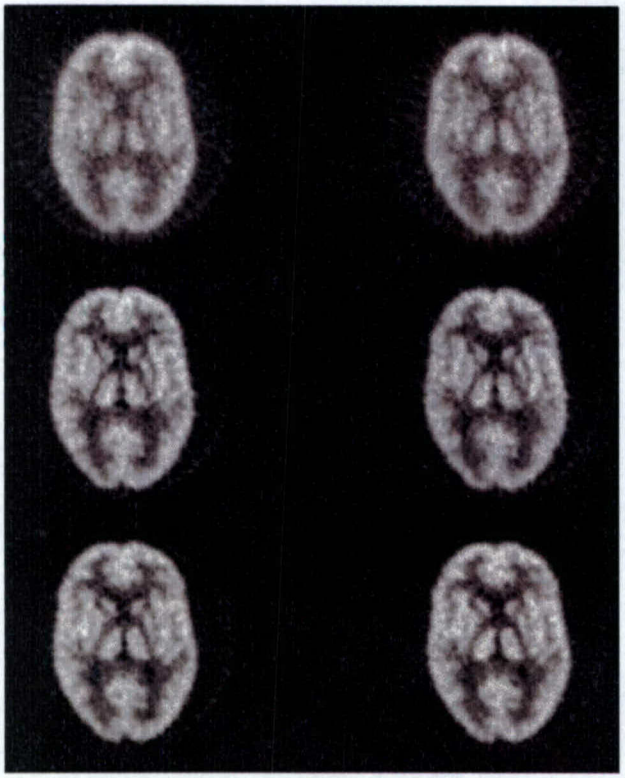

Fig. 3. Two image slices of the Hoffman brain phantom reconstructed with the 3DRP algorithm for three different septa configurations: (top) no-septa, (middle) 5-septa, and (bottom) 7-septa.

Fig. 4 shows two reconstructed image slices with 3 mm (left near edge) and 5 mm (near center) embedded lesion phantoms when the ratio of the activity concentration in the lesions to brain background (gray matter) was 6. In order to improve visualization of smaller lesions, the 8.6 mm lesion phantom was placed such that it did not appear in the same image slices as the others.

Fig. 5 shows two reconstructed image slices with 5 mm embedded lesion phantom when the ratio of the activity concentration in the lesions to background (gray matter) was 2.5. Fig. 6 shows two reconstructed image slices with 8.6 mm lesion when the activity concentration in the lesions to the brain background was 2.5.

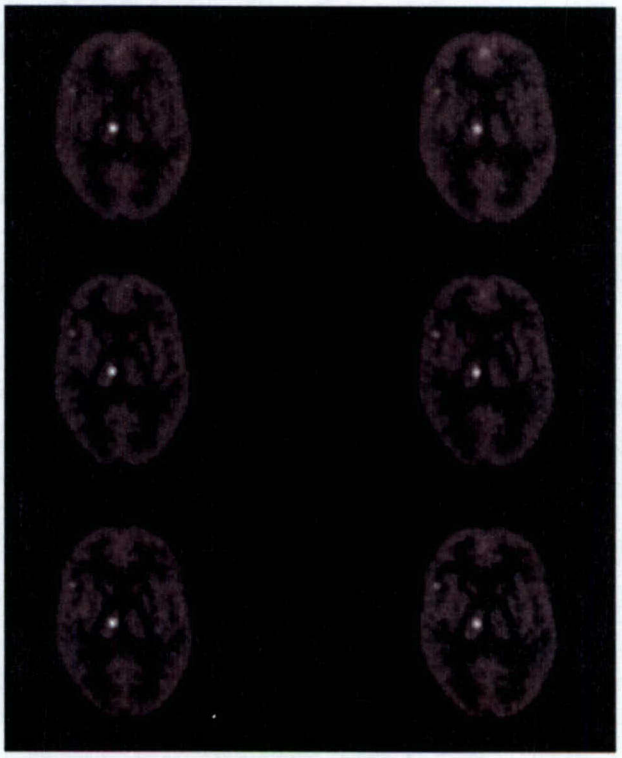

Fig. 4. Two image slices of the Hoffman brain phantom with 3 mm and 5 mm lesions for the three different septa configurations: (top) no-septa, (middle) 5-septa, and (bottom) 7-septa. The ratio of activity concentration of the lesions to brain gray matter was 6.

Visual comparison of the images did not show any significant differences between no-septa and the partial-septa configurations in terms of detection of lesions; however partial-septa images had less background noise compared to no-septa case.

Fig. 7 shows the normalized horizontal profiles running through the middle of the images of 3 mm lesion in warm background for no-septa and partial-septa configurations when the ratio of the activity in the hot lesion to the warm background was 6 (Fig. 4). Figs. 8 and 9 show the normalized horizontal profiles running along the middle of the 5 mm lesion image at activity ratios of 6 and 2.5, respectively. Figs. 10 and 11 show the normalized horizontal profiles through

the middle of the 8.6 mm lesion image at activity ratios of 6 and 2.5, respectively. In profiles shown in Figs. 7 to 11 no averaging over rows or columns was done. The profile data for each image was normalized according to the average count in the background for each case.

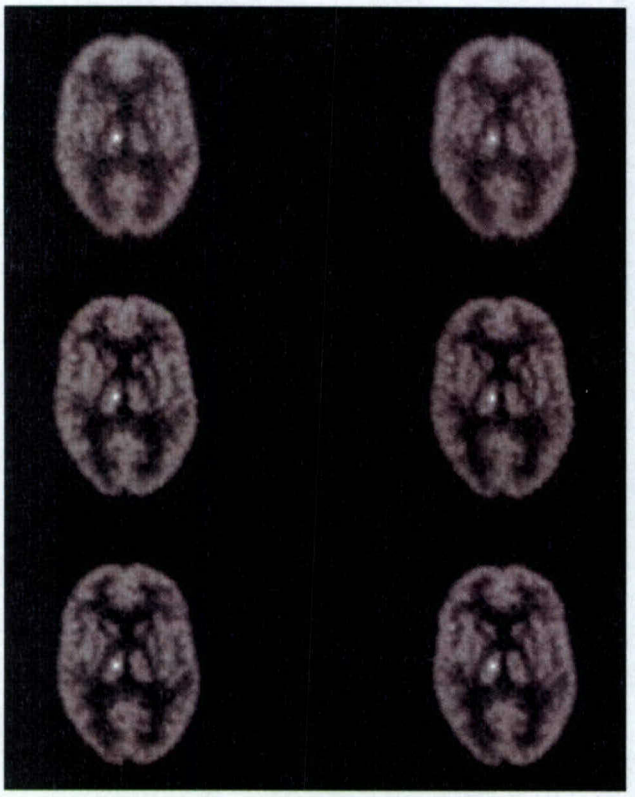

Fig. 5. The same as Fig. 4 but the ratio of activity concentration of the lesions to gray matter was 2.5.

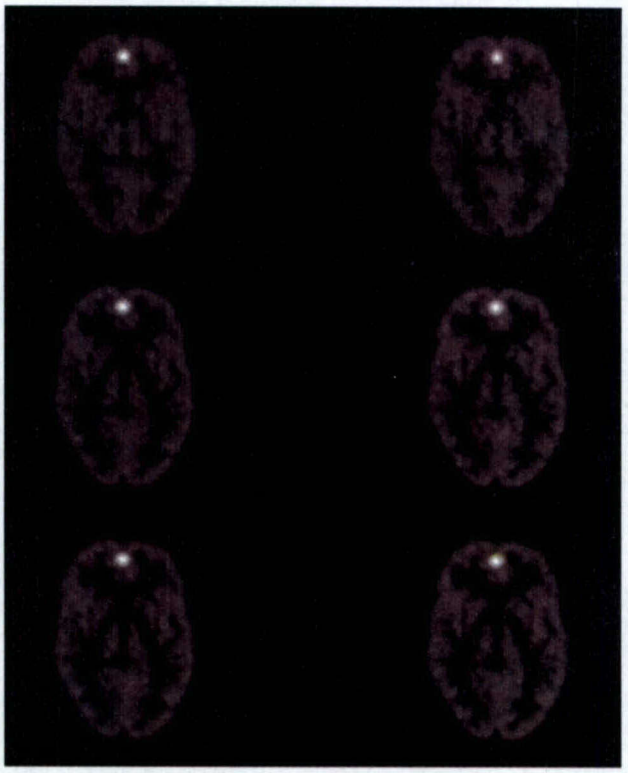

Fig. 6. Two image slices of the Hoffman brain phantom with 8.6 mm lesions for the three different configurations: (top) no-septa, (middle) 5-septa, and (bottom) 7-septa. The ratio of activity concentration of the lesions to gray matter was 2.5.

The profile figures showed that the ratio of the peak (lesion activity) to the background (gray matter) was slightly higher for the partial-septa configuration.

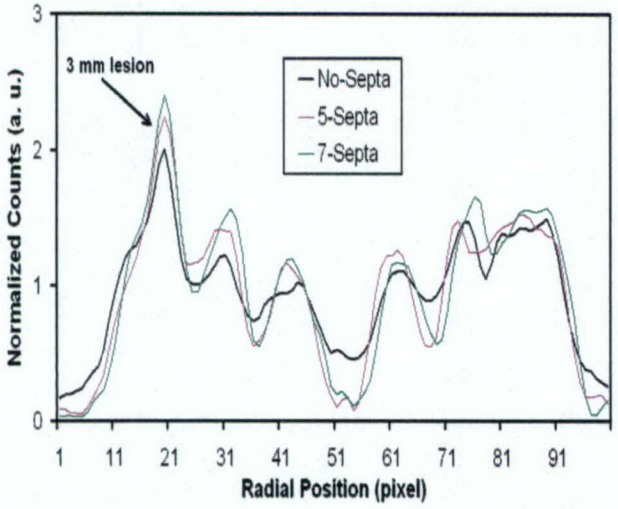

Fig. 7. Horizontal profiles through the middle of the images of 3 mm hot lesion in warm background showed in figure 4 for no-septa and partial -septa configurations. Ratio of activity concentration of the lesions to background (gray matter) was 6.

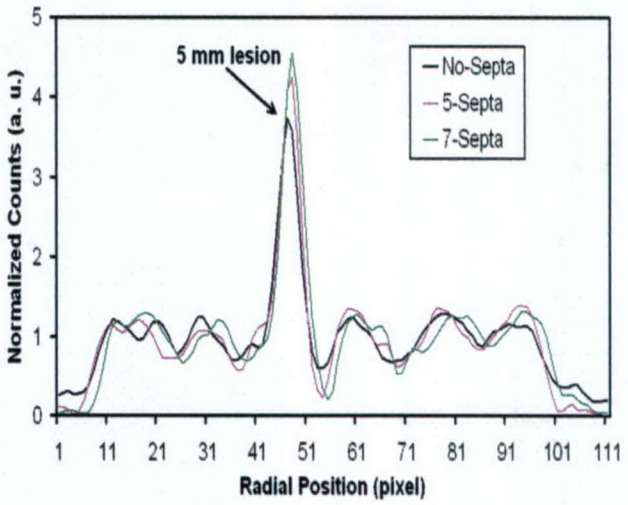

Fig. 8. Horizontal profiles through the middle of the images of the 5 mm hot lesion in cold background for no-septa and partial-septa configurations. Activity concentration of the 5 mm lesion was the same as data in Fig. 7.

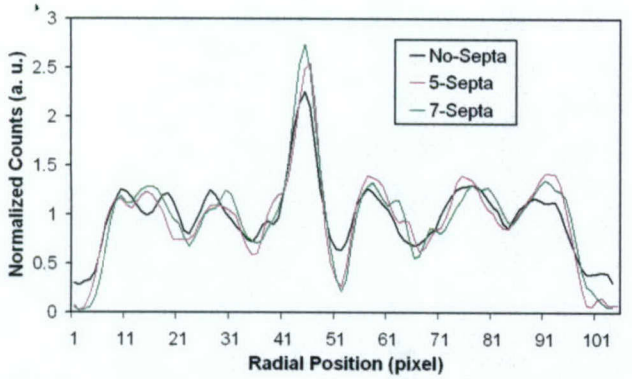

Fig. 9. Same as Fig. 8 but the ratio of activity concentration of the lesions to gray matter was 2.5.

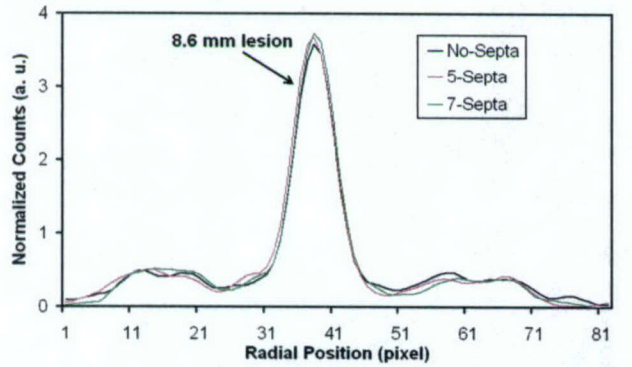

Fig. 10. Horizontal profiles through the middle of the 8.6 mm lesion images for no-septa and partial-septa configurations. Ratio of activity concentration of the lesions to gray matter was 6.

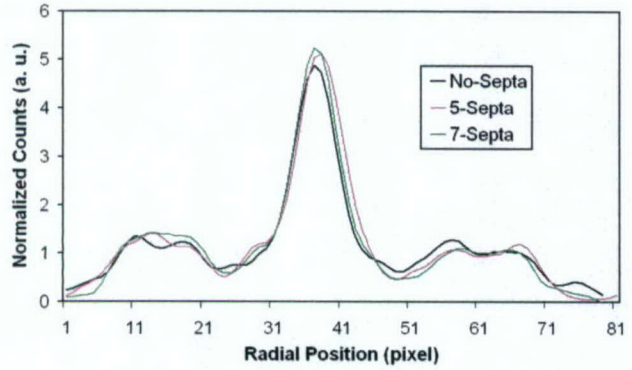

Fig. 11. Horizontal profiles through the middle of the 8.6 mm lesion image slices shown in figure 6 for no-septa and partial-septa configurations. Ratio of activity concentration of the lesions to gray matter was 3.5.

IV. Conclusions

The MDAPET camera operating in brain mode, in the presence of outside FOV activity, performed slightly better with partial-septa configurations: 1) The use of septa, as expected, reduced the background noise outside the brain area and in the white matter regions of the Hoffman brain phantom and image quality visually improved; and 2) the use of septa slightly improved the visual detection of the brain lesions and lesions contrast recovery.

V. References

[1] D. J. Kadrmas, P. E. Christian, S. D. Wollenweber, S. G. Kohlmyer, C. W. Stearns, "Comparative evaluation of 2D and 3D lesion detectability on a full-ring BGO PET scanner," *J. Nucl. Med.*, vol. 43, no. 5, p. 56P, May 2002.

[2] S. Pajevic, M.E. Dauve-Witherspoon, S. L. Bacharach, and R. E. Carson, "Noise characteristics of 3-D and 2-D PET images," *IEEE Trans. Med. Imag.*, vol. 17, pp. 9-23, February 1998.

[3] D. L. Baily, T. Jones, T. J. Spinks, M. C. Gilardi, and D. W. Townsend, "Noise equivalent count measurements in a neuro-PET scanner with retractable septa," *IEEE Trans. Med. Imag.*, vol. 10, pp. 256-260, 1991.

[4] C. W. Stearns, S. R. Cherry, C. J. Thompson, "NECR analysis of 3D brain PET scanner designs," *IEEE Trans. Nucl. Sci.*, vol. 42, no. 4, pp. 1075-1079, Aug. 1995.

[5] J. E.Tanaka, T.Hasegawa, T.Yamashita, H.Okada and H.Murayama "A 2D/3D hybrid PET scanner with rotating partial slice-septa and its quantitative procedures", *Phys. Med. and Biol.*, vol. 45, pp. 2821-2841, 2000.

[6] Turkington,T.G., Sampson, W.H., "Optimizing septal spacing for gamma camera PET imaging", *IEEE MIC Record*, v. 3 pp. 1767, 2000.

[7] S.J.Glick, C.J.Groiselle, J.A.Kolthammer, R.Z.Stodilka, "Optimization of septal spacing in hybrid PET using estimation task performance", *IEEE Medical Imaging Conference Record*, 2001.

[8] M. Aykac, J. Uribe, H. Baghaei, H. Li, Y. Wang, Y. Liu, T. Xing and W-H. Wong, "Septa design study for volumetric imaging in positron emission tomography," *IEEE Trans. Nucl. Sci.*, vol. 49, no. 5, pp. 2097-2102, October 2002.

[9] H. Baghaei, W-H. Wong, J. Uribe, H. Li, M. Aykac, Y. Wang , Y. Liu, and T. Xing, "Brain Lesion Dectctability studies with a high resolution PET operating in no-septa and partial-septa configurations," *IEEE Trans. Nucl. Sci.*, vol. 50, no. 5, pp 1364 -1369, October 2003.

[10] W.-H. Wong, "A positron camera detector design with cross-coupled scintillators and quadrant sharing photomultipliers," *IEEE Trans. Nucl. Sci*, vol. 40, pp.962-966, August 1993.

[11] W-H. Wong, J. Uribe, W. Lu, and K. Hicks, "Design of a variable field prototype PET Camera," *IEEE Trans. Nucl. Sci.*, vol. 43, pp. 1915-1920, June 1996.

[12] W-H. Wong, J. Uribe, K. Hicks, and M. Zambelli, "A 2-dimensional detector decoding study on BGO arrays with quadrant sharing photomultipliers," *IEEE Trans. Nucl. Sci.*, vol. 41, pp. 1453-1457, June 1994.

[13] W-H. Wong, G. Hu, N. Zhang, J. Uribe, J. Wang, H. Li, H. Baghaei, and S. Yokoyama, "Front end electronics for a variable field PET camera using the PMT-quadrant-sharing detector array design," *IEEE Trans. Nucl. Sci.*, vol. 44, pp. 1266-1270, June 1997.

[14] R. H. Li, W-H Wong, N. Zhang, J. Wang, J. Uribe, H. Baghaei, and S. Yokoyama, "Prototype electronics for a variable field of view PET camera using the PMT-quadrant-sharing detector array," *IEEE Trans. Nucl. Sci.*, vol. 46, pp. 546-550, June 1999.

[15] J. Uribe, H. Baghaei, H. Li, S. Yokoyama, N. Zhang, J. Wang, F. Dobbs, and W-H. Wong, "Basic imaging characteristics of a variable field of view PET camera using quadrant sharing detector design," *IEEE Trans. Nucl. Sci.*, vol. 46, pp. 491-497, June 1999.

[16] H. Baghaei, W-H. Wong, J. Uribe, H. Li, N. Zhang, and Y. Wang, "Breast cancer studies with a variable field of view PET camera," *IEEE Trans. Nucl. Sci.*, vol. 47, pp. 1080-1084, June 2000.

[17] R.S. Miyaoka, S.G. Kohlmyer, T.K. Lewellen, "Hot Sphere Detection Limits for a Dual Head Coincidence Imaging System," *IEEE Trans. Nucl. Sci.*, vol. 46, pp.2185-2191, December 1999.

[18] H. Baghaei, W-H. Wong, J. Uribe, H. Li, N. Zhang, and J. Wang, "The correction factors for a high resolution variable field of view PET camera," *J. Nucl. Med.*, vol. 40, p.279P, May 1999.

[19] P. E Kinahan, J. G. Rogers, "Analytic 3D Image Reconstruction Using all Detected Events," *IEEE Trans. Nucl. Sci*, vol. 46 pp.964-968, 1989.

[20] H. Baghaei, W-H. Wong, H. Li, J. Uribe, Y. Wang, M. Aykac, Y. Liu, and T. Xing, "Evaluation of the effect of filtering apodization for volume PET imaging using the 3DRP algorithm," *IEEE Trans. Nucl. Sci.*, vol. 50, no.1, pp. 3-8, February 2003.

Characteristics of 40,000 Quadrant-Sharing BGO Detectors Made by the Slab-Sandwich-Slice Technique

R. Ramirez, W-H. Wong, *Member, IEEE,* J. Uribe, *Member, IEEE, H. Li, Member, IEEE,* T. Xing, Y. Wang, *Member, IEEE,* Y. Liu, H. Baghaei, *Member, IEEE,* S. Xie, S. Kim, Y. Zhang

Abstract— We produced 40,000 high-resolution position-sensitive BGO detectors with a new method (slab-sandwich-slice or SSS). The detectors will be used in a high-resolution human PET system. The detectors were 2.68 x 2.68 mm (18 mm deep) encapsulated in about 800 detector blocks. There were three types of blocks/arrays made, 7x7, 7x8, 8x8. We studied the optical and physical characteristics of the production to evaluate the SSS production method. We also analyzed the data relative to production experience and time. We found that for the *7x7 symmetric blocks:* the average block-composite energy resolution was 35%; the average individual-crystal energy resolution was 23%. Mean intra-block light-collection variation of individual crystals was 23% FWHM. The average number of clearly-decoded crystals was 47 out of a possible 49 for the 7x7 block in the early production, which was improved to 49 in late production. For the *7x8 asymmetric blocks*, the average blocks-composite energy resolution was 32%. Mean intra-block light-collection variation was 23% FHWM. The average number of clearly decoded crystals was 51 for the early production improving to 55 for the late production (out of a possible 56). For the *8x8 asymmetric blocks*, the average blocks-composite energy resolution was 29%. Mean intra-block light-collection variation was 18% FHWM. The average number of clearly decoded crystals was 59 in early production improving to 62 for the late production (out of 64). We have also studied other production quality issues and found production variability and imperfection in the areas of size, shape and color. We observed a (a) "darkness effect" that for a block with poor crystal-position decoding map there was generally darker regions within the blocks and several size and shape errors were also found, as (b) "X-Y thickness-difference effect", which is the difference between the axial and transaxial block dimensions, (c) "pyramid-effect" with the PMT-end of the block (top) and the patient-end of the block (bottom) had different sizes, (d) besides the pyramid-effect, the 4 sidewalls might not orthogonal due to a systematic lateral shift between slices, or "laminar-shift dislocation effect" (e) the "slice-serration effect" which is caused by the variation in slice-widths between different sandwich types, (f) "paint-edge effect", where there was paint material build-up at the edge of the painting mask..

I. Introduction

The PET instrumentation group at MD Anderson Cancer Center has been developing a second generation, very-high resolution and versatile PET camera (HOTPET) for clinical and research applications. The camera can be transformed into different imaging modes: whole-body mode, or high-sensitivity brain/breast mode with 21-cm axial field of view [1] or in a pediatric application. It consists of 12 independent modules with 3,168 BGO detectors per module for a total of 38016 crystals. To achieve a cost-effective detector system for this system, we adopted the lower cost "photomultiplier-quadrant-sharing" detector design (PQS) [2-4]. The PQS design allows a highly pixilated system to be built, hence higher resolution, with 70% less PMT. The large number of crystals of this PET system, however, warranted the development of a more efficient production method so that the detection system can be built with a more affordable budget. Recently we proposed a new and less expensive "slab-sandwich-slice" (SSS) technique for building the detectors of the system [4]. The production started with long BGO slabs of 50 mm that was about the width of 18-19 crystal elements (fig.1). The slabs were coated with white-paint, to create shaped optical windows/reflectors; with different sizes and shapes to form internal light guides for distributing scintillation light for position decoding. The painted slabs were glued together with optical glue, into different crystal-sandwich types. After that we cut the sandwiches into slices and repeat the painting process with the slices to make the final BGO detector block.

With the SSS method, we built about 800 PQS position-sensitive BGO detector blocks with about 40,000 crystal elements (2.68 x 2.68 mm x 18 mm, average). We studied the optical and physical characteristics of these detector blocks to evaluate the SSS production method. This paper presents the results of the optical and physical evaluation for all 800 BGO blocks. The statistics of the detectors blocks were compiled and the data were examined relative to production experience and time also.

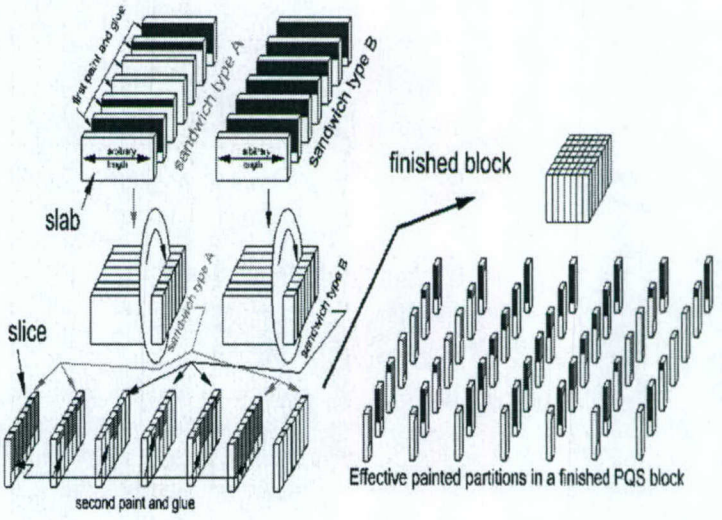

Fig. 1 The 7x7 PQS block was made from two types of sandwich constructions each with a different reflector-window pattern. Slices cut from type-A were used for the 4 outer slices of the 7x7 blocks. Slices cut from type-B were for the 3 inner slices of the block.

II. MATERIALS AND METHODS

The study involved three "big sub process": (a) building the BGO crystal slabs into different sandwich types, (b) cutting the slices to build the final detector block, and (c) testing the optical and physical characteristics of everyone block. These steps provided the parameters for evaluating the SSS technique, for determining the efficiency of the SSS technique, for finding production problems, and for improving the SSS technique for mass-production. The blocks produced were filed in the order of their production time. All the blocks were examined for their sizes, shape, color, light output and position-decoding ability.

With standard NIM-bin electronics and four standard 19-mm round photomultipliers (our laboratory-reference PMT), the block-composite pulse height spectra (sum of all the signals from all the crystals in a block) were collected for all 800 blocks. The crystal-position decoding maps were also collected for all the blocks with the same experimental setup. From each of the block-composite pulse-height spectrum, we extracted the block-composite energy resolution (FWHM). From each crystal-position-decoding map, we extracted a "decoding-resolution parameter" as quantified by observing the number of clearly delineated crystals in the crystal-position decoding map. This decoding parameter is then divided by the total number of crystals in the block to obtain a "quality %" as the figure of merit. The 800 block-composite pulse-height spectra with their corresponding energy resolutions and the 800 crystal-position decoding map with their corresponding decoding resolution parameter are what we called "***macroscopic block data***".

For some typical blocks, we also collected the crystal-position decoding map in list-mode data format. A region of interest (ROI) was drawn for each crystal on the crystal-decoding map. From the list-mode data, we extracted the events inside the ROI of each crystal to extract the individual pulse-height spectra for each crystal to measure the individual crystal energy resolution and photo peak pulse height. These are the "***microscopic block data***". Since extracting the microscopic block data was very tedious, it was impractical to measure and extract the microscopic spectral data for all 40,000 crystals. We only sampled some typical blocks to represent the microscopic characteristics.

For the "other production quality", we measured all the physical dimensions of the detector blocks, gauged the parallelism of the block planes, and noted observable geometrical irregularities. We also observed the color of all the blocks and correlated the color to the crystal-decoding resolution parameters. All the statistics were also compiled and examined according to the time of production for each block to gauge the effect of production experience

III. RESULTS

For 7x7 symmetry blocks, the average block-composite energy resolution was 35% (90% between 28-45%). From sampled typical blocks, the average individual-crystal energy resolution was 23% and the light-collection of individual crystals had a mean variation of 23% (FWHM). On average, the number of clearly decoded crystals was 48 out of 49. At the beginning of production (least production experience), the average number of clearly decoded crystals was 47 out of 49. Near the end of production (most production experience), the average number of clearly decoded crystal was 49 out of 49. The results are summarized in Table-1.

Table-1 Macroscopic optical data for 7x7 blocks

Module Number (time of assembly)	Photo peak	Block Composite FWHM%	Decoded crystals	Decoding Quality %	Indiv. Cryst Energy Resolution Average
05 (1)	93	39	46	95	29
06 (2)	94	44	47	96	36
07 (3)	103	37	47	96	27
08 (4)	113	34	49	99	23
09 (5)	103	35	46	95	24
10 (6)	104	35	49	99	24
11 (7)	88	31	49	99	17
12 (8)	60	34	49	99	20
01 (9)	70	33	48	99	20
2 (10)	60	32	49	99	19
3 (11)	57	35	49	99	23
4 (12)	58	31	49	100	16
12-module averag	84	35	48	98	23

The crystal-decoding performance of the early production and later production of the 7x7 blocks are shown in fig. 2.

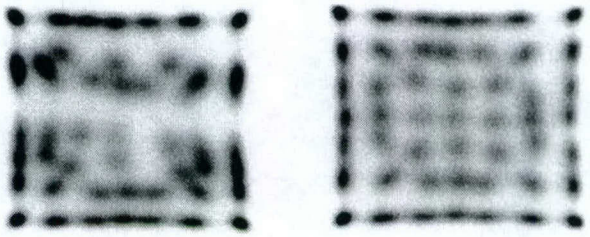

Fig. 2 7x7 blocks - early production (left) and later production (right)

For 7x8 asymmetry blocks (used along the edge of a detector panel/module), the average blocks-composite energy resolution was 32% (range of 26-40%). The mean intra-block light-collection variation was 23% FHWM (range of 10-32%). The average number of clearly decoded crystals was 53 out of 56. At the beginning of production, the average number of clearly decoded crystals was 51 out of 56. Near the end of production, the average number of clearly decoded crystal was 55 out of 56. The results are summarized in Table-2.

Table-2 Macroscopic optical data for 7x8 asymmetric blocks

Module Number (time of assembly)	Photo peak	Block Composite FWHM%	Decoded crystals	Decoding Quality %	Indiv. Cryst Energy Resolution Average
05 (1)	117	33	52	92	23
06 (2)	121	36	51	91	27
07 (3)	99	34	51	91	25
08 (4)	133	33	52	94	24
09 (5)	119	32	52	93	22
10 (6)	122	33	52	93	24
11 (7)	67	28	55	98	16
12 (8)	64	32	54	96	22
01 (9)	68	34	51	92	24
2 (10)	67	31	54	96	20
3 (11)	63	32	54	96	21
4 (12)	62	32	55	98	22
12-module averag	92	32	53	94	23

The crystal-decoding performance of the early production and later production of 7x8 asymmetric blocks are shown in fig. 3.

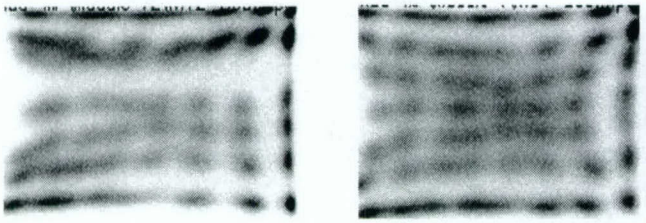

Fig. 3 Blocks 7x8: in early and later production

For 8x8 asymmetric blocks (used at the corners of a module), the average blocks-composite energy resolution was 29% (range of 23-38%). The mean intra-block light-collection variation was 18% FHWM (range of 10-32%). The average number of clearly decoded crystals was 60 out of 64. At the beginning of production, the average number of clearly decoded crystals was 59 out of 64. Near the end of production, the average number of clearly decoded crystal was 62 out of 64. The results are summarized in Table-3.

The crystal-decoding performance of the early production and later production of the 7x8 asymmetric blocks are shown in fig.4.

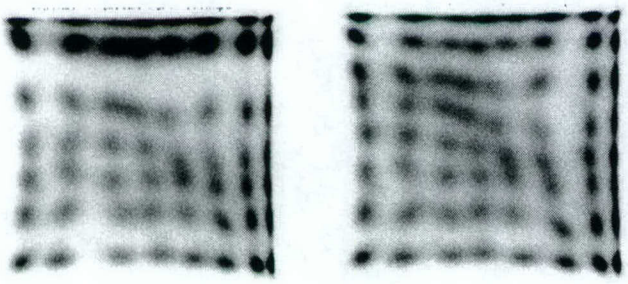

Fig. 4 Blocks 8x8: in early and later production

Table-3 Macroscopic optical data for 8x8 asymmetric blocks

Module Number (time of assembly)	Photo peak.	Block Composite FWHM%	Decoded crystals	Decoding Quality %	Indiv. Cryst Energy Resolution Average
05 (1)	122	33	58	90	24
06 (2)	128	31	61	95	22
07 (3)	130	30	60	93	20
08 (4)	127	31	61	95	22
09 (5)	130	29	58	91	19
10 (6)	133	29	59	93	18
11 (7)	72	28	62	96	15
12 (8)	66	27	60	93	15
01 (9)	68	30	61	96	20
02 (10)	67	27	62	97	15
03 (11)	70	28	62	97	18
04 (12)	68	28	61	96	17
12-module averag	99	29	60	94	19

The crystal decoding maps of the latest production is shown in fig 5. The crystal decoding resolution was excellent.

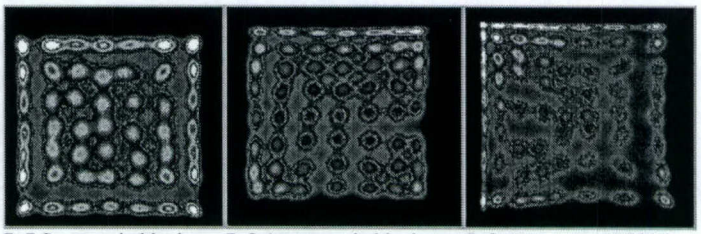

7x7 Symmetric block 7x8 Asymmetric block 8x8-Asym.-corner-block

Fig. 5 Typical examples of crystal-decoding map for the different types pf blocks in the latest production modules (7x7, 7x8, 8x8-corner).

Other Production Quality Qualities:

(a) **"Darkness effect"**: It was caused by a combination of physical and optical problem. For the blocks that had a poor crystal-position decoding map, there were generally darker regions in these detector blocks. Such darker regions can be traced to problems/mistakes made during the production process. These problems included:

(i) Trapped air bubbles during the gluing process,

(ii) External surface contamination from the laboratory environment,

(iii) Assembling errors due to faulty positions or orientations of placing the slabs into the sandwiches.

Near the end of the production, after we rectified and minimized such problems, very good blocks without such darkness effects were made for the last three detector panels/modules. (fig.6)

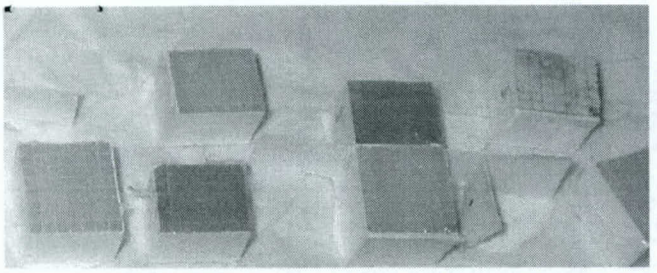

Fig. 6 "Darkness effect" for the blocks that also had a poor crystal-position decoding map

(b) **"X-Y thickness-difference effect":** We observed differences between the axial and transaxial block dimensions. It is caused by,

(i) Variations in the thickness of paint layers, and/or glue layers, contamination, time of curing of the optical glue, and air-compressor pressure for the air-paint brush.

(ii) Difference in thickness of the slabs/slices in the cutting process.

(iii) Paint build-up along the edge of the paint-mask

(iv) Differences in the length slices, before painting and after that, due to the variation in number of masks painted for light distribution on the BGO Detectors. This is a systematic error in the SSS method causing blocks sizes biggest that the one was in our preliminary calculation; as is the case of 8x8 or asymmetric corners blocks that are biggest in 1.6 mm at each dimension. (fig.7)

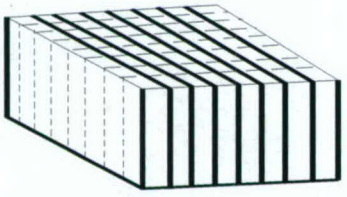

Fig. 7 "X-Y thickness-difference effect"

(c) **"Pyramid-effect":** This occurred when the PMT-end (block top) and the patient-end (block bottom) had different sizes. It was due to the fact that the paint-reflectors are applied to the patient end of the detector block, and there was nothing on the PMT end of the block to make up for this extra space. Therefore, the slices can tilt if there was an inadequate constraint in the gluing jig to prevent these displacements of the slices (fig.8)

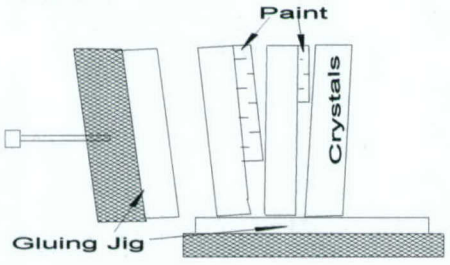

Fig. 8 "Pyramid effect"

d) **"Laminar-shift dislocation effect"**: This occurred when the 4 sidewalls were not orthogonal to each other due to a systematic lateral shift between slices. The ideal square became a slanted parallelogram (fig.9). This was caused by unequal forces from the compression pieces of the **gluing jig** along the axial and transaxial directions.

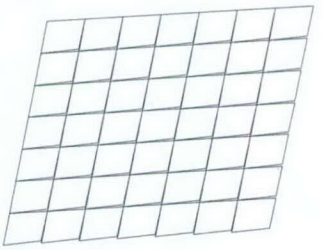

Fig. 9 "Lamina-shift dislocation effect"

(e) **"Slice-serration effect":** This is the variation in slice-widths between different sandwich types caused by the design difference in the number/size of the paint-reflectors of different sandwich (fig.10)

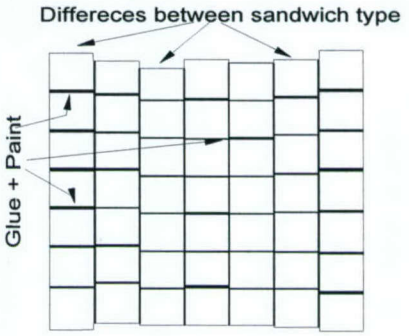

Fig. 10 "Slice-serration effect"

(f) **"Paint-edge effect":** This is caused by paint-material build-up at the edge of the painting mask caused by capillary force along the edge of the mask. (fig.11)

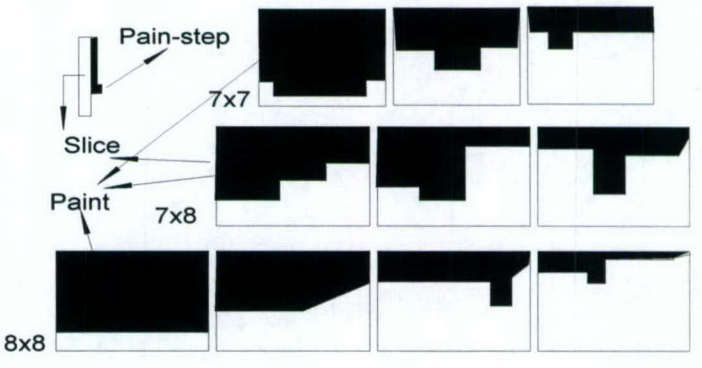

Fig. 11 "Paint edge effect"

V. CONCLUSION AND DISCUSSIONS

- The slab-sandwich-slice production method (SSS) for building PQS position-sensitive detector has been evaluated by building and testing of 800 BGO blocks (40 000 crystals).

- The performance of these production-detector arrays has been measured and studied to gauge detector design and the efficacy of the SSS Technique.

- Many common mistakes were uncovered in the building process, which could generally be rectified with changes made in the production tools or assembly technique. The last 3 modules built had excellent optical and mechanical properties.

- With this large population performance statistics, we concluded that the quadrant-sharing detector design and SSS production technique can yield high quality, lower cost, ultrahigh resolution PET detectors in mass production. The timeline study showed that the production experience did improve the production of the detector and the efficiency of the SSS production technique.

REFERENCES

Wong, W-H., Uribe, J., Li, H., Baghaei, H., Wang, Y., Aykac, M., Liu, Y., Xing, T., Bilgen, D., Rocio Ramirez. The Design of a High Resolution Transformable Whole body PET Camera. IEEE Transactions on Nuclear Science, *49*(5), 2079-2084, October 2002.

Wong, W-H. A positron camera detector design with cross-coupled scintillators and quadrant sharing photomultipliers. IEEE Transactions on Nuclear Science, *40*(4), August 1993.

Wong, W-H., Uribe, J., Hicks, K., Zambelli, M., Hu, G. A 2-dimensional detector decoding study on BGO array with quadrant sharing photomultipliers. IEEE Transactions on Nuclear Science, *41*(4), pp. 1453-1457, August 1994

Wong, W-H., Uribe, J., Hicks, K., Hu, G. An analog decoding BGO block detector using circular photomultipliers. IEEE Transactions on Nuclear Science, *42*(4), 1095-l 101, August, 1995

Uribe, J., Wong, W-H., Li, H., Baghaei, H., Wang, Y., Liu, Y., Xing, T., Rocio Ramirez. An Efficient Detector Production Method For Position-Sensitive Scintillation Detector Arrays with 98% Detector Packing Fraction. IEEE Transactions on Nuclear Science, *50(5),* 1469-1476, October 2003.

White Reflecting Paint BC-620 and Optical Cement C-600, Saint-Gobain Crystals and Detectors, Newbury, OH.

A Simulation Study on Optically Decoding Reflecting Windows for PMT Quadrant Sharing Scintillation Detector Block

Hongdi Li, *Member, IEEE*, Wai-Hoi Wong, *Member, IEEE*, Soonseok Kim, Rocio Ramirez, Shuping Xie, Yu Wang, *Member, IEEE*, Tao Xing, Jorge Uribe, *Member, IEEE*, Hossain Baghaei, *Member, IEEE*, Yuxuan Zhang

***Abstract*—A large number of decodable crystals per photomultiplier tube (PMT) can be achieved using the PMT-quadrant-sharing (PQS) technique with proper optically reflecting windows to channel light distribution in scintillation detector block. However, to develop brand new optically decoding reflecting windows for a detector block with different crystal material, PMT size or decoding resolution, is still very time-consuming and also requires much experience. This study is to develop a computer software tool that can simulate an expected 2-dimensional crystal decoding map before implementing a real detector block with a new set of decoding reflectors. After comparing the experimental decoding data to the simulated results with the same reflector set, data are feed to adjust the software parameters. More accurate decoding reflectors will then be created using the adjusted parameters. A 13 x 13 detector block was evaluated and our preliminary study shows this simulation tool is very promising which can significantly reduce a new product developing time; only a few development cycles are needed to get to the final optimized decoding reflectors.**

I. INTRODUCTION

IN the last few years, we have demonstrated that the PMT-quadrant-sharing (PQS) design can achieve very high resolution with lower cost [1]-[3]. In the PQS design, the four cylindrical surfaces of each scintillation crystal inside a detector block are covered by different sizes of optically reflecting windows using white painted-mask or multilayer polymer mirror foil. In fig. 1, all the individual masked crystals will be glued together as one block and coupled to four PMTs in PQS (fig.2). Scintillation light from each crystal is uniquely distributed to the four PMTs through these optically reflecting windows, and the individual crystal position will be decoded by the signals collected by the four PMTs.

We have successfully developed 7 x 7 (2.7 x 2.7 x 18 mm^3 crystal size) and 8 x 8 (2.3 x 2.3 x 10 mm^3 crystal size) BGO blocks. A higher resolution block requires very fine reflecting window design and fabrication onto 200 or more crystals. A 13 x 13 block requires about 364 masks (two neighbor crystals share a same mask). A higher resolution detector block significantly increases the developing cycle. The experimental time for each iteration of reflector trial is very long and tedious (handing 1-2mm needles). A better decoding resolution can be achieved using higher light output material such as GSO or LSO.

The purpose of this study is to develop a software tool which is able to evaluate a decoding mask design before assembling a real block and eventually to find out the optimized decoding reflecting windows design.

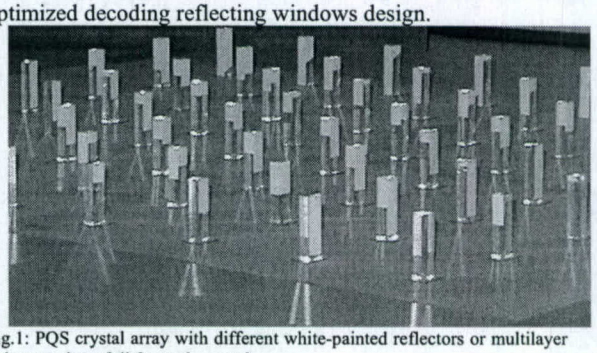

Fig.1: PQS crystal array with different white-painted reflectors or multilayer polymer mirror foil for each crystal.

II. METHODS

A. The photoelectron statistics

As suggested by Wong [1], in PQS detector (fig.2) each photoelectron exhibits a bi-nomial distribution with probability P of going to PMT (A+C), and probability (1-P) to PMT (B+D). Therefore, the photoelectron probability distribution in x and y dimension can be described by the following equations:

$$P(m)=\frac{N!}{(N-m)!m!}\left(\frac{N_{AC}}{N}\right)^{m}\left(1-\frac{N_{AC}}{N}\right)^{(N-m)} \quad (1)$$

$$P(n)=\frac{N!}{(N-n)!n!}\left(\frac{N_{AB}}{N}\right)^{n}\left(1-\frac{N_{AB}}{N}\right)^{(N-n)} \quad (2)$$

Where N = the total number of photoelectrons generated in a scintillation event; N_{AC}= expected photoelectrons going to PMT A and C; N_{AB} = expected photoelectrons going to PMT A and B; m, n range from 0 to N.

Manuscript received November 3, 2004. This work is support in part by the NIH-CA58980 PHS Grant, NIH-CA61880 PHS Grant, NIH-CA76246 PHS Grant, NIH-CA58980S PHS Grant, NIH-EB01481 PHS Grant, NIH-EB00217 PHS Grant, NIH-EB01038 PHS Grant, U.S. Army-Breast Cancer Research Grant, Texas ARP/ATP Grant 003657-0058-2001.

H. Li, W.-H. Wong, S. Kim, R. Ramirez, S. Xie, Y. Wang, T. Xing, J. Uribe, H. Baghaei, and Y. Zhang are with the Department of Experimental Diagnostic Imaging, University of Texas M.D. Anderson Cancer Center, Houston, TX 77030 USA (H. Li's telephone: 713-745-3732, e-mail: hli@di.mdacc.tmc.edu).

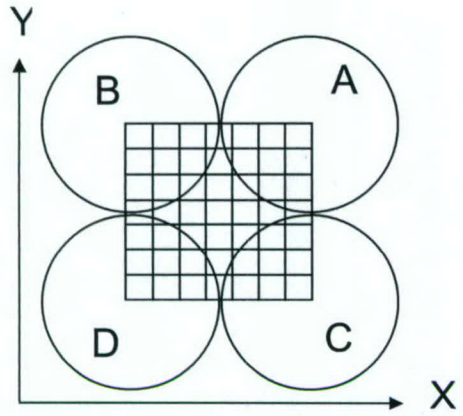

Fig.2: 7 x 7 crystal array coupled to four PMTs A, B, C, D using PQS technology.

2-dimensional photoelectron probability distribution is given by:

$$P(m, n) = P(m)\, P(n) \qquad (3)$$

The normalized decoding position is given by:

$$X = n / N,\ Y = m / N \qquad (4)$$

Fig.3 compares the decoding probability for 10 BGO crystals in one dimension with different light distribution ratio or expected positions and it shows the optimized light distribution ratio can generate a better crystal decoding. The optimized ratio in fig. 3 (right) is 0.025, 0.079, 0.164, 0.279, 0.421, 0.579, 0.721, 0.834, 0.921, 0.975.

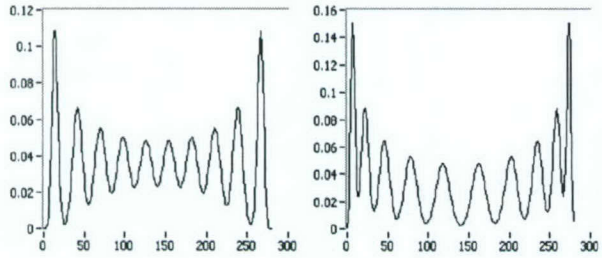

Fig.3: 1-dimensional probability distribution for 10 BGO crystals with linear light distribution ratio (left) and optimized non-linear light distribution ratio (right).

A smaller total number of photoelectron has a larger statistical noise and lower crystal decoding quality. The total number of photoelectrons collected by the four PMTs varies as the crystal location changes. The number of collected photoelectrons from each crystal was assumed proportional to the corresponding photo-peak locations in their experimental energy spectra, and each crystal's photo-peak was measured [4]. In PQS design, PMTs collect more photoelectrons from corner crystals than that from the center ones. Therefore, in equation (1)-(2), the total photoelectron number (N) for every crystal is changed iteratively, and fig. 4 compares the simulated 2-dimensional decoding probability distribution for a block with different light loss at the same light distribution ratios. The result shows the block with mirror foil reflecting windows has better crystal decoding map than that with white painted-masks.

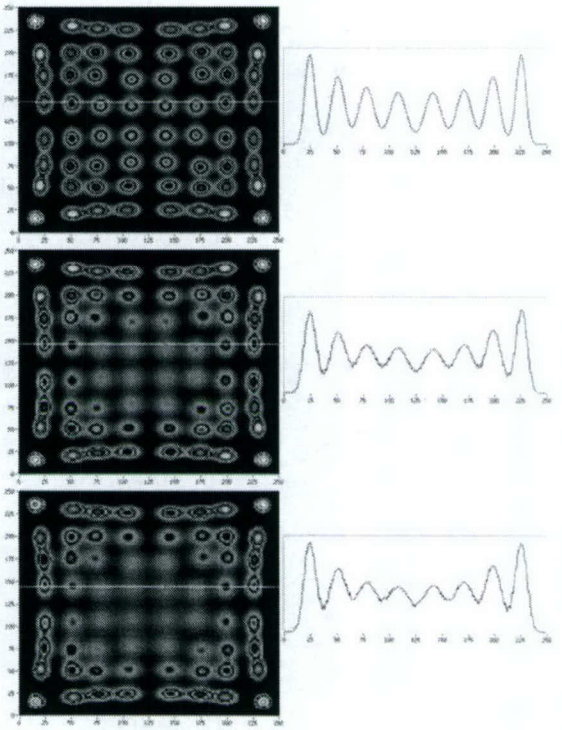

Fig.4: A simulation of 8 x 8 BGO crystal decoding quality for same light distribution ratios with no light loss (upper) vs. with light loss based on experimental photo-peaks for individual crystal using multilayer polymer mirror foil (middle) and white paint (bottom) optical reflecting windows.

B. Estimation of light distribution ratios from the optical decoding reflecting windows

Light distribution ratios of a block can be estimated from the optical reflection windows. Equation (5) describes the light changes from n-th time to (n+1)-th time for a crystal. Part of light inside one crystal will goes to four neighbor crystals and direct PMTs where the crystal sits through the optical windows (fig. 5); some of the light will remain inside the crystal and some will be lost after reflecting many times. This crystal will also accept light from its neighbor crystals.

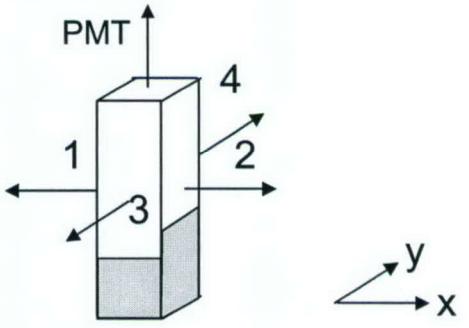

Fig.5: Definitions of optical windows for each crystal. Light can goes through the four side optical windows to its neighbor crystals or pass to the direct PMTs through the top window.

$$R_{n+1}(x,y) = R_n(x,y)\cdot\{\ 1 - P_1(x,y) - P_2(x,y) - P_3(x,y) - P_4(x,y) - P_A(x,y) - P_B(x,y) - P_C(x,y) - P_D(x,y) - P_L(x,y)\ \} + R_n(x-1,y)\cdot P_2(x-1,y) + R_n(x+1,y)\cdot P_1(x+1,y) + R_n(x,y-1)\cdot P_4(x,y-1) + R_n(x,y+1)\cdot P_3(x,y+1) \quad (5)$$

Where $R_n(x, y)$ = remnant light inside crystal (x, y) at n-th time. $P_1..P_4$ = percentage of light goes through four side surfaces by the optical windows; $P_A..P_D$ = percentage of light goes to the direct PMTs through the coupling surface (most of crystals only have one direct PMT; based on different crystal locations, some crystals cross over two or more PMTs, and can have more than one direct PMTs); and P_L = percentage of light loss.

All the percentages of light distribution can be estimated according to the crystal size, optical window sizes, the transmittance from crystal to grease to crystal and the transmittance from crystal to grease to PMT; the light loss percentage is defined in software.

To simulate the expected decoding position for one crystal located at (i, j), a certain number of photoelectrons are initialized to this crystal. In equations (6)-(10), R_0 (i, j) is initialized to N, the rest elements in matrix R_0 for other locations are set to 0. These photoelectrons are then partly distributed to its neighbor crystals and the direct PMTs through the optical windows or coupling surface as described by equation (5). The light that goes into the neighbor crystals will be continuously distributed in the same way. Hence, the initial light will continuously spread among the crystal matrix until the total remnant light inside the entire block is very little (<0.1%) that can not affect the decoding position, then the calculation will be terminated. The accumulated light collected by the four PMTs is used to decode the crystal position. The expected position X (i, j) and Y (i, j) is given by equations (11)-(12).

In the following equations (6)-(13), K is the number of crystals in each dimension, and A(i, j), B(i, j), C(i, j) and D(i, j) are photoelectrons collected by the four PMTs for the crystal (i, j).

$$A(i,j) = \sum_{n=0}^{\infty}\sum_{x=1}^{K}\sum_{y=1}^{K} R_n(x,y)\cdot P_A(x,y) \quad (6)$$

$$B(i,j) = \sum_{n=0}^{\infty}\sum_{x=1}^{K}\sum_{y=1}^{K} R_n(x,y)\cdot P_B(x,y) \quad (7)$$

$$C(i,j) = \sum_{n=0}^{\infty}\sum_{x=1}^{K}\sum_{y=1}^{K} R_n(x,y)\cdot P_C(x,y) \quad (8)$$

$$D(i,j) = \sum_{n=0}^{\infty}\sum_{x=1}^{K}\sum_{y=1}^{K} R_n(x,y)\cdot P_D(x,y) \quad (9)$$

$$R_n(i,j) = \sum_{x=1}^{K}\sum_{y=1}^{K} R_n(x,y) \quad (10)$$

$$E(i,j) = A(i,j) + B(i,j) + C(i,j) + D(i,j) \quad (11)$$

$$X(i,j) = \frac{A(i,j) + C(i,j)}{A(i,j) + B(i,j) + C(i,j) + D(i,j)} \quad (12)$$

$$Y(i,j) = \frac{A(i,j) + B(i,j)}{A(i,j) + B(i,j) + C(i,j) + D(i,j)} \quad (13)$$

C. *Energy composite and block decoding map simulation*

The total energy (photoelectrons) collected by the four PMTs for crystal (i, j) is described by equation (11). This energy is the expected photo-peak value for the crystal. Because of the light loss the collected energy varies as the crystal location changes, although the initial number of scintillation photoelectrons generated by a crystal in different location is almost same. To simulate the energy pulse-height spectra for each single crystal, standard experimental energy spectra (measured by an isolated single crystal) are simply scaled to the simulated photo-peak value mentioned above. More accurate single energy spectra simulation can be carried out by considering the statistical noise for the different photo-peak value. Since the variation of energy resolution for different crystals in the entire PQS detector block is small [3, 5], this simple scaling method for simulating the crystal energy spectra is acceptable. Energy composite spectra for the entire block were obtained by summing all the scaled single crystal's energy spectra.

So far we have discussed the expected decoding positions given by equations (12-13) and total photoelectrons given by equation (11) for each crystal, according to equations (1-4) we can calculate the 2-dimensional decoding probability distribution for the entire block. This 2-dimensional map is the simulated crystal decoding result based on the optical reflecting windows.

III. Results

A software tool has been developed to simulate a 2-dimensional decoding map and energy composite spectra for a PQS detector block using optical reflecting windows. The crystal size, crystal material, PMT size, PMT wall-thickness and the gap between PMTs are able to be adjusted by the software. After compared both the simulated decoding map and the energy composite with the experimental results, parameters in the simulation software such as light lost percentage, the transmittance from crystal to grease to crystal and the transmittance from crystal to grease to PMT were adjusted to have a best match-up. Fig.6 compares the simulated block composite pulse-height spectra with the experimental composite spectra.

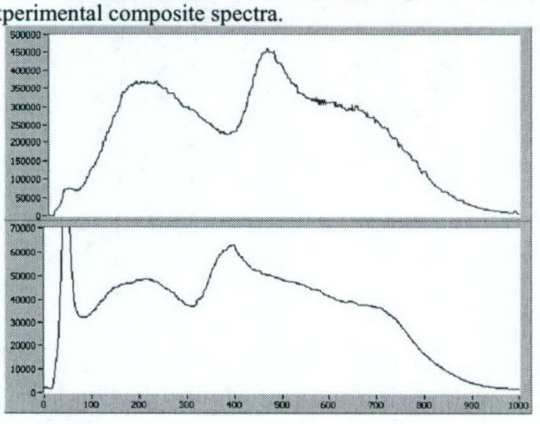

Fig. 6: Composite pulse-height spectra for a 13 x 13 GSO detector block. Upper – simulated result, and bottom – experimental data.

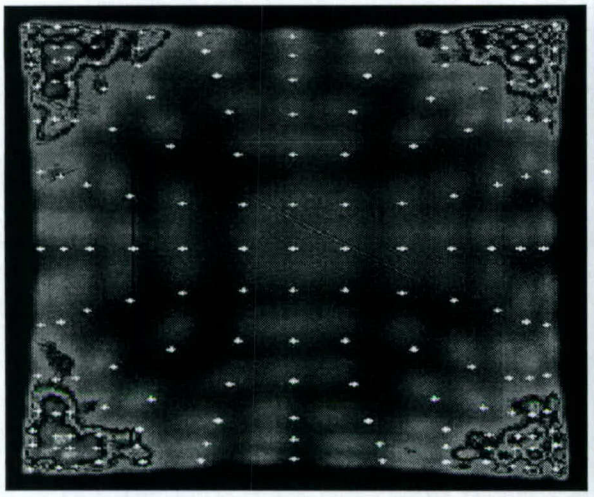

Fig. 7: Comparison of the expected crystal positions from the simulation software (white points) with the experimental crystal decoding map (background image).

The crystal decoding map in fig. 7 (background image) was acquired from a 13 x13 GSO block based on manually developed reflecting windows. This block has already been implemented before the simulation tool was developed (it is not necessary to design a block first for starting a simulation). The simulated crystal positions (white points) were created by the same optical reflecting windows using this software tool and then were projected to the experimental 2-dimentional crystal decoding map (fig.7). We continuously adjusted the software parameters until found a best agreement of simulation result with the experimental data. The overall agreement of the crystal positions are very good (fig. 7), some position offsets are mainly because of the off-center placement of the detector block related to the 4 PMTs and the non-uniformity of PMT photocathode.

After we were satisfied with the software parameters, we played with different sizes of optical reflecting windows to have a better crystal decoding map (better crystal separations) using this simulation tool. If a better simulated decoding map is founded, output the current design of the optical reflecting windows and build a new detector block with these optical reflecting windows. After comparing the simulated result with the experimental data of the new developed block, the software parameters could be further improved and new optical reflecting windows could be found for an even better decoding map. We can go through several development cycles (result comparing, parameter modification, better reflecting windows location and new block assembling) to have a best decoding result. Fig. 8 shows the decoding results of the first and second development cycles. Hence, delivering the final optimized reflector design using this software tool could be much easier and faster than designed by manual iterative experimentation.

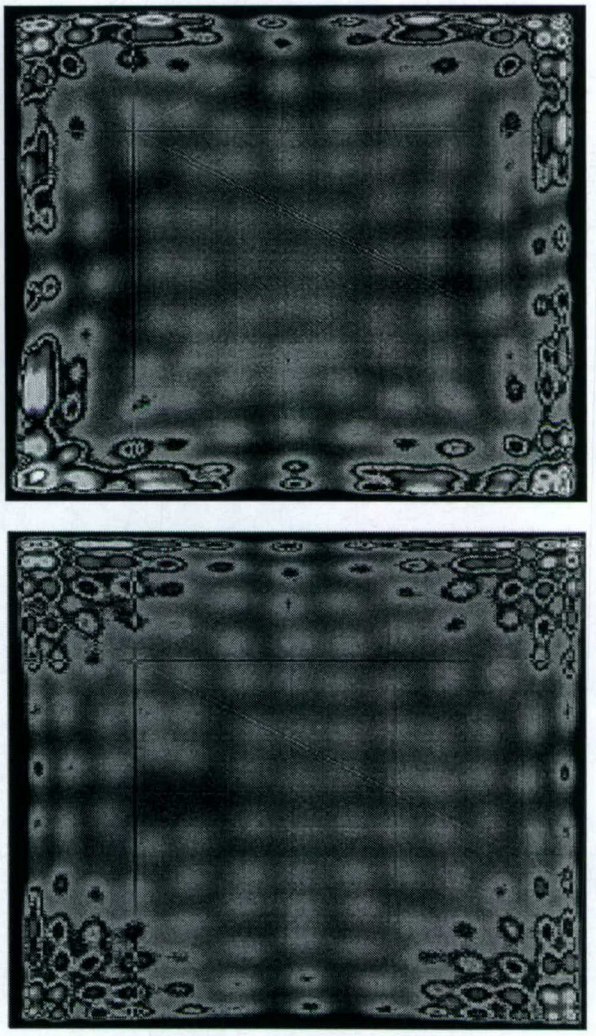

Fig. 8: 2-dimental crystal decoding map of 13 x13 GSO block in PQS design developed by software generated optically decoding reflecting windows. Top: 1st development cycle; bottom: 2nd development cycle.

IV. Conclusions

This paper presented a computer simulation tool for developing optically decoding reflecting windows for detector blocks using PMT-quadrant-sharing design. This tool allows us to evaluate the 2-D decoding map and energy composite spectra before start assembling a real detector block. Our preliminary study showed this simulation tool was very promising which could significantly reduce a new product developing time. Less development cycles are needed to get to the final optimized decoding reflectors by using this tool. A more accurate model will be evaluated by including the PMT regional sensitivities as well as the PMT wall effects. This simulation method can be applied to other detectors with light sharing decoding.

V. REFERENCES

[1] W.-H. Wong, J. Uribe, K. Hicks, M. Zambelli: "A 2-Dimensional Detector Decoding Study on BGO Arrays with Quadrant Sharing Photomultipliers," *IEEE Trans. Nucl. Sci.*, 41(8), pp. 1453-1457, 1994.

[2] W.-H. Wong, J. Uribe, K. Hicks, G. Hu: "An Analog Decoding BGO Block Detector Using Circular Photomultipliers," *IEEE Trans. Nucl. Sci.*, 42(8), pp. 1095-1100, 1995.

[3] S. Xie, R. Ramirez, Y. Liu, T. Xing, J. Uribe, H. Li, Y. Wang, H. Baghaei, S. Kim, W.-H. Wong: "A Pentagon Photomultiplier-Quadrant-Sharing Detector for a Rodent Research PET (RRPET)," 2003 *IEEE Nuclear Science Symposium M3-25*. Accepted for publication.

[4] M. Aykac, H. Li, J. Uribe, Y. Wang, H. Baghaei, Y. Liu, T. Xing, W.-H. Wong: "A Study of Coincidence Line Spread Function (CLSF) Estimation for Small Scintillators Using Quadrant Sharing Technique," *IEEE Trans. Nucl. Sci.*, 50(5), pp1331-1338, 1995.

[5] J. Uribe, H. Li, T. Xing, Y. Liu, H. Baghaei, Y. Wang, M. Aykac, R. Ramirez, W.-H. Wong: "Signal Characteristics of Individual Crystals in a High Resolution BGO Detector Design Using PMT-Quadrant Sharing," *IEEE Trans. Nucl. Sci.*, 50(3), pp355-361, 2003.